CONTINENTAL BASIN AND OROGENIC PROCESSES: TECTONIC DEFORMATION AND ASSOCIATED LANDSCAPE AND ENVIRONMENTAL EVOLUTION

EDITED BY: Xuhua Shi, Hanlin Chen, Rong Yang, Huiping Zhang and Xiaoping Yuan

PUBLISHED IN: Frontiers in Earth Science

frontiers Research Topics

Frontiers eBook Copyright Statement

The copyright in the text of individual articles in this eBook is the property of their respective authors or their respective institutions or funders. The copyright in graphics and images within each article may be subject to copyright of other parties. In both cases this is subject to a license granted to Frontiers.

The compilation of articles constituting this eBook is the property of Frontiers.

Each article within this eBook, and the eBook itself, are published under the most recent version of the Creative Commons CC-BY licence. The version current at the date of publication of this eBook is CC-BY 4.0. If the CC-BY licence is updated, the licence granted by Frontiers is automatically updated to the new version.

When exercising any right under the CC-BY licence, Frontiers must be attributed as the original publisher of the article or eBook, as applicable.

Authors have the responsibility of ensuring that any graphics or other materials which are the property of others may be included in the CC-BY licence, but this should be checked before relying on the CC-BY licence to reproduce those materials. Any copyright notices relating to those materials must be complied with.

Copyright and source acknowledgement notices may not be removed and must be displayed in any copy, derivative work or partial copy which includes the elements in question.

All copyright, and all rights therein, are protected by national and international copyright laws. The above represents a summary only. For further information please read Frontiers' Conditions for Website Use and Copyright Statement, and the applicable CC-BY licence.

ISSN 1664-8714
ISBN 978-2-88976-982-7
DOI 10.3389/978-2-88976-982-7

About Frontiers

Frontiers is more than just an open-access publisher of scholarly articles: it is a pioneering approach to the world of academia, radically improving the way scholarly research is managed. The grand vision of Frontiers is a world where all people have an equal opportunity to seek, share and generate knowledge. Frontiers provides immediate and permanent online open access to all its publications, but this alone is not enough to realize our grand goals.

Frontiers Journal Series

The Frontiers Journal Series is a multi-tier and interdisciplinary set of open-access, online journals, promising a paradigm shift from the current review, selection and dissemination processes in academic publishing. All Frontiers journals are driven by researchers for researchers; therefore, they constitute a service to the scholarly community. At the same time, the Frontiers Journal Series operates on a revolutionary invention, the tiered publishing system, initially addressing specific communities of scholars, and gradually climbing up to broader public understanding, thus serving the interests of the lay society, too.

Dedication to Quality

Each Frontiers article is a landmark of the highest quality, thanks to genuinely collaborative interactions between authors and review editors, who include some of the world's best academicians. Research must be certified by peers before entering a stream of knowledge that may eventually reach the public - and shape society; therefore, Frontiers only applies the most rigorous and unbiased reviews.
Frontiers revolutionizes research publishing by freely delivering the most outstanding research, evaluated with no bias from both the academic and social point of view. By applying the most advanced information technologies, Frontiers is catapulting scholarly publishing into a new generation.

What are Frontiers Research Topics?

Frontiers Research Topics are very popular trademarks of the Frontiers Journals Series: they are collections of at least ten articles, all centered on a particular subject. With their unique mix of varied contributions from Original Research to Review Articles, Frontiers Research Topics unify the most influential researchers, the latest key findings and historical advances in a hot research area! Find out more on how to host your own Frontiers Research Topic or contribute to one as an author by contacting the Frontiers Editorial Office: frontiersin.org/about/contact

CONTINENTAL BASIN AND OROGENIC PROCESSES: TECTONIC DEFORMATION AND ASSOCIATED LANDSCAPE AND ENVIRONMENTAL EVOLUTION

Topic Editors:
Xuhua Shi, Zhejiang University, China
Hanlin Chen, Zhejiang University, China
Rong Yang, Zhejiang University, China
Huiping Zhang, China Earthquake Administration, China
Xiaoping Yuan, GFZ German Research Centre for Geosciences, Germany

Citation: Shi, X., Chen, H., Yang, R., Zhang, H., Yuan, X., eds. (2022). Continental Basin and Orogenic Processes: Tectonic Deformation and Associated Landscape and Environmental Evolution. Lausanne: Frontiers Media SA.
doi: 10.3389/978-2-88976-982-7

Table of Contents

frontiers | Frontiers in Earth Science

EDITORIAL
published: 08 August 2022
doi: 10.3389/feart.2022.957558

Editorial: Continental Basin and Orogenic Processes: Tectonic Deformation and Associated Landscape and Environmental Evolution

Xuhua Shi[1,2,3]*, *Hanlin Chen*[1,2]*, *Rong Yang*[1,2], *Huiping Zhang*[4] and *Xiaoping Yuan*[5]

[1]Key Laboratory of Geoscience Big Data and Deep Resource of Zhejiang Province, School of Earth Sciences, Zhejiang University, Hangzhou, China, [2]Research Center for Structures in Oil and Gas Bearing Basins, Ministry of Education, Hangzhou, China, [3]Xinjiang Pamir Intracontinental Subduction National Observation and Research Station, Beijing, China, [4]State Key Laboratory of Earthquake Dynamics, Institute of Geology, China Earthquake Administration, Beijing, China, [5]School of Earth Sciences, China University of Geosciences, Wuhan, China

Keywords: basin and orogen, coupling, tectonic deformation, landscape evolution, environmental change

Editorial on the Research Topic

Continental Basin and Orogenic Processes: Tectonic Deformation and Associated Landscape and Environmental Evolution

OPEN ACCESS

Edited and reviewed by:
Derek Keir,
University of Southampton,
United Kingdom

***Correspondence:**
Xuhua Shi
shixuhua@zju.edu.cn
Hanlin Chen
hlchen@zju.edu.cn

Specialty section:
This article was submitted to Structural Geology and Tectonics, a section of the journal Frontiers in Earth Science

Received: *31 May 2022*
Accepted: *03 June 2022*
Published: *08 August 2022*

Citation:
Shi X, Chen H, Yang R, Zhang H and Yuan X (2022) Editorial: Continental Basin and Orogenic Processes: Tectonic Deformation and Associated Landscape and Environmental Evolution. Front. Earth Sci. 10:957558. doi: 10.3389/feart.2022.957558

Plate tectonics drives the development of large basins and orogens in the Earth's continents, such as the Tibetan Plateau, the Zagros, the Andes, the Alps and their adjacent basins, and the Basin and Range province in the western United States. Among them, the Circum-Tibetan Plateau basin and orogen system is a typical example (Jia et al., 2013). Tectonic processes in orogenic belts may interact with environmental/climatic changes to affect landscape evolution, through the processes of rock uplift/exhumation, surface erosion and weathering, and associated isostatic deformation (Molnar and England, 1990; Raymo and Ruddiman, 1992; Shi et al., 1999; Ge, 2006; Zheng and Yao, 2006; Bonnet, 2009; Whipple, 2009). These processes can further influence the sediment transportation and deposition in the range-bounding basins, whose changes in space and mass will feedback to deep tectonic processes, leading to basin-orogen coupling processes (Armitage et al., 2011; Leeder, 2011; Li et al., 2003). Despite major progress in recent decades, how these processes interact with each other on different spatiotemporal scales remains a leading scientific issue (Burbank and Pinter, 1999; Willett et al., 2006; Bishop, 2007; National Research Council, 2010). The 14 papers in this Research Topic utilize interdisciplinary approaches to study and improve our understanding of the basin and orogenic processes and their effects on landscape and changes in the paleoenvironment around the Tibetan Plateau, Northeast China, and East China Sea Basin region.

The spatiotemporal evolution of orogenic tectonic deformation constitutes the foundation for studying the basin-orogen processes. Chen Q. et al. attempted to determine the initial deformation of the Atushi anticline within the Kashi foreland thrust-and-fold belt of southwestern Tian Shan. By integrating remote-sensing mapping, field investigation, and $^{26}Al/^{10}Be$ cosmogenic burial dating of the growth strata near the boundary of the Pliocene-Pleistocene Atushi and Xiyu Formations, the authors interpreted that the Atushi anticline started to develop around ~1.8 Ma. Zhao and Pan applied the technique of GPS velocity decomposition and cluster analysis to constrain the strain partition and accommodation in the Qilian fold-and-thrust belt (QFTB) and its tectonic relationship with adjacent blocks. Their work revealed that the East and West QFTB are featured by lateral extrusion and range-normal crustal shortening-lateral

extension, respectively. Such deformation patterns may be attributed to regional simple shear and pure shear, respectively. Jia et al. reconstructed three episodes of compressive tectonic activity of the northeastern Qilian Shan during the Mesozoic and Cenozoic by detailed field mapping of the Sunan and Huangcheng basins bounding the range front. They argue that such a tectonic process may be affected both by the far-field effects of the India-Asia collision and intraplate orogenic processes relating to the collision between the Alashan Block and the Qilian Shan. Tian et al. used detrital apatite fission track thermochronological data to constrain the Meso-Cenozoic tectono-thermal evolution of the Micang Shan-Daba Shan tectonic belt in central China. The authors found that differential across-range exhumation of the Micang Shan and Daba Shan, and a relatively rapid cooling since ~160 Ma in response to the Qinling orogenic uplift, and the occurrence of differential uplift between sedimentary strata and basement may relate to variations in deep structure or intensities of thrust and nappe in different stages.

Sedimentary archives such as sediment provenance signals encode critical records of tectonic and landscape changes and have thus been utilized to study geologic events relating to basin-orogen coupling and surface processes. Pan et al. exploited detrital apatite fission track age distributions obtained from the Jiudong basin in the North Qilian Shan, where a continuous late Cenozoic sediment sequence was deposited with a good post-7 Ma chronologic framework, to examine the expansion of the Tibetan Plateau. Their results of obvious provenance change suggest two phases of significant expansion events of the North Qilian Shan since the Pliocene. Zhuang et al. examined two boreholes in the Taiyuan basin in the Shanxi Rift System bounding the eastern Ordos Block. The borehole stratigraphic analysis demonstrated two mega-transgressions that formed basin-wide paleolakes during ca. 5.8–4.4 and ca. 2.2–1.6 Ma. After a comprehensive analysis of the potential mechanisms for the transgressions, the authors suggested two periods of rifting-induced events of intensive subsidence during the Late Miocene-Quaternary. Liu et al. obtained detrital zircon chronology of sediments from the Pliocene-Pleistocene Sanmen Formation in the Weihe and Sanmenxia basins, and found that the two basins were integrated since the late Pliocene; and the Sanmen Gorge was finally established at ~1 Ma, leading to the formation of the modern Yellow River. Fu et al. analyzed a large number of detrital zircon U-Pb ages of Miocene sediments from the East China Sea Basin (ECSB) and Taiwan to decipher the sediment sources. Their results indicate that the early-middle Miocene sediments in the ECSB and Taiwan share similar sources from the North China and Korean Peninsula, and the sediments in Taiwan were mostly supplied by the ECSB. However, during the late Miocene-Quaternary, the Yangtze River system became the major source of sediments in the ECSB. Such an abrupt provenance change suggests a distinct drainage reorganization and the late Miocene formation of the modern Yangtze River system.

Progress in recent decades on quantitative geomorphology, chronology, and topographic surveys are significantly improving understanding of how landscapes evolve in response to tectonic processes. In the northeastern margin of the Tibetan Plateau, Chen G. et al. integrated techniques of remote-sensing, field mapping, and cosmogenic ^{10}Be chronology, topographic and quantitative geomorphic analysis, to argue that the development of the multi-segmented Dongbatu Shan thrust fault system may control the regional drainage evolution. Dong et al. explored the fluvial response to the regional tectonic uplift, from the perspective of longitudinal variations in grain sizes, lithology, and the roundness of the riverbed gravels of three large rivers flowing through the northern Qilian Shan. They found that the grain-size distribution in these arid/semi-arid areas may be a useful tool for evaluating the fluvial response to active tectonic uplift. Li Y. et al. made use of several geomorphic indices (e.g., channel steepness and χ-elevation data) and fluvial knickpoint celerity to analyze the response time of drainage in the Helan Shan, to the east of the northeastern margin of the Tibetan Plateau. Their results with previous thermochronologic data indicate the tectonic transformation of the Helan Shan from southwest to northwest during the early Quaternary, responding to the northeastward growth of the Tibetan Plateau. In the eastern Tibetan Plateau, field investigation and analyses of river incision and isostasy led Li H. et al. to propose both deep tectonics and the numerous earthquake-induced dams on the surface contribute to developing the regional high-elevation and high-relief landscape. Yu et al. applied the regional channel steepness index to quantify the regional rock uplift rate and its spatial variation in the central part of the grading topography area in the southeastern margin of the Tibetan Plateau. Their results show a southward decrease in channel steepness, hence a decrease in inferred rock uplift rate; and the region's high rock uplift rate may relate to the NE-trending thrust fault system in the region. Collectively, they suggest limited extrusion by thrusting in the region. Outside the Tibetan Plateau, Lin et al. integrated analyses of cosmogenic ^{10}Be-derived basin erosion rates, quantitative geomorphic indices of hypsometric curves, χ values, and channel steepness across the Great Khingan Mountains in NE China to infer the range's asymmetry and disequilibrium state. They further argued that both the inherited Cenozoic tectonics and climate gradient may affect the evolution of the drainage basins capping the Great Khingan Mountains.

In summary, the 14 papers demonstrate the state-of-the-art advances in the research of basin and orogenic processes, from the perspective of interactions between tectonic deformation and associated surface processes and environmental changes. We believe that the results from these papers will contribute to the development of geoscience communities, such as continental tectonics, tectonic geomorphology, and paleoclimate changes.

AUTHOR CONTRIBUTIONS

All the authors listed have made a substantial, direct and intellectual contribution to the work, and approved it for publication.

FUNDING

This work was supported by NSFC grants (41720104003, 51988101, 41941016, 41972227), the China Second Tibetan

Plateau Scientific Expedition and Research (2019QZKK0708) project, Fundamental Research Funds for the Central Universities (2021XZZX005), the Qianjiang Talent Program (QJD190202), and the 100 Talents Program of Zhejiang University.

REFERENCES

Armitage, J. J., Duller, R. A., Whittaker, A. C., and Allen, P. A. (2011). Transformation of tectonic and climatic signals from source to sedimentary archive. *Nat. Geosci.* 4, 231–235. doi:10.1038/ngeo1087

Bishop, P. (2007). Long-term landscape evolution: Linking tectonics and surface processes. *Earth Surf. Process. Landf.* 32, 329–365. doi:10.1002/esp.1493

Bonnet, S. (2009). Shrinking and splitting of drainage basins in orogenic landscapes from the migration of the main drainage divide. *Nat. Geosci.* 2, 766–771. doi:10.1038/ngeo666

Burbank, D., and Pinter, N. (1999). Landscape evolution: The interactions of tectonics and surface processes. *Basin Res.* 11, 1–6. doi:10.1046/j.1365-2117.1999.00089.x

Ge, X. (2006). Multi-stage uplifts of the Qinghai-Tibet plateau and their environmental effects. *Earth Sci. Front.* 13, 118–130. (in Chinese with English abstract).

Jia, C., Li, B., Lei, Y., and Chen, Z. (2013). The structure of Circum-Tibetan Plateau Basin-Range System and the large gas provinces. *Sci. China Earth Sci.* 56, 1853–1863. doi:10.1007/s11430-013-4649-7

Leeder, M. R. (2011). Tectonic sedimentology: Sediment systems deciphering global to local tectonics. *Sedimentology* 58, 2–56. doi:10.1111/j.1365-3091.2010.01207.x

Li, J.-l., Xiao, W.-J., and Yan, Z. (2003). Basin-range coupling and its sedimentation. *Acta Sedimentol. Sin.* 21, 52–60. (in Chinese with English abstract).

Molnar, P., and England, P. (1990). Late cenozoic uplift of mountain ranges and global climate change: Chicken or egg? *Nature* 346, 29–34. doi:10.1038/346029a0

National Research Council (2010). *Landscapes on the edge: New horizons for research on Earth's surface*. Washington, D.C: National Academies Press.

ACKNOWLEDGMENTS

We thank all authors for their contributions, all reviewers for their constructive comments and suggestions, and the Frontiers editorial team for their support.

Raymo, M., and Ruddiman, W. F. (1992). Tectonic forcing of late Cenozoic climate. *Nature* 359, 117–122. doi:10.1038/359117a0

Shi, Y., Li, J., and Li, B. (1999). Uplift of the Qinghai-Xizang (Tibetan) plateau and East Asia environmental change during late Cenozoic. *Acta Geogr. Sin.* 54, 20–28. (in Chinese with English abstract).

Whipple, K. X. (2009). The influence of climate on the tectonic evolution of mountain belts. *Nat. Geosci.* 2, 97–104. doi:10.1038/ngeo413

Willett, S., Hovius, N., Brandon, M., and Fisher, D. (2006). *Tectonics, climate, and landscape evolution*. Boulder, Colorado, United States: Geological Society of America, 449.

Zheng, D., and Yao, T. (2006). Uplifting of Tibetan Plateau with its environmental effects. *Adv. Earth Sci.* 21, 451–458. (in Chinese with English abstract).

Conflict of Interest: The authors declare that the research was conducted in the absence of any commercial or financial relationships that could be construed as a potential conflict of interest.

Publisher's Note: All claims expressed in this article are solely those of the authors and do not necessarily represent those of their affiliated organizations, or those of the publisher, the editors and the reviewers. Any product that may be evaluated in this article, or claim that may be made by its manufacturer, is not guaranteed or endorsed by the publisher.

Copyright © 2022 Shi, Chen, Yang, Zhang and Yuan. This is an open-access article distributed under the terms of the Creative Commons Attribution License (CC BY). The use, distribution or reproduction in other forums is permitted, provided the original author(s) and the copyright owner(s) are credited and that the original publication in this journal is cited, in accordance with accepted academic practice. No use, distribution or reproduction is permitted which does not comply with these terms.

frontiers in Earth Science

ORIGINAL RESEARCH
published: 15 November 2021
doi: 10.3389/feart.2021.754137

New Detrital Apatite Fission Track Thermochronological Constraints on the Meso-Cenozoic Tectono-Thermal Evolution of the Micangshan-Dabashan Tectonic Belt, Central China

Tao Tian[1,2], *Peng Yang*[3]*, *Jianming Yao*[2], *Zhonghui Duan*[2], *Zhanli Ren*[3], *Deliang Fu*[1,2] *and Fu Yang*[1,2]

[1]Key Lab of Coal Resources Exploration and Comprehensive Utilization, MNR, Xi'an, China, [2]Shaanxi Coal Geology Group Co., Ltd., Xi'an, China, [3]State Key Laboratory of Continental Dynamics, Department of Geology, Northwest University, Xi'an, China

OPEN ACCESS

Edited by:
Xuhua Shi,
Zhejiang University, China

Reviewed by:
Jingxing Yu,
Institute of Geology, China
Yuntao Tian,
Sun Yat-sen University, China

***Correspondence:**
Peng Yang
p.yang@nwu.edu.cn

Specialty section:
This article was submitted to Structural Geology and Tectonics, a section of the journal Frontiers in Earth Science

Received: 06 August 2021
Accepted: 14 October 2021
Published: 15 November 2021

Citation:
Tian T, Yang P, Yao J, Duan Z, Ren Z, Fu D and Yang F (2021) New Detrital Apatite Fission Track Thermochronological Constraints on the Meso-Cenozoic Tectono-Thermal Evolution of the Micangshan-Dabashan Tectonic Belt, Central China. Front. Earth Sci. 9:754137. doi: 10.3389/feart.2021.754137

The Micangshan-Dabashan tectonic belt, located in the southern Qinling-Dabie Orogen near the northeastern Tibetan Plateau, is a crucial area for understanding the processes and mechanisms of orogenesis. Previous studies have been focused on the cooling process via thermochronology and the mechanism and process of basement uplift have been investigated. However, the coupling process of basement exhumation and sedimentary cap cooling is unclear. The tectono-thermal history constrained by the detrital apatite fission track (AFT) results could provide valuable information for understanding crustal evolution and the coupling process. In this study, we provided new detrital AFT thermochronology results from the Micangshan-Dabashan tectonic belt and obtained nine high-quality tectono-thermal models revealing the Meso-Cenozoic cooling histories. The AFT ages and lengths suggest that the cooling events in the Micangshan area were gradual from north (N) to south (S) and different uplift occurred on both sides of Micangshan massif. The cooling in Dabashan tectonic zone was gradual from northeast (NS) to southwest (SW). The thermal histories show that a relatively rapid cooling since ca. 160 Ma occurred in the Micangshan-Dabashan tectonic belt, which was a response to the event of Qinling orogenic belt entered the intracontinental orogenic deformation. This cooling event may relate to the northeastward dextral compression of the Yangtze Block. The sedimentary cap of Cambriano-Ordovician strata responded positively to this rapid cooling event and entered the PAZ since ca. 63 Ma. The deep buried samples may be limited affected by climate and water erosion and the accelerated cooling was not obvious in the Late Cenozoic. Collectively, the cooling processes of basement and sedimentary cap in Micangshan-Dabashan tectonic belt were inconsistent. The uplift of the sedimentary area is not completely consistent with that of the basement under thrust and nappe action. The rigid basement was not always continuous and rapidly uplifted or mainly showed as lateral migration in a certain stage because of the different intensities and

modes of thrust and nappe action, and the plastic sedimentary strata rapidly uplifted due to intense folding deformation.

Keywords: detrital apatite fission track, tectono-thermal evolution, differential uplifting, basin-mountain coupling, Micangshan-Dabashan belt

INTRODUCTION

The Micangshan-Dabashan tectonic belt, located at the northeastern margin of the Tibetan Plateau, is a key "basin-mountain coupling" transitional orogenic belt that separates the Qinling orogenic belt to the north and the Sichuan Basin to the south (**Figure 1**). Its tectonic evolution and thermal histories have attracted much attention due to its relevance in understanding the onset of the Asian monsoon, drainage adjustment of the Yangtze River system, growth of the Tibetan Plateau, evolution of the Qinling-Dabie Orogen, erosional lowering of the Sichuan Basin as well as for evaluating the new Frontier exploration potential of lower Cambrian and Neoproterozoic hydrocarbon reservoirs (including shale gas) (Clark et al., 2004; Enkelmann et al., 2006; Shen et al., 2007; Richardson et al., 2008; Tian et al., 2010; Tian et al., 2012; Yang et al., 2013; Yang et al., 2017). The

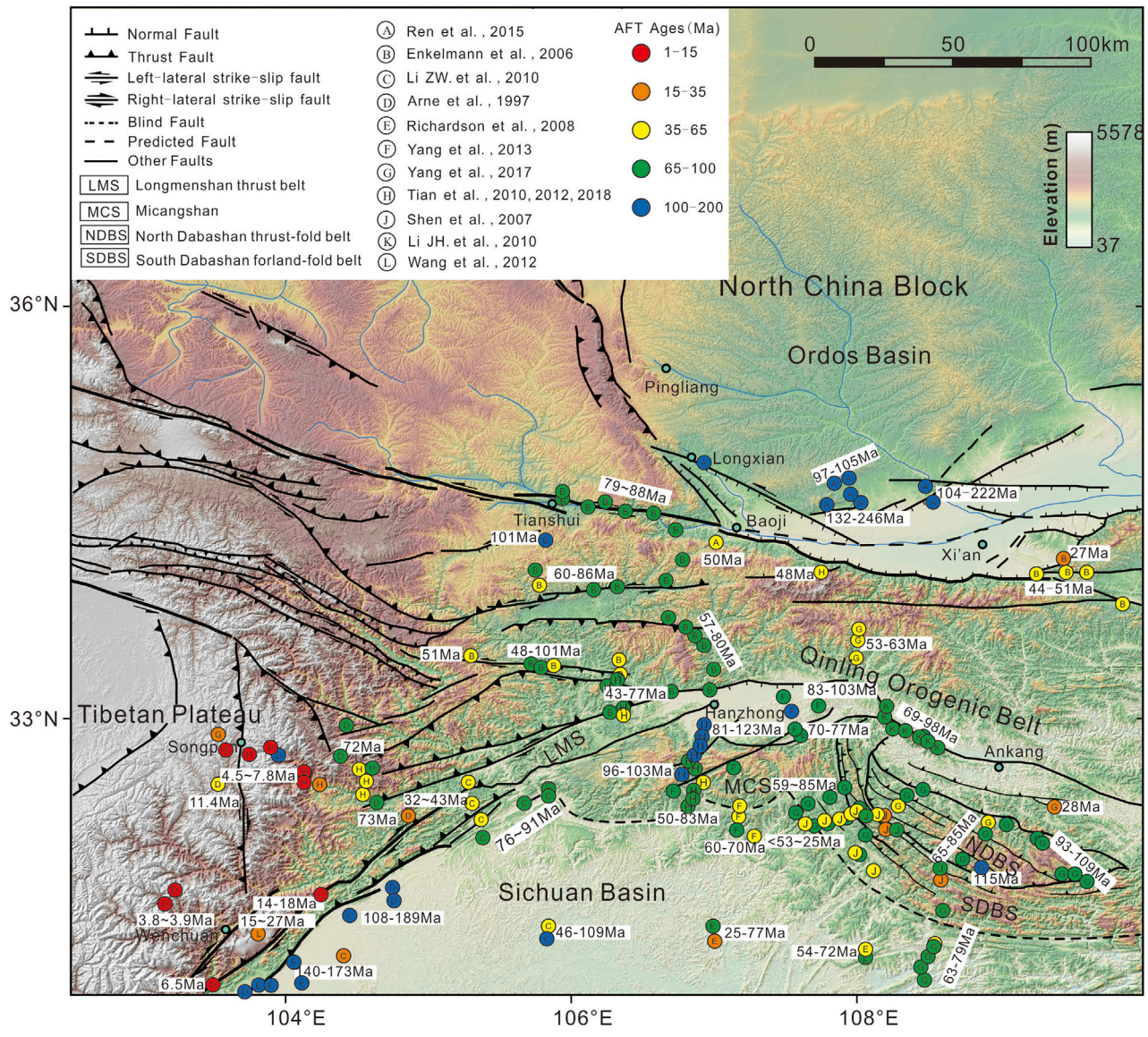

FIGURE 1 | Published apatite fission track (AFT) ages (in Ma) plotted on geologic-tectonic maps of the Micangshan, Dabashan and adjacent regions; different ages are noted in different colours.

Micangshan-Dabashan tectonic belt formed after collision with the South China Block (SCB) and North China Block (NCB) in the Indochina period and intracontinental orogeny in the Yanshanian-Himalayan period (Zhang et al., 1989; Meng and Zhang, 2000; Meng et al., 2005; Tan et al., 2007; Xu et al., 2009; Tian et al., 2010; Tian et al., 2012). The internal structure is complex, and the deformation characteristics are obviously different among different units. The tectono-thermal evolutionary histories need to be addressed in a timely manner, especially given that the evolution of the Micangshan-Dabashan tectonic belt since the Meso-Cenozoic has remained controversial.

As one of the most important thermochronological methods, apatite fission track (AFT) parameters provide quantitative information on cooling and record the thermal history of rocks (Green et al., 1986; Green, 1988; Gallagher, 2003), and these parameters are typically interpreted as a result of surface uplift and erosion (Tian et al., 2010; Tian et al., 2012; Tian et al., 2013; Lei et al., 2012; Ren et al., 2015; Qi et al., 2016; Powell et al., 2017; Tian et al., 2018). Previous work that has focused on the thermal history derived from a variety of thermochronometry dating methods, such as U-Pb, $^{40}Ar/^{39}Ar$, (U-Th)/He and AFT, in the Longmenshan, Micangshan and Dabashan areas has been published, and the dating methods and results have mainly been applied to investigate the cooling events and the coupling process of the Tibetan Plateau uplift (Arne et al., 1997; Enkelmann et al., 2006; Shen et al., 2007; Richardson et al., 2008; Li ZW et al., 2010; Li ZW et al., 2012; Li JH et al., 2010; Li et al., 2011; Chang et al., 2010; Tian et al., 2010; Tian et al., 2012; Tian et al., 2013; Tian et al., 2016; Tian YT et al., 2018; Yang et al., 2013; Yang et al., 2017; Shen et al., 2019). The thermochronometry dating and thermal histories results above and others from the, Tongbai-Dabieshan (Webb et al., 1999; Reiners et al., 2003; Hu et al., 2006), Taibaishan (Wang et al., 2005) and Western Qinling (Zheng et al., 2004; Enkelmann et al., 2006) show that the regional uplift occurred from the Late Jurassic to the Early Cretaceous and an accelerated uplift since the Late Cenozoic which related to the growth of the northeastern Tibetan Plateau. The Longmenshan tectonic defines the eastern margin of the eastern part of the Tibetan Plateauis and the western boundary of the Micangshan tectonic zone. The Longmenshan experienced multiple phases of intracontinental deformation during Mesozoic-Cenozoic (Tian et al., 2013; Tian et al., 2016; Tian YT et al., 2018; Shen et al., 2019), such as the Early Cretaceous (ca.119–131 Ma) and the Late Cenozoic (ca.30–25 Ma, 20 Ma, and 12–5 Ma, Arne et al., 1997; Kirby et al., 2002; Godard et al., 2009; Wang et al., 2012), and these tectonic activities may relate to the uplift and denudation in Micangshan tectonic zone.

Generally, the previous low-temperature thermochronological data was focused on the uplift of basement and show that the timing of the uplift in different areas of the Micangshan-Dabashan tectonic belt during the Mesozoic to Cenozoic was different. Furthermore, the apatite fission track (AFT) ages in the same area were inconsistently affected by factors such as experimental conditions and the nature of the samples (**Figure 1**). In contrast to the abundant thermochronology studies of the basement uplift, few studies have been conducted in the thermal evolution of sedimentary cap and its relationship with the uplift of basement. During the orogenic process, the uplift and denudation of the mountain were closely related to deposition in the nearby basin, which was a coupling process. The basin sediments adjacent to the orogenic belt recorded abundant uplift and denudation information during the late orogenic process. Therefore, the detrital AFT collected from the sedimentary basin could reveal its thermal history and the exhumation cooling history of the orogenic belt in the provenance area (Shen et al., 2005; Homke et al., 2010; Lin et al., 2015; Zhang et al., 2016; Du et al., 2018).

Detrital AFT analysis in the hinterland of the Micangshan and Dabashan areas is rare, and there is a lack of information regarding the tectono-thermal history of the sedimentary area. There are some differences in the results of previous thermochronometry studies related to the timing of cooling events in Micangshan and Dabashan. Therefore, new detrital AFT data and analyses need to be provided as key evidence for the timing of cooling events. In this study, we present a low-temperature thermochronology study of the Micangshan and Northern Dabashan, employing apatite fission track (AFT) data from nine detrital samples to assess the regional cooling history and providing information about the coupling relationship of uplift in basement and sedimentary areas.

GEOLOGICAL SETTING

The Micangshan-Dabashan tectonic belt is located at the junction of the Qinling orogenic belt and Sichuan Basin (**Figures 2A,B**), which was a passive continental margin in the early Paleozoic (Tian et al., 2010; Yang et al., 2013). The South China Block subducted under the North China Block beginning in the late Caledonian, underwent full collision until the Late Triassic, and experienced continuous compression and reconstruction in the Yanshan-Himalayan. Structural phenomena such as continuous fold deformation, differential uplift and thrust-slip faults are widely developed (Shi and Shi, 2014, **Figures 2C,D**).

The Dabashan tectonic belt is an important part of the multilayered thrust nappe tectonic system on the southern margin of the Qinling Orogen. The Late Triassic collision of the South Qinling and Yangtze Block along the Mianlue suture and the large-scale intracontinental subduction of the Yangtze Block beneath the Qinling Orogen during the Yanshanian period (Cheng et al., 2004; Huang and Wu, 1992) resulted in extensive fold and thrust deformation. Usually, the Dabashan tectonic belt is divided into two different tectonic units and sedimentary systems, the Southern Dabashan (SDBS) and the Northern Dabashan (NDBS), and they are bounded by the Chengkou fault (He et al., 1997; Li et al., 2011, Li et al., 2015; Yue, 1998, **Figure 2E**). The Dabashan thrust belt initiated and propagated southwards into the northern Sichuan Basin, which resulted in the formation of the Dabashan foreland basin (Wang et al., 2004). A number of NW-SE-trending faults are developed, and the Chengkou fault is the main active surface stacking the thrusts in the SW direction (Dong et al., 2006; Dong et al., 2008). The thrust belt mainly comprises Proterozoic basement and Sinian-Silurian limestone-dominated cover, which are all intruded by Silurian mafic

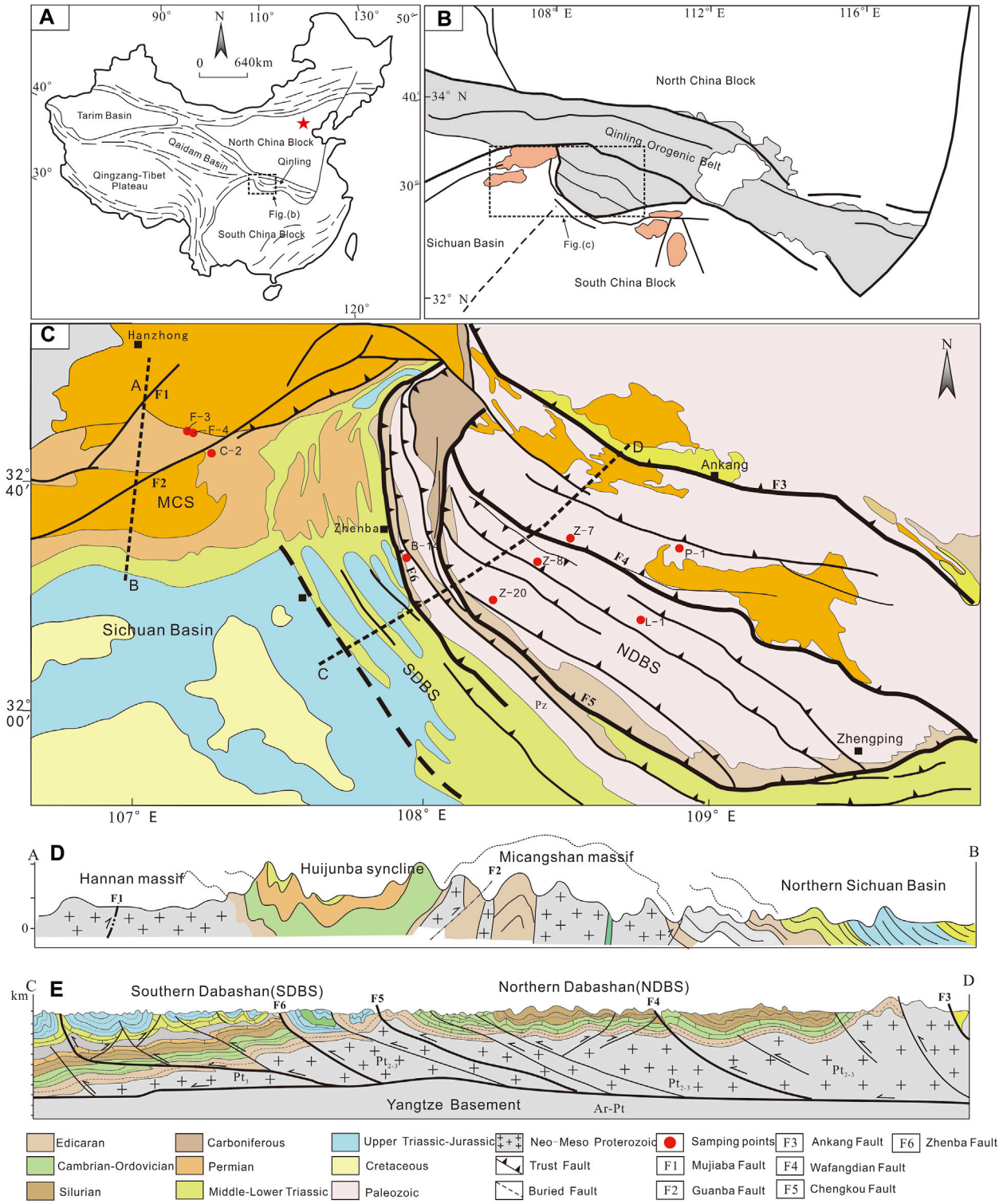

FIGURE 2 | Geological sketch map of the study area and sampling location. **(A)** The study area is located between the SCB and NCB in Central China **(B)** The Dabashan tectonic belt is on the southern margin of the Qinling Orogen. Micangshan is located between the Sichuan Basin and Qinling Orogen **(C)** Sample locations plotted on a geologic-tectonic map of the Micangshan and Dabashan tectonic belts. **(D)**, **(E)** Geologic cross-sections "A-B" and "C-D", modified from Yang et al. (2013) and Shi et al. (2012).

dikes (Zou et al., 2011; Li RX. et al., 2012). Devonian to Middle Triassic strata are exposed only north of the Ankang fault, and lower Paleozoic strata occur along faults and unconformably contact rare Lower to Middle Jurassic strata. Micangshan is located on the northwestern margin of the Upper Yangtze, adjacent to the Longmenshan tectonic belt in the west and to the Southern Dabashan foreland fold-thrust belt in the east. The main structural lines in the area spread out in the NE direction, and most of them behave similarly to thrust faults and slip faults (**Figure 2**). The intersection with the South Qinling block shows a strong dextral arc, with a nearly N-S-trending compound anticline. The Archean-early Proterozoic granitic basement and a small amount of basic intrusive rocks are exposed in the central uplift area of Micangshan, in which there are relatively intact residual synclines, mainly the Permian-Triassic system and the Sinian to Silurian system on the two wings. The overlying strata experienced deformation during the later stage. The lithology of outcrops in the regions varies after uplift and denudation (Chang et al., 2010; Li et al., 2008; Tian YT et al., 2018; Tian et al., 2019). From north to south in the Micangshan tectonic zone, a distinct succession of Neogene-Quaternary sedimentary (Hanzhong Basin), crystalline basement (Hannan and Micangshan massifs), Sinian-Triassic sedimentary (Huijunba syncline) and Sinian-Cretaceous sedimentary cover (Norther Sichuan Basin) can be identified (**Figure 2D**).

SAMPLES AND METHODS

A total of nine outcrop samples were collected for apatite fission track analysis, three of which were from the vicinity of the Huijunba syncline in the Micangshan tectonic belt, and six were from the Dabashan tectonic belt (**Figure 2C**). All the samples were from lower Cambrian to Lower-Middle Ordovician siltstone and sandstone.

Apatite was separated from each sample using standard heavy liquid and magnetic separation techniques. Apatite grains were mounted in epoxy resin on glass slides and then ground and polished to an optical finish to expose internal grain surfaces. Spontaneous fission tracks in the apatite were etched in 6.6% HNO_3 at 25°C for 30 s to reveal the spontaneous fission tracks. Low-U muscovite in close contact with these grains served as an external detector during irradiation (Yuan et al., 2003; Yuan et al., 2006). Neutron fluence was monitored in CN5 U dosimeter glasses (Bellemans et al., 1995). After irradiation in the reactor, the external muscovite detector was detached and etched in 40% HF for 20 min at room temperature to reveal induced tracks. Track densities of both spontaneous and induced fission track populations were measured with a dry objective at ×10015 magnification. Fission track ages were calculated using the IUGS-recommended zeta calibration approach (Hurford, 1990), which is shown in **Eq. 1**. Zeta values used in this study were determined from repeated measurements of standard apatites (Hurford and Green, 1983). The weighted mean zeta value for apatite used by the fission track operator was 391 ± 17.8 a/cm^2 according to the calibration of sample standards. The lengths of the horizontally confined fission tracks were measured exclusively in prismatic apatite crystals because of the anisotropy of annealing of fission tracks in apatite (Green et al., 1986).

$$T_{\text{sample}} = \frac{1}{\lambda_d}\ln\left(1 + \lambda_d \xi \frac{\rho_s}{\rho_i}\rho_d\right) \quad (1)$$

where T_{sample} is the AFT age of the samples; λ_d, which is 1.55125 × 10^{-10}a^{-1}, is the decay constant of ^{238}U; ρ_s is the track density for spontaneous fission tracks; ρ_i is the track density for induced fission tracks; ρ_d is the track density for the CN5 glass standard; and ξ is the Zeta constant, which is 391 ± 17.8 in this study.

Vitrinite reflectance can provide an accurate temperature range for fission track annealing and evidence for thermal history modelling (Sweeney and Burnham, 1990; George et al., 2001). The equivalent vitrinite reflectance calculated by bitumen reflection (Feng and Chen, 1988) in the Lower Camburian Niutitang shale is in the range of 1.86–2.54% (Tian et al., 2019), and the range of 2.98–3.03% in the Lower Cambrian Jianzhuba mudstone which is adjacent to the Lower-Middle Ordovician in NDBS (**Table 1**), reflecting exmaximum paleotemperatures of 233.4°C–273.3°C and 294°C–295 °C according to Barker and Pawlewicz (1986). These results demonstrate that fission tracks in apatite were completely annealed in a geological episode and that the apatite fission tracks were all new tracks through the partial annealing zone (PAZ).

The apparent age of the AFT has no direct geological relevance (Gleadow et al., 2002). However, the thermal history simulation combined with the length distribution of the fission track and the annealing kinetic parameters of apatite itself can well reveal the thermal history experienced by the sample. To achieve robust thermal histories, inverse modelling of AFT data was carried out using the programme HeFTy (version 1.8.3, Ketcham, 2014). Model paths between specified time–temperature constraints were chosen to be monotonic rather than monotonically consistent in HeFTy. This choice provides more freedom in model paths between constraint points. Dpar was used as a kinetic parameter, and thermal histories were calculated using a multikinetic annealing model. The Kolmogorov-Smirnov test function was used to compare measured length histograms to model results (Ketcham et al., 2007). The initial mean track length was calculated based on Dpar (Carlson et al., 1999). The number of fitting curves was set to 20,000. The model quality was judged by the goodness of fit (GOF). Generally, a GOF value greater than 0.05 indicates acceptable simulation results, while a GOF value greater than 0.5 indicates high-quality simulation results (Ketcham, 2005).

RESULTS AND DISCUSSION

Apatite Fission Track Ages and Lengths

The fission track test results of all samples are shown in **Table 2**. The AFT ages of the sandstone and siltstone range from 34 Ma to 50 Ma, which are much younger than the ages of the corresponding sedimentary formations. These results indicate that the samples were all affected by thermal events and annealed after formation. Except for the F-B-4 sample, the other eight samples all pass the age χ^2-test (P (χ^2)>5%),

TABLE 1 | The homogenization temperature and equivalent vitrinite reflectance of samples.

Sample number	Sample location/adjacent strata	Equivalent vitrinite reflectance (*VRo*/%)	Paleogeotemperature (T*max*/°C)	Homogenization temperature (T*h*/°C)
C-2	$\epsilon_1 n$	2.0	242	181.4–194.7
F-B-3	$\epsilon_1 c/\epsilon_1 n$	—	—	368.4–398.7
B-14	$\epsilon_1 n$	2.0	242	189.0–196.7
P-1	$O_1 d/\epsilon_1 j$	< 2.98–3.03	< 294–295	—
L-1	$O_{1\text{-}2} q/\epsilon_1 j$	< 2.98–3.03	< 294–295	278.4–311.6
Z-7	$O_{1\text{-}2} q/\epsilon_1 j$	< 2.98–3.03	< 294–295	248.6–308.7
Z-8	$O_{1\text{-}2} q/\epsilon_1 j$	< 2.98–3.03	< 294–295	271.2–308.7
Z-20	$O_{1\text{-}2} q/\epsilon_1 j$	< 2.98–3.03	< 294–295	—

TABLE 2 | Results of AFT analysis in the Micangshan and Dabashan areas.

Sample number	Elevation/ m	Era	N	ρ_s (10^5/ cm^2)	Ns	ρ_i (10^5/ cm^2)	Ni	ρ_d (10^5/ cm^2)	Nd	P (χ^2) (%)	Pool AFT ages (±1σ) (Ma)	Central AFT age (±1σ) (Ma)	Mean AFT length (μm) (n)	Mean Dpar (Ranger) (μm)
B-14	817.0	$\epsilon_1 n$	35	4.237	516	12.628	1,538	7.428	5,949	82.7	49 ± 3	49 ± 3	13.0 ± 1.6 (110)	1.45 (1.15–1.63)
C-2	1,442.0	$\epsilon_1 n$	35	3.622	277	9.401	719	5.803	5,949	99.3	44 ± 4	44 ± 4	13.2 ± 1.8 (100)	1.62 (1.1–2.1)
F-B-3	1,104.0	$\epsilon_1 c$	35	3.248	508	9.623	1,505	6.13	5,949	8.4	40 ± 3	41 ± 3	12.8 ± 1.8 (101)	1.79 (1.3–2.6)
F-B-4	1,033.0	$\epsilon_1 x$	35	6.105	1,091	15.646	2,796	6.453	5,949	0.7	49 ± 3	49 ± 4	11.7 ± 2.4 (101)	1.67 (1.2–2.3)
Z-7	391.0	$O_1 d$	35	0.856	201	2.64	620	7.103	5,949	100.0	45 ± 4	45 ± 4	12.7 ± 2.3 (64)	1.41 (1.0–2.7)
Z-8	404.0	$O_{1\text{-}2} q$	35	1.748	228	5.044	228	7.428	5,949	65.4	50 ± 5	50 ± 5	12.4 ± 2.2 (51)	1.52 (1.1–2.8)
Z-20	402.0	$O_{1\text{-}2} q$	30	0.983	133	3.149	426	5.722	5,949	76.5	34 ± 4	34 ± 4	12.2 ± 2.3 (10)	1.55 (0.96–2.4)
P-1	489.0	$O_1 d$	35	1.539	128	3.559	296	5.884	5,949	94.9	50 ± 6	50 ± 6	12.0 ± 2.3 (22)	1.68 (1.0–3.2)
L-1	658.2	$O_{1\text{-}2} q$	35	0.679	113	1.864	310	6.13	5,949	100.0	44 ± 5	44 ± 5	12.5 ± 2.5 (38)	1.43 (0.9–2.4)

indicating that the age difference of a single particle is within the statistical error range and is the same age component. The pooled age is generally used as the AFT age. The sample age χ^2-test of F-B-4 is less than 5%, representing the mixed age of different provenance minerals, and the central age can be used to interpret the cooling event (Galbraith and Laslett, 1993; Sobel et al., 2006). The samples collected from the Micangshan area have a short north-south axial distance, and the AFT ages mainly range from 40 Ma to 49 Ma. The ages of the Z-7, Z-8, P-1, and L-1 samples in the northeastern part of the Dabashan belt range from 44 Ma to 50 Ma, which is considerably older than that of sample Z-20 in the southwest with an AFT age of 34 Ma. This difference may indicate that the Dabashan thrust nappe belt was uplifted from NE to SW.

The average measured AFT lengths of the samples are in the range of 11.7–13.2apatite fission trackμm, all of which are less than the original track lengths (generally exceeding 16 μm, Gleadow, 1986; Carlson et al., 1999), indicating that the samples underwent strong annealing. The distribution pattern of track lengths is generally unimodal (**Figure 3A**), and the peak values are mainly distributed in the range of 13–15 μm, indicating that the samples did not experience a multistage thermal history but were in the process of monotonic cooling (Gleadow, 1986), which may reflect rapid stripping and cooling during the later orogeny.

N, induced number of apatite grains; ρ_s, ρ_i and ρ_d, track densities for spontaneous fission tracks, induced fission tracks and CN5 glass standard tracks, respectively; Ns, Ni and Nd, number of spontaneous fission tracks counted, induced fission tracks counted and CN5 glass standards, respectively; P (χ^2), chi-square probability; L, mean track length; n, number of tracks measured.

Collectively, Dpar is a good potential indicator of fission track annealing kinetic properties in natural apatite grains (Carlson et al., 1999). The Dpar content is a routinely used parameter, exhibits a strong and informative correlation with apatite fission-track ages and lengths (**Figure 3B**). It should be noted that the lithological heterogeneity and chemical composition of samples might be different, for example the Dpar with diameters of 1.8–5.0 μm (Richardson et al., 2008), resulting in uncertainty and a negative impact on the basin-scale exhumation and

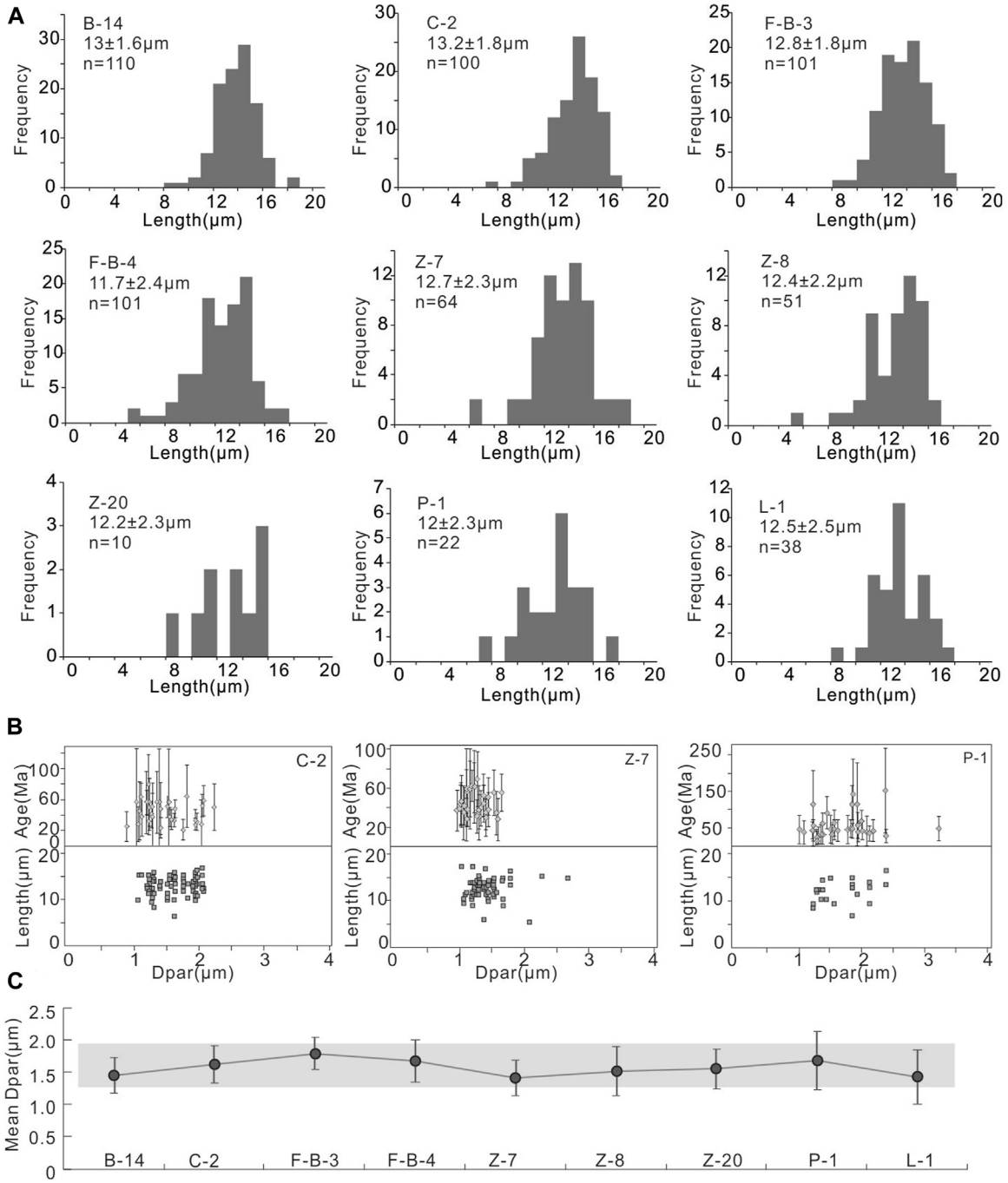

FIGURE 3 | (A) Histogram of the measured track length distribution of all samples, **(B)** relationship between Dpar and length and ages, taking samples C-2, Z-7, and P-1 for example, **(C)** Dpar plots of samples.

tectono-thermal processes. In this study, the Dpar values (mean etch pit size parallel to the c axis, Donelick, 1993) of the samples range from 1.41 to 1.79 μm (**Figure 3C**). No significant Dpar variation was observed among the samples reported in this work, in which the single-grain ages and length came from the same kinetic population. The Dpar results suggest that the differences in AFT age and length are due to the differences in thermal history and may not influenced by nature of apatite itself.

There is a positive correlation between the fission track age and the elevation of the samples, which reflects that the samples in high-altitude localities always passed through the annealing zone of apatite and produced tracks (Shen et al., 2007). However, the study area at the junction of the Qinling orogenic belt and

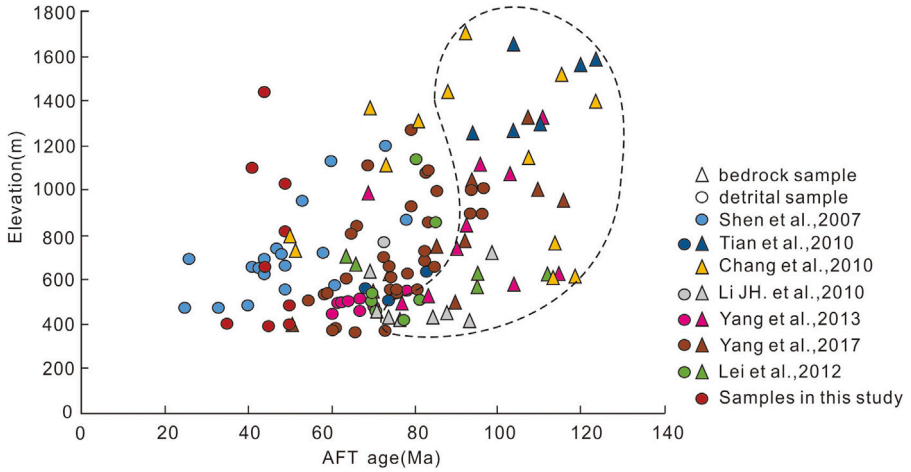

FIGURE 4 | Correlation between AFT ages and elevation.

Sichuan Basin, coupled with continuing subduction collision since the Indo-Chinese epoch and intracontinental orogeny, caused the large-scale thrust nappe (Wang et al., 2004; Shen et al., 2007; Chang et al., 2010). The elevation and distribution of apatite often change due to thrust nappes, uplift, denudation and faulting. Therefore, there is often no correlation between the fission track age and elevation in complex tectonic belts (Green et al., 1986; Shen et al., 2007; Qi et al., 2016).

Statistical analysis of fission track ages and elevations in the study area and its surrounding structural belt indicates that it underwent complex tectonic processes (**Figure 4**). The fission track ages of some sections have a good corresponding relation with altitude, but the slopes are quite different, which shows that the tectonic uplift effect is obviously different in the area. The different uplift effects may be related to the peripheral structural belt of acute Himalayan activity, especially with the far-field effect of the rapid expansion of regional topography and strong reformation from the northeastern margin of the Qinghai-Tibet Plateau (Tian et al., 2010; Tian et al., 2012; Yang et al., 2013, Yang et al., 2017). In this study, there was no linear correlation between AFT age and elevation. In addition to the complex geological process, this lack of correlation may also be related to the concentrated distribution of the topographic elevation of the samples in the smaller ranges of 391–658.2 m and 817–1442.2 m, which are insufficient to reflect the linear relationship between AFT ages and elevation.

In terms of the relationship between sample lithology and age, the ages of the samples from the outcropping area of the bedrock are generally higher than those of the detrital rocks in the sedimentary area (**Figure 4**). The AFT ages of the detrital rocks are mainly distributed in the range of 28.3–85 Ma, and those of the bedrock are mainly distributed in the range of 71–123.5 Ma. As old rigid blocks with weak detachment, the bedrock outburst area in the study area and its surrounding area responds more quickly to tectonic activities such as thrust nappes or intracontinental orogenies that cause formation uplift, and the apatite distributed in the area enters the PAZ earlier and resets its age. Micangshan-Dabashan was a passive continental margin in the early Paleozoic, and the samples from the formation were typical marine sediments. The Micangshan massif formed in the Late Triassic (Tian et al., 2010), and the provenance of the samples was not from this massif. Even if there are other provenance inputs, thermal relocation occurs with increasing burial depth and temperature after the detrital particles are transported and deposited. Therefore, the clastic apatite fission tracks reflect the late tectonic and thermal evolution of the sedimentary area rather than the provenance area. The simulation of the thermal evolutionary history of wells HY-1 and SND-1 in the study area indicates that the maximum paleo-geotemperature exceeded 220°C at 160 Ma. The Cambrian-Ordovician system at 123.5–71 Ma was buried at a depth of more than 4,000 m and had high paleo-geotemperatures ranging from 120°C to 190°C (Tian et al., 2020), and apatite did not enter the annealing zone. Then, the apatite from the Cambrian-Ordovician system entered the annealing zone with subsequent rapid uplift, so the uplift and cooling events recorded by the fission track ages were relatively late. Overall, the Micangshan-Dabashan tectonic belt experienced uplift and denudation from at least 123.5 Ma and affected the surrounding sedimentary strata, entering the PAZ from 85 Ma to 28.3 Ma.

The AFT age and length are positively correlated to a certain extent according to the data in the research area (**Figure 5**). The AFT ages gradually become younger from the Micangshan-Hannan massif to the northern Sichuan Basin, indicating a gradual thrust expansion from north to south in the region as piggyback expansion (Tian et al., 2010; Yang et al., 2013; Wang et al., 2003). In this tectonic framework, the AFT ages of the Cambrian strata samples in the Huijunba syncline should be larger than those in the northern Sichuan foreland area. However, the AFT ages of the Cretaceous-Cambrian stratum samples in the northern Sichuan foreland area range from 61.6 to 85 Ma with the track lengths between 10.6 and 12.2 μm and that in Huijunba syncline at the range of 40–49 Ma with track lengths between 11.7 and 13.2 μm (**Figure 5A**). This distribution of AFT ages and

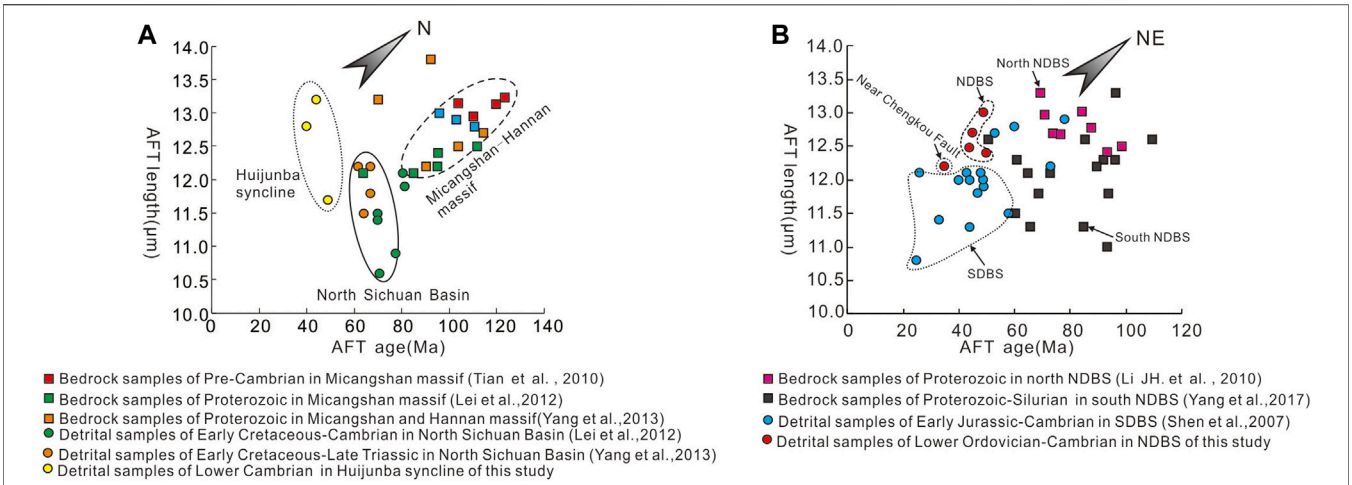

FIGURE 5 | Correlation between AFT ages and lengths of the measured rock samples in the Micangshan area **(A)** and Dabashan area **(B)**.

lengths seems inconsistent with regional tectonic evolution history. Micangshan tectonic zone is a large complex anticline formed by South Qinling collision orogeny since the Triassic and is characterized by the asymmetric structure with a gentle north wing orienting Huijunba syncline and steep south wing orienting north Sichuan foreland (Zhang and Dong, 2009; Zhang, 2019). The samples in the Sichuan foreland area was deeper than samples in the north Huijunba syncline. Therefore, these abnormal AFT ages may be caused by differential basement uplift, as the sedimentary cover in the northern Sichuan foreland area uplifted and entered the PAZ earlier than that in the Huijunba syncline during the overall N-S trending uplift process.

Generally, the AFT age from Dabashan area gradually becomes younger from NE to SW, indicating that the timing of uplift in the NE region was earlier than that in the SW (Shen et al., 2007; Li JH. et al., 2010; Yang et al., 2017, **Figure 5B**). In this study, the AFT age of the NDBS ranges from 35 Ma to 50 Ma, the youngest age of NDBS sample Z-20 is located near the Chengkou fault. Collectively, the AFT ages from the NDBS are older than most ages from the SDBS (**Figure 5B**). This distribution of AFT ages indicates that the uplift process of the sedimentary cap is characterized by earlier to NE and later to SW under the influence of regional uplift. This interpretation is consistent with the thrust nappe of Dabashan from NE to SW (Shen et al., 2007) and the NE-SW trending paleo-tectonic stress during the Late Jurassic to the Early Cretaceous (Shi et al., 2012; Dong et al., 2014). The analysis of AFT provides a new thermochronological constraint for the progressive extension deformation of the thrust nappe structure in the Dabashan area.

Tectono-Thermal History of the Micangshan-Dabashan Tectonic Belt

Geological background constraints are very important for the inversion of the AFT thermal history (Tian et al., 2010). In the study area, many major geological events occurred during the Jurassic and Cretaceous, and the Qinling orogenic belt truly entered the intracontinental orogenic deformation period at approximately 160 Ma (Dong et al., 2006). The Micangshan-Dabashan tectonic belt, as the southern margin of the Qinling orogenic belt, likely responded to this tectonic event. Previous AFT data and thermal simulation results showing that Dabashan area experienced uplift at 180–165 Ma, 170–160 Ma and ca.100 Ma (Shen et al., 2007; Li JH et al., 2010; Xu et al., 2010), and the Micangshan area experienced uplift at 140–100 Ma and 152–150 Ma (Tian et al., 2010; Tian et al., 2012; Xu et al., 2010), which have also provided important constraints for the thermal simulation.

To constrain the maximum paleo-geotemperature experienced by the samples, paleotemperature scales such as vitrinite reflectance are always used along with homogenization temperatures of fluid inclusions in or adjacent to the strata where the samples were located (**Table 1**). In the Micangshan area, the inclusion samples collected from the Lower Cambrian Niutitang Formation were emplaced at 212–166 Ma (Tian et al., 2020). The organic fluids in the Dabashan areas were captured in the Late Triassic to Early-Middle Jurassic (Li RX. et al., 2012). Therefore, the vitrinite reflectance and homogenization temperature of organic fluids were used in this study to constrain the maximum paleogeotemperature in the Late Triassic to Early-Middle Jurassic. The F-B-3 and F-B-4 samples are not representative because of the effect of regional thermal anomalies (Tian et al., 2020), and the AFT age χ^2-test is less than 5%, which reflects the thermal history of different provenances. Thermal history inversion simulations were carried out for samples other than F-B-3 and F-B-4 under the geological constraints in this paper.

The inversely modelled t-T paths for the samples collected from the Micangshan-Dabashan tectonic zone are shown in **Figure 6**. The simulated age and track length GOF values of all samples are greater than 0.5 and indicate that high-quality thermal simulation results are obtained. The sedimentary areas of Micangshan and Dabashan have experienced similar cooling histories since the Late Jurassic (160 Ma), presenting a continuous and single uplift and cooling process. This relatively rapid cooling at ca.160 Ma is consistent with that in Micangshan-Hannan massif at 150 Ma

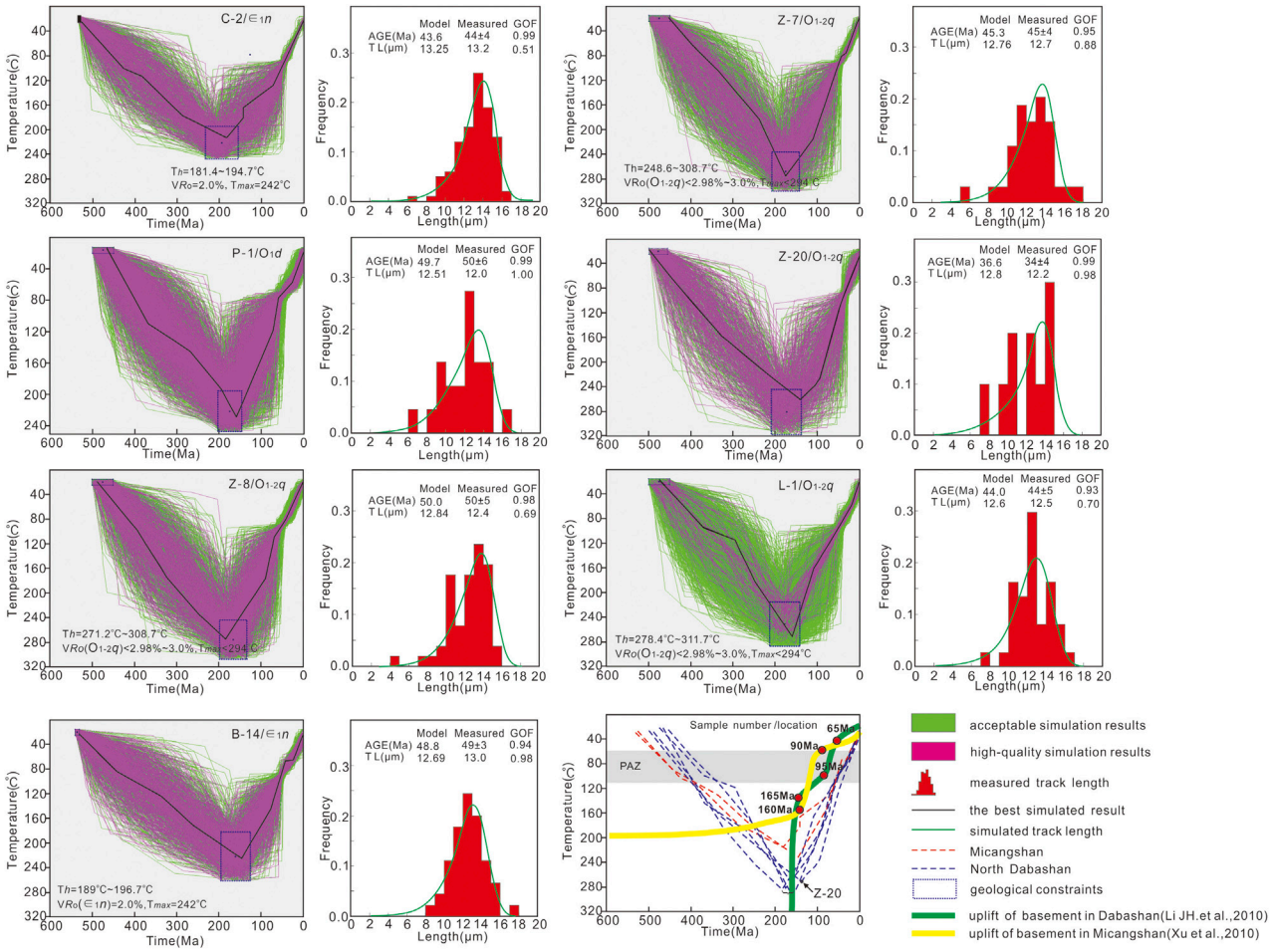

FIGURE 6 | Results of thermal history modelling based on apatite fission track (AFT) data using HeFTy for samples from the Micangshan and Dabashan tectonic belts. The rapid cooling time of sample Z-20 near the Chengkou fault was later than the others, which may indicate the cooling event in the Dabashan area was gradual from northeast to southwest (NS-SW).

and Dabashan tectonic zone at 153 Ma (Xu et al., 2010), which is a precise response to the event of Qinling orogenic belt entered the intracontinental orogenic deformation period (Dong et al., 2006; Li et al., 2013). However, this cooling time is much earlier than that in the southwestern Qinling (Late Cretaceous, Enkelmann et al., 2006), east Qinling-Dabieshan (ca.100 Ma, Hu et al., 2006) and Longmenshan tectonic zone (119–131 Ma, Arne et al., 1997). The previous work shows that it is possibly a response to the combined effects of the Mesozoic tectonism in nearby regions, which probably reactivated pre-existing structures through strike-slip faulting (Webb et al., 1999; Hu et al., 2006; Tian et al., 2012). The Yangtze Block rotated clockwise relative to the north China block through Mesozoic time (Sun et al., 2006) may be an important inducement. The Micangshan-Dabashan area is the core area of the deformation of rotated clockwise that uplift and cooling earlier due to the dextral extrusion. And then spread to the further and more marginal areas such as southwestern Qinling, eastern Qinling-Dabie and Longmenshan tectonic zone. Furthermore, the rapid cooling of Micangshan-Dabashan area at ca.160 Ma was probably the northern source for the early Cretaceous deposition in the northern Sichuan Basin (Meng et al., 2005; Tian et al., 2012). On the background of uplift in the region, the basement and sedimentary cap in Micangshan-Dabashan area also underwent different uplifting processes.

The Micangshan area was uplifted as a whole during 160–90 Ma, and the sedimentary strata and basement experienced a relatively consistent regional uplift process. The sedimentary strata uplifted differently from the basement since 90 Ma. Under the action of thrust and nappe tectonics, the rigid basement uplifted slowly and horizontally, and the plastic strata were squeezed and deformed, which produced the characteristics of folding and uplift since 90 Ma and then entered the PAZ at 63 Ma. Previous study concluded that the displacement of upper structure in Micangshan area is larger than the lower during the progressive deformation process of contraction orogenesis from north to south based on the analysis of structural types and geometric evolution characteristics of folds (Ramsay and Lisle, 2000; Zhang, 2019). And our finding of the different uplifting processes of basement and sedimentary cap is comparable with previous results.

In the Dabashan area, the uplift of sedimentary strata was different from that of the basement during 165–95 Ma. The basement uplifted relatively slowly, while the sedimentary strata uplifted rapidly due to strong fold deformation. The sedimentary strata and the basement experienced a relatively consistent regional uplift process from 95 Ma to 65 Ma. After 65 Ma, the strata experienced differential uplift again (**Figure 6**). In the process of Dabashan nappe extrusion, the rapid uplift of the lower Paleozoic strata in the NDBS since 160 Ma occurred much earlier than that of the Paleozoic strata in the SDBS since ca. 100 Ma (Shen et al., 2007), which reflects the process of nappe uplift from north to south in the Dabashan area. The occurrence of differential uplift between sedimentary strata and basement may reflect the different intensities of thrust and nappe in different stages.

Abundant AFT ages of Late Cenozoic have been used to explain the rapid northeastward growth of Tibetan Plateau, such as ca.20 Ma in northern Longmenshan, 13–15 Ma in central and south Longmenshan and ca.13 Ma in the eastern Tibetan Plateau. Most of the samples which revealed the accelerated cooling were exposed basement samples and shallow buried Cretaceous-Permian samples. However, the simulation results in this study do not show the obvious accelerated cooling in the Late Cenozoic. The accelerated cooling of northeastern Tibet Plateau since Late Cenozoic was the result of multiple factors, which was not only the eastward growth of the Tibetan Plateau, but also intensified by climate change in Southeast Asia (Molnar and Tapponnier, 1975; Tian et al., 2012) and the erodibility of the drainage systems that accelerated the denudation (Richardson et al., 2008; Richardson et al., 2010). Our new samples were from the deep Cambrian-Ordovician strata and they are still buried deeply lager than 2 km (Tian et al., 2020) and was less affected by climate and water erosion in the Late Cenozoic. These may be the reasons why the cooling process was not significantly accelerated in this thermal simulation since the Late Cenozoic.

CONCLUSION

The detrital AFT thermochronological dataset provide new insight into the Meso-Cenozoic tectono-thermal evolution of the Micangshan-Dabashan tectonic belt, central China. New evidence leads us to draw the following conclusions:

1) The AFT ages and lengths suggest that the cooling events in the Micangshan area were gradual from north to south and different uplift occurred on both sides of Micangshan massif. The cooling in Dabashan tectonic zone was from northeast to southwest.
2) A relatively rapid cooling since ca.160 Ma occurred in the Micangshan-Dabashan area which was a precise response to the event of Qinling orogenic belt entered the intracontinental orogenic deformation period. The cooling event may relate to the northeastward dextral compression of the Yangtze Block.
3) The cooling processes of basement and sedimentary cap in Micangshan-Dabashan tectonic belt were inconsistent under the thrust and nappe action. The rigid basement was not always continuous and rapidly uplifted or mainly showed as lateral migration in a certain stage and the plastic sedimentary strata rapidly uplifted due to intense folding deformation and entered the PAZ since ca. 63 Ma.
4) The deep buried samples in Micangshan-Dabashan tectonic belt may be less affected by climate and water erosion what intensified the cooling so that the accelerated cooling was not obvious in the Late Cenozoic as usual.

DATA AVAILABILITY STATEMENT

The original contributions presented in the study are included in the article/Supplementary Material, further inquiries can be directed to the corresponding author.

AUTHOR CONTRIBUTIONS

TT: Conceptualization, Methodology, Resources, Data Curation, Writing-Original Draft, Review and Editing and Project administration. PY: Conceptualization, Methodology, Validation, Formal analysis, Data Curation, Writing-Original Draft, Review and Editing and Visualization. JY: Methodology, Supervision, Project administration and Funding acquisition. ZD: Methodology, Supervision, Writing-Review and Editing, Project administration and Funding acquisition. ZR: Conceptualization, Methodology, Writing-Review and Editing. DF: Formal analysis and Investigation. FY: Formal analysis and Investigation.

FUNDING

This study was supported by the Key Project of Shaanxi Coal Geology Group Co., Ltd., (Grant No. SMDZ (KY)-2020-004), the Independent Project of the Key Laboratory of Coal Exploration and Comprehensive Utilization, MNR (Grant No. ZP 2019-2), and the National Natural Science Foundation of China (Grant No. 41630312, 42102164).

ACKNOWLEDGMENTS

We are grateful to science editor Xuhua Shi for handing with our manuscript. The editors and two reviewers are thanked for critical and constructive comments.

REFERENCES

Arne, D., Worley, B., Wilson, C., Chen, S. F., Foster, D., Luo, Z. L., et al. (1997). Differential Exhumation in Response to Episodic Thrusting along the Eastern Margin of the Tibetan Plateau. *Tectonophysics* 280, 239–256. doi:10.1016/s0040-1951(97)00040-1

Barker, C. E., and Pawlewicz, M. J. (1986). "The Correlation of Vitrinite Reflectance with Maximum Temperature in Humic Organic Matter," in *Paleogeothermics, Heidellberg*. Editors G. Buntebarth and L. Stegena (Berlin: Springer), 79–93.

Bellemans, F., De̋Corte, F., and Van Den̈Haute, P. (1995). Composition of SRM and CN U-Doped Glasses: Significance for Their Use as thermal Neutron Fluence Monitors in Fission Track Dating. *Radiat. Measurements* 24, 153–160. doi:10.1016/1350-4487(94)00100-f

Carlson, W. D., Donelick, R. A., and Ketcham, R. A. (1999). Variability of Apatite Fission-Track Annealing Kinetics; I, Experimental Results. *Am. Mineral.* 84, 1213–1223. doi:10.2138/am-1999-0901

Chang, Y., Xu, C. H., Peter, W. R., and Zhou, Z. Y. (2010). The Exhumation Evolution of the Micangshan-Hannan Uplift since Cretaceous Evidences from apatite(U-Th)/He Dating. *Chin. J. Geophys.* (in Chinese) 53, 912–919. doi:10.3969/j.issn.000125733.2010.04.016

Cheng, R. H., Wang, P. J., Liu, W. Z., Tang, H., Bai, Y., Kong, Q., et al. (2004). Response of Triassic Sequence Stratigraphy of Lower Yangtze to Collision between Yangtze Plate and North China Plate. *Geotectonica et Metallogenia* 29 (2), 174–184.

Clark, M. K., Schoenbohm, L. M., Royden, L. H., Whipple, K. X., Burchfiel, B. C., Zhang, X., et al. (2004). Surface Uplift, Tectonics, and Erosion of Eastern Tibet from Large-Scale Drainage Patterns. *Tectonics* 23, TC1006. doi:10.1029/2002TC001402

Dong, S. W., Hu, J. M., Shi, W., Zhang, Z. Y., and Liu, G. (2006). Jurassic Superposed Folding and Jurassic Foreland in the Daba Mountain, Central China. *Acta Geoscientia Sinica*. (in Chinese) 27, 403–410. doi:10.3321/j.issn:1006-3021.2006.05.003

Dong, S. W., Zhang, Y. Q., Li, Q. S., Gao, R., Hu, J. M., Shi, W., et al. (2014). *Study on the Daba Mountain Intra-continental Orogen belt*. Beijing: Geological Publishing House, 83–108. (in Chinese).

Dong, Y. P., Zha, X. F., Fu, M. Q., Zhang, Q., Yang, Z., and Zhang, Y. (2008). Characteristics of the Dabashan Fold-Thrust Nappe Structure at the Southern Margin of the Qinling, China. *Geol. Bull. China*. (in Chinese) 27, 1493–1508.

Du, D. D., Zhang, C. J., Mughal, M. S., Wang, X. Y., Blaise, D., Gao, J. P., et al. (2018). Detrital Apatite Fission Track Constraints on Cenozoic Tectonic Evolution of the Northeastern Qinghai-Tibet Plateau, China: Evidence from Cenozoic Strata in Lulehe Section, Northern Qaidam Basin. *J. Mt. Sci.* 15, 532–547. doi:10.1007/s11629-017-4692-5

Enkelmann, E., Ratschbacher, L., Jonckheere, R., Nestler, R., Fleischer, M., Gloaguen, R., et al. (2006). Cenozoic Exhumation and Deformation of Northeastern Tibet and the Qinling: Is Tibetan Lower Crustal Flow Diverging Around the Sichuan Basin. *Geol. Soc. America Bull.* 118, 651–671. doi:10.1130/b25805.1

Feng, G. X., and Chen, S. J. (1988). Relationship between the Reflectance of Bitumen and Vitrinite in Rock. *Nat. Gas Industry*. (in Chinese) 3, 30–35.

Galbraith, R. F., and Laslett, G. M. (1993). Statistical Models for Mixed Fission Track Ages. *Nucl. Tracks Radiat. Measurements* 21, 459–470. doi:10.1016/1359-0189(93)90185-c

Gallagher, K. (2003). Fission Track Analysis and its Applications to Geological Problems. *Annu. Rev. Earth Planet. Sci.* 26, 519–572. doi:10.1146/annurev.earth.26.1.519

George, A. D., Marshallsea, S. J., Wyrwoll, K.-H., Jie, C., and Yanchou, L. (2001). Miocene Cooling in the Northern Qilian Shan, Northeastern Margin of the Tibetan Plateau, Revealed by Apatite Fission-Track and Vitrinite-Reflectance Analysis. *Geol* 29, 939. doi:10.1130/0091-7613(2001)0292.0.co;2

Gleadow, A. J. W., Belton, D. X., Kohn, B. P., and Brown, R. W. (2002). Fission Track Dating of Phosphate Minerals and the Thermochronology of Apatite. *Rev. Mineralogy Geochem.* 48, 579–630. doi:10.2138/rmg.2002.48.16

Gleadow, A. J. W., Duddy, I. R., Green, P. F., and Lovering, J. F. (1986). Confined Fission Track Lengths in Apatite: a Diagnostic Tool for thermal History Analysis. *Contr. Mineral. Petrol.* 94, 405–415. doi:10.1007/bf00376334

Godard, V., Pik, R., Lave, J., Cattin, R., Tibari, B., sigoyer, J. D., et al. (2009). Late Cenozoic Evolution of the central Longmen Shan, Eastern Tibet: Insight from (U-Th)/He Thermochronometry. *Tectonics* 28, TC5009. doi:10.1029/2008tc002407

Green, P. F., Duddy, I. R., Gleadow, A. J. W., Tingate, P. R., and Laslett, G. M. (1986). Thermal Annealing of Fission Tracks in Apatite. *Chem. Geology. Isotope Geosci. section* 59, 237–253. doi:10.1016/0168-9622(86)90074-6

Green, P. F. (1988). The Relationship between Track Shortening and Fission Track Age Reduction in Apatite: Combined Influences of Inherent Instability, Annealing Anisotropy, Length Bias and System Calibration. *Earth Planet. Sci. Lett.* 89, 335–352. doi:10.1016/0012-821x(88)90121-5

He, J. K., Lu, H. F., Zhang, Q. L., and Zhu, B. (1997). The Trust Tectonics and Transpressive Geodynamics in Southern Dabashan Mountains. *Geol. J. China Universities*. (in Chinese) 3, 419–428.

Homke, S., Vergés, J., Van Der Beek, P., Fernàndez, M., Saura, E., Barbero, L., et al. (2010). Insights in the Exhumation History of the NW Zagros from Bedrock and Detrital Apatite Fission-Track Analysis: Evidence for a Long-Lived Orogeny. *Basin Res.* 22, 659–680. doi:10.1111/j.1365-2117.2009.00431.x

Hu, S., Kohn, B. P., Raza, A., Wang, J., and Gleadow, A. J. W. (2006). Cretaceous and Cenozoic Cooling History across the Ultrahigh Pressure Tongbai-Dabie belt, central China, from Apatite Fission-Track Thermochronology. *Tectonophysics* 420, 409–429. doi:10.1016/j.tecto.2006.03.027

Huang, W., and Wu, Z. W. (1992). Evolution of the Qinling Orogenic Belt. *Tectonics* 11, 371–380. doi:10.1029/91tc02419

Hurford, A. J., and Green, P. F. (1983). The Zeta Age Calibration of Fission-Track Dating. *Chem. Geology.* 41, 285–317. doi:10.1016/s0009-2541(83)80026-6

Hurford, A. J. (1990). Standardization of Fission Track Dating Calibration: Recommendation by the Fission Track Working Group of the I.U.G.S. Subcommission on Geochronology. *Chem. Geology. Isotope Geosci. section* 80, 171–178. doi:10.1016/0168-9622(90)90025-8

Ketcham, R. A., Carter, A., Donelick, R. A., Barbarand, J., and Hurford, A. J. (2007). Improved Measurement of Fission-Track Annealing in Apatite Using C-axis Projection. *Am. Mineral.* 92, 789–798. doi:10.2138/am.2007.2280

Ketcham, R. A. (2005). Forward and Inverse Modeling of Low-Temperature Thermochronometry Data. *Rev. Mineralogy Geochem.* 58, 275–314. doi:10.2138/rmg.2005.58.11

Ketcham, R. A. (2014). *HeFTy Version 1.8.3*. Austin: University of Texas.

Kirby, E., Reiners, P. W., Krol, M. A., Whipple, K. X., Hodges, K. V., Farley, K. A., et al. (2002). Late Cenozoic Evolution of the Eastern Margin of the Tibetan Plateau: Inferences from 40Ar/39Ar and (U-Th)/He Thermochronology. *Tectonics* 21, 1001. doi:10.1029/2000tc001246

Lei, Y. L., Jia, C. Z., Li, B. L., Wei, G., Chen, Z., and Shi, X. (2012). Meso-Cenozoic Tectonic Events Recorded by Apatite Fission Track in the Northern Longmen-Micang Mountains Region. *Acta Geologica Sinica* 86, 153–165. doi:10.1111/j.1755-6724.2012.00618.x

Li, J., Dong, S., Yin, A., Zhang, Y., and Shi, W. (2015). Mesozoic Tectonic Evolution of the Daba Shan Thrust Belt in the Southern Qinling Orogen, central China: Constraints from Surface Geology and Reflection Seismology. *Tectonics* 34, 1545–1575. doi:10.1002/2014tc003813

Li, J. H., Zhang, Y. Q., Dong, S. W., Shi, W., and Li, H. (2010). Apatite Fission Track Thermochronologic Constraint on Late Mesozoic Uplifting of the Fenghuangshan Basement Uplift. *Chin. J. Geology*. (in Chinese) 45, 969–986.

Li, J., Zhang, Y., Dong, S., and Shi, W. (2013). Structural and Geochronological Constraints on the Mesozoic Tectonic Evolution of the North Dabashan Zone, South Qinling, central China. *J. Asian Earth Sci.* 64, 99–114. doi:10.1016/j.jseaes.2012.12.001

Li, P. Y., Zhang, J. J., Guo, L., and Yang, X. (2011). Structural Features and Deformational Ages in the Front of the Northern Dabashan Thrust belt. *Earth Sci. Front.* 3, 41–49. doi:10.1016/j.gsf.2011.11.002

Li, R. X., Dong, S. W., Zhang, S. N., Zhu, R. J., and Xia, B. (2012). Features and Formation of Organic Fluids during Dabashan Orogenesis. *J. Nanjing Univ. (Natural Science).* (in Chinese) 48, 295–307. doi:10.13232/j.cnki.jnju.2012.03.005

Li, Y. F., Qu, G. S., Liu, S., and Zhang, H. (2008). Strucyural Characters and Mechanism in the Micangshan and Southern Dabashan Mountains Front. *Geotect Metal* 32, 285–292. doi:10.16539/j.ddgzyckx.2008.03.006

Li, Z. W., Liu, S., Chen, H., Deng, B., Hou, M., Wu, W., et al. (2012). Spatial Variation in Meso-Cenozoic Exhumation History of the Longmen Shan Thrust belt (Eastern Tibetan Plateau) and the Adjacent Western Sichuan basin: Constraints from Fission Track Thermochronology. *J. Asian Earth Sci.* 47, 185–203. doi:10.1016/j.jseaes.2011.10.016

Li, Z. W., Chen, H. D., Liu, S. G., Hou, M., and Deng, B. (2010). Differential Uplift Driven by Thrusting and its Lateral Variation along the Longmenshan belt, Western Sichuan, China: Evidence from Fission Track Thermochronology. *Chin. J. Geology*. (in Chinese) 45, 944–968.

Lin, X., Zheng, D., Sun, J., Windley, B. F., Tian, Z., Gong, Z., et al. (2015). Detrital Apatite Fission Track Evidence for Provenance Change in the Subei Basin and Implications for the Tectonic Uplift of the Danghe Nan Shan (NW China) since the Mid-miocene. *J. Asian Earth Sci.* 111, 302–311. doi:10.1016/j.jseaes.2015.07.007

Meng, Q. R., Wang, E., and Hu, J. M. (2005). Mesozoic Sedimentary Evolution of the Northwest Sichuan Basin: Implication for Continued Clockwise Rotation of the south China Block. *Geol. Soc. America Bull.* 117, 396–410. doi:10.1130/b25407.1

Meng, Q. R., and Zhang, G. W. (2000). Geologic Framework and Tectonic Evolution of the Qinling Orogen, central China. *Tectonophysics* 323, 183–196. doi:10.1016/s0040-1951(00)00106-2

Molnar, P., and Tapponnier, P. (1975). Cenozoic Tectonics of Asia: Effects of a Continental Collision: Features of Recent continental Tectonics in Asia Can Be Interpreted as Results of the India-Eurasia Collision. *Science* 189, 419–426. doi:10.1126/science.189.4201.419

Powell, J. W., Schneider, D. A., and Issler, D. R. (2017). Application of Multi-Kinetic Apatite Fission Track and (U-Th)/He Thermochronology to Source Rock thermal History: a Case Study from the Mackenzie Plain, NWT, Canada. *Basin Res.* 30, 497–512. doi:10.1111/bre.12233

Qi, B., Hu, D., Yang, X., Zhang, Y., Tan, C., Zhang, P., et al. (2016). Apatite Fission Track Evidence for the Cretaceous-Cenozoic Cooling History of the Qilian Shan (NW China) and for Stepwise Northeastward Growth of the Northeastern Tibetan Plateau since Early Eocene. *J. Asian Earth Sci.* 124, 28–41. doi:10.1016/j.jseaes.2016.04.009

Ramsay, J. G., and Lisle, R. J. (2000). "The Techniques of Modern Structural Geology," in *Applications of Continuum Mechanics in Structural Geology*, Vol. 3. London: Academic Press, 702–1061.

Reiners, P. W., Zhou, Z., Ehlers, T. A., Xu, C., Brandon, M. T., Donelick, R. A., et al. (2003). Post-orogenic Evolution of the Dabie Shan, Eastern China, from (U-Th)/He and Fission-Track Thermochronology. *Am. J. Sci.* 303, 489–518. doi:10.2475/ajs.303.6.489

Ren, Z. L., Cui, J. P., Guo, K., Tian, T., Li, H., Wang, W., et al. (2015). Fission-track Analysis of Uplift Times and Processes of the Weibei Uplift in the Ordos Basin. *Chin. Sci. Bull.* (in Chinese) 60, 1298–1309. doi:10.1360/N972014-00617

Richardson, N. J., Densmore, A. L., Seward, D., Fowler, A., Wipf, M., Ellis, M. A., et al. (2008). Extraordinary Denudation in the Sichuan basin: Insights from Low Temperature Thermochronology Adjacent to the Easternmargin of the Tibetan Plateau. *J. Geophys. Res.* 113, 1–23. doi:10.1029/2006jb004739,

Richardson, N. J., Densmore, A. L., Seward, D., Wipf, M., and Yong, L. (2010). Did Incision of the Three Gorges Begin in the Eocene. *Geology* 38, 551–554. doi:10.1130/g30527.1

Shen, C. B., Mei, L. F., Fan, Y. F., and Tang, J. G. (2005). Advances and Prospects of Apatite Fission Track Thermochronology. *Geol. Sci. Tech. Information*. (in Chinese) 24, 57–63.

Shen, C. B., Mei, L. F., Xu, Z. P., Tang, J. G., and Tian, P. (2007). Fission Track Thermochronology Evidence for Mesozoic-Cenozoic Uplifting of Daba Mountain, central China. *Acta Petrologica Sinica*. (in Chinese) 23, 2901–2910. doi:10.3969/j.issn.1000-0569.2007.11.020

Shen, X., Tian, Y., Zhang, G., Zhang, S., Carter, A., Kohn, B., et al. (2019). Late Miocene Hinterland Crustal Shortening in the Longmen Shan Thrust Belt, the Eastern Margin of the Tibetan Plateau. *J. Geophys. Res. Solid Earth* 124, 11972–11991. doi:10.1029/2019jb018358

Shi, H. C., and Shi, X. B. (2014). Exhumation Process of Middle-Upper Yangtze since Cretaceous and its Tectonic Significance: Low-Temperature Thermochronology Constraints. *Chin. J. Geophys*. (in Chinese) 57, 2608–2619. doi:10.1002/cjg2.20141

Shi, W., Zhang, Y., Dong, S., Hu, J., Wiesinger, M., Ratschbacher, L., et al. (2012). Intra-continental Dabashan Orocline, Southwestern Qinling, Central China. *J. Asian Earth Sci.* 46, 20–38. doi:10.1016/j.jseaes.2011.10.005

Sobel, E., Chen, J., and Heermance, R. (2006). Late Oligocene-Early Miocene Initiation of Shortening in the Southwestern Chinese Tian Shan: Implications for Neogene Shortening Rate Variations. *Earth Planet. Sci. Lett.* 247, 70–81. doi:10.1016/j.epsl.2006.03.048

Sun, Z., Yang, Z., Yang, T., Pei, J., and Yu, Q. (2006). New Late Cretaceous and Paleogene Paleomagnetic Results from south China and Their Geodynamic Implications. *J. Geophys. Res.* 111, B03101. doi:10.1029/2004JB003455

Sweeney, J. J., and Burnham, A. K. (1990). Evaluation of a Simple Model of Vitrinite Reflectance Based on Chemical Kinetics. *AAPG Bull.* 74, 1559–1570. doi:10.1306/0c9b251f-1710-11d7-8645000102c1865d

Tan, X., Kodama, K. P., Gilder, S., Courtillot, V., and Cogné, J.-P. (2007). Palaeomagnetic Evidence and Tectonic Origin of Clockwise Rotations in the Yangtze Fold belt, South China Block. *Geophys. J. Int.* 168, 48–58. doi:10.1111/j.1365-246x.2006.03195.x

Tian, T., Fu, D. L., Yang, F., Duan, Z., Lin, Y., and Zhao, X. (2018). Relationship between mineral Composition and Micro-pores of Niutitang-Formation Shale in Micangshan-Hannan Uplift. *J. China Coal Soc*. (in Chinese) 43, 236–244. doi:10.13225/j.cnki.jccs.2017.1646

Tian, T., Yang, P., Ren, Z., Fu, D., Zhou, S., Yang, F., et al. (2020). Hydrocarbon Migration and Accumulation in the Lower Cambrian to Neoproterozoic Reservoirs in the Micangshan Tectonic Zone, China: New Evidence of Fluid Inclusions. *Energ. Rep.* 6, 721–733. doi:10.1016/j.egyr.2020.03.012

Tian, T., Zhou, S., Fu, D., Yang, F., and Li, J. (2019). Calculation of the Original Abundance of Organic Matter at High-Over Maturity: A Case Study of the Lower Cambrian Niutitang Shale in the Micangshan-Hannan Uplift, SW China. *J. Pet. Sci. Eng.* 179, 645–654. doi:10.1016/j.petrol.2019.04.071

Tian, Y., Kohn, B. P., Phillips, D., Hu, S., Gleadow, A. J. W., and Carter, A. (2016). Late Cretaceous-Earliest Paleogene Deformation in the Longmen Shan Fold-And-Thrust belt, Eastern Tibetan Plateau Margin: Pre-cenozoic Thickened Crust. *Tectonics* 35, 2293–2312. doi:10.1002/2016tc004182

Tian, Y., Kohn, B. P., Zhu, C., Xu, M., Hu, S., and Gleadow, A. J. W. (2012). Post-orogenic evolution of the Mesozoic Micang Shan Foreland Basin system, central China. *Basin Research* 24, 70–90. doi:10.1111/j.1365-2117.2011.00516.x

Tian, Y. T., Kohn, B. P., Gleadow, A. J. W., and Hu, S. (2013). Constructing the Longmen Shan eastern Tibetan plateau margin: Insights from low-temperature thermochronology. *Tectonics* 32, 576–592. doi:10.1111/j.1365-2117.2011.00516.x

Tian, Y. T., Li, R., Tang, Y., Xu, X., Wang, Y., and Zhang, P. (2018). Thermochronological Constraints on the Late Cenozoic Morphotectonic Evolution of the Min Shan, the Eastern Margin of the Tibetan Plateau. *Tectonics* 37, 1–17. doi:10.1029/2017tc004868

Tian, Y. T., Zhu, C. Q., Xu, M., Rao, S., Kohn, B., and Hu, S. (2010). Exhumation History of the Micangshan-Hannan Dome since Cretaceous and its Tectonic Significance:evidences from Apatite Fission Track Analysis. *Chin. J. Geophys*. (in Chinese) 53, 920–930. doi:10.3969/j.issn.000125733.2010.04.017

Wang, E., Kirby, E., Furlong, K. P., van Soest, M., Xu, G., Shi, X., et al. (2012). Two-phase Growth of High Topography in Eastern Tibet during the Cenozoic. *Nat. Geosci* 5 (9), 640–645. doi:10.1038/ngeo1538

Wang, E., Meng, Q., Clark Burchfiel, B., and Zhang, G. (2003). Mesozoic Large-Scale Lateral Extrusion, Rotation, and Uplift of the Tongbai-Dabie Shan belt in east China. *Geol* 31, 307–310. doi:10.1130/0091-7613(2003)031<0307:mlsler>2.0.co;2

Wang, J. L., Wang, Y., Li, Q., Zheng, D., and Li, D. (2005). Apatite Fission Track Study of Taibai Mountain Uplift in the Mesozoic-Cenozoic. *Nucl. Tech.* 28, 712–716.

Wang, Z. C., Zou, C. N., Tao, S. Z., Li, J., Wang, S. Q., Zhao, C. Y., et al. (2004). Analysis on Tectonic Evolution and Exploration Potential in Dabashan Foreland basin. *Acta Petrolei Sinica* 25, 23–28.

Webb, L. E., Hacker, B. R., Ratschbacher, L., McWilliams, M. O., and Dong, S. (1999). Thermochronologic Constraints on Deformation and Cooling History of High- and Ultrahigh-Pressure Rocks in the Qinling-Dabie Orogen, Eastern China. *Tectonics* 18, 621–638. doi:10.1029/1999tc900012

Xu, H., Liu, S., Qu, G., Li, Y., Sun, G., and Liu, K. (2009). Structural Characteristics and Formation Mechanism in the Micangshan Foreland, south China. *Acta Geol. Sinica* 83, 81–91. doi:10.1111/j.1755-6724.2009.00010.x

Xu, C. H., Zhou, Z. Y., Chang, Y., and Guillot, F. (2010). Genesis of Daba Arcuate Structural Belt Related to Adjacent Basement Upheavals: Constraints from Fission-Track and (U-Th)/He Thermochronology. *Sci China Earth Sci* 53, 1634–1646. doi:10.1007/s11430-010-4112-yL

Yang, Z., Ratschbacher, L., Jonckheere, R., Enkelmann, E., Dong, Y., Shen, C., et al. (2013). Late-stage Foreland Growth of China's Largest Orogens (Qinling, Tibet): Evidence from the Hannan-Micang Crystalline Massifs and the Northern Sichuan Basin, central China. *Lithosphere* 5, 420–437. doi:10.1130/l260.1

Yang, Z., Shen, C., Ratschbacher, L., Enkelmann, E., Jonckheere, R., Wauschkuhn, B., et al. (2017). Sichuan Basin and beyond: Eastward Foreland Growth of the Tibetan Plateau from an Integration of Late Cretaceous-Cenozoic Fission Track and (U-Th)/He Ages of the Eastern Tibetan Plateau, Qinling, and Daba Shan. *J. Geophys. Res. Solid Earth* 122, 4712–4740. doi:10.1002/2016jb013751

Yuan, W. M., Zhang, X. T., Dong, J. Q., Tang, Y. H., Yu, F. S., and Wang, S. C. (2003). A New Vision of the Intracontinental Evolution of the Eastern Kunlun Mountains, Northern Qinghai-Tibet Plateau, China. *Radiat. Measurements* 36, 357–362. doi:10.1016/s1350-4487(03)00151-3

Yuan, W., Carter, A., Dong, J., Bao, Z., An, Y., and Guo, Z. (2006). Mesozoic-Tertiary Exhumation History of the Altai Mountains, Northern Xinjiang, China: New Constraints from Apatite Fission Track Data. *Tectonophysics* 412, 183–193. doi:10.1016/j.tecto.2005.09.007

Yuan, W. M., Du, Y. S., Yang, L. Q., Li, S. R., and Dong, J. (2007). Apatite Fission Track Studies on the Tectonics in Nanmulin Area of Gangdese Terrane, Tibet Plateau. *Acta Petrologica Sinica* 23, 2911–2917.

Yue, G. Y. (1998). Tectonic Characteristics and Tectonic Evolution of Dabashan Orogenic belt and its Foreland basin. *J. Mineralogy Petrol.* (in Chinese) 18, 8–15.

Zhang, G. W., Yu, Z. P., Sun, Y., Cheng, S., Li, T., Xue, F., et al. (1989). The Major Suture Zone of the Qinling Orogenic belt. *J. Southeast Asian Earth Sci.* 3, 63–76.

Zhang, Y. L., Wang, Z. Q., Wang, G., and Wang, K. (2016). Detrital Zircon Geochronology of the Late Paleozoic Taohekou Formation and its Constraints on the Paleozoic Magmatic Events in North Daba Mountains. *Acta Geologica Sinica*. (in Chinese) 90, 728–738.

Zhang, Z. Y., and Dong, S. W. (2009). Superposed Buckle Folding in the Northwestern Daba Mountain, Central China. *Acta Geologica Sinica*. (in Chinese) 83, 923–936. doi:10.1111/j.1755-6724.2009.00008.x

Zhang, Z. Y. (2019). Superposed Buckle Folding at the Upper Structural Levels in Western Dabashan:example from the Jianchi Area in Zhenba County. *Earth Sci. Frontiers*. (in Chinese) 26, 1–15. doi:10.13745/j.esf.sf.2019.3.10

Zheng, D. W., Zhang, P. Z., Wan, J. L., Li, D. M., Wang, F., Yuan, D. Y., et al. (2004). The $^{40}Ar/^{39}Ar$, Fission Track Evidence of Mesozoic Tectonic in Northern Margin of West Qinling Mountain. *Acta Petrologica Sinica* 20, 697–706. doi:10.3321/j.issn:1000-0569.2004.03.034

Zou, X. W., Duan, Q. F., Tang, C. Y., Cao, L., Zhao, W. Q., Wang, L., et al. (2011). SHRIMP Zircon U-Pb Dating and Lithogeochemical Characteristics of Diabase from Zhenping Area in North Daba Mountain. *Geol. China (in Chinese)* 38, 282–291.

Conflict of Interest: Authors TT, JY, ZD, DF and FY are employed by Shaanxi Coal Geology Group Co., Ltd.

The remaining author declares that the research was conducted in the absence of any commercial or financial relationships that could be construed as a potential conflict of interest.

Publisher's Note: All claims expressed in this article are solely those of the authors and do not necessarily represent those of their affiliated organizations, or those of the publisher, the editors, and the reviewers. Any product that may be evaluated in this article, or claim that may be made by its manufacturer, is not guaranteed or endorsed by the publisher.

Copyright © 2021 Tian, Yang, Yao, Duan, Ren, Fu and Yang. This is an open-access article distributed under the terms of the Creative Commons Attribution License (CC BY). The use, distribution or reproduction in other forums is permitted, provided the original author(s) and the copyright owner(s) are credited and that the original publication in this journal is cited, in accordance with accepted academic practice. No use, distribution or reproduction is permitted which does not comply with these terms.

frontiers in Earth Science

ORIGINAL RESEARCH
published: 08 December 2021
doi: 10.3389/feart.2021.796610

Quantifying the Geomorphology of the Drainage Basins Along the Greater Khingan Mountains in NE China

Lingling Lin[1,2]*, *Xuemei Li*[3] and *Zifa Ma*[1]

[1]State Key Laboratory of Earthquake Dynamics, Institute of Geology, China Earthquake Administration, Beijing, China, [2]Hebei Key Laboratory of Earthquake Dynamics, China Institute of Disaster Prevention, Sanhe, China, [3]Institute of Mountain Hazards and Environment, Chinese Academy of Sciences, Chengdu, China

Drainage basins are fundamental elements of the earth's surface, and quantifying their geomorphic features is essential to understand the interaction between tectonics, climatic, and surface processes. In this study, 40 basins of the Greater Khingan Mountains were selected for hypsometric analysis using a 90-m Shuttle Radar Topography Mission digital elevation model. The hypsometric integral values range from 0.13 to 0.44, with an average value of 0.30, and most hypsometric curves exhibit remarkable downward concave shapes. This feature indicates that most drainage basins and the landscape of the Greater Khingan Mountains are approaching the old-age development stage, consistent with the present moderately stable tectonic activity. The spatial distribution of the χ values is characterized by unambiguously higher values on the western flank than those on the eastern flank in the middle and southern segments of the Greater Khingan Mountains. We interpret this as an indicator of the disequilibrium across the main divide. The interpolation of the erosion rates and channel steepness for the catchments on both sides of the Greater Khingan Mountains revealed westward divide migration, which is consistent with the lower χ values, a higher slope, and local relief observed along the eastern flanks. Considering the long-term tectonic evolution pattern between the Greater Khingan Mountains and Songliao Basin, the landscape decay and slow westward divide migration were mostly driven by the inherited Cenozoic tectonics and precipitation gradient across East Asia.

Keywords: Greater Khingan Mountains, geomorphology, hypsometric integral, χ analysis, erosion rates, divide migration

OPEN ACCESS

Edited by:
Xuhua Shi,
Zhejiang University, China

Reviewed by:
Xiaofei Hu,
Lanzhou University, China
Honghua Lu,
East China Normal University, China

***Correspondence:**
Lingling Lin
linlingling@cidp.edu.cn

Specialty section:
This article was submitted to Quaternary Science, Geomorphology and Paleoenvironment, a section of the journal Frontiers in Earth Science

Received: *17 October 2021*
Accepted: *22 November 2021*
Published: *08 December 2021*

Citation:
Lin L, Li X and Ma Z (2021) Quantifying the Geomorphology of the Drainage Basins Along the Greater Khingan Mountains in NE China. Front. Earth Sci. 9:796610. doi: 10.3389/feart.2021.796610

INTRODUCTION

Rivers and drainage basins are the most basic components of geomorphic systems, and the tectonic, climatic and surface processes collaborate to shape their landscape. (Molnar and England, 1990; Willett et al., 2006; Liu-Zeng et al., 2018). Common factors influencing geomorphic features include bedrock type, tectonics, climate, and individual geomorphic events such as river capture (He et al., 2019; Johnson, 2020). Tectonic uplift can increase the terrain slope and provide more potential energy for river erosion. The precipitation change caused by climate change since the Cenozoic can also affect the river erosion efficiency. Furthermore, due to the different lithologies of bedrock, the erosion coefficient and slope index associated with the bedrock river erosion model will be different, affecting the landform of rivers and basins (Chen et al., 2014; Su et al., 2016). Therefore, distinct

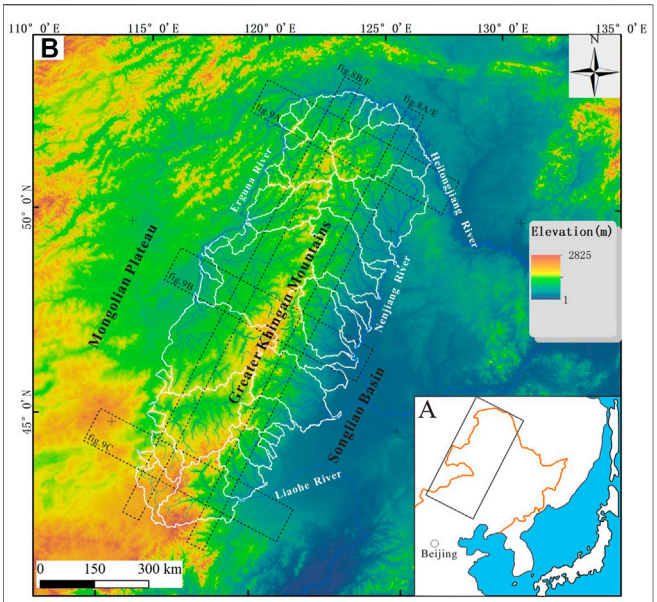

FIGURE 1 | (A) Location of the study area in East Asia; **(B)** Hillshade of 90 m digital elevation model produced from the Shuttle Radar Topography Mission, blue lines show major rivers, white lines show major drainage divides.

features will develop under the same tectonic and climatic conditions. Since the 1990s, with the development of space earth observation and new dating technology, analyzing the relationship among climate, topography, denudation, deposition, and rock deformation in active orogenic belts by quantitatively studying topographic and geomorphic evolution has gradually become one of the frontiers and hot fields in earth sciences (Lv et al., 2014; Liu-Zeng et al., 2018). Digital elevation model (DEM) data and geomorphic parameters were usually utilized to quantitatively reveal the morphology feature, such as extracting the stage of geomorphological evolution within the tectonic active area, especially in the peripheral region of Tibetan Plateau (Zhang et al., 2008, 2011; Hu et al., 2010; Yang et al., 2015; Yang J. et al., 2020; Yang R. et al., 2020; Su, et al., 2015, 2017, Li et al., 2019; Ma et al., 2019). But such studies are still lacking to understand the landscape evolution across different regions rather than the Tibetan Plateau. However, recent researches on geometric indexes (such as channel steepness index and χ plots) were reported on postorogenic landscapes, including the Appalachian Mountains, the Ozark dome of the North American Craton, and the Cape Mountains of South Africa. And these studies have explained how knickpoint migration and channel–hillslope coupling, strong rocks, and asymmetric drainage divides as an important factor in tectonically-inactive (i.e., post-orogenic) orogens for the maintenance of transient landscapes (Gallen et al., 2011; Miller et al., 2013; Beeson et al., 2017; Scharf et al., 2013), which is significant for us to extend our knowledge aside from the actively-uplifting Tibet. In Northeast Asia, the Greater Khingan Mountains are located in the Xing'an East Mongolia block (**Figure 1**). Previous studies indicate that the Greater Khingan Mountains are stable in tectonic activity and the Quaternary tectonic deformation has been relatively weak (Deng et al., 2002,2003; Zhang et al., 2002,2003). What are the features of geomorphic development in a region with a stable tectonic setting and what geomorphic parameters can be used to express geomorphic features of tectonically stable areas? What are the main factors affecting the developmental characteristics? The answers to these questions will be helpful to understand the process and trend of long-term geomorphic evolution in tectonically stable areas. Based on the river system of the Greater Khingan Mountains as the breakthrough point, 40 river basins were selected as research objects using the spatial resolution of a 90-m Shuttle Radar Topography Mission (SRTM)-3 DEM, we have gone through some quantitative calculations, such as slope, hypsometric integral values, χ plots, and a typical swath profile analysis to reveal the watershed geomorphic characteristics of the Greater Khingan Mountains, a relatively tectonically stable region in the mainland. Based on tectonic evolution, lithology, and precipitation, the main controlling factors of this geomorphic development are analyzed and discussed.

GEOLOGICAL SETTING

The NNE–SSW-trending Great Khingan Mountains is located in the western Frontier of Northeast China. It is bounded by the North China Platform North Margin fault in the south, the Mongolian-Okhotsk fold system in the north, and the Nenjiang fault and the Songliao Basin in the east, which determines the small width and steep topography of the eastern flank of the Great Khingan Mountains. However, the western boundary of the Great Khingan Mountains is fuzzy, because the Great Khingan Mountains belongs to the eastern segment of the Tianshan-Xingmeng fold system extending from east to west tectonically, and there is no distinct tectonic boundary to the west. Therefore, the western flank of the Great Khingan Mountains is much wider and slower than the eastern flank topographically (Liu et al., 2004; Fang et al., 2008).

Tectonically, the mountains lie on the junction of the Siberian and North China Plates and are Meso–Cenozoic mountains developed on the Caledonian, Early Hercynian, and Late Hercynian fold belts (Liu et al., 2004; Fang et al., 2008; Qian et al., 2013; Xiang, 2014). In the Paleozoic, the Paleo–Asiatic tectonic domain controlled it, and after Mesozoic, the Pacific and Tethys tectonic domains mostly influenced it (Fang et al., 2008; Wu, 2013). Since the Mesozoic era, the magmatic activity in the area has been intense and Jurassic continental intermediate-acid volcanic rocks and Yanshanian intermediate-acid intrusive rocks have been exposed in large areas. Since the Late Mesozoic era, a tectonic pattern dominated by NW- and NE-trending faults has been formed and the volcanic rocks are distributed along the NE-trending fault. The Cenozoic tectonic activities mostly inherited the Mesozoic faults and developed multiple Cenozoic faults along the NE direction. These inherited faults controlled the distribution of Cenozoic volcanoes and volcanic rocks in the Great Khingan Mountains (Wu, 2013; Yin et al., 1980; Li et al., 2012).

METHODS

Topographic Analysis

We analyzed topographic features from SRTM DEM. Two types of data, namely, SRTM-1 with a 30 m spatial resolution and SRTM-3 with a 90 m spatial resolution, have been widely used in the study of tectonic geomorphology (Liu et al., 2006; Wang et al., 2013; Su et al., 2015,2016). Considering the large selection scope of this study, SRTM-3 data can fully meet the study of macrogeomorphic characteristics in the Greater Khingan Mountains with a resolution of 90 m.

Slope and Local Topographic Relief

Slope and local topographic relief are macroindices of regional topographic features. The slope is constructed by calculating the steepest slope of each DEM pixel. That is, for each pixel, the pixel with the greatest elevation difference near it is searched. The slope angle can be determined according to the elevation difference and horizontal distance between two pixels. Local topographic relief is the elevation difference between the highest peak and valley bottom in a specific area and represents a river or glacier erosive capacity (Deffontains et al., 1994, 1997; Kühni and Pfiffner, 2001). In this study, a square statistical window of 1 × 1 km was selected for statistical study and the highest elevation matrix was subtracted from the minimum elevation matrix using the grid calculation tool of the geographic information system software (Zhang et al., 2011). We will obtain the distribution characteristics of slope and topographic relief in the Greater Khingan Mountains using DEM data.

Hypsometric Analysis

Hypsometric analysis constructed by Strahler in 1952 is considered an effective tool for understanding the stages of geomorphic evolution and geological development of river catchment. Using Davis' erosion cycle theory, Strahler proposed that the drainage basins were in different geomorphic evolution stages have different hypsometric curve and hypsometric integral (*HI*) value: youth stage which had a high hypsometric integral value (where $HI > 0.6$), and a convex upward hypsometric curve; equilibrium or mature stage which had a secondary hypsometric integral value (where $0.35 < HI < 0.6$), and an s-shaped hypsometric curve; pereplain (old) or monadnock stage which had a low hypsometric integral value (where $HI < 0.35$), and a concave upward curve (Davis, 1899; Strahler, 1952; Farhan et al., 2016).

A hypsometric curve is the curve obtained by taking the relative area ratio (a/A) of a basin as the horizontal axis and the relative height ratio (h/H) as the vertical axis. It is a geomorphologic parameter used to describe the three-dimensional volume residual rate of the surface with a two-dimensional curve, where h is the elevation difference between a certain elevation and the lowest elevation in the basin, H is the maximum elevation difference, A is the cross-sectional area of the lowest elevation of the basin (the total area of the basin projected on the horizontal plane), and a is the cross-sectional area of a certain elevation of the basin (Chen, 2008; Su et al., 2015,2016). The area under the hypsometric curve is the hypsometric integral value. In this study, the hydrological analysis module of ArcGIS10.3 was used to extract the water network. We selected 20 basins on the eastern flank and 20 basins on the western flank of the Greater Khingan Mountains. The hypsometric curve and hypsometric integral value was acquired using CalHypso Tools, an ArcGIS add in developed by Pérez-Peña et al. (2009).

χ Plot

During geomorphic evolution, tectonic activity or climate change can change the channel gradient or the river's cross-section area, changing the river's erosion capacity, adjusting the river's hydraulic power, changing the river basin's erosion and transport capacity, and, finally, making the whole basin system gradually tend to equilibrium. For bedrock channels, the downstream erosion capacity of rivers is related to the boundary shear stress of bedrock channels induced by flowing water (Whipple & Tucker, 1999). The downstream erosion rate of rivers, E, can be expressed as a function of basin area A and channel gradient S; channel gradient S can be written in a differential form of elevation and distance, and **Formula 1** can be obtained as follows:

$$E = KA^m \left|\frac{\partial z}{\partial x}\right|^n \tag{1}$$

In **Formula 1**, K is the erosion coefficient, m is the area index, n is the gradient index, Z is the river elevation, A is drainage area, and x is the river's traceability distance (i.e., the direction from the outlet to the watershed). Elevation changes at any point of the bedrock channel with time can be expressed as the difference between uplift rate U and river erosion rate E, and **Formula 2** can be obtained (Flint, 1974; Howard et al., 1983).

$$\frac{\partial z}{\partial t} = U - KA^m \left|\frac{\partial z}{\partial x}\right|^n \tag{2}$$

When the bedrock channel is in equilibrium (i.e., $\partial z/\partial t = 0$) and uplift rate U and erosion coefficient K remain unchanged in space, the channel gradient can be expressed as **Formula 3**.

$$\frac{\partial z}{\partial x} = \left|\frac{U}{KA^m}\right|^{\frac{1}{n}} \tag{3}$$

By integrating **Formula 3** from the outlet x_0 to x along both sides of the river, **Formula 4** can be obtained. To make the integral term in **Formula 4** have the same dimension as the river-tracing distance, the reference watershed area A_0 is introduced, which can take any value (Perron and Royden, 2013).

$$\int_{x_0}^{x} \frac{\partial z}{\partial x} dx = Z(x_0) + \left|\frac{U}{KA_0^m}\right|^{\frac{1}{n}} \int_{x_0}^{x} \left|\frac{A_0}{A(x)}\right|^{\frac{m}{n}} dx \tag{4}$$

$$\chi = \int_{x_0}^{x} \left|\frac{A_0}{A(x)}\right|^{\frac{m}{n}} dx \tag{5}$$

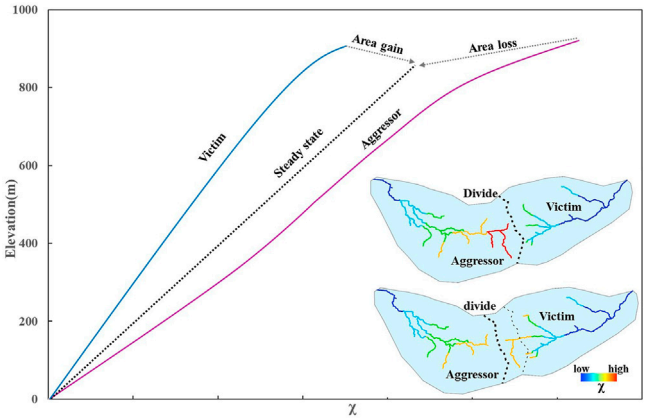

FIGURE 2 | River basins and river profiles in equilibrium and disequilibrium. The parameter χ predicts the steady-state elevation for a given point on a channel. The basin on the left (aggressor) has lower steady-state elevation at channel heads and therefore drives the drainage divide toward the basin on the right (victim) (modified from Willett et al., 2014).

By replacing the integral on the right side of **Formula 4** with χ and assigning the elevation $Z\ (x_0)$ at the outlet of the basin to 0, the formula can be rewritten as **Formula 6**.

$$Z(x) = \left|\frac{U}{KA_0^m}\right|^{\frac{1}{n}}\chi \tag{6}$$

In the stream power model the channel steepness index is defined as $k_s = (\frac{U}{K})^{\frac{1}{n}}$, and the channel concave index is defined as θ = m/n. The normalized steepness index (k_{sn}) can be used for regional comparison when the regional mean concavity index is determined as a reference concavity value (θ_{ref}). Thus, **Eq. 4** can be transformed into :

$$Z(x) = Z(x_0) + \left(\frac{k_{sn}}{A_0^{\theta_{ref}}}\right)\chi \tag{7}$$

From **Formula 6**, the elevation value of each point on the river can be expressed as a function of χ, which only depends on the upstream basin's distribution area, thus avoiding the data deviation caused by elevation noise. Using elevation Z as the ordinate and χ as the abscissa, the plot is called the chi plot (**Figure 2**). When A_0 is 1, the elevation change in the chi plot (slope in chi plot) represents the same meaning as the normalized steepness index obtained in the slope–area log–log plot. Furthermore, Willett et al. proposed in 2014 that the χ difference between the two sides of the divide can be used to analyze the dynamic migration process of the divide, explain the large-scale river capture event, and describe the drainage system's evolution process. River capture changes the watershed area, causing abnormal changes in the χ value. Therefore, the abnormal changes in the χ value can reflect river capture and divide migration. When the water system on both sides of the divide is unbalanced, the χ values of the two sides are different. The divide will migrate from the side with the lower χ value to the side with the higher χ value. Finally, the χ value difference between the two sides of the divide decreases and the drainage system evolution reaches equilibrium (**Figure 2**) (Willett et al., 2014).

In this study, ChiProfiler (Gallen and Wegmann, 2017) was used to calculate the χ values. The parameters were set as follows: m/n = 0.45, A_{cr} = 10 km^2 (the minimum catchment area at the river source was 10 km^2). To ensure that the outlet possesses the same elevation of all basins, we selected a base plane of 300 m. According to the analysis methods and steps developed by Snyder et al. (2000) and Kirby et al. (2003), we extracted the river elevation and watershed area (A) from DEM, selected a 1 km moving window for smoothing, and calculated the river gradient (S) every 20 m vertical elevation difference at first. Then we obtained the normalized steepness index (k_{sn}) (the y-axis intercept) and the channel concave index(θ) (the slope of the straight line) by inversion and regression according to the formula logs = − θ Loga + logks. In order to compare different river channels in the region, We determined θ_{ref} = 0.45 (Snyder et al., 2000; Kirby et al., 2003). Finally, the average normalized steepness index of each sampling basin is calculated.

^{10}Be Basin-Averaged Erosion Rates

To reveal the spatial distribution characteristics of erosion rates in the structurally relatively stable region of the Greater Khingan Mountains, we selected 12 rivers on both sides of the north–central section of the Greater Khingan Mountains in July 2018. We collected modern river sand samples with diameters of 0.25–0.75 mm at their outlets. Preparations of the samples and ^{10}Be/^{9}Be ratios were measured at the Xi'an Accelerator Mass Spectrometry (AMS) Center, China. First, the quartz minerals were extracted using an acid solution and the heavy liquid method and treated with 1% HF and 1% HNO_3 4–5 times to extract pure quartz. After purification, the 9Be carrier was added to quartz particles. HF and HNO_3 digestions were used, and $HClO_4$ was used to remove fluoride. Be was separated by an anion exchange resin and added to ammonia to obtain $Be(OH)_2$ precipitation, which was transferred to a quartz crucible and burned in a muffle furnace at 900°C to generate BeO, and mixed with Niobium powder to press the target sample. Finally, AMS was used to measure the ^{10}Be concentration (Zhang et al., 2012a, 2012b; Corbett et al., 2016; Dong et al., 2016; Dong et al., 2017).

After obtaining the ^{10}Be concentration, we used **Formula 8** to calculate the basin-averaged erosion rates (Granger and Schaller, 2014; Hu et al., 2021).

$$C = \frac{P}{\lambda + \frac{\rho\varepsilon}{\Lambda}} \tag{8}$$

where C is the ^{10}Be concentration measured (atoms/g), P is the average ^{10}Be generation rate in the sampling basin (atoms/g/yr), λ is the decay constant of ^{10}Be (4.997×10^{-7}/a) (Chmeleff et al., 2010), Λ is the decay length of cosmic rays in rocks (~160 g/cm^2) (Gosse and Phillips, 2001; Marrero et al., 2016), and ε is the basin-averaged erosion rates we must obtain. To obtain the

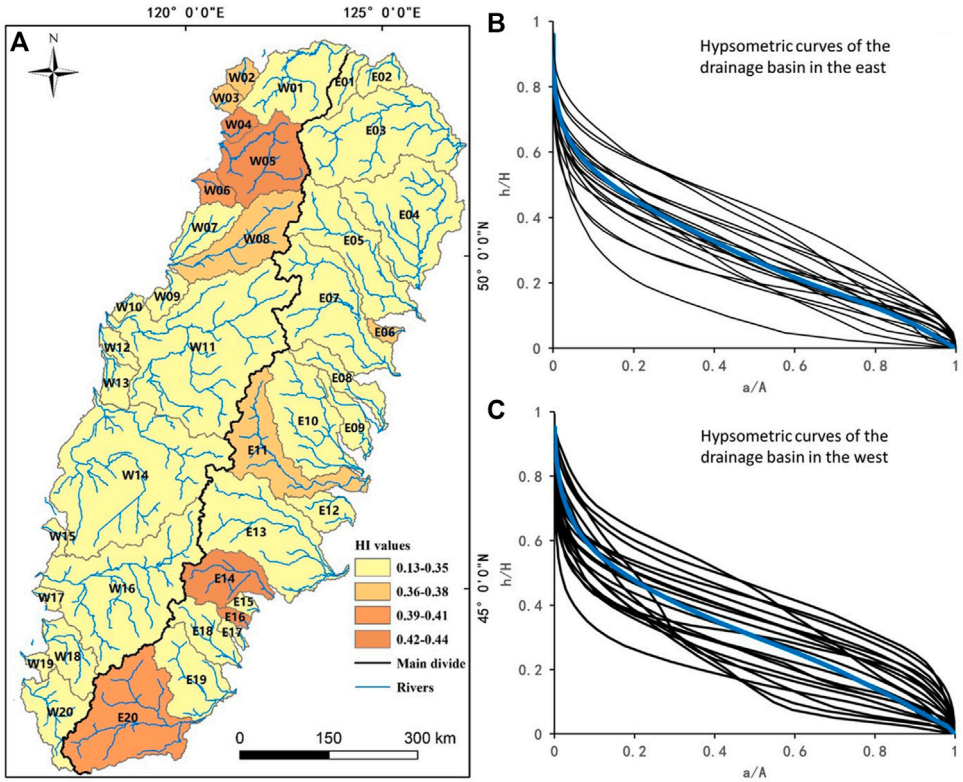

FIGURE3 | Hypsometric curves and hypsometric integral (HI) values. **(A)** Map-view of the HI values. **(B)** Hypsometric curves of 20 drainage basins in the east. **(C)** Hypsometric curves of 20 drainage basins in the west. Hypsometric curves and HI values were obtained using the CalHypso Tools, an ArcGIS add in developed by Pérez-Peña et al. (2009).

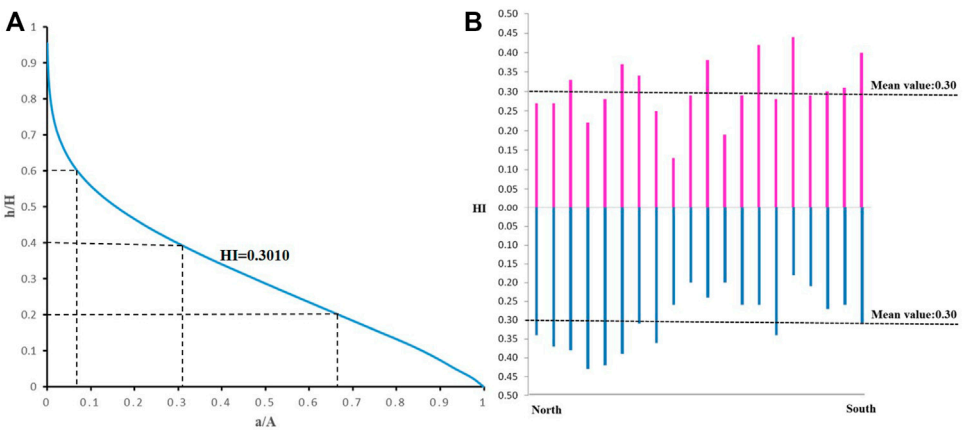

FIGURE 4 | Hypsometric curves of the average topographic development curve in the Greater Khingan Mountains **(A)**; hypsometric integral (HI) and mean values in the Greater Khingan Mountains **(B)**.

basin-averaged erosion rates using the above formula, we must first calculate the average ^{10}Be generation rate of the sampling basin. We calculate the ^{10}Be generation rate of each point in the basin through the standard generation rate of 4.0 atoms/g/yr at high latitude and low altitude (Borchers et al., 2016) and altitudinal scale effect (Lal, 1991; Stone, 2000) and then obtain the generation rate of the entire basin through average processing (Vermeesch, 2007). The topographic self-correcting

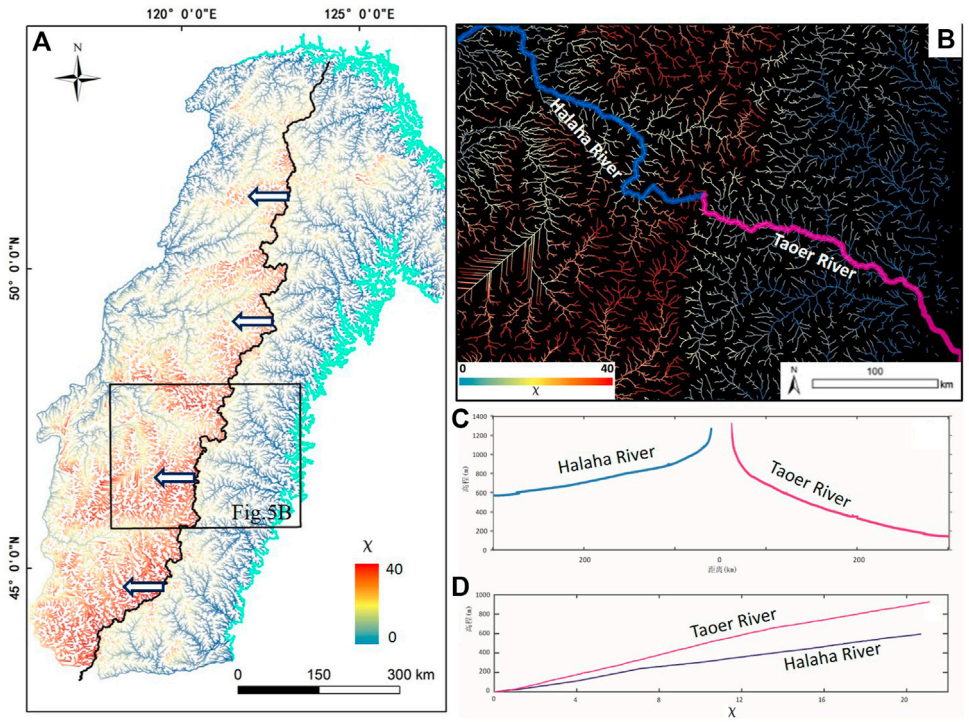

FIGURE 5 | χ map of the Greater Khingan Mountains **(A)**. The typical area with enormous differences in χ values **(B)**. Elevation profile of the main rivers in the typical area **(C)**. Chi plot of the main rivers in the typical area **(D)**.

TABLE 1 | Sample locations and corresponding basin-wide erosion rates.

[a]Sample No	Lat (°N)	Lon (°E)	Mean Elev (m)	Drainage Area (km^2)	^{10}Be Concentration (10^4 at/g)	^{10}Be Erosion rate (mm/kyr)	Mean basin k_{sn} ($m^{0.9}$)
W_1	49.44	121.10	836.06	203.11	38.54 ± 5.64	15.37 ± 2.35	19.56
W_2	49.76	120.13	829.06	1,632.93	67.63 ± 5.86	8.48 ± 0.78	20.46
W_3	50.72	120.32	855.78	1,270.56	42.98 ± 8.92	14.05 ± 3.05	28.60
W_4	50.81	121.52	886.86	17.58	46.44 ± 3.89	13.29 ± 1.16	26.56
W_5	51.26	121.31	980.48	300.81	54.48 ± 2.19	12.15 ± 0.51	23.91
W_6	52.05	122.07	900.08	716.36	42.86 ± 3.70	14.65 ± 1.32	30.90
W_7	52.44	122.53	791.36	288.92	37.20 ± 2.60	15.55 ± 1.13	28.35
W_8	52.88	122.82	653.75	343.44	39.20 ± 2.01	13.12 ± 0.71	24.08
E_1	47.57	122.14	708.30	1839.28	31.21 ± 4.09	16.90 ± 2.31	32.40
E_2	48.57	122.15	801.18	48.38	32.94 ± 4.03	17.42 ± 2.22	38.07
E_3	52.32	124.51	810.33	10,931.40	35.26 ± 4.54	16.70 ± 2.24	33.36
E_4	50.25	124.26	451.34	35.93	37.62 ± 5.06	11.47 ± 1.64	17.17

[a]*W- and E-depict the samples were collected from drainage basins on the western and eastern flanks, respectively.*

regularity within the basin was obtained using previous tools (Codilean, 2006).

RESULTS AND DISCUSSION

Hypsometry and Geomorphic Evolution

To quantitatively explore the stages of geomorphic evolution in the Greater Khingan Mountains, we acquired the hypsometric curve (**Figure 3A**) and *HI* index (**Figures 3B,C**) of 40 basins. The *HI* values range from 0.13 to 0.44, with an average of 0.30. From **Figure 3**, the *HI* values of most basins are less than 0.35. Only some basins on the southeastern and northwestern flanks approach 0.4, and the basins' hypsometry curves are concave, with only some basins being s-shaped.

We analyzed the average topographic development characteristics in the Greater Khingan Mountains following the definition of the hypsometry curve (**Figure 4**). As shown in **Figure 4** the hypsometry curve of the Greater Khingan Mountains is a concave upward curve, it is similar to the hypsometry curve of most basins. The average *HI* value of

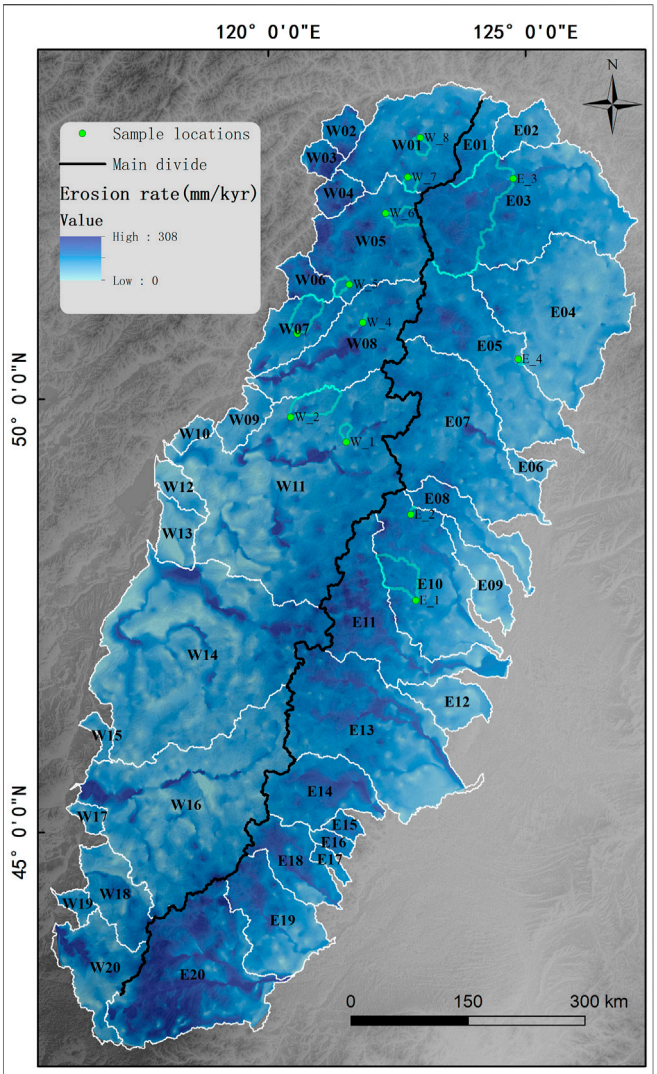

FIGURE 6 | Erosion rate of the Greater Khingan Mountains, basin colors show erosion rates calculated from channel steepness, green lines are basin boundaries and dots are sample locations. Black lines are the main drainage divides.

both flanks in the Greater Khingan Mountains is 0.30. *HI* values indicate the volume residual rate of the basin under the joint influence of tectonism and denudation. So we proposed that the geomorphic evolution stage of the Greater Khingan Mountains is in a pereplain (old) stage. Because the Greater Khingan Mountains are in the inland, affected by West Pacific tectonic domain in the Cenozoic; however, because it is far away from the subduction zone, it has a weak tectonic movement response. In addition, the surface water system is developed with strong weathering.

Significance of χ Values for Watershed Stability

The spatial distribution of the χ value in the Greater Khingan Mountains (the solid black line for the main divide) was shown in **Figure 5A**. No obvious change in the χ value occurs from the north to the south in the eastern flank, but the χ value in the western flank is lower in the north and higher in the south. Across the main divide, the χ values are higher in the western flank than in the eastern flank and the difference in the two flanks increases gradually from the north to the south. The difference in the χ values across the main divide indicates that the river system is in a state of disequilibrium and divide migration and river capture must reorganize the river system to achieve a state of equilibrium.

In the chi plot (plotted with elevation *Z* as the ordinate and χ as the abscissa), the longitudinal profile of equilibrium river channels displays a straight line passing through the origin (**Figure 2**). Due to local structural and climatic disturbances, such changes can be identified from the chi plot to observe whether the river longitudinal profile deviates from the steady linear state (Willet tal. 2014). We selected a typical area in the southern Greater Khingan Mountains, with a maximum difference in χ values across the main divide. We then made a chi plot of the Taoer River and Halaha River (**Figure 5D**). As seen in the graph, the Taoer River and Halaha River channels present near-linear profiles, indicating that the two rivers are in a quasiequilibrium state, coinciding with the hypsometric analysis results. The *HI* value of the Taoer River is 0.29 and that of the Halaha River is 0.26. However, the χ value of the Taoer River is less than that of the Halaha River on the same elevation. According to Willett et al (2014), channel χ values can predict divide migration. When there is a difference in χ values on both sides of a divide, a difference in erosion occurs on both sides, and the side with a small value has a high erosion rate, forcing the divide migrate to the other side (Willett et al., 2014; Yang et al., 2015; Beeson et al., 2017; Mudd, 2017). Therefore, the main divide in the middle and south sections of the Greater Khingan Mountains is unstable and will migrate westward.

Erosion Rates in the Greater Khingan Mountains

Basin-averaged erosion rates calculated based on ^{10}Be concentrations in our study are from 8.48 ± 0.78 to 16.90 ± 2.31 mm/kyr, with a slight difference between basins (**Table 1**; **Figure 6**). The 12 basins are mostly distributed in the middle and to the north of the Greater Khingan Mountains, including 8 basins in the western flank, with an average erosion rate of 13.33 mm/kyr, and 4 basins in the eastern flank, with an average erosion rate of 15.63 mm/kyr. Our results revealed that the basin-averaged erosion rates of the eastern flank of the Greater Khingan Mountains are slightly higher than that of the western flank.

We interpolated the erosion rates and channel steepness for the catchments on both sides of the Greater Khingan Mountains. **Figure 7** shows a positive correlation between the erosion rates and channel steepness.

Probable Drivers of Divide Migration

The present geomorphic form is the result of the interaction of internal and external geological forces in various geological historical periods. Two phases of topographic evolution in the Greater Khingan Mountains existed since the Cenozoic, especially the early period of the Late Pleistocene and the late

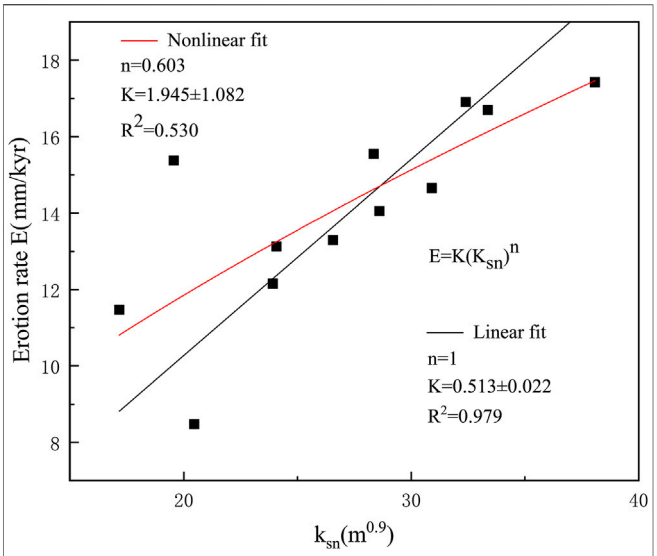

FIGURE 7 | Linear and nonlinear fitting between catchment-averaged erosion rates (*y*-axis) and steepness indices (*x*-axis). The results of fitting indicate a better relevance in linear fitting than nonlinear fitting.

period of the Early Pleistocene tectonic uplift shape the main landform of the Greater Khingan Mountains today. (Geology and Mineral Resources Bureau of Inner Mongolia, 1991). During geomorphic evolution, climate and surface erosion cannot be ignored and have the same significance as tectonic movements in both intensity and quantity. In this study, the geomorphic evolution stage of the Greater Khingan Mountains is in a pereplain (old) stage according to the result of the hypsometry analysis. However, from the spatial distribution of the χ values, the main divide of the southern Greater Khingan Mountains is unsteady and will migrate westward. However, the models applied to tectonic research using these geomorphic parameters are imperfect. They cannot integrate tectonic activity, climate precipitation, lithologic characteristics, and many other factors and cannot distinguish the influence of varied factors on divide migration only from the current geomorphology finally formed (Chen et al., 2014). Therefore, based on topographic factors extracted from the Greater Khingan Mountains, this study comprehensively analyzed regional topographic characteristics, precipitation conditions, and lithologic characteristics to obtain the driving factors of the Greater Khingan Mountains divide migration.

Regional Terrain

To achieve regional terrain information in this study, based on DEM data to calculate the slope and local topographic relief (**Figures 8A,B**), the results showed no obvious change in the spatial distribution of the slope and local topographic relief in the eastern flank, slightly higher in the middle. The slope and local topographic relief of the western flank are high in the north and low in the south.

To further describe and compare the general topographic feature differences between the eastern and western flanks of the Greater Khingan Mountains as well as the northern, middle, and southern sections, two longitudinal swath profiles (50 km wide and 1,350 km long) and three transverse swath profiles (100 km wide and 600 km long) were established (**Figure 1**). For each swath profile, the minimum, mean, and maximum elevations were extracted in a

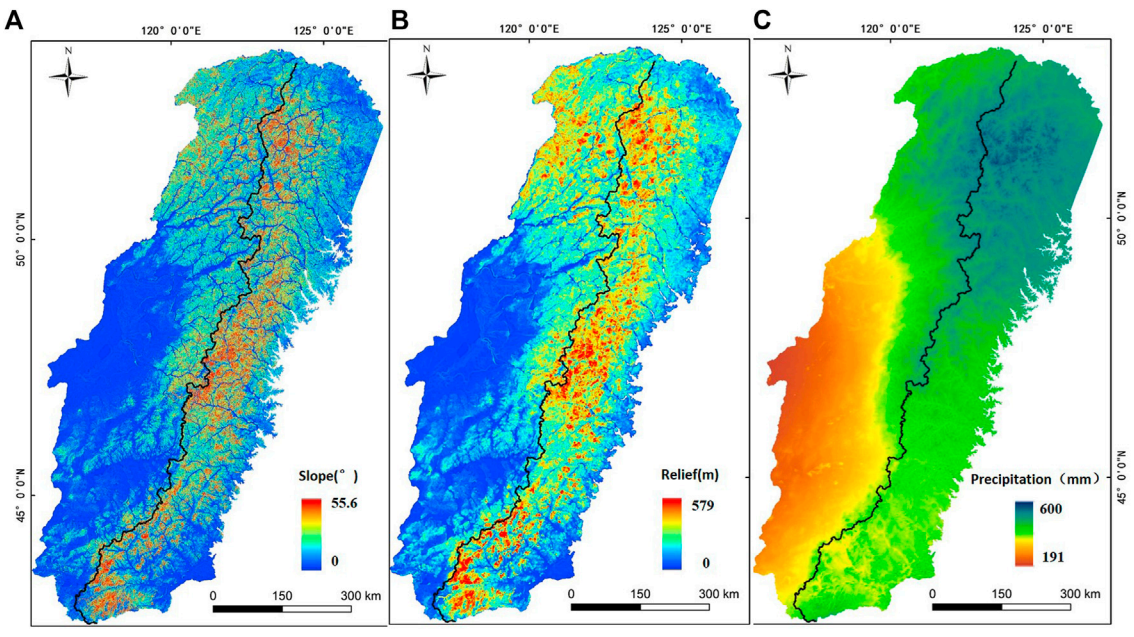

FIGURE 8 | Slope map of the Greater Khingan Mountains **(A)**. Local topographic relief map of the Greater Khingan Mountains **(B)**. Average annual rainfall map of the Greater Khingan Mountains **(C)**.

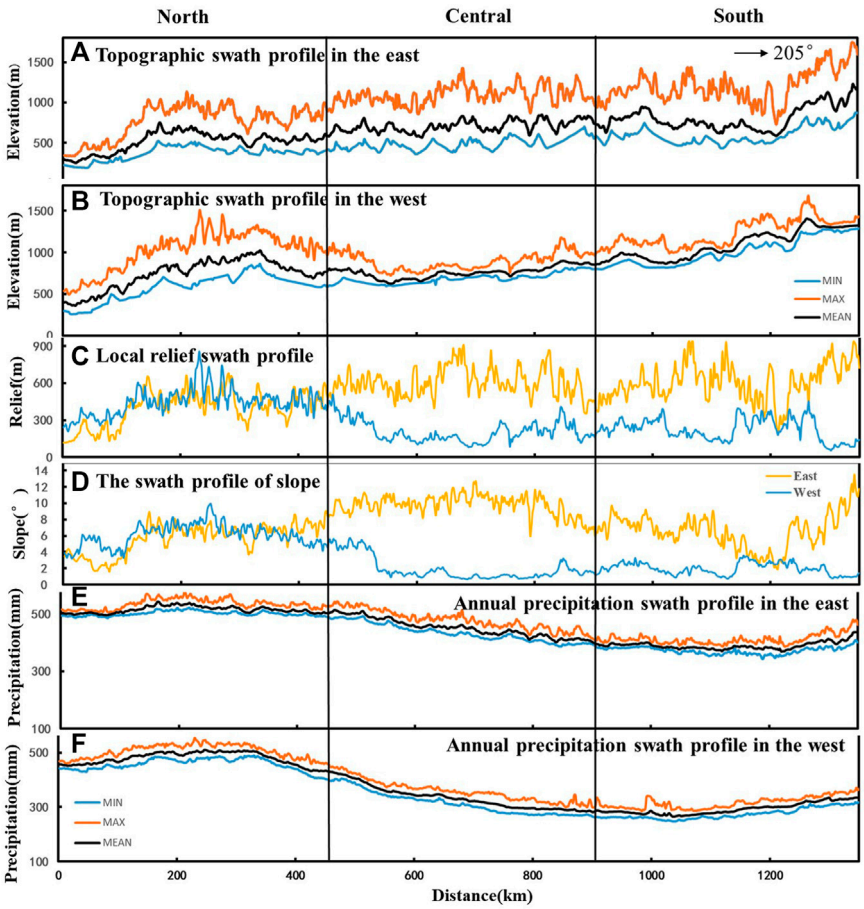

FIGURE 9 | The swath profile in the east of the Greater Khingan Mountains **(A)**. The swath profile in the west of the Greater Khingan Mountains **(B)**. The swath profile of local topographic relief in the Greater Khingan Mountains **(C)**. The swath profile of the slope in the Greater Khingan Mountains **(D)**. The swath profile of average annual rainfall in the east of the Greater Khingan Mountains **(E)**. The swath profile of average annual rainfall in the west of the Greater Khingan Mountains **(F)**.

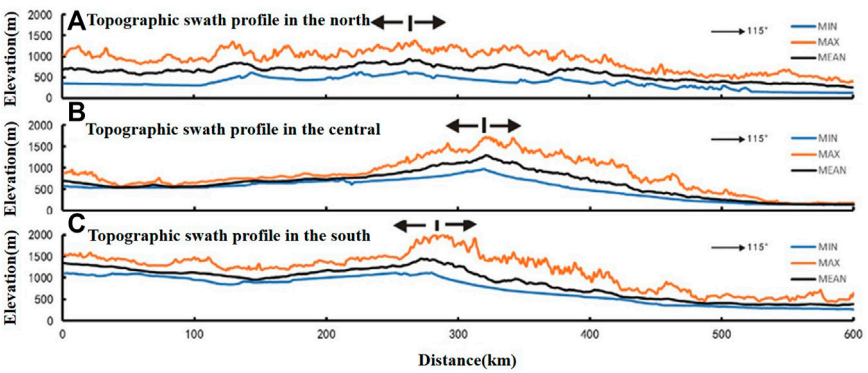

FIGURE10 | Transverse swath profiles across different segments of the Greater Khingan Mountains. The swath is 100 km wide and 600 km long. See **Figure 1** for locations. **(A)** North swath profile; **(B)** central swath profile; **(C)** south swath profile.

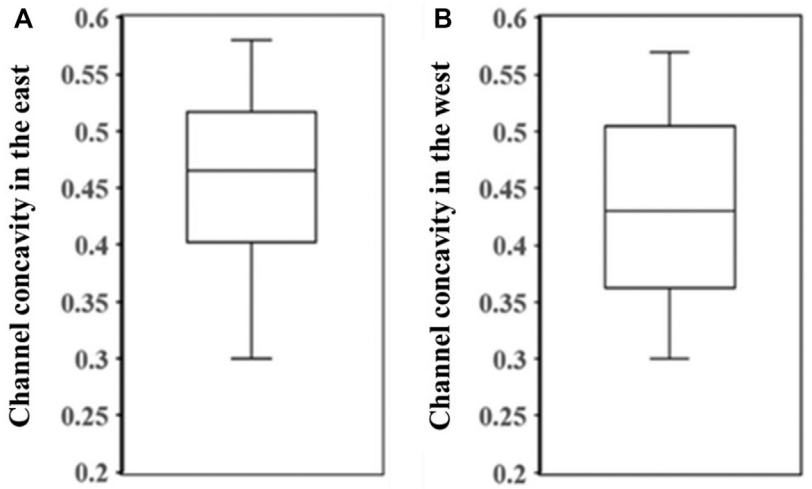

FIGURE 11 | Channel concavity index in the east of the Greater Khingan Mountains **(A)**. Channel concavity index in the west of the Greater Khingan Mountains **(B)**.

50 km-wide rectangular swath and projection in a vertical plane in the midline around the rectangular section (**Figures 9A,B**). Similarly, along the transverse swath profiles, within a 100-km-wide corridor with profile extraction minimum and average and maximum elevation (**Figure 10**). In the swath profile, the maximum elevation information represents the highest mountain summit of river erosion residue in the rectangular area, whereas the minimum elevation information represents the lowest river erosion residue in the rectangular area (Li et al., 2006; Zhang, 2006). The river cutting depth is the height difference between the highest peak elevation and the lowest riverbed left in the river erosion. The results showed that the three transverse swath profiles display a small topographic difference in the eastern flank in the northern section and no significant difference can be observed with respect to the depth of the river cutting between the two flanks. The topographic relief and river cutting depth of the eastern flank in the middle and southern sections are larger than those of the western flank. A quantitative comparison of the slope and local relief of the eastern and western flanks is presented in **Figures 9C,D**. The results showed that the slope of the eastern flank of the Greater Khingan Mountains ranges from 6° to 10°; the northern part is lower, whereas the southern part is slightly higher. The slope of the western flank is between 1° and 6°; the northern section is higher, whereas the southern section is significantly lower. The local topographic relief of the eastern flank of the Greater Khingan Mountains is approximately 600 m, the northern section is lower, and the middle and southern sections are slightly higher. The local topographic relief of the western flank is between 100 and 550 m, the northern section is higher, and the middle and southern sections are significantly lower.

Studies have shown that the average slope and local topographic relief predict the erosion rate in midlatitude basins. The mean slope, local topographic relief, and erosion rate have a linear relationship. Therefore, a higher local topographic relief and steeper slope might result in higher erosion (Ahnert, 1970; Safran et al., 2005; Pan et al., 2010). Although the basin erosion rate measured using cosmogenesis nuclide 10Be did not cover the entire study area, the correlation analysis between the average erosion rate of the 12 basins obtained and the average channel steepness index displayed a strong linear correlation (**Figure 7**). Therefore, the erosion rate of the 40 basins in the study area can be calculated according to the average channel steepness index of the basin (**Figure 6**). The spatial differences in the slope, topographic relief, and erosion rates of the Greater Khingan Mountains are consistent. The slope, topographic relief, and erosion rates in the middle and southern parts of the Greater Khingan Mountains are higher in the east and lower in the west. Furthermore, from the swath profiles, the southern river in the eastern flank has a lower local erosion base level (the river in the eastern flank from the north to the south into the Heilongjiang, Nenjiang, and Liaohe rivers). However, all rivers in the western flank into the Erguna River, the upstream of the Heilongjiang River. Nenjiang River, and Liaohe River flow from north to south, whereas the Erguna River flows in the opposite direction. Therefore, obvious differences are observed in the elevation of the rivers flowing into the main river from the eastern and western flanks of the same divide, causing higher erosion of the eastern flank in the middle and south sections.

Precipitation

Rivers are the most active geological external forces shaping the landform and changing the appearance of the earth. Precipitation conditions are related to the runoff of rivers, which can change the hydrological conditions and sediment supply of river basins and, therefore, the strength of river erosion capacity (Whipple, 2009; Chen et al., 2014). In this study, WorldClim2 data were used to characterize rainfall characteristics in the Greater Khingan Mountains and discuss its impact on divide migration. WorldClim2 is based on data from 9,000 to 60,000 weather stations from 1970 to 2000 using thin-plate splines. High-precision global precipitation and temperature data are interpolated using elevation, distance to the coast, and three covariables (maximum and minimum table temperatures and

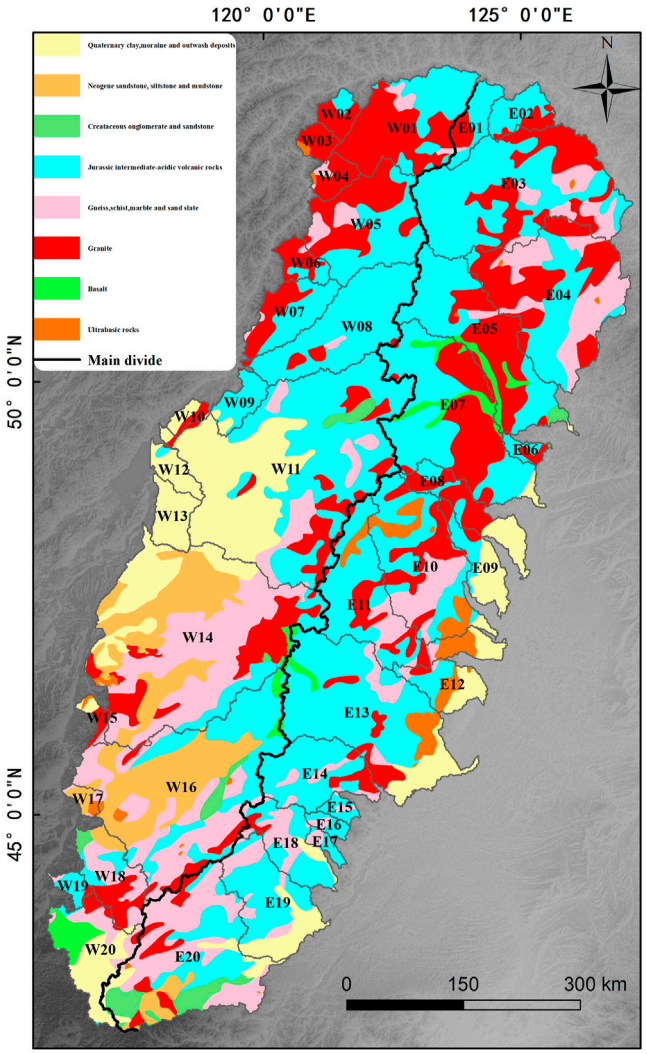

FIGURE 12 | Geological map of the Greater Khingan Mountains.

cloud cover) derived from satellites as variables, the highest spatial resolution meteorological data in the Greater Khingan Mountains currently (https://worldclim.org/; Ficka and Hijmans, 2017).

From **Figures 8C**, **9E**, **8F**, the average annual precipitation is high in the north and low in the south. No significant difference occurs in the average annual precipitation on the eastern and western flanks of the northern section, and the average precipitation is 450–600 mm/a. The average annual precipitation on the western flank of the middle and southern sections is significantly lower than that on the eastern flank. The average precipitation on the western flank of the middle and southern sections is 200–400 mm/a. The annual precipitation on the western flank of the southern section is 200–300 mm/a. The average precipitation on the eastern flank of the south–central section is 400–550 mm/a. Therefore, the main divide of the south–central section of the Greater Khingan Mountains coincides with the equal precipitation line of 400 mm. To the east of the divide is a semihumid monsoon climate zone, and to the west is a semiarid continental climate zone. This is consistent with the spatial distribution of the χ value. The annual average precipitation gradually reduced from the north to the south. The χ value gradually increased from the north to the south, and the average annual precipitation and χ value differences also increase gradually from the north to the south. The average annual precipitation is the dominant factor of different erosions across the divide in the middle and southern Greater Khingan Mountains. However, studies have highlighted that the change in precipitation in mountainous areas is positively correlated with river channel concavity, that is, channels with high erosion rates caused by different rates of precipitation often have high concavity (Bookhagen and Burbank, 2006; Zaprowski et al., 2005; Schlunegger et al., 2011). Our results show that the channel concave values on the eastern and western flanks of the Greater Khingan Mountains are similar without significant differences (**Figure 11**). Although there are significant differences in the precipitation on the eastern and western flanks of the Greater Khingan Mountains, the maximum precipitation on both flanks is no more than 600 mm/a, which is much smaller than the average annual precipitation observed in previous studies, such as in the Southern Himalayas, the Eastern Cordillera, and the eastern American high plains (Bookhagen & Burbank, 2006; Zaprowski et al., 2005; Schlunegger et al., 2011). We propose that the prerequisite for a positive correlation between channel concavity and precipitation is that precipitation in this region reaches above a threshold, although there is no exact value of this threshold in existing studies. Therefore, more abundant precipitation on the eastern flank of the middle and southern sections of the Greater Khingan Mountains promotes the westward migration. Because the Greater Khingan Mountains are in a tectonically stable region, tectonic may be the main factors influence the erosion, relief, and divide migration in early time, and precipitation has gradually become the main factor. In addition, precipitation is the current state, and it is difficult to recover the past climate conditions quantitatively, so the contribution of precipitation in a long time scale is not excluded.

Lithology

Under the same tectonic background and precipitation conditions, rocks with different mineral compositions have different erosion resistances. Due to the lack of measurements of the strength of various rock types in the field, we used rock types formed in different ages to discuss their influence on erosion rates. The strata in this study area include Precambrian metamorphic basal layers dominated by gneiss, granulite, and schist; Paleozoic shallow micrometamorphic volcanic sedimentary rock dominated by schist, sand-slate, marble, and andesite; and Mesozoic, Jurassic, and Cretaceous strata dominated by continental intermediate-acidic volcanic rocks and continental clastic rocks. Jurassic strata of the Mesozoic are the most widely outcropped, mainly distributed on both sides of the main ridge of the northern and the eastern flanks of the middle and southern sections of the Greater Khingan Mountains. The Cenozoic Neogene strata are mainly exposed in the western flank of the middle and southern sections, such as the Hailar Basin, and are scattered in other areas with semicemented clastic and basic volcanic rocks. The Quaternary strata are well developed in the region, mainly distributed in Xing'an, Zhelimu, and Hulunbuir. The lithology is dark clay, moraine–glacial sediments, and lacustrine strata dominated by red clay and subclay (Liu, 2004; Geology and Mineral Resources

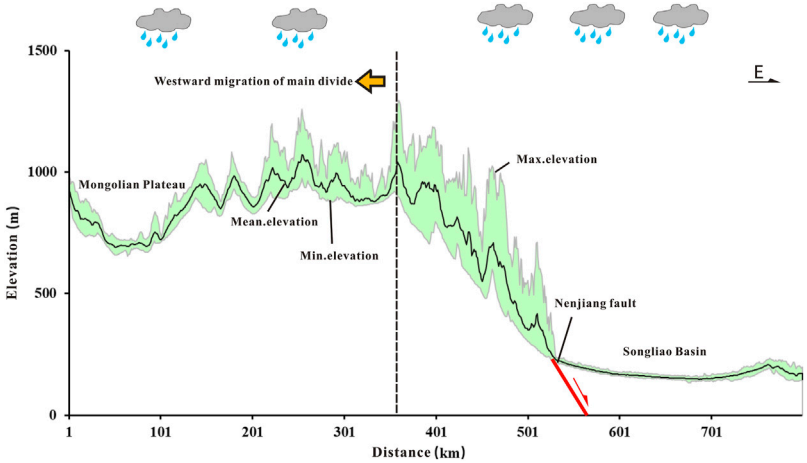

FIGURE 13 | The swath profile across the southern sections of the Greater Khingan Mountains demonstrate that the main divide migrated westward.

Bureau of Inner Mongolia, 1991; Li, 1996). Furthermore, strong magmatic activities occur in this study area, including the out outings of Xingkai, Caledonian, Varician, and Yanshanian rocks. Yanshanian and Hercynian granitic rocks are mainly distributed on the eastern and western flanks of the northern section, and the corresponding ultramafic rocks are scattered in the area (**Figure 12**).

To discuss the influence of lithologic characteristics on divide migration, we focused on analyzing the lithologic characteristics of the area using the largest χ difference between the two sides of the middle and southern divides (**Figure 5A**). In this region, no significant spatial change occurs in the χ values of the eastern flank but the lithology changes. For example, the E13 basin is mainly Jurassic medium acidic volcanic rocks, whereas the E10 and E11 basins are not only Jurassic medium acidic volcanic rocks but also pre-Mesozoic strata and granites. In the E13 and W16 basins on both sides of the divide, the χ value of the E13 basin on the east side is significantly lower than that of the W16 basin on the west side; however, the lithology of the W16 basin is not only Jurassic medium acidic volcanic rocks but also Neozoic semicemented clastic and basic volcanic rocks. From the analysis of mineral stability, the erosion resistance of basic volcanic rocks is weaker than that of medium acidic volcanic rocks. However, the semicemented clastic rocks have a young sedimentary age, loose rock cementation, and low erosion resistance. If the lithologic characteristics of the region are the main factors affecting the erosion rate, the χ value of the eastern basin should be significantly higher than that of the western basin; however, it is the opposite. This phenomenon indicates that lithology is not the main factor controlling the χ values but other factors control the migration of the divide in the middle and southern sections of the Greater Khingan Mountains.

In conclusion, the divide migration in the middle and southern Greater Khingan Mountains is mainly controlled by topography, especially slope and local topographic relief, whereas precipitation conditions push and promote the divide migration. No obvious evidence that bedrock lithology significantly affects the divide migration exists. The terrain is mainly formed by tectonic uplift, although, based on the results of the hypsometric curve and HI index, the Greater Khingan Mountains of today's structure is relatively stable. However, the development of a river terrace series and an uplifting amplitude survey study shows that the eastern flank of the Greater Khingan Mountains in the southern uplift earlier and at a greater rate than the western flank in the Pleistocene (Chen, 2012; Wu, 2013). This is due to the different response times of different elements in the basin to the change in the uplift rate; furthermore, the channel profile is the most sensitive, which is used to detect the impact of tectonic uplifts on geomorphology at the Holocene scale. Slope, divide, and the watershed area are the next factors most sensitive to the uplift rate (Duvall et al., 2004; Whipple et al., 2007; Burbank&Anderson, 2011; Beeson et al., 2017; Pan, 2019). Therefore, although the geomorphic evolution stage of the Greater Khingan Mountains is in a pereplain (old) stage, the divide of the midsouthern sections will continue to migrate westward until it reaches equilibrium (**Figure 13**).

CONCLUSION

Based on the DEM-based topographic analysis and ^{10}Be basin-averaged erosion rate measurement results of the Greater Khingan Mountains, we have reached the following conclusions.

i) The geomorphic evolution stage of the Greater Khingan Mountains is in a pereplain (old) stage. The tectonic activity of this area is stable, and there is no obvious difference between the eastern and western flanks.
ii) The spatial distribution of χ values is generally higher in the west flank and low in the east flank and high in the south and low in the north in case of the western flank, indicating that the river system in the Greater Khingan Mountains has not been adjusted to achieve equilibrium; further, the main divide in the middle and south sections will migrate westward slowly.
iii) The slow westward divide migration is probably in response to the faster uplift rate at the eastern flank during the

Pleistocene, and plentiful rainfall is a contributing factor now.

DATA AVAILABILITY STATEMENT

The original contributions presented in the study are included in the article/Supplementary Material, further inquiries can be directed to the corresponding author.

AUTHOR CONTRIBUTIONS

All authors listed have made a substantial, direct, and intellectual contribution to the work and approved it for publication.

FUNDING

This work was jointly supported by National Natural Science Foundation of China (No. 41888101), the Second Tibetan Plateau Scientific Expeditionand Research (STEP) (2019QZKK0704), Fundamental Research Funds for the Central Universities (ZY20215147).

ACKNOWLEDGMENTS

We gratefully acknowledge the guidance of Doctor Li Zhang and Jiangying Wu for ^{10}Be experiment at the Xi'an Accelerator Mass Spectrometry (AMS) Center, China. We gratefully acknowledge editors and two reviewers provide many valuable advices for our paper.

REFERENCES

Ahnert, F. (1970). Functional Relationships between Denudation, Relief, and Uplift in Large, Mid-latitude Drainage Basins. *Am. J. Sci.* 268 (3), 243–263. doi:10.2475/ajs.268.3.243

Beeson, H. W., McCoy, S. W., and Keen-Zebert, A. (2017). Geometric Disequilibrium of River Basins Produces Long-Lived Transient Landscapes. *Earth Planet. Sci. Lett.* 475, 34–43. doi:10.1016/j.epsl.2017.07.010

Bookhagen, B., and Burbank, D. W. (2006). Correction to "Topography, Relief, and TRMM-Derived Rainfall Variations along the Himalaya". *Geophys. Res. Lett.* 33 (8), 153–172. doi:10.1029/2006GL026944

Borchers, B., Marrero, S., Balco, G., Caffee, M., Goehring, B., Lifton, N., et al. (2016). Geological Calibration of Spallation Production Rates in the Cronus-Earth Project. *Quat. Geochronol.* 31 (4), 188–198. doi:10.1016/j.quageo.2015.01.009

Burbank, D. W., and Anderson, R. S. (2011). *Tectonic Geomorphology*. Second Edition. Hoboken, New Jersey: A John Wiley & Sons, Ltd., Publication.

Chen, L. Z. (2012). *Neotectonism in Solon-Ulanhot Area*. Beijing: China University of Geosciences, 1–60. (in Chinese).

Chen, T., Zhang, H. P., and Wang, W. T. (2014). Topographic Variation along the Minddle-East Segment of Haiyuan Fault Zone and its Implications. *Seismology Geology.* 36 (2), 449–463. doi:10.3969/j.issn.0253-4967.2014.02.014

Chen, Y. (2008).*Morphotectonic Features of Taiwan Mountain Belt Based on Hypsometric Integral, Topographic Fractals and SL Index*. Tainan: The Doctor''s Degree Thesis of National Cheng Kung University, 1–84.

Chmeleff, J., von Blanckenburg, F., Kossert, K., and Jakob, D. (2010). Determination of the 10be Half-Life by Multicollector Icp-Ms and Liquid Scintillation Counting. *Nucl. Instr. Methods Phys. Res. Section B: Beam Interactions Mater. Atoms* 268 (2), 192–199. doi:10.1016/j.nimb.2009.09.012

Codilean, A. T. (2006). Calculation of the Cosmogenic Nuclide Production Topographic Shielding Scaling Factor for Large Areas Using Dems. *Earth Surf. Process. Landforms* 31 (6), 785–794. doi:10.1002/esp.1336

Corbett, L. B., Bierman, P. R., and Rood, D. H. (2016). An Approach for Optimizing *In Situ* Cosmogenic 10be Sample Preparation. *Quat. Geochronol.* 33, 24–34. doi:10.1016/j.quageo.2016.02.001

Davis, W. M. (1899). The Geographical Cycle. *Geographical J.* 14 (5), 481–504. doi:10.2307/1774538

Deffontaines, B., Lee, J.-C., Angelier, J., Carvalho, J., and Rudant, J.-P. (1994). New Geomorphic Data on the Active Taiwan Orogen: a Multisource Approach. *J. Geophys. Res.* 99, 20243–20266. doi:10.1029/94JB00733

Deffontains, B., Lacombe, O., Angelier, J., Chu, H. T., Mouthereau, F., Lee, J. C., et al. (1997). Quaternary Transfer Faulting in the Taiwan Foothills: Evidence from a Multisource Approach. *Tectonophysics* 274, 61–82. doi:10.1016/S0040-1951(96)00298-3

Deng, Q. D., Zhang, P. Z., Ren, Y. K., Yang, X. P., Min, W., and Chen, L. C. (2003). Active Tectonics and Earthquake Activities in china. *Earth Sci. Front.* 10 (U08), 66–73.

Deng, Q. D., Zhang, P. Z., Ren, Y. K., Yang, X. P., Min, W., and Chu, J. Z. (2002). Basic Features of Active Structure in China. *Sci. China Ser. D-Earth* 32 (012), 1020–1030. (in Chinese). doi:10.3321/j.issn:1006-9267.2002.12.007

Dong, G., Huang, F., Yi, C., Liu, X., Zhou, W., and Caffee, M. W. (20162016). Mid-late Pleistocene Glacial Evolution in the Grove Mountains, East Antarctica, Constraints from Cosmogenic 10Be Surface Exposure Dating of Glacial Erratic Cobbles. *Quat. Sci. Rev.* 145, 71–81. doi:10.1016/j.quascirev.2016.05.030

Dong, G., Zhou, W., Yi, C., Zhang, L., Li, M., Fu, Y., et al. (2017). Cosmogenic 10Be Surface Exposure Dating of 'Little Ice Age' Glacial Events in the Mount Jaggang Area, central Tibet. *The Holocene* 27 (10), 1516–1525. doi:10.1177/0959683617693895

Duvall, A., Kirby, E., and Burbank, D. (2004). Tectonic and Lithologic Controls on Bedrock Channel Profiles and Processes in Coastal California. *J. Geophys. Res.* 109 (F3), F03002. doi:10.1029/2003JF000086

Fang, S., Liu, Z. J., Huang, X. T., Guo, W., and Liu, Z. Q. (2008). Uplift and Topography Evolution Research at FT in Cenozoic of South-Eastern Slope of Daxing'anling Mountains. *J. Jinlin University(Earth Sci. Edition)* (05), 771–776. doi:10.3969/j.issn.1671-5888.2008.05.009

Farhan, Y., Elgaziri, A., Elmaji, I., and Ali, I. (2016). Hypsometric Analysis of Wadi Mujib-Wala Watershed (Southern jordan) Using Remote Sensing and Gis Techniques. *Ijg* 07 (2), 158–176. doi:10.4236/ijg.2016.72013

Fick, S. E., and Hijmans, R. J. (2017). WorldClim 2: New 1-km Spatial Resolution Climate Surfaces for Global Land Areas. *Int. J. Climatol* 37, 4302–4315. doi:10.1002/joc.5086

Flint, J. J. (1974). Stream Gradient as a Function of Order, Magnitude, and Discharge. *Water Resour. Res.* 10 (5), 969–973. doi:10.1029/WR010i005p00969

Gallen, S. F., Wegmann, K. W., Frankel, K. L., Hughes, S., Lewis, R. Q., Lyons, N., et al. (2011). Hillslope Response to Knickpoint Migration in the Southern Appalachians: Implications for the Evolution of post-orogenic Landscapes. *Earth Surf. Process. Landforms* 36 (9), 1254–1267. doi:10.1002/esp.2150

Gallen, S. F., and Wegmann, K. W. (2017). River Profile Response to normal Fault Growth and Linkage: an Example from the Hellenic Forearc of South-central crete, greece. *Earth Surf. Dynam.* 5, 161–186. doi:10.5194/esurf-5-161-2017

Geology and Mineral Resources Bureau of Inner Mongolia (1991). *Regional Geology of Inner Mongolia*. Beijing: Geological Publishing House, 189–223. (in Chinese).

Gosse, J. C., and Phillips, F. M. (2001). Terrestrial *In Situ* Cosmogenic Nuclides: Theory and Application. *Quat. Sci. Rev.* 20 (14), 1475–1560. doi:10.1016/S0277-3791(00)00171-2

Granger, D. E., and Schaller, M. (2014). Cosmogenic Nuclides and Erosion at the Watershed Scale. *Elements* 10 (5), 369–373. doi:10.2113/gselements.10.5.369

He, C., Rao, G., Yang, R., Hu, J., Yao, Q., and Yang, C.-J. (2019). Divide Migration in Response to Asymmetric Uplift: Insights from the Wula Shan Horst, north china. *Geomorphology* 339 (AUG.15), 44–57. doi:10.1016/j.geomorph.2019.04.024

Howard, A. D., and Kerby, G. (1983). Channel Changes in Badlands. *Geol. Soc. America Bull.* 94 (6), 739–752. doi:10.1130/0016-7606(1983)94<739:ccib>2.0.co;2

Hu, K., Fang, X., Ferrier, K. L., Granger, D. E., Zhao, Z., and Ruetenik, G. A. (2021). Covariation of Cross-divide Differences in Denudation Rate and χ: Implications for Drainage basin Reorganization in the Qilian Shan, Northeast Tibet. *Earth Planet. Sci. Lett.* 562, 116812. doi:10.1016/j.epsl.2021.116812

Hu, X. F., Pan, B. T., Kirby, E., Li, Q. Y., Geng, H. P., and Chen, J. F. (2010). Spatial Differences in Rock Uplift Rates Inferred from Channel Steepness Indices along the Northern Flank of the Qilian Mountain, Northeast Tibetan Plateau. *Chin. Sci. Bull.* (23), 2329–2338. doi:10.1007/s11434-010-4024-4

Johnson, B. (2020). Stream Capture and the Geomorphic Evolution of the Linville Gorge in the Southern Appalachians, USA. *Geomorphology* 368, 107360. doi:10.1016/j.geomorph.2020.107360

Kirby, E., Whipple, K. X., Tang, W., and Chen, Z. (2003). Distribution of Active Rock Uplift along the Eastern Margin of the Tibetan Plateau: Inferences from Bedrock Channel Longitudinal Profiles. *J. Geophys. Res.* 108 (B4), 2217. doi:10.1029/2001JB000861

Kühni, A., and Pfiffner, O. (2001). The Relief of the Swiss Alps and Adjacent Areas and its Relation to Lithology and Structure: Topographic Analysis from a 250-m DEM. *Geomorphology* 41 (4), 285–307. doi:10.1016/S0169-555X(01)00060-5

Lal, D. (1991). Cosmic ray Labeling of Erosion Surfaces: *In Situ* Nuclide Production Rates and Erosion Models. *Earth Planet. Sci. Lett.* 104 (91), 424–439. doi:10.1016/0012-821X(91)90220-CLi

Li, S. C. (2012). *Study on the Triassic-Jurassic Tectonic Evolution of the Middle Great Xing'an Range*. Beijing: Chinese Academy of Geological Science, 1–112.

Li, W. G. (1996). *Rock Strata in Inner Mongolia*. Beijing: China University of Geosciences Press, 1–344.

Li, Y., Densmore, A. L., Zhou, R. J., Ellis, M. A., Zhang, Y., and Li, B. (2006). Profiles of Digital Elevation Models(DEM) Crossing the Eastern Margin of the Tibetan Plateau and the Irconstra Intson Dissection Depths and Incision Rates of Late Cenizoic Ricers. *Quat. Sci.* 026 (002), 236–243. doi:10.3321/j.issn:1001-7410.2006.02.011

Liu, J., Ding, L., Zeng, L. S., Tapponnier, P., and Gaudemer, Y. (2006). Large-scale Terrain Analysis of Selected Regions of the Tibetan plateau:Discussion on the Origin of Plateau Planation Surface. *Earth Sci. Front.* 13 (5), 285–299. doi:10.3321/j.issn:1005-2321.2006.05.002

Liu, J. M., Zhang, R., and Zhang, Q. Z. (2004). The regional metallogeny of da hinggan ling,china. *Earth Sci. Front.* (01), 269–277. doi:10.3321/j.issn:1005-2321.2004.01.024

Liu-zeng, J., Zhang, J., Ge, Y., Wang, W., Zeng, L., Gen, L., et al. (2018). Tectonic Geomorphology: An Interdisciplinary Study of the Interaction Among Tectonic Climatic and Surface Processes. *Chin. Sci. Bull.* 63 (30), 3070–3088. doi:10.1360/N972018-00498

Lv, H. H., Zhang, T. Q., Chang, Y. C., Wang, W., Zhou, Z. Y., and Zhang, X. M. (2014). Timing of Paleotopogarphic and Geomorphologic Evolution and Paleotopogarphic Recinstruction by Low-Temperature Thernochronologic Approaches. *Mar. Geology&Quaternary Geology.* 34 (03), 175–183. doi:10.3724/SP.J.1140.2014.03175

Ma, Z., Peng, T., Feng, Z., Li, M., Li, X., Guo, B., et al. (2019). Asymmetrical River Valleys and Their Tectonic Significance in the Maxianshan Area, Ne Tibetan Plateau. *Geomorphology* 329 (MAR.15), 70–80. doi:10.1016/j.geomorph.2019.01.001

Marrero, S. M., Phillips, F. M., Borchers, B., Lifton, N., Aumer, R., and Balco, G. (2016). Cosmogenic Nuclide Systematics and the Cronuscalc Program. *Quat. Geochronol.* 31, 160–187. doi:10.1016/j.quageo.2015.09.005

Miller, S. R., Sak, P. B., Kirby, E., and Bierman, P. R. (2013). Neogene Rejuvenation of central Appalachian Topography: Evidence for Differential Rock Uplift from Stream Profiles and Erosion Rates. *Earth Planet. Sci. Lett.* 369-370, 1–12. doi:10.1016/j.epsl.2013.04.007

Molnar, P., and England, P. (1990). Late Cenozoic Uplift of Mountain Ranges and Global Climate Change: Chicken or Egg? *Nature* 346, 29–34. doi:10.1038/346029a0

Mudd, S. M. (2017). Detection of Transience in Eroding Landscapes. *Earth Surf. Process. Landforms* 42, 24–41. doi:10.1002/esp.3923

Norton, K. P., Norton, K. P., and Zeilinger, G. (2011). Climatic Forcing on Channel Profiles in the Eastern Cordillera of the Coroico Region, Bolivia. *J. Geology.* 119, 97–107. doi:10.1086/657407

Pan, B.-t., Geng, H.-p., Hu, X.-f., Sun, R.-h., and Wang, C. (2010). The Topographic Controls on the Decadal-Scale Erosion Rates in Qilian Shan Mountains, N.W. China. *Earth Planet. Sci. Lett.* 292 (1-2), 148–157. doi:10.1016/j.epsl.2010.01.030

Pan, X. M. (2019). *The River Reorganization Based on the Topographic Metrics and Modeling in the central Northern Qilian Mountain*. Lanzhou: Lan zhou Univesity, 1–52.

Pérez-Peña, J. V., Azañón, J. M., and Azor, A. (2009). CalHypso: An ArcGIS Extension to Calculate Hypsometric Curves and Their Statistical Moments. Applications to Drainage basin Analysis in SE Spain. *Comput. Geosciences* 35 (6), 1214–1223. doi:10.1016/j.cageo.2008.06.006

Perron, J. T., and Royden, L. (2013). An Integral Approach to Bedrock River Profile Analysis. *Earth Surf. Process. Landforms* 38 (6), 570–576. doi:10.1002/esp.3302

Qian, C., Cui, T. R., Li, L. C., Chen, H. T., Qin, T., and Lu, L. (2013). Application of Aster-GDEM Data in the Geomorphic Characteristics Analysis of Northern Great Hinggnan Ling Mountains. *J. Geomechanics* 19 (01), 82–92. doi:10.3969/j.issn.1006-6616.2013.01.009

Safran, E. B., Bierman, P. R., Aalto, R., Dunne, T., Whipple, K. X., and Caffee, M. (2005). Erosion Rates Driven by Channel Network Incision in the Bolivian andes. *Earth Surf. Process. Landforms* 30 (8), 1007–1024. doi:10.1002/esp.1259

Scharf, T. E., Codilean, A. T., de Wit, M., Jansen, J. D., and Kubik, P. W. (2013). Strong Rocks Sustain Ancient Postorogenic Topography in Southern Africa. *Geology* 41 (3), 331–334. doi:10.1130/G33806.1

Snyder, N. P., and Whipple, K. X. (2000). Landscape Response to Tectonic Forcing: Digital Elevation Model Analysis of Stream Profiles in the mendocino Triple junction Region, Northern california. *Geol. Soc. America Bull.* 112 (8). doi:10.1130/0016-7606(2000)112<1250:lrttfd>2.0.co;2

Stone, J. O., and John, O. (2000). Air Pressure and Cosmogenic Isotope Production. *J. Geophys. Res.* 105 (B10), 23753–23759. doi:10.1029/2000JB900181

Strahler, A. N. (1952). Hypsometric (Area-Altitude) Analysis of Erosional Topography. *Geol. Soc. America Bull.* 63 (11), 1117. doi:10.1130/0016-7606(1952)63[1117:haaoet]2.0.co;2

Su, Q., Xie, H., Yuan, D.-Y., and Zhang, H.-P. (2017). Along-strike Topographic Variation of Qinghai Nanshan and its Significance for Landscape Evolution in the Northeastern Tibetan Plateau. *J. Asian Earth Sci.* 147 (oct.1), 226–239. doi:10.1016/j.jseaes.2017.07.019

Su, Q., Yuan, D. Y., and Xie, H. (2016). Geomorphic Features of the Heihe River Drainage basin in Western Qilian Shan-Hexi Corridor and its Tectonic Implications. *Seismology Geology.* 38 (2), 560–581. doi:10.3969/j.issn.0253-4967.2016.03.005

Su, Q., Yuan, D. Y., Xie, H., and Shao, Y. X. (2015). Geomorphic Features of the Danghe River Drainage basin in Western Qilian Shan Mountain and its Tectonic Implications. *Quat. Sci.* 35 (1), 48–59. doi:10.11928/j.issn.1001-7410.2015.01.05

Vermeesch, P. (2007). CosmoCalc: An Excel Add-In for Cosmogenic Nuclide Calculations. *Geochem. Geophys. Geosyst.* 8, Q08003. doi:10.1029/2006GC001530

Wang, Q., Wang, R., Zhang, B., Zhang, S., Zheng, Y., and Wang, Z. (2013). Small Organic Molecules Targeting PCAF Bromodomain as Potent Inhibitors of HIV-1 Replication. *Med. Chem. Commun.* 4 (4), 737–745. doi:10.1039/c3md20376j

Whipple, K. X. (2009). The Influence of Climate on the Tectonic Evolution of Mountain Belts. *Nat. Geosci* 2, 97–104. doi:10.1038/ngeo413

Whipple, K. X., and Tucker, G. E. (1999). Dynamics of the Stream-Power River Incision Model: Implications for Height Limits of Mountain Ranges, Landscape Response Timescales, and Research Needs. *J. Geophys. Res.* 104 (B8), 17661–17674. doi:10.1029/1999JB900120

Whipple, K. X., Wobus, C., Crosby, B., Kirby, E., and Sheehan, D. (2007). *New Tools for Quantitative Geomorphology: Extraction and Interpretation of Stream Profiles from Digital Topographic Data*. Boulder, CO: Geological Society of America, Annual Meeting, Short Course Guide. Available at: http://www.geomorphtools.org.

Willett, S. D., Hovius, N., Brandon, M. T., and Fisher, D. (2006). *Tectonics, Climate, and Landscape Evolution*. Boulder, USA: Geological Society of America, 398. doi:10.1130/SPE398

Willett, S. D., Mccoy, S. W., Perron, J. T., Goren, L., and Chen, C.-Y. (2014). Dynamic Reorganization of River Basins. *Science* 343 (6175), 1248765. doi:10.1126/science.1248765

Wu, X. M. (2013). *The Sdudy on Neotactonism and Uplift Mechanism of the Weaern Slope in the Middle South Segment of the Daxinganling*. Beijing: China University of Geosciences, 1–60.

Xiang, T. T. (2014). *Studying on Process of Erosion-Deposition on Eastern Slope of Great Khingan and its Indicative Significance*. Changchun: Jilin Univesity, 1–48.

Yang, J., Zheng, W., Wang, Y., Bi, H., Zhang, D., Zhang, P., et al. (2020). Quantitative Geomorphological Constraints on the Landform Evolution of the Current Active Boundary of the Northeastern Tibetan Plateau. *Geomorphology* 358, 107120. doi:10.1016/j.geomorph.2020.107120

Yang, R., Suhail, H. A., Gourbet, L., Willett, S. D., Fellin, M. G., Lin, X., et al. (2020). Early Pleistocene Drainage Pattern Changes in Eastern Tibet: Constraints from Provenance Analysis, Thermochronometry, and Numerical Modeling. *Earth Planet. Sci. Lett.* 531, 115955. doi:10.1016/j.epsl.2019.115955

Yang, R., Willett, S. D., and Goren, L. (2015). *In Situ* low-relief Landscape Formation as a Result of River Network Disruption. *Nature* 520 (7548), 526–529. doi:10.1038/nature14354

Yin, X. H., Shi, Z. H., Liu, Z. B., and Zhang, Y. M. (1980). The Basic Features of Reginal Gravity Field in Chinese Continent[J]. *Seismology Geology*. (04), 69–75. doi:10.3724/SP.J.1246.2011.00001

Zaprowski, B. J., Pazzaglia, F. J., and Evenson, E. B. (2005). Climatic Influences on Profile Concavity and River Incision. *J. Geophys. Res.* 110 (F3). doi:10.1029/2004JF000138

Zhang, H.-p., Zhang, P.-z., Kirby, E., Yin, J.-h., Liu, C.-r., and Yu, G.-h. (2011). Along-strike Topographic Variation of the Longmen Shan and its Significance for Landscape Evolution along the Eastern Tibetan Plateau. *J. Asian Earth Sci.* 40 (4), 855–864. doi:10.1016/j.jseaes.2010.05.015

Zhang, H. P. (2006). *Study on the Cenozoic Geomorphic Processes of Typical Regions along the Eastern and Northeastern Tibetan Margins*. Beijing: China University of Geosciences, 1–71.

Zhang, H. P., Zhang, P. Z., Wu, Q. L., and Chen, Z. L. (2008). Characteristics of the Huanghe River Longitudinal Profiles Around Xunhua-Guide Area(NE Tibet) and Their Tectonic Significance. *Quat. Sci.* 28 (2), 299–309. doi:10.3321/j.issn:1001-7410.2008.02.012

Zhang, L., Wu, Z. K., Song, S. H., Chang, H., and Zhao, G. Q. (2012). Extraction and Purification of Quartz for *In Situ* Cosmogenic Nuclide Exposure Dating. *Rock Mineral. Anal.* 31 (5), 780–787. doi:10.3969/j.issn.0254-5357.2012.05.005

Zhang, L., Zhou, W. J., Chang, H., Zhao, G. Q., Song, S. H., and Wu, Z. K. (2012). Extraction of *In-Situ* 10 Be and 26 Al from Rock Sample and Accelerator Mass Spectrometric Measurements. *Rock Miner. Anal.* 31 (1), 83–89. doi:10.15898/j.cnki.11-2131/td.2012.01.001

Zhang, P. Z., Deng, Q. D., Zhang, G. M., Ma, J., Gan, W. J., and Min, W. (2003). Strong Earthquake Activities and Active Blocks in Mainland China. *Sci. China Ser. D-Earth* (S1), 12–20. doi:10.3321/j.issn:1006-9267.2003.z1.002

Zhang, P. Z., Wang, Q., and Ma, Z. J. (2002). GPS Velocity Field and Active Crustal Blocks of Contemporary Tectonic Deformation in continental China. *Earth Sci. Front.* 9 (2), 430–441. doi:10.3321/j.issn:1005-2321.2002.02.022

Conflict of Interest: The authors declare that the research was conducted in the absence of any commercial or financial relationships that could be construed as a potential conflict of interest.

Publisher's Note: All claims expressed in this article are solely those of the authors and do not necessarily represent those of their affiliated organizations, or those of the publisher, the editors and the reviewers. Any product that may be evaluated in this article, or claim that may be made by its manufacturer, is not guaranteed or endorsed by the publisher.

Copyright © 2021 Lin, Li and Ma. This is an open-access article distributed under the terms of the Creative Commons Attribution License (CC BY). The use, distribution or reproduction in other forums is permitted, provided the original author(s) and the copyright owner(s) are credited and that the original publication in this journal is cited, in accordance with accepted academic practice. No use, distribution or reproduction is permitted which does not comply with these terms.

frontiers in Earth Science

ORIGINAL RESEARCH
published: 09 December 2021
doi: 10.3389/feart.2021.792504

Drainage Development in the Dunhuang Basin, NE Tibet, Controlled by Multi-Segment Fault Growth

Gan Chen[1,2,3], *Wenjun Zheng*[1,2,3]*, *Jingjun Yang*[1,2,3], *Lei Duan*[1,2,3], *Shumin Liang*[1,2,3], *Zhigang Li*[1,2,3], *Dongli Zhang*[1,2,3] and *Jianguo Xiong*[3]

[1]Guangdong Provincial Key Laboratory of Geodynamics and Geohazards, School of Earth Sciences and Engineering, Sun Yat-Sen University, Guangzhou, China, [2]Southern Marine Science and Engineering Guangdong Laboratory (Zhuhai), Zhuhai, China, [3]State Key Laboratory of Earthquake Dynamics, Institute of Geology, China Earthquake Administration, Beijing, China

The Dongbatu Shan (DBTS, also known as the Nanjie Shan), which interrupts the northern Tibetan foreland in the Dunhuang basin, is an active anticline. It has accommodated the northwestern growth of the eastern Altyn Tagh fault system (ATF). Although several thrust faults have been identified around the DBTS, their evolution history and influence on regional landscape have received little attention during the late-Quaternary. In this study, several geomorphic methods are used to investigate the interaction between drainage development and tectonic movement around DBTS. Based on high-resolution satellite images, field investigation, and cosmogenic nuclide ^{10}Be dating method, the fluvial landform sequences around DBTS were constructed. Using quantitative geomorphology methods including landscape relief profile, asymmetry factor (AF), and transverse topographic symmetry factor (T), we hypothesize that drainage deflection is controlled by multi-segment fault growth. Combining the results of the above-mentioned methods, we propose that Yulin He, flowing across the DBTS, had gone through several abandonments since the late mid-Pleistocene due to the lateral propagation of DBTS. Affected by the discharge of channel and multi-segment fault growth, our research confirms that the direction of river abandonment may have decoupled with the mountain range propagation trend. Based on the chronology dating, the DBTS has gone through two severe uplifts since ~208 ka and the shortening rate across the central DBTS is constrained to be ~1.47 mm/yr since ~83 ka. Given the fact that thrust faults are widely developed around DBTS, we propose that the flower-like structure formed by the northward growth of the eastern ATF could better explain the development of the secondary subparallel faults.

Keywords: drainage development, fault lateral growth, air gap, Dongbatu Shan (Nanjie Shan), Altyn Tagh fault

OPEN ACCESS

Edited by:
Rong Yang,
Zhejiang University, China

Reviewed by:
Gang Rao,
Southwest Petroleum University, China
Haopeng Geng,
Lanzhou University, China

***Correspondence:**
Wenjun Zheng
zhengwenjun@mail.sysu.edu.cn

Specialty section:
This article was submitted to Quaternary Science, Geomorphology and Paleoenvironment, a section of the journal Frontiers in Earth Science

Received: *10 October 2021*
Accepted: *18 November 2021*
Published: *09 December 2021*

Citation:
Chen G, Zheng W, Yang J, Duan L, Liang S, Li Z, Zhang D and Xiong J (2021) Drainage Development in the Dunhuang Basin, NE Tibet, Controlled by Multi-Segment Fault Growth. Front. Earth Sci. 9:792504. doi: 10.3389/feart.2021.792504

INTRODUCTION

The mechanism and kinematics of mountain ranges controlled by fault lateral growth had been a major concern for researchers due to their implications on seismic hazards and hydrocarbon reservoirs (Hetzel et al., 2004; Lacombe et al., 2007; Ramsey et al., 2008; Bretis et al., 2011; Ellis and Barnes, 2015). Drainage networks are sensitive to the surface slope and thus have been used to quantify how tectonic movement controls landform evolution (Keller et al., 1998; Ramsey et al., 2008;

Keller and DeVecchio, 2013). Six landscape criteria were proposed as indications of the propagation of fault-related folds developing above active faults by Keller et al., 1999. Follow-on research suggests that three criteria among them provide the strongest evidence: 1) deformation of progressively younger landforms (Jackson et al., 2002; Bennett et al., 2005); 2) a series of elevation decreased air (wind) gaps (Hetzel et al., 2004; Ramsey et al., 2008); and 3) development of inherited drainage patterns (Ramsey et al., 2008; Keller and DeVecchio., 2013). When the fold lateral propagations happen, tectonic tilting towards the propagating direction would affect the development of drainage basin asymmetry (Schumm et al., 2000; Burbank and Anderson, 2001). Asymmetry factor (AF) (Hare and Gardner, 1985) and transverse topographic symmetry factor (T) (Cox, 1994) are two common quantitative geomorphology indexes used to evaluate drainage basin asymmetry, which have been proven as good indications of tectonic movement in southern Iberian Massif and Taiwan (Salvany, 2004; Ramsey et al., 2007). In addition, many analogue and numerical models also display that curved air gaps could indirectly record fold lateral growth (Grasemann and Schmalholz, 2012; Collignon et al., 2015). However, if we only use a single criterion to detect fold lateral growth, the result could be unreliable and misleading. Therefore, a combination of different geomorphological constraints is needed to distinguish passive exhumation and active fold growth (Burbank and Anderson, 2001).

The Altyn Tagh fault system (ATF), a 1,500 km long sinistral strike-slip fault system that forms a boundary for the Tibetan plateau to the north, plays an important role in accommodating the continental deformation produced by the India/Asia collision (Molnar and Tapponnier, 1975; Avouac and Tapponnier, 1993; Cowgill et al., 2000; Tapponnier et al., 2001; Yin et al., 2002). The style and strike-slip rate of faulting have been a major concern of researchers over the last 3 decades, and till now studies have generally stated that there is a gradual decrease from ~10 ± 2 to 0 ± 2 mm/yr along the eastern section of the ATF (Xu et al., 2005; Cowgill, 2007; Zhang et al., 2007; Cowgill, 2009; Gold et al., 2009; Zheng et al., 2013; Liu et al., 2020). Nevertheless, two main questions derived from the kinematics of the ATF along the north of the eastern end still remain unsolved: 1) how did the fault evolve and 2) what kind of landscape was formed by the movement of ATF? Dongbatu Shan (DBTS) faults, developed in the north pediment of the eastern ATF, is regard as the secondary fault of ATF, and expresses thrust conditions with a sinistral component (Cunningham et al., 2016). Although the magnetotelluric method can provide the fault geometry in depth (Xiao et al., 2011; Xiao et al., 2015; Xiao et al., 2017; Li et al., 2020), and active fault studies reveal fault distribution and activities during the late-Pleistocene (Chen et al., 2020; Yang et al., 2020), the published dataset is not good enough to comprehensively answer how the tectonic activities around DBTS controlled drainage development during the late Quaternary.

In this study, due to the abundant drainages and various kinds of fluvial landforms developed around DBTS, we aim to determine: 1) the geomorphic sequences of landscapes by satellite image analysis, field investigation, and beryllium-10 (^{10}Be) terrestrial cosmogenic nuclides dating; 2) the features of the topography profile along the mountain crestline, drainage pattern, and geomorphic indexes (AF and T); and 3) the landform's evolution and its implication in the regional tectonic movement.

GEOLOGICAL AND TECTONIC SETTING

The Dunhuang basin, located in the northeastern Tibetan plateau, is bounded by the Altyn Tagh fault (ATF) to the south (**Figure 1B**). The basement of the basin belongs to the Paleozoic Dunhuang Orogenic Belt that consists of Archean-Proterozoic rocks, including high-grade tonalite-trondhjemite-granodiorite gneisses, amphibolite, and widespread granite intrusions of the Hercynian period (He et al., 2013; Zhao et al., 2015; Wang et al., 2017). Two mountain ridges composed of the basement rocks, i.e., the Sanwei Shan and Dongbatu Shan, divided the eastern Dunhuang basin into three sub-basins: the Daba, Tashi, and Anxi basins (**Figure 1B**). Jurassic, Cretaceous, and Neogene strata overlay the basement rock with an unconformable contact (Zhuang et al., 2011). With a north-tilted slope, Quaternary conglomerates have been transported by numerous drainages and fulfilled the sub-basins (Wang, 1989). According to the published geological map, the conglomerates can be distinguished into five phases, named Fan1 (early-Pleistocene), Fan 2 and Fan3 (mid-Pleistocene), and Fan4 and Fan5 (late-Pleistocene), respectively (**Figure 1C**).

We focus on the Dongbatu Shan (DBTS) in this study. It strikes east-west with a length of ~100 km and a width of ~10 km. The DBTS, which is believed to have developed no earlier than the early Quaternary (Wang, 1989; Cunningham et al., 2016; Yang et al., 2020), is 100–300 m higher than the surrounding bajada. The uplift and landscape of the DBTS are controlled by several south and north dipping thrust faults, which are possibly reactivations of older fabrics (Cunningham et al., 2016). Based on chronometric dating of the alluvial fans and fluvial terraces, fault scarps and active folds in the western and eastern of the DBTS are found to have been developed during the late-Pleistocene (Chen et al., 2020; Yang et al., 2020). The movement of the DBTS fault in the eastern end has largely affected the asymmetric development of the Shule alluvial fan (Wang et al., 2004). During the Holocene, the activity of the faults around the DBTS remains unclear.

DRAINAGE FEATURES AROUND THE DBTS

Based on bedrock exposure, the DBTS can be divided into three structural domains, namely DBTS-W, DBTS-C, and DBTS-E from west to east, respectively (**Figure 2B**). The Yulin He (the river of Yulin), deflecting towards the west, flows across the western nose of DBTS-C and the eastern nose of DBTS-W, forming a series of fluvial terraces on both sides of the river since the late-Pleistocene (Chen et al., 2020). Several drainages have incised DBTS-W and the river flow turns into groundwater

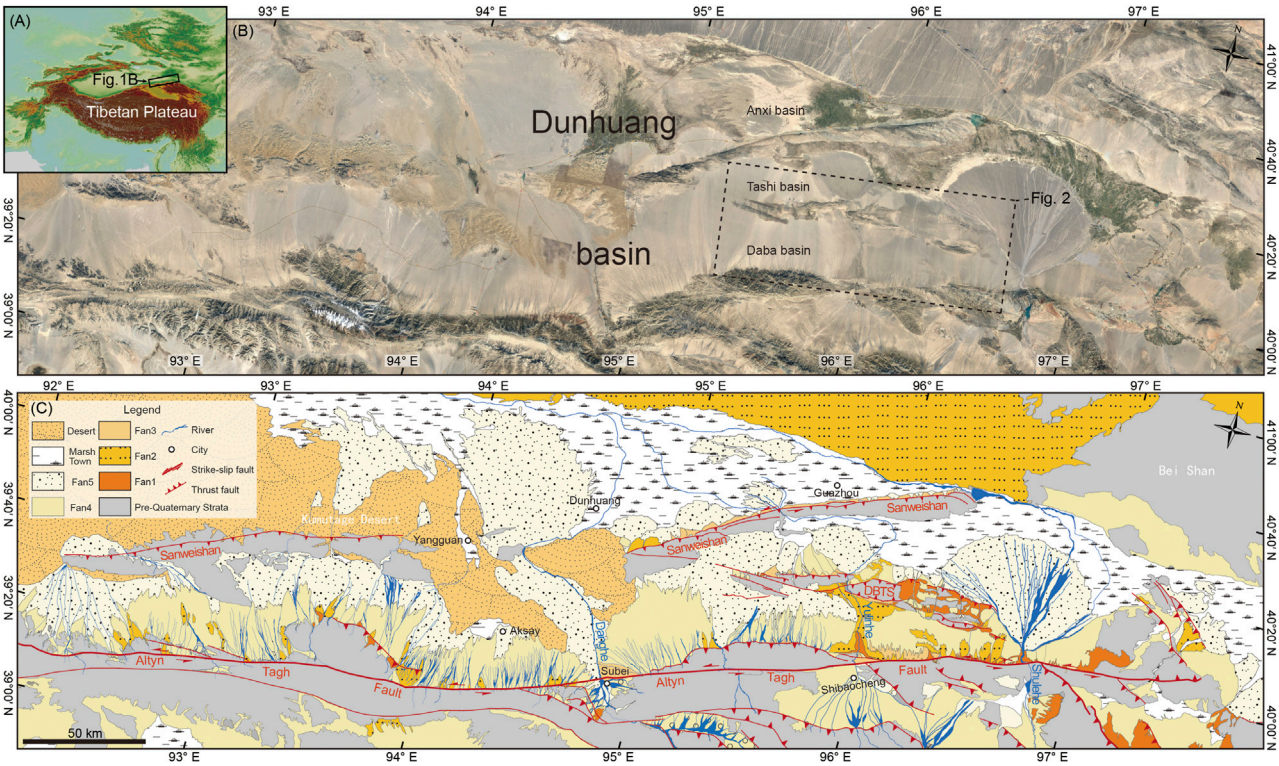

FIGURE 1 | Geomorphic map of the Dunhuang basin. **(A)** Topographic map of the Tibetan plateau. **(B)** Google earth satellite imagery showing the geomorphic features of Dunhuang basin and its surrounding area. **(C)** Interpretation map showing the distribution of Quaternary sediments and active faults around the Dunhuang basin. Active fault locations are modified from "Map of active faults in China" and "Map of active faults in northern Tibet" by Deng et al., 2003 and our own observation.

as it comes into the basin floor. In DBTS-C, paleochannels with a similar scale can be seen on the mountain crestline and the southern alluvial fan. Hanxia and Wudaogou, which had incised across the eastern DBTS-C, are now dry valleys (seasonal channels). In DBTS-E, groundwater overflowed through the Daba basin and then incised across the western and eastern noses of the anticline. Interestingly, seasonal channels around Dushanzi show a dendritic pattern which seems similar to the present Yulin He and paleo-channel preserved on the mid-Pleistocene alluvial fans and mountain crestline.

Field photographs indicate the clear groove shape of air gaps (AG) and water gaps (WG) along the mountain crestline of DBTS-C (**Figure 3A**). The paleo-riverbed of AG2, ~300 m wide, is relatively flat with rounded fluvial conglomerate preserved on it (**Figure 3B**). Paleo-terrace T1 can be found on the western bank (**Figure 3C**). Huge, rounded bedrocks, small rounded fluvial conglomerates reflecting strong hydrodynamic conditions (**Figure 3D**), and fluvial conglomerates preserved on the riverbed of AG3 were observed (**Figure 3E**). At the eastern bank of the Yulin He on the mountain crestline, rounded fluvial conglomerate can also be found on the platform which is ~100 m higher than the present river (**Figures 3F,G**). All these phenomena indicate that paleo-Yulin He had flown across DBTS-C, and were then abandoned due to fault evolution.

METHODS

Mapping Fluvial Landscapes

The landform sequences and distribution are the basis of exploring landscape evolution during different time stages. Due to the absence of vegetation on the surface of landforms in our research area, we can clearly identify different landforms on the satellite images. Combined with field investigation, worldview satellite image with a resolution of 0.5 m was used to distinguish landform sequences and distribution around DBTS. Landform distinguishing was mainly based on the degree of surface erosion and the height above the modern Yulin He. Based on the Shuttle Radar Topography Mission (SRTM) DEM (30 m-resolution), we extracted six topographic profiles along the mountain ridge and alluvial fans. The profiles could help us better distinguish the sequence of alluvial fans and Paleochannels. Two topographic profiles orthogonal to the fault strike are extracted to calculate the amount of fault vertical uplift.

Dating Geomorphic Surfaces

The chronology dating of the geomorphic surface is the most effective way to constrain the process of landscape evolution. We use *in situ* cosmogenic nuclide ^{10}Be dating method to constrain the abandonment ages of Paleo-channels and Paleo terrace. The ^{10}Be dating method hypotheses that ^{10}Be nuclide concentration

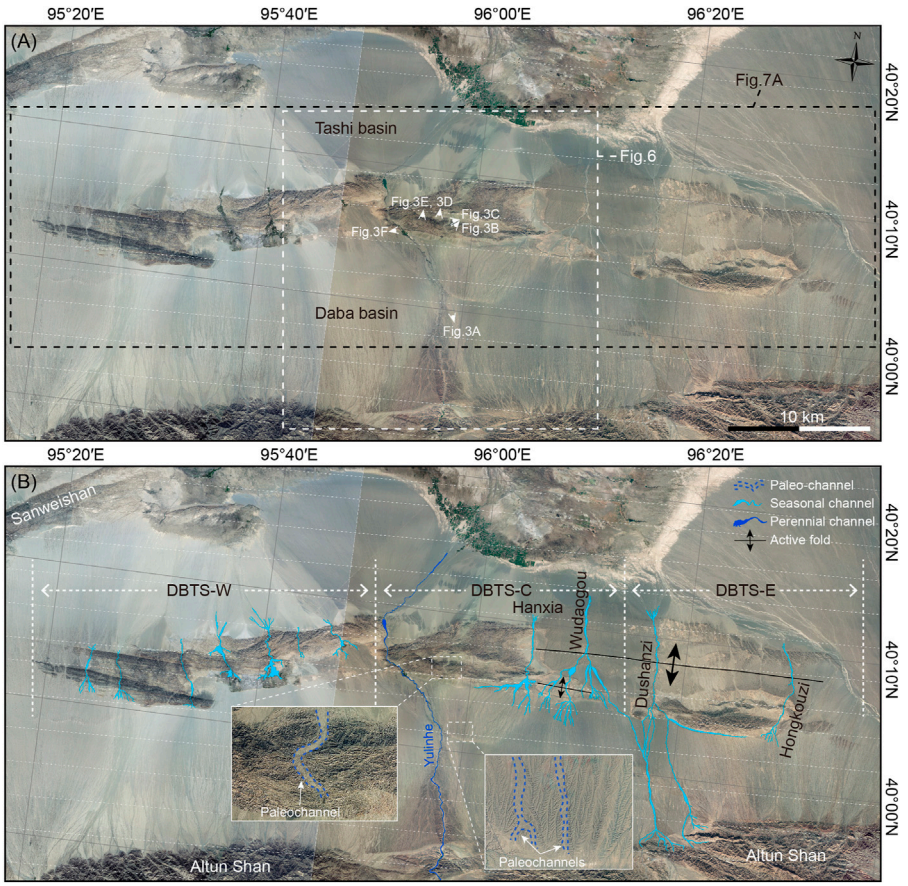

FIGURE 2 | (A) CIRS-P5 satellite images (2.5 m-resolution) around the DBTS. **(B)** Drainage distribution around the DBTS. White dashed lines depict the geographical divisions of DBTS-W, DBTS-C, and DBTS-E.

would accumulate since the riverbed abandoned quartz-rich pebbles exposed to cosmic rays (Gosse and Phillips, 2001). If the inherited nuclide concentration before the riverbed abandoned can be obtained, we could subtract it from the total nuclide concentration to calculate the exposure ages. In the field, we have found that many quartz-rich and sub-round gravel pebbles are well preserved on the surface of the riverbed and terrace at AG2 and AG3 (**Figure 4**). These pebbles, with diameters of ~1–3 cm, are suitable for ^{10}Be dating method to constrain the abandonment age of paleo-channels. At AG2, two superficial ^{10}Be samples are collected, one from the surface of riverbed (YLH-16) and the other from the T1 (YLH-15) (**Figures 4A,B**). At AG3, one superficial ^{10}Be sample is collected on the surface of the riverbed (YLH-17) (**Figure 4C**). We suspect that the inherited nuclide concentration of the paleo-channels is approximately the same as the terrace formed in the Late-Pleistocene incised by Yulin He, which has been simulated by Chen et al., 2020. The pre-process of these samples is performed at the Key Laboratory of the Institute of Crustal Dynamics, China Earthquake Administration (Chen et al., 2020). The ^{10}Be/^{9}Be ratio is tested at CEREGE (Le Centre Européen de Recherche et d'Enseignement des Géosciences de l'Environnement, Laboratoire de Tectonique). After subtracting the inherited nuclide concentration, the CRONUS-Earth online calculator (Balco et al., 2008) (http://hess.ess.washington.edu) and the time-independent scaling model of (Lal, 1991) and (Stone, 2000) are used to calculate the abandonment age of each landform. Dating results are shown in **Table 1**.

Analyzing Drainage Development

If the lateral growth had happened along the strike of DBTS, evidence could have been recorded on drainage development. **Figure 5A** is an idealized cartoon model showing the development of the present river and drainages influenced by the propagating anticlines through time. Fan-shaped drainages form perpendicular to contours on the fold and one river flow across the fold tip at stage I before lateral propagation. With fold propagation along strike (stage II), newly formed drainages are perpendicular to contours, while some deep incised channels formed at stage I may have inherited their curved pattern. These channels, which are not normal for the contours and sometimes nearly parallel to the mountain ridge, are named as "inherited drainages" or "forked drainage" (Keller et al., 1999; Ramsey et al., 2008; Bretis et al., 2011). If the incision rate of the western river can keep pace with the uplift rate, the river would incise a gorge through the nose of the fold (**Figure 5A**). Accompanied by the

FIGURE 3 | Photographs showing paleo-channel geomorphology characters around DBTS. Locations are marked in **Figure 2B**. **(A)** Concave pattern along the mountain crestline showing air gaps and water gaps. **(B)** and **(C)** Paleo-riverbed and terrace T1 at AG2. **(D)** Tributary paleo-river on the top of the mountain. **(E)** Paleo-riverbed of AG3. **(F)** and **(G)** Platforms that are preserved on the eastern bank of the present Yulin He.

consistent fold propagation (stage III and IV), when the river incision rate cannot keep up with the uplift rate, the outlet may be abandoned, leading the river to form a new gorge through the nose of the fold. The abandoned outlet left on the mountain ridge is named AG and the present river gorge is WP (water gap). In such hypotheses, WP represents the nose of the fold and the air gap represents the nose of the fold before propagation. Thus, we could see a decrease in elevation of WPs along the mountain ridge relief (**Figure 5B**). Where such a pattern is recognized, fold lateral propagation could be the likely cause (Keller et al., 1999; Ramsey et al., 2008; Keller and DeVecchio, 2013). Based on the SRTM DEM (30 m resolution), we extract the drainage map of different segment of DBTS to detect inherited channels.

In order to analyze the type and amount of asymmetry of the drainage basins on DBTS, we use two quantitative geomorphic indexes: AF (Hare and Gardner, 1985) and T (Cox, 1994). These two methods are all based on the deflection of the trunk river which may be influenced by

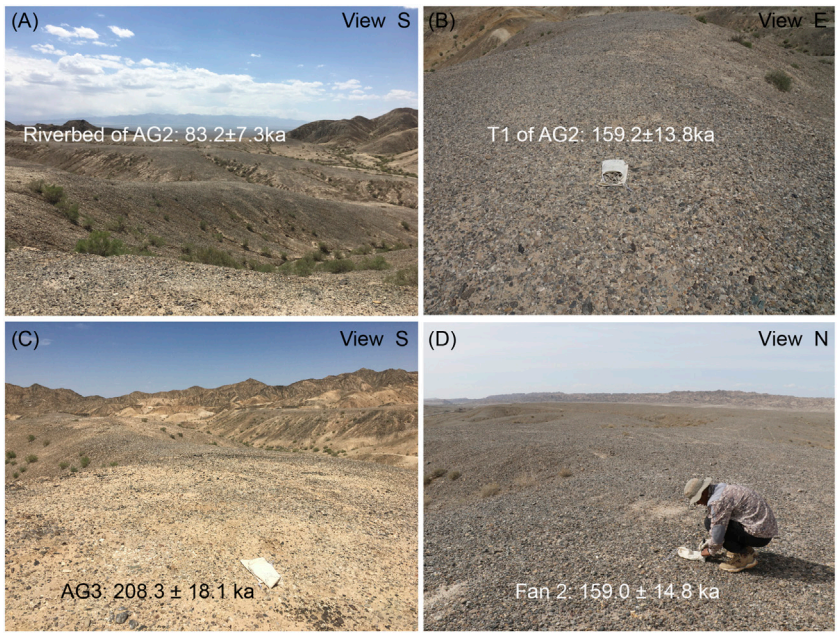

FIGURE 4 | Field photographs showing ^{10}Be samples collected on the surface of **(A)** AG2, **(B)** paleo-terrace T1 at AG2, **(C)** AG3, and **(D)** Fan 2.

tectonic tilting. As different types and different periods of landform are mostly distributed around DBTS-C, we use these two methods to further analyze the drainage basin asymmetry and tectonic information.

The AF—index describes the asymmetry of a drainage basin. It is calculated by AF = 100 (A_r/A_t), where A_r represents the drainage area to the right of the trunk stream towards downstream and A_t is the area of the drainage basin (**Figure 5C**). If the AF is 50 the drainage basin is symmetrical, while if the AF is more or less than 50 this represents the asymmetry of the drainage basins (Ramsey et al., 2007). In this study, an AF > 50 would imply the trunk river is migrating westwards, and conversely an AF < 50 would imply the trunk river is migrating towards the east. We calculate the AF for each of the ten basins in the north of DBTS ridge, and present the results in **Table 2**.

The T - index is used to quantify the amount of asymmetry of the main stream within a drainage basin and how the asymmetry varies in length (**Figure 5C**). We divided the main stream into 300 m for each segment in this study. For each segment, T is the ratio of the distance from the basin midline to the active main stream (Da) and to the basin divide (Dd); T = Da/Dd. If the basin is symmetrical, Da = 0 and T = 0. The asymmetry would increase as the T values approach 1. For each segment, it can be seen as a two-dimensional vector with a length equivalent to Da/Dd, and a direction (bearing) perpendicular to the segment that indicates movement of the segment with regard to the basin midline. We used a MATLAB based toolbox—TecDEM (Shahzad and Gloaguen, 2011) to calculate the value of T and bearing. The mean value of T and bearing could represent overall deflection of the main stream in each drainage basin. The results of this are shown in **Table 2**.

RESULTS

Landform Features and Sequences Around DBTS

Our previous work has identified ten major fluvial terraces developed within alluvial fans along the Yulin He during the late-Pleistocene (Chen et al., 2020). In this work, we extend the research area to collectively cover the overall area around DBTS. To the south of DBTS, mid-Pleistocene alluvial fan (Fan 2) is widely distributed (**Figures 6A,B**) and forms the top surface of the Daba sub-basin (**Figures 6C–E**). Early-Pleistocene alluvial fan (Fan 1) developed beneath it, and is mainly exposed near the mountain front of DBTS and Altun Shan. Late-Pleistocene alluvial fan (Fan 3) is formed in the north of DBTS, which is abandoned at ~30.7 ka (Chen et al., 2020). Five thrust faults, surrounding DBTS, striking approximately west-east direction, are named F1 to F5, respectively. Influenced by the uplift of DBTS-W, the surface of Fan 2 expresses a significantly southward tilting in the south of DBTS-W (**Figure 6F**).

In DBTS-C, the present Yulin He flows across its western nose, and one dry valley-Hanxia incised across its eastern nose (**Figure 7A**). Four possible air gaps exist along the crest DBTS-C (**Figure 7B**). Among them, air gap 2 (AG2), with westward deflection, has the largest scale at ~1,500 m wide and over 70 m deep, while the other air gaps are only 300–500 m wide and ~30 m deep. Topographic profile crossing the AG2 shows that paleo-terrace T1 is ~10 m higher than the Paleo-riverbed (**Figure 7C**). The abandonment age of the riverbed is determined to be 83.2 ± 13.8 ka after eliminating the inherited ^{10}Be concentration (**Figure 4A**), and terrace T1 is 159.2 ± 13.8 ka (**Figure 4B**). Higher possible paleo-terraces cannot be clearly defined as no fluvial conglomerate was

TABLE 1 | Calculating ^{10}Be exposure ages.

Sample ID	ID	Latitude	Longitude	Elev (m)	Depth (m)	Dissolved mass (g)	Carrier mass (mg)	Corrected ^{10}Be/^{9}Be	^{10}Be concentration (atoms g^{-1})	Error (atoms g^{-1})	Inheritance ^{10}Be concentration (atoms g^{-1})	Error (atoms g^{-1})	Age (ka)	Error (ka)
YLH-14	Fan 2	40.050	95.950	1791	0	30.04	0.22	5.8534E-12	2.80E+06	4.76E+04	3.85E+05	+9.93E+04	159.0	14.8
YLH-15	T1	40.095	95.956	1830	0	30.17	0.21	5.9814E-12	2.84E+06	6.51E+04		–5.47E+04	159.2	13.8
YLH-16	AG2	40.094	95.960	1820	0	31.39	0.22	3.56774E-12	1.68E+06	4.49E+04			83.2	7.3
YLH-17	AG3	40.101	95.917	1818	0	26.32	0.22	6.29374E-12	3.36E+06	7.53E+04			208.3	18.1

preserved. To the west at AG3, the abandonment age of the riverbed is 208.3 ± 18.1 ka (**Figure 4C**). Several paleochannels, with similar scales to the present Yulin He, are preserved on the surface of Fan 2 in the southern DBTS. The central alluvial Fan 2 has a convex-up shape shown by topographic profiles P1 to P4 (**Figure 7D**). Along the western segment of Fan 2, some ~10 m higher fan surfaces exist and were abandoned at 159.0 ± 14.8 ka (**Figure 4D**, Chen et al., 2020). The longitudinal profile of AG2 shows a convex shape of the paleo-riverbed and the amount of uplift made by F2 is constrained as ~103 m (**Figure 7E**). For the fault scarp of F4, the vertical displacement is estimated to be 28 ± 2 m (**Figure 7F**).

Drainage Characters on the Flank of DBTS

The drainage network pattern shows some differences in three different segments of DBTS. In DBTS-W, seven major rivers have incised through the mountain and split it into many small segments (**Figure 8A**). The newly formed drainages surrounding the hills in all aspects may have covered the inherited drainages so that we could not observe them. As nearly no terrace was preserved along these gorges, it is difficult to limit the time when the river cuts through the DBTS-W. In DBTS-C, many instances of fan-shaped drainage are overprinted by secondary tributary and formed relatively larger drainage basins on the northern flank of DBTS-C. The tributary pattern on the south flank of DBTS-C is similar to the idealized pattern shown in **Figure 5A** and four inherited drainages are clearly identified (**Figure 8B**). The pattern of drainage network on DBTS-E also shows an idealized pattern so that the inherited drainage approximately parallel to the mountain crestline can be observed (**Figure 8C**).

The results of AF are a great indication of the mountain inclination (**Figure 9A**). Basin 5 to 10 have an AF of 55 to 30 and show a steady decrease in the east direction, indicating an eastern inclination of DBTS-C. But the AF of basin 1 to 5 display an arbitrary value. The AF value of basin 1 and 4 is lower than 50, while basin 2 and 3 is higher. We state that the disordered AF may be affected by the uplift of DBTS-W, which is also shown in the value of T.

The mean value and bearing of T of basin 6 to 10 shows a uniform eastern migration of all trunk rivers (**Figures 9B,C**). Basins 1, 2, and 4 have T of 0.18, 0.14, and 0.27 respectively, and bear towards the southeast. Basins 3 and 5 have T of 0.30 and 0.24, and bear towards the southwest. We believe this phenomenon is influenced by the uplift of the western mountain DBTS-W. In summary, both the value of AF and F seem to be reasonably explained by tectonics.

DISCUSSION

Restoration of Landform Evolution Induced by Fault Growth

The distribution and chronology of different landforms, drainage patterns, and quantitative morphometric indexes help us to establish the landform evolution around DBTS. Based on the inherited drainage pattern, we suggest fold lateral propagation

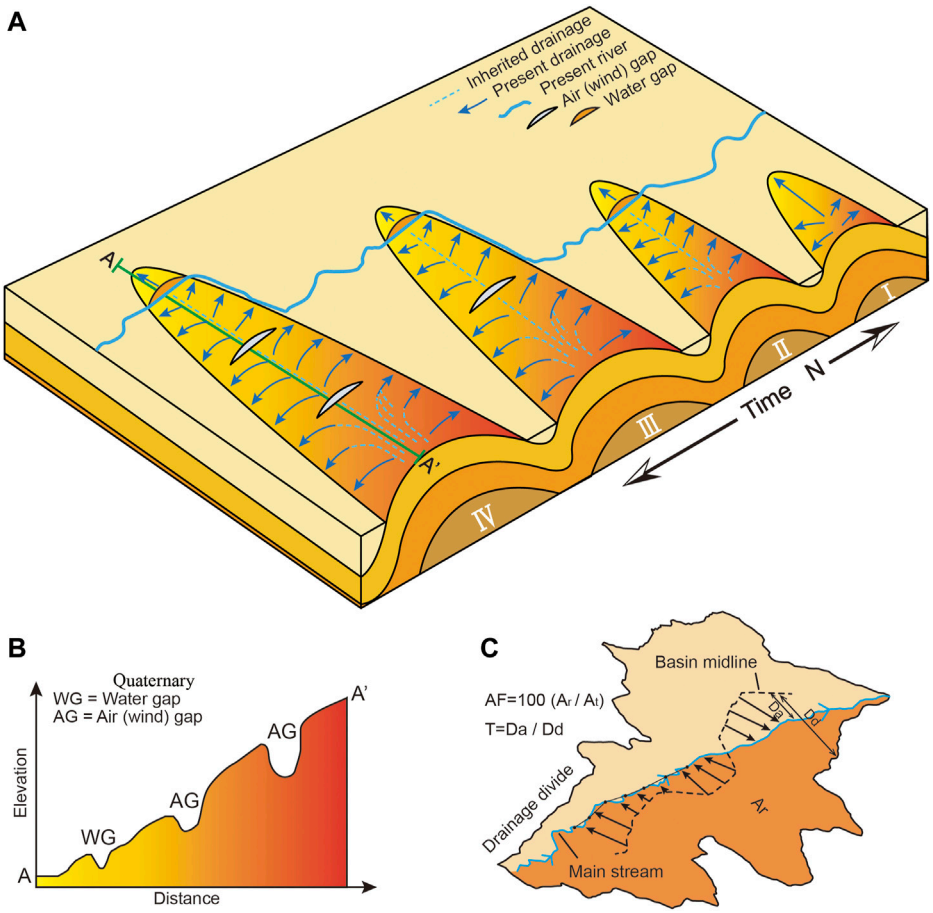

FIGURE 5 | Three conceptual models showing the drainage development controlled by fold lateral propagation. **(A)** A cartoon illustrating fan-shaped drainages on the flanks and river flow across the western nose of a growing fold. At stage II, the fold propagates towards the west. Inherited channels (dotted lines) may be preserved on both flanks of the fold. The incision rate of the western river can keep up with the fold uplift and incised a gorge across the fold nose. At stage III, the western river cannot catch up with the fold uplift such that the gorge is abandoned, leaving one wind gap. A new river would migrate to a new course where it can be incised through. At stage IV, more air gaps are preserved on the mountain crestline due to fold propagation (modified from Ramsey et al., 2008). **(B)** Topographic profiles across the propagating fold crest showing air (wind) gap features (modified from Keller et al., 1999). **(C)** An example of the methods used to calculate asymmetry factor (AF) and transverse topographic symmetry factor (T) of a drainage basin (modified from Cox, 1994; Salvany, 2004).

TABLE 2 | Morphometric values obtained from DBTS-C.

Drainage basin	Asymmetry factor (AF)	Transverse topographic symmetry factor	
		Mean T	Mean bearing
1	45	0.18	133
2	53	0.14	158
3	58	0.30	173
4	43	0.27	157
5	55	0.24	197
6	40	0.13	124
7	32	0.42	157
8	36	0.20	96
9	32	0.47	112
10	30	0.44	120

occurred on DBTS-C and DBTS-E. Combining the terrace deformation with ^{10}Be exposure age, the shortening rate across the west nose of DBTS-E is constrained to be ~0.3 mm/yr since ~50 ka (Yang et al., 2020). At DBTS-C, the value of AF and T show a clear drainage migration towards east active, indicating an eastward titling. To the west flank of DBTS-C, as fault scarp that

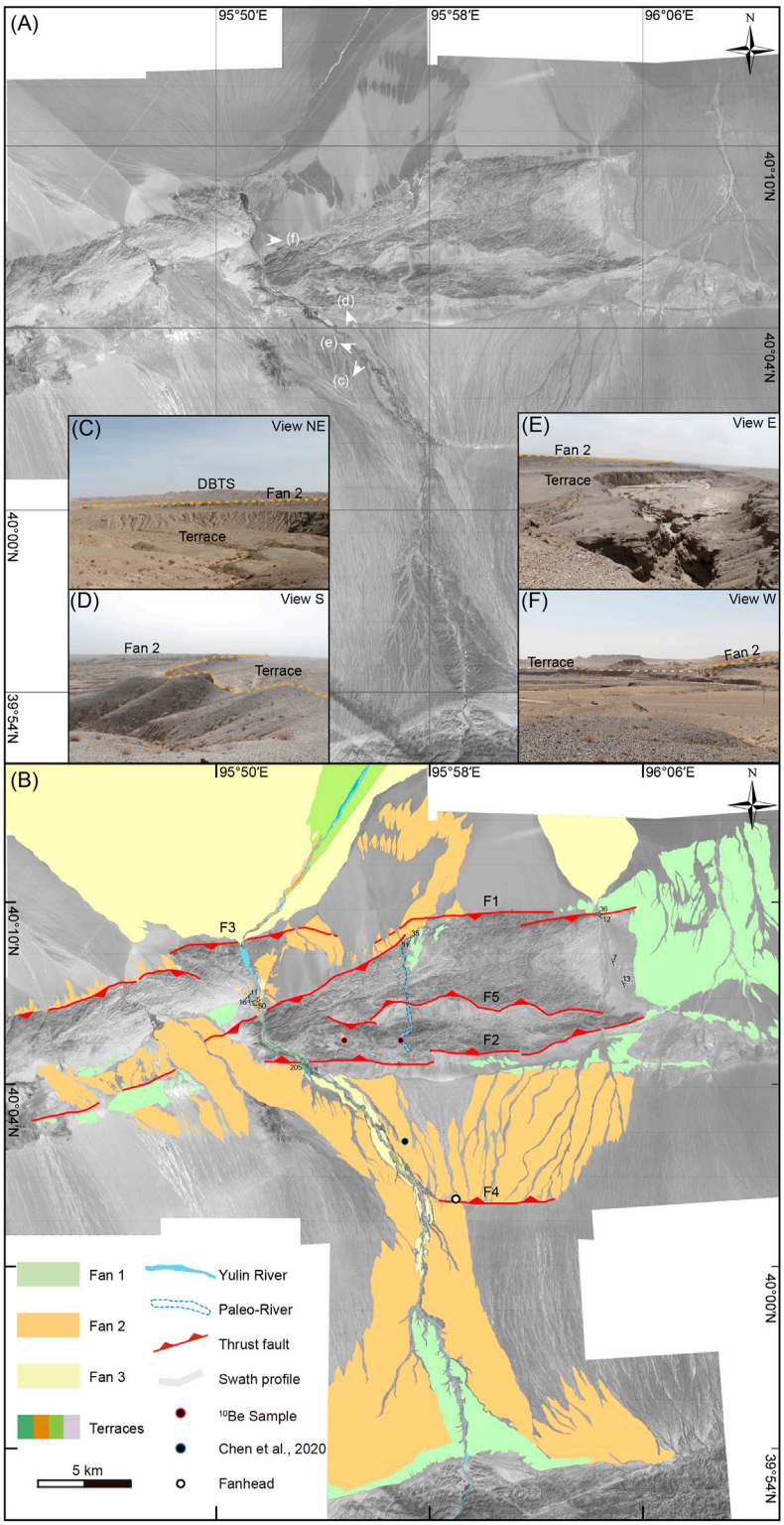

FIGURE 6 | Landform style, sequences, and distribution around DBTS-C. **(A)** Worldview image with 0.5 m-resolution showing the geomorphic feature of the research area. **(B)** Interpretation of the distribution and sequences of drainage landforms. **(C,D)**, and **(E)** Field photographs showing the contact relationship of terraces and alluvial Fan 2 along the upstream of the Yulin He. **(F)** Southward tilting of Fan 2 developed in the south of DBTS-W. Photograph positions are marked in **(A)**.

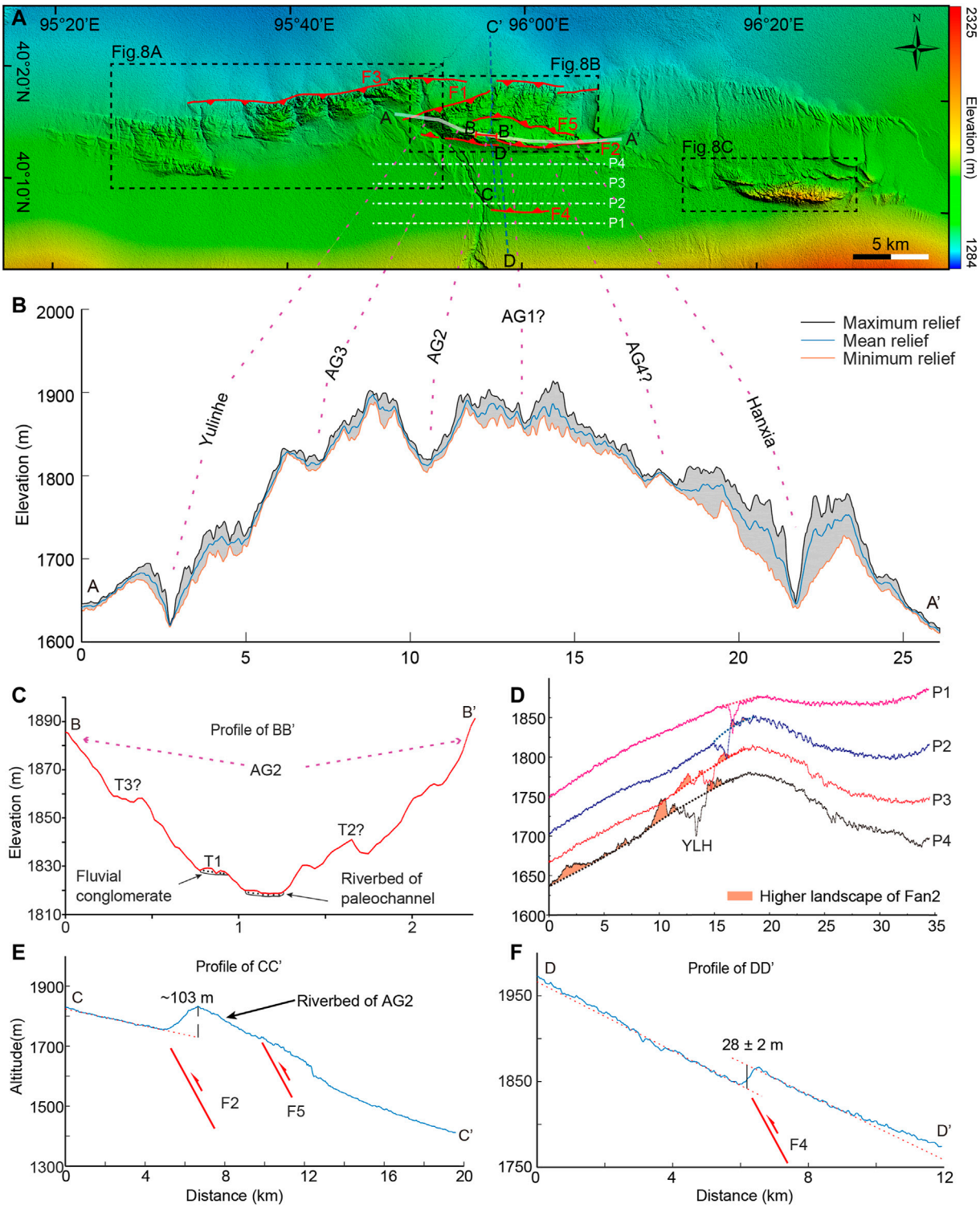

FIGURE 7 | Topographic feature of landscapes around the DBTS. **(A)** Topographic map of DBTS (superimposed on the 30 m-resolution Shuttle Radar Topography Mission DEM; https://lta.cr.usgs.gov/SRTM). **(B)** Topographic profiles along the mountain crestline of DBTS-C. **(C)** Cross profiles of AG2. **(D)** Four relief profiles across Fan 2 in the south DBTS-C. **(E)** and **(F)** Topographic profiles of F2 and F4 fault scarps.

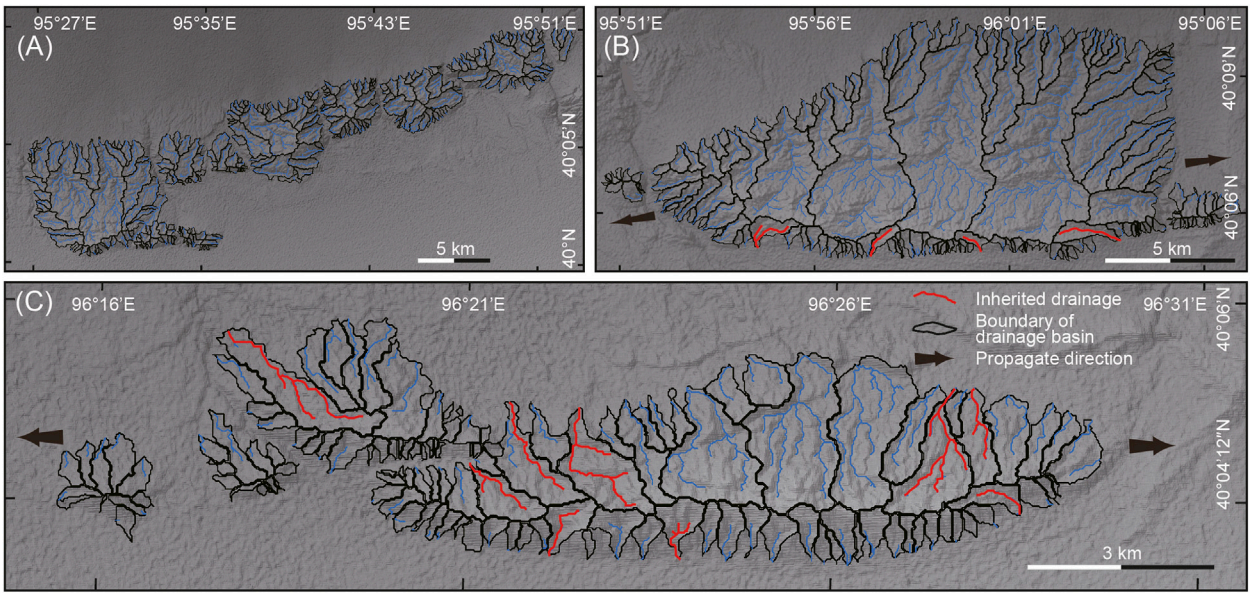

FIGURE 8 | Drainage patterns of the **(A)** DBTS-W, **(B)** DBTS-C, and **(C)** DBTS-E extracted from the 30 m SRTM DEM. Red line represents the inherited drainages.

displaced the alluvial Fan 2 can be clearly observed in the east end of DBTS-W (**Figure 6B**); these two domains have overlapped together. The disordered value of AF and T could reveal the fold superimposition that the uplift of DBTS-W would influence the westward propagation of DBTS-C. Yang et al., 2020 propose that fault uplift of DBTS-W had displaced the alluvial fan at the western end since ~46 ka and may have connected with Sanweishan fault (Cunningham et al., 2016). In the center of DBTS-W, we found the metamorphic rock are thrust on the early-Pleistocene conglomerate, indicating early activity of the fault (Chen et al., 2020). Thus, we regard that the late-Pleistocene fault movement at the east and west end of DBTS-W could indicate a fault lateral growth. In summary, the above evidence reveals that the three segments of DBTS could have gone through east-westward propagation during the late Quaternary. If this supposition is correct, much more evidence would have been recorded on other landforms that surround DBTS.

Under normal conditions, the paleo-river would migrate to AG3 when the AG2 was abandoned. Curiously, the abandonment age of the riverbed at AG3 is ~208.3 ka, which is older than T1 of AG2. The capability of river incision may be influenced by lithology, discharge, and topography relief (Burbank and Anderson, 2001). Since the lithology of DBTS is consistent along the strike, we can exclude the impact of lithology change on river abandonment. Observed from the present mountain crestline relief, the elevation of AG3 is similar with AG2 (**Figure 7B**). As mentioned in the previous paragraph, the uplift of the east end of DBTS-W could influence the topography of the western flank of DBTS-C that could make the riverbed of AG3 higher than AG2 at early stages. The height differences between mountain crestline and sub-basin of DBTS-W and DBTS-C are ~150 and ~200 m, respectively. The higher topography of DBTS-C could reveal a stronger uplift. Then, with the stronger uplift of the DBTS-C, the elevation of AG2 would arise and gradually keep up with AG3. In addition, the scale of AG3 is much smaller than AG2, indicating a weaker incision capability. Thus, we suppose AG3 would be abandoned earlier due to relatively weak hydrodynamics and higher topography. Leading to the acquisition of the abandonment age of Paleo-terrace T1 agreeing well with Fan 2, they may be the same landform and connected before ~160 ka. During that time, river incision could have kept up with mountain uplift and gradually incised the alluvial fan and the bedrock of DBTS to form T1. Until ~83 ka, river incision could not keep up with the mountain uplift of the riverbed of AG2 and river flow on the surface of Fan 2 was abandoned, as the height difference between paleo- T1 and riverbed is the same with the height difference revealed on Fan 2 (**Figures 7C,D**). The present Yulin He has evidently deflected towards the west near fault F4, indicating the uplift of F4 has largely affected the evolution of paleo-rivers. We believe the river would have merged into the present channel of the Yulin He since ~83 ka, where the oldest fluvial terrace found is ~42.8 ka (Chen et al., 2020).

Based on the chronology and topographic data, we had analyzed evolution sequences of the paleo-channels of Yulin He. However, whether the evolution of Yulin He is a single river swinging around or multiple tributaries gradually abandoned needs further discussion. According to the drainage pattern and topographic profile relief, we determined the location of apex of Fan 2 (**Figure 6B**), which corresponds to the position of water outlet in front of the Altun Shan. The phenomenon shows that the upstream position of Yulin He has not changed since Fan 2 was accumulated. Field investigation has found terraces ~100 m higher than the modern riverbed, preserved on the east bank of the Yulin He. Topographic profile of AG2 also shows some possible terraces exist (**Figure 7C**). These phenomena may indicate that paleo-channels of Yulin He may have once flown across these paleo-channels at the same time. In consideration of the present dendritic drainage flow across the

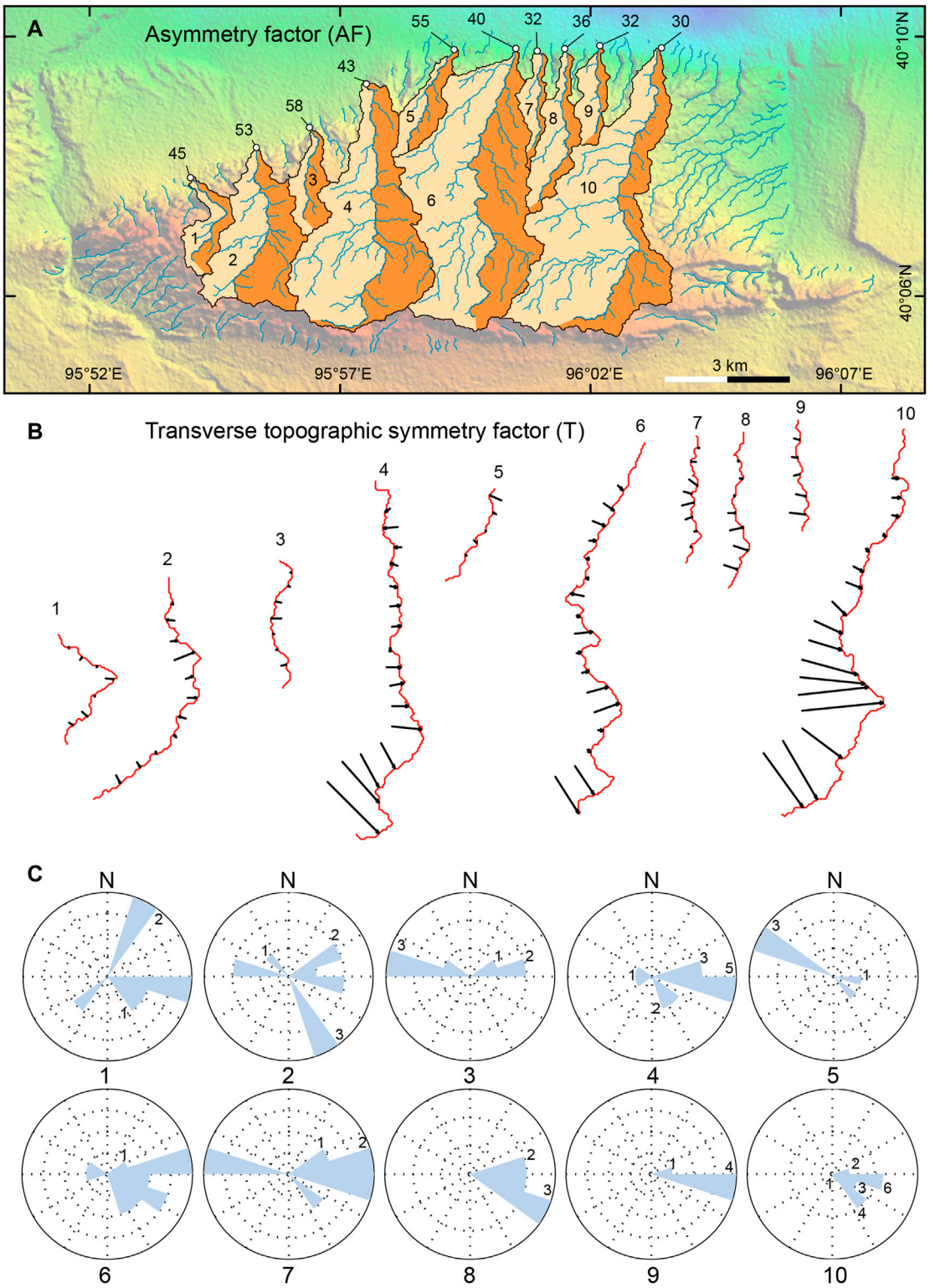

FIGURE 9 | Quantitative morphometric index of the drainage basin on the northern flank of DBTS-C. **(A)** Asymmetry factor (AF) of drainage basin from 1 to 10 outlined in black and the synthetic drainage network shown in blue. **(B)** Trunk river of drainage basin from 1 to 10 showing the migration vector of T in each section. **(C)** Rose and frequency diagram of the T vector.

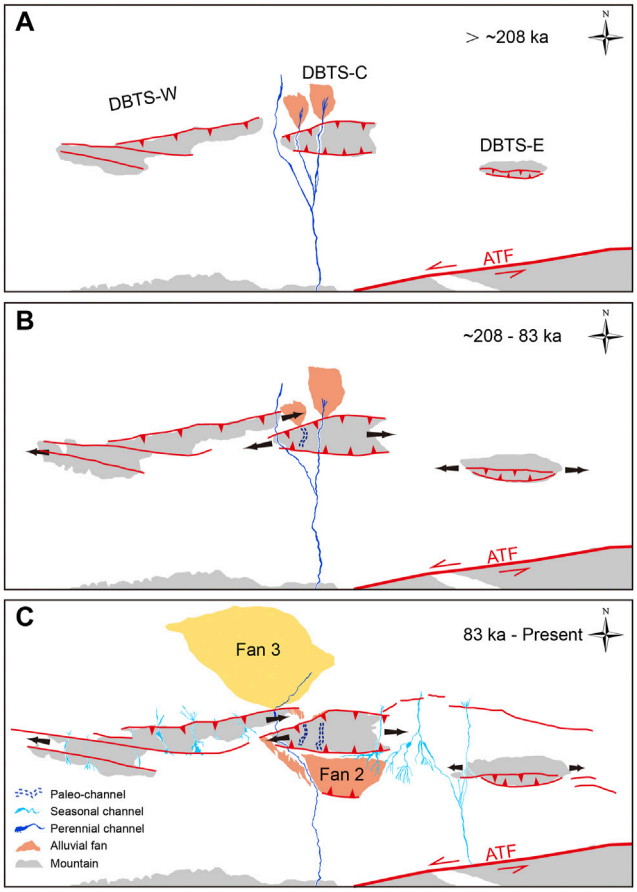

FIGURE 10 | Geomorphic evolution model showing DBTS landscape evolution since ~208 ka. **(A)** In the early stage of ~208 ka, three tributaries flow across DBTS-C on the western flank. **(B)** Accompanied by fold propagation, AG3 was first abandoned at ~208 ka. At ~159 ka, Paleo-terrace T1 was formed by river incision along paleo-river (AG2). **(C)** Until ~83 ka, the incision rate of paleo-river (AG2) cannot keep up with the mountain uplift and the gorge was abandoned on Fan 2 and DBTS-C. The Yulin He would increase its power by accumulating the abandonment flow and deeply incised on alluvial Fans to form a series of terraces since the late-Pleistocene.

Daba sub-basin near Dushanzi (**Figure 2B**), we suppose that the antecedent Yulin He may have a similar pattern.

Figure 10 shows the supposing geomorphic evolution models to illustrate the landform evolution around DBTS since the late mid-Pleistocene. In early 208 ka, the trunk river of the Yulin He flowed across the Daba sub-basin and divided into three tributaries approaching DBTS (**Figure 10A**). All three tributaries flowed across DBTS. Accompanied with the fold propagation of DBTS fault, antecedent river AG3 was firstly abandoned at ~208 ka, leaving two rivers to continue running (**Figure 10B**). At ~159 ka, a continuous incision formed terrace T1 along the alluvial fan and DBTS gorge (AG2). Until ~83 ka, the uplift of F2 and F4 caused the abandonment of the east tributary and left two fault scarps (**Figure 10C**). From then on, only one Yulin He gorge was flowing, and formed Fan 3 and a series of fluvial terraces.

Implications for the Northward Growth of the ATF

Our observations have implications for a new drainage development pattern associated with multi-segment fault growth. Drainages that flow into the bajada could be divided from one stream into several tributaries. Some of the secondary flows have sufficient stream power to cut through propagating anticline and some would have deflected away from the tip. Their abandonment order may not be consistent with the direction of anticline propagation so that the landform relief and stream power would play an important role. Given the fact that the drainages abandoned in an uncommon order, the geomorphic age cannot be used to obtain the fold lateral propagation rate (Bennett et al., 2005). Nevertheless, we could constrain the uplift rate of fault F2 and F4 since ~83 ka, as they deformed the same landscape. Combined with the height of fault scarp, the uplift rate for F2 and F4 since ~83 ka is calculated as 1.24 ± 0.11 and 0.34 ± 0.04 mm/yr, respectively. As we could not obtain the uplift rate of F1, we suggest that the minimum shortening rate across DBTS-C to be ~1.47 mm/yr assuming the fault dips ~47° (Chen, 2018) since ~83 ka. Based on age constraint and displacement measurements, Yang et al., 2020 proposed that the shortening rates in the western and eastern DBTS are approximately 0.3 mm/yr since ~50 ka. A similar shortening rate was also obtained from the deformed terrace along the gorge of Yulin He since ~35.9 ka (Chen et al., 2020). The differences of the shortening rate during the late-Pleistocene indicates that DBTS-C had gone through a relatively severe uplift at ~83 ka.

The fault style, distribution, and deformation pattern along the eastern ATF system has been intensively discussed during the last decade (**Figure 11**) (Yue and Liu, 1999; Zheng et al., 2016; Zhang et al., 2020). To the north of the eastern Altyn Tagh fault there mainly developed the Shanweishan fault and DBTS fault, and to the south developed the Yemahe fault, Daxueshan fault, Yingzuishan fault, Changma fault, and North Qilianshan fault. Several Magnetotelluric and seismic reflection profiles perpendicular across the eastern ATF system indicate that SWSF (Sanweishan fault), DBTSF (Dongbatushan fault), YMHF (Yemahe fault), and YZSF (Yingzuishan fault) are all likely to merge with the ATF at depth of ~30 km (Xiao et al., 2011, 2017; Cunningham et al., 2016; Chen, 2018; Li et al., 2020), and have formed a complex asymmetry flower structure. Yang et al., 2020 used the transgressional duplexing model to illustrate SWSF and NJSF fault kinematics and geometry in the easter ATF. Yun et al., 2020 stated that the Riedel's shear could explain the development of DBTS fault, which stands as the P shear in the model. Their models can well explain the evolution of these faults developed in the shallow lithosphere. However, these secondary faults would merge with the ATF in depth, which may induce the coupling problem between the shallow and deep faults. Based on satellite image of Google earth and seismic reflection profiles, we have found that thrust faults are widely distributed around DBTS, and some are even developed in the Daba sub-basin, such that no sinistral feature has been found since the late mid-Pleistocene. Based on the chronology age of the fault plane and volcanic eruption of

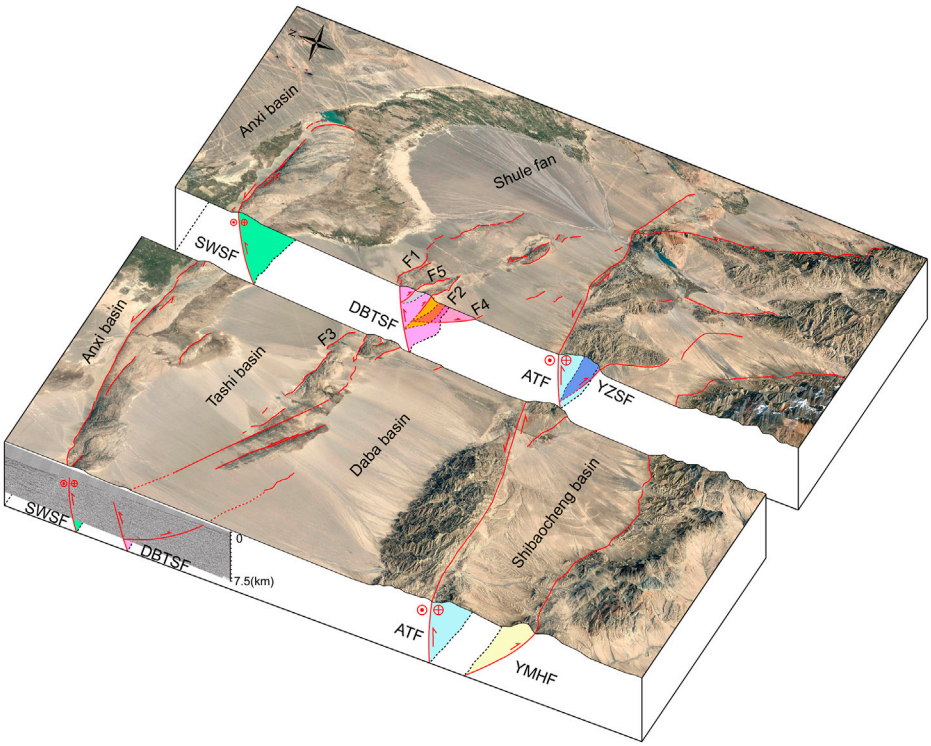

FIGURE 11 | Block diagram with two cross-sections showing downwards projections of sub-parallel faults revealing a flower-like structure along the eastern ATF. The trace of sub-surface fault refers to seismic reflection profiles and magnetotelluric data presented by Chen, 2018 and Xiao et al., 2011.

the Ashkule Volcano Group in west Kunlunshan, Li, 1994 proposed that the ATF had gone through a severe uplift since ~25 ka. Considering the controlling factor of ATF, DBTS region could come under great compression. Thus, we suggest that the pattern of the flower-like structure spreading to both sides under the northward growth of the ATF can better explain the severe uplift of DBTS since ~208 ka.

CONCLUSION

In this study, we investigated the drainage development process and its interaction with the landscape evolution around DBTS based on satellite image interpretation, geomorphic dating, and quantitative geomorphology analysis. We draw the following conclusions:

(1) The course of the Yulin He has gone through several abandonments and left two distinct air gaps along the mountain crestline due to the lateral propagation of DBTS since ~208 ka.
(2) Under multi-segment fault growth and drainage discharge conditions, the direction of drainage abandonment may not be consistent with the fold propagation tendency.
(3) Along the eastern segment of the ATF, the secondary sub-parallel faults developed on both sides of the fault are controlled by a flower-like structure induced by the northward growth of the ATF.

DATA AVAILABILITY STATEMENT

The original contributions presented in the study are included in the article/Supplementary Material, further inquiries can be directed to the corresponding author.

AUTHOR CONTRIBUTIONS

GC did the field work, data processing, and wrote the manuscript. WZ contributed to the conception and provided funding for the study. LD, SL, and JX did the field work. JX, ZL, and LD reviewed and edited the manuscript. All authors contributed to manuscript revision and discussion and approved the submitted version.

FUNDING

This work was supported by the second Tibetan Plateau Scientific Expedition and Research program (STEP) (2019QZKK0901), National Key Research and Development Program of China (2017YFC1500101), the National Science

Foundation of China (41774049, 41874020, 41590861), and Guangdong Province Introduced Innovative R&D Team of Geological Processes and Natural Disasters around the South China Sea (2016ZT06N331).

ACKNOWLEDGMENTS

We would like to express thanks to Yu Zhou for his valuable suggestions.

REFERENCES

Avouac, J.-P., and Tapponnier, P. (1993). Kinematic Model of Active Deformation in central Asia. *Geophys. Res. Lett.* 20 (10), 895–898. doi:10.1029/93GL00128

Balco, G., Stone, J. O., Lifton, N. A., and Dunai, T. J. (2008). A Complete and Easily Accessible Means of Calculating Surface Exposure Ages or Erosion Rates from 10Be and 26Al Measurements. *Quat. Geochronol.* 3 (3), 174–195. doi:10.1016/j.quageo.2007.12.001

Bennett, E. R., Youngson, J. H., Jackson, J. A., Norris, R. J., Raisbeck, G. M., Yiou, F., et al. (2005). Growth of South Rough Ridge, Central Otago, New Zealand: Using *In Situ* Cosmogenic Isotopes and Geomorphology to Study an Active, Blind Reverse Fault. *J. Geophys. Res. Solid Earth* 110 (B2). doi:10.1029/2004JB003184

Bretis, B., Bartl, N., and Grasemann, B. (2011). Lateral Fold Growth and Linkage in the Zagros Fold and Thrust belt (Kurdistan, NE Iraq). *Basin Res.* 23 (6), 615–630. doi:10.1111/j.1365-2117.2011.00506.x

Burbank, D. W., and Anderson, R. S. (2001). *Tectonic Geomorphology*. Massachusetts: Blackwell Science. doi:10.1002/9781444345063

Chen, G., Zheng, W., Xiong, J., Zhang, P. Z., Li, Z. G., and Yu, J. X. (2020). Late Quaternary Fluvial Landform Evolution and Controlling Factors along the Yulin River on the Northern Tibetan Plateau. *Geomorphology* 363, 107213. doi:10.1016/j.geomorph.2020.107213

Chen, G. (2018). *The Evolution of the Yulin River and its Defomation to the Northwestward Growth of the Altyn Tagh Fault*. Beijing: Institute of Geology, China Earthquake Administration. Master thesis.

Collignon, M., Fernandez, N., and Kaus, B. J. P. (2015). Influence of Surface Processes and Initial Topography on Lateral Fold Growth and Fold Linkage Mode. *Tectonics* 34 (7-8), 1622–1645. doi:10.1002/2015TC003843

Cowgill, E., Yin, A., Wang, X. F., and Zhang, Q. (2000). Is the North Altyn Fault Part of a Strike-Slip Duplex along the Altyn Tagh Fault System? *Geology* 28 (3), 255–258. doi:10.1130/0091-7613(2000)028<0255:itnafp>2.3.co;2

Cowgill, E., Gold, R. D., Xuanhua, C., Xiaofeng, W., Arrowsmith, J. R., and Southon, J. (2009). Low Quaternary Slip Rate Reconciles Geodetic and Geologic Rates along the Altyn Tagh Fault, Northwestern Tibet. *Geology* 37 (7), 647–650. doi:10.1130/G25623A.1

Cowgill, E. (2007). Impact of Riser Reconstructions on Estimation of Secular Variation in Rates of Strike-Slip Faulting: Revisiting the Cherchen River Site along the Altyn Tagh Fault, NW China. *Earth Planet. Sci. Lett.* 254 (3–4), 239–255. doi:10.1016/j.epsl.2006.09.015

Cox, R. T. (1994). Analysis of Drainage-basin Symmetry as a Rapid Technique to Identify Areas of Possible Quaternary Tilt-Block Tectonics: an Example from the Mississippi Embayment. *GSA Bull.* 106 (5), 571–581. doi:10.1130/0016-7606(1994)106<0571:aodbsa>2.3.co;2

Cunningham, D., Zhang, J., and Li, Y. (2016). Late Cenozoic Transpressional Mountain Building Directly north of the Altyn Tagh Fault in the Sanweishan and Nanjieshan, North Tibetan Foreland, China. *Tectonophysics* 687, 111–128. doi:10.1016/j.tecto.2016.09.010

Deng, Q. D., Zhang, P. Z., Ran, Y. K., Min, W., Yang, X. P., and Chu, Q. Z. (2003). Basic Characteristics of Active Tectonics of China. *Sci. China Ser. D Earth Sci.* 46 (4), 357–372. (in Chinese with English abstract). doi:10.1360/03yd9032

Ellis, M. A., and Barnes, J. B. (2015). A Global Perspective on the Topographic Response to Fault Growth. *Geosphere* 11 (4), 1008–1023. doi:10.1130/GES01156.1

Gold, R. D., Cowgill, E., Arrowsmith, J. R., Gosse, J., Chen, X., and Wang, X. F. (2009). Riser Diachroneity, Lateral Erosion, and Uncertainty in Rates of Strike-Slip Faulting: A Case Study from Tuzidun along the Altyn Tagh Fault, NW China. *J. Geophys. Res.–Solid Earth* 114 (B4), B04401. doi:10.1029/2008JB005913

Gosse, J. C., and Phillips, F. M. (2001). Terrestrial *In Situ* Cosmogenic Nuclides Theory and Application. *Quat. Sci. Rev.* 20 (14), 1475–1560. doi:10.1016/S0277-3791(00)00171-2

Grasemann, B., and Schmalholz, S. M. (2012). Lateral Fold Growth and Fold Linkage. *Geology* 40 (11), 1039–1042. doi:10.1130/G33613.1

Hare, P. H., and Gardner, T. W. (1985). "Geomorphic Indicators of Vertical Neotectonism along Converging Plate Margins, Nicoya Peninsula, Costa Rica," in *Tectonic Geomorphology*. Editors M Morisawa and J. T Hack (Boston: Allen & Unwin), 75–104.

He, Z. Y., Zhang, Z. M., Zong, K. Q., and Dong, X. (2013). Paleoproterozoic Crustal Evolution of the Tarim Craton: Constrained by Zircon U-Pb and Hf Isotopes of Meta-Igneous Rocks from Korla and Dunhuang. *J. Asian Earth Sci.* 78, 54–70. doi:10.1016/j.jseaes.2013.07.022

Hetzel, R., Tao, M., Niedermann, S., Strecker, M., Ivy-Ochs, S., and Kubik, P. W. (2004). Implications of the Fault Scaling Law for the Growth of Topography: Mountain Ranges in the Broken Foreland of north-east Tibet. *Terra Nova* 16, 157–162. doi:10.1111/j.1365-3121.2004.00549.x

Jackson, J., Ritz, J. F., Siame, L., Raisbeck, G., Yiou, F., and Norris, R. (2002). Fault Growth and Landscape Development Rates in Otago, New Zealand, Using *In Situ* Cosmogenic ^{10}Be. *Earth Planet. Sci. Lett.* 195, 185–193. doi:10.1016/S0012-821X(01)00583-0

Keller, E. A., and DeVecchio, D. E. (2013). "Tectonic Geomorphology of Active Folding and Development of Transverse Drainages," in *Treatise on Geomorphology* (Elsevier), 129–147. doi:10.1016/B978-0-12-374739-6.00088-9

Keller, E. A., Zepeda, R. L., Rockwell, T. K., Ku, T. L., and Dinklage, W. S. (1998). Active Tectonics at Wheeler Ridge, Southern San Joaquin Valley, California. *Geol. Soc. Am. Bull.* 110, 298–310. doi:10.1130/0016-7606(1998)110<0298:atawrs>2.3.co;2

Keller, E. A., Gurrola, L., and Tierney, T. E. (1999). Geomorphic Criteria to Determine Direction of Lateral Propagation of Reverse Faulting and Folding. *Geology* 27, 515–518. doi:10.1130/0091-7613(1999)027<0515:gctddo>2.3.co;2

Lacombe, O., Roure, F., and Lavé, J. (2007). Thrust Belts and Foreland Basins: From Fold Kinematics to Hydrocarbon Systems. *Front. Earth Sci.* 14 (5), 205–228. doi:10.1007/978-3-540-69426-7

Lal, D. (1991). Cosmic ray Labeling of Erosion Surfaces *In Situ* Nuclide Production Rates and Erosion Models. *Earth Planet. Sci. Lett.* 104, 424–439. doi:10.1016/0012-821X(91)90220-C

Li, M., Xiao, Q. B., and Yu, G. (2020). Electrical Structure of the Altyn Tagh Fault at the Changma Section and its Tectonic Significance. *Chin. J. Geophys.* 63 (11), 4125–4143. doi:10.6038/cjg2020N0413

Li, Z. Z. (1994). Formation and Evolution of the Tectonic Landforms in the Altun Mountain and its Neighboring Region. *Geogr. Res.* 13 (3), 35–42.

Liu, J., Ren, Z., Zheng, W., Min, W., Li, Z., and Zheng, G. (2020). Late Quaternary Slip Rate of the Aksay Segment and its Rapidly Decreasing Gradient along the Altyn Tagh Fault. *Geosphere* 16 (6), 1538–1557. doi:10.1130/GES02250.1

Molnar, P., and Tapponnier, P. (1975). Cenozoic Tectonics of Asia: Effects of a continental Collision: Features of Recent continental Tectonics in Asia Can Be Interpreted as Results of the India-Eurasia Collision. *Science* 189 (4201), 419–426. doi:10.1126/science.189.4201.419

Ramsey, L. A., Walker, R. T., and Jackson, J. (2007). Geomorphic Constraints on the Active Tectonics of Southern Taiwan. *Geophys. J. Int.* 170 (3), 1357–1372. doi:10.1111/j.1365-246X.2007.03444.x

Ramsey, L. A., Walker, R. T., and Jackson, J. (2008). Fold Evolution and Drainage Development in the Zagros Mountains of Fars Province, SE Iran. *Basin Res.* 20 (1), 23–48. doi:10.1111/j.1365-2117.2007.00342.x

Salvany, J. M. (2004). Tilting Neotectonics of the Guadiamar Drainage basin, SW Spain. *Earth Surf. Process. Landforms* 29 (2), 145–160. doi:10.1002/esp.1005

Schumm, S. A., Dumont, J. F., and Holbrook, J. M. (2000). *Active Tectonics and Alluvial Rivers*. Cambridge: Cambridge University Press.

Shahzad, F., and Gloaguen, R. (2011). TecDEM: A MATLAB Based Toolbox for Tectonic Geomorphology, Part 2: Surface Dynamics and Basin Analysis. *Comput. Geosci.* 37 (2), 261–271.

Stone, J. O. (2000). Air Pressure and Cosmogenic Isotope Production. *J. Geophys. Res.* 105, 23753–23759. doi:10.1029/2000JB900181

Tapponnier, P., Zhiqin, X., Roger, F., Meyer, B., Arnaud, N., and Wittlinger, G. (2001). Oblique Stepwise Rise and Growth of the Tibet Plateau. *Science* 294 (5547), 1671–1677. doi:10.1126/science.105978

Wang, P., Lu, Y., Ding, G., Chen, J., and Wyrwoll, K. H. (2004). Response of the Development of the Shule River Alluvial Fan to Tectonic Activity. *Quat. Sci.* 24 (1), 74–81. (in Chinese with English abstract). doi:10.3969/j.issn.0253-4967.2004.04.017

Wang, H. Y. C., Wang, J., Wang, G. D., Lu, J. S., Chen, H. X., and Peng, T. (2017). Metamorphic Evolution and Geochronology of the Dunhuang Orogenic belt in the Hongliuxia Area, Northwestern China. *J. Asian Earth Sci.* 135, 51–69. doi:10.1016/j.jseaes.2016.12.014

Wang, Y. T. (1989). The Research of Quaternary basin of Dunhuang in the Western Gansu. *Gansu Geol.* (10), 39–55. (in Chinese with English abstract).

Xiao, Q., Zhao, G., and Dong, Z. (2011). Electrical Resistivity Structure at the Northern Margin of the Tibetan Plateau and Tectonic Implications. *J. Geophys. Res. Solid Earth* 116 (B12). doi:10.1029/2010JB008163

Xiao, Q., Shao, G., Liu-Zeng, J., Oskin, M. E., Zhang, J., and Zhao, G. (2015). Eastern Termination of the Altyn Tagh Fault, Western China: Constraints from a Magnetotelluric Survey. *J. Geophys. Res. Solid Earth* 120 (5), 2838–2858. doi:10.1002/2014JB011363

Xiao, Q., Yu, G., Liu-Zeng, J., Oskin, M. E., and Shao, G. (2017). Structure and Geometry of the Aksay Restraining Double bend along the Altyn Tagh Fault, Northern Tibet, Imaged Using Magnetotelluric Method. *Geophys. Res. Lett.* 44 (9), 4090–4097. doi:10.1002/2017GL072581

Xu, X., Wang, F., Zheng, R., Chen, W., Ma, W., Yu, G., et al. (2005). Late Quaternary Sinistral Slip Rate Along the Altyn Tagh Fault and Its Structural Transformation Model. *Sci. China Ser. D* 48 (3), 14. doi:10.1360/02yd0436

Yang, H., Yang, X., Cunningham, D., Hu, Z., Huang, X., and Huang, W. (2020). A Regionally Evolving Transpressional Duplex along the Northern Margin of the Altyn Tagh Fault: New Kinematic and Timing Constraints from the Sanweishan and Nanjieshan, China. *Tectonics* 39 (2). doi:10.1029/2019tc005749

Yin, A., Rumelhart, P. E., Butler, R., Cowgill, E., Harrison, T. M., and Foster, D. A. (2002). Tectonic History of the Altyn Tagh Fault System in Northern Tibet Inferred from Cenozoic Sedimentation. *Geol. Soc. Am. Bull.* 114, 1257–1295. doi:10.1130/0016-7606(2002)114<1257:thotat>2.0.co;2

Yue, Y., and Liu, J. G. (1999). Two-stage Evolution Model for the Altyn Tagh Fault, China. *Geology* 27 (3), 227–230. doi:10.1130/0091-10.1130/0091-7613(1999)027<0227:tsemft>2.3.co;2

Yun, L., Zhang, J., Wang, J., Yang, X. P., Qu, J. F., and Zhang, B. H. (2020). Active Deformation to the north of the Altyn Tagh Fault: Constraints on the Northward Growth of the Northern Tibetan Plateau. *J. Asian Earth Sci.* 198, 104312. doi:10.1016/j.jseaes.2020.104312

Zhang, P. Z., Molnar, P., and Xu, X. (2007). Late Quaternary and Present-Day Rates of Slip along the Altyn Tagh Fault, Northern Margin of the Tibetan Plateau. *Tectonics* 26 (5), TC5010.1–TC5010.24. doi:10.1029/2006TC002014

Zhang, J., Yun, L., Zhang, B., Qu, J. F., Zhao, H., and Hui, J. (2020). Deformation at the Easternmost Altyn Tagh Fault: Constraints on the Growth of the Northern Qinghai–Tibetan Plateau. *Acta Geol. Sin.-English Ed.* 94 (4), 988–1006. doi:10.1111/1755-6724.14555

Zhao, Y., Diwu, C., Ao, W., Wang, H., Zhu, T., and Sun, Y. (2015). Ca. 3.06 Ga Granodioritic Gneiss in Dunhuang Block. *Chin. Sci. Bull. (Chin. Vers.)* 60 (1), 75–87. (in Chinese). doi:10.1360/n972014-00382

Zheng, W. J., Zhang, P. Z., He, W. G., Yuan, D. Y., Shao, Y. X., and Zheng, D. W. (2013). Transformation of Displacement between Strike-Slip and Crustal Shortening in the Northern Margin of the Tibetan Plateau: Evidence from Decadal GPS Measurements and Late Quaternary Slip Rates on Faults. *Tectonophysics* 584, 267–280. doi:10.1016/j.tecto.2012.01.006

Zheng, W. J., Yuan, D. Y., Zhang, P. Z., Yu, J. X., Lei, Q. Y., and Wang, W. T. (2016). Tectonic Geometry and Kinematic Dissipation of the Active Faults in the Northeastern Tibetan Plateau and Their Implications for Understanding Northeastward Growth of the Plateau. *Quat. Sci.* 34 (4), 775–788. (in Chinese).

Zhuang, G. S., Hourigan, J. K., Ritts, B. D., and Kent-Corson, M. L. (2011). Cenozoic Multiple-phase Tectonic Evolution of the Northern Tibetan Plateau: Constraints from Sedimentary Records from Qaidam basin, Hexi Corridor, and Subei basin, Northwest China. *Am. J. Sci.* 311 (2), 116–152. doi:10.2475/02.2011.02

Conflict of Interest: The authors declare that the research was conducted in the absence of any commercial or financial relationships that could be construed as a potential conflict of interest.

Publisher's Note: All claims expressed in this article are solely those of the authors and do not necessarily represent those of their affiliated organizations, or those of the publisher, the editors and the reviewers. Any product that may be evaluated in this article, or claim that may be made by its manufacturer, is not guaranteed or endorsed by the publisher.

Copyright © 2021 Chen, Zheng, Yang, Duan, Liang, Li, Zhang and Xiong. This is an open-access article distributed under the terms of the Creative Commons Attribution License (CC BY). The use, distribution or reproduction in other forums is permitted, provided the original author(s) and the copyright owner(s) are credited and that the original publication in this journal is cited, in accordance with accepted academic practice. No use, distribution or reproduction is permitted which does not comply with these terms.

frontiers in Earth Science

ORIGINAL RESEARCH
published: 18 January 2022
doi: 10.3389/feart.2021.820674

The Changes in Drainage Systems of Weihe Basin and Sanmenxia Basin Since Late Pliocene Give New Insights Into the Evolution of the Yellow River

Jin Liu[1], Ping Wang[2], Xingqiang Chen[3], Wei Shi[4], Lijun Song[5] and Jianmin Hu[4]*

[1]School of Civil and Architecture Engineering, Xi'an Technological University, Xi'an, China, [2]School of Geography, Nanjing Normal University, Nanjing, China, [3]China Railway First Survey & Design Institute Group Co., Ltd., Xi'an, China, [4]Institute of Geomechanics, Chinese Academy of Geological Sciences, Beijing, China, [5]School of Earth Sciences and Engineering, Xi'an Shiyou University, Xi'an, China

The formation of the Yellow River involved the draining of a series of ancestral local lakes along their course, substantially changing the regional, geomorphic, and paleoenvironmental evolution. However, the evolution of the Weihe-Sanmenxia Basin section of the Yellow River remains indistinct as previous studies regard the Weihe and Sanmenxia Basin as one integral basin of the Late Cenozoic. Here, we present the detrital zircon age spectra from the Pliocene-Pleistocene Sanmen Formation to clarify the drainage system evolution of the two basins since the Late Pliocene. The results reveal that these two basins belonged to different drainage systems in the Late Pliocene because no sediments from the marginal mountains of the Weihe Basin accumulated in the Sanmenxia Basin. At 2.8/2.6 Ma, the currents presented at the edge of the basins and transported the sediment of east Hua Mountain into the Sanmenxia Basin, where it was deposited. This integration likely leads to a mismatch between the deposition and regional paleoclimate in previous studies. At ~1.0 Ma, the Sanmenxia Gorge was traversed and the Yellow River finally formed, depositing Jinshaan Gorge sediment into the Sanmenxia Basin and lower reaches of the Yellow River.

Keywords: Yellow river (Huanghe), Sanmen Fm., Sanmenxia Basin, Weihe Basin, river formation

OPEN ACCESS

Edited by:
Xiaoping Yuan,
GFZ German Research Centre for Geosciences, Germany

Reviewed by:
Lei Wu,
Zhejiang University, China
Maodu Yan,
Institute of Tibetan Plateau Research (CAS), China

****Correspondence:***
Jin Liu
358198000@qq.com

Specialty section:
This article was submitted to Structural Geology and Tectonics, a section of the journal Frontiers in Earth Science

Received: *23 November 2021*
Accepted: *22 December 2021*
Published: *18 January 2022*

Citation:
Liu J, Wang P, Chen X, Shi W, Song L and Hu J (2022) The Changes in Drainage Systems of Weihe Basin and Sanmenxia Basin Since Late Pliocene Give New Insights Into the Evolution of the Yellow River. Front. Earth Sci. 9:820674. doi: 10.3389/feart.2021.820674

INTRODUCTION

The Yellow River is the second-longest river in China and the sixth-longest river in the world. Previous studies suggested that the Yellow River achieved its present geometry by integrating a series of ancestral local drainages (Craddock et al., 2010; Pan et al., 2012) and has long been related to the uplift of the northeastern Tibetan Plateau (Wang et al., 2013; Xiao et al., 2020).

In the middle reaches of the Yellow River, many studies have been carried out in Jinshaan Gorge (Fu et al., 2013; Hu et al., 2017) and Sanmenxia Gorge (Wang et al., 2002; Pan et al., 2005; Jiang et al., 2007; Zheng et al., 2007; Kong et al., 2014; Hu et al., 2016). Jinshaan Gorge connects the Hetao Basin and Weihe Basin, whereas Sanmenxia Gorge connects Weihe Basin and Huabei Plain. However, the integration of the Weihe Basin and Sanmenxia Basin remains indistinct, which makes the Yellow River bend significantly (nearly 90°) in Tongguan County (**Figure 1**).

Previous studies have regarded the Weihe Basin and Sanmenxia Basin as one integral basin, belonging to the Sanmen Paleolake since ~5 Ma, having been deposited with the fluvio-

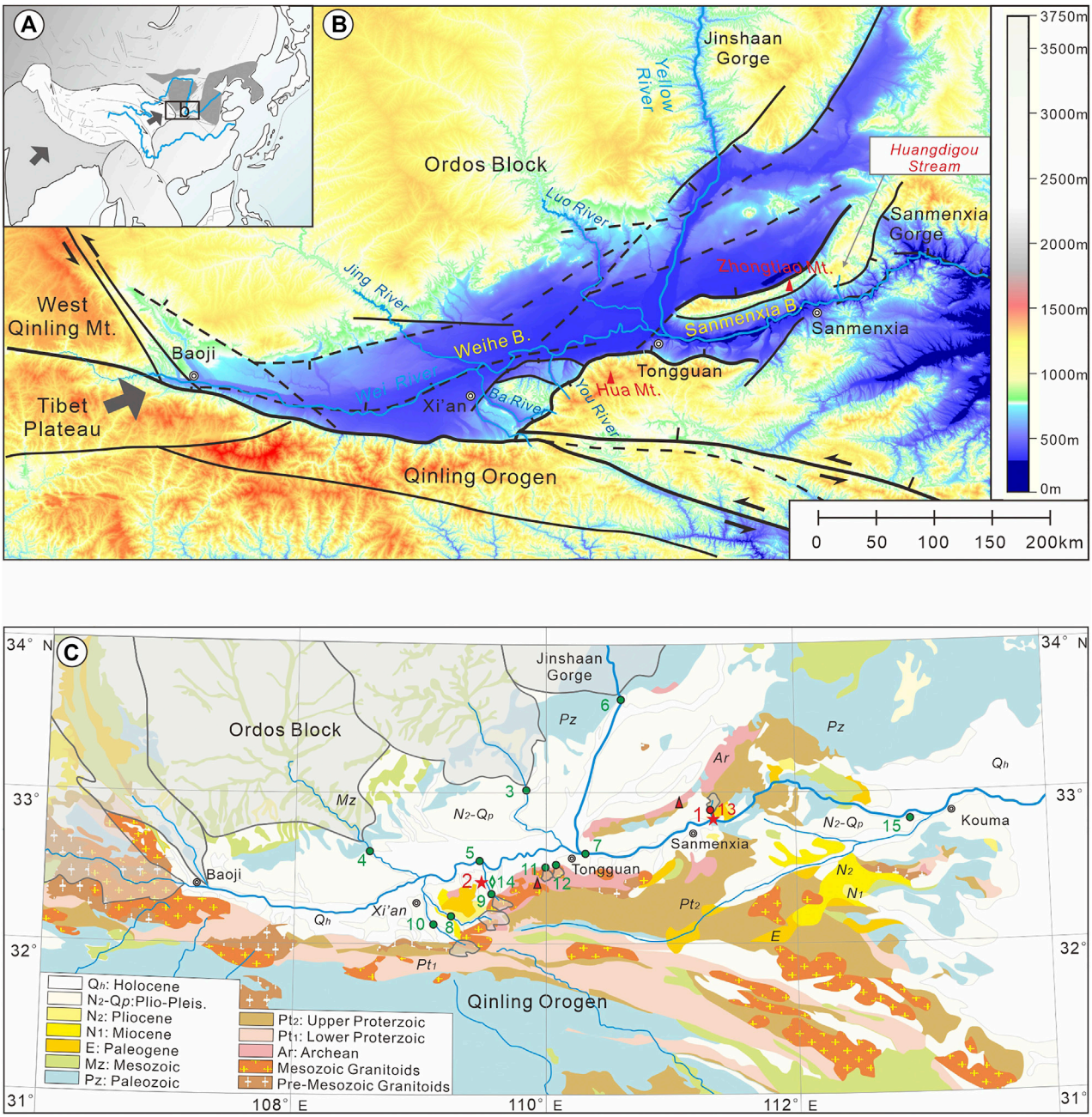

FIGURE 1 | (A), Locating of the Yellow River and the study area. **(B)**, Tectonic setting and geomorphic features of the Weihe Basin and Sanmenxia Basin. **(C)**, Lithostratigraphy of the study area and the sampling location. The stars indicate the study site in this article (1. Huangdigou section; 2. Songjiabeigou section). The open circles and numbers are the locations of published modern river samples, and the diamonds indicate the locations of the sites of previously studied samples from basin or terrace sediments (see **Supplementary Table S1** for sample information).

lacustrine Sanmen Formation (Sm Fm.) (Wang et al., 2004; Wang et al., 2013). However, the Sm Fm. in these two basins show different sedimentary characteristics and are considered to have different deposition locations. The paleogeomorphic study (Zhu, 1989) and sedimentary facies of drilled cores (Liu and Zhou, 2015) indicated that the Weihe Basin and Sanmenxia Basin were isolated during the Pliocene but belonged to the same Sanmen Paleolake during the Early Pleistocene (Han et al., 2002). To determine that the Weihe Basin and Sanmenxia Basin belong to the same drainage system at 5 Ma or Early Pleistocene, the sedimentary character of the Sm Fm. should be studied. Because the Weihe Basin is located upstream and the Sanmenxia Basin is located downstream, once the two basins are integrated, the

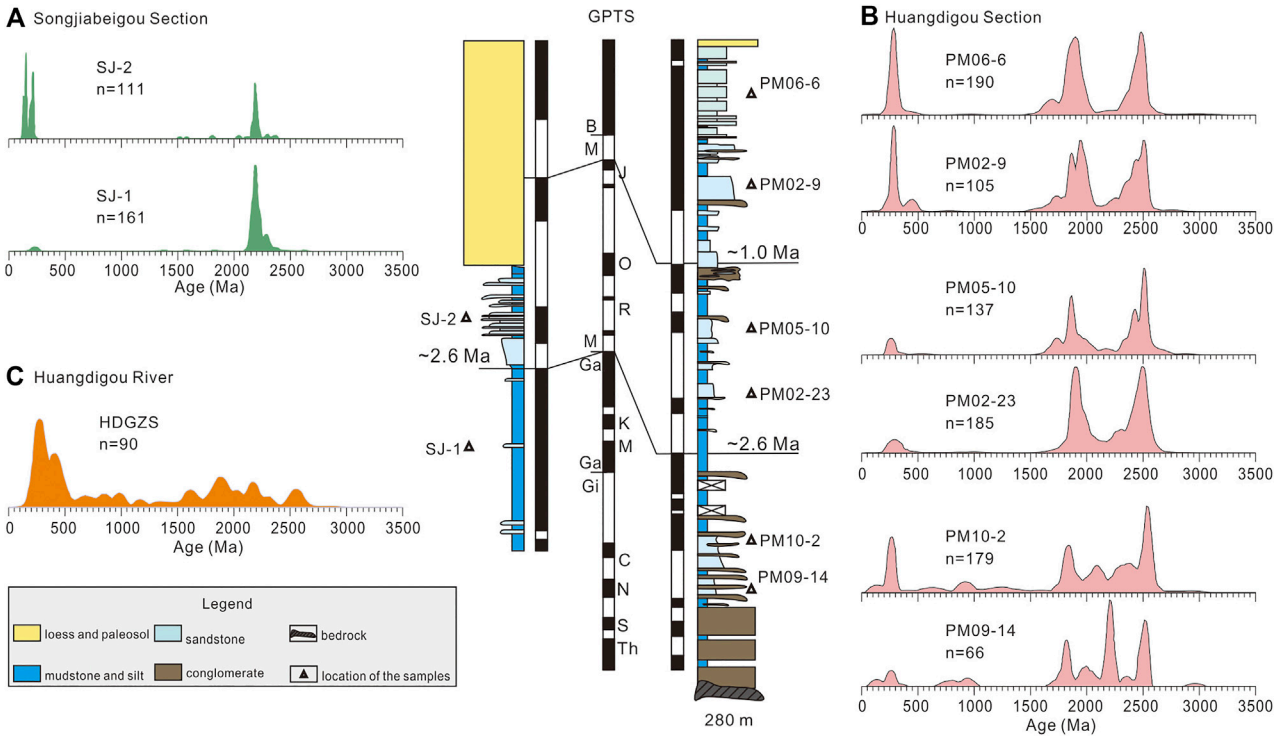

FIGURE 2 | Kernel density estimation plots of the zircon U-Pb ages from the Songjiabeigou Section **(A)**, Huangdigou Section **(B)**, and Huangdigou Stream **(C)** and the corresponding lithostratigraphy and chronological framework [referenced by Hu et al. (1993) and Wang et al. (1999)].

water in the Weihe Basin will flow into the Sanmenxia Basin, resulting in sedimentary facies and provenance of the Sm Fm. in the two basins changed simultaneously. Studies of sedimentary facies and heavy minerals in the Sm Fm. of the Huangdigou section in the Sanmenxia Basin and Songjiabeigou section in the Weihe Basin have been carried out in our previous studies (Liu et al., 2019; Liu et al., 2020). Based on the reported paleomagnetic ages (Hu et al., 1993; Wang et al., 1999) and our previous work, the sections could be divided into five and three sediment environments in the Sanmenxia Basin and Weihe Basin, respectively. The Huangdigou section consists mainly of gray conglomerates, yellowish sands, green or yellowish mud, and minor yellow silt and could be divided into alluvial fan (~5–2.8 Ma), a shallow lake (~2.8–1.8 Ma), a lake shore environment (~1.8–1.0 Ma), a fluvial setting (~1.0–0.15 Ma), and eolian loess (younger than ~0.15 Ma) from bottom to top. The Songjiabeigou section contains mainly yellowish sand and green and blue clay, which can be divided into deep lake environment (prior ~2.6 Ma), fluvial environment (~2.6–1.5 Ma), and eolian loess (younger than ~1.5 Ma) from bottom to top. However, the single-grain zircon U-Pb age spectra, a diagnostic tool for identifying the source areas in East Asia (e.g., Stevens et al., 2013; Nie et al., 2015; Licht et al., 2016), are still poorly understood. In this study, we measured nine detrital zircon ages from two well-dated sections and one from Huangdigou Stream to represent sediment from Zhongtiao Mountain and compared the results with published zircon ages of the modern river sand samples to determine the evolution of the basin drainage system.

MATERIALS AND METHODS

Clastic deposits started to be accumulated in the Weihe and Sanmenxia Basins since the Paleogene (Chen et al., 2021). Extensive fluvial-lacustrine Sanmen Formation was developed continuously since the Late Pliocene (Wang et al., 2013), providing reliable material for the basin paleoenvironmental evolution research. The different lithology and chronology of the surrounding mountains make the region an ideal site for tracing the provenance (see detailed information from **Supplementary Figure S1**).

In the field, we explored the Songjiabeigou section (109°30′43″E, 34°25′53″N) and the Huangdigou section (111°16′54″–111°16′56″E, 34°49′38″–34°49′48″N) in the Weihe and Sanmenxia Basins, respectively. Nine samples were collected from the coarse channel or floodplain deposits of these two basins. Six of them were from the Huangdigou section of the Sanmenxia Basin (two from the lower Sm Fm. and four from the upper Sm Fm.) and two from the Songjiabeigou section of the Weihe Basin (one from the lower Sm Fm. and one from the upper Sm Fm.) (see the positions of the samples in **Figure 2**). Another sample was collected from the modern stream sediment in Huangdigou Stream (shown in **Figure 1**) to represent the provenance of Zhongtiao Mountain.

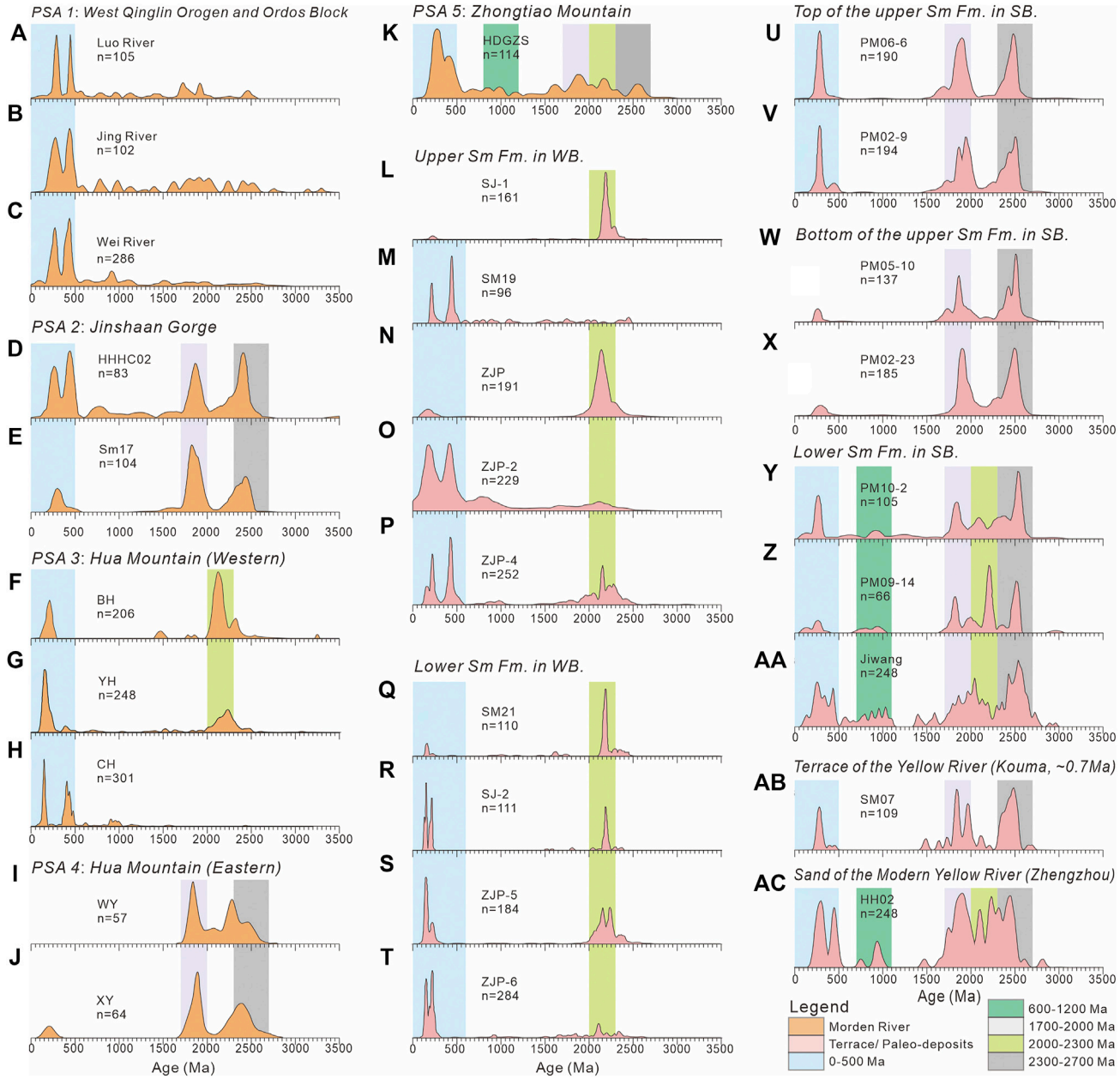

FIGURE 3 | Zircon U-Pb ages of the Sm Fm. and potential source areas of the region. The bands show different age ranges of zircon grains indicated by colors defined in the lower panel. **A–C, D–E, F–H, I–J, and K** show the sediments from potential source areas of western Qinling Orogen and Ordos, Jinshaan Gorge, the western part of Hua Mountain, the eastern part of Hua Mountain, and Zhongtiao Mountain, respectively. **L–M and N–T** show the sediments from the upper and lower parts of the Sm Fm. in Weihe Basin. **U-V, W-X, and Y-AA** show the sediments from the upper, middle, and lower parts of the Sm Fm. in the Sanmenxia Basin. **AB and AC** show the sediments from the terrace of the Yellow River and modern Yellow River, respectively.

RESULTS OF THE DETRITAL ZIRCON U–PB GEOCHRONOLOGY

The U–Pb ages of each sample are presented by kernel density estimation in **Figure 2** using the DensityPlotter software (Vermeesch, 2012). These large age clusters indicate that the grains in these samples were derived from a number of heterogeneous and varying sources. In Sanmenxia Basin, the lower Sm Fm. (PM09-14 and PM10-2) show eight age clusters at ~100 Ma, ~250 Ma, ~800 Ma, ~950 Ma, ~1,800 Ma, ~2,000 Ma, ~2,200 Ma, and ~2,500 Ma, with four large peaks at ~250 Ma, ~1,800 Ma, ~2,200 Ma, and ~2,500 Ma. However, the upper Sm Fm. can be divided into two units: the bottom of the formation (PM05-10 and PM02-23) exhibits two age clusters at ~1,800 Ma and ~2,500 Ma, whereas the top of the formation (PM 02-9, PM 06-6) shows three obvious clusters at ~250 Ma,

~1,800 Ma, and ~2,500 Ma. Nevertheless, in the Weihe Basin, the data for the lower (SJ1) and upper Sm Fm. (SJ2) show the same pattern, with no more than/only two clusters at ~250 Ma and ~2,200 Ma, but with a different ratio. SJ2 sediment consists of younger age components, which account for approximately 28% of the sediment, whereas SJ1 accounts for approximately 3%.

The modern fluvial sample HDGZS-1 shows one distinct peak at ~250 Ma and four small clusters at ~900 Ma, ~1,800 Ma, ~2,200 Ma, and ~2,600 Ma. See detailed chronologies in **Supplementary Table S2**.

AGE COMPARISON AND INTERPRETATION OF THE POTENTIAL SOURCE AREAS

Detrital zircon U-Pb geochronology has long been regarded as a powerful tool to constrain the provenance of terrigenous sediments and the evolution of sedimentary basins (Dickinson et al., 1983; Gehrels et al., 2003; Zheng et al., 2020; Shang et al., 2021). Comparing zircon ages with sediments that accumulate from potential source areas could provide a comprehensive view of potential source areas (Gehrels, 2012). Rivers can mix all the bedrock lithology of potential sources (He et al., 2013), and analyses of modern river sands can be used to reflect the comprehensive characteristics of potential source areas and help track the long-term evolution of the region (Nie et al., 2012; Chen et al., 2017). Therefore, in order to better determine the provenance changes, published detrital zircon U-Pb ages in modern river sediments were compiled and compared with our studies (**Supplementary Table S1**, **Figure 3**).

From **Figure 3**, the provenance of the western Qinling Orogen and Ordos Block, represented by the modern Luo River and Jing River (Zhang et al., 2019) and Wei River (Zhang et al., 2021), shows obvious clusters at ~250 Ma and ~450 Ma. The zircon spectrum of modern Yellow River sediments, collected at Hancheng (HHHC02, Yang et al., 2009) and Tongguan (SM 17, Kong et al., 2014), demonstrates great similarities with three clusters at ~250 Ma, ~1,800 Ma, and ~2,500 Ma and are regarded as the provenance character of the Jinshaan Gorge. The sediments from the Ba River, You River, and Chan River (BH, Zhang et al., 2018; YH and CH, Zhang et al., 2021), which originate from western Hua Mountain, show two distinct peaks at ~150 Ma and ~2,200 Ma. In addition, the sediments from two valleys (WY and XY) at the eastern Hua Mountain exhibit two obvious age peaks at ~1,800 Ma and ~2,200 Ma (Zhang, 2008). The sediments from Huangdigou Valley of Zhongtiao Mountain show five age ranges: ~250 Ma, ~900 Ma, ~1,800 Ma, ~2,200 Ma, and ~2,600 Ma.

From the U-Pb age spectrum of different potential provenance regions, sediments from the western Qinling Orogen and Ordos Block are relatively young and seldom contain old zircon. Sediments from western Hua Mountain and Zhongtiao Mountain contain an age peak at ~2,200 Ma, which is absent in modern Yellow River sediments. The North China Craton formed at ~2,500 Ma; thus, the regional zircon spectrum revealed the peak at 2,300~2,700 Ma widespread. At approximately ~2,200 Ma, the region experienced a long-term magma quiet period (Zhai and Peng, 2007) with occasional rifting, accretion, and collision processes in Zhongtiao Mountain and Hua Mountain (Zhai and Santosh, 2011; Du et al., 2016; Peng et al., 2017; Du et al., 2018). This indicated that the sediment with a peak at ~2,200 Ma could be regarded as a representative feature of the Zhongtiao Mountain and Hua Mountain provenance. These differences make it possible to identify potential provenance regions by the U-Pb age.

The spectrum characteristics of potential provenance regions were compared with those of Sm Fm. to trace the provenance. The sediments of Sm Fm. in the Weihe Basin were mainly from the western areas of the Hua Mountain, with no obvious changes. For Sanmenxia Basin, there were two provenance shifts at 2.8 Ma and 1.0 Ma, respectively. At 2.8 Ma, the sediments changed from Zhongtiao Mountain to eastern Hua Mountain, indicating that the sediment provenance changed from near-source deposition to west of the Weihe Basin. This implies that water from the Weihe Basin began to flow into the Sanmenxia Basin. At 1.0 Ma, sediments are very similar to the modern Yellow River, indicating that the Jinshaan Gorge drainage system was connected to the region (**Figure 4**). This hypothesis is also supported by the evolution of the Yellow River in the Jinshaan Gorge, which revealed that the final incision of Jinshaan Gorge was ~1.2 Ma (Hu et al., 2016). Following the Yellow River formation, the sediment discharged by the Wei River occupied only about 30% of the Yellow River (Zhang et al., 2018); therefore, the sediment in the Sanmenxia Basin did not exhibit many Weihe Basin characteristics.

DISCUSSION

The Timing of the Connection of the Weihe and the Sanmenxia Basins

The apparent difference in sediment provenance in the Sanmenxia and Weihe Basins before 2.8 Ma indicated that they belonged to different drainage systems. Previous studies of the sedimentary facies (Liu et al., 2019) indicated that the lake level in the Weihe Basin decreased, whereas in the Sanmenxia Basin, the level increased at 2.8 Ma; this study further revealed that the sediment provenance of the Sanmenxia Basin changed from Zhongtiao Mountain to eastern Hua Mountain. The zircon ages verified that a paleocurrent originated from the eastern Hua Mountain and transported the sediments into the Sanmenxia Basin at 2.8 Ma. Thus, we regarded the two basins as belonging to the same Paleo-Sanmen Lake drainage system not earlier than 2.8 Ma. After the connection of drainage systems, a great volume of water in Weihe Basin flowed into the Sanmenxia Basin, therefore explaining the formation of the oldest terrace (~2.6 Ma) in Weihe Basin (Sun, 2005). Moreover, this connection resulted in a decrease in regional erosion, which may prompt the traversing of Jinshaan Gorge.

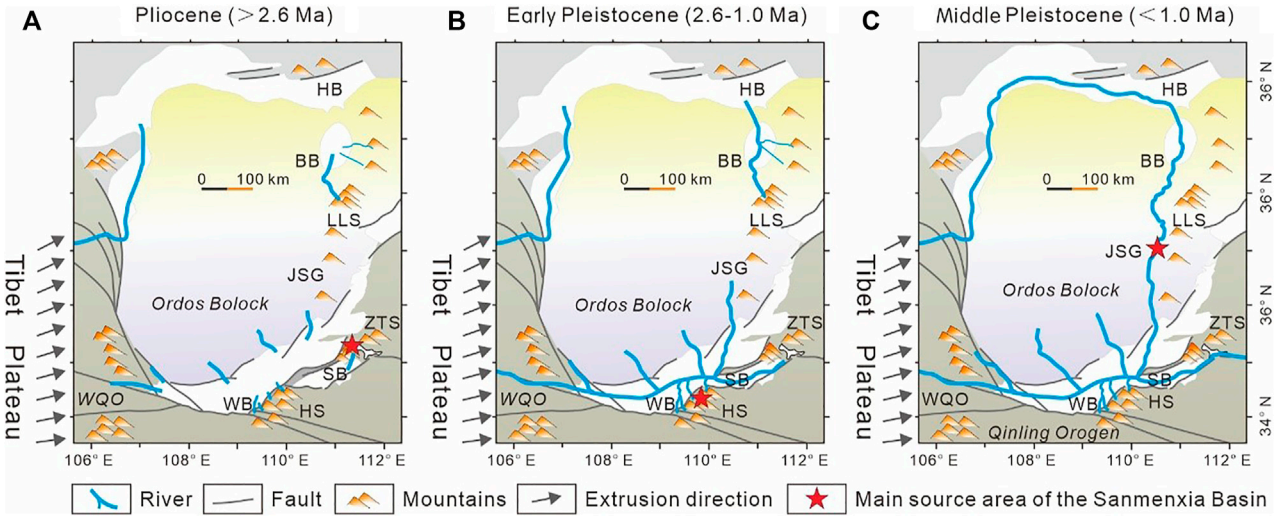

FIGURE 4 | Sketch maps illustrating formation processes of the middle reach of the Yellow River. **(A)** Short rivers developed surrounding local lakes during the early Pliocene. **(B)** Regional drainage started to connect during Early Pleistocene. **(C)** Modern Yellow River finally formatted at ~1.0 Ma. HB: Hetao Basin; BB: Baode Basin; LLS: Lvliang Mountain; JSG: Jinshaan Gorge; WQO: West Qinling Orogen; WB: Weihe Basin; SB: Sanmenxia Basin; HS: Hua Mountain; ZTS: Zhongtiao Mountain.

Implication for the Formation of the Modern Yellow River

The traversal of the Sanmenxia Gorge is regarded as the final formation of the Yellow River (Pan et al., 2005; Jiang et al., 2007; Wang et al., 2016). However, this date is still debated, from Early Pleistocene (Xue, 1996; Yang et al., 2001) to ~1.2 Ma (Zhu, 1989; Pan et al., 2005; Fu et al., 2008; Pan et al., 2012; Hu et al., 2017) or even 0.15 Ma (Wang et al., 2002; Jiang et al., 2007). The sediment of the Sanmenxia Basin after 1.0 Ma shows great consistency with Jinshaan Gorge (HHHC02; Yang et al., 2009), Tongguan County (SM17; Kong et al., 2014), and Yellow River terrace with the age of 0.7 Ma (SM07; Kong et al., 2014) (**Figure 3**). The studies of the detrital zircon U-Pb ages in the Sanmenxia Basin indicate that the traversing time of the Sanmenxia Gorge is ~1.0 Ma. This conclusion reveals that the sedimentary facies in the Sanmenxia Basin changed from shallow lake to fluvial (Liu et al., 2019; Liu et al., 2020) and led to the extensive development of terraces in the Weihe Basin after ~1.2 Ma (Hu et al., 2017).

However, the age spectrum of sediments collected from Zhengzhou (HH02, ac of **Figure 3**; Yang et al., 2009) is quite different from the sediments of the upper Sm Fm. in the Sanmenxia Basin and Jinshaan Gorge but is similar to Zhongtiao Mountain. We believe that the construction of the Sanmenxia Reservoir could probably be the main reason for the blockage of sediment from the middle reach of the Yellow River transported downstream.

Implications for the Environmental Change

The integration of the Sanmenxia Basin and Weihe Basin until 2.8 Ma indicates that the sediment before 2.8 Ma in the Sanmenxia Basin was a local record and could not be regarded as a record of paleo-Yellow River. This integration led to the decline of the Weihe Basin lake level, and the sediment from the western Qinling or Ordos Block transported by the Yellow River, Jing River, and Luo River could accumulate into the depocenter of the Weihe Basin. Therefore, the sediment with a young cluster of ~200 Ma increased remarkably after 2.6 Ma. The decline of the water table was also recorded in the variation of pollen (Tong et al., 2000; Zhao et al., 2018), ostracods (Wang et al., 2010), and paleosalinity (Liu et al., 2006), which was interpreted as a dry climate after 2.6 Ma. However, the decline may also be attributed to water outflow, thus creating a significant shift in the understanding of the paleoclimate evolution in this region. These landform changes led to changes in the provenance of the sediment, meaning that the Sanmenxia Basin after 2.8/2.6 Ma could not be used as an indicator of local paleoclimate.

CONCLUSION

1) Zircon chronology results revealed the drainage of Weihe Basin and Sanmenxia Basin began to connect at ~2.8 Ma and the middle reach of Yellow River finally formed at ~1.0 Ma.
2) This study showed that the traversing time of the Sanmen Gorge was ~1.0 Ma, and sediments from Jinshaan Gorge were deposited in the lower reaches of the Yellow River. However, the sediment character of the lower reaches varies obviously nowadays and could probably be attributed to dam construction.
3) The integration in the middle reaches of the Yellow River changed the regional landform and sediment provenance

significantly and likely led to a mismatch between the deposition and regional paleoclimate.

DATA AVAILABILITY STATEMENT

The original contributions presented in the study are included in the article/**Supplementary Material**; further inquiries can be directed to the corresponding author.

AUTHOR CONTRIBUTIONS

JL performed the data analyses and wrote the article; PW performed the experiment; XC contributed to the conception of the study; WS and LS contributed significantly to analysis and manuscript preparation; JH helped perform the analysis with constructive discussions.

FUNDING

This study was supported by the National Natural Science Foundation of China No. 42072242, and No. 41672203, Research Foundation of Education Bureau of Shaanxi Province, China (Grant No. 19JK0404).

SUPPLEMENTARY MATERIAL

The Supplementary Material for this article can be found online at: https://www.frontiersin.org/articles/10.3389/feart.2021.820674/full#supplementary-material

REFERENCES

Chen, Y., Yan, M., Fang, X., Song, C., Zhang, W., Zan, J., et al. (2017). Detrital Zircon U-Pb Geochronological and Sedimentological Study of the Simao Basin, Yunnan: Implications for the Early Cenozoic Evolution of the Red River. *Earth Planet. Sci. Lett.* 476, 22–33. doi:10.1016/j.epsl.2017.07.025

Chen, X., Dong, S., Shi, W., Zuza, A. V., Li, Z., Chen, P., et al. (2021). Magnetostratigraphic Ages of the Cenozoic Weihe and Shanxi Grabens in north china and Their Tectonic Implications. *Tectonophysics* 813 (6833), 228914. doi:10.1016/j.tecto.2021.228914

Craddock, W. H., Kirby, E., Harkins, N. W., Zhang, H., Shi, X., and Liu, J. (2010). Rapid Fluvial Incision along the Yellow River during Headward basin Integration. *Nat. Geosci.* 3, 209–213. doi:10.1038/ngeo777

Dickinson, W. R., Beard, L. S., Brakenridge, G. R., Erjavec, J. L., Ferguson, R. C., Inman, K. F., et al. (1983). Provenance of North American Phanerozoic Sandstones in Relation to Tectonic Setting. *Geol. Soc. Am. Bull.* 94, 222–235. doi:10.1130/0016-7606(1983)94<222:ponaps>2.0.co;2

Du, L., Yang, C., Wyman, D. A., Nutman, A. P., Lu, Z., Song, H., et al. (2016). 2090-2070Ma A-type Granitoids in Zanhuang Complex: Further Evidence on a Paleoproterozoic Rift-Related Tectonic Regime in the Trans-North China Orogen. *Lithos* 254-255, 18–35. doi:10.1016/j.lithos.2016.03.007

Du, L., Yang, C., Song, H., Zhao, L., Lu, Z., Li, L., et al. (2018). Petrogenesis and Tectonic Setting of 2. 2 ~2. 1Ga Granites in Wutai Area, North China Craton. *Acta Petrol. Sin.* 34, 1154–1174 (in Chinese with English abstract).

Fu, J., Wang, S., Jiang, F., and Cai, Y. (2008). Age of Aeolian Deposition on the Highest Terrace in Yuanqu Basin and its Tectonic Significance. *Quat. Sci.* 28, 841–853 (in Chinese with English abstract).

Fu, J., Zhang, K., Ma, Z., Wang, S., and Wu, Y. (2013). The Terrace (T5 and T4) Formation since the Late Middle Pleistocene and its Implication in the through Cutting of the Middle Reach of Yellow River. *Earth Sci. Front.* 20, 166–181.

Gehrels, G. E., Yin, A., and Wang, X.-F. (2003). Detrital-zircon Geochronology of the Northeastern Tibetan Plateau. *GSA Bull.* 115, 881–896. doi:10.1130/0016-7606(2003)115<0881:dgotnt>2.0.co;2

Gehrels, G. (2012). "Detrital Zircon U-Pb Geochronology: Current Methods and New Opportunities," in *Tectonics of Sedimentary Basins: Recent Advances*. Editor U. Chichester (New Jersey: Wiley-Blackwell), 47–62 (in Chinese with English abstract).

Han, H., Zhang, Y., and Yuan, Z. (2002). The Evolution of Weihe Down-Faulted basin and the Movement of the Fault Blocks. *J. Seismol. Res.* 25, 362–368 (in Chinese with English abstract).

He, M., Zheng, H., and Clift, P. D. (2013). Zircon U-Pb Geochronology and Hf Isotope Data from the Yangtze River Sands: Implications for Major Magmatic Events and Crustal Evolution in Central China. *Chem. Geol.* 360–361, 186–203. doi:10.1016/j.chemgeo.2013.10.020

Hu, W., Yue, L., and Tian, X. (1993). On the Magnetostratigraphy of the Songjiabeigou Section, Youhe, Weinan. *Geol. Shaanxi* 11, 26–32 (in Chinese with English abstract).

Hu, Z., Pan, B., Guo, L., Vandenberghe, J., Liu, X., Wang, J., et al. (2016). Rapid Fluvial Incision and Headward Erosion by the Yellow River along the Jinshaan Gorge during the Past 1.2 Ma as a Result of Tectonic Extension. *Quat. Sci. Rev.* 133, 1–14. doi:10.1016/j.quascirev.2015.12.003

Hu, Z., Pan, B., Bridgland, D., Vandenberghe, J., Guo, L., Fan, Y., et al. (2017). The Linking of the Upper-Middle and Lower Reaches of the Yellow River as a Result of Fluvial Entrenchment. *Quat. Sci. Rev.* 166, 324–338. doi:10.1016/j.quascirev.2017.02.026

Jiang, F., Fu, J., Wang, S., Sun, D., and Zhao, Z. (2007). Formation of the Yellow River, Inferred from Loess-Palaeosol Sequence in Mangshan and Lacustrine Sediments in Sanmen Gorge, China. *Quat. Int.* 175, 62–70. doi:10.1016/j.quaint.2007.03.022

Kong, P., Jia, J., and Zheng, Y. (2014). Time Constraints for the Yellow River Traversing the Sanmen Gorge. *Geochem. Geophys. Geosyst.* 15, 395–407. doi:10.1002/2013gc004912

Licht, A., Pullen, A., Kapp, P., Abell, J., and Giesler, N. (2016). Eolian Cannibalism: Reworked Loess and Fluvial Sediment as the Main Sources of the Chinese Loess Plateau. *Geol. Soc. Am. Bull.* 128, B31371–B31375. doi:10.1130/b31375.1

Liu, Z., and Zhou, L. (2015). The Cenozoic Tectonic and Sedimentary Framework and Preliminary Study on the Hydrocarbon Accumulation Potential of the Weihe basin. *J. Fuzhou Univ. (Natural Sci. Edition)* 43, 708–714 (in Chinese with English abstract).

Liu, H., Xue, X., and andLi, Y. (2006). Calculation on the Paleosalinity of the Ancient Sanmen Lake in the Weinan Area of Weihe River Basin. *J. Northwest Univ. (Natural Sci. Edition)* 36, 112–114 (in Chinese with English abstract). doi:10.3799/dqkx.2020.112

Liu, J., Chen, X., Shi, W., Chen, P., Zhang, Y., Hu, J., et al. (2019). Tectonically Controlled Evolution of the Yellow River Drainage System in the Weihe Region, North China: Constraints from Sedimentation, Mineralogy and Geochemistry. *J. Asian Earth Sci.* 179, 350–364. doi:10.1016/j.jseaes.2019.05.008

Liu, J., Chen, X., Wang, P., and Li, T. (2020). Sedimentary Characteristics, Provenance and Tectonic Significance of the Sanmen Formation in Weihe-Sanmenxia Basin. *Earth Sci.* 45, 2673–2683 (in Chinese with English abstract). doi:10.3799/dqkx.2020.112

Nie, J., Horton, B. K., Saylor, J. E., Mora, A., Mange, M., Garzione, C. N., et al. (2012). Integrated Provenance Analysis of a Convergent Retroarc Foreland System: U-Pb Ages, Heavy Minerals, Nd Isotopes, and sandstone Compositions of the Middle Magdalena Valley basin, Northern Andes, Colombia. *Earth-Science Rev.* 110, 111–126. doi:10.1016/j.earscirev.2011.11.002

Nie, J., Stevens, T., Rittner, M., Stockli, D., Garzanti, E., Limonta, M., et al. (2015). Loess Plateau Storage of Northeastern Tibetan Plateau-Derived Yellow River Sediment. *Nat. Commun.* 6, 700–705 (in Chinese, with English summary). doi:10.1038/ncomms9511

Pan, B., Wang, J., Gao, H., Chen, Y., Li, J., and Liu, X. (2005). Terrace Dating as an Archive of the Run-Through of the Sanmen Gorges. *Prog. Nat. Sci.*, 700–705.

Pan, B., Hu, Z., Wang, J., Vandenberghe, J., Hu, X., Wen, Y., et al. (2012). The Approximate Age of the Planation Surface and the Incision of the Yellow River.

Palaeogeogr. Palaeoclimatol. Palaeoecol. 356-357, 54–61. doi:10.1016/j.palaeo.2010.04.011

Peng, P., Yang, S., Su, X., Wang, X., Zhang, J., and Wang, C. (2017). Petrogenesis of the 2090 Ma Zanhuang Ring and Sill Complexes in North China: A Bimodal Magmatism Related to Intra-continental Process. *Precambrian Res.* 303, 153. doi:10.1016/j.precamres.2017.03.015

Shang, Y., Nian, X., Zhang, W., and Wang, F. (2021). Yellow River's Contribution to the Building of Yangtze Delta during the Last 500 Years-Evidence from Detrital Zircon U-Pb Geochronology. *Geophys. Res. Lett.* 48, e2020G–e91896G. doi:10.1029/2020GL091896

Stevens, T., Carter, A., Watson, T. P., Vermeesch, P., Andò, S., Bird, A. F., et al. (2013). Genetic Linkage between the Yellow River, the Mu Us Desert and the Chinese Loess Plateau. *Quat. Sci. Rev.* 78, 355–368. doi:10.1016/j.quascirev.2012.11.032

Sun, J. (2005). Long-term Fluvial Archives in the Fen Wei Graben, central China, and Their Bearing on the Tectonic History of the India? Asia Collision System during the Quaternary. *Quat. Sci. Rev.* 24 (10-11), 1279–1286. doi:10.1016/j.quascirev.2004.08.018

Tong, G., Wu, X., and Chen, Y. (2000). Palynoevents since Late Cenozoic in Weihe Valley and Climate Changes. *J. Geomech.* 6, 18–65 (in Chinese, with English abstract).

Vermeesch, P. (2012). On the Visualisation of Detrital Age Distributions. *Chem. Geol.* 312-313, 190–194. doi:10.1016/j.chemgeo.2012.04.021

Wang, S., Jiang, F., and Wu, X. (1999). A Study on the Age of Sanmen Group in Sanmenxia Area. *J. Geomech.* 5, 65–71 (in Chinese, with English abstract).

Wang, S., Wu, X., Zhang, Z., Jiang, F., Xue, B., Tong, G., et al. (2002). Sedimentary Records of Environmental Evolution in the Sanmen Lake Basin and the Yellow River Running through the Sanmenxia Gorge Eastward into the Sea. *Sci. China Ser. D-Earth Sci.* 45, 595–608 (in Chinese with English abstract). doi:10.1360/02yd9061

Wang, S., Jiang, F., Wu, X., Wang, S., and Tian, G. (2004). The Connotation and Significance of Sanmen Formation. *Quat. Sci.* 24, 116–123.

Wang, Z., Wang, P., and Wang, X. (2010). Study on the Neogene-Quaternary Ostracoda Fossils of Sanmen Formation in Songjiabeigou, Weinan, Shaanxi. *J. Xi'an Shiyou Univ. (Natural Sci. Edition)* 1, 10 (in Chinese with English abstract).

Wang, S., Jiang, F., Fu, J., Li, C., Cai, Y., Yao, H., et al. (2013). Some Knowledge of the Formation of the Yellow River. *Quat. Sci.* 33, 705–714. doi:10.3724/sp.j.1140.2013.05053

Wang, S., Fu, B., Piao, S., Lü, Y., Ciais, P., Feng, X., et al. (2016). Reduced Sediment Transport in the Yellow River Due to Anthropogenic Changes. *Nat. Geosci.* 9 (1), 38–41. doi:10.1038/ngeo2602

Xiao, G., Sun, Y., Yang, J., Yin, Q., Dupont-Nivet, G., Licht, A., et al. (2020). Early Pleistocene Integration of the Yellow River I: Detrital-Zircon Evidence from the North China Plain. *Palaeogeogr. Palaeoclimatol. Palaeoecol.* 546, 109691. doi:10.1016/j.palaeo.2020.109691

Xue, T. (1996). Trusting in Traditional Cures. *Nature* 379, 110. doi:10.1038/379110a0

Yang, S., Cai, J., Li, C., and Deng, B. (2001). New Discussion about the Run-Through Time of the Yellow River. *Mar. Geol. Quat. Geol.* 21, 15–20 (in Chinese with English abstract).

Yang, J., Gao, S., Chen, C., Tang, Y., Yuan, H., Gong, H., et al. (2009). Episodic Crustal Growth of North China as Revealed by U-Pb Age and Hf Isotopes of Detrital Zircons from Modern Rivers. *Geochim. Cosmochim. Acta* 73, 2660–2673. doi:10.1016/j.gca.2009.02.007

Zhai, M., and Peng, P. (2007). Paleoproterozoic Events in the North China Craton. *Acta Petrol. Sin.* 23, 2665–2682 (in Chinese, with English abstract).

Zhai, M.-G., and Santosh, M. (2011). The Early Precambrian Odyssey of the North China Craton: A Synoptic Overview. *Gondwana Res.* 20, 6–25. doi:10.1016/j.gr.2011.02.005

Zhang, X., He, M., Wang, B., Rits, S. D., and Zheng, H. (2018). Provenance Study of the Sediments in Wei River Using the Detrital Zircon U-Pb Dating. *Mar. Geol. Quat. Geol.* 38, 202–211. doi:10.16562/j.cnki.0256-1492.2018.01.021

Zhang, X., He, M., Wang, B., Clift, P., Rits, D., Zheng, Y., et al. (2019). Provenance Evolution of the Northern Weihe Basin as an Indicator of Environmental Changes during the Quaternary. *Geol. Mag.* 156, 1915–1923. doi:10.1017/s0016756819000244

Zhang, H., Lu, H., Zhou, Y., Cui, Y., He, J., Lv, H., et al. (2021). Heavy mineral Assemblages and U Pb Detrital Zircon Geochronology of Sediments from the Weihe and Sanmen Basins: New Insights into the Pliocene-Pleistocene Evolution of the Yellow River. *Palaeogeogr. Palaeoclimatol. Palaeoecol.* 562, 110072. doi:10.1016/j.palaeo.2020.110072

Zhang, H. (2008). *The Chronological Study on U-Pb Dating of Modern River Detrital Zircon in North piedmont of Qinling and its Geological Indication*. Northwest University, 74.

Zhao, L., Lu, H., and Tang, L. (2018). Cenozoic Palynological Records and Vegetation Evolution in the Weihe Basin, Central China. *Quat. Sci.* 38, 1083–1093 (in Chinese with English abstract).

Zheng, H., Huang, X., Ji, J., Liu, R., Zeng, Q., and Jiang, F. (2007). Ultra-high Rates of Loess Sedimentation at Zhengzhou since Stage 7: Implication for the Yellow River Erosion of the Sanmen Gorge. *Geomorphology* 85, 131–142. doi:10.1016/j.geomorph.2006.03.014

Zheng, H., Clift, P. D., He, M., Bian, Z., Liu, G., Liu, X., et al. (2020). Formation of the First Bend in the Late Eocene Gave Birth to the Modern Yangtze River, China. *Geology* 49, 35–39. doi:10.1130/g48149.1

Zhu, Z. (1989). The Formation of Terraces in the Middle Reach of the Yellow River and the Drainage System Evolution. *Acta Geograph. Sin.* 61 (4), 429–440 (in Chinese with English abstract).

Conflict of Interest: XC was employed by China Railway First Survey & Design Institute Group Co., Ltd.

The remaining authors declare that the research was conducted in the absence of any commercial or financial relationships that could be construed as a potential conflict of interest.

Publisher's Note: All claims expressed in this article are solely those of the authors and do not necessarily represent those of their affiliated organizations, or those of the publisher, the editors and the reviewers. Any product that may be evaluated in this article, or claim that may be made by its manufacturer, is not guaranteed or endorsed by the publisher.

Copyright © 2022 Liu, Wang, Chen, Shi, Song and Hu. This is an open-access article distributed under the terms of the Creative Commons Attribution License (CC BY). The use, distribution or reproduction in other forums is permitted, provided the original author(s) and the copyright owner(s) are credited and that the original publication in this journal is cited, in accordance with accepted academic practice. No use, distribution or reproduction is permitted which does not comply with these terms.

frontiers in Earth Science

ORIGINAL RESEARCH
published: 02 February 2022
doi: 10.3389/feart.2021.826104

Uplift and Expansion of the North Qilian Shan Recorded by Detrital Fission Tracks in the Jiudong Basin, NW China

Baotian Pan, Qiming Zhao, Xiaofei Hu*, Jiaxin Zhang and Dianbao Chen*

Key Laboratory of Western China's Environmental Systems (Ministry of Education), College of Earth and Environmental Sciences, Lanzhou University, Lanzhou, China

The North Qilian Shan, located in the northeastern front of the Tibetan Plateau, is an ideal region to study the expansion process of the plateau, which is not clearly revealed due to the lack of direct evidence and an accurate age control. In the Jiudong Basin (foreland basin of the North Qilian Shan), a continuous late Cenozoic sedimentary sequence and a reliable chronostratigraphic framework (post-7 Ma) provide us the material to study this process. In this study, we first analyzed the provenance changes of the sediment by detrital apatite fission track age distributions and apatite particle textures. The result shows that the first provenance change occurred at 4.6–3.6 Ma, when the sediment source changed from the southern to the northern parts of the North Qilian Shan, and it indicates that the North Qilian Shan Fault had propagated to its modern location. The second provenance change occurred at 3.0–2.4 Ma, at when the Yumu Shan and its south region began to provide sediments for the Jiudong Basin, and it indicates that the tectonic deformation in the North Qilian Shan had expanded to the North Yumu Shan Fault. Our finding suggests that two significant expansion events happened since the Pliocene for the North Qilian Shan.

Keywords: North Qilian Shan, Jiudong Basin, apatite fission track, provenance change, Tibetan Plateau expansion

OPEN ACCESS

Edited by:
Huiping Zhang,
Institute of Geology, China

Reviewed by:
Lin Xu,
China Three Gorges University, China
Lei Wu,
Zhejiang University, China

****Correspondence:***
Qiming Zhao
zhaoqm16@lzu.edu.cn
Xiaofei Hu
feixhu@lzu.edu.cn

Specialty section:
This article was submitted to Structural Geology and Tectonics, a section of the journal Frontiers in Earth Science

Received: *30 November 2021*
Accepted: *24 December 2021*
Published: *02 February 2022*

Citation:
Pan B, Zhao Q, Hu X, Zhang J and Chen D (2022) Uplift and Expansion of the North Qilian Shan Recorded by Detrital Fission Tracks in the Jiudong Basin, NW China. Front. Earth Sci. 9:826104. doi: 10.3389/feart.2021.826104

INTRODUCTION

The collision of the Indian and Eurasian plates caused the uplift and expansion of the Tibetan Plateau, which has a profound impact on the geomorphic evolution of Asia and the global climate change (e.g., Molnar et al., 1993; An et al., 2001; Pan et al., 2004; Xu et al., 2011). The northeastern margin (the Qilian Shan) of the Tibetan Plateau represents the most-front for the ongoing expansion (Tapponnier et al., 2001), and how this margin grows or expands is key to understanding the formation dynamics for the entire plateau (Burchfiel et al., 1989; Métivier et al., 1998; Yin and Harrison, 2000; Clark, 2012). Although the intense uplift of the Qilian Shan that began at 15–10 Ma is supported by multiple evidences (Zheng et al., 2010; Zheng et al., 2017; Wang et al., 2016; Wang et al., 2020; Zhuang et al., 2018; Pang et al., 2019a; Pang et al., 2019b), the detailed expanding process is still in debate (e.g., Cheng et al., 2019; Hu et al., 2021). Especially for the northward expanding of the North Qilian Shan (e.g., Tapponier et al., 1990; Zheng et al., 2013), several studies tried to answer this question. From apatite fission track (AFT) age distribution across the main range, Pang et al. (2019a) suggest a sequence of thrust faults prograde to the north since Late Miocene (~10 Ma). To the north of the main range, paleomagnetic studies on the exposed Cenozoic strata in the Jiuxi Basin suggest

that the thrust system started to develop in the basin during 4.9–2.6 Ma (Fang et al., 2005) or at ~3.0 Ma (Chen et al., 2006; Zhao et al., 2017). In the Jiudong Basin, Plio-Quaternary deformation of the Yumu Shan is also indicated by coarse-grained sediments at 3.0 Ma (Hu et al., 2019a), the faster cooling at ~4.0 Ma from AFT thermal modeling (Wang et al., 2018), the estimation of 4.6 to 2.0 Ma by dividing the structural relief with the current fault slip rate (Palumbo et al., 2009; Hu et al., 2019b), and the unconformity between 0.8 and 0.9 Ma (Liu et al., 2011). The frame of a northward sequence for the thrust fault across the North Qilian Shan has been found; however, the clear process is still not revealed. This fact is mostly due to a lack of direct evidence from the range, such as the thermochronology method, and the Plio-Quaternary uplift is insufficient to expose complete annealing rocks to the surface (George et al., 2001; Jolivet et al., 2001). It is also due to the great uncertainty in calculating uplift time by recent deformation rate and in estimating the age for the unconformity where the material for dating is missing due to erosion. Therefore, direct evidence and accurate age control are needed to reveal a continuous expansion process of the North Qilian Shan.

In the Jiudong Basin, previous research obtained a continuous late Cenozoic (post-7 Ma) sedimentary sequence from the MH drill core, and it provided a detailed lithostratigraphic and chronostratigraphic framework for the sediments (Hu et al., 2019a). This provides us an ideal material to find the direct evidence for the northward expansion of the range. In this study, detrital AFT ages (Gallagher et al., 1998; Garver et al., 1999; Bernet, 2001) and apatite particle textures are used for a provenance study, and then we use the change of the provenance to reveal the expansion process of the North Qilian Shan from late Miocene to the Pliocene.

Geological Setting

In the northern front of the Qilian Shan, the foreland basins extend southeast to northwest with a length of 1,000 km, and the basin is divided into several sub-basins, the Jiuquan, the Minle, and the Wuwei basins (EGPGYO, 1989; Fang et al., 2005; Wang et al., 2016). The Jiuquan basin can be separated by the Wensu Shan into two parts, the Jiudong Basin in the east and the Jiuxi Basin in the west. The Jiudong Basin has been a depressed area since the Neogene and is filled with >3,000-m-thick terrigenous clastic sediments (Li and Yang, 1998; Bovet et al., 2009). Along the southern edge of the basin close to the Qilian Shan, Cenozoic sedimentary rocks overlie Paleozoic meta-sedimentary rocks. Cenozoic sediments can be divided into the following stratigraphic formations (Fang et al., 2005): Eocene–Oligocene Huoshaogou formation and Oligocene Baiyanghe formation, consisting of fluvio-lacustrine red beds with fine conglomerate to mudstone intercalated by playa gypsum beds; Miocene Shulehe formation, consisting of fluvio-lacustrine gray and brown fine conglomerate, sandstone, and siltstone; the Quaternary Yumen conglomerates, Jiuquan conglomerates, and Gobi conglomerates from bottom to top. The Quaternary conglomerates are characterized by poor roundness in general. MH drill core (3927′47.5″N, 9926′00.1″E, elevation: 1,387 m) is located at the eastern Jiudong Basin and downstream of the Maying River and the Bailang River. The drilling depth was 554 m, and the sediments are dominated by sand and silt, with occasional interbedded layers of medium-coarse sands, gravels, or clays. The sedimentary sequence of MH drill core could be divided into four stratigraphic units based on lithology, sedimentary texture, structure, and their vertical associations (Hu et al., 2019a). Unit 1 (554–465.3 m, 7.0–5.2 Ma) is dominated by clay silt, silt, and sandy silt, which are intercalated with thin and medium bedded sand layers. The facies assemblage suggests the depositional environment is a delta front or shallow lake. Unit 2 (465.3–395.6 m, 5.2–4.1 Ma) mainly consists of alternating layers of thin to medium bedded silt and sand. This unit is interpreted as a delta plain or littoral lake facies. Unit 3 (395.6–292.5 m, 4.1–3.0 Ma) consists of alternating layers of medium to thick bedded sand and silt, and this unit is interpreted as meandering river facies. The unit 4 (292.5–0 m, 3.0–0 Ma) is dominated by thick sand layers intercalated with several medium to thick bedded gravel layers and thin layers of clay and silt. It is inferred that this unit was deposited within a braided river environment (Hu et al., 2019a).

The thick late Cenozoic deposition in Jiuquan basin is controlled by the uplift and erosion of the Qilian Shan (**Figure 1A, B**). The Qilian Shan had experienced a long and complex tectonic history, including early Paleozoic oceanic sutures and continental collision events during the late Paleozoic, Mesozoic, and Cenozoic intraplate orogeny events (Li, 2003; Yang et al., 2007; Chen et al., 2019). The Cenozoic deformation process of the Qilian Shan started to occur in the early Cenozoic (Yin et al., 2002), with rapid exhumation during the Oligocene (Wan et al., 2011; Zhuang et al., 2018) and the Miocene (Wang et al., 2017; Zhuang et al., 2018). Stratigraphy studies suggest that the Qilian Shan expanded southwards to the Qaidam basin during 12–7 Ma (Wang et al., 2017; Pang et al., 2019b). At the north part of the Qilian Shan, a growing number of low-temperature thermochronology evidence indicate that significant orogeny began in the Miocene (Zheng et al., 2010; Baotian et al., 2013; Li et al., 2013; Qi et al., 2016; Zheng et al., 2017; Pang et al., 2019a; Yu et al., 2019; Li et al., 2020). The conglomerate accumulation in the south Jiuquan basin during 4.5–0.9 Ma or 3.6–0.9 Ma (Zhao et al., 2001; Fang et al., 2005) suggests that the North Qilian Shan had reached a high topographic relief in Pliocene. The basin-ward growth of the deformation system to the north of the main range is represented by the uplift of the Yumu Shan that began at 2.5–4 Ma (Palumbo et al., 2009; Wang et al., 2018; Hu et al., 2019a; Hu et al., 2019b) and the formation of the Laojunmiao Anticline that began at 3.66 Ma (Fang et al., 2005). The evidence probably indicated that the intense uplift of the Qilian Shan started during the Miocene and the mountains began to expand to the foreland basin from late Miocene to the Pliocene. However, due to the lack of direct evidence, the specific uplift and expansion process of the Qilian Shan are not clear.

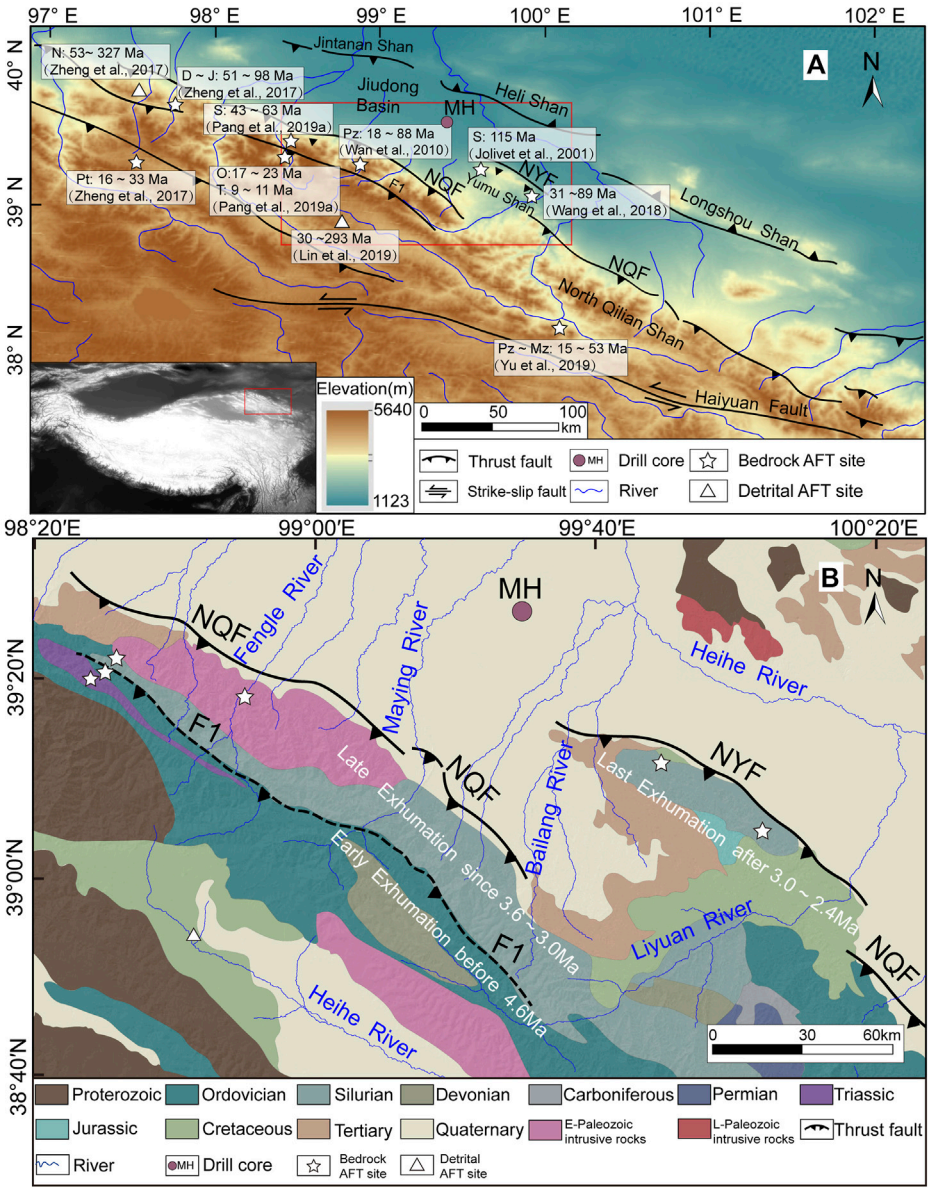

FIGURE 1 | (A) Topography of North Qilian Shan and the Hexi Corridor basin. Also shown is the distribution of major active faults, NQF—North Qilian Fault and NYF—North Yumu Shan Fault (Yuan et al., 2013), and major rivers. The numbers in the rectangles show AFT ages and the lithology unit where the sample was taken from: Pt—Proterozoic, Pz—Paleozoic, O—Ordovician, S—Silurian, D—Devonian, Mz—Mesozoic, T—Triassic, J—Jurassic, and N—Tertiary. **(B)** Simplified geologic map of the Jiudong Basin and the surrounding area (modified from the 1:500,000 geologic map of China).

MATERIALS AND METHODS

In this study, we adopted the external detector method (Gleadow and Lovering, 1977) to obtain the AFT age of the sample. The standard equation to calculate the age is

$$t = \frac{1}{\lambda_d} \ln\left[\frac{\lambda_d \phi \sigma I \rho_s}{\lambda_f \rho_i} + 1\right] \quad (1)$$

In **Eq. 1**, λ_d is the total decay constant of ^{238}U (λ_d = 1.55125 × 10–10a-1, Steiger and Jäge, 1977), λ_f is the spontaneous fission constant, ρ_s is the spontaneous fission track density, ρ_i is the induced fission track density, and "I" is the ratio of ^{235}U and ^{238}U under natural conditions, and has a value of 7.2527 × 10^{-3} (Cowan and Adler, 1976). ϕ is the thermal neutron flux; σ is the effective area irradiated by thermal neutrons, as a constant. Among the aforementioned parameters, only the values of λ_d and I are universally recognized, but the value of λ_f is still controversial at present. Besides, it is very difficult to determine the thermal neutron flux ϕ. Therefore, zeta (ζ) parameter calibration was proposed to calculate the AFT age (Hurford and Green, 1981). This method could eliminate the

error caused by the uncertainty of thermal neutron irradiation and spontaneous fission track decay constant λ_f.

In **Eq. 1**, let $\zeta = \frac{\phi\sigma I}{\lambda_f \rho_d}$, then **Eq. 1** can be transformed into equation

$$t = \frac{1}{\lambda_d}\ln\left[\lambda_d \zeta \frac{\rho_s}{\rho_i}\rho_d + 1\right] \quad (2)$$

Put the standard apatite sample with a certain age of t_{STD} into the reactor together with a uranium glass detector, and thermal neutron irradiation produced induced fission track in the standard apatite and uranium glass detector. Calculate the spontaneous fission track density A and the induced fission track density B of the standard apatite sample and the fission track density of uranium glass detector. The value of ζ could be obtained by equation

$$\zeta = \frac{e^{\lambda_d t_{STD}} - 1}{\lambda_d (\rho_s/\rho_i)_{STD}\rho_d} \quad (3)$$

Substituting the obtained zeta (ζ) parameter into **Eq. 2**, we could calculate the AFT age of the geological sample.

In this study, we collected 10 samples at different depths from the MH core. These samples are taken from different sedimentary facies or at the position where the facies significantly change. By correlating to the magnetostratigraphic analysis (Hu et al., 2019a), the depositing age for each sample is determined and they range from 5.9 to 0.045 Ma. Each sample mainly consists of fine and medium sands and has a weight of 2–3 kg. All samples were collected from the sand layers. The bulk sample was washed and separated by magnetic and heavy liquid to purify heavy minerals, and then pure apatite crystals were manually picked. The selected apatite crystals were mounted on a slide with epoxy resin and polished to expose their internal surface. The polished mount was etched with HNO_3 for 20 s at 21°C to reveal the spontaneous fission track. All samples were dated by the external detector method (Hurford and Green, 1981); low-U mica external detectors covered the standard sample (Durango apatite with age of 31.4 ± 0.5 Ma), apatite mounts, and glass dosimeters (IRMM-540R), and then they were irradiated by the reactor at Oregon State University. After irradiation, mica detectors were etched in 40% HF at 20°C for 40 min to reveal the induced fission tracks. Tracks were measured using the Auto scan Professional Automated System in the Key Laboratory of Western China's Environmental Systems (Ministry of Education), Lanzhou University. Spontaneous and induced fission track densities of all samples (including standard samples) and fission track densities of uranium glass detectors were calculated. The zeta (ζ) parameter was calculated as 328.24 ± 1.24, and then we used it to obtain AFT ages of all samples.

Because the clastic deposits mostly come from multiple provenances, the AFT central age of detrital sample would be a mixed age, which does not have clear geological significance (Braun et al., 2006). For a bulk age data, the p (χ^2) test (Galbraith and Green, 1990) is performed to determine whether there are unique or multiple age components. Samples fail the p (χ^2) test, the p (χ^2) probability less than 5%, indicating that the sample contains several age components. In such case, Density Plotter (Spencer et al., 2014), a program integrated mathematical fitting method, could be used to obtain the best-fitting age peaks of different components. The lag time, which is defined as the AFT fitting age peak minus the depositional age of sample (Garver et al., 1999), was introduced to measure the time from closure depth in the range to the deposit region of basin (Bernet, 2001). Generally, progressively shortened lag time indicates enhanced tectonic activity and accelerated exhumation rate of the source region, whereas constant lag time indicates that the exhumation rate of the source region is steady. Another special case is that a stable or decreasing lag time increases suddenly over a short period, and the depositional age corresponding to the overturn point could be the time when the sediment recycled (Garver et al., 1999; Zheng et al., 2017).

In general, unweathered euhedral apatite particle is a hexagonal column; the shape is column or regular hexagon under the microscope. For terrigenous clastic sediments, the roundness and surface textures of apatite particles will change due to abrasion, mechanical crushing, and chemical weathering (Liu, 1980; Zhu, 2008; Andò et al., 2012). The roundness of detrital apatite particles usually becomes better with the increase of transporting distance and time, and the content of the euhedral particles decreases. Aiming to identify source differences for the samples, we measured the number of euhedral apatite particles and the roundness of apatite particles of each sample under the microscope (**Figure 2**), according to the catalog for optical analysis of corrosion of heavy minerals (Andò et al., 2012) and the roundness scale for sedimentary particles (Powers, 1953). The number of total measured apatite particles were greater than 75 in most samples, except MH1(36), MH4(58), and MH7(51).

RESULTS

The AFT age results of 10 samples are shown in **Table 1**. The single grain AFT ages of all samples range from 35 to 324.5 Ma, and most of them were distributed in the range of 100–180 Ma. According to the age distribution, the samples can be divided into three sections (**Figure 3D**). The lower section includes two samples from 5.9 to 4.6 Ma, and AFT ages are mostly distributed in 60–160 Ma; the middle section includes three samples from 3.6 to 3.0 Ma, and AFT ages are mostly distributed in 100–180 Ma; and the upper section includes five samples from 2.4 to 0 Ma, and AFT ages have a wider distribution in 60–300 Ma. After 3.0 Ma, apatite grains with AFT age older than 200 Ma began to emerge. The apatite grain roundness (**Figure 3E**) and crystal morphology (**Figure 3F**) also show the change. From 5.9 to 4.6 Ma, apatite particles have moderate roundness (with certain number of very-rounded particles), and the euhedral apatite particle content is about 7%. During 3.6–3.0 Ma, apatite particles have worse roundness (with large amount of sub-angular particles and no very-round particles), and the content of euhedral apatite particles is the highest of 10–12%. From 2.4 Ma to present, the five samples have best roundness (rounded particles dominant and with very-round particles), and the content of euhedral apatite particles is the lowest at 3–5%.

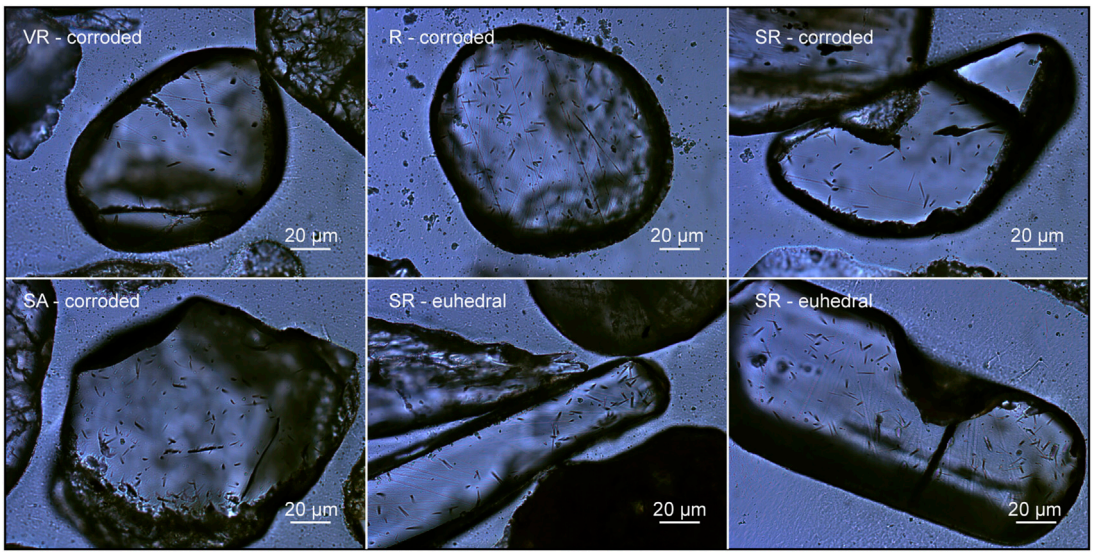

FIGURE 2 | Roundness and crystal textures characteristics of apatite particles.

TABLE 1 | Apatite fission track data from the MH drill core

Sample	Depth (m)	D age (Ma)	N	Age range (Ma)	Central age (Ma)	P (χ^2)	P1 (Ma)	P2 (Ma)	P3 (Ma)	P4 (Ma)
MH1	7.3–8.2	0.045	36	43.3–283.2	118.1 ± 9.5	0	67.5 ± 6.9	117.0 ± 14.0	–	196 ± 22
MH2	97.6–100.1	0.6	76	51.1–282.2	148.8 ± 5.9	0	59.1 ± 7.9	103.0 ± 10.0	–	172 ± 12
MH3	191.7–194.2	1.3	78	40.2–288.4	96.4 ± 4	0	62.7 ± 7.4	108.0 ± 11.0	–	272 ± 74
MH4	222.1–224.7	1.6	58	53.8–233.0	127.8 ± 5.8	0	69.0 ± 10.0	109.0 ± 15.0	–	158 ± 14
MH5	260.1–261.4	2.4	76	35–324.5	104.2 ± 4.5	0	52.6 ± 6.2	108.5 ± 8.7	–	208 ± 33
MH6	289.7–291.4	3.0	76	67.5–190.5	137.6 ± 4	0.99	–	–	137.6 ± 4	–
MH7	328.3–330.8	3.4	51	50.2–197.2	131.7 ± 6.7	0	70.3 ± 9.5	–	144 ± 11	–
MH8	348.3–350.8	3.6	83	67.1–170.6	129 ± 3.6	0.35	–		129 ± 3.6	–
MH9	437.9–440.5	4.6	82	44.2–161.6	100.8 ± 3.8	0	62.7 ± 7.6	116.0 ± 11.0	–	–
MH10	511.8–513.3	5.9	78	46.5–171.7	112 ± 4.2	0	66.3 ± 7.9	121.3 ± 9.3	–	–

P (χ^2) test result shows that eight of 10 samples did not pass p (χ^2) test (**Figure 4**), suggesting they have multiple age components and provenances. For the two samples passing the test, MH6 and MH8, we considered that they contain only one age component. Although the sample MH7 did not pass the p (χ^2) test, its age distribution is relatively narrower and most age data are concentrated in the range similar to MH6 and MH8, and thus it can be grouped with MH6 and 8, which have a single provenance. We decomposed the observed age distributions into four best-fitting age component peaks, P1 (52.6–70.3 Ma), P2 (103–121 Ma), P3 (129–144 Ma), and P4 (>158 Ma). After the decomposition, the different age component combination for these samples (**Table 1**) shows a similar pattern as previous separation of the three parts (**Figure 3**). The four age components also suggest that these apatite grains in the basin sediment came from four different sources.

Since the content of P3 and P4 component is relatively older, which may have undergone recycles in the geological process, it cannot reflect the recent uplifting process of the mountain. Therefore, we only consider the younger components to analyze the pattern of the lag time. As shown in **Figure 5**, the lag time of P1 and P2 showed a trend of decreasing during 5.9–2.4 Ma and a trend of increasing since 2.4 Ma. The depositional age corresponding to the inflection point is 2.4 Ma, suggesting that the previous sediments were recycled.

DISCUSSION

The Provenance Changes of the Sediment

The bottom of the MH core is 554 m, considered the geothermal gradient of Jiuquan basin that ranged 25–30°C/km (Ren et al., 2000), and the temperature of the sediment is far from the depth of annealing for AFT of 60–120°C (Wagner et al., 1989). Thus, we believe that all samples in this study did not suffer annealing after deposition, and their AFT ages reflect the cooling age for the provenance of the sediment.

Modern drainage pattern in the Jiudong Basin (**Figure 1B**) indicates that the modern river for transporting sediments into the MH core includes the Maying River, two smaller rivers to the east of the Maying River, and probably the Bailang River. According to previous studies in the basin sediment (Pan et al., 2016; Hu et al., 2019a), no sediment from the Heihe

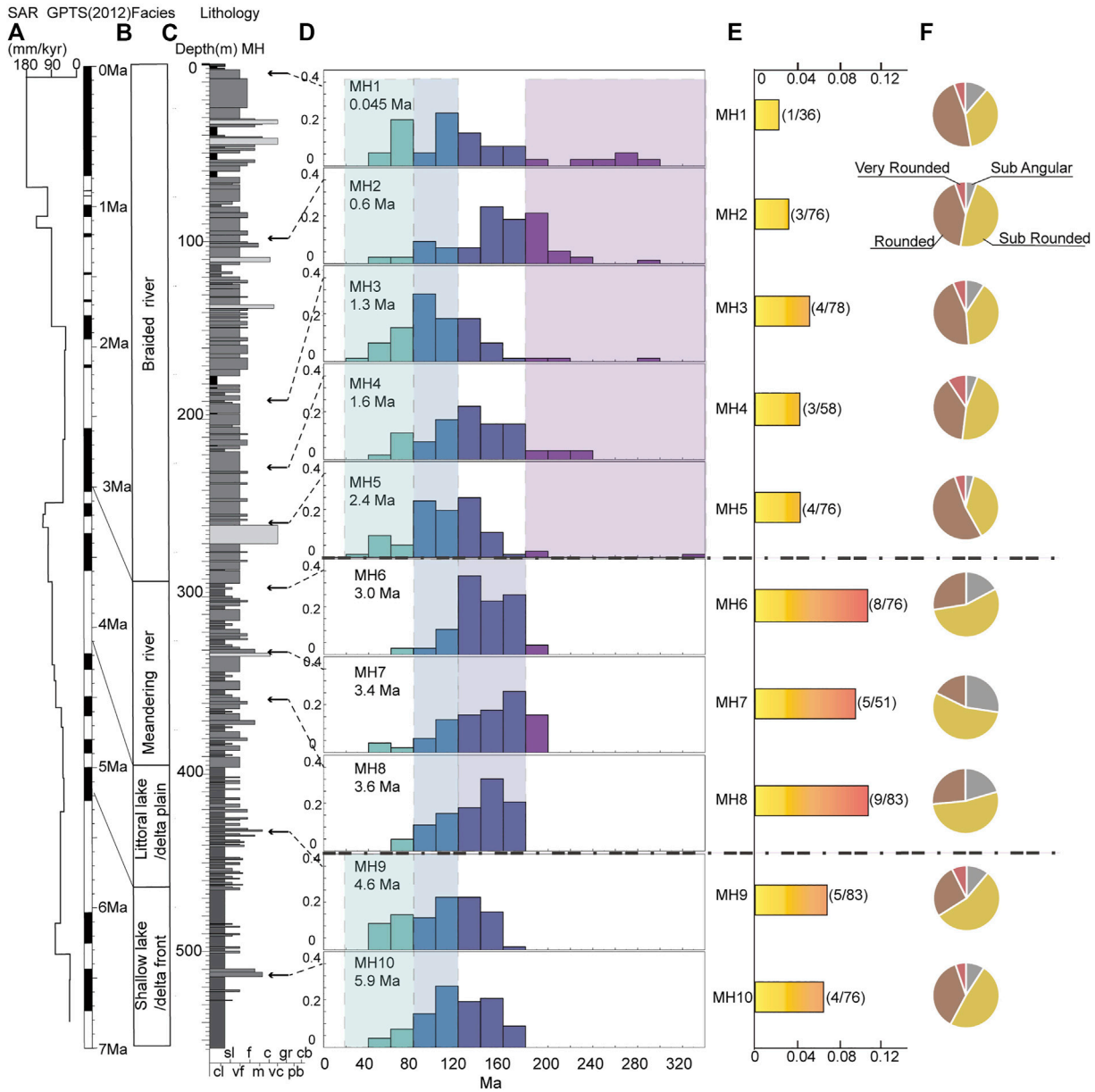

FIGURE 3 | (A) Comparison of the sediment accumulation rate (SAR). **(B)** Sedimentary facies. **(C)** Lithology: cl—clay; sl—silt; vf—very fine sand; f—fine sand; m—medium sand; c—coarse sand; vc—very coarse sand; gr—granule; pb—pebble; cb—cobble (Hu et al., 2019a). **(D)** The single grain age distribution. **(E)** The content of euhedral apatite particles (euhedral apatite particles/all observed apatite particles). **(F)** The roundness of apatite particles.

River was deposited in the MH core, so the source of the deposition can be constrained to the regions ranging from the Maying to the Bailang. During the recent period, 2.4–0 Ma, the AFT age distribution shows a wide range and multiple sources, which suggest it was not from a single river. For the samples in this stage, the roundness of apatite particles is very well and the content of euhedral apatite particles is very low (**Figure 3**), suggesting that the sediments had been transported over long distances or had experienced multiple transport-deposition processes. A distinguished pattern in this period is the appearance of apatite grains with ages older than 200 Ma. In the Qilian Shan range, samples containing AFT age older than 200 Ma were reported from Tertiary strata in the Jiuxi Basin (Zheng et al., 2017) and modern sediments of the upper reaches of Heihe River (Lin et al., 2019), where the main exposed strata are the Cretaceous sandstones (**Figure 1B**). Among the possible sources for the MH core, only the Bailang River is draining the Cretaceous and Tertiary sediments in the Yumu Shan and its south range. Besides, the lag time inflection point suggested that the recycled sediments have appeared in MH core since 2.4 Ma, and it is consistent with the time of provenance change and the time of sedimentary facies change. Thus, the evidence indicates

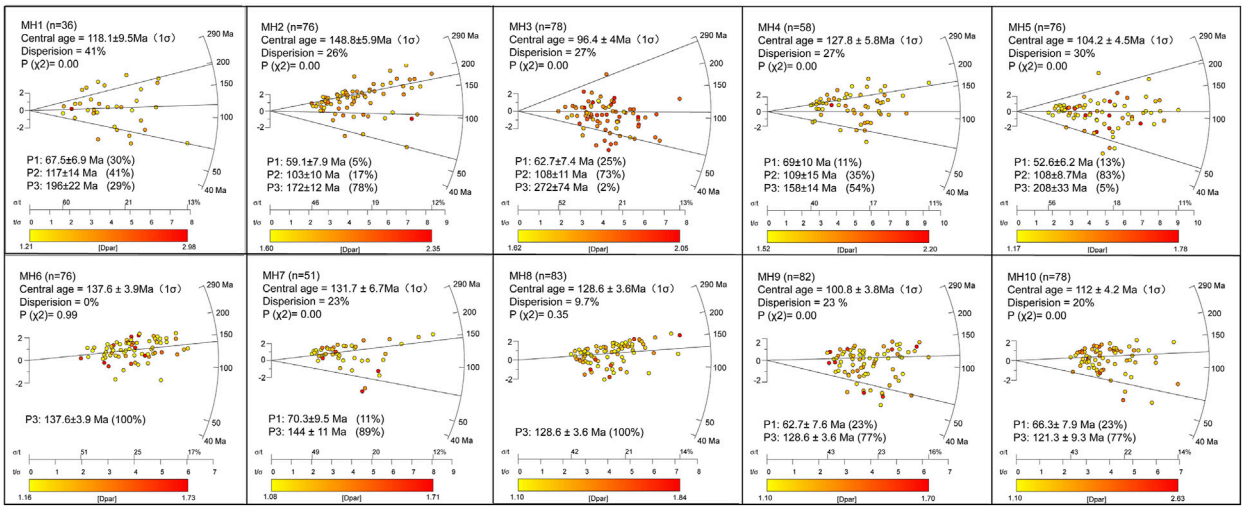

FIGURE 4 | Fitting age peaks by Density Plotter.

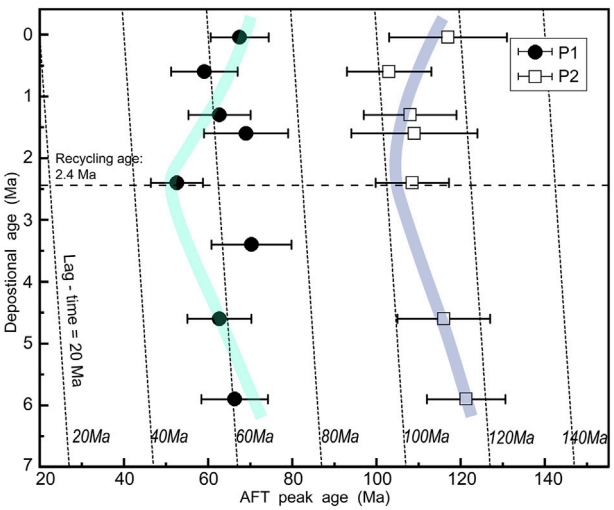

FIGURE 5 | Apatite fission track (AFT) fitting age peaks versus depositional age plot.

that the Yumu Shan range supplied sediments to the Jiudong Basin by the Bailang River during 2.4–0 Ma, and the North Qilian Shan also supplied sediments to the basin by the Maying River and the two smaller rivers.

During the period of 3.6–3.0 Ma, the single component pattern of AFT ages is greatly different with the upper and the lower section (**Figure 3** and **Figure 4**), suggesting a single source region different from the previous or late period. The roundness of apatite particles is poorer and the content of euhedral apatite particles is less than that of the other two sections; it indicates that the sediments had not suffered intense weathering and abrasion during the process of erosion and transportation. These evidences suggest that apatite particles in the section were mostly from a simple source and transported by a relatively small drainage that originated in front of the North Qilian Shan. The simple bedrock of Silurian (**Figure 1B**) drained by the two smaller rivers is the most suitable source. To the west of the studied region, the AFT study across the range of the North Qilian Shan suggests that the Silurian rock in the north has older age than other exposed rocks to the south attributing to a later activation of the northern thrust (Pang et al., 2019a). Comparing with the Maying River draining a large area containing Proterozoic to Devonian rock, rivers only draining the Silurian rock would supply the sediments to the Jiudong Basin, probably the two smaller rivers and the Bailang River without the drainage area of the Yumu Shan range.

During the period of 5.9–4.6 Ma, AFT ages are distributed in a relatively younger range, and can be divided into two age components P1 and P2. These two components appear in all samples and with high content; it means that this provenance has continuously provided numerous sediments for the Jiudong Basin at least since 5.9 Ma. For the rocks to the south of the F1 fault, published AFT data of *in situ* bedrock (Jolivet et al., 2001; Guo et al., 2009; Wan et al., 2010; Li et al., 2013; Baotian et al., 2013; Qi et al., 2016; Zheng et al., 2017; Li et al., 2020) are mainly distributed in the range of 20–120 Ma, which is in agreement with the age range of two samples from 5.9 to 4.6 Ma (**Figure 3**). The only possible river that brought these sediments is the Maying River, and thus we suggest that the provenance for the sediment during 5.9–4.6 Ma was the southern part of the North Qilian Shan, transported by a river similar to the modern Maying River.

Northward Expansion of the North Qilian Shan

Previous studies on basin sediments have found a coarsen-upward trend (Liu et al., 2011; Hu et al., 2019a), showing a northward propagation for the deposition system in recent 7 Ma, and our results infer a more clear dynamics for the propagation. The first change of the source for the sediment happened at 4.6–3.6 Ma, and this source change from the south to the north of the North Qilian Shan probably indicates the northward propagation of the thrust

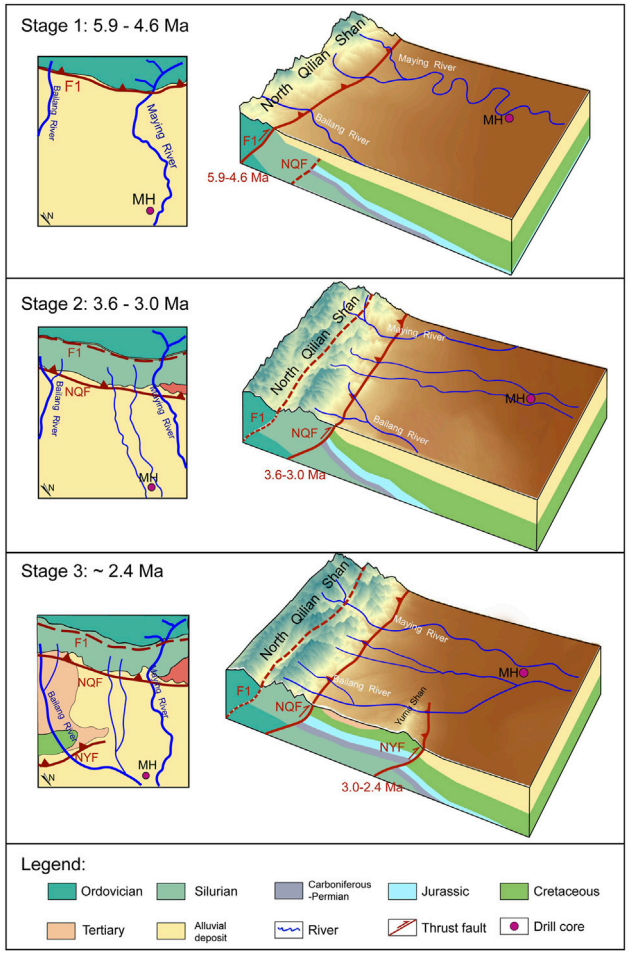

FIGURE 6 | The progressive deformational model of the North Qilian Shan during late Cenozoic. NQF—North Qilian Shan Fault; NYF—North Yumu Shan Fault. Stratigraphic texture modified from the 1:500,000 geologic map of China (EGPGYO, 1989) and seismic sections in the Jiuquan Basin (Yang et al., 2007; Zuza et al., 2016).

fault, from the F1 to the modern NQF (**Figure 1B** and **Figure 6**). The activation of the NQF uplifted the Silurian rock and supplied the sediment to the Jiudong Basin. The second change of the source during 3.0–2.4 Ma indicates the uplift and erosion of the Yumu Shan range, and this situation was caused by the further northward propagation of the thrust system, from the NQF to the NYF.

The first propagation of the Qilian range at 4.6–3.6 Ma corresponds to the large unconformity at 5.2–3.6 Ma in the depositing sequence at the western Yumu Shan (Liu et al., 2011), and also corresponds to the sedimentary phase change in basin center at ~4.1 Ma from lake/delta to rivers (Hu et al., 2019a). The second propagation to the Yumu Shan range at 3.0–2.4 Ma received various supports. AFT thermochronology on the Yumu Shan shows that it initiated growth during the Pliocene (Wang et al., 2018). At the MH core, the sedimentary environment changed from meandering river to braided river at 3.0 Ma, but the sediment accumulation rate abrupt decreased, indicating the uplift of the basin region (Hu et al., 2019a). In the Yumu Shan range, combining the geometry of the fault and fold with age control for the terraces (Palumbo et al., 2009), the rock uplift rate in the Yumu Shan was calculated as 1.2 ± 0.1 mm/a, indicating an onset age of 2.5 ± 0.5 Ma for the uplift of the Yumu Shan (Hu et al., 2019b). Our investigation, in a more confident way, provides a narrower time range for the onset of the uplift of the Yumu Shan at 3.0–2.4 Ma.

CONCLUSION

Detrital AFT investigation of the MH drill core in the Jiudong Basin provides credible supplementary evidence to understand the clear expansion process of the North Qilian Shan. The single grain AFT age distribution, together with lag time of younger AFT fitting age peaks and the roundness and crystal surface texture of apatite particles, marked that two obvious provenance changes happened in the Jiudong Basin at 4.6–3.6 Ma and at 3.0–2.4 Ma. Combining published thermochronological data along the Qilian Shan and sedimentary records in the Hexi Corridor, we infer that the thrust fault propagated to the modern North Qilian Fault during 4.6–3.6 Ma and propagated to the North Yumu Shan Fault during 3.0–2.4 Ma.

DATA AVAILABILITY STATEMENT

The original contributions presented in the study are included in the article/supplementary material further inquiries can be directed to the corresponding authors.

AUTHOR CONTRIBUTIONS

BP: conceptualization, formal analysis, writing—original draft, visualization. QZ: conceptualization, formal analysis, investigation, writing—original draft, visualization. XH: investigation, formal analysis, investigation, writing—original draft. JZ: investigation, writing—review and editing. DC: investigation, writing—review and editing.

FUNDING

This work was supported by National Natural Science Foundation of China (41730637), the Second Tibetan Plateau Scientific Expedition and research program (STEP) (2019QZKK0704), National Natural Science Foundation of China 42001005, China Postdoctoral Science Foundation (2020M673529), and the Fundamental Research Funds for the Central Universities (lzujbky-2021-it38 and lzujbky-2018-it77).

ACKNOWLEDGMENTS

We are grateful to Jian Zhang, Jiakun Wu, and Yang Hong for their assistance in the treatment; and Xiuxi Wang and Jianzhang Pang for their assistance with the analysis of data.

REFERENCES

Andò, S., Garzanti, E., Padoan, M., and Limonta, M. (2012). Corrosion of Heavy Minerals during Weathering and Diagenesis: A Catalog for Optical Analysis. *Sediment. Geo.* 280, 165–178. doi:10.1016/j.sedgeo.2012.03.023

An, Z., Kutzbach, J. E., Prell, W. L., and Porter, S. C. (2001). Evolution of Asian Monsoons and Phased Uplift of the Himalaya -Tibetan Plateau since Late MioceneTimes. *Nature* 411, 62–66. doi:10.1038/35075035

Baotian, P., Qingyang, L., Xiaofei, H., Haopeng, G., Zibian, L., Shaofei, J., et al. (2013). Cretaceous and Cenozoic Cooling History of the Eastern Qilian Shan, north-eastern Margin of the Tibetan Plateau: Evidence from Apatite Fission-Track Analysis. *Terra Nova* 25, 431–438. doi:10.1111/ter.12052

Bernet, M. (2001). Tracking the Evolution of Convergent Mountain Belts with Detrital Geo-Thermochronology. *Metalurgija* 43, 17–22. doi:10.1130/0091-7613(2001)029<0035:SSEOTE>2.0.CO;2

Bovet, P. M., Ritts, B. D., Gehrels, G., Abbink, A. O., Darby, B., and Hourigan, J. (2009). Evidence of Miocene Crustal Shortening in the North Qilian Shan from Cenozoic Stratigraphy of the Western Hexi Corridor, Gansu Province, China. *Am. J. Sci.* 309, 290–329. doi:10.2475/00.4009.02

Braun, J., Beek, P., and Batt, G. E. (2006). "Numerical Methods for the Interpretation of Thermochronological Data," in *Quantitative Thermochronology* (Cambridge, UK: Cambridge University Press).

Burchfiel, B. C., Quidong, D., Molnar, P., Royden, L., Yipeng, W., Peizhen, Z., et al. (1989). Intracrustal Detachment within Zones of continental Deformation. *Geol* 17, 748–752. doi:10.1130/0091-7613(1989)017<0448:idwzoc>2.3.co;2

Chen, J., Wyrwoll, K. H., Lu, Y., Krapez, B., Wan, J., and Liu, J. (2006). Magnetochronology of the Yumen Conglomerates and Multi-Pulsed Folding and Thrusting in the Northern Qilian Shan (In Chinese). *Quat. Sci.* 26, 20–31. doi:10.3321/j.issn:1001-7410.2006.01.004

Chen, X., Shao, Z., Xiong, X., Gao, R., Liu, X., Wang, C., et al. (2019). Fault System, Deep Structure and Tectonic Evolution of the Qilian Orogenic Belt, Northwest China (In Chinese). *Geo. China* 46 (5), 995–1020. doi:10.12029/gc20190504

Cheng, F., Garzione, C. N., Mitra, G., Jolivet, M., Guo, Z., Lu, H., et al. (2019). The Interplay between Climate and Tectonics during the Upward and Outward Growth of the Qilian Shan Orogenic Wedge, Northern Tibetan Plateau. *Ear.-Sci. Rev.* 198, 102945. doi:10.1016/j.earscirev.2019.102945

Clark, M. K. (2012). Continental Collision Slowing Due to Viscous Mantle Lithosphere rather Than Topography. *Nature* 483, 74–77. doi:10.1038/nature10848

Cowan, G. A., and Adler, H. H. (1976). The Variability of the Natural Abundance of 235U. *Geo. et Cosmo. Acta* 40, 1487–1490. doi:10.1016/0016-7037(76)90087-9

EGPGYO (1989). "Yumen Oilfeld," in *Petroleum Geology of China (In Chinese) 13* (Beijing, China: Petroleum Industry Press), 441.

Fang, X., Zhao, Z., Li, J., Yan, M., Pan, B., Song, C., et al. (2005). Magnetostratigraphy of the Late Cenozoic Laojunmiao Anticline in the Northern Qilian332w3 Mountains and its Implications for the Northern Tibetan Plateau Uplift. *Sci. China Ser. D* 48, 1040–1051. doi:10.1360/03yd0188

Galbraith, R. F., and Green, P. F. (1990). Estimating the Component Ages in a Finite Mixture. *Int. J. Radiat. Appl. Instrument. D. Nucl. Tracks Radiat. Measure.* 17, 197–206. doi:10.1016/1359-0189(90)90035-V

Gallagher, K., Brown, R., and Johnson, C. (1998). Fission Track Analysis and its Applications to Geological Problems. *Annu. Rev. Earth Planet. Sci.* 26, 519–572. doi:10.1146/annurev.earth.26.1.519

Garver, J. I., Brandon, M. T., Roden-Tice, M., and Kamp, P. J. J. (1999). Exhumation History of Orogenic highlands Determined by Detrital Fission-Track Thermochronology. *Geol. Soc. Lond. Spec. Pub.* 154, 283–304. doi:10.1144/GSL.SP.1999.154.01.13

George, A. D., Marshallsea, S. J., Wyrwoll, K.-H., Jie, C., and Yanchou, L. (2001). Miocene Cooling in the Northern Qilian Shan, Northeastern Margin of the Tibetan Plateau, Revealed by Apatite Fission-Track and Vitrinite-Reflectance Analysis. *Geol* 29, 939–942. doi:10.1130/0091-7613(2001)029<0035:SSEOTE>2.0.CO;2

Gleadow, A. J. W., and Lovering, J. F. (1977). Geometry Factor for External Detectors in Fission Track Dating. *Nucl. Track Detect.* 1, 99–106. doi:10.1016/0145-224x(77)90003-5

Guo, Z., Lu, J., and Zhang, Z. (2009). Cenozoic Exhumation and Thrusting in the Northern Qilian Shan, Northeastern Margin of the Tibetan Plateau: Constraints from Sedimentological and Apatite Fission-Track Data. *J. Geol.* 83, 562–579. doi:10.1111/j.1755-6724.2009.00045.x

Hu, X., Cao, X., Li, T., Mao, J., Zhang, J., He, X., et al. (2021). Late Quaternary Fault Slip Rate within the Qilian Orogen, Insight into the Deformation Kinematics for the NE Tibetan Plateau. *Tectonics* 40, e2020TC006586. doi:10.1029/2020TC006586

Hu, X., Chen, D., Pan, B., Chen, J., Zhang, J., Chang, J., et al. (2019a). Sedimentary Evolution of the Foreland basin in the NE Tibetan Plateau and the Growth of the Qilian Shan since 7 Ma. *Geol. Soc. Am. Bull.* 131, 1744–1760. doi:10.1130/B35106.1

Hu, X., Wen, Z., Pan, B., Guo, L., and Cao, X. (2019b). Constraints on Deformation Kinematics across the Yumu Shan, NE Tibetan Plateau, Based on Fluvial Terraces. *Glob. Planet. Change* 182, 103023. doi:10.1016/j.gloplacha.2019.103023

Hurford, A. J., and Green, P. F. (1981). A reappraisal of neutron dosimetry and uranium-238 λf values in fission-track dating. *Nuc. Tracks* 5, 53–61. doi:10.1016/0191-278X(81)90026-3

Jolivet, M., Brunel, M., Seward, D., Xu, Z., Yang, J., Roger, F., Tapponnier, P., Malavieille, J., Arnaud, N., and Wu, C. (2001). Mesozoic and Cenozoic tectonics of the northern edge of the Tibetan plateau: fission-track constraints. *Tectonophysics* 343, 111–134. doi:10.1016/S0040-1951(01)00196-2

Li, B., Zuza, A. V., Chen, X., Hu, D., Shao, Z., Qi, B., Wang, Z.-z., Levy, D. A., and Xiong, X. (2020). Cenozoic multi-phase deformation in the Qilian Shan and out-of-sequence development of the northern Tibetan Plateau. *Tectonophysics* 782-783, 228423. doi:10.1016/j.tecto.2020.228423

Li, F. (2003). New evidences for the presence of the NS-trending extensional structures in northwestern China: An example from the Early Cretaceous half-graben fault depressions in Jiuquan Gansu (in Chinese). *Sedimentary Geology and Tethyan Geology* 23 (2), 8. doi:10.3969/j.issn.1009-3850.2003.02.007

Li, Q., Pan, B., Hu, X., Hu, Z., Li, F., Yang, S., et al. (2013). Apatite fission track constraints on the pattern of faulting in the north Qilian Mountain. *J. Earth Sci.* 24, 569–578. doi:10.1007/s12583-013-0350-1

Li, Y., and Yang, J. (1998). Tectonic geomorphology in the Hexi Corridor, northwest China. *Basin Res.* 10, 345–352. doi:10.1046/j.1365-2117.1998.00070.x

Lin, X., Tian, Y., Donelick, R. A., Liu-Zeng, J., Cleber, S. J., Li, C. a., et al. (2019). Mesozoic and Cenozoic Tectonics of the Northeastern Edge of the Tibetan Plateau: Evidence from Modern River Detrital Apatite Fission-Track Age Constraints. *J. Asian Earth Sci.* 170, 84–95. doi:10.1016/j.jseaes.2018.10.028

Liu, B. (1980). *Sedimentary Petrology (In Chinese)*. Beijing, China: Geology Publishing House, 45–48.

Liu, D., Yan, M., Fang, X., Li, H., Song, C., and Dai, S. (2011). Magnetostratigraphy of Sediments from the Yumu Shan, Hexi Corridor and its Implications Regarding the Late Cenozoic Uplift of the NE Tibetan Plateau. *Quat. Int.* 236, 13–20. doi:10.1016/j.quaint.2010.12.007

Métivier, F., Gaudemer, Y., Tapponnier, P., and Meyer, B. (1998). Northeastward Growth of the Tibet Plateau Deduced from Balanced Reconstruction of Two Depositional Areas: The Qaidam and Hexi Corridor Basins, China. *Tectonics* 17, 823–842. doi:10.1029/98TC02764

Molnar, P., England, P., and Martinod, J. (1993). Mantle Dynamics, Uplift of the Tibetan Plateau, and the Indian Monsoon. *Rev. Geophys.* 31, 357–396. doi:10.1029/93RG02030

Palumbo, L., Hetzel, R., Tao, M., Li, X., and Guo, J. (2009). Deciphering the Rate of Mountain Growth during Topographic Presteady State: An Example from the NE Margin of the Tibetan Plateau. *Tectonics* 28, TC4017.1–TC4017.18. doi:10.1029/2009TC002455

Pan, B., Chen, D., Hu, X., Cao, X., Chen, J., and Mao, j. (2016). Drainage Evolution of the Heihe River in Western Hexi Corridor, China, Derived from Sedimentary and Magnetostratigraphic Results. *Quat. Sci. Rev.* 150, 250–263. doi:10.1016/j.quascirev.2016.08.036

Pan, B., Gao, H., Li, B., and Li, J. (2004). Step-like Landforms and Uplift of the Qinghai-Xizang Plateau (In Chinese). *Quat. Sci.* 24, 50–58. doi:10.3321/j.issn:1001-7410.2004.01.006

Pang, J., Yu, J., Zheng, D., Wang, W., Ma, Y., Wang, Y., et al. (2019b). Neogene Expansion of the Qilian Shan, north Tibet: Implications for the Dynamic Evolution of the Tibetan Plateau. *Tectonics* 38, 1018–1032. doi:10.1029/2018TC005258

Pang, J., Yu, J., Zheng, D., Wang, Y., Zhang, H., Li, C., et al. (2019a). Constraints of New Apatite Fission-Track Ages on the Tectonic Pattern and Geomorphic Development of the Northern Margin of the Tibetan Plateau. *J. Asian Earth Sci.* 181, 103909. doi:10.1016/j.jseaes.2019.103909

Powers, M. C. (1953). A New Roundness Scale for Sedimentary Particles. *Sepm Jsr* 23, 117–119. doi:10.1306/D4269567-2B26-11D7-8648000102C1865D

Qi, B., Hu, D., Yang, X., Zhang, Y., Tan, C., Zhang, P., et al. (2016). Apatite Fission Track Evidence for the Cretaceous-Cenozoic Cooling History of the Qilian Shan (NW China) and for Stepwise Northeastward Growth of the Northeastern Tibetan Plateau since Early Eocene. *J. Asian Earth Sci.* 124, 28–41. doi:10.1016/j.jseaes.2016.04.009

Ren, Z., Liu, C., Zhang, X., Wu, H., Chen, G., Li, J., et al. (2000). Recovery and Comparative Research of thermal History on Jiuquan basin Group (In Chinese). *Chin. J. Geophys.* 43, 635–645. doi:10.1002/cjg2.82

Spencer, C. J., Prave, A. R., Cawood, P. A., and Roberts, N. M. W. (2014). Detrital Zircon Geochronology of the Grenville/Llano Foreland and Basal Sauk Sequence in West Texas, USA. *Geol. Soc. America Bull.* 126, 1117–1128. doi:10.1130/B30884.1

Steiger, R. H., and Jäger, E. (1977). Subcommission on Geochronology: Convention on the Use of Decay Constants in Geo- and Cosmochronology. *Earth Planet. Sci. Lett.* 36, 359–362. doi:10.1016/0012-821X(77)90060-7

Tapponier, P., Meyer, B., Avouac, J. P., Peltzer, G., Gaudemer, Y., Guo, S., et al. (1990). Active Thrusting and Folding in the Qilian Shan, and decoupling Between Upper Crust and Mantle in Northeastern Tibet. *Earth Planet. Sci. Lett.* 97, 382–407. doi:10.1016/0012-821x(90)90053-z

Tapponnier, P., Zhiqin, X., Roger, F., Meyer, B., Arnaud, N., Wittlinger, G., et al. (2001). Oblique Stepwise Rise and Growth of the Tibet Plateau. *Science* 294, 1671–1677. doi:10.1126/science.105978

Wagner, G. A., Gleadow, A. J. W., and Fitzgerald, P. G. (1989). The Significance of the Partial Annealing Zone in Apatite Fission-Track Analysis: Projected Track Length Measurements and Uplift Chronology of the Transantarctic Mountains. *Chem. Geology. Isotope Geosci. Sec.* 79, 295–305. doi:10.1016/0168-9622(89)90035-3

Wan, J., Zheng, D., Zheng, W., and Wang, W. (2011). Modeling thermal History during Low Temperature by K-Feldspar MDD and Fission Track: Example from Meso-Cenozoic Tectonic Evolution in Saishiteng Shan in the Northern Margin of Qaidam Basin (In Chinese). *Seismology Geology.* 33, 370–382. doi:10.3969/j.issn.0253-4967.2011.02.010

Wan, J., Zheng, W., Zheng, D., Wang, W., and Wang, Z. (2010). Low Closure Temperature Thermochronology Study on the Late Cenozoic Tectonic Active of Northern Qilian Shan and its Implication for Dynamics of Tibetan Plateau Growth (In Chinese). *Geochimica* 39, 439–446. doi:10.19700/j.0379-1726.2010.05.004

Wang, W., Zhang, P., Pang, J., Garzione, C., Zhang, H., Liu, C., et al. (2016). The Cenozoic Growth of the Qilian Shan in the Northeastern Tibetan Plateau: A Sedimentary Archive from the Jiuxi Basin. *J. Geophys. Res. Solid Earth* 121, 2235–2257. doi:10.1002/2015JB012689

Wang, W., Zheng, D., Li, C., Wang, Y., Zhang, Z., Pang, J., et al. (2020). Cenozoic Exhumation of the Qilian Shan in the Northeastern Tibetan Plateau: Evidence from Low-Temperature Thermochronology. *Tectonics* 39, e2019TC005705. doi:10.1029/2019TC005705

Wang, W., Zheng, W., Zhang, P., Li, Q., Kirby, E., Yuan, D., et al. (2017). Expansion of the Tibetan Plateau during the Neogene. *Nat. Commun.* 8, 15887. doi:10.1038/ncomms15887

Wang, Y., Zheng, D., Pang, J., Zhang, H., Wang, W., Yu, J., et al. (2018). Using Slope-Area and Apatite Fission Track Analysis to Decipher the Rock Uplift Pattern of the Yumu Shan: New Insights into the Growth of the NE Tibetan Plateau. *Geomorphology* 308, 118–128. doi:10.1016/j.geomorph.2018.02.006

Wen-Jun, Z., Hui-Ping, Z., Pei-Zhen, Z., Molnar, P., Xing-Wang, L., and Dao-Yang, Y. (2013). Late Quaternary Slip Rates of the Thrust Faults in Western Hexi Corridor (Northern Qilian Shan, China) and Their Implications for Northeastward Growth of the Tibetan Plateau. *Geosphere* 9, 342–354. doi:10.1130/GES00775.1

Xu, Z., Yang, J., Li, H., Ji, S., Zhang, Z., and Liu, Y. (2011). On the Tectonics of the India-Asia Collision (In Chinese). *Acta Geol. Sin.* 85, 1–33.

Yang, S., Chen, H., Cheng, X., Xiao, A., He, G., and Chen, J. (2007). Deformation Characteristics and Rules of Spatial Change for the Northern Qilian Shan Thrust belt (In Chinese). *Earth Sci. Front.* 14, 211–221. doi:10.3321/j.issn:1005-2321.2007.05.021

Yin, A., and Harrison, T. M. (2000). Geologic Evolution of the Himalayan-Tibetan Orogen. *Annu. Rev. Earth Planet. Sci.* 28, 211–280. doi:10.1146/annurev.earth.28.1.211

Yin, A., Rumelhart, P. E., Butler, R., Cowgill, E., Harrison, T. M., Foster, D. A., et al. (2002). Tectonic History of the Altyn Tagh Fault System in Northern Tibet Inferred from Cenozoic Sedimentation. *Geol. Soc. Am. Bull.* 114, 1257–1295. doi:10.1130/0016-7606(2002)114<1257:thotat>2.0.co;2

Yu, J., Pang, J., Wang, Y., Zheng, D., Liu, C., Wang, W., et al. (2019). Mid-Miocene Uplift of the Northern Qilian Shan as a Result of the Northward Growth of the Northern Tibetan Plateau. *Geosphere* 15, 423–432. doi:10.1130/GES01520.1

Yuan, D. Y., Ge, W. P., Chen, Z. W., Li, C. Y., Wang, Z. C., Zhang, H. P., et al. (2013). The Growth of Northeastern Tibet and its Relevance to Large-scale continental Geodynamics: A Review of Recent Studies. *Tectonics* 32, 1358–1370. doi:10.1002/tect.20081

Zhao, Z., Fang, X., and Li, J. (2001). Late Cenozoic Magnetic Polarity Stratigraphy in the Jiudong Basin, Northern Qilian Mountain. *Sci. China Ser. D-earth Sci.* 44, 243–250. doi:10.1007/BF02911993

Zhao, Z., Granger, D. E., Chen, Y., Shu, Q., Liu, G., Zhang, M., et al. (2017). Cosmogenic Nuclide Burial Dating of an Alluvial Conglomerate Sequence: An Example from the Hexi Corridor, NE Tibetan Plateau. *Quat. Geochronol.* 39, 68–78. doi:10.1016/j.quageo.2017.02.007

Zheng, D., Clark, M. K., Zhang, P., Zheng, W., and Farley, K. A. (2010). Erosion, Fault Initiation and Topographic Growth of the North Qilian Shan (Northern Tibetan Plateau). *Geosphere* 6, 937–941. doi:10.1130/GES00523.1

Zheng, D., Wang, W., Wan, J., Yuan, D., Liu, C., Zheng, W., et al. (2017). Progressive Northward Growth of the Northern Qilian Shan-Hexi Corridor (Northeastern Tibet) during the Cenozoic. *Lithosphere* 9, 408–416. doi:10.1130/L587.1

Zhu, X. (2008). *Sedimentary Petrology*. 4th edition. Beijing, China: Petroleum Industry Press, 23–24.

Zhuang, G., Johnstone, S. A., Hourigan, J., Ritts, B., Robinson, A., and Sobel, E. R. (2018). Understanding the Geologic Evolution of Northern Tibetan Plateau with Multiple Thermochronometers. *Gondwana Res.* 58, 195–210. doi:10.1016/j.gr.2018.02.014

Zuza, A. V., Cheng, X., and Yin, A. (2016). Testing Models of Tibetan Plateau Formation with Cenozoic Shortening Estimates across the Qilian Shan-Nan Shan Thrust belt. *Geosphere* 12, 501–532. doi:10.1130/GES01254.1

Conflict of Interest: The authors declare that the research was conducted in the absence of any commercial or financial relationships that could be construed as a potential conflict of interest.

Publisher's Note: All claims expressed in this article are solely those of the authors and do not necessarily represent those of their affiliated organizations, or those of the publisher, the editors, and the reviewers. Any product that may be evaluated in this article, or claim that may be made by its manufacturer, is not guaranteed or endorsed by the publisher.

Copyright © 2022 Pan, Zhao, Hu, Zhang and Chen. This is an open-access article distributed under the terms of the Creative Commons Attribution License (CC BY). The use, distribution or reproduction in other forums is permitted, provided the original author(s) and the copyright owner(s) are credited and that the original publication in this journal is cited, in accordance with accepted academic practice. No use, distribution or reproduction is permitted which does not comply with these terms.

frontiers in Earth Science

ORIGINAL RESEARCH
published: 16 February 2022
doi: 10.3389/feart.2022.821367

Evaluation of the Rock Uplift Pattern in the Central Yunnan Subblock, SE Tibetan Plateau: Based on the Bedrock Channel Profile

*Liang Yu, Youpu Dong *, Weiwei Zhou *, Dongyue Zhang, Dan Wang, Huayu Yu, Yangyang Ren and Jiangtao Li*

Faculty of Land Resource Engineering, Kunming University of Science and Technology, Kunming, China

The uplift pattern of the southeastern Tibetan Plateau is strongly related to the topographic evolution stemming from the India–Eurasia collision. However, whether strain is localized along major faults that bound large tectonic blocks or is accommodated across regions has been strongly debated. In this study, we used stream power incision models to obtain the distribution pattern of the channel steepness indices to understand the rock uplift pattern across the area, as increased channel steepness indices often correlate with the rock uplift rates. In this study, the river longitudinal profiles were analyzed to obtain the distribution of the channel steepness indices in the Central Yunnan subblock. The results suggested very weak correlations between the steepness indices and the lithology, precipitation, sediment flux, or channel concavity indices. Along the Xiaojiang strike–slip fault and the interior subblock, the uplift rate was slower, while the northern part had uplifted faster and was controlled by thrust fault systems. The channel steepness increased gradually from south to north. Thus, the distribution pattern of the normalized channel steepness, k_{sn}, index within the Central Yunnan subblock provides notable support for the argument for the thrusting transformation-limited extrusion model of the Tibetan Plateau.

Keywords: stream power incision model, channel steepness index, the Central Yunnan subblock, river longitudinal profile, rock uplift

OPEN ACCESS

Edited by:
Rong Yang,
Zhejiang University, China

Reviewed by:
Lei Wu,
Zhejiang University, China
Yang Wang,
Sun Yat-sen University, China

****Correspondence:***
Youpu Dong
dongypsd@126.com
Weiwei Zhou
605316200@qq.com

Specialty section:
This article was submitted to Quaternary Science, Geomorphology and Paleoenvironment, a section of the journal Frontiers in Earth Science

Received: *24 November 2021*
Accepted: *07 January 2022*
Published: *16 February 2022*

Citation:
Yu L, Dong Y, Zhou W, Zhang D, Wang D, Yu H, Ren Y and Li J (2022) Evaluation of the Rock Uplift Pattern in the Central Yunnan Subblock, SE Tibetan Plateau: Based on the Bedrock Channel Profile. Front. Earth Sci. 10:821367. doi: 10.3389/feart.2022.821367

INTRODUCTION

The Tibetan Plateau is one of the most studied natural laboratories for examination of the relationship between continental collision and landscape evolution (Clark et al., 2005; Clark, 2012; Allen et al., 2013; Zheng et al., 2013; Liu et al., 2008; Molnar and England, 1990; Liu-Zeng et al., 2018; Wang et al., 2019). Although there has been much work done in the region, it is still poorly understood how the southeastern margin of the Tibetan Plateau responded to the India–Eurasia continental collision. Additionally, whether the strain is mainly localized along the boundary faults of large blocks (Tapponnier, 2001) or accommodated within the block (Houseman and England, 1993; Royden et al., 1997; Clark et al., 2005; Clark et al., 2004; Wang et al., 2017) has been strongly debated.

Research on the bedrock channel fluvial systems has examined the relationships between climate variations, surface processes, and tectonic evolution (Raymo and Ruddiman, 1992; Hartshorn et al., 2002; Dibiase and Whipple, 2011; Ferrier et al., 2013; Dibiase, 2014; Finnegan et al., 2014; Pan et al.,

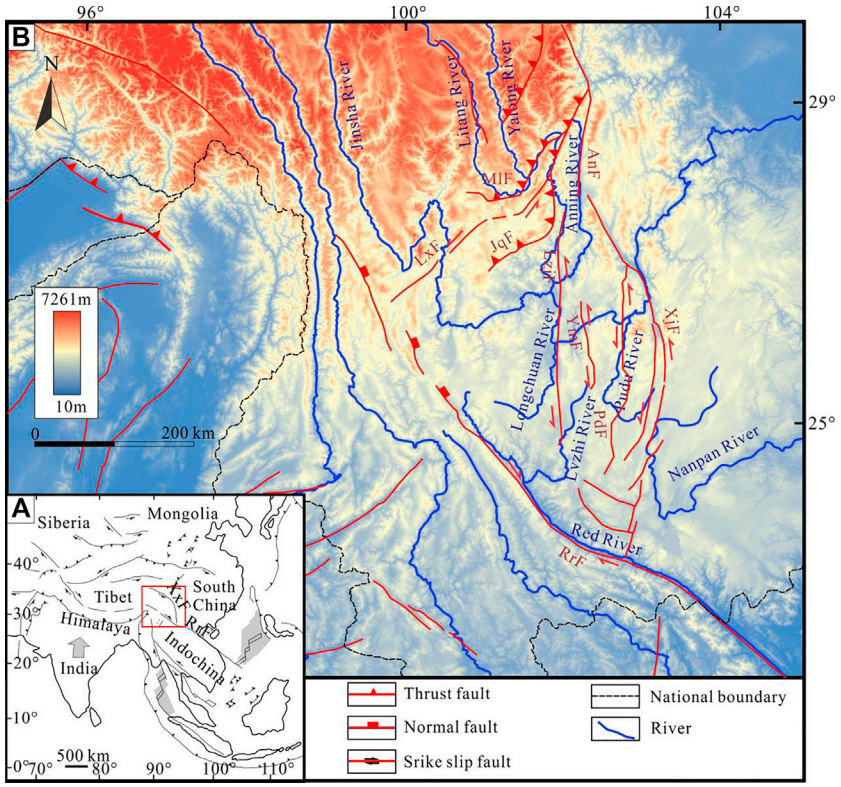

FIGURE 1 | Topographic map of the Central Yunnan subblock. **(A)** Location of the study area. **(B)** Topography, major faults, and rivers in the southeastern Tibetan Plateau. *XxF*, Xianshuihe–Xiaojiang Fault; *AnF*, Anninghe Fault; *LxF*, Lijiang–Xiaojinhe Fault; *MlF*, Muli Fault; *JqF*, Jinhe–Qinghe Fault; *LzjF*, Lvzhijiang Fault; *YmF*, Yimen Fault; *PdF*, Pudu Fault; *XjF*, Xiaojiang Fault; *RrF*, Red River Fault.

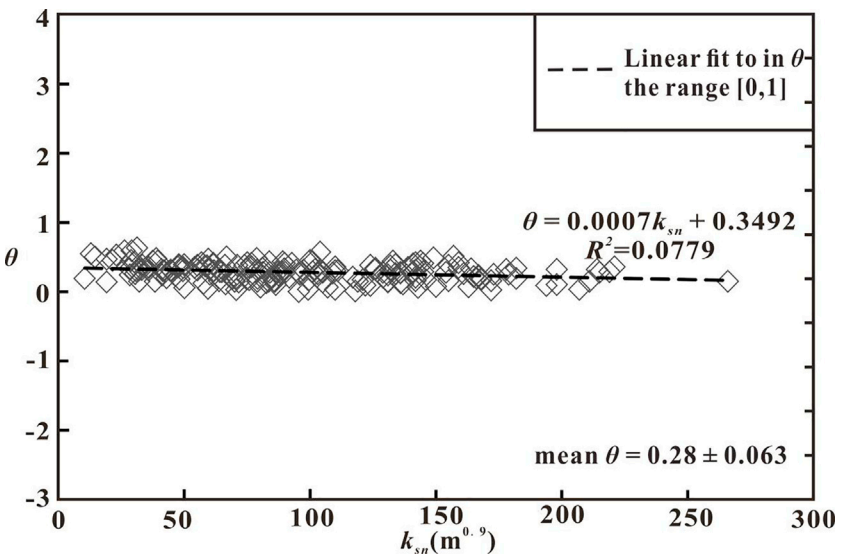

FIGURE 2 | Normalized channel steepness calculated for a reference concavity (θ_{ref} = 0.45) plotted against the actual concavity (θ) of the profile. The streams extracted for river profile analysis and the steepness and concavity indices of each segment are in the *Supplementary File*.

2015; Kirby and Ouimet, 2011; Kirby et al., 2007; Lave and Avouac, 2001) and has been used to interpret the relationships between topography, elevation, and denudation rates (Pritchard et al., 2009; Schwanghart and Scherler, 2020). In this study, we selected the Central Yunnan subblock as our study area (**Figure 1**). We extracted longitudinal river profiles from 320

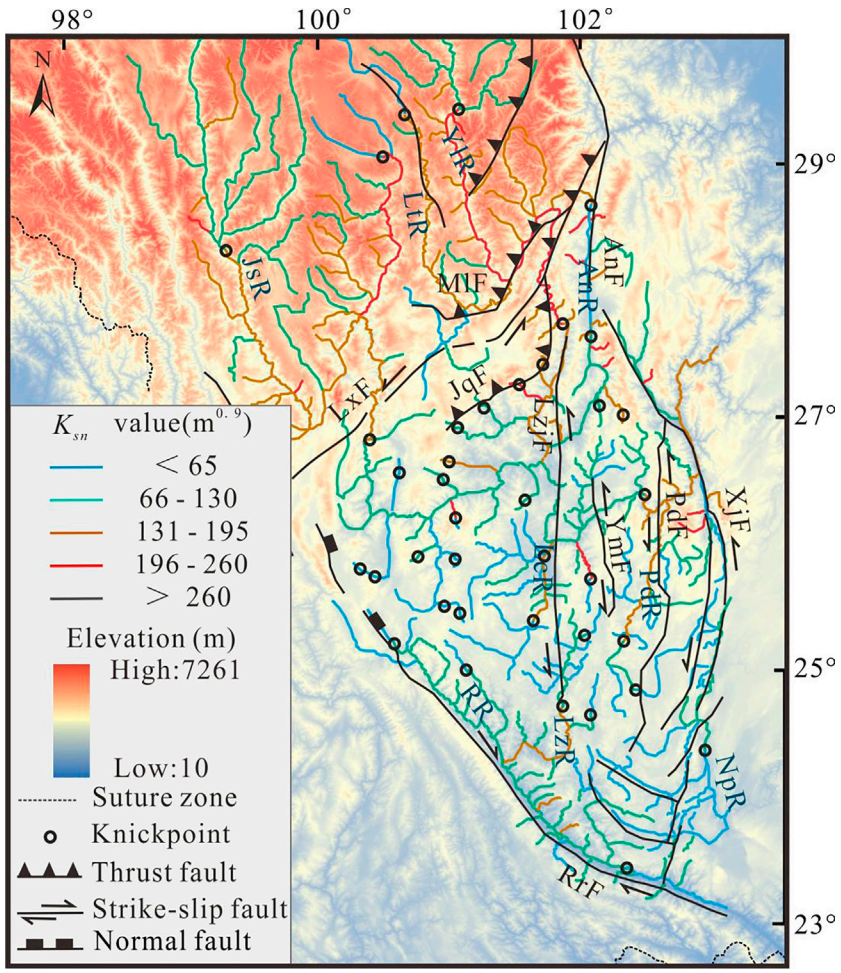

FIGURE 3 | Spatial pattern of the normalized channel steepness across the Central Yunnan subblock. *AnF*, Anninghe Fault; *LxF*, Lijiang–Xiaojinhe Fault; *MlF*, Muli Fault; *JqF*, Jinhe–Qinghe Fault; *LzjF*, Lvzhijiang Fault; *YmF*, Yimen Fault; *PdF*, Pudu Fault; *XjF*, Xiaojiang Fault; *RrF*, Red River Fault; *AnR*, Anning River; *LcR*, Longchuan River; *PuR*, Pudu River; *LzR*, Lvzhi River; *NpR*, Nanpan River; *RrR*, Red River; *JsR*, Jinsha River; *LtR*, Litang River.

rivers and calculated the channel steepness indices and concavities to determine the uplift patterns in this area (e.g., Kirby and Whipple, 2001; Whipple, 2004; Wobus et al., 2006; Oskin et al., 2014; Su et al., 2016) based on the digital elevation model data of the 90-m Shuttle Radar Topography Mission (downloaded from http://srtm.csi.cgiar.org/) by ArcGIS 10.2 and MATLAB R2015b. Thereafter, the influence of lithology resistance, precipitation, and sediment flux on channel steepness indices was analyzed to obtain the distribution pattern of the rock uplift within the subblock.

Regional Setting

The Sichuan–Yunnan rhombic block is located in the southeastern margin of the Tibetan Plateau. The Lijiang–Xiaojinhe Fault cuts the block into two parts: the Central Yunnan subblock in the south and the northwestern Sichuan subblock in the north (Xu et al., 2003) (**Figure 1**). In this paper, we mainly studied the Central Yunnan subblock.

The average elevation of the Central Yunnan subblock is about 2,000 m. The geotectonic location belongs to the southeastern margin of the Tibetan Plateau. It is adjacent to the Simao block in the south and the Caledonian fold belt in southeastern Yunnan to the east (Huangfu and Qin, 2006; He et al., 2009; Wang et al., 2015). For most parts of the area, annual rainfall ranges from 600 to 1,100 mm and gradually increases from north to south. Owing to the abundant rainfall, the study area has developed a dense river network, with many large rivers originating in the area (e.g., Longchuan River, Red River, Nanpan River, Pudu River, Anning River, and Xiaohedi River) (**Figure 1**).

The lithology of the central region of the subblock is relatively homogenous (consisting of Cretaceous–Jurassic sandstones and mudstones), while the lithology of the border region of the Central Yunnan subblock is complex (including Paleozoic shales, schists, and gneiss, Cambrian limestones and dolomites, and Triassic phyllites and mudstones). The subblock is

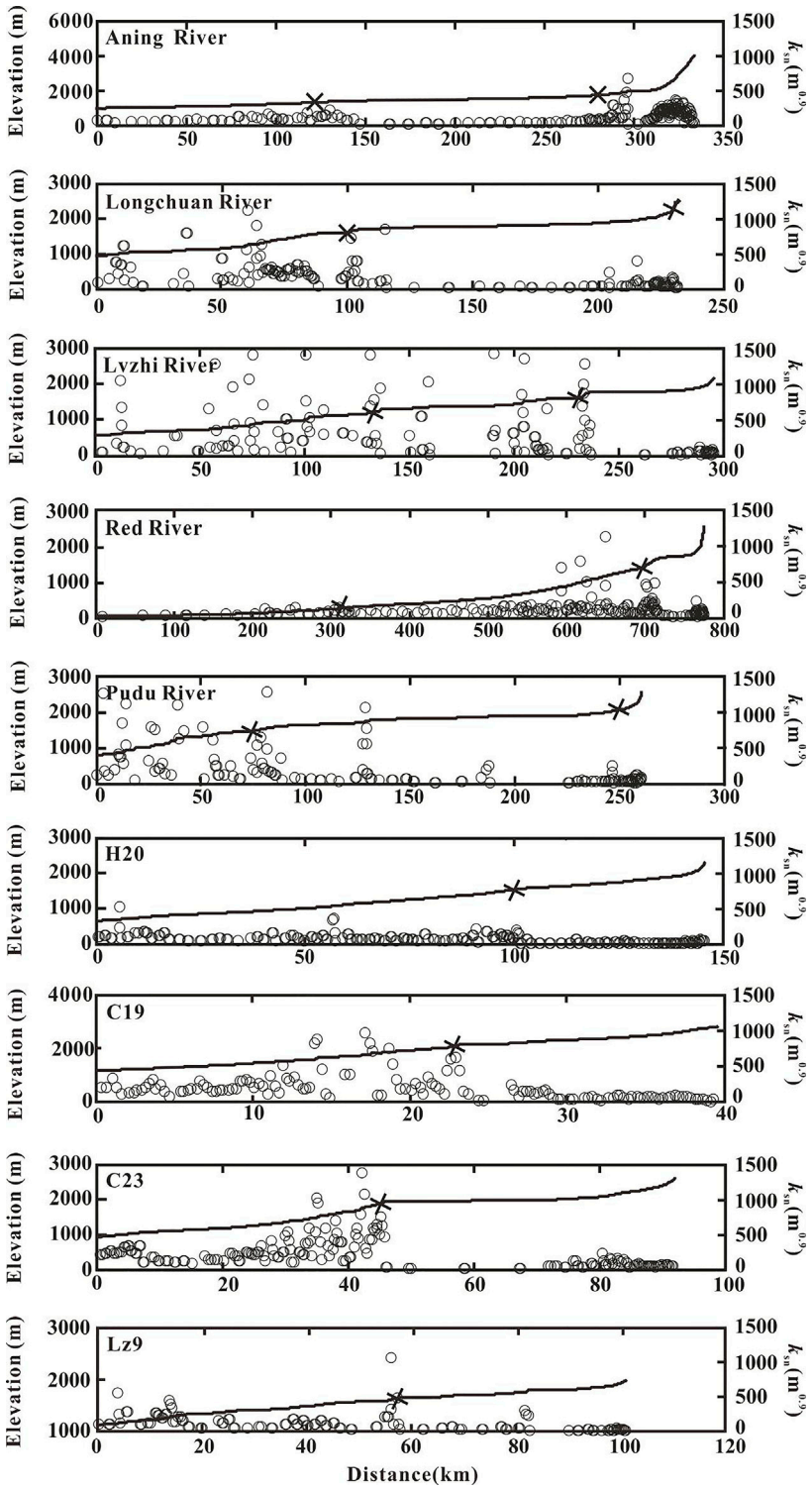

FIGURE 4 | Channel steepness of representative river profiles. *Black crosses* are knickpoints.

constrained by the Xiaojiang Fault, Lijiang–Xiaojinhe Fault, and the Red River Fault. The northern region of the block is cut by a series of thrust faults (the Jiulong, the Muli, and Jinhe–Qinghe thrusting faults) (**Figure 1**). The central region of the block is cut by a series of strike–slip faults (the Xiaojiang, Lvzhijiang, and Yimen strike–slip faults) (**Figure 1**).

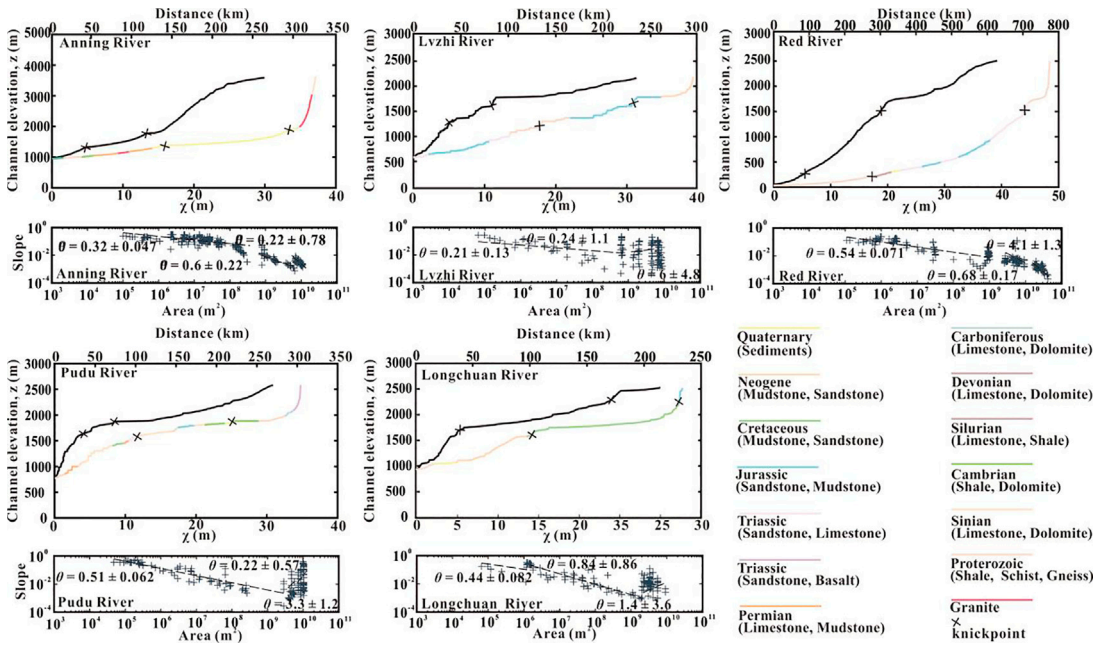

FIGURE 5 | Stream profile analysis for the trunk rivers of the five large drainage basins. The *colored curve* is a river profile with variable lithologies.

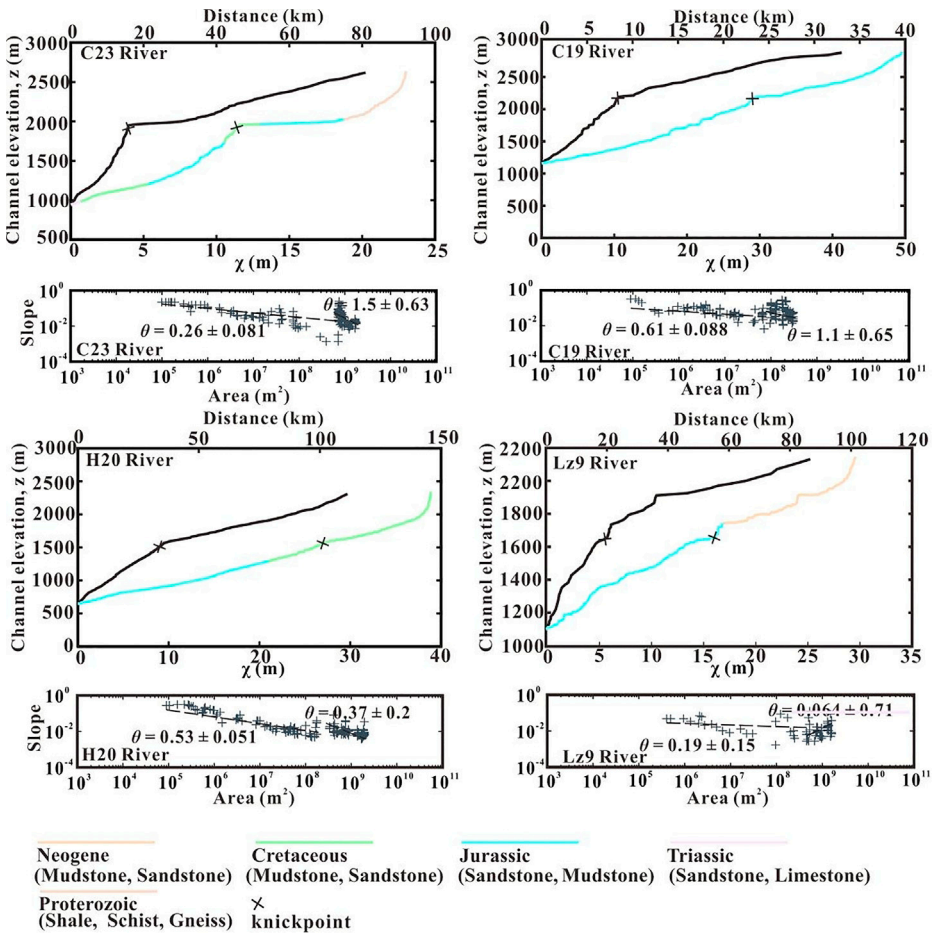

FIGURE 6 | Stream profile analysis for the four middle-scale rivers. The *colored curve* is a river profile with variable lithologies.

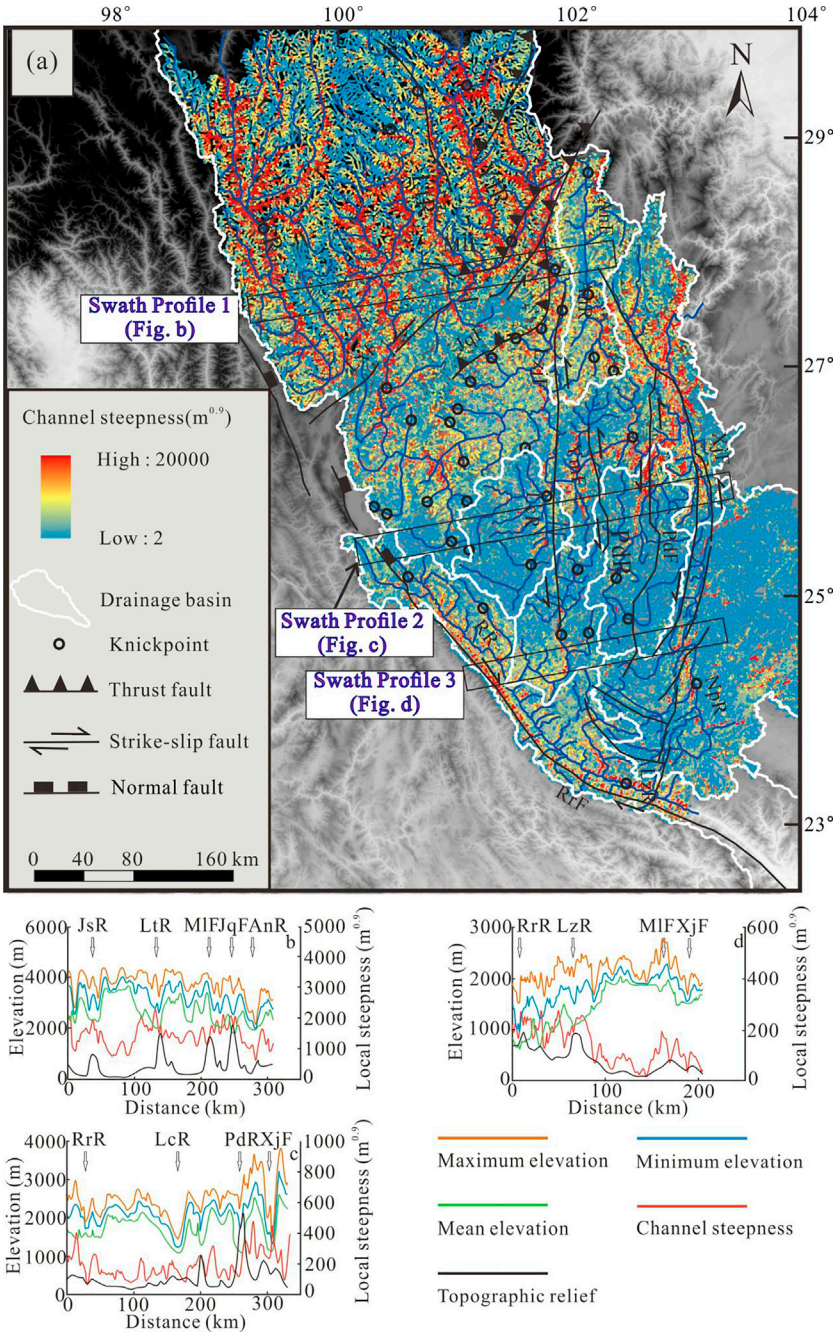

FIGURE 7 | (**A**) Map of local channel steepness values calculated under an elevation interval of 100 m. **(B–D)** Geological cross-sections and swath profiles of the elevation and local channel steepness indices along the section in **(A)**: swath profile 1 **(B)**; swath profile 2 **(C)**; and swath profile 3 **(D)**. The maximum, minimum, mean elevation, and topographic relief are shown in *orange*, *green*, *blue*, and *red*, respectively. Major faults and rivers are as follows: *RrR*, Red River; *LtF*, Litang Fault; *MlF*, Muli Fault; *JqF*, Jinhe–Qinghe Fault; *JsR*, Jinsha River; *LtR*, Litang River; *LcR*, Longchuan River; *LzR*, Lvzhi River; *PdR*: Pudu River; *XjR*, Xiaojiang River. Average local steepness indices are shown in *black*.

In the Cenozoic, most of the fault zones and orogenic belts of the Tibetan Plateau were active due to the strong collision between India and Eurasia (Wang et al., 2012; Shen et al., 2016; Zhang et al., 2016; Zhang et al., 2017; Liu-Zeng et al., 2018). The Xianshuihe–Xiaojiang Fault is a very large left lateral strike–slip fault (e.g., Xiang et al., 2002; Li and Zhang, 2013; Yan and Lin, 2015; Xu et al., 2007). In the Late Cenozoic, the Xianshuihe–Xiaojiang Fault offset the NE–SW Longmenshan thrust fault by as much as 60 km, splitting it into the north Longmenshan (NLM) and south Longmenshan (SLM) thrust

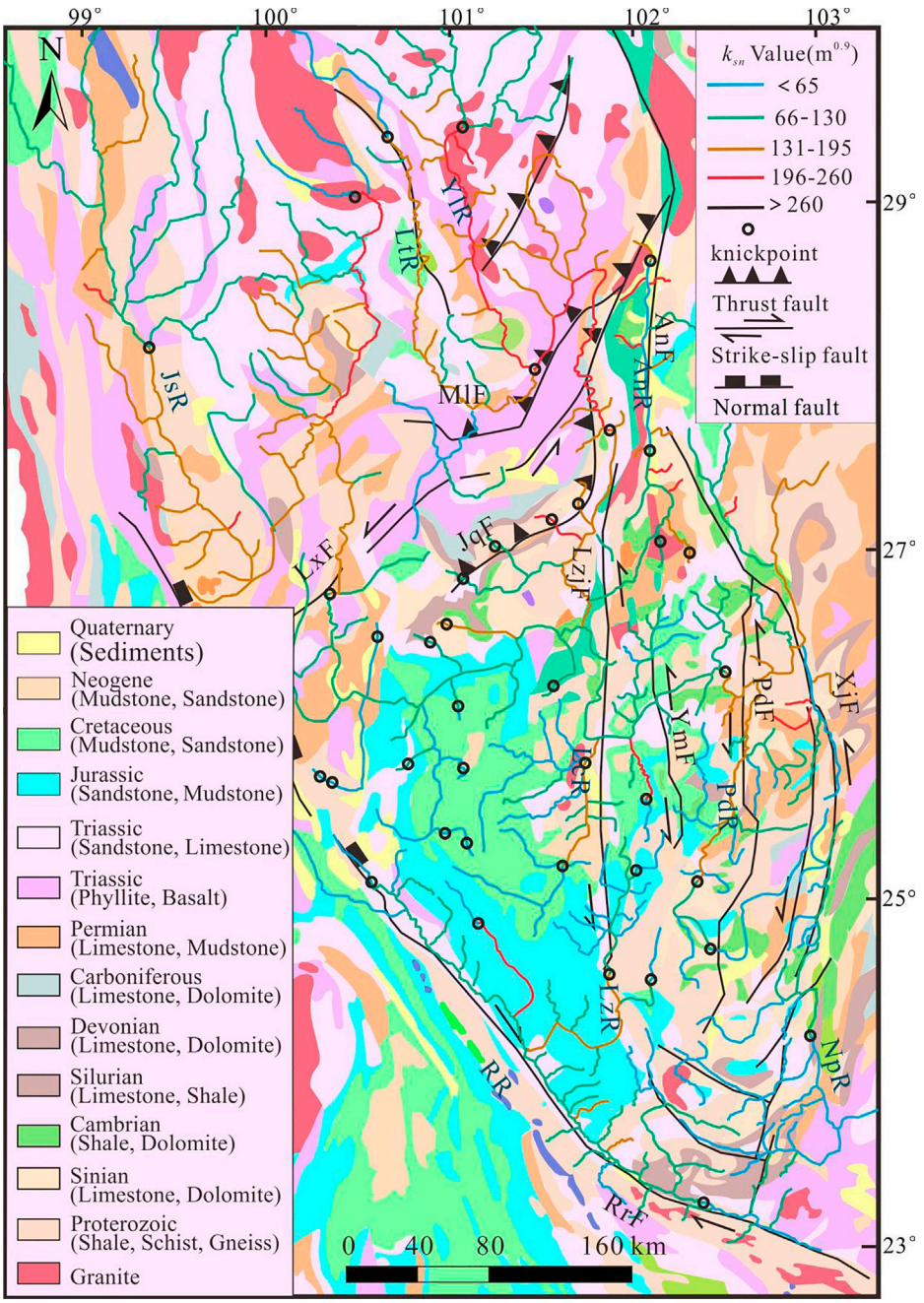

FIGURE 8 | Comparison of normalized channel steepness (k_{sn}) to lithologic variability in the Central Yunnan subblock. *AnF*, Anninghe Fault; *LxF*, Lijiang–Xiaojinhe Fault; *MlF*, Muli Fault; *JqF*, Jinhe–Qinghe Fault; *LzjF*, Lvzhijiang Fault; *YmF*, Yimen Fault; *PdF*, Pudu Fault; *XjF*, Xiaojiang Fault; *RrF*, Red River Fault; *AnR*, Anning River; *LcR*, Longchuan River; *PuR*, Pudu River; *LzR*, Lvzhi River; *NpR*, Nanpan River; *RrR*, Red River; *JsR*, Jinsha River; *LtR*, Litang River.

belts (Burchfiel et al., 1995; Wang et al., 1998). The SLM includes the Muli Fault, Lijiang–Xiaojinhe Fault, and Jinhe–Qihe Fault (Yin et al., 2020; Wang et al., 2012).

The uplift history and the expansion of the southeastern margin of the Tibetan Plateau have been studied intensely using several methods. Analysis of the ^{18}O isotopes of carbonate rocks in Cenozoic sedimentary basins (Li et al., 2015; Tang et al., 2017; Hoke, 2018) interpreted that the palaeo-elevation of the southeastern margin of the plateau reached its present height prior to the Eocene. In addition, episodic periods of uplifts have occurred in the region since the Late Cenozoic, determined through various thermochronometers (e.g., Xu and Kamp, 2000; Chen et al., 2006; Wilson and Fowler, 2011; Wang et al., 2012; Tian et al., 2013, Tian et al., 2014, Tian et al., 2015; Shen et al., 2016; Zhang et al., 2016; Zhang et al., 2017; Liu-Zeng et al., 2018; Wu et al., 2020).

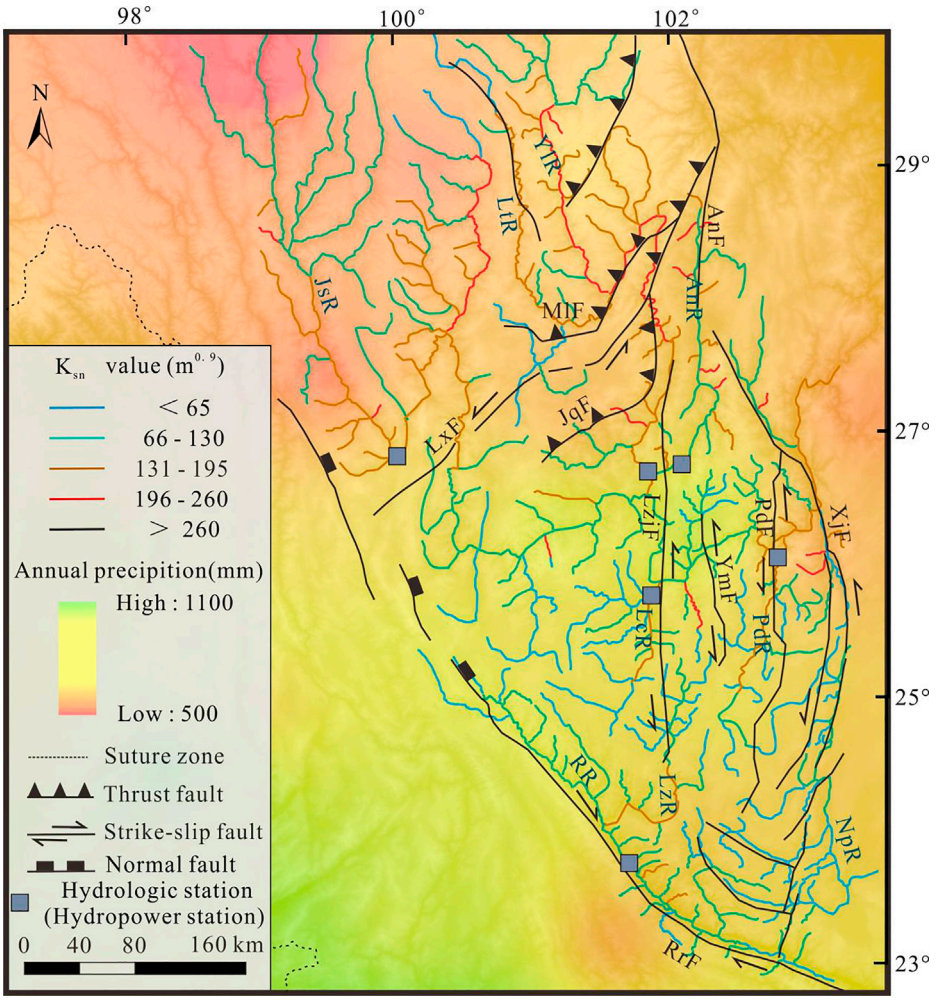

FIGURE 9 | Comparison of normalized channel steepness (k_{sn}) to annual precipitation in the Central Yunnan subblock. The precipitation data (timescale: from 1970 to 2019) were downloaded from http://data.cma.cn. The tributary catchments (*white boundary*) were selected randomly for correlation analysis between channel steepness with precipitation and drainage area. *AnF*, Anninghe Fault; *LxF*, Lijiang–Xiaojinhe Fault; *MlF*, Muli Fault; *JqF*, Jinhe–Qinghe Fault; *LzjF*, Lvzhijiang Fault; *YmF*, Yimen Fault; *PdF*, Pudu Fault; *XjF*, Xiaojiang Fault; *RrF*, Red River Fault; *AnR*, Anning River; *LcR*, Longchuan River; *PuR*, Pudu River; *LzR*, Lvzhi River; *NpR*, Nanpan River; *RrR*, Red River; *JsR*, Jinsha River; *LtR*, Litang River.

METHODS

The stream power incision model relates rock uplift and river incision over time along the longitudinal profile of the channel (Howard and Kerby, 1983; Howard et al., 1994), and it can be represented by **Eq. 1**:

$$\frac{\partial z}{\partial t} = U - KA^m\left(\frac{\partial z}{\partial x}\right)^n \tag{1}$$

where z represents the channel elevation, x represents the upstream distance, t represents time, U is the rock uplift rate, and K is the bedrock erodibility and is related to the channel width, the water discharge, the sediment load, and the lithologic resistance (Howard and Kerby, 1983; Howard et al., 1994). m and n are constant exponents, and A is the drainage area.

For a steady state, channel elevation at a particular point does not change, and then $\partial z/\partial t$ equals 0. From this, we can obtain **Eq. 2**.

$$\frac{dz}{dx} = k_s A^{-\theta} \tag{2}$$

$$K_s = \left(\frac{U}{K}\right)^{1/n} \tag{3}$$

$$\theta = \frac{m}{n} \tag{4}$$

where k_s and θ are the channel steepness and concavity indices, respectively. Generally, θ oscillated between 0.3 and 0.6 (Snyder et al., 2000; Snyder et al., 2006; Whipple, 2002; Kirby et al., 2003; Wobus et al., 2003). K_s is usually proportional to the rock uplift rates (**Eq. 3**). Although the longitudinal profile analysis was

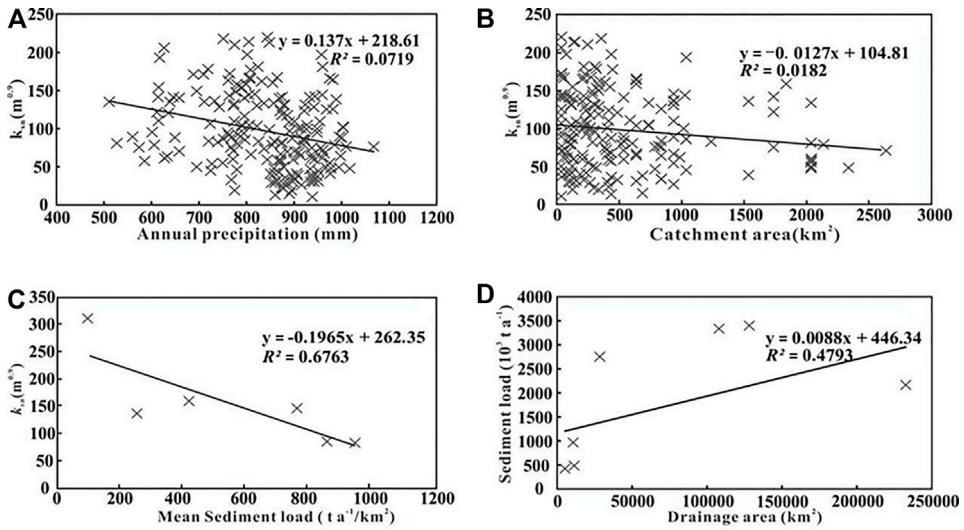

FIGURE 10 | Bi-variant linear regression of channel steepness (k_{sn})–annual precipitation **(A)**, channel steepness–catchment area **(B)**, mean sediment load–channel steepness **(C)**, and sediment load–drainage area **(D)**.

developed under steady-state assumptions, it has been extended to transient systems as well (e.g., Pan et al., 2015; Wang et al., 2017; Wang et al., 2019; Ma et al., 2020), and several studies (e.g., Snyder et al., 2000; Kirby et al., 2003; Wobus et al., 2003; Hu et al., 2010; Burbank and Anderson, 2011; Kirby and Whipple, 2012) showed that K_s is a useful index for denoting rock uplift rates at transient states.

θ can be gained by a log transformation to **Eq. 2** by Wobus et al. (2003).

$$\log\left(\frac{dz}{dx}\right) = -\theta \cdot \log(A) + \log(K_s) \tag{5}$$

The concavity and steepness indices are the slope and intercept of **Eq. 5**, respectively. K_s can be gained using **Eq. 6** (Perron and Royden, 2013).

$$z = z_b + \left(\frac{U}{KA_0^m}\right)^{\frac{1}{n}} \cdot \chi \tag{6}$$

$$\chi = \int_0^x \left(\frac{A_0}{A(x')}\right)^{\frac{m}{n}} dx' \tag{7}$$

where A_0 is the area factor and z_b is the channel elevation at river outlets ($x = 0$). $A_0/A_{(x)'}$ is dimensionless. Setting $A_0 = 1\ m^2$, the slope of **Eq. 6** is k_s.

We first used the ArcGIS 10.2 and MATLAB 2015b scripts (www.geomorphtools.org) to derive the concavity indices (**Figure 2**), steepness indices (**Figure 3**), and the longitudinal profiles (**Figures 4–6**). The steepness indices were determined using log*S*–log*A* plots according to the methods described by Wobus et al. (2003). Then, we interpolated the normalized channel steepness, k_{sn}, values of the river basins in the Central Yunnan subblock and created three swath profiles of the elevation and local steepness (**Figure 7**) (the profiles are E/W-directed, 220–350 km long and 20 km wide), finally presenting a distribution pattern over the Central Yunnan subblock. Due to the strong dependence of k_s on θ, a fixed reference concavity of 0.45 (a typical value used in many studies, e.g., Wobus et al., 2003; Hu et al., 2010; Perron and Royden, 2013) was used to generate *x*–*z* plots and to calculate the k_{sn} indices in order to compare the channels and channel segments of varying drainage areas (Whipple and Tucker, 1999). We resampled the elevation data at 20-m contour intervals with a 250-m smoothing window to decrease data noise (e.g., Wang et al., 2017).

RESULTS

In the Central Yunnan subblock, the 320 extracted river profiles had a mean concavity of 0.28 ± 0.063 (1σ), with a total range of 0.014–0.63 (**Figure 2**). In this section, however, we just described the most representative stream longitudinal profiles in the subblock (**Figures 3–7**). The detailed results are depicted in the **Supplementary Material** (**Supplementary Figure S1** and **Supplementary Table S1**). Furthermore, the k_{sn} and θ values are also listed in the **Supplementary Material** (**Supplementary Figure S1** and **Supplementary Table S1**).

In the northern areas controlled by a series of NE–SW thrust faults (such as the Jiulong and Muli thrust fault belts and the Jinhe–Qinghe thrust fault zone), these rivers had higher k_{sn} values (**Figure 3**), which can also be found from profile 1 (**Figure 7B**). The upper reaches of the Anning River also had high k_{sn} values, which may stem from their close proximity to areas of thrust faults (Muli Fault and Jinhe–Qinghe Fault) (**Figure 3**).

However, in the south areas controlled by the strike–slip faults and within the block, the rivers had lower k_{sn} values (**Figures 3**,

7). The lower reaches of the Anning River near the Xiaojiang strike–slip fault zone had low k_{sn} values. Similarly, the Pudu River and Lvzhi River and the Red River, which are close to the Pudu River Fault and Lvzhi River Fault, respectively, also had lower k_{sn} values in this area. From swath profiles 2 and 3, we can see that the k_{sn} values were low on both sides of the Xiaojiang fault zone, the Lvzhijiang Fault, and the Red River Fault and exhibited little change across the area (**Figures 7C, D**).

Based on the distribution pattern of the k_{sn} indices along the Central Yunnan subblock (**Figure 7A**), an approximate trend of change has been outlined, in which the average k_{sn} indices showed a general and gradual decrease from north to south.

DISCUSSION

The K_{sn} values were higher in the northern region controlled by the thrust faults and on both sides of the Jinsha River and were lower within the block and near strike–slip faults. The results suggest that the longitudinal river profiles correlated strongly with the underlying tectonic regime and may be used to make inferences regarding the tectonic setting or structure. However, if we want to attribute the variation of k_{sn} to the rock uplift rates, the influence of the lithology, precipitation, and sediment flux should be excluded.

Lithology

Channel bedrock erodibility is largely controlled by the lithologic resistance (Stock and Montgomery, 1999; Palumbo et al., 2010; Wang, 2014; Wang et al., 2018). As river incision through more resistant rocks (low K) requires greater stream power compared to less resistant rocks (high K), knickpoints are usually observed near the contact between rocks, with higher k_{sn} values in areas underlain by harder units (Duvall et al., 2004). Therefore, we analyzed the relationship between nine representative rivers with different lithologies (**Figures 5**, **6**) and their k_{sn} values to assess the influence of lithologic resistance.

Although the knickpoints observed along the Longchuan River (large-scale river, basin area $> 10^4$ km^2), C23 and Lz9 (middle-scale river, $10^3 <$ basin area $< 10^4$), are located near lithologic boundaries (**Figures 5**, **6**), the influences of variable lithologies on the channel profiles were weak. Along these rivers, the extracted k_{sn} values did not match the mapped lithologies (**Figure 8**). For example, in the lower reaches of the Anning River, although the lithology varied, we did not find an obvious knickpoint (**Figure 5**). But an obvious knickpoint was extracted from H20 (**Figure 6**), where the bedrock lithology of these channels is uniform.

Therefore, regional lithology does not appear to be a major influence on the channel profile of the subblock.

Precipitation

The effect of climate (mainly precipitation) on the channel profiles must be examined, as increased rates of rainfall often lead to increased river discharge and erosion of the bedrock beneath the channel. Ultimately, increased rainfall rates will decrease channel steepness, as channel steepness is often inversely proportional to the erodibility (**Eq. 3**). Here, the monthly precipitation data of 15 meteorological stations were collected from the China Meteorological Data Network (timescale: 1970–2019; downloaded from http://data.cma.cn) (**Figure 9**). These data were interpolated to derive the spatial distribution of average precipitation across the Central Yunnan subblock. The annual rainfall in the study area decreased from >1,200 mm (close to the Red River fault zone in the south) to <500 mm (close to the Lijiang–Xiaojinhe fault zone in the north) (**Figure 9**). This may be related to monsoons from the Indian Ocean being blocked by the Himalayas, promoting increased southeastern compared to northwestern rainfall. Increased runoff can be seen in the numerous river channels that have developed in Southwest China, such as the Yarlung Zangbo River Grand Canyon, the Lancang River Valley, the Jinsha River Valley, and other south-to-north valleys (Nie, 2018; Li, 1999).

From these data, there were two reasons to exclude precipitation as having a key role in controlling the k_{sn} values in the subblock. Firstly, by extracting the k_{sn} values from a small watershed in the study area, we found that the k_{sn} values in the northern part of the study area were higher than those in the southern part of the subblock (**Figure 7**). However, the rainfall in the southern part of the study area is higher than that in the northern part, which is inconsistent with our observation results of k_{sn} values (**Figure 9**). Secondly, we selected catchment basins with approximately 200 tributaries to quantify the relationship between rainfall and k_{sn} values. Rainfall in these basins ranges from 600 to 1,100 mm (**Figure 10A**), and the k_{sn} values had a wide range from 10.5 to 207 m$^{0.9}$. **Figure 10A** shows that the correlation between the k_{sn} values and precipitation was very weak ($R^2 = 0.0719$). As such, precipitation did not seem to control the distribution of k_{sn} values.

Sediment Flux

Abrupt changes in drainage area, water discharge, and sediment flux at tributary junctions might trigger knickpoint initiation. This behavior has been suggested in theoretical river incision models that included a dual sediment flux dependence (e.g., Gasparini and Brandon, 2011). In these models, the efficiency of bedrock incision increased with additional sediment flux up until the point when the increasing sediment no longer functioned as a tool to abrade the bed, but rather covered and armored the bed from further incision. The sediment flux in rivers mainly depends on the interplay between the actual total sediment flux (ATSF) and the river sediment capacity (RSC) (Willgoose, 1994; Tucker and Slingerland, 1996; Slingerland et al., 1997; Sklar and Dietrich, 2001; DiBiase et al., 2010). If ATSF < RSC, the materials carried by the river will erode the base of the river and increase the erosion rates (Wang et al., 2019). If ATSF > RSC, the material carried by the river will be deposited on the river bottom, thus protecting the riverbed from further erosion (Whipple, 2002) and lessening the rate at which the knickpoints move headwaters (Wang et al., 2019). As a result, the channel will become flatter and have a low concave.

Knickpoints along the Anning River (**Figure 8**) are located at the transition from the base of the channel, being characterized by

TABLE 1 | Locations of the hydrologic stations shown in **Figure 7**

Hydrologic station (hydropower station)	Drainage basin name	Sediment load (10^4 t annum^{-1})	Drainage area (km^2)	Record history	Channel steepness ($m^{0.9}$)
Tongzilin	Yalong	3,420	128,363	1954–1987	135
Xiaohuangguayuan	Longchuan	426	5,560	Multi-year average	146
Jiasa	Red River	2,772	28,816	Multi-year average	76.6
Wantan	Anning	973	11,037	1954–1987	81.3
Jiayan	Pudu	488.8	11,752	Multi-year average	160
Shigu	Jinsha	2,180	232,651	1954–1987	310

sediment characterized by bedrock. However, the k_{sn} values across the Central Yunnan subblock are not controlled by sediment flux.

We compared the k_{sn} and concavity values extracted for each class of lithology through a statistical analysis derived from **Figure 2**. Comparison of the concavity and k_{sn} values showed no linear relationship. In a normalized height–distance coordinate system, the concavity indices are close to a constant and represent similar channel shapes (Whipple and Tucker, 1999; Duvall et al., 2004; Kirby and Whipple, 2012).

The records of sediment load and drainage area were from Qin et al. (2019) and Pan (1997). Channel steepness values are shown in **Figure 6**.

We also found no systematic change of the k_{sn} values with varying sediment concentrations and the basin area. We obtained the sediment load data (including bed load, suspended load, and solute) from hydrological stations and hydroelectric stations of the Central Yunnan subblock and calculated the k_{sn} values of the channel portions downstream of the knickpoints (**Table 1**) (Pan, 1997; Qin et al., 2019). The soil erosion modulus of the Jinsha River basin in Yunnan is 1,530 t/km^2 (Huang et al., 2006), and the calculated sediment transport capacity is far greater than the actual sediment transport capacity. We found no obvious relevance between the watershed area and the k_{sn} values in the tributary catchments ($R^2 = 0.0182$) (**Figure 10B**). The calculated sediment transport capacity is far greater than the actual sediment transport. Therefore, k_{sn} should increase with the increase of the mean sediment load, but the trend cannot be seen from **Figure 10C**. Despite limited data, the sediment loads increased with the watershed area ($R^2 = 0.4793$) (**Figure 10D**).

Therefore, sediment flux did not appear to have dominant control on the k_{sn} value in the channel profile.

Patterns of Rock Uplift

Non-tectonic factors (e.g., lithologic resistance, precipitation, and sediment flux) could not fully explain the k_{sn} distribution. The most active areas of the interpreted uplift are scattered in the region controlled by the NE/SW-trending thrust faults in the north of the Central Yunnan subblock. Therefore, the distribution of the k_{sn} values is likely tectonically controlled.

The Xianshuihe–Xiaojiang Fault accommodates the shortage from the India–Eurasia collision by the left lateral strike–slip motion (e.g., Molnar and Tapponnier, 1975; Molnar et al., 1987; Deng et al., 2002; Xu et al., 2003; Wen et al., 2003). Since 13 Ma, the maximum slip rate of the north part of the Xiaojiang fault system has reached up to 10 mm/annum (Xu et al., 2003), and this rate has decreased progressively southward. At the south end of the Xiaojiang Fault, no obvious slip can be found (Wang et al., 1998). In the growth model for the Tibetan Plateau of Tapponnier et al. (1982) and Tapponnier (2001), the strain was mainly localized along the boundary faults of large blocks (Tapponnier, 2001). Fast erosion rates in the adjacent zone of the strike–slip fault belt can be found (Wang et al., 2017; 2021); however, the k_{sn} values were low on both sides of the strike–slip faults and exhibited little change across the area (**Figure 7A**). This may be due to the limited vertical slip and fast strike–slip rate (Molnar and Tapponnier, 1975; Molnar et al., 1987; Deng et al., 2002; Xu et al., 2003) in the strike–slip fault zone (Zhang, 2008; Wu et al., 2014).

Along the transition between the Xianshuihe Fault and Xiaojiang Fault, some active thrust faults with a NE trend were cut by this Xianshuihe–Xiaojiang Fault and propagated southwestward (**Figure 1**). Slip vector analyses argued that the sinistral slip rates from west to east across these thrust faults have decreased (Xu et al., 2003). Their loss has been considered to be transformed into local crustal shortening perpendicular to the active thrust faults. As a result, the distribution pattern of k_{sn} along the Xiaojiang Fault, obtained in this study, is in good agreement with the thrusting transformation-limited extrusion model of the Tibetan Plateau.

The slope–area regression of the longitudinal profiles revealed that the rock uplift in the interior of the block is lower compared to the north part controlled by a series of NE–NW thrust faults (such as the Jiulong, Muli, and Jinhe–Qinghe thrust faults) where rivers have high k_{sn} values and contain several knickpoints along their profiles, suggesting that the tectonic signals have propagated upstream in the landscape by knickpoint recession. This process resulted in higher indices in the downstream, along trunk and tributary channels (Wang et al., 2017; Zhang et al., 2020). The lower part of the Jinsha River trunk also showed high channel steepness, and the region east of the Xianshuihe Fault also had high channel steepness, although distant from the thrust faults, which appears to be the products of the knickpoint recession (Zhang et al., 2022).

We postulated that, in the interior of the block, the rivers experienced successive base-level uplifts that have migrated upslope, reaching the headwater (e.g., Clark et al., 2005; Schoenbohm et al., 2006; Royden et al., 2008; Wang et al., 2017). The distribution of lower k_{sn} values at the headwaters, the unperturbed reaches with a tight slope–area regression with low k_{sn} values, suggest that, in the growth model for the Tibetan Plateau of Tapponnier et al. (1982) and Tapponnier (2001), the

great crustal shortening between the Indian and Eurasian plates was mainly absorbed by a series of strike–slip fault systems and the related thrust faults.

CONCLUSION

In this study, we calculated the distribution pattern of normalized channel steepness by the stream power incision model of 300 rivers in the Central Yunnan subblock. The distribution pattern has been clearly observed to represent a general increase in value from north to south in this subblock. Higher k_{sn} values were associated with the NE/SW-trending Cenozoic thrust faults (including the Muli Fault, Lijiang–Xiaojinhe Fault, and Jinhe–Qihe Fault). Lower k_{sn} values were found on both sides of the Xiaojiang fault zone and the Red River fault zone. The influences of non-tectonic factors were discussed and excluded. We suggested that very weak correlations were found between the steepness indices and the lithology, precipitation, sediment flux, or channel concavity indices. Along the Xiaojiang strike–slip fault and the interior subblock, the uplift rate was slower, while the northern part had uplifted faster and was controlled by thrust fault systems. The channel steepness increased gradually from south to north. Thus, the distribution pattern of the K_{sn} index within the Central Yunnan subblock provides notable support for the argument for the thrusting transformation-limited extrusion model of the Tibetan Plateau.

DATA AVAILABILITY STATEMENT

The original contributions presented in the study are included in the article/**Supplementary Material**, further inquiries can be directed to the corresponding authors.

AUTHOR CONTRIBUTIONS

LY and YD conceived of the presented idea. YD and WZ developed the theoretical framework. LY, DZ, and DW developed the theory, analyzed the data, and performed the computations. HY, YR, and JL verified the analytical methods. All authors discussed the results and contributed to the final manuscript.

FUNDING

This study is supported by the National Natural Science Foundation of China (nos. 41802215 and 41762017).

SUPPLEMENTARY MATERIAL

The Supplementary Material for this article can be found online at: https://www.frontiersin.org/articles/10.3389/feart.2022.821367/full#supplementary-material

REFERENCES

Allen, G. H., Barnes, J. B., Pavelsky, T. M., and Kirby, E. (2013). Lithologic and Tectonic Controls on Bedrock Channel Form at the Northwest Himalayan Front. *J. Geophys. Res. Earth Surf.* 118 (3), 1806–1825. doi:10.1002/jgrf.20113

Burbank, D. W., and Anderson, R. S. (2011). *Tectonic Geomorphology*. Massachusetts: Blackwell Science, 247–251.

Burchfiel, B. C., Zhiliang, C., Yupinc, L., and Royden, L. H. (1995). Tectonics of the Longmen Shan and Adjacent Regions, Central China. *Int. Geology. Rev.* 37, 661–735. doi:10.1080/00206819509465424

Chen, W., Zhan, Y., Zhang, Y. Q., Jin, G. S., and Wang, Q. L. (2006). Late Cenozoic Episodic Uplifting in southeastern Part of the Tibetan Plateau - Evidence from Ar-Ar Thermochronology. *Acta Petrologica Sinica.* 73 (4), A1512. doi:10.1016/j.sedgeo.2005.11.021

Clark, M. K., Schoenbohm, L. M., Royden, L. H., Whipple, K. X., Burchfiel, B. C., Zhang, X., et al. (2004). Surface Uplift, Tectonics, and Erosion of Eastern Tibet from Large-Scale Drainage Patterns. *Tectonics.* 23 (1), 6. doi:10.1029/2002tc001402

Clark, M. K. (2012). Continental Collision Slowing Due to Viscous Mantle Lithosphere rather Than Topography. *Nature.* 483 (7387), 74–77. doi:10.1038/nature10848

Clark, M. K., House, M. A., Royden, L. H., Whipple, K. X., Burchfiel, B. C., Zhang, X., et al. (2005). Late Cenozoic Uplift of Southeastern Tibet. *Geol.* 33 (6), 525–528. doi:10.1130/g21265.1

Deng, Q., Zhang, P., Ran, Y., Yang, X., Min, W., and Chu, Q. (2002). Basic Characteristics of Active Tectonics of China. *Sci. China Ser. D Earth Sci.* 32 (12), 1020–1030. doi:10.3969/j.issn.1674-7313.2003.04.005

Dibiase, R. A. (2014). River Incision Revisited. *Nature.* 505 (7483), 294–295. doi:10.1038/505294a

DiBiase, R. A., Whipple, K. X., Heimsath, A. M., and Ouimet, W. B. (2010). Landscape Form and Millennial Erosion Rates in the San Gabriel Mountains, CA. *Earth Planet. Sci. Lett.* 289 (1-2), 134–144. doi:10.1016/j.epsl.2009.10.036

Dibiase, R. A., and Whipple, K. X. (2011). The Influence of Erosion Thresholds and Runoff Variability on the Relationships Among Topography, Climate, and Erosion Rate. *J. Geophys. Res. Earth Surf.* 116 (F4), F04036. doi:10.1029/2011jf002095

Duvall, A., Kirby, E., and Burbank, D. (2004). Tectonic and Lithologic Controls on Bedrock Channel Profiles and Processes in Coastal California. *J. Geophys. Res. Earth Surf.* 109 (F3), F03002. doi:10.1029/2003jf000086

Ferrier, K. L., Huppert, K. L., and Perron, J. T. (2013). Climatic Control of Bedrock River Incision. *Nature.* 496 (7444), 206–209. doi:10.1038/nature11982

Finnegan, N., Schumer, R., and Finnegan, S. (2014). A Signature of Transience in Bedrock River Incision Rates over Timescales of 10^4–10^7 Years. *Nature* 505 (7483), 391. doi:10.1038/nature12913

Gasparini, N. M., and Brandon, M. T. (2011). A Generalized Power Law Approximation for Fluvial Incision of Bedrock Channels. *J. Geophys. Res.* 116, F02020. doi:10.1029/2009jf001655

Hartshorn, K., Hovius, N., Dade, W. B., and Slingerland, R. L. (2002). Climate-Driven Bedrock Incision in an Active Mountain Belt. *Science.* 297 (5589), 2036–2038. doi:10.1126/science.1075078

He, J., Lu, S., and Wang, X. (2009). Mechanical Relation between Crustal Rheology, Effective Fault Friction, and Strike-Slip Partitioning Among the Xiaojiang Fault System, southeastern Tibet. *J. Asian Earth Sci.* 34 (3), 363–375. doi:10.1016/j.jseaes.2008.06.003

Hoke, G. D. (2018). Geochronology Transforms Our View of How Tibet's Southeast Margin Evolved. *Geology (Boulder).* 46 (1), 95–96. doi:10.1130/focus012018.1

Houseman, G., and England, P. (1993). Crustal Thickening versus Lateral Expulsion in the Indian-Asian continental Collision. *J. Geophys. Res.* 98 (B7), 12233–12249. doi:10.1029/93jb00443

Howard, A. D., Dietrich, W. E., and Seidl, M. A. (1994). Modeling Fluvial Erosion on Regional to continental Scales. *J. Geophys. Res.* 99 (B7), 13971–13986. doi:10.1029/94jb00744

Howard, A. D., and Kerby, G. (1983). Channel Changes in Badlands. *Geol. Soc. America Bull.* 94 (6), 739–752. doi:10.1130/0016-7606(1983)94<739:ccib>2.0.co;2

Hu, X., Pan, B., Kirby, E., Li, Q., and GengChen, H. J. (2010). Spatial Differences in Rock Uplift Rates Inferred from Channel Steepness Indices along the Northern Flank of the Qilian Mountain, Northeast Tibetan Plateau. *Chin. Sci. Bull.* 55 (27–28), 3205–3214. doi:10.1007/s11434-010-4024-4

Huang, Y., Guo, Y., and Fang, S. (2006). "Analysis on the Variation Characteristics of Water and Sediment in Jinsha River Basin in Yunnan Province, Chinese Hydraulic Society 2006 Annual Conference and 2006 Hydrology Symposium," in Proceedings of 2006 Annual Conference of Chinese Hydraulic Society and 2006 Hydrology Symposium (Application of New Technologies in Hydrology and Water Resources) (Anhui Province, China: Hefei), 6.

Huangfu, G., and Qin, J. (2006). Study of the Seismicity of Strong Earthquakes in the Yunnan Area. *Earthq. res. China* 28 (1), 37–47.

Kirby, E., Johnson, C., and Heimsath, A. (2007). Transient Channel Incision along Bolinas Ridge, California: Evidence for Differential Rock Uplift Adjacent to the San Andreas Fault. *J. Geophys. Res. Earth Surf.* 112, F03S07. doi:10.1029/2006jf000559

Kirby, E., and Ouimet, W. (2011). Tectonic Geomorphology along the Eastern Margin of Tibet: Insights into the Pattern and Processes of Active Deformation Adjacent to the Sichuan Basin. *Geol. Soc. Lond. Spec. Publications.* 353 (1), 358–361. doi:10.1144/sp353.9

Kirby, E., and Whipple, K. (2001). Quantifying Differential Rock-Uplift Rates via Stream Profile Analysis. *Geol.* 29 (5), 415–418. doi:10.1130/0091-7613(2001)029<0415:qdrurv>2.0.co;2

Kirby, E., and Whipple, K. X. (2012). Expression of Active Tectonics in Erosional Landscapes. *J. Struct. Geology.* 44, 54–75. doi:10.1016/j.jsg.2012.07.009

Kirby, E., Whipple, K. X., Tang, W. Q., and Chen, Z. L. (2003). Distribution of Active Rock Uplift along the Eastern Margin of the Tibetan Plateau: Inferences from Bedrock Channel Longitudinal Profiles. *J. Geophys. Res. Solid Earth.* 108 (B4), 2217. doi:10.1029/2001jb000861

Lavé, J., and Avouac, J. P. (2001). Fluvial Incision and Tectonic Uplift Across the Himalayas of central Nepal. *J. Geophys. Res.* 106 (B11), 26561–26591. doi:10.1029/2001jb000359

Li, H., and Zhang, Y. (2013). Zircon U-Pb Geochronology of the Konggar Granitoid and Migmatite: Constraints on the Oligo-Miocene Tectono-Thermal Evolution of the Xianshuihe Fault Zone, East Tibet. *Tectonophysics.* 606, 127–139. doi:10.1016/j.tecto.2013.07.007

Li, S., Currie, B., Rowley, D., and Ingalls, M. (2015). Cenozoic Paleoaltimetry of the SE Margin of the Tibetan Plateau: Constraints on the Tectonic Evolution of the Region. *Earth Planet. Sci.* 432, 415–424. doi:10.1016/j.epsl.2015.09.044

Li, J. (1999). Studies of the Geomorphological Evolution of the Qinghai-Xizang (Tibetan) Plateau and Asian Monsoon. *Mar. Geol. Quater. Geol.* 19 (2), 1–12.

Liu, J., Zeng, L., Ding, L., Tapponnier, P., Gaudemer, Y., Wen, L., et al. (2009). Tectonic geomorphology, active tectonics and lower crustal channel flow hypothesis of the southeastern Tibetan Plateau. *Journal of Geology (Scientia Geologica Sinica)* 44 (4), 1227–1255. doi:10.3321/j.issn:0563-5020.2009.04.014

Liu, Z. J., Tapponnier, P., Gaudemer, Y., and Ding, L. (2008). Quantifying Landscape Differences across the Tibetan Plateau: Implications for Topographic Relief Evolution. *J. Geophys. Res. Earth Surf.* 113 (F4), F04018. doi:10.1029/2007jf000897

Liu-Zeng, J., Zhang, J., McPhillips, D., Reiners, P., Wang, W., Pik, R., et al. (2018). Multiple Episodes of Fast Exhumation since Cretaceous in Southeast Tibet, Revealed by Low-Temperature Thermochronology. *Earth Planet. Sci. Lett.* 490 (15), 62–76. doi:10.1016/j.epsl.2018.03.011

Ma, Z., Zhang, H., Wang, Y., Tao, Y., and Li, X. (2020). Inversion of Dadu River Bedrock Channels for the Late Cenozoic Uplift History of the Eastern Tibetan Plateau. *Geophys. Res. Lett.* 47, e2019GL086882. doi:10.1029/2019gl086882

Molnar, P., Burchfiel, B. C., K'uangyi, L., and Ziyun, Z. (1987). Geomorphic Evidence for Active Faulting in the Altyn Tagh and Northern Tibet and Qualitative Estimates of its Contribution to the Convergence of India and Eurasia. *Geol.* 15 (3), 249–253. doi:10.1130/0091-7613(1987)15<249:gefafi>2.0.co;2

Molnar, P., and England, P. (1990). Late Cenozoic Uplift of Mountain Ranges and Global Climate Change: Chicken or Egg? *Nature.* 346 (6279), 29–34. doi:10.1038/346029a0

Molnar, P., and Tapponnier, P. (1975). Cenozoic Tectonics of Asia: Effects of a Continental Collision: Features of Recent continental Tectonics in Asia Can Be Interpreted as Results of the India-Eurasia Collision. *Science.* 189, 419–426. doi:10.1126/science.189.4201.419

Nie, J. (2018). Rapid Incision of the Mekong River in the Middle Miocene Linked to Monsoonal Precipitation. *Nat. Geoence.* 11, 944. doi:10.1038/s41561-018-0244-z

Oskin, M. E., Burbank, D. W., Phillips, F. M., Marrero, S. M., Bookhagen, B., and Selander, J. A. (2014). Relationship of Channel Steepness to Channel Incision Rate from a Tilted and Progressively Exposed Unconformity Surface. *J. Geophys. Res. Earth Surf.* 119 (2), 366–384. doi:10.1002/2013jf002826

Palumbo, L., Hetzel, R., Tao, M., and Li, X. (2010). Topographic and Lithologic Control on Catchment-Wide Denudation Rates Derived from Cosmogenic 10Be in Two Mountain Ranges at the Margin of NE Tibet. *Geomorphology.* 117 (1-2), 130–142. doi:10.1016/j.geomorph.2009.11.019

Pan, B., Li, Q., Hu, X., Geng, H., and Gao, H. (2015). Bedrock Channels Response to Differential Rock Uplift in Eastern Qilian Mountain along the Northeastern Margin of the Tibetan Plateau. *J. Asian Earth Sci.* 100, 1–19. doi:10.1016/j.jseaes.2014.12.009

Pan, J. (1997). Study on Sediment Transport Characteristics in Jinsha River Basin. *Bull. soll Water conservation.* 17 (5), 35–39. doi:10.13961/j.cnki.stbctb.1997.05.008

Perron, J. T., and Royden, L. (2013). An Integral Approach to Bedrock River Profile Analysis. *Earth Surf. Process. Landforms.* 38 (6), 570–576. doi:10.1002/esp.3302

Pritchard, D., Roberts, G. G., White, N. J., and Richardson, C. N. (2009). Uplift Histories from River Profiles. *Geophys. Res. Lett.* 36 (24), L24301. doi:10.1029/2009gl040928

Qin, L., Dong, X., Du, Z., and Chen, X. (2019). Processes of Water-Sediment and Deposition in cascade Reservoirs in the Lower Reach of Jinsha River. *J. Sediment Res.* 44 (03), 24–30. doi:10.16239/j.cnki.0468-155x.2019.03.005

Raymo, M. E., and Ruddiman, W. F. (1992). Tectonic Forcing of Late Cenozoic Climate. *Nature.* 359 (6391), 117–122. doi:10.1038/359117a0

Royden, L., Burchfiel, B., and Hilst, R. (2008). The Geological Evolution of the Tibetan Plateau. *Science* 321 (5892), 1054–8. doi:10.1126/science.1155371

Royden, L. H., Burchfiel, B. C., King, R. W., Wang, E., Chen, Z., Shen, F., et al. (1997). Surface Deformation and Lower Crustal Flow in Eastern Tibet. *Science.* 276 (5313), 788–790. doi:10.1126/science.276.5313.788

Schoenbohm, L., Burchfiel, B. C., and Chen, L. (2006). Propagation of Surface Uplift, Lower Crustal Flow, and Cenozoic Tectonics of the Southeast Margin of the Tibetan Plateau. *Geology* 34, 813–816. doi:10.1130/G22679.1

Schwanghart, W., and Scherler, D. (2020). Divide Mobility Controls Knickpoint Migration on the Roan Plateau (Colorado, USA). *Geology.* 48 (7), 698. doi:10.1130/g47054.1

Shen, X., Tian, Y., Li, D., Qin, S., Vermeesch, P., and Schwanethal, J. (2016). Oligocene-Early Miocene River Incision Near the First bend of the Yangze River: Insights from Apatite (U-Th-Sm)/He Thermochronology. *Tectonophysics.* 687, 223–231. doi:10.1016/j.tecto.2016.08.006

Sklar, L. S., and Dietrich, W. E. (2001). Sediment and Rock Strength Controls on River Incision into Bedrock. *Geol.* 29 (12), 1087–1090. doi:10.1130/0091-7613(2001)029<1087:sarsco>2.0.co;2

Slingerland, R., Willett, S. D., and Hennessey, L. H. (1997). A New Fluvial Bedrock Erosion Model Based on the Work-Energy Principle. *Eos Trans. AGU* 78 (46), Suppl., F299.

Snyder, E., Johnson, N., Spyropolou, J., Crosby, K., and Sheehan, D. (2006). Tectonics from Topography: Procedure, Promise, and Pitfalls. *Geol. Soc. Am. Spec.* 398 (12), 55–74. doi:10.1130/2006.2398(04)

Snyder, N. P., Whipple, K. X., Tucker, G. E., and Merritts, D. J. (2000). Landscape Response to Tectonic Forcing: Digital Elevation Model Analysis of Stream Profiles in the Mendocino Triple junction Region, Northern California. *Geol. Soc. America Bull.* 112 (8), 1250–1263. doi:10.1130/0016-7606(2000)112<1250:lrttfd>2.0.co;2

Stock, J. D., and Montgomery, D. R. (1999). Geologic Constraints on Bedrock River Incision Using the Stream Power Law. *J. Geophys. Res. Solid Earth.* 104 (B3), 4983. doi:10.1029/98jb02139

Su, Q., Yuan, D., and Xie, H. (2016). Geomorphic Features of the Heihe River Drainage basin in Western Qilian Shan-Hexi Corridor and its Tectonicimplications. *Seismology Geology* 38 (3), 560–581. doi:10.3969/j.issn.0253-4967.2016.03.005

Tang, M., Liu-Zeng, J., Hoke, G. D., Xu, Q., Wang, W., Li, Z., et al. (2017). Paleoelevation Reconstruction of the Paleocene-Eocene Gonjo basin, SE-central Tibet. *Tectonophysics.* 712-713, 170–181. doi:10.1016/j.tecto.2017.05.018

Tapponnier, P., Peltzer, G., and Le Dain, A. Y. (1982). Propagating Extrusion Tectonics in Asia, New Insights from Simple Experiments with Plasticine. *Geology* 10 (12), 611–617. doi:10.1130/0091-7613(1982)10<611:PETIAN>2.0.CO;2

Tapponnier, P., Zhiqin, X., Roger, F., Meyer, B., Arnaud, N., Wittlinger, G., et al. (2001). Oblique Stepwise Rise and Growth of the Tibet Plateau. *Science.* 294 (5547), 1671–1677. doi:10.1126/science.105978

Tian, Y., Kohn, B. P., Gleadow, A. J. W., and Hu, S. (2014). A Thermochronological Perspective on the Morphotectonic Evolution of the southeastern Tibetan Plateau. *J. Geophys. Res. Solid Earth.* 119 (1), 676–698. doi:10.1002/2013jb010429

Tian, Y., Kohn, B. P., Hu, S., and Gleadow, A. J. W. (2015). Synchronous Fluvial Response to Surface Uplift in the Eastern Tibetan Plateau: Implications for Crustal Dynamics. *Geophys. Res. Lett.* 42, 29. doi:10.1002/2014gl062383

Tian, Y. T., Kohn, B. P., and Gleadow, A. J. W. (2013). Constructing the Longmenshan Eastern Tibetan Plateau Margin: Insights from Low-Temperature Thermochronology. *Tectonics.* 32, 572–596. doi:10.1002/tect.20043

Tucker, G. E., and Slingerland, R. (1996). Predicting Sediment Flux from Fold and Thrust Belts. *Basin Res.* 8 (3), 329–349. doi:10.1046/j.1365-2117.1996.00238.x

Wang, E., Burchfiel, B. C., Royden, L. H., Chen, L., Chen, J., Li, W., et al. (1998). *The Cenozoic Xianshuihe–Xiaojiang,Red River, and Dali Faultsystems of Southwestern Sichuan and central Yunnan*, 327. China: Geological Society of America Special Paper, 108.

Wang, F., Wang, M., Wang, Y., and Shen, Z.-K. (2015). Earthquake Potential of the Sichuan-Yunnan Region, Western China. *J. Asian Earth Sci.* 107, 232–243. doi:10.1016/j.jseaes.2015.04.041

Wang, S., Jiang, G., Xu, T., Tian, Y., Zheng, D., and Fang, X. (2012). The Jinhe–Qinghe Fault-An Inactive branch of the Xianshuihe–Xiaojiang Fault Zone, Eastern Tibet. *Tectonophysics* 544545, 93–102.

Wang, Y., Liu, C., Zheng, D., Zhang, H., Yu, J., Pang, J., et al. (2021). Multistage Exhumation in the Catchment of the Anninghe River in the SE Tibetan Plateau: Insights from Both Detrital Thermochronology and Topographic Analysis. *Geophys. Res. Lett.*, 48. doi:10.1029/2021GL092587

Wang, Y., Schoenbohm, L. M., Zhang, B., Granger, D. E., Zhou, R., Zhang, J., et al. (2017). Late Cenozoic Landscape Evolution along the Ailao Shan Shear Zone, SE Tibetan Plateau: Evidence from Fluvial Longitudinal Profiles and Cosmogenic Erosion Rates. *Earth Planet. Sci. Lett.* 472 (1), 323–333. doi:10.1016/j.epsl.2017.05.030

Wang, Y. Z. (2014). Controls on Decadal Erosion Rates in Qilian Shan: Re-evaluation and New Insights into Landscape Evolution in north-east Tibet. *Geomorphology.* 223 (October15), 117–128. doi:10.1016/j.geomorph.2014.07.002

Wang, Y., Zheng, D., Pang, J., Zhang, H., Wang, W., Yu, J., et al. (2018). Using Slope-Area and Apatite Fission Track Analysis to Decipher the Rock Uplift Pattern of the Yumu Shan: New Insights into the Growth of the NE Tibetan Plateau. *Geomorphology.* 308 (MAY1), 118–128. doi:10.1016/j.geomorph.2018.02.006

Wang, Y., Zheng, D., Zhang, H., Li, C., Xiao, L., Li, Y., et al. (2019). The Distribution of Active Rock Uplift in the interior of the Western Qilian Shan, NE Tibetan Plateau: Inference from Bedrock Channel Profiles. *Tectonophysics.* 759, 15–29. doi:10.1016/j.tecto.2019.04.001

Wen, X., Xu, X., and Zheng, R. (2003). Average Slip-Rate and Recent Large Earthquake Ruptures along the Garzê-Yushu Fault. *Sci. China Earth Sci.* 46 (0z2), 276–288. doi:10.1360/03dz0022

Whipple, K. X. (2004). Bedrock Rivers and the Geomorphology of Active Orogens. *Annu. Rev. Earth Planet. Sci.* 32, 151–185. doi:10.1146/annurev.earth.32.101802.120356

Whipple, K. X. (2002). Implications of Sediment-flux-dependent River Incision Models for Landscape Evolution. *J. Geophys. Res.* 107 (B2), 2039. doi:10.1029/2000jb000044

Whipple, K. X., and Tucker, G. E. (1999). Dynamics of the Stream-Power River Incision Model: Implications for Height Limits of Mountain Ranges, Landscape Response Timescales, and Research Needs. *J. Geophys. Res.* 104 (B8), 17661–17674. doi:10.1029/1999jb900120

Willgoose, G. (1994). A Physical Explanation for an Observed Area-slope-elevation Relationship for Catchments with Declining Relief. *Water Resour. Res.* 30, 151. doi:10.1029/93wr01810

Wilson, C., and Fowler, A. P. (2011). Denudational Response to Surface Uplift in East Tibet: Evidence from Apatite Fission-Track Thermochronology. *Geol. Soc. America Bull.* 123 (9-10), 1966–1987. doi:10.1130/b30331.1

Wobus, C., Whipple, K., Kirby, E., Snyder, N., Jhonson, J., Spyropolou, K., et al. (2006). Tectonics From Topography: Procedures, Promise, and Pitfalls. *Geol. Soc. Am. Spec. Pap.* 398, 55–74. doi:10.1130/2006.2398(04)

Wobus, C. W., Hodges, K. V., and Whipple, K. X. (2003). Has Focused Denudation Sustained Active Thrusting at the Himalayan Topographic Front? *Geol.* 31 (10), 861–864. doi:10.1130/g19730.1

Wu, Z., Zhou, C., Feng, H., Zhang, K., Li, J., Ye, P., et al. (2014). Active Faults and Earthquake Around Yushu in Eastern Tibetan Plateau. *Geological Bulletin of China* 33 (4), 419–469.

Wu, K., Dong, Y., Duan, J., Ru, X., Zhang, D., and Wang, D. (2020). Cenozoic Uplift of the Central Yunnan Fragment, Southwestern China, Revealed by Apatite. *J. Earth Sci.* 31 (04), 735–742. doi:10.1007/s12583-020-1328-4

Xiang, H., Xu, X., Guo, S., Zhang, W., Li, H., and Yu, G. (2002). Sinistaral Thrusting along the Lijiang-Xiaojinhe Fault since Quaternary and its Geologic-Tectonic Significance-Shielding Effect of Transverse Structure of Intracontinental Active Block. *Seismoseismology Geology.* 24 (2), 188–198. doi:10.1080/12265080208422884

Xu, G., and Kamp, P. J. J. (2000). Tectonics and Denudation Adjacent to the Xianshuihe Fault, Eastern Tibetan Plateau: Constraints from Fission Track Thermochronology. *J. Geophys. Res.* 105, 19231–19251. doi:10.1029/2000jb900159

Xu, X., Cheng, G., Yu, G., Song, F. M., and Wen, X. Z. (2003). Tectonic and Paleomagnetic Evidence for the Clockwise Rotation of the Sichuan-Yunnan Rhombic Block. *Seismology Geology.* 25 (1), 61–70. doi:10.1016/S0955-2219(02)00073-0

Xu, Z., Yang, J., Li, H., Zhang, J., and Wu, C. (2007). *Orogenic Plateaux-Terrane Amalgamation, Collision and Uplift in the Qinghai-Tibet Plateau*. Beijing, China: Geological Publishing House, 1–458. doi:10.1130/2006.2398(04)

Yan, B., and Lin, A. (2015). Systematic Deflection and Offset of the Yangtze River Drainage System along the Strike-Slip Ganzi-Yushu-Xianshuihe Fault Zone, Tibetan Plateau. *J. Geodynamics.* 87, 13–25. doi:10.1016/j.jog.2015.03.002

Yin, Q., Li, H., and Wang, Q. (2020). The Study of the Dextral Oblique-Slip Deformation of the Jinhe-Qinghe Fault, Southeast Tibet, and its Tectonic Significance. *Acta Geoscientica Sinica.* 41 (3), 371–383. doi:10.3975/cagsb.2020.012201

Zhang, L., Li, T., Wang, G., Kwang, J., Parker, G., et al. (2020). How Canyons Evolve by Incision into Bedrock: Rainbow Canyon, Death Valley National Park, United States. *Proc. Natl. Acad. Sci.* 117 (26), 201911040. doi:10.1073/pnas.1911040117

Zhang, D., Dong, Y., Jiao, Q., Duan, J., Wang, D., Yu, L., et al. (2022). Three Periods of Cenozoic Tectonic Uplift in the Southeastern Margin of the Tibetan Plateau-Evidence from Fluvial Longitudinal Profile Analysis. *Geotectonic Et Metallogenia.* In press.

Zhang, P. (2008). The Current Tectonic Deformation, Strain Distribution and Deep Dynamic Process in Western Sichuan Province in the East of Qinghai-Tibet Plateau. *Science in China Series D-Earth Sciences (in Chinese)* 38 (9), 1041–1056.

Zhang, H., Oskin, M., Oskin, M. E., Liu-Zeng, J., Zhang, P., Reiners, P. W., et al. (2016). Pulsed Exhumation of interior Eastern Tibet: Implications for Relief Generation Mechanisms and the Origin of High-Elevation Planation Surfaces.

Earth Planet. Sci. Lett. 449 (September1), 176–185. doi:10.1016/j.epsl.2016.05.048

Zhang, Y.-Z., Replumaz, A., Replumaz, A., Leloup, P. H., Wang, G.-C., Bernet, M., et al. (2017). Cooling History of the Gongga Batholith: Implications for the Xianshuihe Fault and Miocene Kinematics of SE Tibet. *Earth Planet. Sci. Lett.* 465, 1–15. doi:10.1016/j.epsl.2017.02.025

Zheng, H., Clift, P. D., Wang, P., Tada, R., Jia, J., He, M., et al. (2013). Pre-Miocene Birth of the Yangtze River. *Proc. Natl. Acad. Sci. U S A.* 110 (19), 7556–7561. doi:10.1073/pnas.1216241110

Conflict of Interest: The authors declare that the research was conducted in the absence of any commercial or financial relationships that could be construed as a potential conflict of interest.

Publisher's Note: All claims expressed in this article are solely those of the authors and do not necessarily represent those of their affiliated organizations, or those of the publisher, the editors and the reviewers. Any product that may be evaluated in this article, or claim that may be made by its manufacturer, is not guaranteed or endorsed by the publisher.

Copyright © 2022 Yu, Dong, Zhou, Zhang, Wang, Yu, Ren and Li. This is an open-access article distributed under the terms of the Creative Commons Attribution License (CC BY). The use, distribution or reproduction in other forums is permitted, provided the original author(s) and the copyright owner(s) are credited and that the original publication in this journal is cited, in accordance with accepted academic practice. No use, distribution or reproduction is permitted which does not comply with these terms.

frontiers in Earth Science

ORIGINAL RESEARCH
published: 14 February 2022
doi: 10.3389/feart.2022.825849

Early Quaternary Tectonic Transformation of the Helan Shan: Constraints Due To Quantitative Geomorphology

Yige Li[1,2,3], *Wenjun Zheng*[1,2,3]*, *Jingjun Yang*[1,2,3], *Dongli Zhang*[1,2,3], *Haoyu Zhou*[1,2,3] and *Ting Liu*[1,2,3]

[1]Guangdong Provincial Key Laboratory of Geodynamics and Geohazards, School of Earth Science and Engineering, Sun Yat-sen University, Guangzhou, China, [2]Southern Marine Science and Engineering Guangdong Laboratory, Zhuhai, China, [3]State Key Laboratory of Earthquake Dynamics, Institute of Geology, China Earthquake Administration, Beijing, China

The Helan Shan is located on the front edge of the expanding Tibetan Plateau. However, how the topography here responds to this propagation and its precise time constraints remain unknown. Based on the response process of fluvial landforms and tectonic evolution, we conducted a quantitative landform analysis of the Helan Shan region. Here, the spatial distribution features of various geomorphic indices were coupled, demonstrating that the mountain is tilting toward the west and north. The steeper downstream and gentle upper reaches indicate that the fluvial landforms have experienced an accelerated incision event, which can be attributed to the tectonic activity along the East Helan Shan Fault. Furthermore, the response time of the tectonic knickpoints ranges from 0.1 to 1.4 Ma based on the paleochannel reconstruction method. Combined with previous studies on low temperature thermochronology and active tectonics, we proposed a tectonic transformation model where the Helan Shan shifted the tilting model from the southwest to the northwest, as induced by the northeast expansion of the Tibetan Plateau from 0.1 to 1.4 Ma.

Keywords: Helan Shan, tectonic transformation, fluvial landforms, tectonic geomorphology, Tibetan Plateau

OPEN ACCESS

Edited by:
Xuhua Shi,
Zhejiang University, China

Reviewed by:
Xiaohui Shi,
Northwest University, China
Zhongtai He,
Ministry of Emergency Management, China

***Correspondence:**
Wenjun Zheng
zhengwenjun@mail.sysu.edu.cn

Specialty section:
This article was submitted to Structural Geology and Tectonics, a section of the journal Frontiers in Earth Science

Received: *30 November 2021*
Accepted: *20 January 2022*
Published: *14 February 2022*

Citation:
Li Y, Zheng W, Yang J, Zhang D, Zhou H and Liu T (2022) Early Quaternary Tectonic Transformation of the Helan Shan: Constraints Due To Quantitative Geomorphology. Front. Earth Sci. 10:825849. doi: 10.3389/feart.2022.825849

INTRODUCTION

The uplift of the Tibetan Plateau is one of the most significant tectonic processes that occurred in the Cenozoic: a formation that shaped the tectonic and climatic framework of Eurasia (Molnar and Tapponnier, 1975; Yin and Harrison, 2000; Royden et al., 2008) and has continued to expand since its establishment (Tapponnier et al., 2001; Zheng et al., 2006; Yin et al., 2008; Clark et al., 2010; Duvall et al., 2011; Rohrmann et al., 2012). Although its dynamic mechanism remains controversial, the scientific community widely accepts the view that the northeastern Tibetan Plateau is the outermost component of accretion and uplift (Liu et al., 2010; Zheng et al., 2010; Wang et al., 2011; Lei et al., 2016; Zheng et al., 2016). Recent studies on active tectonics suggest that the current active boundary of the Tibetan Plateau is the South Heli Shan Fault, North Longshou Shan Fault, and Sanguankou–Niushou Shan Fault, which developed during the Late Cenozoic (2–3 Ma) (Lei et al., 2016; Zheng et al., 2021). The geomorphological response to this tectonic event has been observed in the Niushou Shan area (Liang et al., 2013). The West Helan Shan Fault is generally regarded as the continuation of the arc-shaped tectonic belt periphery (Sanguankou–Niushou Shan

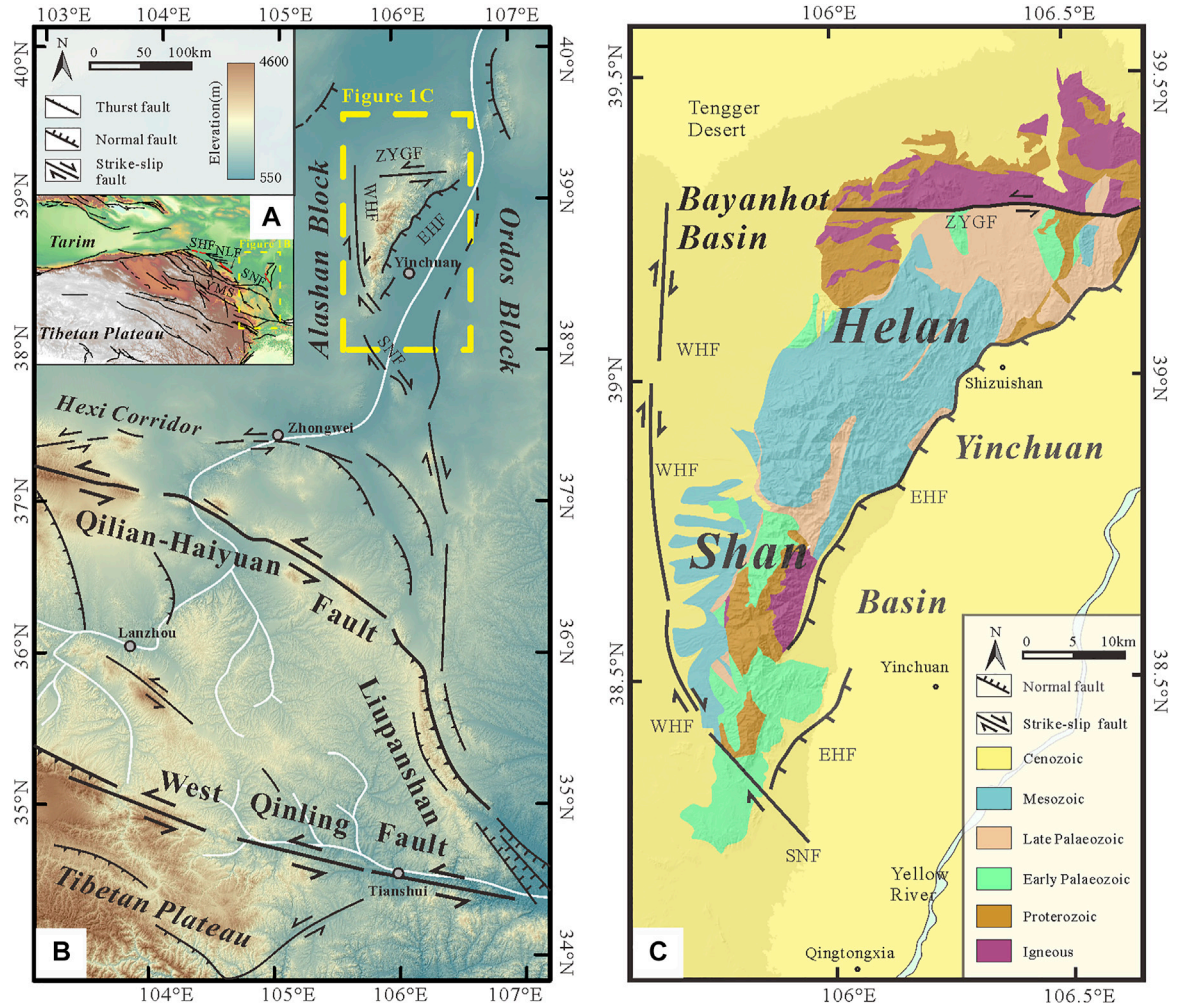

FIGURE 1 | (A) Tectonic location of the study area. **(B)** Active tectonic features of the northeastern margin of the Tibetan Plateau, modified from Zheng et al. (2016) and Yu et al. (2016). **(C)** Geological map of the Helan Shan area, modified from Geological Map of Ningxia Hui Autonomous Region, the People's Republic of China (2014). Fault names: SHP, South Heli Shan Fault; NLP, North Longshou Shan Fault; WHF, West Helan Shan Fault; EHF, East Helan Shan Fault; SNF, Sanguankou-Niushoushan Fault; ZYGF, Zhengyiguan Fault.

Fault) on the northeastern margin of the Tibetan Plateau to the north. However, how the Helan Shan responded to this plateau propagation event in the Late Cenozoic, and precise constraints on the corresponding timing remain unclear. Hence, the evolution of active orogenic belts located along the current boundary of the northeastern Tibetan Plateau is significant for understanding the expansion process of the Tibetan Plateau.

The fluvial landscapes in the active orogenic belt result from the combined effects of surface processes, tectonics, and climate, thus recording the tectonic-climate evolutional history across geological periods (Hack, 1957; Whipple, 2004; Kirby and Whipple, 2012). Rapid progress in quantitative research on fluvial landscapes in the past 10 years has allowed us to extract tectonic information from the many factors that control the evolution of fluvial landforms (Schwanghart and Kuhn, 2010; Schwanghart and Scherler, 2014; Willett et al., 2014; Forte and Whipple, 2019). Previous studies on quantitative geomorphology have shown that the Yumu Shan and Heli Shan began uplift at 4 and 0.6–2.1 Ma, respectively (Wang et al., 2018; Yang et al., 2020). Therefore, examining the interaction between fluvial landforms and active orogenies provides a practical approach for revealing the regional spatial–temporal tectonic patterns.

In this study, we utilized bedrock river profile analysis and paleochannel reconstruction to decipher the tectonic patterns of the Helan Shan. We first extracted the geomorphic index, for example, the normalized channel steepness index, and χ of the Helan Shan to quantify the spatial variation in the rock uplift rates and direction of divide migration. We then calculated the response time of the knickpoints confined within a range. Finally, we combined multiple lines of evidence to suggest that the tectonic transformation of the Helan Shan may have occurred in the Pleistocene as a result of Tibetan Plateau expansion.

GEOLOGIC SETTING

The Helan Shan extends from the NE to the SW for approximately 100 km, surrounded by tectonically stable blocks, with the Alashan block to the west and the Ordos block to the east. To the southwest, numerous active strike-slip and thrust faults constitute the northeastern margin of the Tibetan Plateau (**Figure 1A**) (Yang and Dong, 2018). A variety of dynamic factors have restricted the special composite junction, which has experienced a long-term intracontinental deformation process (Darby and Ritts, 2002; Liu et al., 2010). As a result, the area is characterized by complex tectonic phenomena, accompanied by the development of folds, faults, and strong active tectonics since the Quaternary (Zhang et al., 1990; Deng and Liao, 1996; Deng et al., 2003).

The main component of the Helan Shan is under the clamping control of the East and West Helan Shan faults on both sides. The East Helan Shan Fault is a normal fault with a northeast–southwest strike and an eastward dip, whose hanging wall is the Yinchuan Basin and footwall is the Helan Shan (Yang and Dong, 2018). All methods used by previous studies, such as thermoluminescence, cosmogenic radionuclide dating, trenches, and sedimentology, among others, have shown that without exception, the vertical slip rate of the southern section of the East Helan Shan Fault is higher than that of the northern section (Du, 2010; Zhang et al., 2010; Lei et al., 2016). The currently active West Helan Shan Fault is a Holocene right lateral strike-slip fault with horizontal and vertical sliding rates of approximately 0.28 and 0.64 mm/a, respectively (Du, 2010; Lei et al., 2016). The West Helan Shan Fault is the northern extension of the Sanguankou–Niushoushan Fault. They have the same structural deformation process and tectonic properties, i.e., the leading edge of plateau extension are toward the northeast. The Yinchuan Basin is mirror-symmetrical to the Helan Shan in terms of its tectonic attributes, tending to be synchronized with respect to important tectonic deformation events (Zhang et al., 2010). During the 12–10 Ma active tectonic period, fault depression and shrinkage in the Yinchuan Basin accompanied the rapid uplift of the Helan Shan (Liu et al., 2010). The traditional view is that the Alashan block is stable with weak tectonic activity (Yu et al., 2016; Zheng et al., 2016). However, recent results show that the northeastward propagation of the Tibetan Plateau intersected the Hexi Corridor and reached the southern edge of the Alashan Block at 3–2 Ma, gradually becoming the newest part of the northeastern edge of the Tibetan Plateau (Zheng et al., 2013, 2021; Lei et al., 2016).

The Helan Shan mainly exposes Paleozoic–Mesozoic strata, accompanied by a series of intrusive rocks. Proterozoic strata include high-grade metamorphic rocks in the north and carbonate rocks in the south. The high-grade metamorphic rocks and igneous rock are referred to as the khondalite belts (Zhao et al., 2005; Zhou and Geng, 2009), which contain mélange, S-type granite, schist, and gneiss, among others. The early Paleozoic strata of Helan Shan are mainly exposed in the south, where the main lithology comprises limestone and dolomite. The upper Paleozoic and Mesozoic strata are exposed in the middle of the Helan Shan, where the lithology is dominated by clastic rocks. Additionally, a large number of alluvial fan groups contained in the Cenozoic strata developed at the front of the mountain (**Figure 1C**).

In terms of the topography, the west is relatively flat, the east is steeper, the north is wider, and the south is narrower. The highest peak is 3,556 m above sea level, with an average elevation of 1,800 m, which is significantly higher than the Bayanhot and Yinchuan basins on both sides, with a height difference of >2,200 m. The rivers in the Helan Shan generally have a narrow width, limited runoff, and poor tributary development. As the climate of the Helan Shan is characterized by its location in the transitional zone of the monsoon and non-monsoon climate, the rivers in the area have relatively limited runoff and relatively rapid flow. The Helan Shan is at a transitional position between the desert-grassland and desert areas. This region mainly depends on summer precipitation for water supply. The main rainfall occurs in June, July, and August. Therefore, the surface runoff that develops at the two foothills of the Helan Shan is seasonal (Liu et al., 2004). Rivers at the western foot of the Helan Shan flow westward into the Tengger Desert. Rivers at the eastern foot of the Helan Shan flow into the Yinchuan Basin and then merge into the Yellow River. We considered the rivers along the eastern and western slopes of the Helan Shan for quantitative analysis of the fluvial landscapes.

METHODS

Stream Power Model

The stream power law (Stock and Montgomery, 1999; Whipple, 2001; Kirby and Whipple, 2012) assumes that the incision progress of detachment-limited stream (longitudinal profiles) can be approximated as follows (Whipple and Tucker, 1999; Whipple, 2004; Wang et al., 2017):

$$E = KA^m S^n, \tag{1}$$

where K is the fluvial erodibility of the bedrock channel affected by climatic conditions, rock properties, and channel geometry; A is the contributing drainage area; S is the local channel gradient; and m and n are positive parameters.

However, the vertical evolution of a detachment-limited bedrock channel is determined by the rock uplift (U) and stream trenching (E) rates (England and Molnar, 1990):

$$\frac{\partial z}{\partial t} = U(x, t) - KA^m \left(\frac{\partial z}{\partial x}\right)^n. \tag{2}$$

When the fluvial landform reaches a steady state, the topographic elevation is no longer a function of time. **Eq. 2** reduces to the following expression (Perron and Royden, 2013):

$$0 = \mathrm{U(x)} - \mathrm{K}A^m \left(\frac{\partial z}{\partial x}\right)^n. \tag{3}$$

For a single river channel, the regional uplift rate (U) basically does not change in space, such that we obtained the following:

$$U = KA^m\left(\frac{\partial z}{\partial x}\right)^n \text{ and} \tag{4a}$$

$$\frac{\partial z}{\partial x} = \left(\frac{U}{K}\right)^{\frac{1}{n}} A^{-\frac{m}{n}}. \tag{4b}$$

The channel steepness index, k_s (or the normalized steepness index, i.e., k_{sn}), can be used to simplify **Eq. (4a)** and directly express the uplift rate:

$$k_s = \left(\frac{U}{K}\right)^{\frac{1}{n}} \text{and} \tag{5a}$$

$$S = \frac{dz}{dx} = k_s A^{-\theta}, \tag{5b}$$

where θ is the concavity of the river channel and S is the slope of the river channel. The steepness index, k_s, has a notable power–law relationship with the bedrock uplift rate (U). Therefore, both k_s and k_{sn} can be used to obtain the uplift rate (Kirby and Whipple, 2012).

The χ-analysis method is widely used to obtain the steepness index of the channel. We integrated both sides of **Eq. (4b)** to obtain (Royden and Perron, 2013) the following:

$$\int dz = \int \left(\frac{U(x)}{K(x)A(x)^m}\right)^{\frac{1}{n}} dx. \tag{6}$$

Taking the position of x_b as the initial definite integral and simplifying, we obtained the following:

$$z(x) = z(x_b) + \left(\frac{U}{X}\right)^{\frac{1}{n}} \int_{x_b}^{x} \frac{dx}{A(x)^{\frac{m}{n}}}. \tag{7}$$

We set parameter A_0 as the reference area, which is usually 1 m^2 to facilitate a simplified calculation. Parameter χ was introduced to represent topological information on the river:

$$\chi = \int_{x_b}^{x} \left(\frac{A_0}{A(x)}\right)^{\frac{m}{n}} dx. \tag{8}$$

Eq. 7 can be rewritten as follows:

$$z(x) = z(x_b) + \left(\frac{U}{X}\right)^{\frac{1}{n}} \chi, \tag{9}$$

where χ is the abscissa, the river elevation, z, is the ordinate, and the slope is k_s. Compared with the traditional logarithmic method, this method avoids repeated errors caused by the elevation differential. At the same time, the slope of the straight line directly represents the steepness index (Royden and Perron, 2013). Therefore, we used the χ-plot method to calculate the k_s value and examine the river profile.

Additionally, recent research indicates that the χ value can be used to analyze the evolution of water systems in active orogenic belts (Willett et al., 2014). Here, the model assumes that runoff from both sides of the active orogen flows into the same datum. Therefore, the elevations of the watersheds should be equal. The watershed with a large χ value has a relatively small erosion rate, E, and the channel steepness index, k_s, is often relatively small owing to the equilibrium of the channel. Numerical simulation studies have shown that the erosion rate of the watershed gradually becomes lower, which has also been confirmed by field observations (Willett, 1999). Therefore, the χ values of the basins can be used to identify the direction of watershed migration (Yang et al., 2015).

Paleochannel Reconstruction Method

When bedrock channels reach steady state, the longitudinal fluvial profile of the steady channel shows a smooth concave shape (Hack, 1973; Whipple, 2004). However, differences in the lithology, climate, and tectonic activity may alter the original balance between river erosion and the regional tectonic uplift rate, leading to discontinuities in the river, that is, knickpoints (Whipple and Tucker, 1999; Berlin and Anderson, 2007). As discussed by Kirby and Whipple (2012), knickpoints can be grouped into two end-member morphologies: vertical-step knickpoints and slope-break knickpoints. The reasons for the formation of these two knickpoint types are divergent; there are significant differences in the shape of the river longitudinal profile (**Figure 2**).

A vertical-step knickpoint is characterized by a sharply increasing slope near the knickpoint area, but there is no change in the steepness index of the river course upstream or downstream of the knickpoint. In contrast, there is a notable difference in the steepness index near a slope-break knickpoint. We mainly distinguished the knickpoint type based on the longitudinal river profile and analyzed its genesis and tectonic indications in combination with geological and geomorphological data.

A slope-break of tectonic origin is the most common in an active orogenic belt. At present, research and applications of the unsteady water erosion equation have mostly focused on this type of knickpoints. The paleochannel projection is the most basic application (Kirby and Whipple, 2012; Kent et al., 2017; Zhang et al., 2017). This method assumes that the original vertical slip rate of active faults in the orogenic belt is U2, the channel is in equilibrium at this time, and its erosion rate, E2, is equivalent to U2. After tectonic movement occurs, the regional uplift rate increases from U2 to U1, knickpoints are generated, and the downstream attains an equilibrium state. At this time, the downstream erosion rate, E2, is equal to the new fault activity rate, U1. Therefore, the upstream and downstream channels of the knickpoints are in equilibrium with the original, U2, and current, U1, uplift rates, respectively. The upstream channel of the knickpoints refers to the previous channel before acceleration of the regional uplift rate (Goren et al., 2014a; Fox et al., 2014).

The elevation of the knickpoint is Z, and the distance from the knickpoints to the mountain pass is χ (**Figure 3**). On the χ-elevation map or the distance–elevation map, the river channel upstream of the knickpoint was fitted and extended to the water outlet position to obtain the previous channel projection. The height difference between the elevation projected on the outlet and the elevation, Z, of the knickpoint is z'. The only difference (ΔZ) with respect to the elevation of the outlet is the quantity of erosion owing to the knickpoint; the undercut depth (ΔZ) of the knickpoint can be expressed as follows (Kirby and Whipple, 2012):

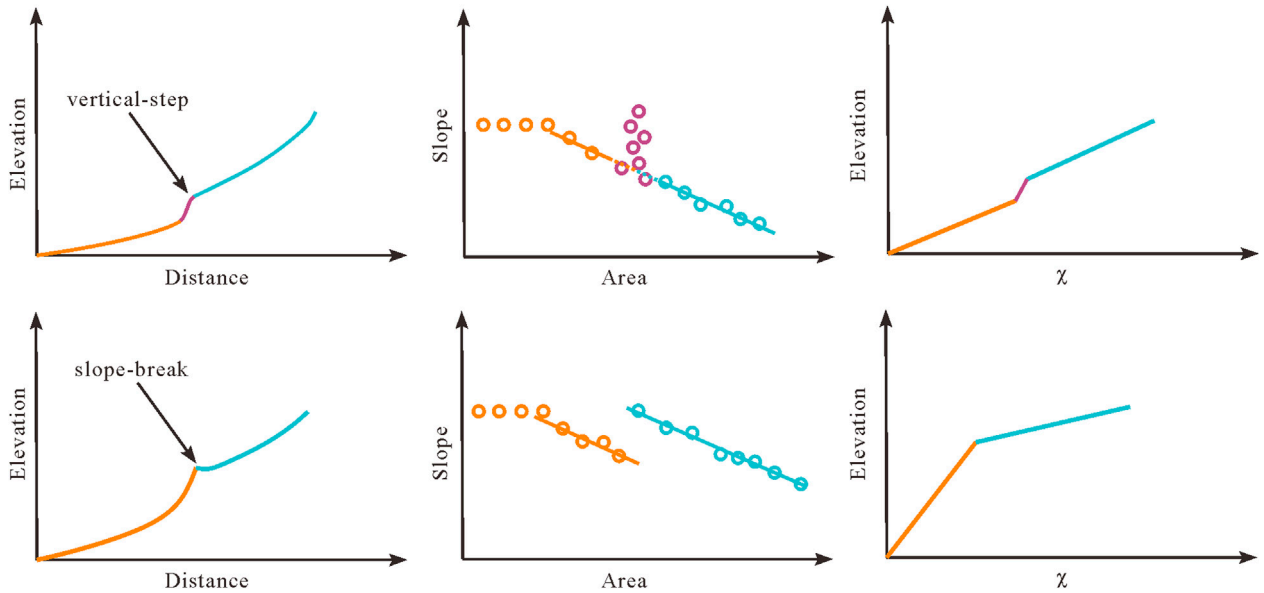

FIGURE 2 | Channel profile differences between the two types of knickpoints (blue indicates the upstream channel of the crack; orange indicates the channel downstream of the crack; purple indicates the knickpoints) [modified from Kirby and Whipple, (2012)].

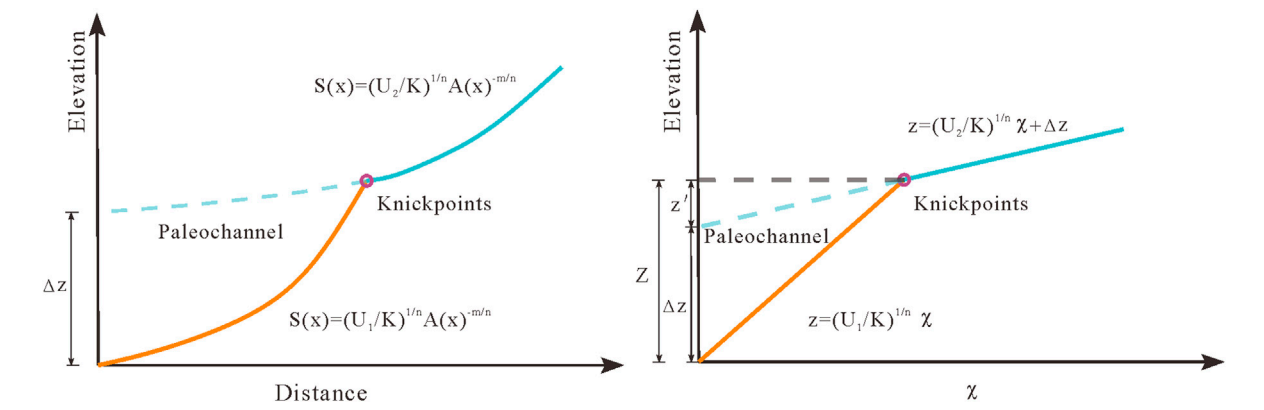

FIGURE 3 | Paleochannel reconstruction in two coordinate systems [modified from Kirby and Whipple, (2012)].

$$\Delta Z = (U - E)\tau, \tag{10}$$

where τ is the response time of the split point, which can be expressed as follows (Yang et al., 2020):

$$\tau = \frac{\Delta Z}{U - E} = \frac{Z - k_{sn2} \cdot \chi}{U1 - \frac{k_{sn2n}}{k_{sn1}}}. \tag{11}$$

RESULTS

We used the 90 m resolution digital elevation model (DEM) provided by the Shuttle Radar Topography Mission (SRTM) to extract 43 rivers in the Helan Shan, of which 1–26 and 27–43 are located at the eastern and western piedmont of the Helan Shan, respectively (**Figure 4A**). Most rivers flow through a single lithological area: only seven rivers (7–12 and 26) flow through two different lithological areas.

We extracted and interpolated the χ value of the river channel using the χ-analysis method, obtaining the spatial distribution characteristics of the χ value for the Helan Shan watershed (**Figure 4D**). The difference in the χ value between both sides of the main divide (N-S direction) showed that the χ value on the western side was notably higher than that on the eastern side.

The relief, k_{sn}, and slope of the Helan Shan were calculated. We generated five combined swath profiles with a width of 10 km, one of which was parallel to the mountain range while the others

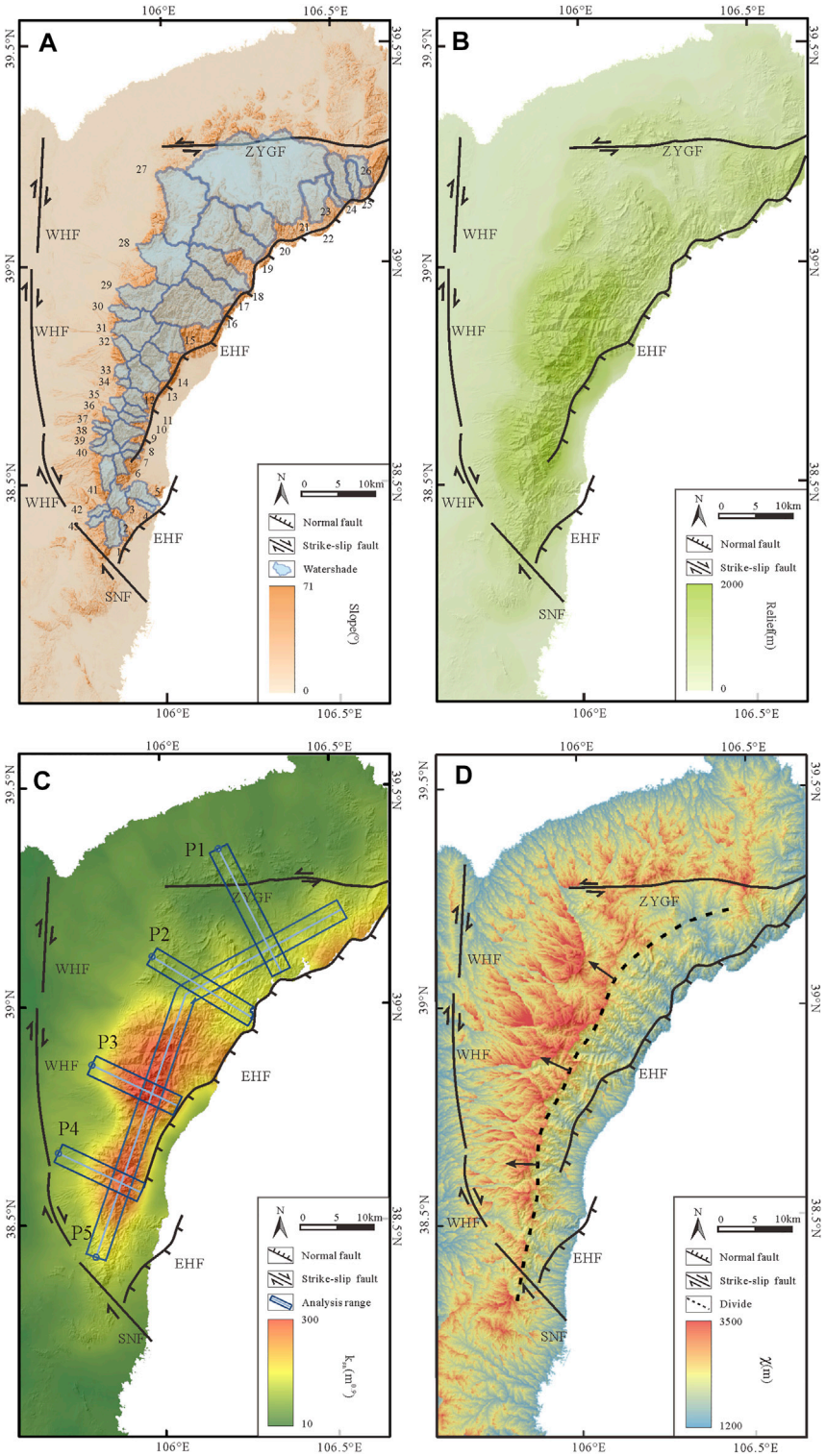

FIGURE 4 | (A) Slope map showing the locations of the studied drainage areas. 1–26 are located at the eastern foot of the Helan Shan, and 27–43 are located at the western foot of the Helan Shan. **(B)** Relief map obtained by calculating the difference between the maximum and minimum elevation values within a radius of 5 km. **(C)** Normalized steepness index map. The dark blue frame, the blue circle, and the light blue line represent the sampling range starting point and the centerline of the strip, respectively. **(D)** χ map of the Helan Shan with the active faults. The black lines represent the active faults, black-dotted line represents the divide position, and black arrows represent the divide migration direction.

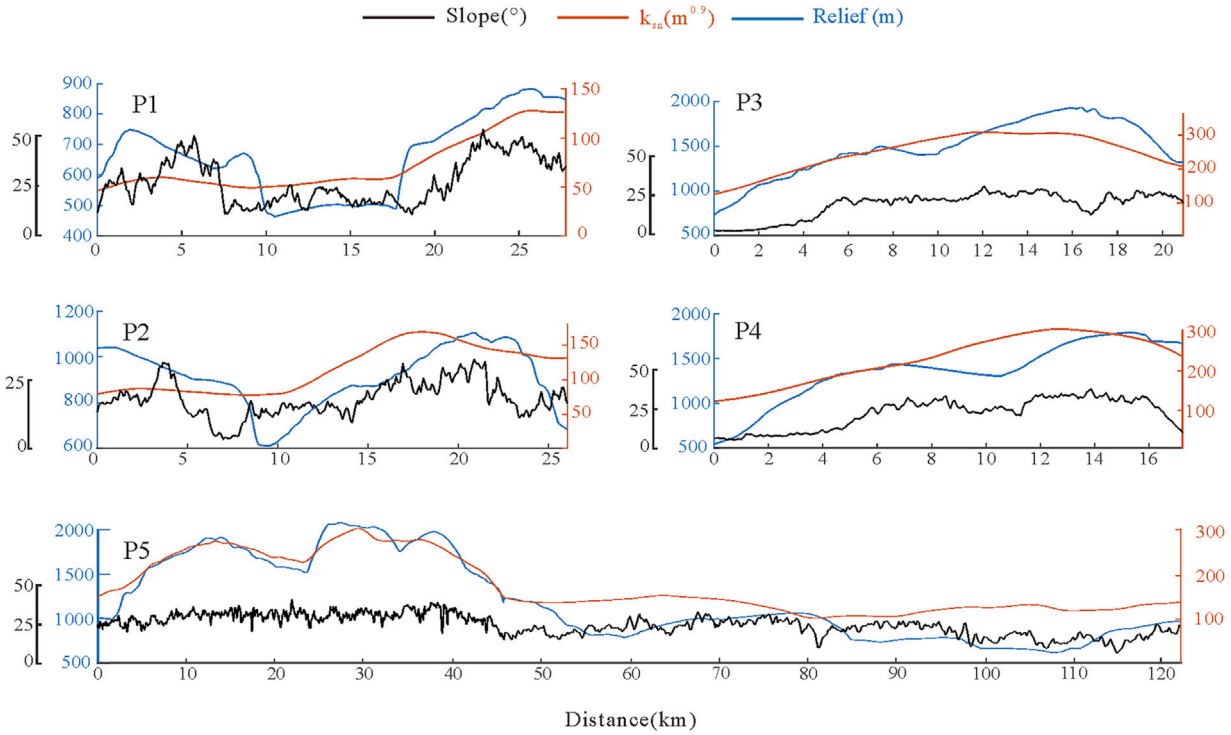

FIGURE 5 | Five strip analysis profiles. Strip analysis profiles include the relief, k_{sn}, and slope. Black, orange, and blue present the slope, k_{sn}, and relief, respectively.

were perpendicular (**Figure 4C**). The spatial distribution of geomorphic indices showed that the k_{sn} in the southern Helan Shan was >150 $m^{0.9}$ and there were two peaks at approximately 8 and 12 km along the mountain range, which is close to the northern side. The strip analysis profiles showed that the k_{sn} in the western Helan Shan was slightly less than that in the eastern Helan Shan. The local relief was also higher along the southern side of the Helan Shan, which was maintained at > 1,200 m, while it ranged from 800 to 1,000 m on the northern side. The slope generally ranged from 15 to 25°, whose distribution was coupled to the topography, local relief, and normalized steepness index (**Figure 5**).

Trunk streams within each watershed were analyzed using the χ-z methodology with a reference concavity of 0.45 (Whipple and Tucker, 1999; Wobus et al., 2006; Kirby and Whipple, 2012; Perron and Royden, 2013) (**Figures 6C–H**). Some bedrock channels (streams 42 and 43 in the western Helan Shan; streams 4 and 5 in the eastern Helan Shan) were stable and had no notable knickpoints; these channels had continuous and concave-up longitudinal profiles. Channels with knickpoints occurred in lower reaches with a high steepness index of ~120 $m^{0.9}$ in the eastern Helan Shan and ~109 $m^{0.9}$ in the western Helan Shan. The upper reaches had lower steepness index values of ~67 $m^{0.9}$ in the eastern Helan Shan and ~68 $m^{0.9}$ in the western Helan Shan, approximately half of that of downstream areas. The similar k_{sn} values in the upper reaches may indicate an equal rate of tectonic uplift in terms of the latitude before tectonic activity. The spatial distribution of the knickpoints showed that no knickpoint was located on lithological contacts or along faults, indicating that knickpoint formation had no relationship with lithology.

We extracted and analyzed a large number of knickpoint parameters (**Table 1**). The average relative elevation of the knickpoints was approximately 317 m in the eastern Helan Shan and approximately 230 m in the western Helan Shan. Here, ΔZ was calculated based on the k_{sn} and relative elevation, with an average of approximately 143 m in the eastern Helan Shan and approximately 74 m in the western Helan Shan. Both parameters showed a downward trend from the south to the north. The χ-analysis yielded a good linear relationship between χ and elevation, with a mean R2 of ~0.99.

DISCUSSION

Implication of Spatial Variance in Geomorphic Index

The normalized steepness index is proportional to the strength of tectonic activity. The result of the normalized steepness index distribution may indicate that the tectonic uplift rate in the southern and eastern Helan Shan was higher than that in the northern and western Helan Shan, which is consistent with the current topography, local relief, and slope. However, lithology also had an influence on the slope index, n, and erosion coefficient, K, thereby controlling the river incision process, which consequently affected the channel shape and steepness

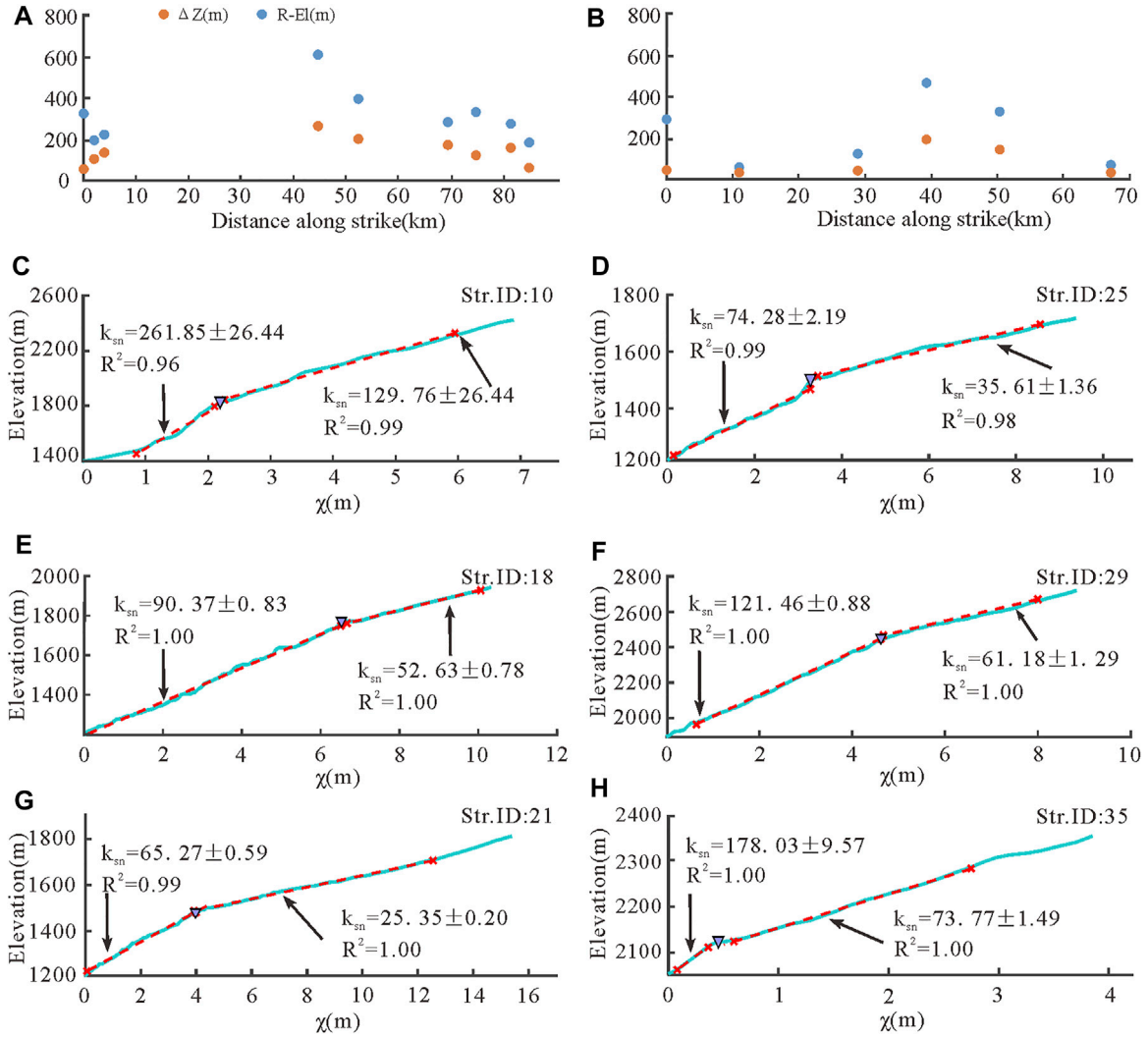

FIGURE 6 | (A–B) ΔZ and R–El along the direction of the scatter point distribution map. R–El indicates the relative knickpoint elevation. The abscissa represents the projection distance of the streams along strike from the southernmost stream to the northernmost stream. Here, A represents the eastern Helan Shan, using stream 10 as the starting point; B represents the western Helan Shan, using stream 40 as the starting point. **(C–H)** Analysis results of the fluvial longitudinal profiles. Typical river longitudinal profiles in different parts of the study area are shown in the figure. The Str. ID is the stream number shown in **Figure 4A**. Blue lines indicate the original χ-z profiles, red-dashed lines indicate the regressed χ-z profiles, and the red cross represents the start and end of the fitting. Abrupt changes in the slope were classified as knickpoints denoted by dark blue triangles.

index (Di Biase, 2018; Forte et al., 2016). Precipitation can affect the erosion coefficient, K, and concavity, θ; increased precipitation often results in a decrease in topographic undulations and the steepness coefficient (Zaprowski, 2005; Whipple 2009; Chen et al., 2019). As the precipitation was mainly concentrated in mountainous areas with small changes (**Figure 7B**), this had a limited effect on divide migration. The relative arid climatic conditions in the Helan Shan (i.e., the annual precipitation is relatively uniform and <330 mm/yr), where carbonate rocks have stronger erosion resistance than clastic rocks, reduce the steepness index. The carbonate rocks of the Helan Shan are mainly distributed in the south (**Figure 7A**); therefore, the increased steepness index in the south than that in the north is not due to differences in the lithology. As the normalized steepness is a reflection of the tectonic strength, we suggest that the eastern piedmont normal fault has mainly controlled the tectonic activity in the Helan Shan. The mountain range has tilted toward the north and west, which has been induced by the spatial differences in the uplift rate. Moreover, previous studies on active tectonics in the Helan Shan have revealed the spatial distribution of the tectonic intensity, whose results are also consistent with those presented here.

Furthermore, χ values are widely used to determine the stability of the drainage divide; therefore, the variance on different sides of the main divide indicates that the divide tended to migrate westward. The stability of the watershed of the basin may be affected by many factors, such as differences in precipitation or lithology (Willett, 1999; Goren et al., 2014b; Forte

TABLE 1 | Results of the stream profile analysis in the Helan Shan.

Site	Str.ID	Downstream		Upstream		Knickpoints						
		k_{sn} ($m^{0.9}$)	R^2	k_{sn} ($m^{0.9}$)	R^2	Elevation (m)	R–El (m)	χ (m)	ua (km^2)	dfm (km)	dfd (km)	Δz (m)
Eastern Helan Shan	10	261.85	0.96	129.76	0.99	1,787	329	2.10	9.45	3.12	6.04	56
	11	215.26	0.87	105.81	1.00	1,644	225	0.83	18.86	1.62	7.92	137
	12	133.43	0.94	112.62	0.99	1,644	198	0.81	18.86	1.58	7.92	106
	18	90.37	1.00	52.63	1.00	1,800	616	6.63	16.87	18.49	7.16	267
	19	94.63	0.98	56.68	0.95	1,620	400	3.46	89.56	15.45	16.51	204
	21	65.27	0.99	25.35	1.00	1,503	287	4.41	160.89	28.21	24.65	175
	23	103.41	0.99	60.61	0.99	1,567	336	3.49	7.69	5.07	7.86	125
	24	47.32	0.98	26.76	0.97	1,591	187	4.66	7.74	7.85	6.68	62
	25	74.28	0.99	35.61	0.98	1,507	278	3.28	11.53	5.95	8.71	161
Western Helan Shan	27	63.01	0.97	36.11	0.99	1,616	72	1.08	61.49	4.62	15.72	33
	28	87.63	1.00	47.32	0.96	2,103	338	4.01	17.29	13.34	7.28	148
	29	121.46	1.00	61.18	1.00	2,457	482	4.62	13.23	11.67	6.49	199
	31	125.78	1.00	92.58	0.99	2,236	127	0.91	61.02	2.95	12.95	43
	35	178.03	1.00	73.77	1.00	2,123	60	0.37	10.33	0.53	4.96	33
	40	97.40	0.99	81.81	1.00	2,231	299	3.09	10.67	5.55	4.78	46

Str. ID, R-El, ua, dfm, and dfd are the stream number, relative knickpoint elevation, upstream area, distance from mouth, and distance from divide, respectively.

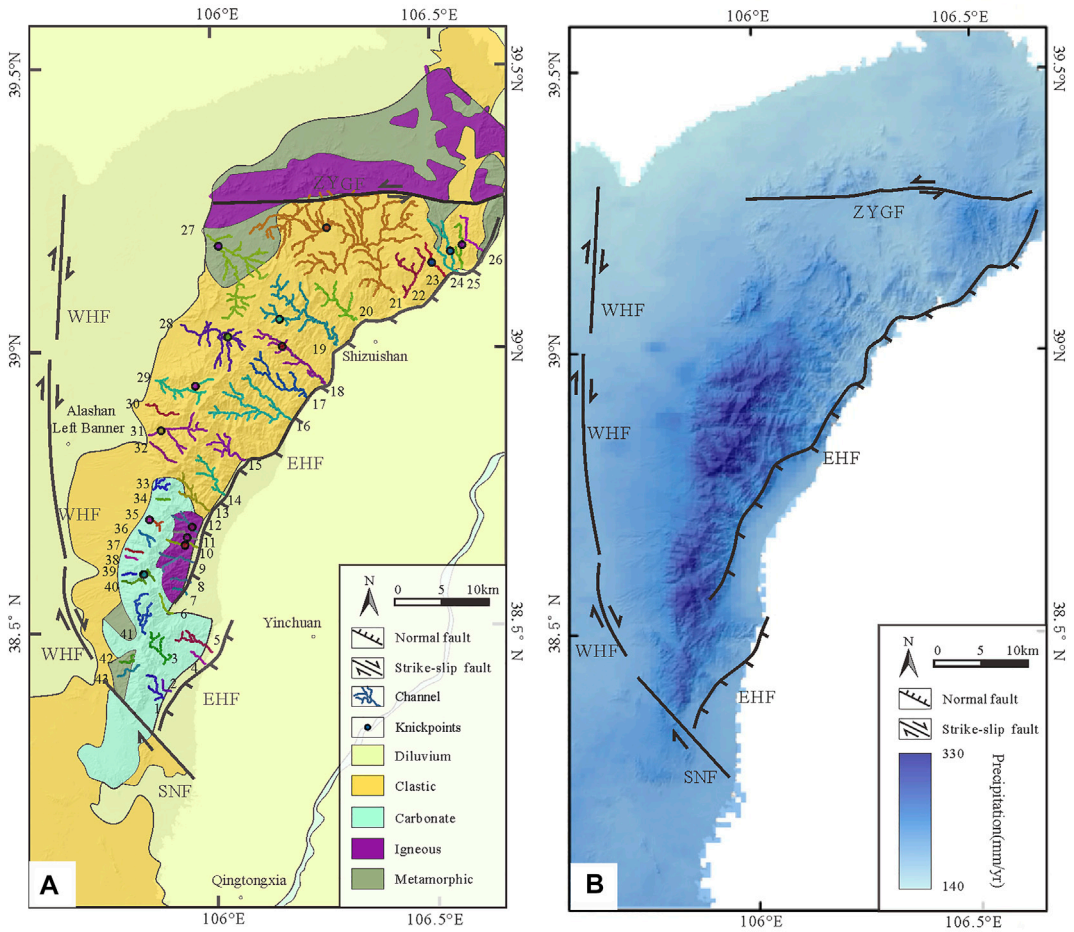

FIGURE 7 | (A) The lithology and knickpoints distribution map. The distribution of lithology is modified from Geological Map of Ningxia Hui Autonomous Region, the People's Republic of China (2014). The knickpoints were identified from the χ-analysis of each stream. No knickpoints were located on lithological contacts or faults. **(B)** Mean annual rainfall shown over hillshade. Data comes from http://climatedataguide.ucar.edu/.

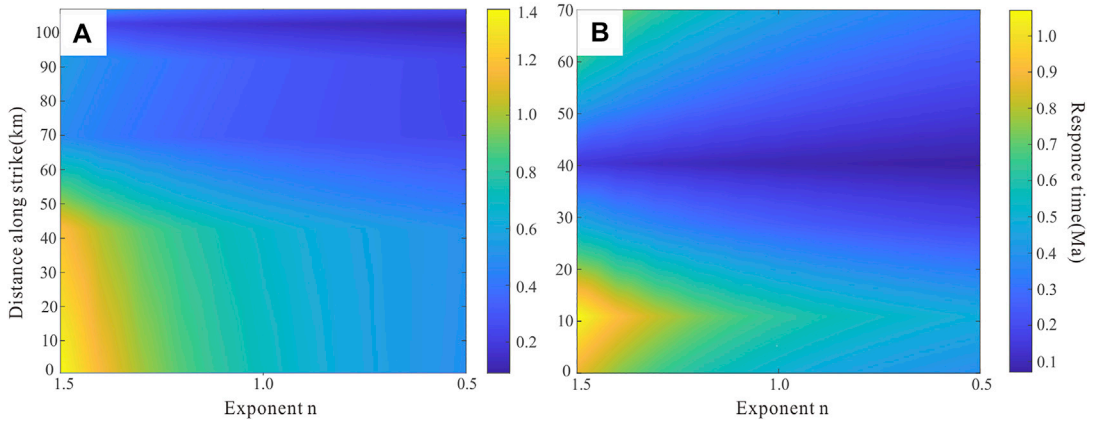

FIGURE 8 | Calculated response time along the direction of the Helan Shan. Yellow represents a larger response time while blue represents a smaller response time. The ordinate represents the projection distance of the streams along strike from the southernmost stream to the northernmost stream. **(A)** represents the eastern Helan Shan, using stream 10 as the starting point and **(B)** represents the western Helan Shan, using stream 40 as the starting point.

and Whipple, 2018), changes in erosion base levels (Goren et al., 2014b; Forte and Whipple, 2018), and asymmetric tectonic uplift (Goren et al., 2014b; Willett et al., 2014; Whipple et al., 2017). The lithology and precipitation of the Helan Shan is basically symmetrically distributed along the divide (**Figures 7A,B**), and rivers in the two foothills have the Yellow River as the same erosion base level. These factors are difficult to explain the divide migration in the Helan Shan. Given that the Helan Shan is bound by the western and eastern piedmont fault, we suggest that the difference in the tectonic intensity of the two boundary faults influenced the divide migration (i.e., the tectonic strength of the eastern piedmont fault was higher than that of the western piedmont fault); the eastern piedmont fault dominantly shaped the fluvial landform. The χ-map was also coupled to the result of the k_{sn} distribution characteristics.

Geologic Significance of Knickpoint Origin and Ages

Knickpoints on the channel profiles in the 46 watersheds were associated with an abrupt change in the slope of the χ-elevation plots. The normalized steepness index downstream of the knickpoints was approximately twice as high as that upstream; the longitudinal profiles of these channels had a notable broken line with steep downward and gentle upward characteristics, implying the occurrence of a river incision-accelerated event. Most of the rivers in the Helan Shan flow through a single lithological unit; almost all of the knickpoints are distributed at non-lithological boundaries, which eliminates lithological differences as a potential cause (**Figure 7A**). Moreover, the dryer and colder climate based on $\delta^{18}O$ records from the strata causes difficulties when attempting to interpret the origin of the knickpoints (Zachos et al., 2001; Zhang et al., 2010; Peng et al., 2016). Therefore, climatic factors and lithology cannot explain the accelerated incision of the bedrock channels in this area. Knickpoint origination is a response to tectonic acceleration events.

Additionally, we calculated the response time of the Helan Shan knickpoints based on the paleochannel reconstruction method. The results showed that the average response time of the knickpoints was 0.38 Ma in the eastern Helan Shan and 0.33 Ma in western Helan Shan when the slope index n, was set to/predefined as 1. However, as various conditions, such as lithology and climate, affect the slope index n, its value may not be 1 under ideal conditions. Here, we changed the slope index, n, from 0.5 to 1.5 at steps of 0.1 based on previous studies (**Figure 8**). Finally, the response time of the knickpoint was limited to 0.1–1.4 Ma (**Figure 8**). The response time of the bedrock channel located at the northern side of the Helan Shan was later than that located at the southern side, which may suggest that the acceleration of Helan tectonic activity was not simultaneous, that is, tectonic activity first affected the southern area and then propagated northward.

Transformation of Tectonic Pattern in the Helan Shan

Previous studies on neotectonics indicate that the Helan Shan experienced a rapid southwest tilting tectonic pattern from 10 to 20 Ma (Liu et al., 2010) (**Figure 9**). However, the active tectonics and k_{sn} index show that the uplift rate of the southern part of the Helan Shan is currently faster than that of the northern part, which indicates that the spatial pattern of the tectonic activity has experienced at least one transformation. Moreover, the northeastward propagation of the Tibetan Plateau has controlled the tectonic deformation and evolution along the northeastern margin of the plateau, inducing a series of tectonic events in chronological order. Current research has shown that northeast extension reached the Niushou Shan fault at approximately the end of the Pliocene (~2.7 Ma). Additionally, the Yellow River in the Niushou Shan area also responded to this event in the early Pleistocene (Liang et al., 2013). The knickpoints in the Helan Shan formed in the Pleistocene, which demonstrates that they most likely occurred during tectonic pattern transformation in the Helan Shan and when the Tibetan Plateau reached the Helan Shan (**Figure 9**). We

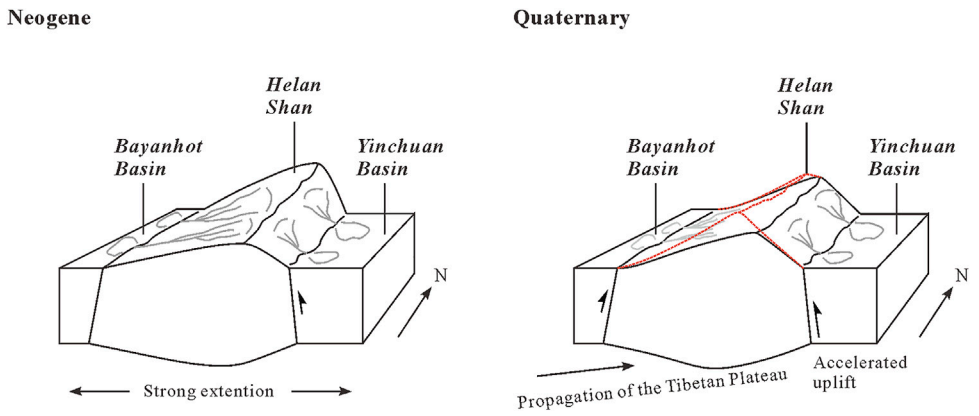

FIGURE 9 | Tectonic transformation model of the Helan Shan. The orange-dashed lines indicate the future topography. The embryo of the Helan Shan formed via a strong extension of the Ordos Block in the late Neogene, which appeared as a tilting tectonic model in the southwest direction (Liu et al., 2010). In the early Quaternary, expansion of the Tibetan Plateau affected the Helan Shan; the uplift rate of its southern end increased and the pattern of tectonic uplift changed to a northwest tilt. The Helan Shan will likely form topography characterized by a high in the south and a low in the north in the future.

suggest that the tectonic transformation of the Helan Shan may have occurred in the Pleistocene as a result of Tibetan Plateau expansion.

CONCLUSION

In this study, we investigated the various geomorphic indices and the response of channels based on quantitative geomorphology analysis. We draw the following conclusions:

1. The bedrock channel of the Helan Shan is segmented, which indicates that the channel has experienced an accelerated incision event. Based on the influence of lithology and climate, we suggest that this is the result of accelerated tectonic uplift.
2. The development and evolution characteristics of the Helan Shan drainage basin show that the main divide tended to migrate toward the western Helan Shan, which demonstrates that the EHF was the main controlling fault with respect to tectonic uplift and deformation.
3. The spatial variance in the geomorphic index of the Helan Shan reflects the occurrence of at least one tectonic transformation event that shifted the tilting tectonic model from the southwest to the northwest during the Pleistocene (0.1–1.4 Ma), which may have been caused by the outward expansion of the northeastern Tibetan Plateau.

DATA AVAILABILITY STATEMENT

The raw data supporting the conclusion of this article will be made available by the authors, without undue reservation.

AUTHOR CONTRIBUTIONS

WZ and YL contributed to the conception of this study. WZ and DZ provided funding for the study. YJ provided the basic code and polished the study. YL completed the experiment with the help of HZ and TL. YL and WZ wrote the manuscript. All authors contributed to manuscript revision and discussion and approved the submitted version.

FUNDING

This work was supported by the National Key Research and Development Program of China (2017YFC1500101), the National Science Foundation of China (42174062, 41774049, 41872204), the second Tibetan Plateau Scientific Expedition and Research program (STEP) (2019QZKK0901), and Guangdong Province Introduced Innovative R&D Team of Geological Processes and Natural Disasters around the South China Sea (2016ZT06N331).

REFERENCES

Berlin, M., and Anderson, R. (2007). Modeling of Knickpoint Retreat on the Roan Plateau, Western Colorado. *J. Geophys. Res. Earth Surf.* 112 (3), 1–16. doi:10.1029/2006jf000553

Chen, S.-A., Michaelides, K., Grieve, S. W. D., and Singer, M. B. (2019). Aridity Is Expressed in River Topography Globally. *Nature* 573 (7775), 573–577. doi:10.1038/s41586-019-1558-8

Clark, M., Farley, K., Zheng, D., Wang, Z., and Duvall, A. (2010). Early Cenozoic Faulting of the Northern Tibetan Plateau Margin from Apatite (U-Th)/He Ages. *Earth Planet. Sci. Lett.* 296 (1–2), 78–88. doi:10.1016/j.epsl.2010.04.051

Darby, B., and Ritts, B. (2002). Mesozoic Contractional Deformation in the Middle of the Asian Tectonic Collage: the Intraplate Western Ordos Fold–Thrust belt, China. *Earth Planet. Sci. Lett.* 205 (1), 13–24. doi:10.1016/s0012-821x(02)01026-9

Deng, Q., and Liao, Y. (1996). Paleoseismology along the Range-Front Fault of Helan Mountains, north central China. *J. Geophys. Res.* 101 (B3), 5873–5893. doi:10.1029/95jb01814

Deng, Q., Zhang, P., Ran, Y., Yang, X., Min, W., and Chu, Q. (2003). Basic Characteristics of Active Tectonics of China. *Sci. China, Ser. D: Earth Sci.* 46 (4), 356–372. doi:10.1360/03ys9030

DiBiase, R. A. (2018). Short Communication: Increasing Vertical Attenuation Length of Cosmogenic Nuclide Production on Steep Slopes Negates Topographic Shielding Corrections for Catchment Erosion Rates. *Earth Surf. Dynam.* 6 (4), 923–931. doi:10.5194/esurf-6-923-2018

Du, P. (2010). *Studying on the Active Characteristics and Paleoearthquake of the Eastern piedmont Fault of Helan Mountain in the Late Quaternary*. Beijing: China University of Geosciences. [dissertation/master's thesis].

Duvall, A., Clark, M., Pluijm, B., and Li, C. (2011). Direct Dating of Eocene Reverse Faulting in Northeastern Tibet Using Ar-Dating of Fault Clays and Low-Temperature Thermochronometry. *Earth Planet. Sci. Lett.* 304 (3–4), 520–526. doi:10.1016/j.epsl.2011.02.028

England, P., and Molnar, P. (1990). Surface Uplift, Uplift of Rocks, and Exhumation of Rocks. *Geol* 18 (12), 1173–1177. doi:10.1130/0091-7613(1990)018<1173:suuora>2.3.co;2

Forte, A. M., and Whipple, K. X. (2018). Criteria and Tools for Determining Drainage divide Stability. *Earth Planet. Sci. Lett.* 493, 102–117. doi:10.1016/j.epsl.2018.04.026

Forte, A. M., and Whipple, K. X. (2019). Short Communication: The Topographic Analysis Kit (TAK) for TopoToolbox. *Earth Surf. Dynam.* 7 (1), 87–95. doi:10.5194/esurf-7-87-2019

Forte, A. M., Yanites, B. J., and Whipple, K. X. (2016). Complexities of Landscape Evolution during Incision through Layered Stratigraphy with Contrasts in Rock Strength. *Earth Surf. Process. Landforms* 41, 1736–1757. doi:10.1002/esp.3947

Fox, M., Goren, L., May, D. A., and Willett, S. D. (2014). Inversion of Fluvial Channels for Paleorock Uplift Rates in Taiwan. *J. Geophys. Res. Earth Surf.* 119 (9), 1853–1875. doi:10.1002/2014jf003196

Goren, L., Fox, M., and Willett, S. D. (2014a). Tectonics from Fluvial Topography Using Formal Linear Inversion: Theory and Applications to the Inyo Mountains, California. *J. Geophys. Res. Earth Surf.* 119 (8), 1651–1681. doi:10.1002/2014jf003079

Goren, L., Willett, S. D., Herman, F., and Braun, J. (2014b). Coupled Numerical-Analytical Approach to Landscape Evolution Modeling. *Earth Surf. Process. Landforms* 39 (4), 522–545. doi:10.1002/esp.3514

Hack, J. (1957). Studies of Longitudinal Profiles in Virginia and Maryland. *J. Res. US Geol. Surv.* 294, 208–209.

Hack, J. (1973). Stream-Profile Analysis and Stream-Gradient Index. *J. Res. US Geol. Surv.* 1 (04), 421–429.

Kent, E., Boulton, S. J., Whittaker, A. C., Stewart, I. S., and Cihat Alçiçek, M. (2017). Normal Fault Growth and Linkage in the Gediz (Alaşehir) Graben, Western Turkey, Revealed by Transient River Long-Profiles and Slope-Break Knickpoints. *Earth Surf. Process. Landforms* 42, 836–852. doi:10.1002/esp.4049

Kirby, E., and Whipple, K. X. (2012). Expression of Active Tectonics in Erosional Landscapes. *J. Struct. Geol.* 44, 54–75. doi:10.1016/j.jsg.2012.07.009

Lei, Q., Zhang, P., Zheng, W., Chai, C., Wang, W., Du, P., et al. (2016). Dextral Strike-Slip of Sanguankou-Niushoushan Fault Zone and Extension of Arc Tectonic belt in the Northeastern Margin of the Tibet Plateau. *Sci. China Earth Sci.* 59 (5), 1025–1040. doi:10.1007/s11430-016-5272-1

Liang, H., Zhang, K., and Fu, J. (2013). The Neotctonics in the Niushou Mountains, the Northeastern Margin of the Tibetan Plateau, China and its Impact on the Evolution of the Yellow River. *Earth Sci. Front.* 20 (4), 182–189.

Liu, Y., Shishov, T., Shi, J., Vaganov, E., Sun, J., Cai, Q., et al. (2004). Prediction of Precipitation Trend in Helan Mountain in Western Inner Mongolia and Baiyin Obao in Eastern Inner Mongolia in the Next 20 Years. *Chin. Sci. Bull.* 49 (3), 270–274. doi:10.1007/bf02900326

Liu, J., Zhang, P., Zheng, D., Wan, J., Wang, W., Du, P., et al. (2010). Pattern and Timing of Late Cenozoic Rapid Exhumation and Uplift of the Helan Mountain, China. *Sci. China Earth Sci.* 53 (3), 345–355. doi:10.1007/s11430-010-0016-0

Molnar, P., and Tapponnier, P. (1975). Cenozoic Tectonics of Asia: Effects of a Continental Collision: Features of Recent continental Tectonics in Asia Can Be Interpreted as Results of the India-Eurasia Collision. *Science* 189 (4201), 419–426. doi:10.1126/science.189.4201.419

Peng, T., Li, J., Song, C., Guo, B., Liu, J., Zhao, Z., et al. (2016). An Integrated Biomarker Perspective on Neogene-Quaternary Climatic Evolution in NE Tibetan Plateau: Implications for the Asian Aridification. *Quat. Int.* 399, 174–182. doi:10.1016/j.quaint.2015.04.020

Perron, J. T., and Royden, L. (2013). An Integral Approach to Bedrock River Profile Analysis. *Earth Surf. Process. Landforms* 38 (6), 570–576. doi:10.1002/esp.3302

Rohrmann, A., Kapp, P., Carrapa, B., Reiners, P. W., Guynn, J., Ding, L., et al. (2012). Thermochronologic Evidence for Plateau Formation in central Tibet by 45 Ma. *Geology* 40 (2), 187–190. doi:10.1130/g32530.1

Royden, L., and Taylor Perron, J. (2013). Solutions of the Stream Power Equation and Application to the Evolution of River Longitudinal Profiles. *J. Geophys. Res. Earth Surf.* 118 (2), 497–518. doi:10.1002/jgrf.20031

Royden, L. H., Burchfiel, B. C., and van der Hilst, R. D. (2008). The Geological Evolution of the Tibetan Plateau. *Science* 321 (5892), 1054–1058. doi:10.1126/science.1155371

Schwanghart, W., and Kuhn, N. J. (2010). TopoToolbox: A Set of Matlab Functions for Topographic Analysis. *Environ. Model. Softw.* 25, 770–781. doi:10.1016/j.envsoft.2009.12.002

Schwanghart, W., and Scherler, D. (2014). Short Communication: TopoToolbox 2 - MATLAB-Based Software for Topographic Analysis and Modeling in Earth Surface Sciences. *Earth Surf. Dynam.* 2 (1), 1–7. doi:10.5194/esurf-2-1-2014

Stock, J. D., and Montgomery, D. R. (1999). Geologic Constraints on Bedrock River Incision Using the Stream Power Law. *J. Geophys. Res.* 104 (B3), 4983–4993. doi:10.1029/98jb02139

Tapponnier, P., Xu, Z., Roger, F., Meyer, B., Arnaud, N., Wittlinger, G., et al. (2001). Oblique Stepwise Rise and Growth of the Tibet Plateau. *Science* 294 (5547), 1671–1677. doi:10.1126/science.105978

Wang, W., Zhang, P., Kirby, E., Wang, L., Zhang, G., Zheng, D., et al. (2011). A Revised Chronology for Tertiary Sedimentation in the Sikouzi basin: Implications for the Tectonic Evolution of the Northeastern Corner of the Tibetan Plateau. *Tectonophysics* 505 (1), 100–114. doi:10.1016/j.tecto.2011.04.006

Wang, Y., Schoenbohm, L. M., Zhang, B., Granger, D. E., Zhou, R., Zhang, J., et al. (2017). Late Cenozoic Landscape Evolution along the Ailao Shan Shear Zone, SE Tibetan Plateau: Evidence from Fluvial Longitudinal Profiles and Cosmogenic Erosion Rates. *Earth Planet. Sci. Lett.* 472, 323–333. doi:10.1016/j.epsl.2017.05.030

Wang, Y., Zheng, D., Pang, J., Zhang, H., Wang, W., Yu, J., et al. (2018). Using Slope-Area and Apatite Fission Track Analysis to Decipher the Rock Uplift Pattern of the Yumu Shan: New Insights into the Growth of the NE Tibetan Plateau. *Geomorphology* 308, 118–128. doi:10.1016/j.geomorph.2018.02.006

Whipple, K. X., and Tucker, G. E. (1999). Dynamics of the Stream-Power River Incision Model: Implications for Height Limits of Mountain Ranges, Landscape Response Timescales, and Research Needs. *J. Geophys. Res.* 104 (B8), 17661–17674. doi:10.1029/1999jb900120

Whipple, K. X., Forte, A. M., Dibiase, R. A., Gasparini, N. M., and Ouimet, W. B. (2017). Timescales of Landscape Response to divide Migration and Drainage Capture: Implications for the Role of divide Mobility in Landscape Evolution. *J. Geophys. Res. Earth Surf.* 122 (1), 248–273. doi:10.1002/2016jf003973

Whipple, K. X. (2001). Fluvial Landscape Response Time: How Plausible Is Steady-State Denudation? *Am. J. Sci.* 301 (4–5), 313–325. doi:10.2475/ajs.301.4-5.313

Whipple, K. X. (2004). Bedrock Rivers and the Geomorphology of Active Orogens. *Annu. Rev. Earth Planet. Sci.* 32, 151–185. doi:10.1146/annurev.earth.32.101802.120356

Whipple, K. X. (2009). The Influence of Climate on the Tectonic Evolution of Mountain Belts. *Nat. Geosci.* 2, 97–104. doi:10.1038/ngeo413

Willett, S. D., McCoy, S. W., Perron, J. T., Goren, L., and Chen, C. Y. (2014). Dynamic Reorganization of River Basins. *Science* 343 (6175), 1248765. doi:10.1126/science.1248765

Willett, S. D. (1999). Orogeny and Orography: The Effects of Erosion on the Structure of Mountain Belts. *J. Geophys. Res.* 104 (B12), 28957–28981. doi:10.1029/1999jb900248

Wobus, C., Whipple, K., Kirby, E., Snyder, N., Johnson, J., Spyropolou, K., et al. (2006). Tectonics from Topography: Procedures, Promise, and Pitfalls. *Spec. Paper Geol. Soc. Am.* 398, 55–74. doi:10.1130/2006.2398(04)

Yang, X., and Dong, Y. (2018). Mesozoic and Cenozoic Multiple Deformations in the Helanshan Tectonic Belt, Northern China. *Gondwana Res.* 60, 34–53. doi:10.1016/j.gr.2018.03.020

Yang, R., Willett, S. D., and Goren, L. (2015). *In Situ* low-relief Landscape Formation as a Result of River Network Disruption. *Nature* 520 (7548), 526–529. doi:10.1038/nature14354

Yang, J., Zheng, W., Wang, Y., Bi, H., Zhang, D., Zhang, P., et al. (2020). Quantitative Geomorphological Constraints on the Landform Evolution of the Current Active Boundary of the Northeastern Tibetan Plateau. *Geomorphology* 358, 107120. doi:10.1016/j.geomorph.2020.107120

Yin, A., and Harrison, T. M. (2000). Geologic Evolution of the Himalayan-Tibetan Orogen. *Annu. Rev. Earth Planet. Sci.* 28, 211–280. doi:10.1146/annurev.earth.28.1.211

Yin, A., Dang, Y., Wang, L., Jiang, W., Zhou, S., Chen, X., et al. (2008). Cenozoic Tectonic Evolution of Qaidam basin and its Surrounding Regions (Part 1): The Southern Qilian Shan-Nan Shan Thrust belt and Northern Qaidam basin. *Bull. Geol. Soc. Am.* 120 (7–8), 813–846. doi:10.1130/b26180.1

Yu, J., Zheng, W., Kirby, E., Zhang, P., Lei, Q., Ge, W., et al. (2016). Kinematics of Late Quaternary Slip along the Yabrai Fault: Implications for Cenozoic Tectonics across the Gobi Alashan Block, China. *Lithosphere* 8 (3), 199–218. doi:10.1130/l509.1

Zachos, J., Pagani, M., Sloan, L., Thomas, E., and Billups, K. (2001). Trends, Rhythms, and Aberrations in Global Climate 65 Ma to Present. *Science* 292 (5517), 686–693. doi:10.1126/science.1059412

Zaprowski, B. J. (2005). Climatic Influences on Profile Concavity and River Incision. *J. Geophys. Res.* 110 (F3), 1–21. doi:10.1029/2004jf000138

Zhang, P., Burchfiel, B., Molnar, P., Zhang, W., Jiao, D., Deng, Q., et al. (1990). Late Cenozoic Tectonic Evolution of the Ningxia-Hui Autonomous Region, China. *GSA Bull.* 102 (11), 1484–1498. doi:10.1130/0016-7606(1990)102<1484:lcteot>2.3.co;2

Zhang, J., Dickson, C., and Chen, H. (2010). Sedimentary Characteristics of Cenozoic Strata in central-southern Ningxia, NW China: Implications for the Evolution of the NE Qinghai–Tibetan Plateau. *J. Asian Earth Sci.* 39 (6), 740–759. doi:10.1016/j.jseaes.2010.05.008

Zhang, H., Kirby, E., Pitlick, J., Anderson, R. S., and Zhang, P. (2017). Characterizing the Transient Geomorphic Response to Base-level Fall in the Northeastern Tibetan Plateau. *J. Geophys. Res. Earth Surf.* 122 (2), 546–572. doi:10.1002/2015jf003715

Zhao, G., Sun, M., Wilde, S. A., and Sanzhong, L. (2005). Late Archean to Paleoproterozoic Evolution of the North China Craton: Key Issues Revisited. *Precambrian Res.* 136 (2), 177–202. doi:10.1016/j.precamres.2004.10.002

Zheng, D., Zhang, P., Wan, J., Yuan, D., Li, C., Yin, G., et al. (2006). Rapid Exhumation at ~8 Ma on the Liupan Shan Thrust Fault from Apatite Fission-Track Thermochronology: Implications for Growth of the Northeastern Tibetan Plateau Margin. *Earth Planet. Sci. Lett.* 248 (1), 198–208. doi:10.1016/j.epsl.2006.05.023

Zheng, D., Clark, M. K., Zhang, P., Zheng, W., and Farley, K. A. (2010). Erosion, Fault Initiation and Topographic Growth of the North Qilian Shan (Northern Tibetan Plateau). *Geosphere* 6 (6), 937–941. doi:10.1130/ges00523.1

Zheng, W., Zhang, P., He, W., Yuan, D., Shao, Y., Zheng, D., et al. (2013). Transformation of Displacement between Strike-Slip and Crustal Shortening in the Northern Margin of the Tibetan Plateau: Evidence from Decadal GPS Measurements and Late Quaternary Slip Rates on Faults. *Tectonophysics* 584, 267–280. doi:10.1016/j.tecto.2012.01.006

Zheng, W., Yuan, D., Zhang, P., Yu, J., Lei, Q., Wang, W., et al. (2016). Tectonic Geometry and Kinematic Dissipation of the Active Faults in the Northeastern Tibetan Plateau and Their Implications for Understanding Northeastward Growth of the Plateau. *Quat. Sci.* 36 (4), 775–788. doi:10.11928/j.issn.1001-7410.2016.04.01

Zheng, W., Zhang, B., Yuan, D., Chen, G., Zhang, Y., Yu, J., et al. (2021). Tectonic Activity in the Southern Alashan Block and the Latest Boundary of Outward Expansion on the Northeastern Tibetan Plateau,China. *J. Earth Sci. Environ.* 43 (2), 224–236. doi:10.19814/j.jese.2021.01039

Zhou, X., and Geng, Y. (2009). Metamorphic Age of the Khondalite Series in the Helanshan Region Constraints on the Evolution of the Western Block in the North China Craton. *Acta Petrol. Sin.* 25 (08), 1843–1852.

Conflict of Interest: The authors declare that the research was conducted in the absence of any commercial or financial relationships that could be construed as a potential conflict of interest.

Publisher's Note: All claims expressed in this article are solely those of the authors and do not necessarily represent those of their affiliated organizations, or those of the publisher, the editors, and the reviewers. Any product that may be evaluated in this article, or claim that may be made by its manufacturer, is not guaranteed or endorsed by the publisher.

Copyright © 2022 Li, Zheng, Yang, Zhang, Zhou and Liu. This is an open-access article distributed under the terms of the Creative Commons Attribution License (CC BY). The use, distribution or reproduction in other forums is permitted, provided the original author(s) and the copyright owner(s) are credited and that the original publication in this journal is cited, in accordance with accepted academic practice. No use, distribution or reproduction is permitted which does not comply with these terms.

frontiers in Earth Science

ORIGINAL RESEARCH
published: 22 February 2022
doi: 10.3389/feart.2022.791264

Chain Actions Generated High-Elevation and High-Relief Topography of the Eastern Margin of the Tibetan Plateau: From Deep Earth Forces to Earthquake-Induced Dams

Hailong Li[1]*, *Yujun Sun*[1]* and *Yueqiao Zhang*[2]

[1]Chinese Academy of Geological Sciences, Beijing, China, [2]School of Earth Sciences and Engineering, Nanjing University, Nanjing, China

High-elevation and high-relief topography is the most prominent geomorphological features of the eastern margin of the Tibetan Plateau. This paper proposes that the interaction of the endogenic and exogenic forces jointly determines the formation of such high and steep landform. Eastward propagation of the Tibetan Plateau has been portioned by NW-striking, large-scaled sinistral strike-slip faults due to resistance of rigid Yangtze craton to the east of the eastern margin of the Tibetan Plateau. The transpressional stress has emerged in eastern margin of the Tibetan Plateau and has resulted in several large-scale active faults. The transpressional behavior has changed the flowing direction of the rivers from NW-SE to nearly N-S. The transport capacity of these southward-flowing rivers decreases correspondingly. Since the late Cenozoic, intensive seismic events have occurred on the active faults of the eastern Tibetan Plateau which resulted in geohazards such as slope failures, landslides along these southward-flowing rivers. This resulted in the formation of a large number of dammed lakes in the eastern margin of the Tibetan Plateau. To a certain degree, these dammed lakes play an important role in lowering the upstream erosion rate and in accelerating downstream river incision which yields gravity unloading and uplift of the bedrock. The frequently and widely distributed damming events, therefore, forms an important supplementary factor with respect to the formation of high and steep landforms.

Keywords: Eastern tibet, continental transpressional zone, Earthquake-induced dammed lakes, step-pool system, high-elevation and high-relief topography

OPEN ACCESS

Edited by:
Xiaoping Yuan, GFZ German Research Centre for Geosciences, Germany

Reviewed by:
Gang Rao, Southwest Petroleum University, China
Haopeng Geng, Lanzhou University, China

***Correspondence:**
Hailong Li
13811539443@126.com
Yujun Sun
sunyujunabc@163.com

Specialty section:
This article was submitted to Quaternary Science, Geomorphology and Paleoenvironment, a section of the journal Frontiers in Earth Science

Received: *08 October 2021*
Accepted: *24 January 2022*
Published: *22 February 2022*

Citation:
Li H, Sun Y and Zhang Y (2022) Chain Actions Generated High-Elevation and High-Relief Topography of the Eastern Margin of the Tibetan Plateau: From Deep Earth Forces to Earthquake-Induced Dams. Front. Earth Sci. 10:791264. doi: 10.3389/feart.2022.791264

INTRODUCTION

Rapid uplift around eastern margin of the Tibetan Plateau generated a high-elevation and high-relief topography in the formation of NE-trending mountain chains (Kirby et al., 2002), including Minshan Mountain, Longmenshan Mountain, and Gonggarshan Mountain. The elevation drops nearly 4,000 m from the Bayan Har block to the Yangtze craton over a distance of 30–50 km, which marks the geomorphological boundary in the East Tibetan Plateau (Liu-Zeng et al., 2008). However, there are still many controversies about the formation and preservation of such high and steep landforms.

Previous studies have proposed at least two typical models to explain the formation of high and steep landforms. One is the crustal shortening model. Hubbard and Shaw (2009) report that crustal shortening across the high and steep landscape varies from around 2–40%, which dramatically increases upon approaching and crossing Longmenshan Mountain. Tian et al., 2016 shows the similar evidence of late Cenozoic thrusting along major Longmenshan faults. However, a comparative analysis was conducted and the results showed that the crustal-shortening strain in eastern Tibetan Plateau is much lower than that in the northeastern Tibetan Plateau, where crustal shortening can reach up to 46% (Gao et al., 2013) and varies from 20% to >60% across the southern Qilian Shan–Nan Shan thrust belt and northern Qaidam Basin (Yin et al., 2008). In fact, the eastern margin of the Tibetan Plateau is much higher and steeper than northeastern Tibetan Plateau. Thus, The shortening of the crust is not the only determinant of the formation of high and steep landforms. Another model is the lower crustal flow model. The model proposes that lower crustal material flows around the strong crust of the Sichuan Basin and "piles up" the material above to create narrow and steep margins (Clark and Royden, 2000; Royden et al., 2008). However, recent seismological results indicate that lower crustal flow does not universally exist, with the deformation of Eastern Tibetan Plateau also being influenced by oblique thrusting of major NW-striking faults (Gao et al., 2013; Liu et al., 2015). In addition, some studies have assumed that climate-induced surface erosion is a predominant factor that determines the formation of high and steep landforms in eastern margin of the Tibetan Plateau (England and Molnar, 1990; Molnar and England, 1990). However, the premise of this assumption is that there should be a pre-existing high elevation difference in the terrain.

Therefore, while previous studies have provided us with possible causes, no single process offers a satisfactory interpretation to the formation and preservation of such terrain, which means the responsible dynamic mechanisms remain unclear.

DEEP EARTH FORCES AND LANDFORM CHANGES

A Continental Transpressional Zone in Eastern Margin of the Tibetan Plateau

The formation of landforms comes from the interactions between deep Earth forces and surface processes (Cloetingh et al., 2013; Cloetingh and Willett, 2013). During the Indo-Asian collision, strong south-north shortening in the Tibetan Plateau occurred (Yin and Harrison, 2000; Tapponnier et al., 2001; Wang et al., 2002). However, slight shortening occurred on the western side of the Yangtze craton, which is adjacent to the eastern Tibetan Plateau. Such great differences in deformation will inevitably lead to a tectonic transition zone which will show special neotectonic characteristics between Tibetan Plateau and the Yangtze craton. Some tectonic processes show the formation of this transition zone.

On one hand, the eastern Tibetan Plateau is cut a series of relatively independent blocks by a series of NW-striking faults

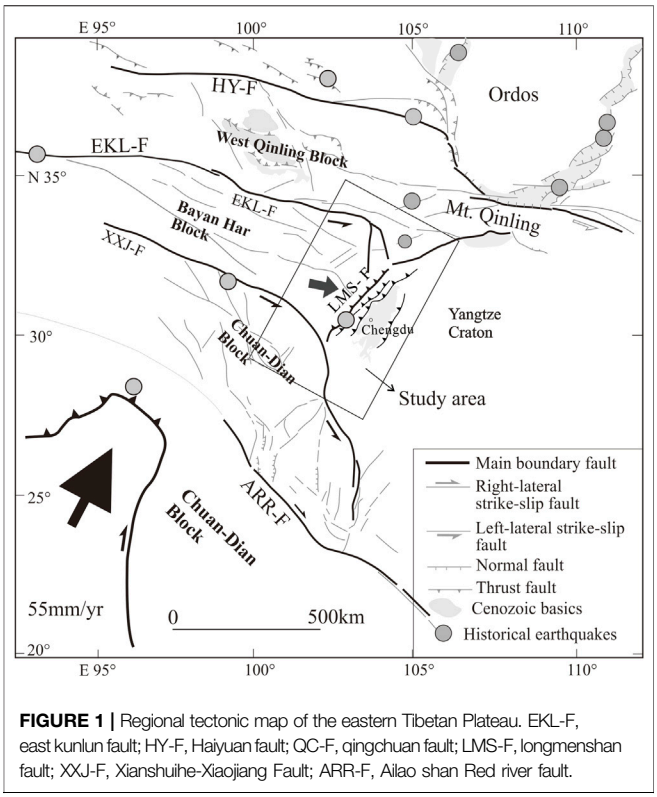

FIGURE 1 | Regional tectonic map of the eastern Tibetan Plateau. EKL-F, east kunlun fault; HY-F, Haiyuan fault; QC-F, qingchuan fault; LMS-F, longmenshan fault; XXJ-F, Xianshuihe-Xiaojiang Fault; ARR-F, Ailao shan Red river fault.

(**Figure 1**). GPS velocity data shows that material of the Tibetan Plateau is extruding from west to east (Shen et al., 2005; Gan et al., 2007). Due to the resistance of the stable Yangtze craton on the eastern side of the Tibetan Plateau, crustal material accumulated and created a broad and steep margin in eastern Tibetan Plateau (Clark and Royden, 2000). On the other hand, the eastward extrusion was approximately orthogonal to the convergence vector and extended along several major sinistral strike-slip fault zones on the eastern Tibetan Plateau (Tapponnier et al., 2001). The regional principal compressive stress is not perpendicular to the western boundary of the Yangtze craton, which promotes the formation of an oblique convergence between the two blocks. Under the common restriction of the two aspects mentioned above, there formed a comparatively restricted transperessional zone, showing a macroscale NE-trending. along eastern margin of the Tibetan Plateau (as seen in the white rectangle of **Figure 2**). In the transperessional zone, there are two large, arc-shaped fault systems named as the Xianshuihe-Xiaojiang fault zone and the East Kunlun-Minjiang/Huya fault zone. Both of them show N-NW striking trends in the interior of the plateau and then near NS-striking along eastern margin of the Tibetan Plateau (**Figure 1**).

The Great Bent Rivers in the Eastern Margin of the Tibetan Plateau

The morphological characteristics and evolutionary history of the fluvial systems are also controlled by surface uplift, especially in actively deforming regions (Clark et al., 2004). The upstream of

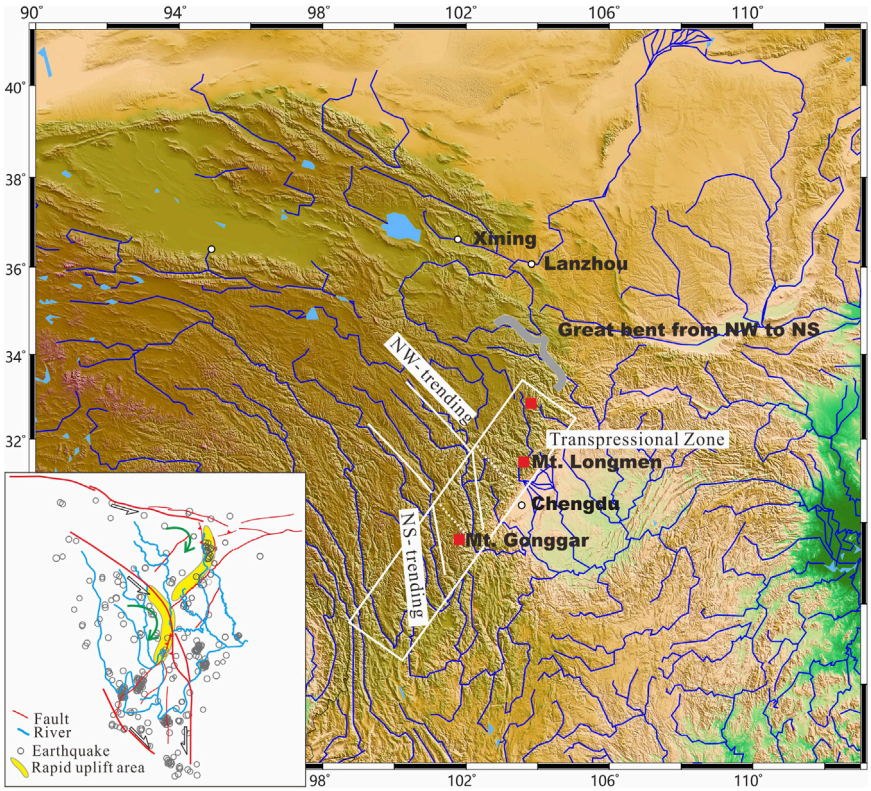

FIGURE 2 | Characteristics of the continental transpressional zone in the eastern margin of the Tibetan Plateau. White dots denote the main cities in this region. The insert map in the lower-left corner shows the fault systems, river systems, and past earthquakes of eastern margin of the Tibetan Plateau.

the Yangtze River is composed of different branches. From east to west, they include the Tuojiang, Minjiang, Qingyijiang, Daduhe, Yalongjiang, and Jingshajiang Rivers. These rivers are neither perpendicular to the NE-trending mountain chain in the eastern margin of the Tibetan Plateau nor parallel to it. On the contrary, they generally show the characteristics of strong curve in their flow direction (**Figure 2**). In particular, the remarkable bend from a southeastward to near southwards flow direction geographically, Clark et al. (2004) calls it the superposition of eastward and southward draining rivers. The sudden changing of river flow from NW-flowing to nearly NS-flowing caused by fault zone in the east edge of the rivers exists in a universal way. Such as in Ya-lung River and in Jinsha River (**Figure 2**). This paper focuses more on the macro hydrographic distribution characteristics. However, such characteristics can't always be observed in a river, such as in the upstream of Min-Jiang River. We prone to consider the feature of NW-to-NS is the primary form of antecedent stream as the latest study by Zhao et al. (2021). In the process of landform uplifting, the hydrographic system of original Tibet Plateau showed NW-to-NS flowing and endured spatial transformation lately (Zhao et al., 2021). These south-flowing rivers coincides with the active faults in the eastern Tibetan Plateau and affected by active fault (Li et al., 2010; Yan and Lin, 2015), showing similar features as those of the two large arc-shaped fault zone aforementioned (**Figures 1**, **2**).

Assuming that the migration of the rivers would only be controlled generally by gravity, the flow direction of these rivers should be perpendicular to the NE trending gravity gradient zone, hence flowing NW, rather than a uniform macro bend from NW to near NS. The universal drainage pattern in eastern margin of the Tibetan Plateau reflects the general and macro-control of the transpressional stress during the Indo-Asian collision (Brookfield, 1998). A simple comparison shows that the length and tortuosity of these bent rivers may increase by 20–30% under the existence of tectonic forces. Since the length and tortuosity of a river defines the associated hydrodynamic forces, the slope, current speed, and transport capacity of these rivers decreased.

ACTIVE FAULT AND LANDSLIDE DAM

Landslide dam or dammed lake caused by earthquake are widely developed within intraplate orogenic belts, active belts, and active continental margins, such as the southern Himalayas (Hewitt, 1998; Srivastava et al., 2013; Draganits et al., 2014), Taiwan Island (Lin et al., 2008; Hsu and Hsu, 2009; Hsieh et al., 2012), the Cordillera orogenic belt (García-García et al., 2011), New Zealand (Adams, 1981; Korup, 2004), and the West Bank of *Argentina* (Bookhagen et al., 2001; Hermanns and Strecker, 1999; Trauth and Strecker, 1999). The eastern margin of the Tibetan Plateau belongs to the NS-

trending Earthquake Belt in China, where many N-S striking active faults have developed (Deng et al., 2002; Deng et al., 2003). In some occasions, NW-striking high-slipping active faults overprint the N-S fault belts. Both of these have hosted many large to moderate earthquakes in the eastern margin of the Tibetan Plateau (Ma et al., 1989; Deng, 2008; Zhang, 2008; Zhang et al., 2009). For example, more than 10 strong earthquakes with magnitudes greater than 7 have occurred on the Xianshuihe- Xiaojiang fault over the past 150 years (Ma et al., 1989; Deng, 2008; Zhang, 2008; Zhang et al., 2009), which have caused a series of landslides and dammed lakes. On 1 June 1786, an earthquake of M 7.75 occurred in the Xianshuihe fault zone, forming a large, dammed lake in the Daduhe River, Sichuan Province, China. The subsequent failure of the dammed lakecaused great damage, with around 100,000 people lost (Dai et al., 2005; Korup and Tweed, 2007). The M 7.5 Diexi earthquake, 25 August 1933, also lead to a dammed lake, whereabout 45 days later, the landslide dam, with a height of around 160 m, collapsed due to aftershocks and rainstorms, causing thousands of casualties (Tang et al., 1983; Wang et al., 2005; Wang et al., 2007). Strong seismic events around Longmenshan Mountain brought about mass movements, such as slope failure, landslides, and damming events (Guo et al., 2016a). The Ms 7.9 Wenchuan earthquake provides us with a vivid example, in which approximately 400 million m^3 of loose sediments were deposited during the earthquake, with dammed lakes diffused throughout the southward-flowing rivers (Huang and Fan, 2013; Guo et al., 2016b).

The formation of earthquake-induced landside dams is the most important component for the landform (Chai et al., 2000; Huang, 2007). The eastern margin of the Tibetan Plateau is one of the most seismically active areas in the world. In addition to the large elevation difference, this area is also have a high stress state (An et al., 2010) and a significant gravity imbalance within the deep crust. It is undoubtedly one of the steepest terrains in the world, with the most complex surface geometries of all orogenic belts. Such remarkable topographic gradients provide the most favorable locations for the occurrence of landslides, with about 80% of the large-scale landslides in China occurring around eastern margin of the Tibetan Plateau (Huang, 2007). In short, the strong interweaving and transformation of the endogenic and exogenic forces in this region promote the development of large landslides and dammed lakes (Huang, 2007).

DAMMING PRESERVATION AND LANDFORM EVOLUTION

Dammed lakes are usually sustained for a short time: about 27% break down within 1 day, 41% within 1 week, more than half within 10 days, 80% within half a year, and 93% within 1 year (Schuster and Costa, 1986). Those dammed lakes that survive for more than 100 years are termed steady-state dammed lakes (Nie et al., 2004). This is because the dam-body mainly consists of loose and unconsolidated rock and soils that are rapidly deposited and accumulated in the river. Thus, the dam may be damaged rapidly due to overflow, piping, seepage, or overtopping (Costa and Schuster, 1988; Casagli et al., 2003; Nie et al., 2004; Shi et al., 2010). However, at the upstream of the Yangtze River, there are still many dammed lakes

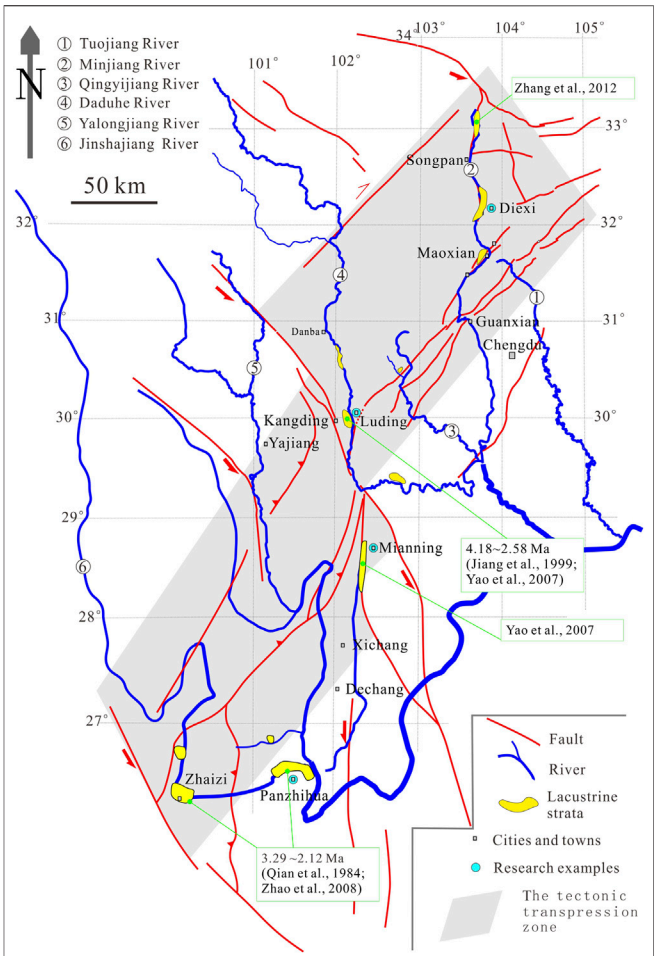

FIGURE 3 | River system and its associated dammed lakes in eastern margin of the Tibetan Plateau (modified from Liu et al., 2015). The shaded part is the approximate range of the tectonic transpression zone.

that have survived for tens of thousands or even for millions of years. What impact they have on river evolution is therefore an important scientific issue worthy of attention. The following two examples are presented to clarify the overlooked impact of such features.

The Diexi Dammed Lake

The Diexi dammed lake developed in the upstream of the Minjiang River (**Figures 4**). The maximum thickness of the lacustrine strata is around 200 m. Field distribution characteristics of the lacustrine strata and remote sensing analysis show that the dammed lake is around 20 km in length (Li et al., 2010). Geochronological dating of the lake deposits show that it formed between around 30 to 74 ka. BP (Wang et al., 2005; Li et al., 2010; Wang et al., 2011a). In the interior of the dammed lake, the secondary dam-body formed by landslide can also be found (**Figure 4C**). On the northern side of the dam, the detachment or the slip plane can be observed in the bedrock (**Figures 3**, **4D**). Meanwhile, the inclined bedrock is almost parallel to the slope, showing the form of typical bedding-controlled landslides. Interior of the dam show bedding of giant gravels which maintained the overall shape of the

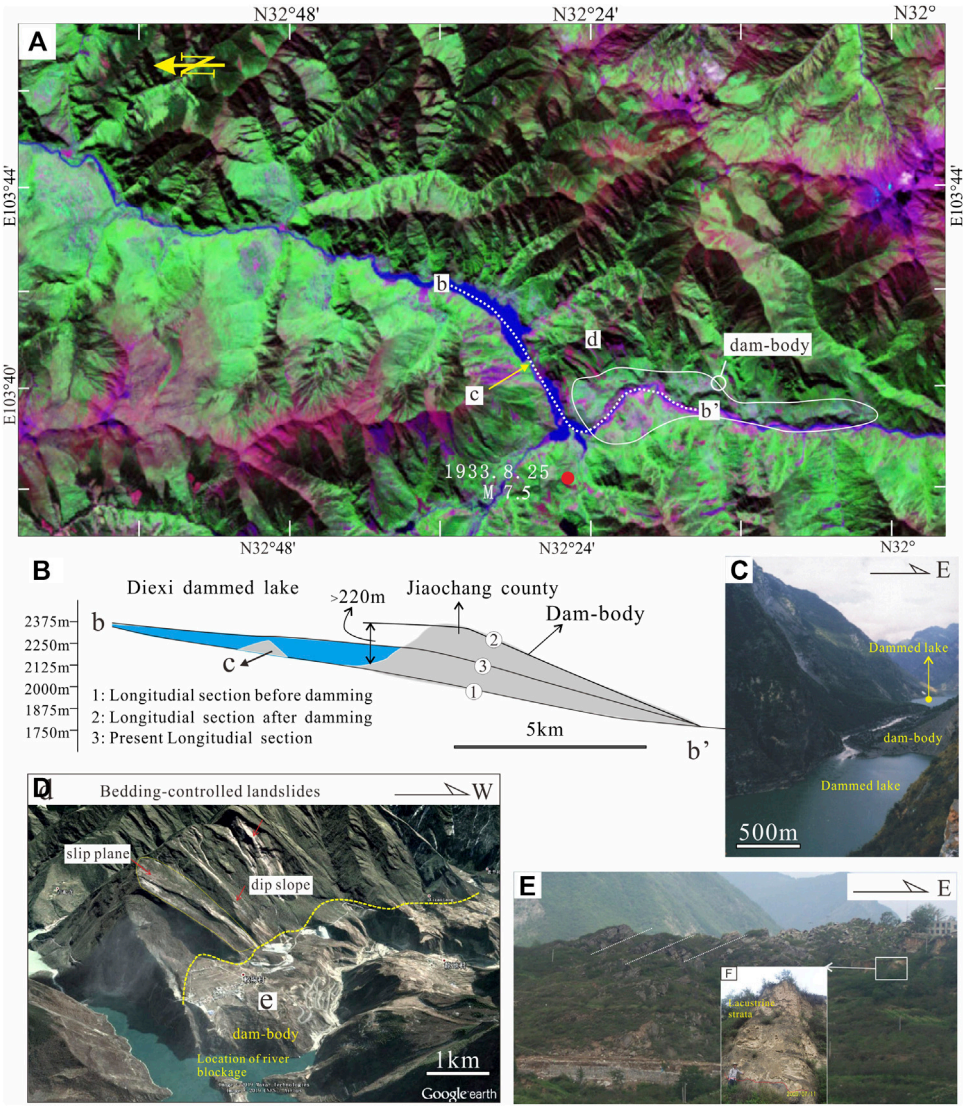

FIGURE 4 | (A) Satellite image and sections of the Diexi dammed lake along the Minjiang River (modified from Li et al., 2010). **(B)** The conceptual longitudinal section across the Diexi dammed lake (modified from Li et al., 2014). **(C)** Field photos of the Diexi dammed lake. **(D)** Landslide surface on the north side of the dammed lake. **(E,F)** Examples of the huge gravel in the debris that consisting the dam.

bedrock structure (**Figure 4E**). This suggests that these gravels come from a great landslide of bedrock from the east (**Figure 4D**), which was probably caused by a large earthquake. Lacustrine strata showing approximately horizontal and parallel bedding are deposited above these gravels (**Figure 4F**), which implies that the area was once submerged by the dammed lake.

When a dammed lake is full, it will form a waterfall at the facade and then incision occurs. In terms of the erosion rate, the average vertical incision rate on the downstream of the Diexi dammed lake is around 1810 m/Ma (Zhang et al., 2005). However, until now, the Minjiang River has not completely cut through the lacustrine strata. On the contrary the dammed lake is now being cut. This means that the incision rate of the upstream near the dammed lake is nearly zero after around 30 ka (if we regarded 30 ka as the formation time of the dam).

From the interior of these lacustrine strata, some evidences have been obtained to show the existence of paleo-earthquakes in the region, with each of the disturbance layers in the lacustrine strata representing a paleo-earthquake event that disturbed the unconsolidated strata (Wang et al., 2011b). It needs to be noted that the epicenters of these paleo-earthquakes may not just be in Diexi Country. In 1933, an *Ms*. 7.5 earthquake occurred and formed a new dammed lake superimposed on the ancient dammed lake (Ren et al., 2018). This makes the dammed lake bigger and the crest stronger. As a result, it will continue to affect the river's geomorphology.

The Xigeda Dammed Lake

The Xigeda formation is a set of lacustrine strata with considerable thickness widely distributed in the upstream of

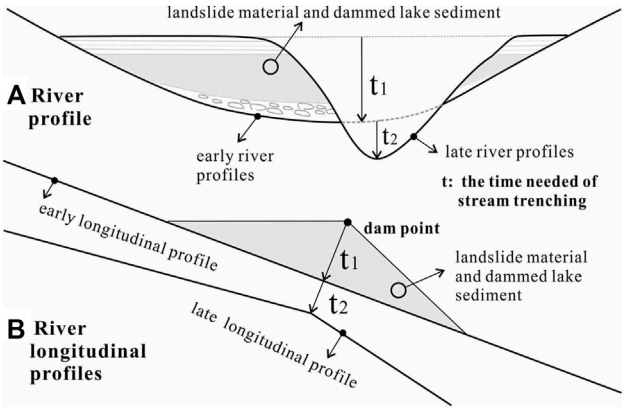

FIGURE 5 | A conceptual model about the changes between river profile and river longitudinal profile after the formation of a dammed lake (Assuming that the unconsolidated lacustrine strata will be cut through a very short period, t1 should be a short time during the stage of dam-break).

the Yangtze River in eastern Tibetan Plateau. It is also considered to have formed as a dammed lake (Chen et al., 2004; Xu, 2011; Xu and Liu, 2011; Deng et al., 2021).

The Xigeda Dammed Lake in Dadu River

The age and thickness of the Xigeda formation vary across different reaches. For example, the Xigeda formation is 930 m higher than the current riverbed around the Dadu River which is a tributary of the upper reaches of the Yangtze River. The thickness of the Xigeda formation in this area is more than 400 m. Paleomagnetism studies show that the formation age is between 4.18 and 2.58 Ma (Jiang et al., 1999; Yao et al., 2007). It can be inferred from the data that the duration of the former dammed lake is up to 1.6 Ma. From the point of view of hydrodynamics, the upstream channel of a dammed lake is in an aggradation state during the life span of the lake. After around 2.58 Ma, when the dammed lake broke, the river began to down-cut. Here, this paper draws a conceptual model about the changes between river profile and river longitudinal profile after the formation of a dammed lake (**Figure 5**). Assuming that the incision rate was constant and that the unconsolidated lacustrine strata will be cut through a very short period, the minimum incision rate of the Dadu river should be 930 m/2.58 Ma = 360 /Ma, while the maximum incision rate should be equal to (930 m + 400 m)/2.58 Ma = 515 m/Ma. The maximum time the river needs to cut through the dam should be equal to 400 m/(515 m/Ma) = 0.78 Ma.

Calculated in this way, it can be determined that the incision rate is between 360 m/Ma and 515 m/Ma after 2.58 Ma. It can also be estimated that a single-loop process of the dammed lake, from emerging to breaking down completely, takes a time which equal to (4.18–2.58 + 0.78) Ma = 2.38 Ma. Thus, the impact time of the lake is between ~1.6 Ma to ~2.38 Ma under conservative estimates.

The Xigeda Dammed Lake in the Jinshajiang River

Xigeda dammed lake near Panzhihua City is also found along the main stream of the Jinshajiang River, a branch of the Yangtze River. The maximum thickness of the Xigeda lacustrine strata here is around 300 m. Paleomagnetic studies show that the dammed lake formed between 3.29 Ma to 2.12 Ma (Qian et al., 1984). At present, the height difference between the riverbed and the bottom of the lacustrine layer is around 100 m (Zhao et al., 2008). The incision rate following the formation of the dammed lake is (300 m + 10 0 m)/2.12 Ma ≈ 188 m/Ma. It can be inferred that the maximum value of influence derived from the dammed lake on the river's evolution can reach about (3.29–2.12) Ma+ 2.12 Ma* 300 m/(300 m + 100 m) = 2.76 Ma. The real impact time is therefore between around 1.07 Ma to 2.76 Ma.

The Xigeda Dammed Lake in the Others River

Since the formation of a dammed lake, there has been both erosion and sedimentation in the lake. We have also found Xigeda formationin Mianning City along the Anninghe River (**Figure 3**). The measurable thickness of the Xigeda formation is more than 300 m (Yao et al., 2007). However, the bottom of the lacustrine stratum is lower than current riverbed in several sites. This shows the Xigeda formation has not been exposed completely. Another example in the upper reaches of the Minjiang River, where a borehole has revealed that the thickness of the Xigeda lacustrine strata is more than 100 m in the current river channel (Zhang et al., 2012).

Recently, it has been reported that different age ranges have been obtained for the Xigeda formation, such as 1.34 to 1.58 Ma (Kong et al., 2009) and 200 to 700 ka (Wang et al., 2011a). Such a dispersed range of ages is, on the one hand, due to the limitations of current dating technology, especially for late Cenozoic sediments, while also reflecting the complexity of these lacustrine strata.

Similar to the Diexi dammed lake, these dammed-lake deposits for a multi-stage dam-break loop circulation process until it completely disappears. From the perspective of river evolution, Zhao et al. (2008) pointed out that the gravel layer at the bottom of the Xigeda formation was found close to the bottom of the Jinshajiang River. This indicates that the river had been down-cut to a depth that was close to the bottom of the current valley several million years ago, which requires the pre-existing channel was filled and downcutted again. While these rivers are still experiencing ongoing incision, over the long term, namely, from the emergence to the final disappearance of the dammed lake, the incision rate was close to zero. These data, therefore, provide us with a fact that the amount of incision in the eastern margin of the Tibet Plateau is quite small. However, many thermochronological studies suggest ~10 Ma initiation of the last phase of rock uplift on the eastern margin of the Tibetan Plateau (much strongly uplifted since around 5 to 3 Ma), and shows the relatively deep exhumation of rocks along its eastern margin, by about 8–10 km (Kirby et al., 2002; Wang et al., 2012; Yang et al., 2020).

The strong uplift should have resulted in relatively rapid erosion or incision due to the river and deeply incise the bedrock in the high and steep eastern margin of the Tibetan Plateau. This is in contradiction with the previously introduced long-term preserved dammed lakes. To better understand this conundrum, a simple experiment is conducted. We present two terms: ***Unloading Capacity*** and ***Unloading Ratio***. The former

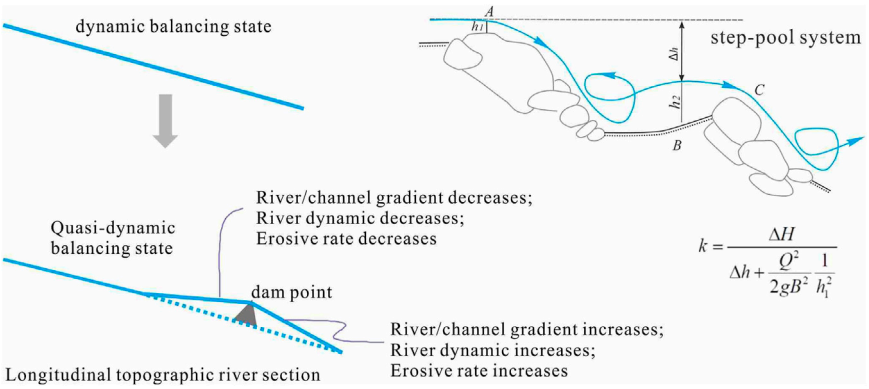

FIGURE 6 | Energy dissipation in a dammed river. Energy dissipation $k = \Delta H/(\Delta h + Q^2/2gB^2h_1^2)$, where Δh is the difference between two surface elevations from point A to point C, Q is the water flow, B is the width of the river, and h_2 is the depth of the water (Xu and Wang, 2004).

refers to the carrying capacity which can be measured by the amount of unloading of a river. The latter refers to the ratio between carrying capacity and loose sediment. A lot of loose sediments, rocks, debris, and landslides, which are derived from the strong earthquakes and weathering in the region, are accumulated and fill up these rivers' branches. However, these rivers could not unload this added material immediately or quickly. After the Wenchuan earthquake, Parker et al. (2011) estimated that coseismic landslides produced amounts of erodible material which were greater than the net volume added to the orogen by coseismic rock uplift, even if only a fraction of landslide debris is removed from the orogen over the earthquake recurrence period. Although the unloading amount is very large in the eastern Tibetan Plateau, the unloading ratio is not high enough. This indicates that frequent damming behavior and strong unloading can cause river accretion, which can counteract a river's incision because of the rock uplift. Beyond our intuitive knowledge, the unloading ratios of these rivers were not as strong as expected. To a certain degree, eastern margin of the Tibetan Plateau plays a role as a large-scaled damming or blocking system, over the last around 4 Ma.

LANDSCAPE DEFORMATION AND ENERGY CONVERSION

To illustrate the energy conversion process of the dammed lakes, we should trace back to the beginning when a dammed lake formed. The formation of a dammed lake is accomplished within a short time. Earthquakes are one form of the internal energy released by the deep Earth. Driven or triggered by seismic energy, landslides, rock collapses, and debris flows are other forms of potential energy release. After the formation of the dammed lake, the river water level rises and the potential energy increases. Hence, the formation and destruction of earthquake-induced dammed lakes reflect instantaneous energy transformation in nature.

In the process of river evolution, the formation of knickpoints could raise the erosion basis and slow down the erosion rate of the upstream channel. Earthquakes can create dammed lakes and then form a knickpoint in the long profile whenever a damming event occurs on a river, which caused the ups and downs of the river in the long profile and can reduce the kinetic energy of rivers (**Figure 5**). This phenomenon is similar to the "step-pool system" (**Figure 5**) (Xu and Wang, 2004; Wang et al., 2006; Zhang et al., 2011). As shown in **Figure 5**, the energy dissipation ratio k of the reach ABC is given by:

$$k = \frac{\Delta H}{\left(\Delta h + \frac{Q^2}{2gB^2h_1^2}\right)} \quad (1)$$

where $\Delta H = \Delta h + \frac{Q^2}{2gB^2}\left(\frac{1}{h_1^2} - \frac{1}{h_2^2}\right)$, Δh is the height difference of the water surface at the top of two consecutive steps, and Q is the rate of flow (Xu and Wang, 2004). According to the formula, k is always larger than 1 in the "step-pool system," that is to say, the system always consumes water energy and slows down river erosion. In particular, continuous damming behaviors can also cause cumulative effects of hydrodynamic attenuation, which can decrease the erosion rate in the upstream areas of these rivers, where the riverbed is then protected. However, for the downstream areas, the damming events usually form a waterfall and enhance the hydrodynamic force. These effects will increase river incision in the downstream parts and lead to the unloading and uplift of bedrock. In fact, there always exist many step-pool systems in a river. In the Minjiang River, for example, there are several dammed lakes on the downstream side of the Diexi dammed lake. The influence of continuous step-pool systems on river hydrodynamic forces should not be underestimated. The longer the retention of the step-pool system, the greater the change in hydrodynamic force and the stronger the ability to shape the landforms.

The Diexi dammed lake, with a height of ~200 m (**Figure 4**) and an impact time of >40 to 70 ka, will continue to affect the river landforms for a long time. The height of the dammed lake in Jinsha River is ~300 m, and the duration of its impaction is greater than 1.16 Ma. The Xigeda dammed lake on the Dadu River, with a height of around 400 m, has an impact time of more

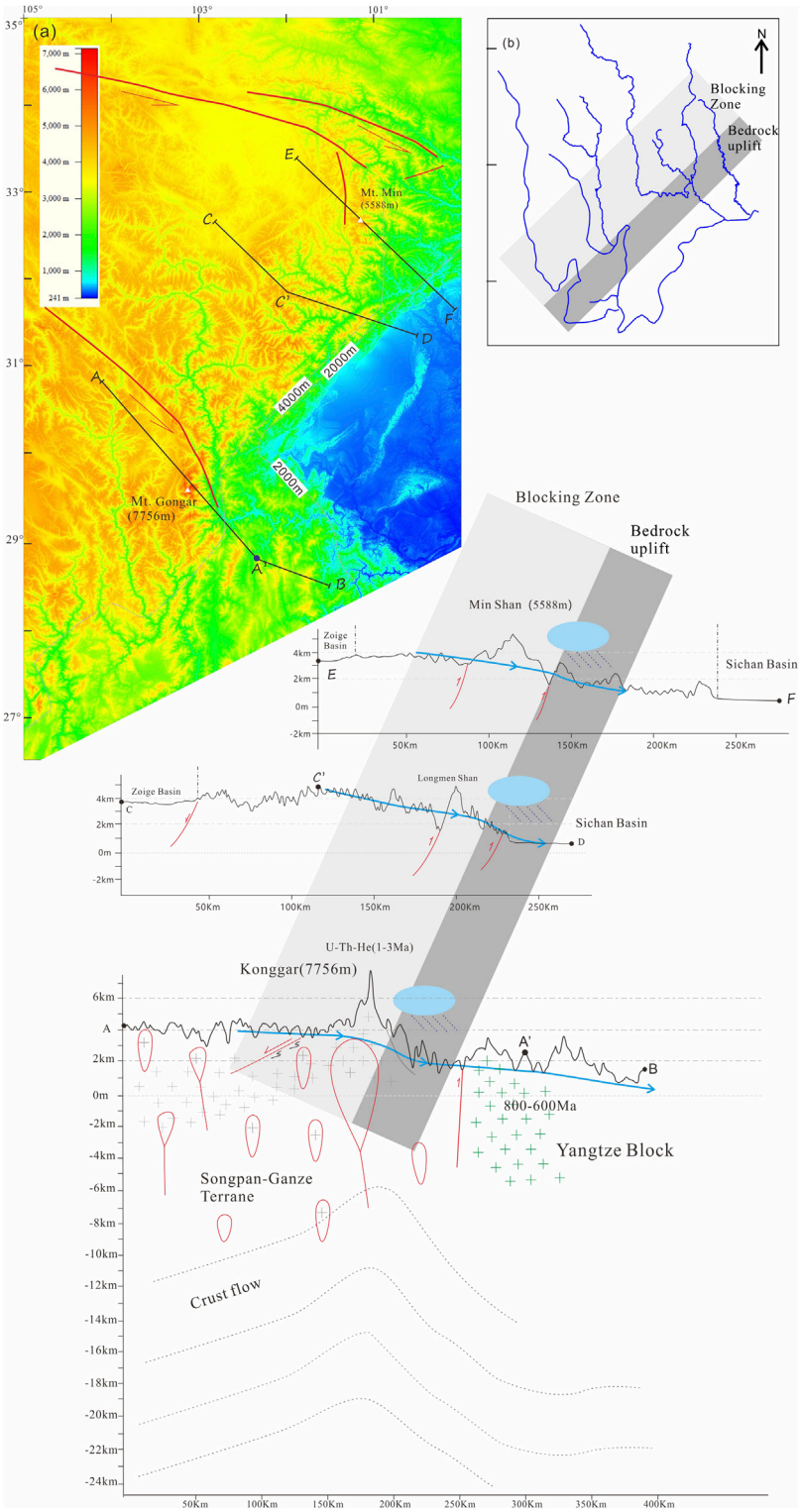

FIGURE 7 | Landform analysis of the eastern Tibetan Plateau (The map summarizes the causes of the high and steep landform on the East Tibet. The approximate spatial position of the blocking area is marked in the map. From the perspective of exogenic forces, heavy rainfall frequently occurs in the piedmont of the eastern margin of Tibet Plateau, which speeds up the denudation rate and makes an obvious contribution to high and steep landform. From the perspective of endogenic forces, three topographical sections are provided here. Profile A-B passes through the Gonggar mountain. Scholars believe that there is lower crustal flow in its deep part (Clark

(*Continued*)

FIGURE 7 | and Royden, 2000; Zhang 2008; Liu et al., 2015)., which is the influence of deep structure on landform. Profile C-D passes through Longmenshan mountain, and the compressive uplift of thrust fault zone is the main controlling factor of geomorphic uplift (Tian et al., 2016; Gao et al., 2013). Profile E-F passes through the Minshan mountain, one of the highest peaks in the northeast margin of Tibet Plateau, and is controlled by two boundary faults (the Minjiang and Huya fault). The data of this figure comes from the following websites: http://dds.cr.usgs.gov/srtm/and http://glcf.umiacs.umd.edu/data.

than 1.6 Ma. During these periods, it can be considered that the river cutting rate is near zero for the upstream areas of a dammed lake, at least within the range of tens or even near a hundred kilometer from it. Macroscopically speaking, the cutting rate during these periods will also be very low. From the point of view of river incision ratios, during this period of around 4 to 3 Ma, there must be a sharp decrease or a gap in the average incision rate. This had been discovered by the research on the Dadu River (Ouimet et al., 2007; Ma et al., 2020). These examples also reflect the basic fact that once a large-scale dammed lake has formed, it will play a continuous role in the evolution of river geomorphology over long timescales. It is therefore definitely the case that damming behaviors associated with frequent earthquake events are closely related to processes of mountain building.

DISCUSSION

How should we understand the formation of high and steep landform in the eastern margin of the Tibetan Plateau? We thought that the process was similar to building a skyscraper, adding materials bit by bit. From this point of view, the primary reason for the formation of high and steep landforms is the accumulation of materials within the body and to reduce material erosion on its surface. There are four ways for material accumulation.

The first way is the overlapping of crustal materials from horizontal contraction deformation, such as the thrust caused by the extrusion of the eastern Tibetan Plateau. The second way is the upwelling of deep materials in the vertical direction. The third way is the weakening of erosion in terms of external dynamics, and the fourth way is the strengthening of the aforementioned three ways by the coupling of internal and external dynamics. These aspects will now be discussed.

First, compression deformation is always the essential cause of geomorphic uplift, because it is the most effective means of material accumulation, not only in the eastern margin of the Tibetan Plateau but in all orogenic belts around the world. The structural pattern is an important factor in the process of material accumulation. Compression stress in the eastern Tibetan Plateau has shown the characteristics of transpressional deformation since the middle to late Cenozoic. As a result, the convergence deformation in the upper crust has seen dramatic shortening, for example, up to 40% for Longmenshan Mountain (Hubbard and Shaw, 2009) while also resulting in the characteristics of the strike-slip and oblique thrust of the Longmenshan fault zone. Li et al. (2008) showed that oblique thrust is the most effective way of controlling the rapid rise of the mountains through a large number of case studies, such as the Altun fault, the East Kunlun fault, and the Longmenshan fault.

Secondly, deep material upwelling also plays a role in material accumulation. Our previous findings have shown that the youngest magma (14.4–3.6 Ma) in the Tibetan Plateau is emplaced under Mt. Gonggar (unpublished data), where unroofing is dated from 11 to 1 Ma by low-temperature thermochronological dating (Xu and Kamp, 2000; Lai et al., 2007). We are inclined to believe that transpressional behavior plays a vital role in the ascent and emplacement of magma (or deep-earth materials) and provides the space occupied by the upwelling of the youngest magma. This space is eventually transformed by the uplift of the landscape, such as lower crustal flow (**Figures 6**, **7**).

In this paper, we noted that the highest mountain peaks, for example, Mt. Gonggar (7,756 m) and Mt. Min (5,588 m), as well as the fastest-growing places in eastern margin of the Tibetan Plateau, are all located at the bend of the two big arc-shaped faults aforementioned (**Figure 7**). Also, analog experiments (Mazzarini et al., 2010) and a large number of field examples indicate that strike–slip deformation is favorable for magma emplacement (Cao and Neubauer, 2016).

Thirdly, there can be no doubt that the formation of high and steep landforms is the result of the influence of internal and external dynamics. Molnar and England (1990) first noted the frequent rainfall around Longmenshan Mountain. Under the action of gravity equilibrium, the crustal material rebounds and causes the uplift of the landscape (Molnar and England, 1990; Zhang et al., 1994). In subsequent research, Korup and Montgomery (2008) showed that moraine-dammed lakes not only inhibit bedrock incision during their lifetime but also promote the upstream aggradation and burial of bedrock valley floors under glaciofluvial sediment long after the dam's formation. Reviewing these mechanisms (Korup and Montgomery, 2008) and combining them with the results of this paper, we conclude several key points that can help us to understand the high and steep landforms in the eastern margin of the Tibetan Plateau.

1) When a dammed lake is formed, it can be considered that the river changes from a dynamic balancing state to a quasi-dynamic balancing state (**Figure 6**). Taking the dammed lake as a knickpoint, the trunk can be divided into upstream and downstream sections where the hydrodynamic processes change between the ups and downs correspondingly. This is closely related to the erosional or incisional processes and represents the mechanism of the step-pool system (**Figure 6**).
2) In longitudinal sections, there should be many big dammed lakes in a river system. Therefore, the decrease in hydrodynamic forces has a cumulative effect.
3) With regards to the evolution of landforms, the impact of one single damming event is insignificant, yet, frequent and

continuous damming events can result in the sustained effect of external forces which can be observed in the eastern margin of the Tibetan Plateau, where frequent seismic events occur.
4) The long-term retention of loose materials can protect the riverbed and lead to weakening denudation. However, this is an extremely complex proposition. We have presented in-depth discussions on this issue (Li et al., 2010; Li and Zhang, 2015), and the conclusion can be summarized into two points, namely that the transpressional structures increase the bending of these rivers and that deep valleys result from rapid crustal uplift.

Finally, comparing the earthquake-induced damming behavior with that resulting from glacial dam in the Yarlung River (Korup and Tweed, 2007; Korup and Montgomery, 2008; Owen, 2008), this paper emphasizes that the effect of these events are similar to river morphology and the hydrodynamic environment. Meanwhile, this paper describes how transpressional stress causes overlapping in crustal materials, as well as spatial adjustment and provides a channel or space for the upwelling of material from the deep Earth, both of which eventually transform into landform uplift. Transpressional behavior therefore strongly affects and bridges surface and deep geological processes. Hence, it provides a new insight into a logical link between the endogenetic and exogenetic forces on the Earth's surface, which results in the high elevation and steep relief in the eastern margin of the Tibetan Plateau.

CONCLUSION

1) Geological coupling between endogenetic and exogenetic forces has resulted in the formation and maintenance of the high-elevation and high-relief topography of eastern margin of the Tibetan Plateau.
2) The continental transpressional stress between the Tibetan Plateau and the Yangtze block, showing contraction deformation and oblique thrusting, strongly affects and bridges surface and deep geological processes.
3) Frequent seismic activity has resulted in widespread large-scale damming events, offering an important insight into the evolution of landscape.

DATA AVAILABILITY STATEMENT

The original contributions presented in the study are included in the article/Supplementary Material, further inquiries can be directed to the corresponding authors.

AUTHOR CONTRIBUTIONS

All authors listed have made a substantial, direct, and intellectual contribution to the work and approved it for publication.

FUNDING

This study was jointly supported by the National Natural Science Foundation of China (grant number 41872223, 41874114), and the Fundamental Research Funds for the Chinese Academy of Geological Sciences.

ACKNOWLEDGMENTS

We thank the Editors and the reviewers for their constructive reviews and encouragement. We hereby to express our sincere gratitude toward Dr. Hongdan Deng, professor Yue Zhao and professor Yuntao Tian.

REFERENCES

Adams, J. (1981). Earthquake-dammed Lakes in New Zealand. *Geol* 9 (5), 215–219. doi:10.1130/0091-7613(1981)9<215:elinz>2.0.co;2

An, M., Feng, M., and Long, C. (2010). Deep Ruptures Around the Hypocenter of the 12 May 2008 Wenchuan Earthquake Deduced from Aftershock Observations. *Tectonophysics* 491 (1–4), 96–104. doi:10.1016/j.tecto.2009.12.024

Bookhagen, B., Haselton, K., and Trauth, M. H. (2001). Hydrological Modelling of a Pleistocene Landslide-Dammed lake in the Santa Maria Basin, NW Argentina. *Palaeogeogr. Palaeoclimatol. Palaeoecol.* 169 (1), 113–127. doi:10.1016/s0031-0182(01)00221-8

Brookfield, M. E. (1998). The Evolution of the great river Systems of Southern Asia during the Cenozoic India-Asia Collision: Rivers Draining Southwards. *Geomorphology* 22 (3), 285–312. doi:10.1016/s0169-555x(97)00082-2

Cao, S., and Neubauer, F. (2016). Deep Crustal Expressions of Exhumed Strike-Slip Fault Systems: Shear Zone Initiation on Rheological Boundaries. *Earth-Science Rev.* 162, 155–176. doi:10.1016/j.earscirev.2016.09.010

Casagli, N., Ermini, L., and Rosati, G. (2003). Determining Grain Size Distribution of the Material Composing Landslide Dams in the Northern Apennines: Sampling and Processing Methods. *Eng. Gelogy* 69 (1), 83–97. doi:10.1016/s0013-7952(02)00249-1

Chai, H., Liu, H., and Zhang, Z. (2000). The Temporal-Soatial Distribution of Damming Landslides in China. *J. Mountain Sci.* 18 (Z1), 51–54. (In Chinese with English Abstract). doi:10.16089/j.cnki.1008-2786.2000.s1.011

Chen, Z., Sun, Z., Royden, L. H., and Zhang, X. (2004). Landslide Blocked lake: Origin of the Xigeda Formation in Luding, Sichuan and its Significance. *Quat. Res.* 24 (6), 614–620. (In Chinese with English Abstract). doi:10.3901/cjme.2004.04.614

Clark, M. K., Schoenbohm, L. M., Royden, L. H., Whipple, K. X., Burchfiel, B. C., Zhang, X., et al. (2004). Surface Uplift, Tectonics, and Erosion of Eastern Tibet from Large-Scale Drainage Patterns. *Tectonics* 23 (1), TC1006. doi:10.1029/2002tc001402

Clark, M. K., and Handy Royden, L. (2000). Topographic Ooze: Building the Eastern Margin of Tibet by Lower Crustal Flow. *Geology* 28 (8), 703–706. doi:10.1130/0091-7613(2000)028<0703:tobtem>2.3.co;2

Cloetingh, S., Burov, E., and Francois, T. (2013). Thermo-mechanical Controls on Intra-plate Deformation and the Role of Plume-Folding Interactions in continental Topography. *Gondwana Res.* 24 (3-4), 815–837. doi:10.1016/j.gr.2012.11.012

Cloetingh, S., and Willett, S. D. (2013). TOPO-EUROPE: Understanding of the Coupling between the Deep Earth and continental Topography. *Tectonophysics* 602, 1–14. doi:10.1016/j.tecto.2013.05.023

Costa, J. E., and Schuster, R. L. (1988). The Formation and Failure of Natural Dams. *GSA Bull.* 100 (7), 1054–1068. doi:10.1130/0016-7606(1988)100<1054:tfafon>2.3.co;2

Dai, F., Lee, C., Deng, J., and Tham, L. (2005). The 1786 Earthquake-Triggered Landslide Dam and Subsequent Dam-Break Flood on the Dadu River, Southwestern China. *Geomorphology* 73 (3), 277–278. doi:10.1016/j.geomorph.2004.08.011

Deng, Q. (2008). Sone Thoughts on the M*s* 8.0 Wenchuan, Earthquake. *Seismology Geology*. 30 (4), 811–827. (In Chinese with English Abstract).

Deng, Q., Zhang, P. Z., Ran, Y., Yang, X., Min, W., and Chu, Q. (2002). Basic Characteristics of Active Tectonics of China. *Sci. China (Series D)* 32 (12), 1020–1030. (In Chinese). doi:10.1360/zd2002-32-12-1020

Deng, Q., Zhang, P., Ran, Y., Yang, X., Min, W., and Chen, L. (2003). Active Tectonics and Earthquake Activities in china. *Earth Sci. Front.* 10 (z1), 66–73. (In Chinese with English Abstract). doi:10.3321/j.issn:1005-2321.2003.z1.012

Deng, B., Chew, D., Mark, C., Liu, S., and Li, J. (2021). Late Cenozoic Drainage Reorganization of the Paleo-Yangtze River Constrained by Multi-Proxy Provenance Analysis of the Paleo-lake Xigeda. *Geol. Soc. America Bull.* 133 (1-2), 199–211. doi:10.1130/b35579.1

Draganits, E., Grasemann, B., Janda, C., Hager, C., and Preh, A. (2014). 300 MW Baspa II - India's Largest Private Hydroelectric Facility on Top of a Rock Avalanche-Dammed Palaeo-lake (NW Himalaya): Regional Geology, Tectonic Setting and Seismicity. *Eng. Geology*. 169, 14–29. doi:10.1016/j.enggeo.2013.11.009

England, P., and Molnar, P. (1990). Right-lateral Shear and Rotation as the Explanation for Strike-Slip Faulting in Eastern Tibet. *Nature* 344 (6262), 140–142. doi:10.1038/344140a0

Gan, W., Zhang, P., Shen, Z. K., Niu, Z. J., Wang, M., Wan, Y. G., et al. (2007). Present-day Crustal Motion within the Tibetan Plateau Inferred from GPS Measurements. *J. Geophys. Res.* 112 (B8), 582–596. doi:10.1029/2005jb004120

Gao, R., Wang, H., Yin, A., Dong, S., Kuang, Z., Zuza, A. V., et al. (2013). Tectonic Development of the Northeastern Tibetan Plateau as Constrained by High-Resolution Deep Seismic-Reflection Data. *Lithosphere* 5 (6), 555–574. doi:10.1130/l293.1

García-García, F., Sánchez-Gómez, M., Navarro, V., and Pla, S. (2011). Formation, Infill, and Dissection of a Latest-Pleistocene Landslide-Dammed Reservoir (Betic Cordillera, Southern Spain): Upstream and Downstream Geomorphological and Sedimentological Evidence. *Quat. Int.* 233 (1), 61–71. doi:10.1016/j.quaint.2010.07.010

Guo, X., Cui, P., Li, Y., Zou, Q., and Kong, Y. (2016a). The Formation and Development of Debris Flows in Large Watersheds after the 2008 Wenchuan Earthquake. *Landslides* 13 (1), 116–125. doi:10.1007/s10346-014-0541-6

Guo, X., Cui, P., Li, Y., Ma, L., Ge, Y., and Mahoney, W. B. (2016b). Intensity-duration Threshold of Rainfall-Triggered Debris Flows in the Wenchuan Earthquake Affected Area, China. *Geomorphology* 253, 208–216. doi:10.1016/j.geomorph.2015.10.009

Hermanns, R. L., and Strecker, M. R. (1999). Structural and Lithological Controls on Large Quaternary Rock Avalanches (Sturzstroms) in Arid Northwestern Argentina. *GSA Bull.* 111 (6), 934–948. doi:10.1130/0016-7606(1999)111<0934:salcol>2.3.co;2

Hewitt, K. (1998). Catastrophic Landslides and Their Effects on the Upper Indus Streams, Karakoram Himalaya, Northern Pakistan. *Geomorphology* 26 (1), 47–80. doi:10.1016/s0169-555x(98)00051-8

Hsieh, M.-L., Lai, L. S.-H., Lin, C. D.-J., and Shyu, J. B. H. (2012). Late Quaternary Landscape Evolution and Genesis of the 2009 Catastrophic Landslide in the Hsiao-Lin Area, Southwestern Taiwan. *Geomorphology* 179, 225–239. doi:10.1016/j.geomorph.2012.08.014

Hsu, Y., and Hsu, Y. (2009). Impact of Earthquake-Induced Dammed Lakes on Channel Evolution and Bed Mobility. Case Study of the Tsaoling Landslide Dammed lake. *J. Hydrol.* 374 (1), 43–55. doi:10.1016/j.jhydrol.2009.05.020

Huang, R., and Fan, X. (2013). The Landslide story. *Nat. Geosci* 6 (5), 325–326. doi:10.1038/ngeo1806

Huang, R. (2007). Large-scale Landslides and Their Sliding Mechanisms in China since the 20th century. *Chin. J. rock Mech. Eng.* 26 (3), 433–454. doi:10.3321/j.issn:1000-6915.2007.03.001

Hubbard, J., and Shaw, J. H. (2009). Uplift of the Longmen Shan and Tibetan Plateau, and the 2008 Wenchuan (M = 7.9) Earthquake. *Nature* 458 (7235), 194–197. doi:10.1038/nature07837

Jiang, F., Wu, X., Xiao, H., and Zhao, Z. (1999). On the Age of the Xigeda Formation in Luding, Sichuan and its Neotectonic Significance. *Acta Geol. Sinica* 73 (1), 1–6. (In Chinese with English Abstract).

Kirby, E., Reiners, P. W., Krol, M. A., Whipple, K. X., Hodges, K. V., Farley, K. A., et al. (2002). Late Cenozoic Evolution of the Eastern Margin of the Tibetan Plateau: Inferences from $^{40}Ar/^{39}Ar$ and (U-Th)/He Thermochronology. *Tectonics* 21 (1), 1001. doi:10.1029/2000tc001246

Kong, P., Granger, D. E., Wu, F., Caffee, M. W., Wang, Y., Zhao, X., et al. (2009). Cosmogenic Nuclide Burial Ages and Provenance of the Xigeda paleo-lake: Implications for Evolution of the Middle Yangtze River. *Earth Planet. Sci. Lett.* 278 (1–2), 131–141. doi:10.1016/j.epsl.2008.12.003

Korup, O. (2004). Geomorphometric Characteristics of New Zealand Landslide Dams. *Eng. Geology*. 73 (1), 13–35. doi:10.1016/j.enggeo.2003.11.003

Korup, O., and Montgomery, D. R. (2008). Tibetan Plateau River Incision Inhibited by Glacial Stabilization of the Tsangpo Gorge. *Nature* 455 (7214), 786–789. doi:10.1038/nature07322

Korup, O., and Tweed, F. (2007). Ice, Moraine, and Landslide Dams in Mountainous Terrain. *Quat. Sci. Rev.* 26 (25), 3406–3422. doi:10.1016/j.quascirev.2007.10.012

Lai, Q. Z., Ding, L., Wang, H. W., Yue, Y. H., and Cai, F. L. (2007). Constraining the Stepwise Migration of the Eastern Tibetan Plateau Margin by Apatite Fission Track Thermochronology. *Sci. China Ser. D* 36 (9), 785–796. doi:10.1007/s11430-007-2048-7

Li, H., and Zhang, Y. (2015). Analysis of the Controlling Factors of Landslide Damming and Dam Failure: an Analysis Based on Literature Review and the Study on the Meridional River System of Eastern Tibetan Plateau. *Quat. Sci.* 35 (1), 71–87. (In Chinese with English Abstract). doi:10.11928/j.issn.1001-7410.2015.01.07

Li, H., Fu, X., Jvan Der Woerd, R. O. M., Si, J., Wang, Z., Hou, L., et al. (2008). Co-seisimic Surface Rupture and Dextral-Slip Oblique Thrusting of the MS 8.0 Wenchuan Earthquake. *Acta Geologica Sinica* 82 (12), 1623–1643. (In Chinese with English Abstract). doi:10.3321/j.issn:0001-5717.2008.12.002

Li, H., Zhang, Y., and Li, J. (2010). Meridional River Systems and Ancient Dammed Lakes on the East Margin of the Tibetan Plateau. *Quat. Sci.* 30 (4), 812–824. (In Chinese with English Abstract). doi:10.3969/j.issn.1001-7410.2010.04.16

Lin, W., Lin, C., Tsai, J., and Huang, P. (2008). Eco-environmental Changes Assessment at the Chiufenershan Landslide Area Caused by Catastrophic Earthquake in Central Taiwan. *Ecol. Eng.* 33 (3), 220–232. doi:10.1016/j.ecoleng.2008.04.002

Liu, Q. Y., Hilst, R. D. V. D., Li, Y., Yao, H. J., Chen, J. H., Guo, B., et al. (2015). Eastward Expansion of the Tibetan Plateau by Crustal Flow and Strain Partitioning across Faults. *Nat. Geosci.* 7 (5), 361–365. doi:10.1038/ngeo2130

Liu-Zeng, J., Tapponnier, P., Gaudemer, Y., and Ding, L. (2008). Quantifying Landscape Differences across the Tibetan Plateau: Implications for Topographic Relief Evolution. *J. Geophys. Res.* 113, F04018. doi:10.1029/2007JF000897

Ma, J., Ma, S. L., and Lei, X. L. (1989). Fault Geometry and its Relationship with Seismicity in the Xianshuihe Fault Zone. *Phys. Chem. Earth* 17, 131–142. doi:10.1016/0079-1946(89)90018-9

Ma, Z., Zhang, H., Wang, Y., Tao, Y., and Li, X. (2020). Inversion of Dadu River Bedrock Channels for the Late Cenozoic Uplift History of the Eastern Tibetan Plateau. *Geophys. Res. Lett.* 47 (4), e2019GL086882. doi:10.1029/2019gl086882

Mazzarini, F., Musumeci, G., Montanari, D., and Corti, G. (2010). Relations between Deformation and Upper Crustal Magma Emplacement in Laboratory Physical Models. *Tectonophysics* 484 (1-4), 139–146. doi:10.1016/j.tecto.2009.09.013

Molnar, P., and England, P. (1990). Late Cenozoic Uplift of Mountain Ranges and Global Climate Change: Chicken or Egg. *Nature* 346 (6279), 29–34. doi:10.1038/346029a0

Nie, G., Gao, J., and Deng, Y. (2004). Preliminary Study on Earthquake-Induced Dammed lake. *Quat. Sci.* 24 (3), 293–301. (In Chinese with English Abstract). doi:10.3321/j.issn:1001-7410.2004.03.008

Ouimet, W. B., Whipple, K. X., Royden, L. H., Sun, Z., and Chen, Z. (2007). The Influence of Large Landslides on River Incision in a Transient Landscape: Eastern Margin of the Tibetan Plateau (Sichuan, China). *Geol. Soc. America Bull.* 119, 1462–1476. doi:10.1130/b26136.1

Owen, L. A. (2008). How Tibet Might Keep its Edge. *Nature* 455 (7214), 748–749. doi:10.1038/455748a

Parker, R. N., Densmore, A. L., Rosser, N. J., de Michele, M., Li, Y., Huang, R., et al. (2011). Mass Wasting Triggered by the 2008 Wenchuan Earthquake Is Greater Than Orogenic Growth. *Nat. Geosci* 4 (7), 449–452. doi:10.1038/ngeo1154

Qian, F., Xu, S., Chen, F., and Zhao, Y. (1984). Study on the Paleomagnetion of the Xigeda Formation. *Mountain Res.* 2 (4), 275–282. (In Chinese with English Abstract). doi:10.16089/j.cnki.1008-2786.1984.04.012

Ren, J., Xu, X., Zhang, S., Yeats, R. S., Chen, J., Zhu, A., et al. (2018). Surface Rupture of the 1933 M 7.5 Diexi Earthquake in Eastern Tibet: Implications for Seismogenic Tectonics. *Geophys. J. Int.* 212 (3), 1627–1644. doi:10.1093/gji/ggx498

Royden, L. H., Burchfiel, B. C., and van der Hilst, R. D. (2008). The Geological Evolution of the Tibetan Plateau. *Science* 321 (5892), 1054–1058. doi:10.1126/science.1155371

Schuster, R. L., and Costa, J. E., 1986. Effects of Landslide Damming on Hydroelectric Projects, in Proceedings 5th International Association of Engineering Geology Congress, 1295–1307.

Shen, Z., Lü, J., Wang, M., and Bürgmann, R. (2005). Contemporary Crustal Deformation Around the Southeast Borderland of the Tibetan Plateau. *J. Geophys. Res.* 110, B11. doi:10.1029/2004jb003421

Shi, Z., Li, J., Lu, C., Wang, Y., and Xu, Q. (2010). Research Status and prospect of the Stability of Landslide Dam. *J. Eng. Geology*. 18 (5), 657–663. (In Chinese with English Abstract).

Srivastava, P., Ray, Y., Phartiyal, B., and Sharma, A. (2013). Late Pleistocene-Holocene Morphosedimentary Architecture, Spiti River, Arid Higher Himalaya. *Int. J. Earth Sci. (Geol Rundsch)* 102 (7), 1967–1984. doi:10.1007/s00531-013-0871-y

Tang, R., Liu, S., and Jiang, N. (1983). *The 1933 Diexi Earthquake: Chengdu*. Chengdu: Sichuan Science and Technology Press. (In Chinese).

Tapponnier, P., Zhiqin, X., Roger, F., Meyer, B., Arnaud, N., Wittlinger, G., et al. (2001). Oblique Stepwise Rise and Growth of the Tibet Plateau. *Science* 294, 1671–1677. doi:10.1126/science.105978

Tian, Y., Kohn, B. P., Phillips, D., Hu, S., Gleadow, A. J. W., Carter, A., et al. (2016). Late Cretaceous-earliest Paleogene deformation in the Longmen Shan fold-and-thrust belt, eastern Tibetan Plateau margin: Pre-Cenozoic thickened crust?. *Tectonics* 35 (10), 2293-2312. doi:10.1002/2016TC004182

Trauth, M. H., and Strecker, M. R. (1999). Formation of Landslide-Dammed Lakes during a Wet Period between 40,000 and 25,000 Yr B.P. In Northwestern Argentina. *Palaeogeogr. Palaeoclimatol. Palaeoecol.* 153 (1), 277–287. doi:10.1016/s0031-0182(99)00078-4

Wang, C., Liu, Z., Yi, H., Liu, S., and Zhao, X. (2002). Tertiary Crustal Shortening and Peneplanation in the Hoh Xil Region: Implications for the Tectonic History of the Northern Tibetan Plateau. *J. Asian Earth Sci.* 20 (3), 211–223. doi:10.1016/s1367-9120(01)00051-7

Wang, L., Dun, L., Yang, L., and Wang, X. (2005). Discovery of Huge Ancient Dammed lake on Upstream of Minjiang River in Sichuan, China. *J. Chengdu Univ. Technol. (science Technol. edition* 32 (1), 1–11. (In Chinese with English Abstract). doi:10.3969/j.issn.1671-9727.2005.01.001

Wang, Z., Cheng, D., He, Y., and Wang, H. (2006). A Study of the Ecological Functions of Step-Pool System in Southwest Mountain Streams. *Adv. Earth Sci.* 21 (4), 409–416. (In Chinese with English Abstract). doi:10.3321/j.issn:1001-8166.2006.04.010

Wang, L., Wang, X., Xu, X., and Cui, J. (2007). What Happened on the Upstream of Minjiang River in Sichuan Province 20 000 Years Ago. *Earth Sci. Front.* 14 (4), 189–196. (In Chinese with English Abstract). doi:10.1016/s1872-5791(07)60037-2

Wang, P., Li, J., Wang, J., Liu, C., Han, F., and Gao, L. (2011a). Quartz Ti-center in ESR Dating of Xigeda Formation in Sichuan and Contrast with Magnetic Stratigraphic Profiles. *Nucl. Tech.* 34 (2), 111–115. (In Chinese with English Abstract).

Wang, P., Zhang, B., Qiu, W., and Wang, J. (2011b). Soft-sediment Deformation Structures from the Diexi Paleo-Dammed Lakes in the Upper Reaches of the Minjiang River, East Tibet. *J. Asian Earth Sci.* 40 (4), 865–872. doi:10.1016/j.jseaes.2010.04.006

Wang, E., Kirby, E., Furlong, K. P., van Soest, M., Xu, G., Shi, X., et al. (2012). Two-phase Growth of High Topography in Eastern Tibet during the Cenozoic. *Nat. Geosci* 5 (9), 640–645. doi:10.1038/ngeo1538

Xu, G., and Kamp, P. J. J. (2000). Tectonics and Denudation Adjacent to the Xianshuihe Fault, Eastern Tibetan Plateau: Constraints from Fission Track Thermochronology. *J. Geophys. Res.* 105 (B8), 19231–19251. doi:10.1029/2000jb900159

Xu, J., and Wang, Z. (2004). Formation and Mechanism of Step-Pool System. *J. Hydraulic Eng.* 35 (10), 48–55. (In Chinese with English Abstract). doi:10.3321/j.issn:0559-9350.2004.10.008

Xu, Z. (2011). Deposits of Zhaizicun Landslide-Dammed Lake along Jinsha River and its Implication for the Genesis of Xigeda Formation. *Geol. Rev.* 57 (5), 675–686. (In Chinese with English Abstract). doi:10.1007/s10114-011-0511-z

Xu, Z., and Liu, W. (2011). Some Problems in the Study of the Genesis of the Xigeda Formation. *Earth Sci. Front.* 18 (5), 256–270. (In Chinese with English abstract).

Yan, B., and Lin, A. (2015). Systematic Deflection and Offset of the Yangtze River Drainage System along the Strike-Slip Ganzi-Yushu-Xianshuihe Fault Zone, Tibetan Plateau. *J. Geodynamics* 87, 13–25. doi:10.1016/j.jog.2015.03.002

Yang, R., Suhail, H. A., Gourbet, L., Willett, S. D., Fellin, M. G., Lin, X., et al. (2020). Early Pleistocene Drainage Pattern Changes in Eastern Tibet: Constraints from Provenance Analysis, Thermochronometry, and Numerical Modeling. *Earth Planet. Sci. Lett.* 531, 115955. doi:10.1016/j.epsl.2019.115955

Yao, H., Zhao, Z., Qiao, Y., Li, C., Wang, S., Wang, Y., et al. (2007). Magnetostratigraphic Dating of the Xigeda Formation in Mianning. *Sichuan and its significance* 27 (1), 74–84. (In Chinese with English abstract). doi:10.3321/j.issn:1001-7410.2007.01.009

Yin, A., Dang, Y. Q., Wang, L. C., Jiang, W. M., Zhou, S. P., Chen, X. H., et al. (2008). Cenozoic Tectonic Evolution of Qaidam basin and its Surrounding Regions (Part 1): The Southern Qilian Shan-Nan Shan Thrust belt and Northern Qaidam basin. *GSA Bull.* 120 (7), 813–846. doi:10.1130/b26180.1

Yin, A., and Harrison, T. M. (2000). Geologic Evolution of the Himalayan-Tibetan Orogen. *Annu. Rev. Earth Planet. Sci.* 28 (1), 211–280. doi:10.1146/annurev.earth.28.1.211

Zhang, P. (2008). The Present Day's Deformation, Strain Distribution and Deep Dynamic Process on the Western Sichuan, Eastern Tibetan Plateau. *Sci. China Ser. D* 38 (9), 1041–1056. (In Chinese). doi:10.1360/zd2008-38-9-1041

Zhang, P., Molnar, P., and Downs, W. R. (1994). Increased Sedimentation Rates and Grain Sizes 2–4? Myr Ago Due to the Influence of Climate Change on Erosion Rates. *Nature* 410 (6831), 891–897. doi:10.1038/35073504

Zhang, Y., Yang, N., and Meng, H. (2005). Deep-incised Valleys along the Minjiang River Upstream and Their Responses to the Uplift of the West Sichuan Plateau, China. *J. Chengdu Univ. Tech. (Science Tech. edition* 32 (4), 331–339. (In Chinese with English abstract). doi:10.3969/j.issn.1671-9727.2005.04.001

Zhang, Y., Dong, S., and Yang, N. (2009). Active Faulting Pattern, Present-Day Tectonic Stress Field and Block Kinematics in the East Tibetan Plateau. *Acta Geologica Sinica* 83 (4), 694–712. doi:10.1111/j.1755-6724.2009.00093.x

Zhang, K., Wang, Z., Liu, H., and Yu, G. (2011). Effect of Knickpoint Development in Controlling the Stability of the Landslide Dam. *J. Mountain Sci.* 29 (4), 474–482. doi:10.3969/j.issn.1008-2786.2011.04.012

Zhang, Y., Li, H., Wu, M., and Liao, C. (2012). Late Cenozoic Thrust and Nappe Structure along the Minjiang Upstream: Evidence from a Drill Hole. *Geol. Rev.* 58 (2), 215–223. (In Chinese with English abstract). doi:10.3969/j.issn.0371-5736.2012.02.003

Zhao, X., Hu, D., and Zhang, Y. (2008). Genesis and Age of the Gravels Underlying the Xigeda Formation of Panzhihua, Sichuan , China , and Valley Development of the Ancient Jinsha River. *Acta Geoscientia Sinica* 29 (1), 1–12. (In Chinese with English abstract). doi:10.3321/j.issn:1006-3021.2008.01.001

Zhao, X., Zhang, H., Hetzel, R., Kirby, E., Duvall, A. R., Whipple, K. X., et al. (2021). Existence of a continental-scale River System in Eastern Tibet during the Late Cretaceous-Early Palaeogene. *Nat. Commun.* 12 (1), 7231. doi:10.1038/s41467-021-27587-9

Conflict of Interest: The authors declare that the research was conducted in the absence of any commercial or financial relationships that could be construed as a potential conflict of interest.

Publisher's Note: All claims expressed in this article are solely those of the authors and do not necessarily represent those of their affiliated organizations, or those of the publisher, the editors and the reviewers. Any product that may be evaluated in this article, or claim that may be made by its manufacturer, is not guaranteed or endorsed by the publisher.

Copyright © 2022 Li, Sun and Zhang. This is an open-access article distributed under the terms of the Creative Commons Attribution License (CC BY). The use, distribution or reproduction in other forums is permitted, provided the original author(s) and the copyright owner(s) are credited and that the original publication in this journal is cited, in accordance with accepted academic practice. No use, distribution or reproduction is permitted which does not comply with these terms.

frontiers in Earth Science

ORIGINAL RESEARCH
published: 24 February 2022
doi: 10.3389/feart.2022.847921

Tectonic Deformation of an Intraplate Orogenic Belt: Mesozoic Sedimentary Basins in the Northeastern Qilian Shan, China

Jiabao Jia[1,2], Wenjun Zheng[1,2], Yipeng Zhang[1,2], Shiqi Wei[1,2], Shumin Liang[1,2], Changhuan Feng[1,2], Yu Zhu[1,2], Qing Tang[1,2] and Weitao Wang[1,2]*

[1]Guangdong Provincial Key Laboratory of Geodynamics and Geohazards, School of Earth Sciences and Engineering, Sun Yat-sen University, Guangzhou, China, [2]Southern Marine Science and Engineering Guangdong Laboratory (Zhuhai), Zhuhai, China

The Qilian Shan, located in the northeastern Tibetan Plateau, is an intraplate orogenic belt that underwent several episodes of fold and thrust deformation, particularly during the Mesozoic and Cenozoic. However, the deformation styles and relationships between the basin and mountains remain controversial. Therefore, in the current study, we conducted detailed field mapping of the sedimentary basins in Sunan and Huangcheng, and observed three episodes of compressive tectonic activity. We also restored a deformed section to determine the shortening rate of the Cretaceous sedimentary Sunan Basin. The first thrust episode, during the Paleogene, involved a southwestward thrust motion, comprising the Yumu Shan and Gaizhangdaban thrust systems. The second Neogene episode involved the northeastern thrust belt in the northern Qilian Shan, which comprises the Northern Qilian thrust system. The third episode produced NW-trending strike-slip activity that became the major tectonic deformation style; thus, the entire block rotated clockwise. Additionally, the restored section revealed that the Cretaceous strata have been shortened by ~3.56%. Collectively, these results indicate that the Sunan and Huangcheng area on the northeastern Tibetan Plateau is influenced by the far-field effects of the collision between the Indian and Asian continents, as well as the effects of intraplate orogenic processes related to the collision of the Alashan Block and the Qilian Shan. Therefore, the current study has defined the deformation style in the northeastern Qilian Shan region, so we wish to give a clarification of the tectonic evolution and forecast the tectonic propagation in the Qilian Shan region.

Keywords: tectonic deformation style, thrust system, intraplate orogenesis, deformation model, orogenic topography

OPEN ACCESS

Edited by:
Xuhua Shi,
Zhejiang University, China

Reviewed by:
Lei Wu,
Zhejiang University, China
Feng Cheng,
University of Nevada, Reno, United States

***Correspondence:**
Wenjun Zheng
zhengwenjun@mail.sysu.edu.cn

Specialty section:
This article was submitted to Structural Geology and Tectonics, a section of the journal Frontiers in Earth Science

Received: *03 January 2022*
Accepted: *07 February 2022*
Published: *24 February 2022*

Citation:
Jia J, Zheng W, Zhang Y, Wei S, Liang S, Feng C, Zhu Y, Tang Q and Wang W (2022) Tectonic Deformation of an Intraplate Orogenic Belt: Mesozoic Sedimentary Basins in the Northeastern Qilian Shan, China. Front. Earth Sci. 10:847921. doi: 10.3389/feart.2022.847921

1 INTRODUCTION

The Tibetan Plateau is a region with a complex tectonic deformation history. Before the Late Cretaceous, the deformation style of the Qilian Block was a multiple-accretionary orogenic belt (Xiao et al., 2009), while the northern Tibetan Plateau underwent two phases of extensional deformation that were not transmitted to northern Qilian Shan (Chen et al., 2003). Additionally, two phases of continental collision occurred in the central Qilian Shan before the Cretaceous (Zuza et al., 2019). It is believed that the northern Qilian Shan region formed higher topography than the central Qilian

Shan region during the Mesozoic (Wang et al., 2021). Moreover, based on reports from the Bureau of Mineral Resources of Gansu Province (BMRGP, Regional Geological Survey) (1982), Bureau of Mineral Resources of Inner Mongolia Province (BMRIMP, Regional Geological Survey) (1991) and Bureau of Mineral Resources of Qinghai Province (BMRQP, Regional Geological Survey) (1991), it is clear that the data pertaining to the geometry of the faults and strata constitute the geological background, while the relationships between the faults and folds remains unclear. To address this gap in knowledge, we began performing detailed map fielding to characterize the tectonic activities responsible for causing the specific strata and fault geometry. Although an uplift event was identified during the Late Cretaceous in the eastern Qilian Shan (Pan et al., 2013), and a slow and continuous cooling period was observed in the Eastern Qinghai Nan Shan (Jolivet et al., 2001; Lin et al., 2021), it remains unclear whether the Sunan Basin and Huangcheng Basin in northeastern Tibet formed during this period.

Previous studies have focused on the uplift of the Tibetan Plateau following collision of the Indian plate with the Eurasian plate (Zhong and Ding, 1996), which is thought to have begun from 60 to 55 Ma (Zuza et al., 2018a, 2018b). Moreover, based on the trench sediments in the west Himalaya, the orogeny likely began at the middle Paleocene (Hu et al., 2015). Although the entire plateau has continued to grow owing to this collision (Yin, 2006; Yuan et al., 2013), another view states that the timing of the Qilian Shan deformation coincided with the collision of the Indo-Eurasian (Yin et al., 2008a, 2008b; Dayem et al., 2009; Clark et al., 2010; He et al., 2021). Moreover, the eastern Kunlun Shan is thought to be serve as the roots when the strike-slip event occurs (Cheng et al., 2021). Meanwhile, on the northeastern Tibetan Plateau, the tectonic blocks underwent shear, extrusion, and rotation from the Mesozoic to the Cenozoic during the Late Jurassic to Cretaceous (Cheng et al., 2019b).

The Qilian Shan fold and thrust system records the effects of changes in the deformation style of the Indian and Eurasian blocks during the Cenozoic. That is, the deformation patterns within the strata are well preserved and capable of reflecting the evolution of the Qaidam Basin, which is in the western Qilian Shan (Cheng et al., 2021). However, the tectonic deformation style present during the Cretaceous in the Sunan Basin and Huangcheng Basin remains poorly understood. To investigate the older topography, it is necessary to determine the deformation architecture of the Late Cretaceous strata. Thus, in the current study, based on the divisions of the tectonic belt and the sedimentary background (BMRGP, 1982; Zhou et al., 2002; Dai et al., 2006; Jin et al., 2010; Wang et al., 2017), we selected two typical areas in the northeast Qilian Shan region, namely, the Sunan, and Huangcheng basins, for further analysis. Both areas share the deformation style of a fold–thrust system.

Above all, the tectonic evolution in the northern Tibetan Plateau remains unclear, with the tectonic deformation style in the northeastern Qilian Shan during the Late cretaceous currently unknown. In this study, we focused on the period preceding the Indo-Eurasian collision and addressed the fault planes and fault-related folds using field work and field mapping to investigate fold deformation in the study area. The aim of this study is to characterize the tectonic deformation architecture of the basin and to determine a tectonic evolutionary model for the Sunan Basin.

2 GEOLOGIC SETTING

The Qilian Shan is located on the northeastern margin of the Tibetan Plateau and controls the propagation of the northeastern Tibetan Plateau with an NW-trending fold and thrust system (Zhang et al., 2004; Wang et al., 2014). The northeastern Qilian Shan is bounded by the Alashan Block to the north, the Ordos Block to the northeast, and the Kunlun-Qiangtang Block to the south (**Figure 1**). The Qilian Shan–Hexi corridor experienced a collision between the Alashan Block and the Songpan-Ganzi Block of the Tibetan Plateau. The northeast Qilian Shan is located on the northern margin of the Nan Shan–Qilian Shan deformation belt.

In the study area, the sedimentary basin, which is covered by 1.5–2 km of thick Cretaceous sandstones, conglomerates, and siltstones, unconformably overlies Paleozoic sandstones and conglomerates. The Cretaceous strata, which are covered by Neogene strata, are located in the Sunan, northern Huangcheng, and Longshou Shan areas. The Cretaceous strata in the Sunan area differ from those in the Huangcheng area. According to geological mapping surveys (BMRGP, 1982), the Cretaceous strata include the Xinminpu Formation (K_1xn) in the Sunan area, while the Hekou Formation (K_1hk) is found in the Huangcheng area. The Malianggou Formation (K_2ml) is also exposed in the Huangcheng area, characterized by sandstones and conglomerates that are more well-cemented than those in the Neogene strata.

The Neogene strata are horizontally trending sandstones and conglomerates that unconformably overlie the Cretaceous strata. The Neogene strata unconformably cover the Cretaceous strata in both study areas along the southern Yumu Shan and in the southern Gaizhangdaban area. Along the Northern Qilian thrust system, Neogene strata are exposed primarily in the Yumen, Sunan, Jiuquan, and southern Gaizhangdaban areas (**Figure 1**). Based on data from the BMRGP (1982), the Neogene strata include the Houshaogou ($E_{1\text{-}2}h$), Baiyanghe (E_3b), and Shulehe (Ns) formations, which are characterized by red to red-brown sandstones and conglomerates. The characteristics of the Neogene deformation style include the growth strata that developed along the fault systems around the basin.

The Sunan Basin is bounded by thrust systems on the north, south, and east sides, which form elevated topography around the basin. From north to south, the major thrust faults and their associated tectonic deformation are the Yumu Shan thrust system (YMT), and the Northern Qilian thrust system (NQT). Yang (2007) found that the YMT is a regional thrust system, while the NQT is a northward thrusting system that comprises Cambrian and Ordovician klippes. On the northern and southern margins of the Sunan Basin, lightly metamorphosed limestones are thrust up against the Cretaceous basin on the hanging wall of the fault. The eastern side of the basin is bounded by metamorphosed Ordovician strata.

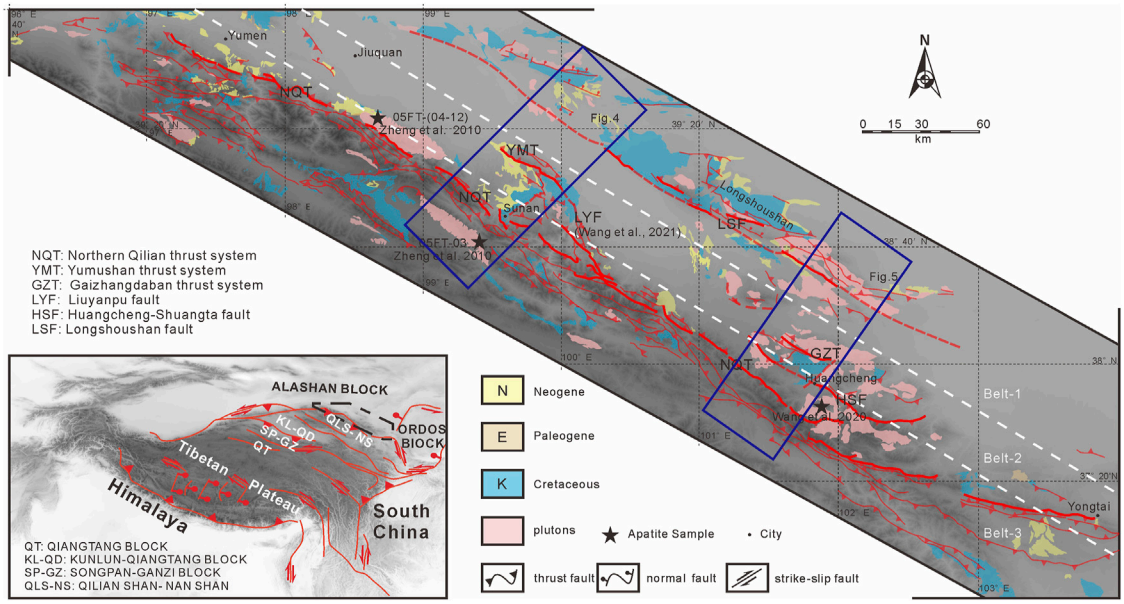

FIGURE 1 | Geologic map of the Qilian Shan–Hexi corridor. Map based on data from the Bureau of Mineral Resources of Gansu Province (BMRGP, Regional Geological Survey) (1982), BMRIMP (1991), Bureau of Mineral Resources of Qinghai Province (BMRQP, Regional Geological Survey) (1991), and fieldwork conducted for this study.

3 ACQUISITION OF DATA AND THE ESTABLISHMENT OF DEFORMATION LAYERS

We first collected 20 field maps (scale 1:200,000) to summarize the geometric characteristics of the fault system and the location of the target strata. We then generated detailed field work, including images that were meant to depict the relationships between the fold and thrust. Moreover, to define the kinematic characteristics, we selected the clean fault planes to accumulate the plunge data of the scratch to demonstrate the strain field. Upon completion of the field work, we reconstructed the geological mapping based on our observations and adjusted the geometry of the faults and folds.

Based on the field surveys and mapping, we defined three fault–fold deformation belts in the Qilian Shan–Hexi corridor deformation zone. The first belt (belt-1) in the north is the deformation zone closer to the Alashan terrane, where the Longshou Shan and Heli Shan are the central aspects of the Alashan orogenic belt. This belt is thought to be controlled by the Longshou Shan fault (LSF), which thrusts southwestward toward the Tibetan Plateau. In the northern part of belt-1, the Alashan terrane is weakly deformed and the crust is more stable. The second belt (belt-2) includes the Yumu Shan and Gaizhangdaban areas, both of which exhibit the same tectonic activities as in the adjacent Alashan Block and along the southern margin of the Alashan terrane thrust system. This region is controlled by both the Alashan Block and the Qilian Shan orogenic belt, forming southwestward thrusting faults and active northward faults along the northern margin of the Yumu Shan and Gaizhangdaban areas. The third deformation belt (belt-3) is the northern Qilian Shan thrust fault system, which is thought to be the edge of the Qilian Shan–Nan Shan thrust system that is affected by the propagation of the northeastern Tibetan Plateau.

Therefore, to study the deformation history more clearly, we divided the strata into three structure deformation layers (SDLs) according to the contact relationships between each stratum (**Figure 2**). The first SDL is Permian–Jurassic (SDL-1), which we defined as the basement sediment. The second SDL is the Cretaceous, which comprises the major strata in the basin as footwall, is dominated by folds topping to the central basin that cause a portion of the shortening. This SDL (SDL-2) differs in the two study areas. The Cretaceous strata in both study areas are unconformably overlain by Neogene strata (SDL-3). SDL-3 is Eogene–Neogene, which includes tectonic deformation caused by the active fault system, and is gently dipping (**Figure 3**).

After concluding that the strata occurrence data was insufficient, we selected a cross-section of the basin from northeast to southwest, and accumulated detailed data regarding strata trends and dips, including specific altitude, longitude data, and latitude data. Based on the data strata, we used line balancing to simulate each fold hinge of the Cretaceous strata in the Sunan Basin to restore the section across the Sunan Basin. To ensure that the area of the Cretaceous strata was consistent (Elliott, 1983), we altered the thickness of the strata to fit current day measurements.

The detailed mapping allowed us to perform detailed statistical analysis of the poles for each strata occurrence, and simulate the most proximate fold hinge using the stereographic projection to show the geometry of the fold hinge, which depicted the strain orientation. Finally, based on the geological background generated by predecessors, as well as our current field work, we simulated a tectonic propagation model to represent the evolution history of the Sunan Basin.

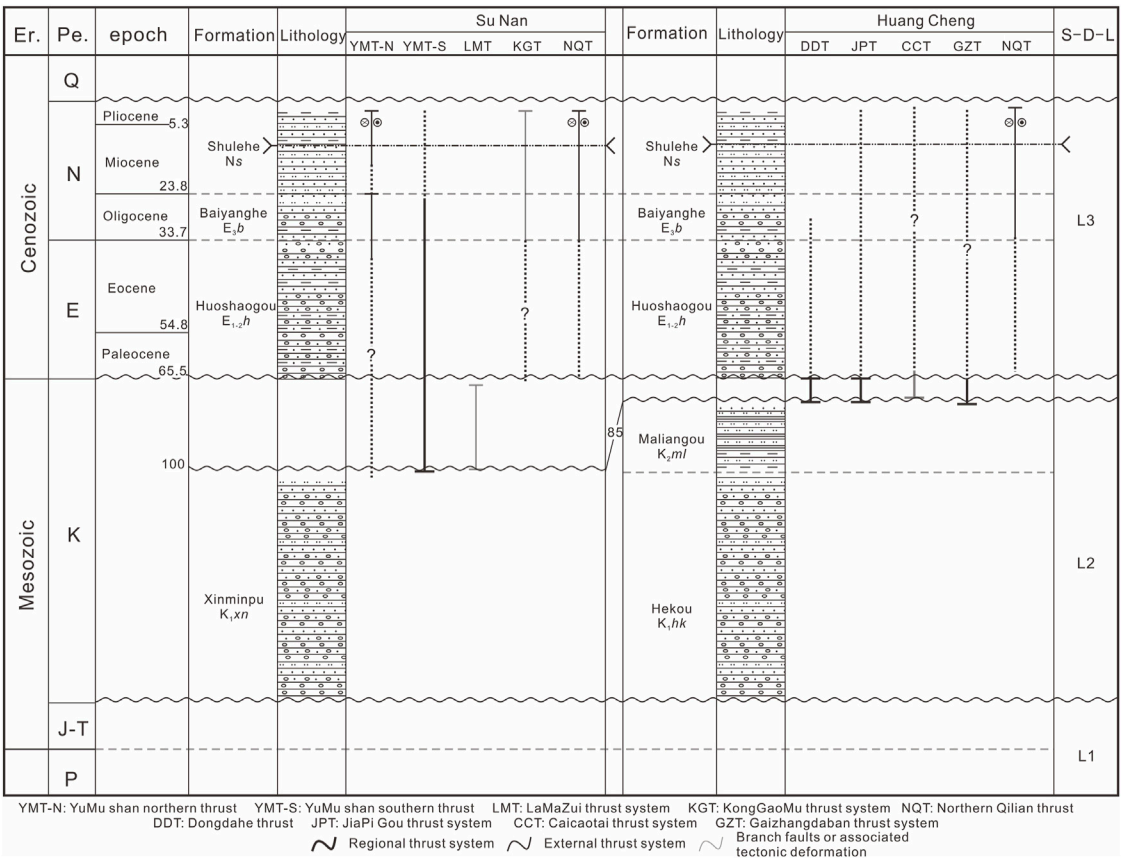

FIGURE 2 | Chronology of thrust faulting and sequence stratigraphy in Sunan and Huangcheng. Lithologic age constraints were obtained from the Bureau of Mineral Resources of Gansu Province (BMRGP, Regional Geological Survey) (1982). The time of faulting are based on the faults, strata and unconformity contacting relations from the geological map (Bureau of Mineral Resources of Gansu Province (BMRGP, Regional Geological Survey), 1982; BMRIMP, 1991; Bureau of Mineral Resources of Qinghai Province (BMRQP, Regional Geological Survey), 1991) and the field observation.

4 IDENTIFICATION OF MAJOR TECTONIC COMPONENTS

Deformation of the Cretaceous strata and the NW–SE thrust systems between the Paleozoic and Mesozoic control the shape of the basin, record far-field deformation influenced by the collision between the Indian and Asian plates, and can be used to determine the shortening of the northeastern Tibetan Plateau.

In the Sunan Basin, prominent tectonic structures include NW-trending thrust faults and folds. The Sunan Basin is dustpan shaped and consists of Permian–Cretaceous fold deformation and Neogene strata. The older strata are generally exposed along the northern and eastern margins of the basin, which is believed to be a basin formed by the thrust system as its footwall. The fold deformation present along the northern and southern margins of the basin manifests as folds topping to the central basin in the Cretaceous strata, which are more severely deformed around the YMT and NQT, however, are less deformed toward the center of the Sunan Basin.

The Yumu Shan Fault is located adjacent to the southern and northern margins of the Sunan Basin. The southern Yumu Shan Fault (YMT-S) is ~35 km long and cuts through Neogene, Cretaceous, Permian, and Silurian strata. The southern portion of the YMT-S is a Cretaceous and Neogene sedimentary basin. Along the YMT-S, the northern part of the Silurian metamorphosed mudstones has been thrust southward over Permian strata. The northern Yumu Shan Fault (YMS-N) is ~40 km long and is located along the northern margin of the Yumu Shan, which is likely affected by the propagation of the Tibetan Plateau and is rotated clockwise. The current fault dip angle is 65°–70° (BMRGP, 1982), while the dip angle is ~45° in the adjacent areas of the Yumu Shan. Along the YMT-N, Silurian, Carboniferous, and Devonian strata have been thrust northward toward the Jiuquan Basin (Yang, 2007), which comprises Quaternary sediments. However, the deformation style of the Yumu Shan remains unclear. It has been proposed that the Yumu Shan klippes were derived from the nappe system of the NQT (Wang et al., 2021); however, we postulate that the Yumu Shan was controlled by the YMT-S to form the southward thrust system, thereby leaving the LMK in the basin.

In the Huangcheng Basin, regional tectonics are controlled by the Gaizhangdaban thrust system (GZT) and the Caicaotai thrust system (CCT; **Figure 5**). The Huangcheng Basin consists of SDL-2, and the deformation primarily comprise folds topping to the

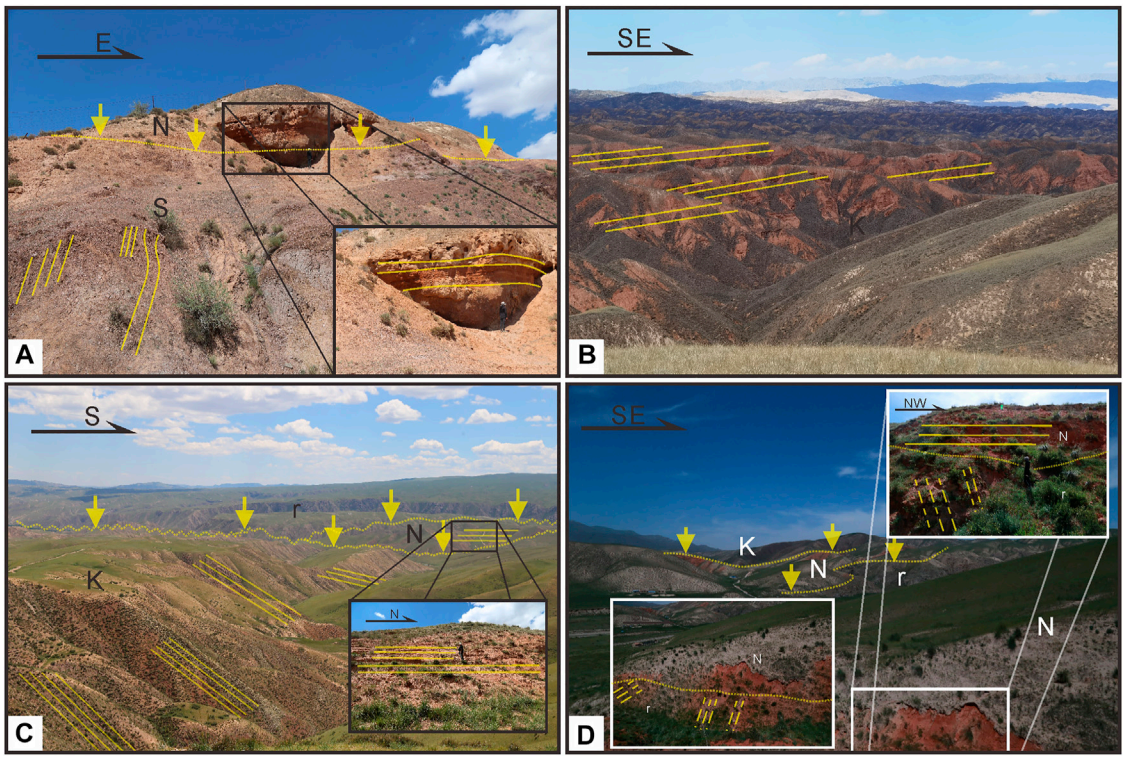

FIGURE 3 | Field photos of stratigraphic relationships in the study area. Yellow lines mean bedding. (**Figure 4** and **Figure 5** for regional location of this map). **(A)** Strata of the Lamazui klippe. Neogene strata almost horizontally overlie Silurian strata. This shows the contact relationship between the SDL-3 and SDL-1. **(B)** Dipping Cretaceous strata that underwent little deformation in the central Sunan Basin. **(C)** Cretaceous strata in the Huangcheng Basin. From north to south, the dip angle changed from ~50° to ~20°. In the central basin, Neogene strata horizontally overlie Cretaceous strata and have an unconformable contact with the pluton. **(D)** Pluton in the Huangcheng Basin overlain by red Neogene sandstones. The Neogene strata contact the Cretaceous strata and pluton unconformably in the eastern part of the Huangcheng Basin. K: Cretaceous strata. N: Neogene strata. r: plutons.

central basin. The Huangcheng Basin is bounded by thrust faults to the north, south, east, and northwest, unlike the Sunan Basin. The GZT is located along the northern margin of the basin, and by the branch fault of the GZT along the northwestern margin. The plutons were thrust southward toward the basin along the GZT, and Permian strata were thrust southeastward over Cretaceous strata along the CCT, forming elevated topography. On the eastern side of the basin, the Dongdahe River nearly bounds the eastern margin, while the plutons that form the elevated topography are located on the eastern side of the river. Part of the plutons remain on the western side of the river, which were covered by SDL-1 and SDL-2 (**Figure 2**). As in the Sunan Basin, the southern basin is bounded by the eastern segment of the NQT while the hanging wall strata are the basement strata that were thrust over the Quaternary strata. A NW-trending thrust fault cuts through the basin, which is thought to be the Huangcheng-Shuangta Fault. At the center of the basin, the basement strata have been thrust up as the hanging wall along the Huangcheng-Shuangta Fault (HSF). Moreover, the footwall has also formed a fold topping to the central basin.

In the Huangcheng Basin, the plutons are often present as the hanging wall of the faults. The elevated topography comprises the Gaizhangdaban granite plutons, which are located in the northern Huangcheng Basin. The Gaizhangdaban plutons are located ~35 km northwest and ~15 km northeast of the lateral ramp. The Huangcheng-Shuangta granite pluton is also located around the Huangcheng Basin, located 25 km to the northwest. Apatite He ages have suggested that the uplift of the HSF occurred at 12.9–14.6 Ma (Wang et al., 2020).

Similar to the YMT-S, the GZT is believed to be a fault system that thrust southward in the Huangcheng Basin during the Late Cretaceous. The GZT represents the thrust edge of the Longshou Shan thrust system.

The thrust fault system proposed in this study can be divided into two parts. Stage 1 includes motion on the YMT and the GZT, representing the older southward thrust system. Stage 2 includes motion on the NQT, which uplifted rapidly during the Cenozoic and formed elevated topography in the southern basin.

4.1 Older Southward Vergent Thrust System

Based on the detailed field work and mapping (**Figure 4** and **Figure 5**), as well as the relationships between the faults and folds, we determined that the deformation styles of the Cretaceous strata and Neogene strata differ. For instance, the Neogene strata is mildly deformed, while the Cretaceous strata exhibited strong deformation near the faults plane. Hence, two separate compression events occurred in the study area, resulting in the formation of unique deformation architecture. Meanwhile, the

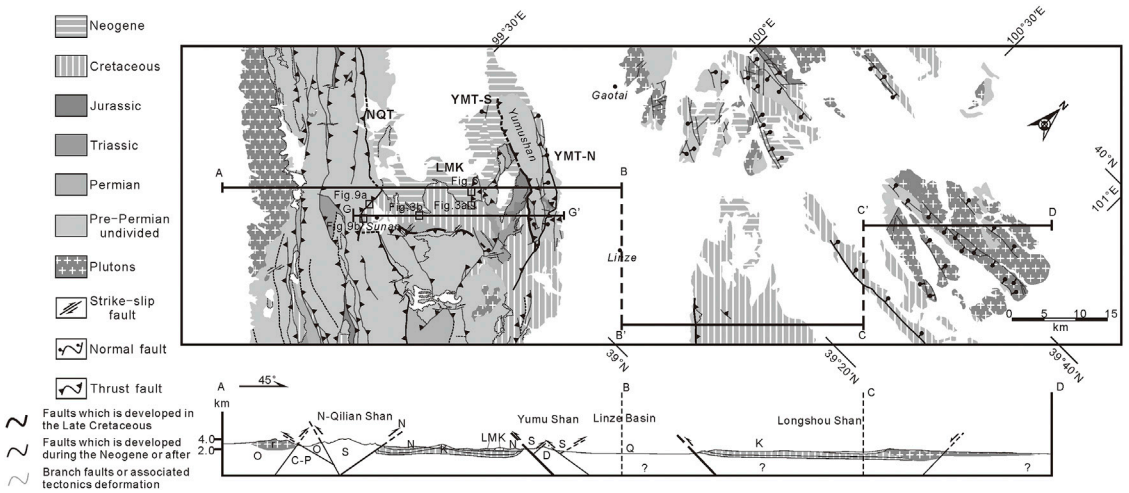

FIGURE 4 | Field map of the Sunan area. (Map based on data from the Bureau of Mineral Resources of Gansu Province (BMRGP, Regional Geological Survey) (1982), BMRIMP (1991), Bureau of Mineral Resources of Qinghai Province (BMRQP, Regional Geological Survey) (1991) and fieldwork conducted for this study).

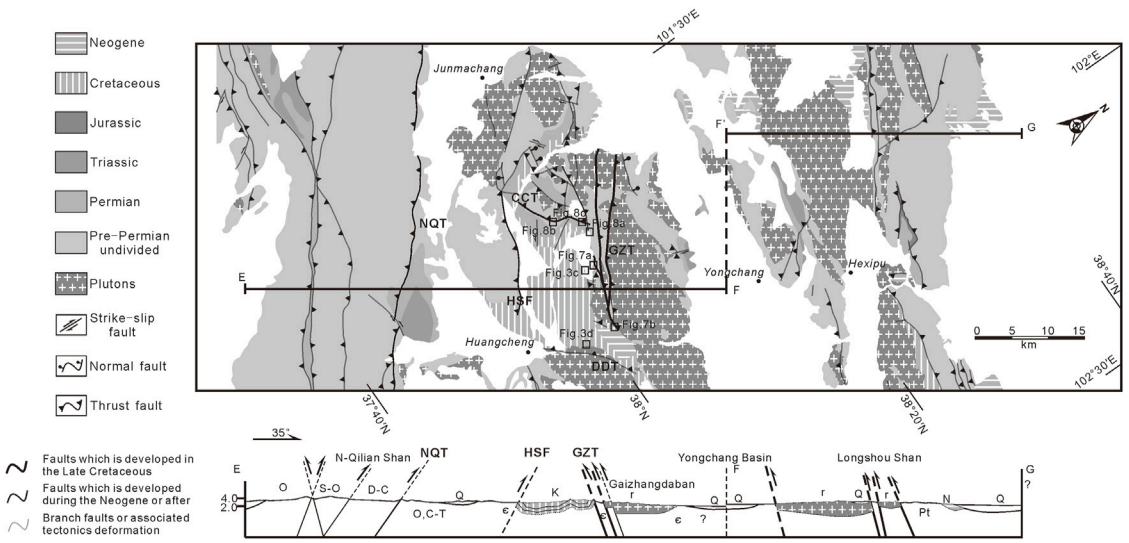

FIGURE 5 | Field map of the Huangcheng area. (Map based on data from the Bureau of Mineral Resources of Gansu Province (BMRGP, Regional Geological Survey) (1982), BMRIMP (1991), Bureau of Mineral Resources of Qinghai Province (BMRQP, Regional Geological Survey) (1991) and fieldwork conducted for this study).

southward propagation faults influence both the Cretaceous strata and Neogene strata. Additionally, the southward vergent thrust formed during the Late Cretaceous shortening event.

4.1.1 Lamazui Klippe

The LMK is located on the southern side of the YMT-S in the Sunan Basin (**Figure 6**) and extends nearly 5 km from east to west and ~1 km from north to south. The strata in the klippe include Silurian lightly metamorphosed mudstones, which overlie Cretaceous sandstones. The Cretaceous strata are slightly deformed around the klippes, indicating that the footwall was not affected by the hanging wall.

The Silurian strata dip steeply around the margin and connect with the Cretaceous strata near the fracture zone. Many fault planes were observed in the fracture zone. We also observed two sets of fault planes and two sets of scratches on the planes. The scratches indicate that the thrust experienced almost NE–SW strain, which is nearly vertical to the trend along the YMT-S. In the upper wall, the klippes are covered by Neogene strata (**Figure 2A**), implying that the YMT-S was active between the Cretaceous and Neogene.

4.1.2 Gaizhangdaban Thrust System

The GZT system is located in southern Gazhangdaban, which contains the highest peak of the pluton mountains. It has a

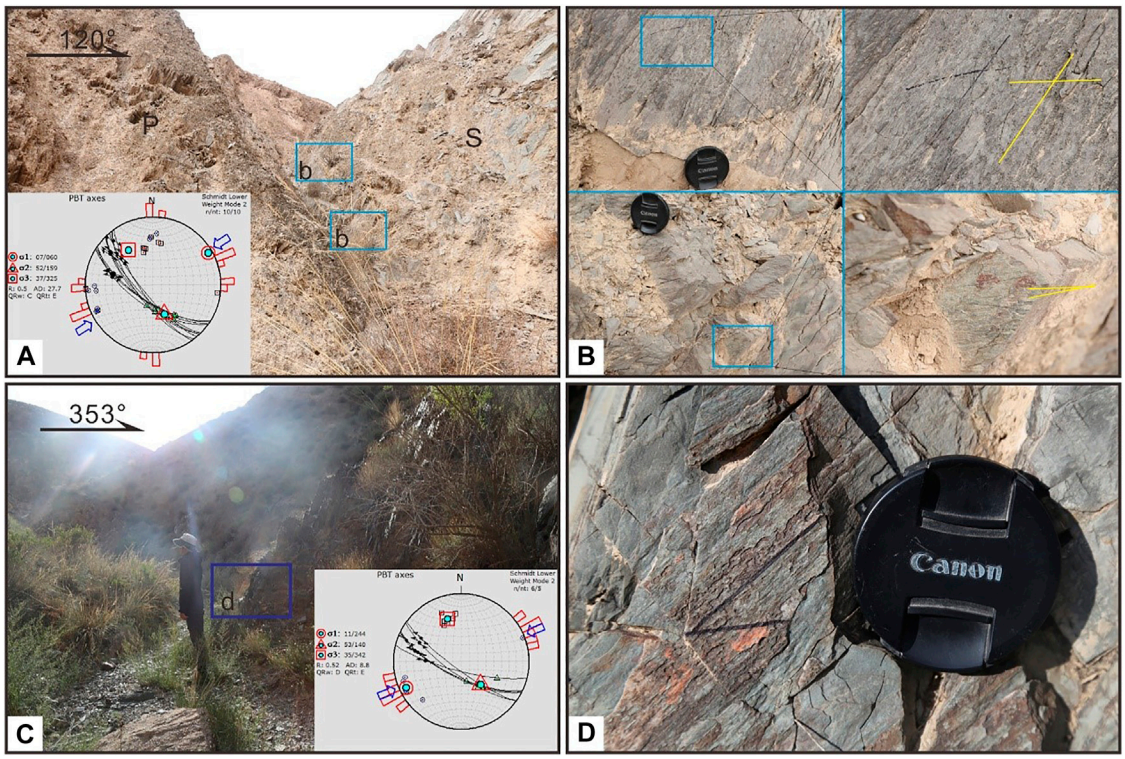

FIGURE 6 | Field photos of fault planes and scratches in the Lamazui klippe (LMK). Yellow lines mean bedding. (**Figure 4** for regional location of this map). **(A)** Fault planes located on the southern margin of the LMK. The scratches indicate that the area underwent NE–SW compression. **(B)** Two sets of scratches on the fault planes. The upper scratches indicate that the tectonic activity was dominated by thrust motion, while the other set indicates that tectonic deformation was dominated by strike-slip motion. **(C)** Fault plane on the northern margin of the LMK. The scratches indicate that this region experienced nearly NE–SW compression. **(D)** Scratches on the fault plane, indicating that the fault underwent a combination of thrust and strike-slip motion. K: Cretaceous strata. N: Neogene strata.

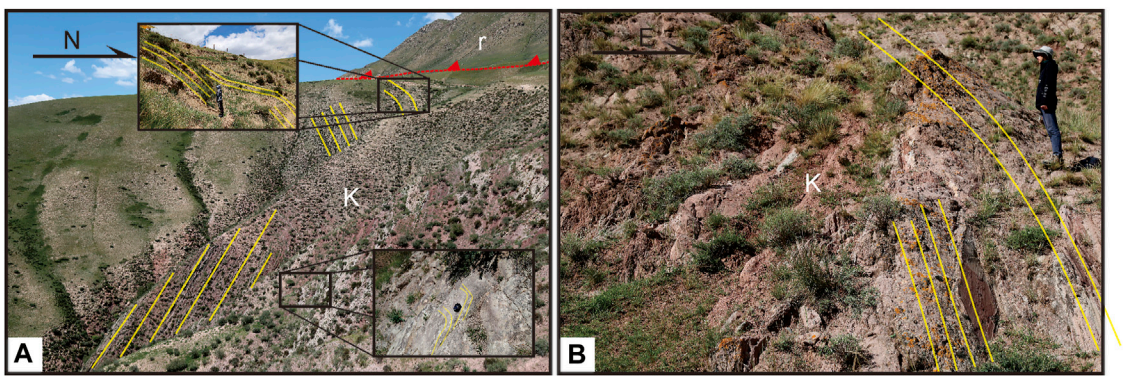

FIGURE 7 | Field photos of the GZT fault and related deformation. Yellow lines mean bedding. (**Figure 5** for regional location of this map). **(A)** Fault plane in the southern Gaizhangdaban area, where Cretaceous strata are deformed near the fault plane. The lower strata dip ~50° southward, but become vertical in the middle strata. The upper strata dip northward ~60°. The deformation exhibits a southward tectonic polarity, thereby indicating that deformation was related to southward thrust motion. **(B)** Folds topping to the central basin in the Shagousi area. Near the GZT, the Cretaceous strata dip vertically, while the upper strata are reversed. This fold also exhibits tectonic polarity toward the basin. K: Cretaceous strata. N: Neogene strata.

NW–SE strike and dips ~70° around the Gaizhangdaban area. The GZT marks the northern boundary of the Huangcheng sedimentary basin. Along this fault, the granite plutons were thrust southward over Cretaceous sandstones. This fault cuts through the plutons and overlies the Neogene strata in the southern adjacent area, indicating that the fault was not largely affected during the Neogene.

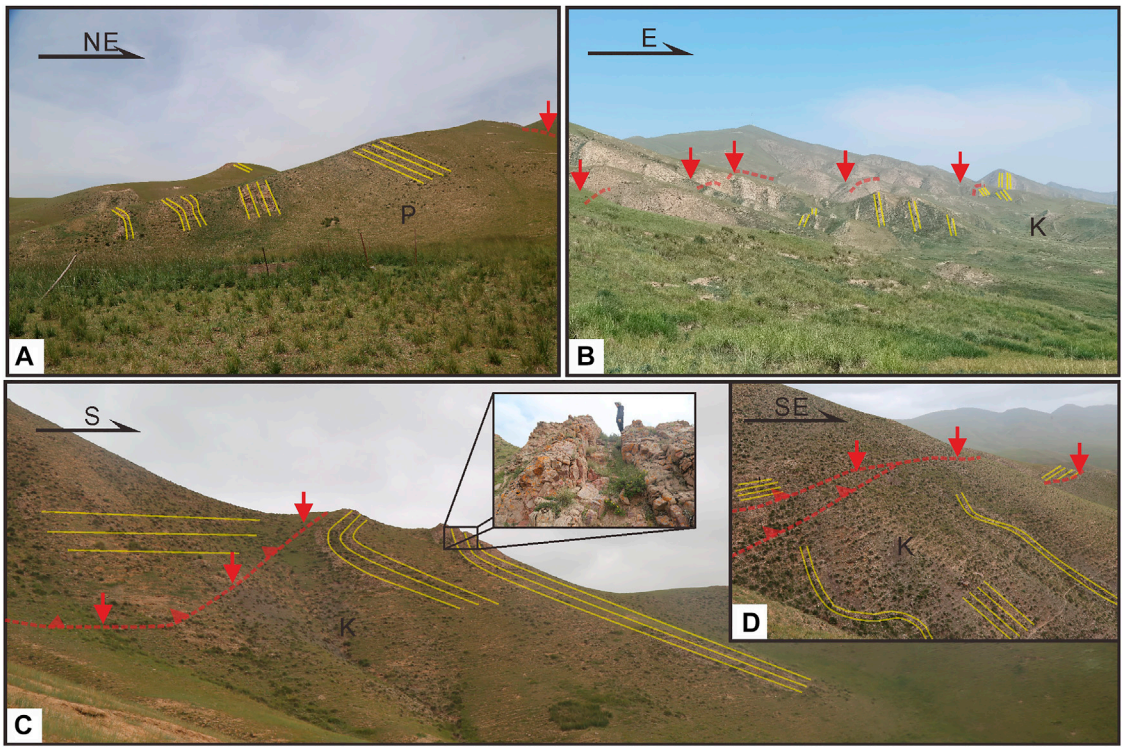

FIGURE 8 | Field photos of the CCT and related deformation. Yellow lines mean bedding. (**Figure 5** for regional location of this map). **(A)** The CCT, located on the southern GZT, trends NE–SW. The pluton was thrust over the Permian strata and formed a fold topping to the central basin. The upper strata are reversed and become vertical in the middle part of the section. **(B)** The CCT, located in the western Huangcheng Basin, trends NE–SW and the fault plane is not exposed clearly. The fold topping to the central basin emerges at the eastern end of this fault, and has a SE-trending tectonic polarity that points toward the center of the basin. **(C)** The CCT fault, which is located in the northwestern part of the sedimentary basin in Caicaotai. The fault plane is not exposed clearly, and the footwall strata deformed as a fold topping to the central basin with a SW tectonic polarity. **(D)** Fault plane located at the northern end of **(C)**. Here, the footwall deformed to produce a kink fold. the upper strata dip steeply, but become more horizontal in the middle of the section. K: Cretaceous strata. N: Neogene strata.

The footwall comprises Cretaceous thinly layered purple sandstones, which dip vertically in the middle of the section and are reversed in the upper section, forming a fold topping to the central basin at the end of the thrust fault (**Figure 7**). Moreover, the fold has a tectonic polarity toward the central basin. Based on these findings, we postulated that the fault was most active from the Cretaceous to the Neogene.

4.1.3 Caicaotai Thrust System

The CCT system is located in the southern portion of the GZT, and is thought to be a branch fault of the GZT. The fault plane is ~10 km from the Huangcheng Basin and trends NNE–SSW. The CCT nearly bounds the Cretaceous basin in the northwest, and is cut by the HSF in the south (**Figure 5**).

The upper wall comprises Cambrian and Permian lightly metamorphosed sandstones, which were thrust southeastward over Cretaceous dark red sandstones. Near the fault plane, the Cretaceous strata are reversed, and some portions of the strata are vertical, indicating a southward tectonic polarity. Meanwhile, a fault broken block is present in another section of this fault, under which Cretaceous strata form a bend fold. Moreover, away from the fault plane, strata dip ~20° and are more stable toward the basin (**Figure 8**).

4.2 Younger Northward Vergent Thrust Fault

Based on the detailed field work and mapping (**Figure 4** and **Figure 5**), as well as the detected relationships between the faults and folds, the younger northward vergent thrust fault represented by the Qilian Shan thrust system (NQT). the Neogene strata deposit along the NQT, as well as the faults, seldom affect the Cretaceous strata. Through examination of previous study findings, it is believed that the NQT underwent intense shortening during Neogene (Zheng et al., 2010; Wang et al., 2013, 2020). We, therefore, postulate that the NQT was active later than the older south vergent thrust system.

The NQT comprises the western and eastern segments (Yang, 2007), which cover almost the entire margin of the northern Qilian Shan region. In this study, we focused on the western segment of the NQT, which is located in the southern Jiuquan Basin. The southern side of the Sunan Basin is controlled by the Fodongmiao-Hongyazi thrust segment of the NQT (Yang, 2007), which trends NW. The fault plane dips at 60°–75° (BMRGP, 1982). The NQT thrust belt formed imbricate fans and thrust northward over Cretaceous strata.

The western segment of the NQT, located in southern Sunan Province, is the leading edge of the Qilian Shan thrust system. In

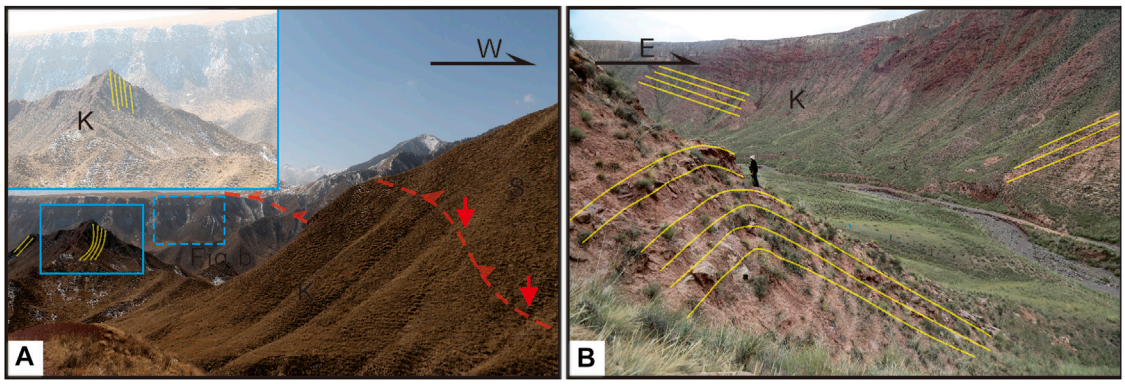

FIGURE 9 | Field photos of the NQT and its folds in the footwall strata. Yellow lines mean bedding. (**Figure 4** for regional location of this map). **(A)** Field photos of the NQT and Cretaceous strata in the footwall of the fault. The upper section's Cretaceous strata deformed and are steeply dipping. **(B)** Field photos of Cretaceous strata near the NQT fault plane. K: Cretaceous strata. N: Neogene strata.

the western area around Sunan Province, the NQT is thrust over Neogene strata and dips NE at ~60°. In the middle section of the NQT, Triassic strata are present and believed to be tectonic windows. The structural style of the NQT is an imbricate fan along the northeastern Qilian Shan region (**Figure 1**). The hanging wall comprises lightly metamorphosed Silurian mudstones that overlie Cretaceous sandstones and are covered by Neogene strata, in which the strata reverse and form a NE-trending tectonic polarity. The upper strata of the Cretaceous footwall were affected by the NQT and became reversed, then became steeper in the middle section, and finally became vertical (**Figure 9**).

5 POLYCYCLIC MODEL AND THRUST MECHANISM

In the study area, we observed two sets of fold and thrust fault systems. One set of faults is believed to be an older regional thrust system that was active after the Cretaceous and before the Neogene. The other set of thrust systems (comprising the YMT-N, NQT, and HSF) is believed to result from the northeastward propagation of the Tibetan Plateau, which has been active since the Neogene. In addition to the thrust systems, the older thrusts formed the LMK, while the Yumu Shan and Gaizhangdaban serve as the upper walls of the southward thrust edge. The younger thrust system propagated northward and is expected to cut through, or reactivate, the older thrust system, forming multiple tectonism episodes. The most typical deformation style in this orogenic belt is northward thrust, which includes the NQT and the HSF.

The sedimentary basins are dustpan shaped and filled with Cretaceous and Neogene strata. Based on the field mapping, the strata of the Cretaceous strata revealed that the fold hinge is NW-trending, indicating that the field strain is NE-trending. With the appearance of the extrusion events, the fold hinge rotated.

5.1 Polycyclic Model for the Basin

The shortening rate of the Neogene Qilian Shan strata during the Cenozoic can be used to answer questions regarding the Qilian Shan uplift (Zhang et al., 2004). We observed two sets of fold and thrust pairs in the Sunan and Huangcheng basins. If the tectonic style of each tectonic activity can be identified, the tectonic deformation in the study area can be used to characterize the older tectonic mechanisms and forecast future tectonic evolution. Three main features are common to recognizing out of sequence thrust faults: basic ramp-flat geometry, fault-related folds, and detachments between the basement and upper covering strata (Li et al., 2016).

Based on these features, the YMT and LMK belong to the regional thrust system in the Sunan Basin, whereas the GZT and CCT belong to the regional thrust system in the Huangcheng Basin, which is the fold and thrust system that was present prior to the Cenozoic thrust system (NQT). The regional system comprised a set of low-angle thrust faults and produced regional shortening of the Cretaceous strata, which are deformed more strongly near the thrust faults, however, are more stable in the interior aspect of the basin. All of the regional thrust systems dip steeply northward and were present along the northern margin of the basin. We, therefore, propose that these regional thrust systems experienced the northward propagation of Cenozoic thrust tectonism that formed southward-dipping thrust systems (YMT-N and HSF). These systems are still developing, being reactivated, and becoming more steeply dipping.

We observed a fold topping to the central basin in the southern GZT, indicating that the YMT-S and GZT controlled the northern basin during the Late Cretaceous and formed elevated topography. By analyzing the relationships between the unconformities and the fold and thrust system, we established a fault evolution model for the Sunan Basin and compared the deformation style with those of regional thrusting and the NQT.

When the model was initiated, hinterland rifted systems were present (Yang, 2007), wherein the Cretaceous strata trended W–E

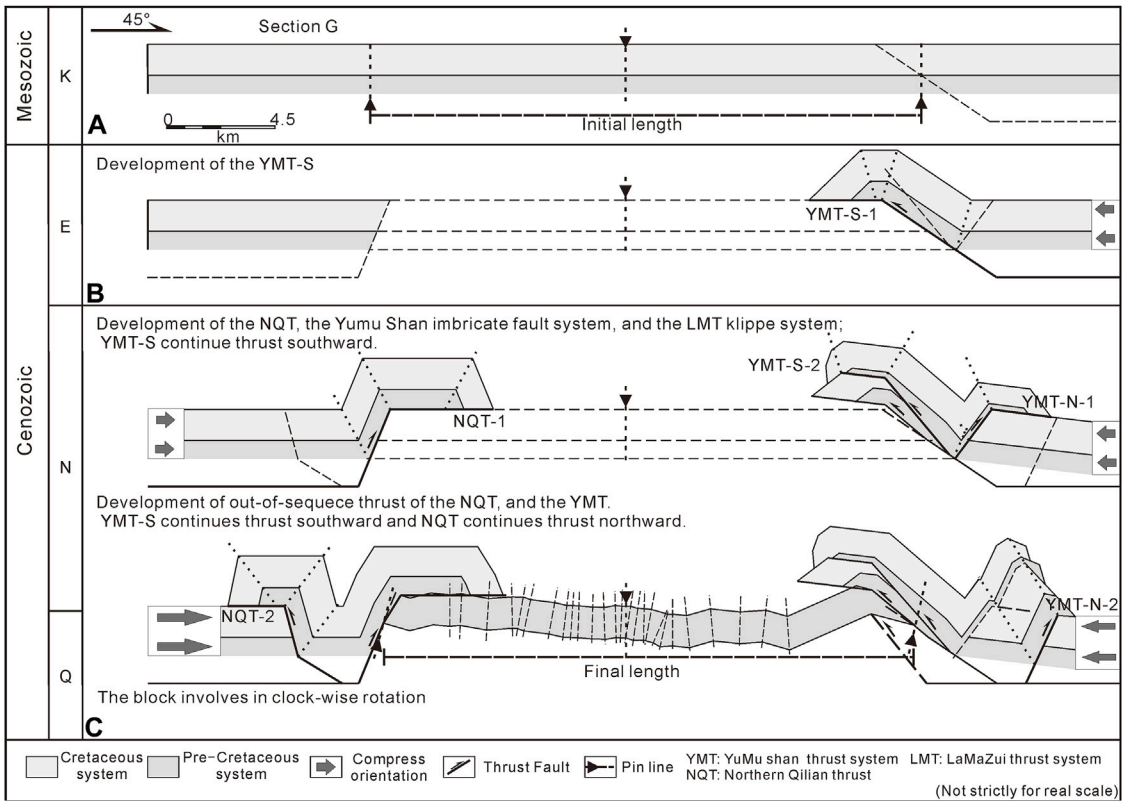

FIGURE 10 | Model of the fault system development in the study area. **(A–C)** Fault propagation and strata deformation process. **(A)** The restored initial length of the Cretaceous strata is shown (based on the strata data of this study); **(C)** The final length of the Cretaceous strata of this section. Each of the dotted lines represent the fold hinge, based on the field work of this study and the thickness of the strata is based on the Bureau of Mineral Resources of Gansu Province (BMRGP, Regional Geological Survey) (1982).

(**Figure 10A**). Owing to the collision between the Alashan and Qiangtang blocks, southward propagation of the thrusting began, forming a regional thrust system (YMT-S and GZT) (**Figure 10B**). At this stage, slight differences can be observed between the Sunan and Huangcheng basins. The YMT-S developed during the Late Triassic (~100 Ma) to the early Neogene (**Figure 2**); however, the GZT in the Huangcheng Basin developed later, possibly since 80 Ma. Both thrust faults are not currently well-exposed, owing to the burial of the Neogene strata, and the fault surface is not well preserved. However, their deformation styles can be defined by the fault-related folds described above, which indicate that these faults are at their farthest extents during this time. During this process, the Yumu Shan and Gaizhangdaban areas began uplifting forming elevated topography.

As the collision between the two blocks continued, the YMT developed more branch faults, forming an imbricate fan in the Yumu Shan region (**Figure 10C**). In the Huangcheng Basin, along the propagation of the GZT, volcanism formed plutons. This phase of shortening stopped after ~65.5 Ma when an unconformity formed between the Cretaceous and Neogene strata (**Figure 1**). The Cenozoic thrust system may have developed after the deposition of the Eogene conglomerates, which were uplifted rapidly at ~10 Ma in the western Sunan Basin (Zheng et al., 2010), at ~15 Ma in the Huangcheng Basin along the HSF (Wang et al., 2020), and at 17–15 Ma along the Tuolai Shan in the central Qilian Shan region (Yu et al., 2019).

With the northward propagation of the NQT, the YMT may have formed the YMT-N, after which the YMT-S, GZT, and CCT began to tilt, reactivate, and steepen (**Figure 10**). Moreover, the development of the back-thrust fault in the NQT and the uplift of the YMT and GZT caused the Cretaceous strata in the basin to undergo folding.

Several cross sections have been restored using seismic reflection data, indicating that the northern margin of the Tibetan Plateau accumulated the majority of its compressive strain from the Jurassic to the Cretaceous (Zuza et al., 2016). From the Cretaceous to the present, the northeastern Tibetan Plateau has shortened by approximately 50% (Yang, 2007; Zuza et al., 2016), 43–49% shortening in the Altyn Tagh-Qilian Shan (Cheng et al., 2015) and 48% in the west Qaidam Basin (Yin et al., 2008b). The restored cross sections also indicate that the middle and upper crust exhibit strike-slip deformation and tectonic extrusion (Guo et al., 2016). However, the shortening rate of the Cenozoic strata in the Sunan Basin remains controversial.

Through our detailed field mapping and data from geologic maps (BMRGP, 1982), in the last tectonic evolutionary stage, we restored Section G (extending across the Sunan Basin) with the Cretaceous strata in the initial length (**Figure 10A**), and compared it with the final length of the cross-section map (**Figure 10C**). Our results revealed that the Cretaceous folding system accumulated ~3.56% of the regional shortening in the Sunan Basin from northeast to southwest, which was significantly less than the ~50% crustal shortening accumulated through thrust propagation (Zuza et al., 2020). Taken together, these findings suggest that the block in the Qilian Shan did not only absorb the shortening through the north and south vergent thrust-fold system, but also through extrusion, strike-slip, and block rotation tectonic activities. However, the NQT propagation is ongoing and may reactivate older thrust faults with the potential to cause the formation of active faults along the northern margin of the Yumu Shan and Gaizhangdaban areas.

5.2 Deformation Response of the Simulated Fold Hinge

For the regional thrust system, the deformation style is believed to be that of a traditional thrust system, which forms in the hinterland (Davis et al., 1998). However, both basins exhibited different deformation styles in the foreland fold and thrust belts. The sedimentary basins are dustpan shaped and filled with Cretaceous and Neogene strata. However, it is unknown whether this topography formed before the Cretaceous or in the Cenozoic because of the India–Eurasian plate collision. In addition to the sedimentary basins, the hanging walls of the regional thrusts were exposed differently. The hanging walls mark the area adjacent to the basin on the northern, eastern, and southern sides, and on the northern and eastern sides of the hanging walls. The strata appear to have experienced clockwise rotation, as well as thrust motion.

To address these issues, we generated sets of stereographic projections, which suggest that the strike trends and the fold hinge are located in different parts of the Cretaceous strata (**Figure 11**). In the Sunan Basin, the thrust fault system trends almost NW–SE as the fold hinges. In the eastern portion of the Yumu Shan (S-4 and S-5) near the Liyuanpu Fault (LYF) (Wang et al., 2021), the fold hinge has a ~133° trend and a ~23° plunge that is right-laterally rotated by ~13°. In the northern aspect of the Sunan Basin (S-1), the fold hinge trends almost W and has a 15° plunge that has been left-laterally rotated ~25° from the NW. In the central portion of the basin (S-2), the fold hinge is almost undefinable and the strata are nearly parallel, at ~12° toward the north. Hence, we suggest that the strata in Sunan area are the southern limb of the syncline fold (S-1). In the southern part of the Sunan Basin, where folding primarily occurred as folds topping to the central basin, the fold hinges trend ~327° and have a 6° plunge that was right-laterally rotated by ~24°. Based on these data, we suggest that the Sunan Basin was dominated by NE–SW compression from the Late Cretaceous to the Neogene. The fold hinge trend is the opposite in the Sunan Basin and around the LYF; thus, fold deformation was altered by the NW–SE compressive strain. During the most recent tectonic stage, the fold deformation evolved as the block gently rotated. Meanwhile, some researchers have postulated that the Qilian Shan is not involved in block rotation (Wang et al., 2002).

In the Huangcheng Basin, fold deformation throughout the area differs from that in the Sunan Basin. We believe that both study areas are dominated by the NE–SW trending compression. In the Huangcheng Basin, this formed the GZT and HSF. The fold hinges in the basin (H-2, H-3, and H-4) trend ~130° and plunge ~20°, all of which are seldomly rotated. Based on the plunge, the thrust of the CCT influenced the entire area and formed elevated topography in the northwestern portion of the basin. In addition to the southeastward trending folds in the southern aspect of the basin (H-1), the Cretaceous strata trend 39° northeastward and plunge ~4°. Thus, the fold deformation in this area remains unclear.

5.3 Thrust System Mechanism

We established a model to explain the topography observed in the study area (**Figure 12**). Prior to the Cretaceous, crustal shortening of the craton in the Alashan Block thrust downward into the northern Qilian Shan (Yin and Harrison, 2000; Zuza et al., 2016). Two phases of N–S tectonic extension (Chen et al., 2003) formed rifted basins or topographic depressions (Wang et al., 2021) in the Sunan and Huangcheng basins, which resulted from the evolution of the suture belt. The rifted basins were then filled with Cretaceous and Neogene strata. During compression, due to the Songpan-Ganzi and Alashan blocks, the regional thrust faults began to thrust southward and vertically to the eastern margin of the rifted basin, thereby causing the basin margin to become a lateral ramp and forming a tear fault. The Cenozoic strata in the northern Qaidam basin may source from Qilian Shan and the southern Qaidam Basin (Lu et al., 2018), and it indicates that the strata materials in the Qaidam Basin are severed by the northern Qaidam thrust belt (Cheng et al., 2021). According to the source trace of the Lower Cretaceous strata, the ages of the Cretaceous strata are consistent with those of the basement rocks in the Alashan area and in the North China Block (Wang et al., 2021) and most of the materials in the northern Sunan Basin originate from the Bei Shan (Cheng et al., 2019a), indicating that the Alashan Block had a higher topography during the Mesozoic than the current location of the Qilian Shan.

The thrust faults continued to thrust southward and form elevated topography along the northern margin of the sedimentary basin. As for the lateral ramp, the thrust fault plane was rotated and torn apart, forming a tear fault to accommodate the shortening, which then created elevated topography on the eastern side of the basin and lower topography toward the center of the sedimentary basin. Based on the source trace of the strata in the basin, this belt may have developed higher topography than that of the northern Qilian Shan prior to the Cretaceous (Wang et al., 2021).

During the Early Cenozoic, regional southward thrusting seldom propagated, and Neogene strata were deposited on top of the YMT and GZT. The source trace of the Miocene strata indicates that the sediment source was the plutons in the Alashan

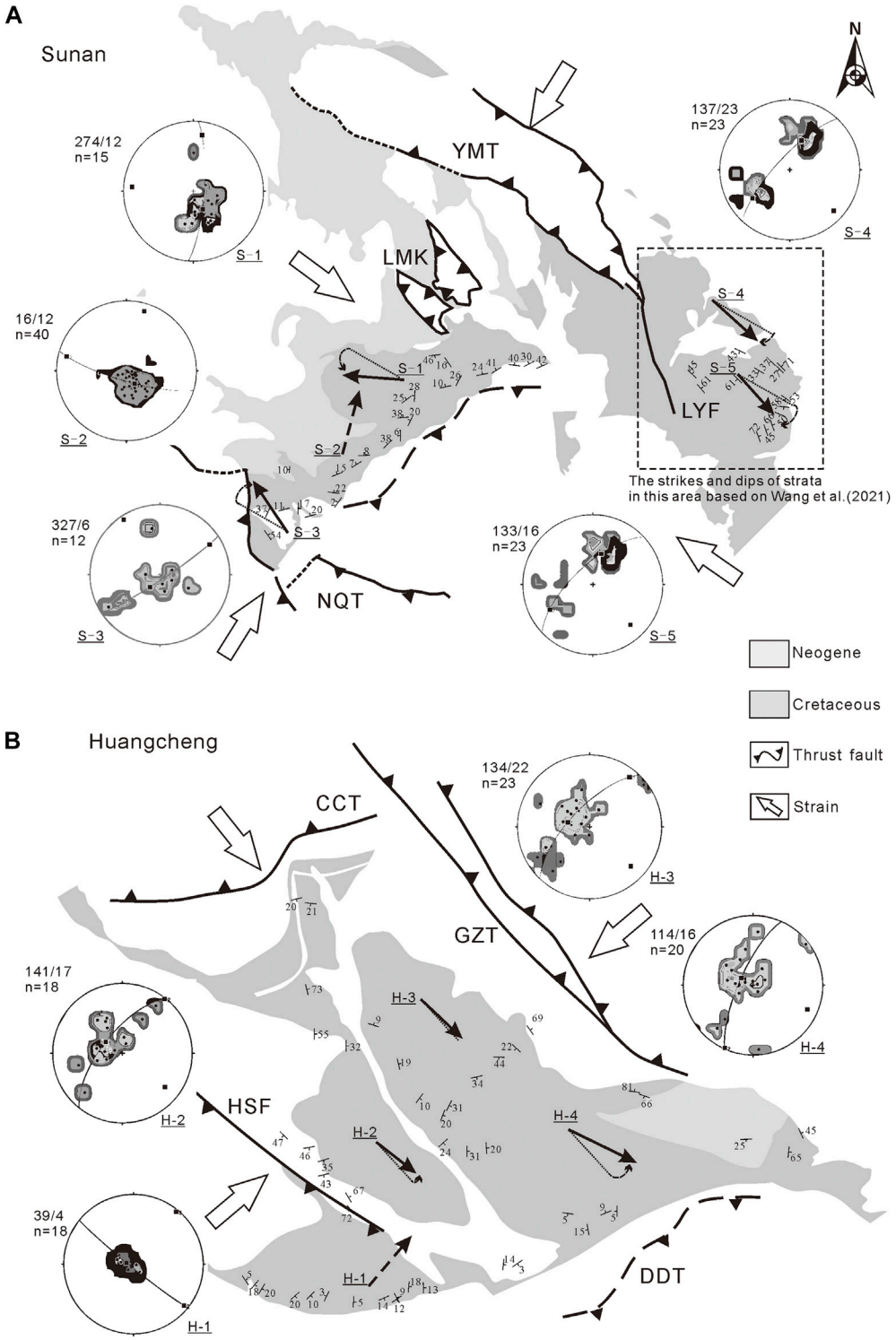

FIGURE 11 | Stereographic projection of the study area. Based on data from the Bureau of Mineral Resources of Gansu Province (BMRGP, Regional Geological Survey) (1982), Wang et al. (2021), and fieldwork conducted for this study. The dots in the stereographic projection represent strata data while circles represent the best fit transection of the fold; thus, the pole of the circle is the simulated fold hinge, which shows the plunge. Arrows indicate the simulated fold hinge. **(A)** Stereographic projection of the Sunan basin. **(B)** Stereographic projection of the Huangcheng basin.

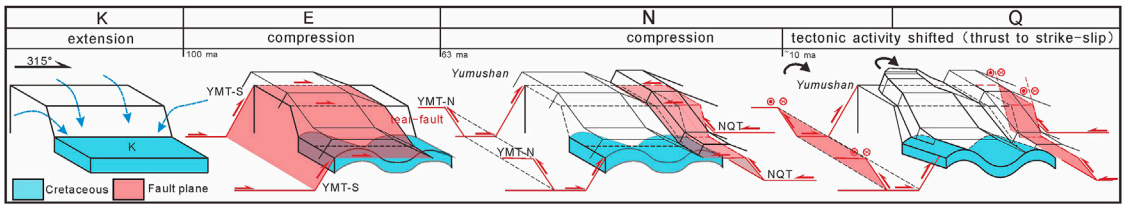

FIGURE 12 | Model of the tectonic evolution of the Sunan area (not strictly to scale). Cretaceous strata deformation history of Sunan Basin, fault plane propagation history, and kinematic characteristics of the strata block through time and tectonic activities, are shown.

area (Wang et al., 2021), which indicates that the strata were uplifted and volcanism, controlled by the YMT and GZT, occurred before the uplift of the Qilian Shan. The hanging walls in the basin are also eroded more than those on the eastern side of the basin, owing to water erosion. Thus, a portion of the hanging wall strata remains on the eastern side of the adjacent rifted basin and forms rivers in the adjacent area, including the Dongdahe River, located along the lateral ramp (**Figure 12**).

The convergence of the Indian and Eurasian plates began at ~50 Ma (Yin, 2000), and produced volcanism along with thrust. The Qilian Shan experienced a NE–SW trending compression strain in the Early Cenozoic (Cheng et al., 2019a). Apatite He ages of the plutons around the western segment of the NQT indicate that the NQT in the Sunan area initially created steep topography at ~10 Ma (Zheng et al., 2010). The intense exhumation events occurred at the beginning of the Mesozoic (Lin et al., 2021). Meanwhile, the sedimentary history of basin has indicated that shortening began at ~10 Ma (Wang et al., 2013; Wang et al., 2017). The Qilian Shan may have been uplifted during the Late Miocene, based on the rapid accumulation in the Sikouzi Basin at ~ 10.5 Ma (Wang et al., 2011) and rapid exhumation of faults in the northeastern Qilian Shan at ~15 Ma (Zheng et al., 2010; Wang et al., 2020), forming high topography. The deformation propagation continues toward the Longshou Shan and Heli Shan regions (Zheng et al., 2013).

On the eastern segment of the NQT in the southern Huangcheng Basin, the HSF is thought to be a branch fault of the NQT, which remains active today. Moreover, the Apatite He ages indicate that the HSF was rapidly exhumed at ~15 Ma (Wang et al., 2020). Moreover, the thrust system on the northeastern margin of the Tibetan Plateau maintained thrust and strike-slip motions (Zheng et al., 2010; Wang et al., 2020). This resulted in strata rotation and left-lateral thrust faults, thereby causing the folding and rotation of the Cretaceous strata in the Sunan and Huangcheng basins. The most likely mechanism for the propagation of the plateau is far-field stress related to the tectonic plate collision. As a result of the propagation of the NQT, the northern regional thrust planes (YMT-S and GZT) dipped more steeply and developed back-thrust faults (YMT-N), enabling the potential reactivation of older thrust faults and topographic uplifts throughout the area.

Based on thermochronological results, the Haiyuan Fault, which is located in the eastern Qilian Shan, shifted from thrust to left-lateral strike-slip motion (Wang et al., 2020). This kind of tectonic shift might have affected the western and central portions of the Qilian Shan–Hexi corridor, which accumulates crustal shortening by eastward block extrusion and rotation in the upper crust. Based on the evidence obtained herein, we postulate that the older Tibetan Plateau growth boundary terminates at the northern margins of the Yumu Shan and Gaizhangdaban by forming an active fault and reproducing the older regional fault. The outgrowth of the Tibetan Plateau may still propagate northeastward, combined with block extrusion toward the east. We also suggest that the subduction of the Alashan Block is ongoing.

6 CONCLUSION

The Qilian Shan orogenic belt is a typical continental collision area characterized by vergent fold and thrust deformation. Older southward vergent thrusts were reactivated by a younger northward thrust system and covered by Neogene strata. The first shortening event was characterized by southward regional thrust systems that developed from the Late Cretaceous to the Neogene, which were constrained by the thrust fault planes covered by Neogene strata. The older regional thrusts are the YMT and GZT, which are characterized by steep fault planes and folds topping to the central basin. The second shortening event began in the Neogene, in which the Qilian Shan propagated northeastward toward the Hexi corridor and rapidly uplifted the NQT, which was produced by the Indian–Eurasian tectonic collision. After two phases of convergence, deformation of the Cretaceous sedimentary basin occurred, and the basin developed fault-related folds that accommodated ~3.56% of the NE–SW shortening in this area.

To investigate the basin shape, we established a deformation model of the study area. Initially, the development of a rifted basin established a depositional setting; thus, the northern Qilian Shan region has lower topography. Subsequently, southward thrust motion and the development of a tear fault formed the contours of the basin and produced elevated topography in the northern and eastern aspects of the basin. When tectonic strain shifted in the Miocene, the deformation (including folds and thrusts) was reactivated by the strike-slip activity and block rotation.

The Qilian Shan–Hexi corridor exhibits typical continental orogenic deformational characteristics. These opposing vergent thrust faults and fault-related folds accommodated the shortening of the propagating Tibetan Plateau, and can be used to define the tectonic evolution of the northeastern Tibetan Plateau.

DATA AVAILABILITY STATEMENT

The raw data supporting the conclusion of this article will be made available by the authors, without undue reservation.

AUTHOR CONTRIBUTIONS

JJ did the field work, field mapping, and wrote the manuscript. WZ contributed to the conception and provided funding for the study. SL, QT, SW, CF, and YZ did the field work. SL, QT, and SW and reviewed and edited the manuscript. All authors contributed to manuscript revision and discussion and approved the submitted version.

FUNDING

This work is supported by the Second Tibetan Plateau Scientific Expedition and Research Program (STEP) (2019QZKK0901), National Natural Science Foundation of China (Grant Nos 42030301, 41872204, 41590861), and Guangdong Province Introduced Innovative R&D Team of Geological Processes and Natural Disasters around the South China Sea (2016ZT06N331).

ACKNOWLEDGMENTS

We are grateful to Yigen Qin and Gan Chen for their guidance during the manuscript writing process.

REFERENCES

Bureau of Mineral Resources of Gansu Province (1982). *BMRGP, Regional Geological Survey*. Beijing, China: Ministry of Geology of China.

Bureau of Mineral Resources of Inner Mongolia Province (1991). *BMRIMP, Regional Geological Survey*. Beijing, China: Ministry of Geology of China.

Bureau of Mineral Resources of Qinghai Province (1991). *BMRQP, Regional Geological Survey*. Beijing, China: Ministry of Geology of China.

Chen, X., Yin, A., Gehrels, G. E., Cowgill, E. S., Grove, M., and Harrison, T. M. (2003). Two Phases of Mesozoic north–south Extension in the Eastern Altyn Tagh Range, Northern Tibetan Plateau. *Tectonics* 22. doi:10.1029/2001TC001336

Cheng, F., Garzione, C., Jolivet, M., Wang, W., Dong, J., Richter, F., et al. (2019a). Provenance Analysis of the Yumen Basin and Northern Qilian Shan: Implications for the Pre-collisional Paleogeography in the NE Tibetan Plateau and Eastern Termination of Altyn Tagh Fault. *Gondwana Res.* 65, 156–171. doi:10.1016/j.gr.2018.08.009

Cheng, F., Jolivet, M., Dupont-Nivet, G., Wang, L., Yu, X., and Guo, Z. (2015). Lateral Extrusion along the Altyn Tagh Fault, Qilian Shan (NE Tibet): Insight from a 3D Crustal Budget. *Terra Nova* 27, 416–425. doi:10.1111/ter.12173

Cheng, F., Jolivet, M., Guo, Z., Lu, H., Zhang, B., Li, X., et al. (2019b). Jurassic–Early Cenozoic Tectonic Inversion in the Qilian Shan and Qaidam basin, North Tibet: New Insight from Seismic Reflection, Isopach Mapping, and Drill Core Data. *J. Geophys. Res. Solid Earth*. 124, 12077–12098. doi:10.1029/2019jb018086

Cheng, F., Jolivet, M., Guo, Z., Wang, L., Zhang, C., and Li, X. (2021). Cenozoic Evolution of the Qaidam basin and Implications for the Growth of the Northern Tibetan Plateau: A Review. *Earth Sci. Rev.* 220. doi:10.1016/j.earscirev.2021.103730

Clark, M. K., Farley, K. A., Zheng, D., Wang, Z., and Duvall, A. R. (2010). Early Cenozoic Faulting of the Northern Tibetan Plateau Margin from Apatite (U–Th)/He Ages. *Earth Planet. Sci. Lett.* 296, 78–88. doi:10.1016/j.epsl.2010.04.051

Dai, S., Fang, X., Dupont-Nivet, G., Song, C., Gao, J., Krijgsman, W., et al. (2006). Magnetostratigraphy of Cenozoic Sediments from the Xining basin: Tectonic Implications for the Northeastern Tibetan Plateau. *JGR Solid Earth* 111, B11102. doi:10.1029/2005jb004187

Davis, G. A., Wang, C., Zheng, Y., Zhang, J., Zhang, C., and Gehrels, G. E. (1998). The Enigmatic Yinshan Fold-And-Thrust belt of Northern China: New Views on its Intraplate Contractional Styles. *Geology* 26. doi:10.1130/0091-7613(1998)026<0043:teyfat>2.3.co;2

Dayem, K. E., Molnar, P., Clark, M. K., and Houseman, G. A. (2009). Far-field Lithospheric Deformation in Tibet during continental Collision. *Tectonics* 28, TC6005. doi:10.1029/2008tc002344

Elliott, D. (1983). The Construction of Balanced Cross-Sections. *J. Struct. Geol.* 5, 101. doi:10.1016/0191-8141(83)90035-4

Guo, X., Gao, R., Li, S., Xu, X., Huang, X., Wang, H., et al. (2016). Lithospheric Architecture and Deformation of NE Tibet: New Insights on the Interplay of Regional Tectonic Processes. *Earth Planet. Sci. Lett.* 449, 89–95. doi:10.1016/j.epsl.2016.05.045

He, P., Song, C., Wang, Y., Wang, D., Chen, L., Meng, Q., et al. (2021). Early Cenozoic Activated Deformation in the Qilian Shan, Northeastern Tibetan Plateau: Insights from Detrital Apatite Fission-track Analysis. *Basin Res.* 33, 1731–1748. doi:10.1111/bre.12533

Hu, X., Garzanti, E., Moore, T., and Raffi, I. (2015). Direct Stratigraphic Dating of India–Asia Collision Onset at the Selandian (Middle Paleocene, 59 ± 1 Ma). *Geology* 43, 859–862. doi:10.1130/g36872.1

Jin, Z., Cunningham, D., and Hongyi, C. (2010). Sedimentary Characteristics of Cenozoic Strata in central-southern Ningxia, NW China: Implications for the Evolution of the NE Qinghai–Tibetan Plateau. *J. Asian Earth Sci.* 39, 740–759. doi:10.1016/j.jseaes.2010.05.008

Jolivet, M., Brunel, M., Seward, D., Xu, Z., Yang, J., Roger, F., et al. (2001). Mesozoic and Cenozoic Tectonics of the Northern Edge of the Tibetan Plateau: Fission-Track Constraints. *Tectonophysics* 343, 111–134. doi:10.1016/s0040-1951(01)00196-2

Li, C., Zhang, C., Cope, T. D., and Lin, Y. (2016). Out-of-sequence Thrusting in Polycyclic Thrust Belts: An Example from the Mesozoic Yanshan belt, North China Craton. *Tectonics* 35, 2082–2116. doi:10.1002/2016tc004187

Lin, X., Jolivet, M., Liu-Zeng, J., Cheng, F., Tian, Y., and Li, C. a. (2021). Mesozoic–Cenozoic Cooling History of the Eastern Qinghai Nan Shan (NW China): Apatite Low-Temperature Thermochronology Constraints. *Palaeogeogr. Palaeoclimatol. Palaeoecol.* 572. doi:10.1016/j.palaeo.2021.110416

Lu, H., Ye, J., Guo, L., Pan, J., Xiong, S., and Li, H. (2018). Towards a Clarification of the Provenance of Cenozoic Sediments in the Northern Qaidam basin. *Lithosphere* 11, 252–272. doi:10.1130/l1037.1

Pan, B., Li, Q., Hu, X., Geng, H., Liu, Z., Jiang, S., et al. (2013). Cretaceous and Cenozoic Cooling History of the Eastern Qilian Shan, north-eastern Margin of the Tibetan Plateau: Evidence from Apatite Fission-Track Analysis. *Terra Nova* 25, 431–438. doi:10.1111/ter.12052

Wang, E., Meng, K., Su, Z., Meng, Q., Chu, J. J., Chen, Z., et al. (2014). Block Rotation: Tectonic Response of the Sichuan basin to the Southeastward Growth of the Tibetan Plateau along the Xianshuihe–Xiaojiang Fault. *Tectonics* 33, 686–718. doi:10.1002/2013tc003337

Wang, Q., Wang, W., Cui, D., Zhu, G., and Liang, W. (2002). Present-day Crustal Movement of Northeastern Margin of Qinghai-Tibet Block. *J. Geod. Geodynamic.* 22.

Wang, W., Kirby, E., Zhang, P., Zheng, D., Zhang, G., Zhang, H., et al. (2013). Tertiary basin Evolution along the Northeastern Margin of the Tibetan Plateau: Evidence for basin Formation during Oligocene Transtension. *Geol. Soc. Am. Bull.* 125, 377–400. doi:10.1130/b30611.1

Wang, W., Zhang, P., Kirby, E., Wang, L., Zhang, G., Zheng, D., et al. (2011). A Revised Chronology for Tertiary Sedimentation in the Sikouzi basin: Implications for the Tectonic Evolution of the Northeastern Corner of the Tibetan Plateau. *Tectonophysics* 505, 100–114. doi:10.1016/j.tecto.2011.04.006

Wang, W., Zheng, D., Li, C., Wang, Y., Zhang, Z., Pang, J., et al. (2020). Cenozoic Exhumation of the Qilian Shan in the Northeastern Tibetan Plateau: Evidence from Low-Temperature Thermochronology. *Tectonics* 39. doi:10.1029/2019tc005705

Wang, W., Zheng, W., Zhang, P., Li, Q., Kirby, E., Yuan, D., et al. (2017). Expansion of the Tibetan Plateau during the Neogene. *Nat. Commun.* 8, 15887. doi:10.1038/ncomms15887

Wang, X., Deng, L., Zattin, M., Ji, M., and Li, J. (2017). Palaeogene Growth of the Northeastern Tibetan Plateau: Detrital Fission Track and Sedimentary Analysis of the Lanzhou basin, NW China. *J. Asian Earth Sci.* 147, 322–331. doi:10.1016/j.jseaes.2017.07.020

Wang, Y., Chen, X., Zhang, Y., Yin, Z., Zuza, A. V., Yin, A., et al. (2021). Superposition of Cretaceous and Cenozoic Deformation in Northern Tibet: A Far-Field Response to the Tectonic Evolution of the Tethyan Orogenic System. *GSA Bull.* 134, 501–525. doi:10.1130/b35944.1

Xiao, W., Windley, B. F., Yong, Y., Yan, Z., Yuan, C., Liu, C., et al. (2009). Early Paleozoic to Devonian Multiple-Accretionary Model for the Qilian Shan, NW China. *J. Asian Earth Sci.* 35, 323–333. doi:10.1016/j.jseaes.2008.10.001

Yang, S. (2007). *Structural Features and Petroleum Prospects of Thrust belt in the Northern Margin of Qilian Mountains*. Beijing: Science Press. (in Chinese).

Yin, A. (2006). Cenozoic Tectonic Evolution of the Himalayan Orogen as Constrained by Along-Strike Variation of Structural Geometry, Exhumation History, and Foreland Sedimentation. *Earth-Science Rev.* 76, 1–131. doi:10.1016/j.earscirev.2005.05.004

Yin, A., Dang, Y. Q., Wang, L. C., Jiang, W. M., Zhou, S. P., Chen, X. H., et al. (2008a). Cenozoic Tectonic Evolution of Qaidam basin and its Surrounding Regions (Part 1): The Southern Qilian Shan–Nan Shan Thrust Belt and Northern Qaidam basin. *Geol. Soc. America Bull.* 120, 813–846. doi:10.1130/b26180.1

Yin, A., Dang, Y. Q., Zhang, M., Chen, X. H., and McRivette, M. W. (2008b). Cenozoic Tectonic Evolution of the Qaidam basin and its Surrounding Regions (Part 3): Structural Geology, Sedimentation, and Regional Tectonic Reconstruction. *Geol. Soc. America Bull.* 120 (7–8), 847–876. doi:10.1130/b26232.1

Yin, A., and Harrison, T. M. (2000). Geologic Evolution of the Himalayan-Tibetan Orogen. *Annu. Rev. Earth Planet. Sci.* 28, 211–280. doi:10.1146/annurev.earth.28.1.211

Yin, A. (2000). Mode of Cenozoic East–West Extension in Tibet Suggesting a Common Origin of Rifts in Asia during the Indo-Asian Collision. *J. Geophys. Res.* 105, 21745–21759. doi:10.1029/2000jb900168

Yu, J., Pang, J., Wang, Y., Zheng, D., Liu, C., Wang, W., et al. (2019). Mid-Miocene Uplift of the Northern Qilian Shan as a Result of the Northward Growth of the Northern Tibetan Plateau. *Geosphere* 15, 423–432. doi:10.1130/ges01520.1

Yuan, D. Y., Ge, W. P., Chen, Z. W., Li, C. Y., Wang, Z. C., Zhang, H. P., et al. (2013). The Growth of Northeastern Tibet and its Relevance to Large-Scale continental Geodynamics: A Review of Recent Studies. *Tectonics* 32, 1358–1370. doi:10.1002/tect.20081

Zhang, P., Shen, Z., Wang, M., Gan, W., Bürgmann, R., Molnar, P., et al. (2004). Continuous Deformation of the Tibetan Plateau from Global Positioning System Data. *Geology* 32, 809–812. doi:10.1130/g20554.1

Zheng, D., Clark, M. K., Zhang, P., Zheng, W., and Farley, K. A. (2010). Erosion, Fault Initiation and Topographic Growth of the North Qilian Shan (Northern Tibetan Plateau). *Geosphere* 6, 937–941. doi:10.1130/ges00523.1

Zheng, W., Zhang, P., Ge, W., Molnar, P., Zhang, H., Yuan, D., et al. (2013). Late Quaternary Slip Rate of the South Heli Shan Fault (Northern Hexi Corridor, NW China) and its Implications for Northeastward Growth of the Tibetan Plateau. *Tectonics* 32, 271–293. doi:10.1002/tect.20022

Zhong, D., and Ding, L. (1996). Discussion on the Uplift Process and Mechanism of the Qinghai-Tibet Plateau. *Sci. China (Earth Sci.* 26, 289–295. (in Chinese).

Zhou, J., Wang, J., An, Y., Spurlin, M. S., and Horton, B. K. (2002). Depositional Patterns and Tectonic Setting of Early Tertiary Basins in the NE Margin of the Tibetan Plateau: A Case Study of the Nangqian and Xialaxiu Basins (In Chinese). *Acta Sed Sin* 20, 85–91.

Zuza, A. V., Cheng, X., and Yin, A. (2016). Testing Models of Tibetan Plateau Formation with Cenozoic Shortening Estimates across the Qilian Shan–Nan Shan Thrust belt. *Geosphere* 12, 501–532. doi:10.1130/ges01254.1

Zuza, A. V., Gavillot, Y., Haproff, P. J., and Wu, C. (2020). Kinematic Evolution of a continental Collision: Constraining the Himalayan-Tibetan Orogen via Bulk Strain Rates. *Tectonophysics* 797. doi:10.1016/j.tecto.2020.228642

Zuza, A. V., Wu, C., Reith, R. C., Yin, A., Li, J., Zhang, J., et al. (2018a). Tectonic Evolution of the Qilian Shan: An Early Paleozoic Orogen Reactivated in the Cenozoic. *Geol. Soc. Am. Bull.* 130, 881–925. doi:10.1130/b31721.1

Zuza, A. V., Wu, C., Wang, Z., Levy, D. A., Li, B., Xiong, X., et al. (2019). Underthrusting and Duplexing beneath the Northern Tibetan Plateau and the Evolution of the Himalayan-Tibetan Orogen. *Lithosphere* 11, 209–231. doi:10.1130/l1042.1

Conflict of Interest: The authors declare that the research was conducted in the absence of any commercial or financial relationships that could be construed as a potential conflict of interest.

Publisher's Note: All claims expressed in this article are solely those of the authors and do not necessarily represent those of their affiliated organizations, or those of the publisher, the editors and the reviewers. Any product that may be evaluated in this article, or claim that may be made by its manufacturer, is not guaranteed or endorsed by the publisher.

Copyright © 2022 Jia, Zheng, Zhang, Wei, Liang, Feng, Zhu, Tang and Wang. This is an open-access article distributed under the terms of the Creative Commons Attribution License (CC BY). The use, distribution or reproduction in other forums is permitted, provided the original author(s) and the copyright owner(s) are credited and that the original publication in this journal is cited, in accordance with accepted academic practice. No use, distribution or reproduction is permitted which does not comply with these terms.

frontiers in Earth Science

ORIGINAL RESEARCH
published: 09 March 2022
doi: 10.3389/feart.2022.833585

Depositional Record and Geochemistry Constraints on the Late Miocene–Quaternary Evolution of the Taiyuan Basin in Shanxi Rift System, China

Qitian Zhuang[1,2], *Rongzhu Wei*[3] *and Honglin He*[1,2]*

[1]State Key Laboratory of Earthquake Dynamics, Institute of Geology, China Earthquake Administration, Beijing, China, [2]Shanxi Taiyuan Continental Rift Dynamics National Observation and Research Station, Taiyuan, China, [3]Shanxi Institute of Geological Survey, Taiyuan, China

The formation and evolution of the Shanxi Rift System are topics of interest because of its unique geometry and critical position in the North China Plate. However, it is not easy to delineate the late Cenozoic tectonic processes. This is partly because it is difficult to preserve the normal faults' movement evidence and related deposits for dating in the outcrop. Besides, the current studies are heavily weighted in the low-temperature thermochronology, whereas it is insensitive to the exhumation after the late Miocene. To decipher the late Cenozoic evolution, we offer a case of detailed depositional recording from the boreholes of the Taiyuan Basin in the Shanxi Rift System. Fluvial, deltaic, and lacustrine environments were identified by the systematic stratigraphic analysis of boreholes. Two mega transgressions generated basin-wide lakes at ca. 5.8–4.4 and ca. 2.2–1.6 Ma. We attribute the lake expansion events to tectonism because climatic variations from reconstruction of the paleoclimate with geochemistry index and previous work exhibited asynchronous processes with the transgression. Thus, the basin experienced two stages of extensive subsidence after the rift occurred. This result is conducive to obtaining a more complete late Cenozoic tectonic evolution of the Shanxi Rift System.

Keywords: shanxi rift system, cenozoic, geochemistry, sedimentary environment, palaeoclimate

OPEN ACCESS

Edited and reviewed by:
Xuhua Shi,
Zhejiang University, China

***Correspondence:**
Honglin He
honglinhe123@vip.sina.com

Specialty section:
This article was submitted to Quaternary Science, Geomorphology and Paleoenvironment, a section of the journal Frontiers in Earth Science

Received: *11 December 2021*
Accepted: *24 January 2022*
Published: *09 March 2022*

Citation:
Zhuang Q, Wei R and He H (2022) Depositional Record and Geochemistry Constraints on the Late Miocene–Quaternary Evolution of the Taiyuan Basin in Shanxi Rift System, China. Front. Earth Sci. 10:833585. doi: 10.3389/feart.2022.833585

1 INTRODUCTION

The Cenozoic intracontinental extension around the Ordos Block of the western North China Plate is a significant component of the Eurasian continent deformation (Tapponnier and Molnar, 1977; Tapponnier et al., 1982; Peltzer et al., 1985; Yin, 2010). A range of basins have been generated since the early Eocene in the periphery of the Ordos Block, and they are commonly related to the evolution of the Tibet Plateau (Deng et al., 1973; Tapponnier and Molnar, 1977; Ma et al., 1982; Tapponnier et al., 1986; Zhang et al., 2003; Kusky et al., 2007). The Shanxi Rift System, which situates in the east margin of the Ordos Block, is usually believed as the latest formed basin system (Zhang et al., 1998; Deng et al., 1999; Wei et al., 2020). Therefore, discrepancies of development time and evolution processes between the Shanxi Rift System and other basins around the Ordos Block have drawn researchers' attentions (The Research Group on Active Fault System around Ordos MassifState

Seismological Bureau, 1988; Xu and Ma, 1992; Zhang et al., 1998; Zhang et al., 2003; Zhang et al., 2006; Shi et al., 2020), and this raises the need for an integrated knowledge of the rift evolution.

Works of predecessors, such as the low-temperature thermochronology (Li Bin et al., 2015; Zhao et al., 2016; Chang et al., 2018; Clinkscales et al., 2020; Clinkscales et al., 2021; Su et al., 2021), revealed that the rift could have experienced multiple uplift events from the Late Cretaceous to Miocene. However, it is challenging to constrain the cooling history after Miocene due to the annealing temperature limitation. In addition, analysis of fault kinematics (Zhang et al., 1998; Zhang and Liao, 2006; Shi et al., 2015; Shi et al., 2020) presented the regional stress transition of multiple phases, illustrating the Pacific Plate and/or Indian Plate dynamic source. Nevertheless, most of the results above were more likely to delineate the pre-rift episodes than the syn-rift processes since no corresponding deposits prior to the mid-Miocene were found in the Shanxi Rift System (Wei et al., 2020). On the other hand, detailed sedimentology researches are mainly from limited and incomplete outcrops (Sun, 2005; Deng et al., 2007; Liu et al., 2012; Chen et al., 2016; Chen et al., 2021), which is insufficient for a comprehensive understanding of the evolution. Hence, analysis based on a complete depositional succession in the basin is vital in basin evolution research (Liu and Zhang, 2005). Furthermore, it requires the establishment of the basin filling succession and the sedimentary environment evolution.

Sedimentary basins are regions of prolonged subsidence on Earth's surface (Allen and Allen, 2013). Subsidence provides accommodation for the storage of detritus from adjacent ranges suffering weathering and erosion (Allen and Allen, 2013). While the sediments, in turn, record the history of mountain uplift and the degree of weathering in the source area. Therefore, there is an inextricably linked liaison between climate, process of denudation–transportation–deposition, and tectonic settings in the basin-range research field (Zhang et al., 2001; Pan et al., 2003; Weltje and Von Eynatten, 2004; Clift and Jonell, 2021).

In order to obtain a complete sedimentary sequence, we conducted borehole ZK01 in the east part of Taiyuan Basin, which lies in the middle of the Shanxi Rift System. The geochemistry of sediments from the drill was analyzed to reveal the palaeoenvironment (Singer, 1980; Armstrong-Altrin, 2009; Wang et al., 2021) of the Taiyuan Basin. In addition, many boreholes have been carried out by the Shanxi Oil Team before ZK01. Thereinto, borehole J2, J7, and T2 perforate the Cenozoic and are distributed in different basin parts. Although their age data are absent, a relatively detailed record compiling can be used to stratigraphic division and correlation, which is helpful for a more integrated study of the evolution of Taiyuan Basin. We aim to fetch the paleoenvironment information *via* elements analysis, and then recognize the sedimentary environments and establish the sedimentary sequence in Taiyuan Basin. Furthermore, we attempt to discuss whether the shifts of the environments result from climate-driven or tectonic-driven processes.

2 GEOLOGICAL SETTING

The Shanxi Rift System is located on the eastern margin of the Ordos basin and the west side of the North China Plain (**Figure 1**). The rift system terminates at the Yinshan–Yanshan ("shan" = mountain) orogenic belt on the north and is connected with Weihe Basin and Qinling Mountain on the south. The western Lvliang Mountain and eastern Taihang Mountain separate the Ordos basin and the North China Plain from the Rift System, respectively. According to the drill data (Xu et al., 1993; Wei et al., 2020; Yan et al., 2020), aeolian red clay and gravels (Xu et al., 2009; Yue et al., 2004), and the Cenozoic basalt (Chen, 1987; Wang et al., 1996), the Shanxi Rift System were developed from late Miocene. The thermochronologic data also denoted the time of the most recent rapid cooling event around the Shanxi Rift System at about 10 Ma (white stars and time labels in **Figure 1**). A total of five en echelon basins (from north to south, Datong Basin, Xin-Ding Basin, Taiyuan Basin, Linfen Basin, and Yuncheng Basin) in left stepped form extend for >700 km. Basins are separated by mountain or push-up swells (Xu and Ma, 1992; Xu et al., 1993). The range-front steep faults, as the boundaries between ranges and basins, are characterized by dip-slip and perhaps accompanied by a small amount of dextral strike-slip component (Hu et al., 2012; Jiang et al., 2012; Xu, 2012; Zhang and Liu, 2012; Huang et al., 2018). The active normal faults control the subsidence of basins, and the maximal thickness of Cenozoic sediments is more than 4 km (Xu and Ma, 1992). Although the active faults are believed only started in late Neogene (Wang et al., 1996; Zhang et al., 1998; Zhang et al., 2003), the location and geometry of the basins are likely to be dependent in part on the pre-existing fold-thrust belt structures (Clinkscales and Kapp, 2019) of the Indosinian (235–200 Ma old) orogeny and the Yanshanian (150–60 Ma old) orogeny (Xu and Ma, 1992; Xu et al., 1993; Zhang et al., 1998).

The Taiyuan Basin lies in the central part of the Shanxi Rift System. Two high-angle normal faults on the NW (i.e., the Jiaocheng Fault) and SE sides (i.e., the Taigu Fault) restrict the basin in a typical rhombic shape (Xu et al., 1993). The striking difference between the sedimentary thickness of the western and eastern part of the basin indicates asymmetrical subsidence (Zhang et al., 1998; Shi et al., 2015; Wei et al., 2020), revealing that the Jiaocheng Fault is more active than the Taigu Fault. The Fen River originates from the northern Lvliang Mountain, passing through the Jiaocheng Fault into Taiyuan Basin, then joining the Yellow River further downstream. Deep incised meander is created in Lvliang Mountain before where the Fen River drains into the basin. In the north, the Shilingguan Uplift occurs in the joint of the Taiyuan Basin and the Xin-Ding Basin, consisting mainly of Paleozoic limestone and overlying Quaternary unconsolidated deposits (Shanxi Bureau of Geology and Mineral Resources, 1989; Wang et al., 1996). It is disputed that whether the Shilingguan Uplift was a paleocourse of Hutuo River into Taiyuan Basin from Xin-Ding Basin or not (Willis, 1907; Li and Liang., 1965; Cheng, 1983; Wu, 1996). In the south, the Fen River flows into the Linfen Basin through the narrow Lingshi Uplift, cutting a canyon with hundreds of meters

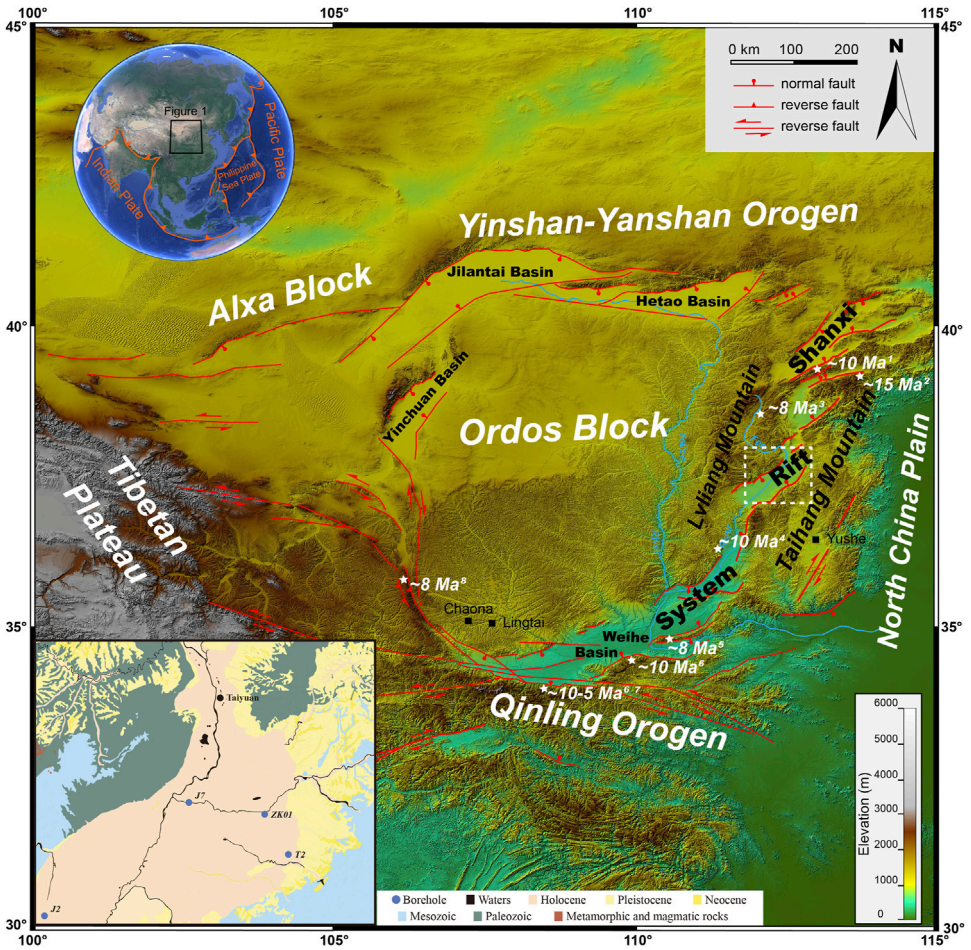

FIGURE 1 | Regional tectonic setting and digital elevation (SRTM 90 m resolution) of North China and adjacent regions. The Shanxi Rift System and the other basin systems around the Ordos Block are mapped out. The white stars denote the published thermochronological data of rapid cooling events after late Miocene: (1) Clinkscales et al. (2020), (2) Qing et al. (2008), (3) Zhao et al. (2009), (4) Li Jianxing et al. (2015), (5) Su et al. (2021), (6) Liu et al. (2013), (7) Heberer et al. (2014), (8) Zheng et al. (2006). The dotted white box refers to the location of the Taiyuan Basin, and its stratigraphic map is shown at the bottom left corner (after Shanxi Bureau of Geology and Mineral Resources, 1989).

in height in the Paleozoic strata. Pre-Cenozoic strata form the main body of surrounding ranges. Nevertheless, the Archean–Paleoproterozoic igneous and metamorphic basement rocks are exposed mainly to the north of the Taiyuan Basin and in the southernmost of the Shanxi Rift System, as well as the low-grade metamorphic Proterozoic rocks (Shanxi Bureau of Geology and Mineral Resources, 1989). Unlike the Precambrian rocks, Paleozoic marine–continental strata and Mesozoic fluvial-lacustrine strata are widely distributed with a dominant position. The pre-Cenozoic strata were folded to form the northeast-southwest trending Taihang-Lvliang fold belt in Yanshanian (Clinkscales and Kapp, 2019). Afterward, the fold belt was unconformably covered by late Cenozoic deposits. Around the Taiyuan Basin, most of the Cenozoic sediments are buried in the basin with a depth up to 4,000 m (Xu et al., 1993; Wang et al., 1996). The residual outcrop of Cenozoic sediments is primarily in the eastern piedmont platform. However, rare outcrop can be seen around the west rim of Taiyuan Basin (Wang et al., 1996), which may have a causal link with the intense activity of the Jiaocheng Fault. The paleomagnetic chronology of the bottom sediments in Taiyuan Basin presents ca. 8.1 Ma (Wei et al., 2020), manifesting a late Miocene sedimentary formation.

3 STRATIGRAPHY AND SEDIMENTARY ENVIRONMENTS

3.1 Stratigraphy

The ZK01 drill hole locates in the northeastern part of the Taiyuan Basin (**Figure 1**). A total length of 850 m of borehole core reveals a complete Cenozoic stratigraphic succession of Taiyuan Basin. From bottom to top, the section is divided into six formations [i.e., Xiatuhe Formation (Xt Fm.), Xiaobai

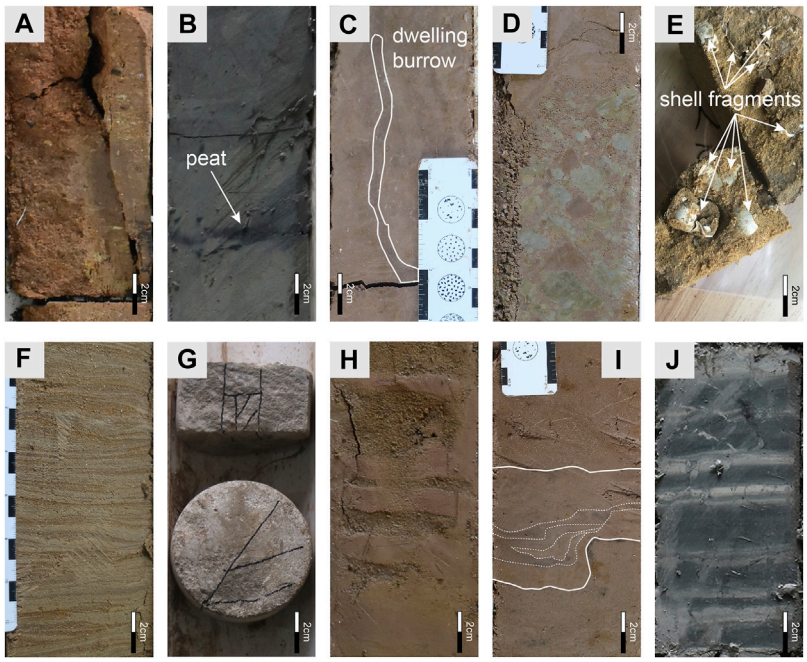

FIGURE 2 | Photographs of typical sedimentary features in ZK01 core. **(A)** Paleosol in Xiatuhe Formation (Xt Fm.). **(B)** Black organic-rich clay in Xiaobai Formation (Xb Fm.). Note the peat layer to which the arrow points. **(C)** Mud-filled dwelling burrow in Hongya Formation (Hy Fm.). **(D)** Mud clasts in Hy Fm., with rough normal-grading. **(E)** Shell fragments in Dagou Formation (Dg Fm.). **(F)** Wavy beddings of sand and clayey silt in Mugua Formation (Mg Fm.). **(G)** Rigid and compact calcareous cement in Fenhe Formation (Fh Fm.). **(H)** Contorted beds commonly seen on delta front. **(I)** Tidal rhythmite consisting of silts and muds. **(J)** Lacustrine rhythmite of pale carbonate-rich and dark organic-rich stratifications.

Formation (Xb Fm.), Hongya Formation (Hy Fm.), Dagou Formation (Dg Fm.), Mugua Formation (Mg Fm.), and Fenhe Formation (Fh Fm.)] (Wei et al., 2020).

3.1.1 Xiatuhe formation (853–584 m)

The Xt Fm. is unconformably overlaid on the Yanchang Formation of the Upper Triassic, with a thickness of 270 m. The lower part (853–788 m) is characterized by brown pebbles and sands that alternate stratigraphically. Erosional surfaces are common at the base of the coarse fraction. The pebbles are moderately to well rounded and mainly composed of sandstone. The sands range from silts to coarse sands with poor sorting. It is worth noting that an interval of paleosol is recorded between the pebble layers (**Figure 2A**). A decrease of particle size occurs upward to form a granule–silt succession. The upper part (788–584 m) consists of massive light brick-red silts and clayey silts, with a few thin clay interlayers. The silts are granularity uniform and enriched with calcium masses. The deposits are colored light red by iron oxides. Besides, mud-clasts are common, implying the presence of high-energy flows. Fossils are rarely found.

3.1.2 Xiaobai formation (584–399 m)

As the finest section on granularity in the whole drill core, the lower part (584–508 m) of Xb Fm. is whitish-gray to gray-olive-green clay in the majority, while the upper part (508–399 m) includes dark gray-green clay and pale brown silts–silty clay. Rhythmites are common in the lower part. On the whole, this section presents a coarsening-upward tendency. The pale gray color of the sediment may be attributed to the large amount of calcium it contains, which has a remarkable distinction with the underlying light brick-red Xt Fm. Most of the Xb Fm. sections are massive thick layers, with a handful of finely laminated rhythmites. The fragments of Corbicula, which live in freshwater are common. Black organic-rich clay layers appear on the upper part of the section (**Figure 2B**).

3.1.3 Hongya Formation (399–264 m)

The Hy Fm. has a large particle size variation. It starts with pebbly medium sand of normal grading and is overlaid by brown massive clay–silty clay (399–338 m). The middle part (338–320 m) is featured by dark brown silts–medium sands interbedded with silty clay. Many rust-colored spots appear in the silty clay. There are mud-filled dwelling burrows perpendicular to the bedding in the silts at the top of this part (**Figure 2C**). This part constitutes the coarsest-grained fraction in the Hy Fm. The upper part (320–264 m) comprises gray-brown silts and clay. Yellowish green spots are observed in clay layers. A 10-cm-thick layer of pebble-shaped mud clasts is sandwiched between silt layers. The mud clasts are poorly sorted and subangular, with irregular bedding planes (**Figure 2D**). The Hy Fm. contains a small amount of Viviparus.

3.1.4 Dagou formation (264–182)

The Dg Fm. is also characterized by a fusiform granularity distribution pattern. At the bottom (264–246 m), gray and

dark brown silty clay is the majority, with a thin bed of weakly developed cross-lamination. A large number of shell fragments are visible. The coarse part (246–215 m) consists mainly of brown fine sands and silts. Rounded granules are sporadic in pure and closely graded sands, usually with distinct normal grading. Erosion surfaces are common on the bottom of the normal grading sequences. The upper part (215–182) consists of light brown silts and silty clay, with few thin layers of fine sands. This part is marked by plentiful yellowish-green mottles, bands, and masses. Laminated structures can be seen in intercalated thin silts and clay, which may be attributed to climatic variations. The silts usually have a sharp base and lenticular form, presenting ripples on their upper surface. Abundant shell fragments (**Figure 2E**) are visible in silts.

3.1.5 Mugua formation (182–127 m)

The Mg Fm. is composed mainly of brown to grayish-black clay and silty clay. Plentiful broken shells spread among very thin fine sand layers. In the lower part (172–173), massive rust stains are very extensive. Parallel beddings are well developed, especially in the finest portion. In the upper part of the formation, black organic-rich bands are common in the gray clay unit. The well-developed wavy beddings of sand and clayey silt occur at the top (**Figure 2F**).

3.1.6 Fenhe formation (127–0 m)

Brown and beige silty clay–silts and fine sands are the central features of the Fh Fm. Noteworthy increase of sand content differs significantly from the underlying Mg Fm., which is mainly clay and silty clay. It is gradually varied from the dark gray clay of the uppermost of Mg Fm., to the silty clay of the downmost of Fh Fm. Rigid and compact white calcareous cement (**Figure 2G**) appears in the lower part (127–118 m) of the Fh Fm. In the middle part (118–18 m), light brown silty clay–silts and dark brown fine–medium sands appear alternately. Most sediments are massive, while scour-filling structures are common. Subangular granules are sparse in silts and sands. The fragments of *Corbicula* are visible at the top of the part. The top (18–0 m) of the Fh Fm. is composed mainly of silts and clay, whereas with the mixture of very fine loess, the sediments present mess and obscurity.

3.2 Sedimentary environments

Emphasis is placed on grain size, color, fossils, bed geometry, texture, and structures of the deposits to assess sedimentary environments comprehensively. Sedimentary systems are divided into fluvial, deltaic, and lacustrine environments on a sketchy description of the Taiyuan Basin. Each system is further subdivided to bear out its reasonability.

3.2.1 Fluvial environment

The fluvial environment consists of channel deposits and overbank deposits, which are components of meandering river on low gradient terrain (Miall, 1980; Miall, 1985; Reading, 2009). The channel deposits are dominated by coarse-grained sediments, which usually have a larger particle size than silt, while overbank deposits are primarily of fine-grained sediments such as clay and silt. The channel and overbank sediments are typically treated as combination of binary structure (i.e., substratum and top stratum).

3.2.1.1 Channel deposits

The channel deposits consist of channel-fill and channel bar sediments. Channel-fill sediments are localized in the channel and divided into coarse-grained and fine-grained deposits (Middleton et al., 2003), depending on whether the channels are abandoned gradually or abruptly (Reading, 2009).

The coarse-grained channel deposits contain gravels lying on floors directly (also called lag deposits) and overlying sands. They are characterized by large grain size, thin layer, and lateral discontinuity. In the ZK01 core, the lag sediments are mainly distributed in the lower Xt Fm. They are composed mainly of sub-rounded pebbles, with sands overlying on the pebbles. Apparent erosive surfaces are common at the base of pebbles. The lag deposits are also seen in the upper Xt Fm. and in the base of Hy Fm. These deposits mark the position of abandoned channels.

The fine-grained channel deposits consist of silt and clay that are deposited in oxbow lakes. As channels are abandoned due to neck cutoff, they would provide relatively enclosed space for still water (Fisk, 1947), leading to the accumulation of overbank fines in oxbow lakes with an upward-fining sequence as the mud is laid on the top (Reading, 2009). Accordingly, the oxbow lake sediments in the Xt Fm. are hardly distinguished from the flood plain sediments in the core.

Channel-bar, also known as point bar, is the sediments of river migration on the floodplain. They usually emerge with the lag deposits, constituting upward-fining sequences. The sand bars from the core are mainly fine–coarse sand of normal grading, with relatively low textural maturity. However, distinct trough cross-beddings and planar cross-beddings are absent, which may be attributed to the limitation of the borehole core. The thickness of the sand bar horizon is usually less than 1 m. Brownish red is the dominant tone of the sands, reflecting subaerial deposition under oxidation. The sand bars deposits are mainly in the lower part of Xt Fm. and Fh Fm. Unlike the widespread development in Xt Fm., sand bars deposits are infrequent in Fh Fm., indicating a farther depositional site from the active river.

3.2.1.2 Overbank deposits

The overbank deposits are sediments out of channels, including nature levees, crevasse splays, and floodplain sediments. Generally, deposits of overbank are much finer than that of channels. Besides, the recognition of paleosols is also helpful to distinguish these deposits in overbank sediments (Kraus, 1999).

The nature levees are featured by intercalated thin muds and fine sands (Farrell, 1987; Collison et al., 2006). They are formed during major floods as the suspended materials spill out of the channel and then accumulate on the banks (Jordan and Pryor, 1992). In the lower part of the Xt Fm., the levee deposits are uncommon and very thin, probably eroded by overlying channel deposits. It is noteworthy that a suspected paleosol layer of the levee in the lower part of the Xt Fm. demonstrates a subaerial

exposure environment. In the Fh Fm., the nature levees are characterized by thin mud interfingered with thin silt.

Commonly, the channel is confined by bilateral levees. However, floodwaters may overtop the levees and destroy the banks. In this case, the flood deposits extend down the levees and spread onto the floodplain as crevasse splays (Jordan and Pryor, 1992; Reading, 2009). The crevasse splay deposits are dominantly of silt and fine sand, and coarse sand at the base. They usually lie between silt and mud layers with scour-filling structures at the base in the upper Xt Fm. The existence of mud clasts further exemplifies the scouring on levees or floodplain deposits. The crevasse splay deposits are also visible in the upper part of Xb Fm. and Fh Fm.

The floodplain deposits are the finest-grained fractions, which are typically of clay and silt in the non-lacustrine settings. Bioturbation and paleosols are well developed on account of slow sediment accumulation rates (Middleton et al., 2003). The floodplain deposits achieve a dominant position in the upper Xt Fm. and the Fh Fm. Muds of the floodplain encase sand bodies of crevasse splays and channels. Small and multichannel floodplain streams, instead of large-scale meandering channels represented by large tabular cross-bedding sands, dominate the floodplain construction in the east Taiyuan Basin. The light brick-red silts and clay in the upper Xt Fm. indicate an oxidized exposure environment. In addition, the paleosols further prove the exposure environment just as what the color has stated.

3.2.2 Deltaic environment

The deltaic environment is the product of interactions of various environments, such as rivers, lakes, and alluvial fans (Moore and Asquith, 1971). It is divided into delta plain, delta front, and prodelta subenvironments. However, it is difficult to distinguish the microfacies in the core so that the subenvironments are depicted concisely. The delta deposits are usually fine-upward or coarsening-upward sequences, depending on transgression or regression of the lake.

3.2.2.1 Delta plain deposits

The delta plain deposits are similar to that of the river because the delta plain is in the transition zone between river and lake. Hence, the recognition features of a delta can follow that of a river. Nevertheless, deposits of delta plain are finer in grain size and smaller in scale, which are mainly composed of sands, silts, and muds. The black organic-rich beds in the Xb Fm. are interpreted as swamp environments in interdistributary bays along the edge of the delta plain (Fielding, 1984; Nichols, 2009). Besides, the calcareous duricrusts are arrested in unconsolidated sediments. They present as highly resistant surfaces that develop under subaerial weathering environments over long periods in semi-arid climate (Nichols, 2009), emerging on channel or delta (Carlisle, 1983). They jointly constitute the delta plain environment with abundant erosive structures, paleosols, and fining-upward sands in strata.

3.2.2.2 Delta front deposits

The deposits in the delta front environment are strongly affected by wave and tide action (Nichols, 2009). Consequently, the wavy bedding and tidal rhythmite in the Xb Fm (**Figure 2H**) consisting of intercalation of thin silts and muds are the significant identification markers. Broken shells are also present, which represent high-energy environments, the beach pounding by waves, for instance (Jones, 2014). Although the channels are not developed as in the delta plain environment, the subaqueous channels are still visible in the form of finer materials and their erosive undersurfaces. Contorted beds from the upper part of the Hy Fm (**Figure 2I**) occur on the delta front surface when subjected to vibration such as earthquake, since the high slope angle of the delta front provides such an unstable sedimentary condition (Mills, 1983).

3.2.2.3 Prodelta deposits

The prodelta deposits are mainly suspended sediment traveling away from the delta front (Nichols, 2009). Hence, it is similar to the lacustrine muds, both featured by massive and horizontal beddings (e.g., lower part of the Mg Fm.). Nevertheless, the prodelta deposits have more silts and fewer clays than that of the lake (e.g., Xt Fm. and Xb Fm.).

In conclusion, the delta deposits from the borehole core are generally fine grained, distinct from fan delta or braided river delta (Schomacker et al., 2010; Gobo et al., 2015; Lin et al., 2018). We attribute it to the low energy of the meandering river delta. On the other hand, the absence of steeply dipping foreset beds exemplifies a gentle slope basin margin of a finer-grained fluvial delta rather than a typical Gilbert-type coarse-grained delta. Furthermore, it is also in accordance with the tectonic setting of the half-graben basin, as the drill hole is on the inactive side of the basin, which has a low gradient slope and subsidence rate (Allen and Allen, 2013).

3.2.3 Lacustrine environment

3.2.3.1 Lacustrine deposits

The lacustrine deposits consist of interlaminated muds, silts, and very fine sands. The content of coarser materials depends on their depth in the lake basin. In the drill core, thick massive muds are interpreted as the lacustrine deposits, while the thinly interbedded silts with erosive bottoms as subaqueous channel deposits or sandy turbidity current deposits that went deep into the lake during floods or seismic activity (Mills, 1983). The lacustrine deposits are mainly in the lower part of Xb Fm. and Mg Fm. Rhythmites are the most characteristic sedimentary structures of deep lacustrine facies composed of pale carbonate-rich and dark organic-rich stratifications (**Figure 2J**). The interlayers of carbonates and organic matters reveal a characteristic facies of deep basin (Eugster and Kelts, 1983). However, lower Mg Fm. deposits containing more erosive structures and shell fragments are more likely to be a shallower lake environment. Indeed, they even failed to be distinguished from the prodelta deposits.

According to the distributions of the rhythmites, two great-lake periods can be distinguished in the lower Xb Fm. and lower Mg Fm., respectively (**Figure 3**). The lacustrine deposits in the Xb Fm. demonstrate a deep lake environment. They are swiftly

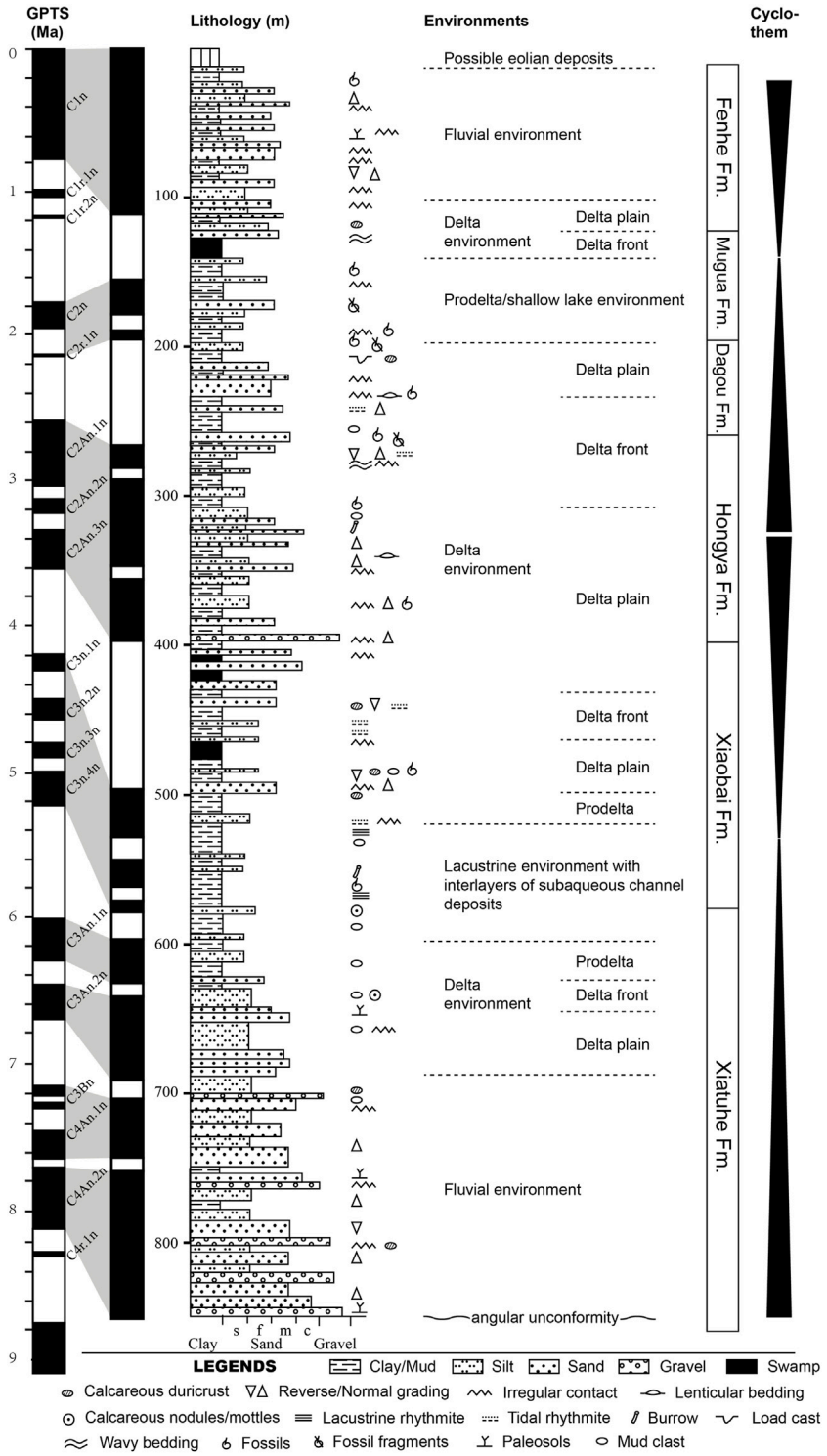

FIGURE 3 | Sedimentary column of ZK01 with time scale (Wei et al., 2020) and sedimentary environments division. Identified depositional markers are plotted where they were found. A simplified cyclothem division and detrital maturity are attached as well.

shifted from brown silts–clays to whitish and dark gray muds, which indicate sudden subsidence of the Taiyuan Basin. The vertical changes of the lake level can be dramatic and rapid on account of a steeper lake basin margin in such a rift-basin setting (Reading, 2009). Beside of the lake level, facies changes are synchronous.

4 DRILL CORE GEOCHEMISTRY

A total of 34 bulk samples were collected for the analysis of major and trace element concentrations from the drill core of ZK01. Most samples came from clay and silts in the fluvial–lacustrine deposits, seldom from sand, and no samples were collected in conglomeratic units. Geochemical analysis was carried out at Taiyuan Mineral Resources Supervision and Testing Center of Ministry of Land and Resources. Samples were powdered to less than 200 mesh in an agate mortar and then placed in an oven at 105°C for drying for 12 h. Major oxides were tested by XRF analysis and had the analytical precision of 1%–2%. Trace element analyses were conducted on Agilent 7700e ICP-MS. Sample powder (50 mg) was disposed of to make the final solution for ICP-MS testing. Detailed procedures (see Cullen et al., 2001) are omitted here. The analytical precision is better than 5%.

4.1 Major elements concentration

The major element contents of the samples are listed in the **Supplementary Table S1**. The variations of element compositions along the depth of the drill core are plotted in **Supplementary Figure S1**. The SiO_2 content varies between 16.36 and 84.08 wt%, with an average of 57.92 wt%. Al_2O_3 content varies from 4.40 to 18.31 wt% with an average of 12.80. Compared with the upper continental crust (UCC) average content (Taylor and McLennan, 1985) (dash line in **Supplementary Figure S1**), SiO_2, Al_2O_3, Fe_2O_3, and TiO_2 are apparently lower in content at a depth of about 120–180 m (i.e., Mg Fm.) and 480–580 m (i.e., the lower part of Xb Fm.). Considerable loss appears at around 570 m. While it is exactly reverse for MgO and CaO, which are prominently enriched at the lower part of Xb Fm. All samples for Na_2O are depleted. SiO_2, Al_2O_3, Fe_2O_3, and TiO_2 content have similar curves in shape, indicating a statistically significant correlation (r = 0.45 to 0.96; n = 34; **Supplementary Table S2**). CaO and MgO content (r = 0.47; n = 34) have similar curves in shape but exactly opposite to that of the SiO_2 series (r = −0.5 to −0.93, and −0.19 to −0.70, respectively; n = 34), marking complementary features with the SiO_2 series. In addition to the two complementary series, no distinct changing trends are displayed between MnO, Na_2O, and P_2O_5.

4.2 Trace elements concentration

Trace element concentrations of the samples are listed in the **Supplementary Table S1**. The normalized patterns of each strata formation's average trace element concentrations against average UCC values are shown in **Supplementary Figure S2**. In comparison with the UCC, the samples are generally low in Zr, Ni, Cr, V, Sc, Co, and Mo. On the contrary, Rb, Th, Pb, Zn, La, and Ce are enriched with a few exceptions. Zn is highly consistent with most trace elements other than Mo, Ba, and U (r = 72 to 0.96; n = 34) (**Supplementary Table S3**). In comparison, Zr and Mo are little related to other trace elements (r = −0.56 to 0.52 and r = −0.35 to 0.33, respectively; n = 34). Samples from Mg Fm. manifest that the average content is depleted in most trace elements. Nb, La, Ce, and Y of all samples plot a concentrated distribution, while the others exhibit a wide variation.

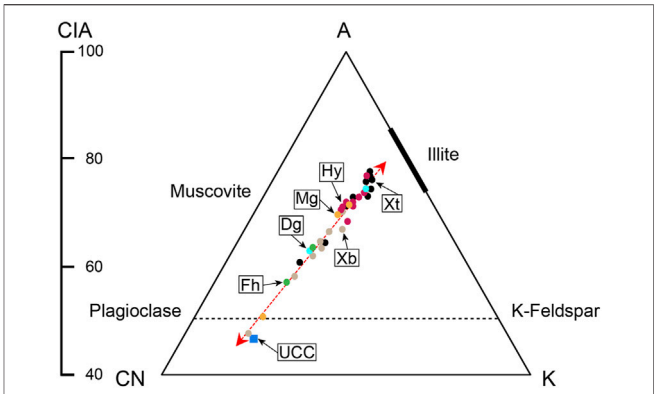

FIGURE 4 | The proportion of Al_2O_3–(CaO* + Na_2O)–K_2OA-CN-K) ternary plot and CIA index for the sand samples (after Nesbitt and Young, 1982 and Fedo et al., 1995).

5 DISCUSSION

5.1 Paleoenvironment condition

5.1.1 Paleoweathering condition

The chemical index of alteration, namely, CIA (Nesbitt and Young, 1982), which reflects the ratio of immobile alumina to mobile alkalis, is widely used to measure the degree of weathering (Gallet et al., 1998; Tao et al., 2014; Wang et al., 2018; Armstrong-Altrin et al., 2019). The CIA values can be calculated by the formula $[Al_2O_3/(Al_2O_3 + CaO^* + Na_2O + K_2O)] \times 100$, using molecular proportions. Cao* herein is the amount of CaO in silicates alone, ensuring inorganic carbon derivation. The CaO content was calculated according to Martinez et al. (2010). High CIA values reflect the removal of labile cations relative to stable residual constituents during weathering (Nesbitt and Young, 1982). Conversely, low CIA values indicate the near absence of chemical alteration, and consequently might reflect cool and/or arid conditions. In this work, CIA values of all samples range from 48 to 78 with an average of 68 (**Supplementary Table S1**), indicating a low to moderate degree of chemical weathering of the source area.

The proportion of Al_2O_3–(CaO* + Na_2O)–K_2O can also be plotted as the A-CN-K ternary diagram (Fedo et al., 1995) (**Figure 4**). In the A-CN-K plot, most samples plot well above the plagioclase-K-feldspar join line (black dashed line), indicating that chemical weathering, rather than abrasion, has primarily affected bedrock by destroying feldspars (Nesbitt and Young, 1996). The samples are clustered toward illite, signifying the removal of Na_2O and CaO from the bulk composition due to chemical weathering, and the increase of illite minerals. Each Xb Fm. and Mg Fm. contains one sample located on the feldspar join line and near UCC square, respectively, indicating slightly weathered products. However, the Xt Fm. and Hy Fm. samples are closer to the illite end, implying more exhaustive weathering processes.

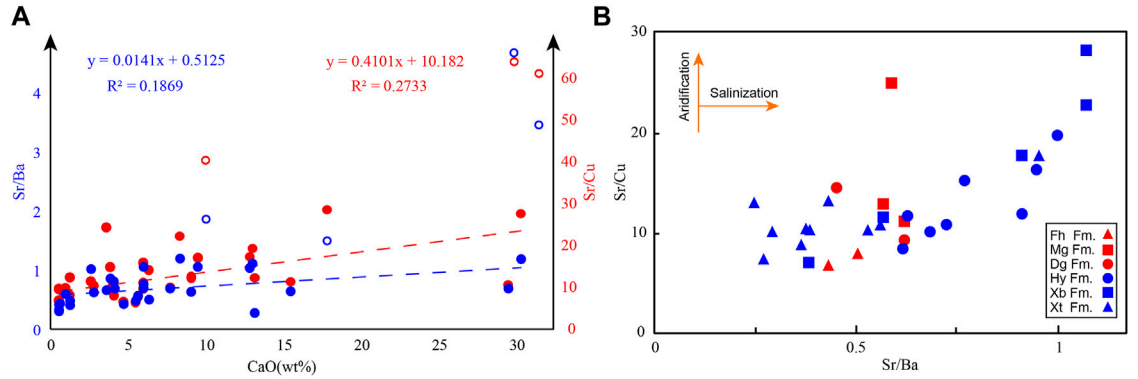

FIGURE 5 | (A) Correlation between Sr/Ba (blue) and Sr/Cu (red) indexes and CaO content. The open circles represent abnormal data, which are influenced by CaO dramatically. **(B)** Sr/Cu and Sr/Ba binary diagram for the ZK01 core (after Lerman 1989) without the discarded data in **(A)**, indicating aridification and salinization conditions, respectively.

5.1.2 Paleoclimate condition

The content and distribution patterns of various elements show differences in different climate conditions. In humid climates, lake levels are high, and water is diluted, with higher contents of Fe, Al, Ba, and Zn in sediments, while in arid climates, the water evaporates, and the aqueous medium becomes strong alkaline, with abundant Na, Ca, Mg, Cu, Sr, and Mn precipitates over the underlying sediment (Meng et al., 2012; Tian and Zhang, 2016). We use the ratio of Sr, Ba, and Cu instead of the value of a single element as the index to analyze paleoclimate, which can minimize the effect of source rock, highlighting the information obtained in sedimentation.

Sr/Ba ratio reflects lake water's concentration degree and, ultimately, the water salinity (Chivas et al., 1985; Sun, 1997; Fu et al., 2016). The ratio of Sr and Cu can be a proxy of aridification (Lerman, 1989; Meng et al., 2012). However, the carbonate-hosted Sr may alter the Sr/Ba and Sr/Cu signals from clay fraction (wei et al., 2018; Wei and Algeo, 2020). Hence, we inspected the correlation between the values of indexes and the content of CaO (**Figure 5A**). We found that only four samples (open circles) had the abnormal Sr/Ba and Sr/Cu values that were affected by CaO obviously. After removing these samples, the rest of the samples (solid circles) showed weak correlation between the indexes and CaO. Thus, we believe that it is reasonable to discuss the salinity using Sr/Ba and Sr/Cu index after we discarded the abnormal samples. Sr/Cu and Sr/Ba show a linear relationship in **Figure 5B**, indicating a good overall evaluation of the paleoclimate. It is worth noting that the Xt Fm. is plotted as relative humid environments, while Xb Fm. is in arid condition. The result demonstrates that the incipient sediments from the fluvial system were deposited under a humid environment, whereas the following lake was developed in arid environments.

The results are not conducive to the rapid development of the lake of the Xb Fm. This indicates that climate change may not be the primary driver in the transition from the fluvial to lacustrine system in Taiyuan Basin. Subsidence derived from tectonic movement provides accommodation and blocks the streams flowing out the basin, which probably builds closer ties with the expansion of the lake.

5.2 Sedimentary environments and controlling factors

5.2.1 Evolution of the sedimentary environments

It is divided into three sections for the correlation of the strata in different boreholes, which are the bottom section of fluvial sediments, the middle section of lacustrine and deltaic sediments, and the top section of fluvial sediments, respectively. Coarse-grained fluvial sediments at the bottom of cores ZK01, J7, and T2, represent the response of the rapid subsidence process in the initial basin faulting stage. As the gravel convert to fine sand and mud upward, the grain size of sediments decrease sharply in the middle section. Because there are almost no thick layers of sand and gravel except for the top and bottom of the boreholes, and scarce typical fluvial beddings, the middle sections of the cores J7, J2, and T2 are mainly of lacustrine and deltaic sediments. Thereinto, there are five periods of lacustrine deposits in cores J2 and J7, twice lacustrine deposits in core ZK01, and only one lacustrine deposits in core T2. It shows obvious regional characteristic. The lacustrine deposits are embedded by the deltaic sediments reflecting the shrinkage of the lakes. Reappearance of thick sand and gravel in the top section of cores represents the run-through of the Fen River. Furthermore, the dramatic decrease of the thickness and amount of mud also confirms the disappearance of the standing water environment. This feature can be observed in the upper section of all four cores, showing spatial comparability.

The sediments of basal alluvial facies converted upward to delta facies with grain size sharply decreased, reflecting the weakening of the tectonic movement. Then, the stable stage was presented by the first transgression of J7 and J2. However, the transgression event lasted for only a short time. It was characterized by thin lacustrine deposition, inconsistent with the deep lacustrine deposition in the lower part of core ZK01 in the NE basin margin. Accordingly, we believe that cores J7 and

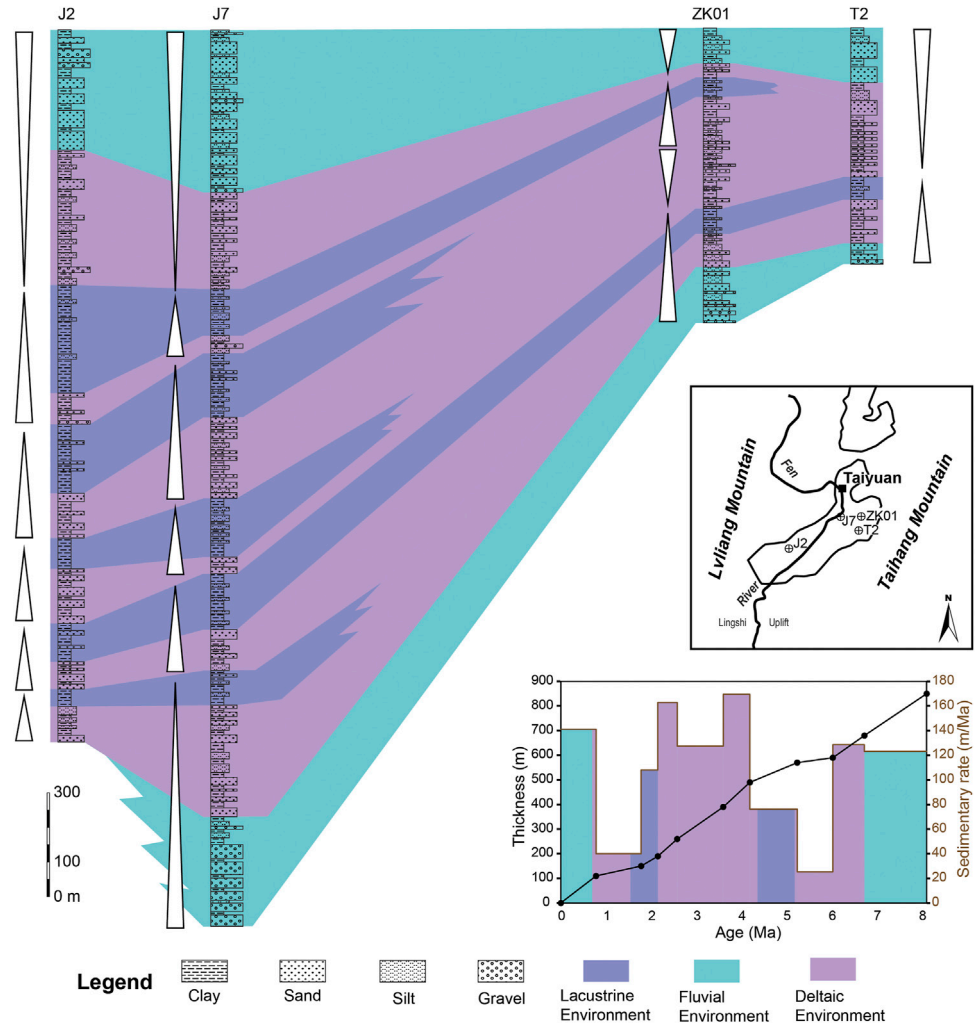

FIGURE 6 | Correlation of stratigraphy and sedimentary environments from boreholes in Taiyuan Basin. The simplified geological map shows the location of the boreholes. The bottom right corner displays sedimentary rates of ZK01.

J2 experienced a small range of lake transgression, which failed to reach the positions of ZK01 and T2.

After the first transgression in J7 and J2, the following coarse-grained delta deposits advanced rapidly along the steep slope of the basin margin, capping the underlying fine-grained lacustrine sediments. Afterward, the accommodation was generated, contributing to the transgression during the subsequent tectonic quiescence. This transgression may be linked to the first transgression in cores ZK01 and T2. In ZK01, abrupt transition of sedimentary environments and relatively large deposition rate (**Figure 6**) exemplify accelerated lake expansion at ~5.2 Ma. Thereby, a lake covering the entire Taiyuan Basin formed during 5.2–6 Ma.

The third and fourth transgressions in J7 and J2 show a considerable thickness of lacustrine deposition. However, after the first lacustrine transgression, ZK01 was dominated by the interaction of delta plain and delta front deposits until~2.2 Ma, and stable lacustrine deposits were no longer developed. Furthermore, the second transgression of ZK01, which started at~2.2 Ma, lasted for a short time and soon transformed into delta deposits and fluvial deposits. Therefore, it is difficult to compare the third and fourth transgression of cores J7 and J2 with the second transgression of ZK01. In the east of the basin, the principal manifestation is only a fluctuation of deepening and shallowing of the water body in the delta environment.

The fifth transgression of J7 and J2 was the last typical transgression event of these two boreholes. Thereinto, core J2 contains 300 m of lacustrine deposits, signifying a long time and large-scale transgression process. Hence, it is comparable to the second transgression of core ZK01. However, the shore-shallow lake sediments of core ZK01 are thin and insignificant with the pro-delta sedimentary characteristics. Moreover, corresponding transgression sediments are absent in core T2. It indicates that the position of T2 is beyond the reach of this transgression, and the west side of the basin has a larger subsidence amplitude than the east.

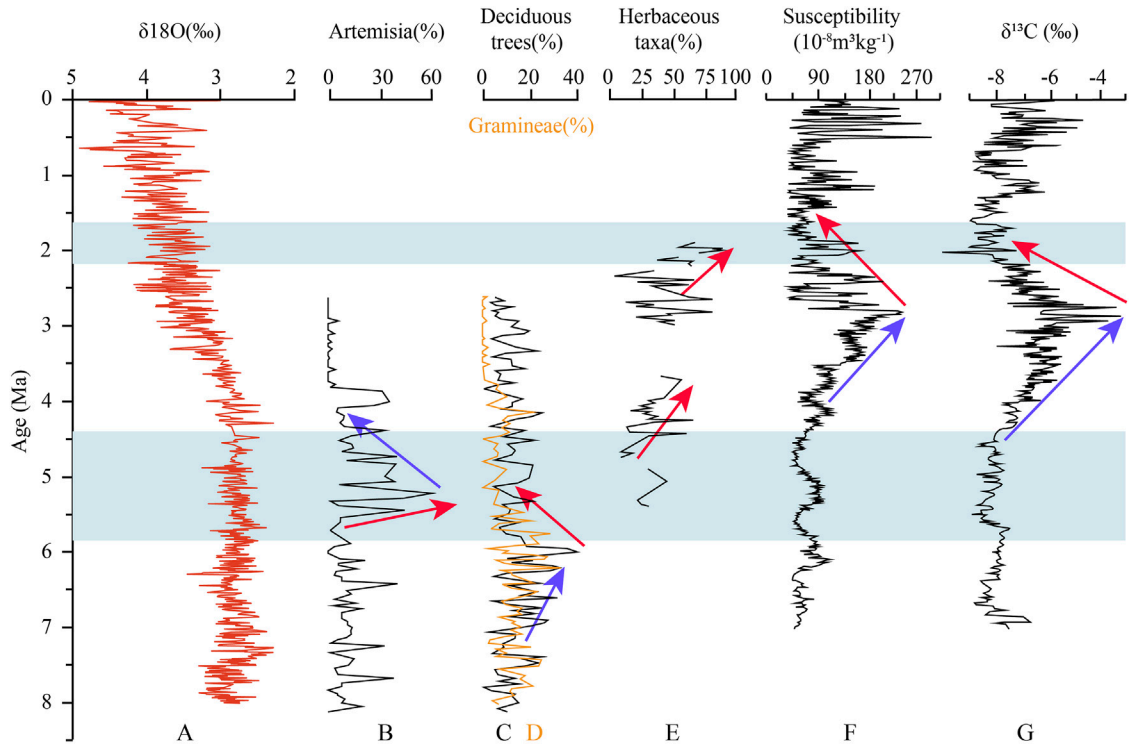

FIGURE 7 | Regional climatic information around the Shanxi Rift System (location of Chaona, Yushe, and Lingtai in **Figure 1**). **(A)** Oxygen isotope records of benthic foraminifera from boreholes 1,147 and 11,488 in the South China Sea (Cheng et al., 2004). **(B)** Pollen content of *Artemisia* of the Chaona section (Ma et al., 2005). The higher values indicate more arid condition. The red arrow and blue arrow signify drought trend and wet trend, respectively, hereinafter the same. **(C)** and **(D)** Pollen content of deciduous trees and Gramineae of the Chaona section (Ma et al., 2005). **(E)** Pollen content of herbaceous taxa from the Yushe Basin (Shi et al., 1993). **(F)** magnetic susceptibility of eolian deposits from Lingtai (An et al., 2005). **(G)** Soil carbonate $\delta^{13}C$ from Lingtai (An et al., 2005).

After that, neither the cores developed typical lacustrine deposits. It shows that the Taiyuan Basin lakes were gradually shrinking. After 0.6 Ma of core ZK01, the delta environment changed into a fluvial environment, and the lake shrank dramatically until it was completely emptied. Thus, there were five large-scale lake transgressions totally in Taiyuan Basin during the late Cenozoic. Two of them reached the basin's eastern edge, forming the super-large lake that almost covered the whole Taiyuan Basin. These two super-large lake periods are late Miocene to early Pliocene (~5.8–~4.4 Ma) and early stage of early Pleistocene (~2.2–1.6 Ma), respectively.

5.2.2 Controlling factors of lake evolution

In a continental basin, the internally sedimentary architecture is most likely under the control of tectonism and climatic variations (Allen and Allen, 2013; Birgenheier et al., 2019). Specifically, lakes are the products of active tectonic and moister climates (Reading, 2009). Here, we attempt to discuss the main controlling factors of lacustrine evolution in the Taiyuan Basin.

From a regional perspective, the East Asia has experienced an overall drying and cooling process (Guo et al., 2002; Deng et al., 2006; Cheng et al., 2004, **Figure 7A**) since the late Miocene, on account of sea ice expansion in the Northern Hemisphere (Jansen and Sjoholm, 1991) and uplift of the Tibetan Plateau (Manabe and Broccoli, 1990; An et al., 2001). Specifically, the Shanxi Rift System is located in the eastern margin of the present Loess Plateau. According to the magnetic grain-size records (Nie et al., 2013), and pollen records of *Artemisia*, deciduous trees and Gramineae (Ma et al., 2005) of the Chaona section, the Loess Plateau is not unusually humid during ~5.8–4.4 Ma, and even has an aridification trend (Ma et al., 2005, **Figures 7B–D**). Although some results depict differing views that the summer precipitation was increased in this period due to enhanced summer monsoon (Wu et al., 2006; Chen et al., 2007; Li Jianxing et al., 2015), simulated summer precipitation for late Miocene and Pliocene presents its difference less than 100 mm/year (Ao et al., 2021) in the Taiyuan Basin. This cannot make a decisive impact on sedimentary environments of the Taiyuan Basin because the most increased precipitation is blocked by the Taihang Mountain. From 2.2 to 1.6 Ma, it is the period of strengthening monsoon with frequent and violent climate fluctuations. The pollen proportion of the herbaceous taxa from the Yushe Basin (**Figure 7E**, Shi et al., 1993), and magnetic susceptibility (**Figure 7F**) and soil carbonate $\delta^{13}C$ (**Figure 7G**) from Lingtai (An et al., 2005) all show a remarkable aridification tendency. It is consistent with what the Sr/Cu index presents and unfavorable for the expansion of the lake. Consequently, climate change is evidently not a direct factor in forming the two super-large lake periods.

Results of depositional environment and depositional cycle division of the drill cores reveal a close relationship between location (distance from active fault) and evolution of the drill holes (**Figure 6**). Cores J7 and J2 lie in the west of the basin, ahead of the steep slope with intense fault depression, developing at least five transgressions. In comparison, ZK01 and T2 are on the gentle slope of the east side with weak subsidence, involving simply two events. Hence, the Jiaocheng Fault activity can be effectively preserved by coarse-grained sediments. The Taigu Fault, however, can be recorded by sediments only during significant events. The close relevance between the sedimentary styles and their tectonic position reflects that tectonism rather than climate variations should mainly control the environmental changes of the Taiyuan Basin. Additionally, the first transgression coincides with the rapid uplift event of the Lvliang Mountain at about 5.7 Ma (Pan et al., 2018), and the second transgression corresponds to the change of stress regime of the rift from ca. 1.8 Ma (Shi et al., 2015). Therefore, the two transgressions represent two major tectonic events.

We speculate that the paleolakes originated from the backwater of the blocked paleorivers due to the differential uplift at the basin rim. At present, the Lingshi Uplift has an average elevation of 1,100 m in the northern mountains area on both sides of Fenhe Valley, much higher than the southern basin with a height of 750 m. In spite lacking the uplift rate, this fact indicates that the Lingshi Uplift blocked the drainage system from entering the Linfen Basin. As the lake in Taiyuan Basin reached its maximum flooding surface, the water overflowed the Lingshi Uplift and spilled southward to the Linfen Basin. Meanwhile, the spillover caused headward erosion at the boundary of Lingshi Uplift and Linfen Basin. When the river incised to the same height as the basin's surface, the ancient lake in Taiyuan Basin was gradually evacuated, and the Fen River recurred and flowed through the whole Taiyuan Basin eventually.

6 CONCLUSION

In the Taiyuan Basin of the Shanxi Rift System, thick deposits accumulated at ca. 8.1 Ma, recording the rift development. Sedimentary environment evolution indicates that two basin-wide lacustrine transgression events occurred at ca. 5.8–4.4 and ca. 2.2–1.6 Ma, respectively. In addition, the parent rock lithology changed significantly when the coarse clastic sediments of the syn-rift phase converted to the lacustrine sediments at ca. 5.8 Ma. It reveals two different depositional systems before and after 5.8 Ma. We believe that these two transgressions are a response to the rapid subsidence of the basin and are controlled mainly by tectonism rather than climate variation. Hence, the Taiyuan Basin experienced at least two tectonic events at ca. 5.8 and 2.2 Ma.

DATA AVAILABILITY STATEMENT

The original contributions presented in the study are included in the article/**Supplementary Material**. Further inquiries can be directed to the corresponding author.

AUTHOR CONTRIBUTIONS

QZ did the field work, data processing, and wrote the manuscript. HH and RW contributed to the conception and provided funding for the study. HH reviewed and edited the manuscript. All authors contributed to the manuscript revision and discussion, and approved the submitted version.

FUNDING

This research was supported by the National Science Foundation of China (41872213, U1939201, 41702221, and 41602206) and Geological Prospecting Fund Project of Shanxi Bureau of National Territory Resources (HXCT01-2018F005). Shanxi Taiyuan Continental Rift Dynamics National Observation and Research Station (NORSTY20-04).

ACKNOWLEDGMENTS

We are grateful to Pengsheng Yang and Xiao Hu for their assistance in core logging and sample collection. We are particularly grateful to Qinmian Xu and Chengfa Lin for their helpful discussions.

SUPPLEMENTARY MATERIAL

The Supplementary Material for this article can be found online at: https://www.frontiersin.org/articles/10.3389/feart.2022.833585/full#supplementary-material

REFERENCES

Allen, J. P., Fielding, C. R., Rygel, M. C., and Gibling, M. R. (2013). Deconvolving Signals of Tectonic and Climatic Controls from Continental Basins: An Example from the Late Paleozoic Cumberland Basin, Atlantic Canada. *J. Sediment. Res.* 83, 847–872. doi:10.2110/jsr.2013.58

Allen, P. A., and Allen, J. R. (2013). *Basin Analysis: Principles and Application to Petroleum Play Assessment*. John Wiley & Sons.

An, Z., Huang, Y., Liu, W., Guo, Z., Steven, C., Li, L., et al. (2005). Multiple Expansions of C4 Plant Biomass in East Asia since 7 Ma Coupled with Strengthened Monsoon Circulation. *Geology* 33 (9), 705–708.

Ao, H., Rohling, E. J., Zhang, R., Roberts, A. P., Holbourn, A. E., Ladant, J.-B., et al. (2021). Global Warming-Induced Asian Hydrological Climate Transition across the Miocene-Pliocene Boundary. *Nat. Commun.* 12 (1), 6935. doi:10.1038/s41467-021-27054-5

Armstrong-Altrin, J. S., Botello, A. V., Villanueva, S. F., and Soto, L. A. (2019). Geochemistry of Surface Sediments from the north Western Gulf of Mexico: Implications for Provenance and Heavy Metal Contamination. *Geol. Q.* 63, 522–538. doi:10.7306/gq.1484

Armstrong-Altrin, J. S. (2009). Provenance of Sands from Cazones, Acapulco, and Bahía Kino Beaches, México. *Revista Mexicana de Ciencias Geologicas* 26, 764–782.

Birgenheier, L. P., Berg, M. D. V., Plink-Björklund, P., Gall, R. D., Rosencrans, E., Rosenberg, M. J., et al. (2019). Climate Impact on Fluvial-Lake System Evolution, Eocene Green River Formation, Uinta Basin, Utah, USA. *GSA Bull.* 132, 562–587. doi:10.1130/b31808.1

Boardman, E. L. (1989). Coal Measures (Namurian and Westphalian) Blackband Iron Formations: Fossil Bog Iron Ores. *Sedimentology* 36, 621–633. doi:10.1111/j.1365-3091.1989.tb02089.x

Carlisle, D. (1983). "Concentration of Uranium and Vanadium in Calcretes and Gypcretes," in *Residual Deposits; Surface Related Weathering Processes and Materials*. Editor R. C. L. Wilson (Geological Society of London Special Publications), 11, 185–195. doi:10.1144/gsl.sp.1983.011.01.19

Chang, J., Qiu, N., Liu, S., Cai, C., Xu, Q., and Liu, N. (2018). Post-triassic Multiple Exhumation of the Taihang Mountains Revealed via Low-T Thermochronology: Implications for the Paleo-Geomorphologic Reconstruction of the North China Craton. *Gondwana Res.* 68, 34–49.

Chen, G. (1987). On the Geotectonic Nature of the Fen-Wei Rift System. *Tectonophysics* 143, 217–223.

Chen, X., Shi, W., Hu, J., and Dong, S. (2016). Sedimentation of the Pliocene–Pleistocene Chaizhuang Section in the central of Linfen Basin, North China and its Tectonic Significance. *J. Geomechanics* 22 (4), 984–994.

Chen, X., Dong, S., Shi, W., Zuza, A. V., Li, Z., Chen, P., et al. (2021). Magnetostratigraphic Ages of the Cenozoic Weihe and Shanxi Grabens in North China and Their Tectonic Implications. *Tectonophysics* 813, 1–12. doi:10.1016/j.tecto.2021.228914

Chen, X., Fang, X., An, Z., Han, W., Wang, X., Bai, Y., et al. (2007). An 8.1Ma Calcite Record of Asian Summer Monsoon Evolution on the Chinese central Loess Plateau. *Sci. China Ser. D* 50, 392–403. doi:10.1007/s11430-007-0016-x

Cheng, S. (1983). Discussion on the Capture of Qingshuihe River and Hutuohe River. *J. Hebei Sch. Geology.* 2, 41–53.

Cheng, X., Zhao, Q., Wang, J., Jian, Z., and Xia, P. (2004). Data Report: Stable Isotopes from Sites 1147 and 1148. *Proc. Odp, Sci. Results.* 184, 1–12. doi:10.2973/odp.proc.sr.184.223.2004

Chivas, A. R., De Deckker, P., and Shelley, J. M. G. (1985). Strontium Content of Ostracods Indicates Lacustrine Palaeosalinity. *Nature* 316 (6025), 251–253. doi:10.1038/316251a0

Clift, P. D., and Jonell, T. N. (2021). Himalayan-Tibetan Erosion Is Not the Cause of Neogene Global Cooling. *Geophys. Res. Lett.* 48, e2020GL087742. doi:10.1029/2020gl087742

Clinkscales, C., and Kapp, P. (2019). Structural Style and Kinematics of the Taihang-Luliangshan Fold belt, North China: Implications for the Yanshanian Orogeny. *Lithosphere* 11, 767–783. doi:10.1130/l1096.1

Clinkscales, C., Kapp, P., Thomson, S., Wang, H., Laskowski, A., Orme, D. A., et al. (2021). Regional Exhumation and Tectonic History of the Shanxi Rift and Taihangshan, North China. *Tectonics* 40 (3), e2020TC006416. doi:10.1029/2020tc006416

Clinkscales, C., Kapp, P., and Wang, H. (2020). Exhumation History of the north-central Shanxi Rift, North China, Revealed by Low-Temperature Thermochronology. *Earth Planet. Sci. Lett.* 536, 116146. doi:10.1016/j.epsl.2020.116146

Collison, J. D., Mountney, N. P., and Thompson, D. B. (2006). *Sedimentary Structures*. Terra Publishing.

Cullen, J. T., Paul Field, M., and Sherrell, R. M. (2001). Determination of Trace Elements in Filtered Suspended marine Particulate Material by Sector Field HR–ICP–MS. *J. Anal. Spectrom.* 16, 1307–1312. doi:10.1039/b104398f

Deng, C., Shaw, J., Liu, Q., Pan, Y., and Zhu, R. (2006). Mineral Magnetic Variation of the Jingbian Loess/paleosol Sequence in the Northern Loess Plateau of China: Implications for Quaternary Development of Asian Aridification and Cooling. *Earth Planet. Sci. Lett.* 241, 248–259. doi:10.1016/j.epsl.2005.10.020

Deng, C., Zhu, R., Zhang, R., Ao, H., and Pan, Y. (2007). Timing of the Nihewan Formation and Faunas. *Quat. Res.* 69, 77–90.

Deng, Q., Chen, S., Min, W., Yang, G., and Reng, D. (1999). Discussion on Cenozoic Tectonics and Dynamics of the Ordos Block. *Int. J. Rock Mech. Min. Sci.* 5 (3), 13–21.

Deng, Q., Wang, K., Wang, Y., Tang, H., Wu, Y., and Ding, M. (1973). Geological Conditions for Earthquakes in Down-Faulted Seismic Zone of Shanxi Uplift Region and Developmental Trend of Seismicity. *Scientia Geologica Sinica* 1, 37–74. (in Chinese with English abstract).

Eugster, H. P., and Kelts, K., (1983). Lacustrine Chemical Sediments. In: *Chemical Sediments and Geomorphology* Ed. by A. S. Goudie and K. Pye, 321–368. Academic Press, London. 4.7.1.

Farrell, K. M. (1987). "Sedimentology and Facies Architecture of Overbank Deposits of the Mississippi River, False River Region, Louisiana," in *Recent Developments in Fluvial Sedimentology* (SEPM (Society of Sedimentary Geology) Special Publication), 39, 111–120. doi:10.2110/pec.87.39.0111

Fedo, C. M., Wayne Nesbitt, H., and Young, G. M. (1995). Unraveling the Effects of Potassium Metasomatism in Sedimentary Rocks and Paleosols, with Implications for Paleoweathering Conditions and Provenance. *Geol* 23 (10), 921–924. doi:10.1130/0091-7613(1995)023<0921:uteopm>2.3.co;2

Fielding, C. R. (1984). A Coal Depositional Model for the Durham Coal Measures of NE England. *J. Geol. Soc.* 141, 919–931. doi:10.1144/gsjgs.141.5.0919

Fisk, H. N. (1947). *Fine-grained Alluvial Deposits and Their Effect on Mississippi River Activity*. Mississippi River Commission: Vicksburg.

Fu, X., Wang, J., Chen, W., Feng, X., and Wang, D. (2016). Elemental Geochemistry of the Early Jurassic Black Shales in the Qiangtang Basin, Eastern Tethys: Constraints for Palaeoenvironment Conditions. *Geol. J.* 51, 443–454.

Gallet, S., Jahn, B.-m., Van Vliet Lanoë, B., Dia, A., and Rossello, E. (1998). Loess Geochemistry and its Implications for Particle Origin and Composition of the Upper continental Crust. *Earth Planet. Sci. Lett.* 156, 157–172. doi:10.1016/s0012-821x(97)00218-5

Gobo, K., Ghinassi, M., Nemec, W., and Walsh, J. P. (2015). Gilbert-type Deltas Recording Short-Term Base-Level Changes: Delta-Brink Morphodynamics and Related Foreset Facies. *Sedimentology* 62, 1923–1949. doi:10.1111/sed.12212

Guo, Z. T., Ruddiman, W. F., Hao, Q. Z., Wu, H. B., Qiao, Y. S., Zhu, R. X., et al. (2002). Onset of Asian Desertification by 22 Myr Ago Inferred from Loess Deposits in China. *Nature* 416, 159–163. doi:10.1038/416159a

Hao, Q., and Guo, Z. (2004). Magnetostratigraphy of a Late Miocene-Pliocene Loess-Soil Sequence in the Western Loess Plateau in China. *Geophys. Res. Lett.* 31, 1–4. doi:10.1029/2003gl019392

Haszeldine, R. S. (1984). Muddy Deltas in Freshwater Lakes, and Tectonism in the Upper Carboniferous Coalfield of NE England. *Sedimentology* 31, 811–822. doi:10.1111/j.1365-3091.1984.tb00888.x

Heberer, B., Anzenbacher, T., Neubauer, F., Genser, J., Dong, Y., and Dunkl, I. (2014). Polyphase Exhumation in the Western Qinling Mountains, China: Rapid Early Cretaceous Cooling along a Lithospheric-Scale Tear Fault and Pulsed Cenozoic Uplift. *Tectonophysics* 617, 31–43. doi:10.1016/j.tecto.2014.01.011

Hu, Z., Pan, B., Wang, J., Cao, B., and Gao, H. (2012). Fluvial Terrace Formation in the Eastern Fenwei Basin, China, during the Past 1.2Ma as a Combined Archive of Tectonics and Climate Change. *J. Asian Earth Sci.* 60, 235–245. doi:10.1016/j.jseaes.2012.09.016

Huang, Y., Wang, Q., Hao, M., and Zhou, S. (2018). Fault Slip Rates and Seismic Moment Deficits on Major Faults in Ordos Constrained by GPS Observation. *Sci. Rep.* 8, 16192–16199. doi:10.1038/s41598-018-34586-2

Jansen, E., and Sjøholm, J. (1991). Reconstruction of Glaciation over the Past 6 Myr from Ice-Borne Deposits in the Norwegian Sea. *Nature* 349, 600–603. doi:10.1038/349600a0

Jiang, W., Guo, H., Xie, X., Zhang, L., and Xu, J. (2012). *Report of 1: 50000 Active Fault Mapping of Jiaocheng Fault Zone in Shanxi*. Institute of Crustal Stress, China Earthquake Administration Publication.

Jones, S. J. (2014). *Introducing Sedimentology*. Dunedin Academic Press Ltd.

Jordan, D. W., and Pryor, W. A. (1992). Hierarchical Levels of Heterogeneity in a Mississippi River Meander belt and Application to Reservoir Systems. *AAPG Bull.* 76 (10), 1601–1624. doi:10.1306/bdff8a6a-1718-11d7-8645000102c1865d

Kraus, M. J. (1999). Paleosols in Clastic Sedimentary Rocks: Their Geologic Applications. *Earth-Science Rev.* 47, 41–70. doi:10.1016/s0012-8252(99)00026-4

Kusky, T. M., Windley, B. F., and Zhai, M.-G. (2007). "Tectonic Evolution of the North China Block: from Orogen to Craton to Orogen," in *Mesozoic Sub-Continental Lithospheric Thinning under Eastern Asia: Geol*. Editors M. Zhai, B. F. Windley, T. M. Kusky, and Q. Meng (Geological Society, London: Special PublicationsSoc. London Special Publication), 280, 1–34. doi:10.1144/sp280.1

Lerman, A. (1989). *Lakes, Chemistry, Geology, Physics*. Springer-Verlag Berlin Heidelberg Gmbh.

Li, B., Sørensen, M. B., and Atakan, K. (2015). Coulomb Stress Evolution in the Shanxi Rift System, North China, since 1303 Associated with Coseismic, post-seismic and Interseismic Deformation. *Geophys. J. Int.* 203, 1642–1664. doi:10.1093/gji/ggv384

Li, J., Liu, C., Yue, L., and Wang, J. (2015). Apatite Fission Track Evidence for the Cenozoic Uplift of the Lüliang Mountains and a Discussion on the Uplift Mechanism. *Chin. Geol.* 42 (4), 960–972. (in Chinese with English abstract).

Li, P., and Liang, Q. (1965). New Information on Channel Change of the Upstream of Hutuohe River and Mumahe River. *Geol. Rev.* 23 (3), 240–241.

Lin, C., Liu, S., Zhuang, Q., and Steel, R. J. (2018). Sedimentation of Jurassic Fan-Delta Wedges in the Xiahuayuan Basin Reflecting Thrust-Fault Movements of the Western Yanshan Fold-And-Thrust Belt, China. *Sediment. Geology.* 368, 24–43. doi:10.1016/j.sedgeo.2018.03.005

Liu, J., Zhang, P., Lease, R. O., Zheng, D., Wan, J., Wang, W., et al. (2013). Eocene Onset and Late Miocene Acceleration of Cenozoic Intracontinental Extension in the North Qinling Range-Weihe Graben: Insights from Apatite Fission Track Thermochronology. *Tectonophysics* 584, 281–296. doi:10.1016/j.tecto.2012.01.025

Liu, P., Deng, C., Li, S., Cai, S., Cheng, H., Baoyin, Y., et al. (2012). Magnetostratigraphic Dating of the Xiashagou Fauna and Implication for Sequencing the Mammalian Faunas in the Nihewan Basin, North China. *Palaeogeogr. Palaeoclimatol. Palaeoecol.* 315-316, 75–85. doi:10.1016/j.palaeo.2011.11.011

Liu, S., and Zhang, G. (2005). Fundamental Ideas, Contents and Methods in Study of basin and Mountain Relationships. *Earth Sci. Front.* 12, 101–111. (in Chinese with English abstract).

Ma, X., Deng, Q., Wang, Y., and Liu, H. (1982). Cenozoic Graben System in north China. *Z. Geomorphy. N.F.* 42, 99–116.

Ma, Y., Wu, F., Fang, X., Li, J., An, Z., and Wang, W. (2005). Pollen Record from Red clay Sequence in the central Loess Plateau between 8.10 and 2.60 Ma. *Chin.Sci.Bull.* 50 (19), 2234–2243. doi:10.1007/bf03182675

Manabe, S., and Broccoli, A. J. (1990). Mountains and Arid Climates of Middle Latitudes. *Science* 247 (4939), 192–195. doi:10.1126/science.247.4939.192

Martinez, N. C., Murray, R. W., Thunell, R. C., Peterson, L. C., Muller-Karger, F., Lorenzoni, L., et al. (2010). Local and Regional Geochemical Signatures of Surface Sediments from the Cariaco Basin and Orinoco Delta, Venezuela. *Venezuela. Geology.* 38, 159–162. doi:10.1130/g30487.1

Meng, Q., Liu, Z., Bruch, A. A., Liu, R., and Hu, F. (2012). Palaeoclimatic Evolution during Eocene and its Influence on Oil Shale Mineralisation, Fushun basin, China. *J. Asian Earth Sci.* 45, 95–105. doi:10.1016/j.jseaes.2011.09.021

Miall, A. D. (1985). Architectural-element Analysis: a New Method of Facies Analysis Applied to Fluvial Deposits. *Earth-Science Rev.* 22 (4), 261–308. doi:10.1016/0012-8252(85)90001-7

Miall, A. D. (1980). Cyclicity and the Facies Model Concept in Fluvial Deposits. *Bull. Can. Petrol. Geol.* 28, 59–80.

Middleton, G. V., Church, M. J., Coniglio, M., Hardie, L. A., and Longstaffe, F. J. (2003). *Encyclopedia of Sedimentary Rocks*. Dordrecht: Kluwer Academic Publishers, 286.

Mills, P. C. (1983). Genesis and Diagnostic Value of Soft-Sediment Deformation Structures-A Review. *Sediment. Geology.* 35 (2), 83–104. doi:10.1016/0037-0738(83)90046-5

Moore, G. T., and Asquith, D. O. (1971). Delta: Term and Concept. *Geol. Soc. America Bull.* 82, 2563–2568. doi:10.1130/0016-7606(1971)82[2563:dtac]2.0.co;2

Nesbitt, H. W., and Young, G. M. (1982). Early Proterozoic Climates and Plate Motions Inferred from Major Element Chemistry of Lutites. *Nature* 299, 715–717. doi:10.1038/299715a0

Nesbitt, H., and Young, G. (1996). Petrogenesis of Sediments in the Absence of Chemical Weathering: Effects of Abrasion and Sorting on Bulk Composition and Mineralogy. *Sedimentology* 43, 341–358. doi:10.1046/j.1365-3091.1996.d01-12.x

Nichols, G. (2009). *Sedimentology and Stratigraphy*. John Wiley & Sons.

Nie, J., Song, Y., King, J. W., Zhang, R., and Fang, X. (2013). Six Million Years of Magnetic Grain-Size Records Reveal that Temperature and Precipitation Were Decoupled on the Chinese Loess Plateau during ~ 4.5-2.6 Ma. *Quat. Res.* 79 (3), 465–470. doi:10.1016/j.yqres.2013.01.002

Pan, B., Burbank, D., Wang, Y., Wu, G., Li, J., and Guan, Q. (2003). A 900 k.Y. Record of Strath Terrace Formation during Glacial-Interglacial Transitions in Northwest China. *Geology* 31, 957–960. doi:10.1130/g19685.1

Pan, F., Li, J., Xu, Y., Wingate, M. T. D., Yue, L., Li, Y., et al. (2018). Uplift of the Lüliang Mountains at Ca. 5.7 Ma: Insights from Provenance of the Neogene Eolian Red clay of the Eastern Chinese Loess Plateau. *Palaeogeogr. Palaeoclimatol. Palaeoecol.* 502, 63–73. doi:10.1016/j.palaeo.2018.04.024

Peltzer, G., Tapponnier, P., Zhitao, Z., and Qin, X. Z. (1985). Neogene and Quaternary Faulting in and along the Qinling Shan. *Nature* 317, 500–505. doi:10.1038/317500a0

Qing, J.-C., Ji, J.-Q., Wang, J.-D., Peng, Q.-L., Niu, X.-L., and Ge, Z.-H. (2008). Apatite Fission Track Study of Cenozoic Uplifting and Exhumation of Wutai Mountain, China. *Chin. J. Geophys.* 51, 256–264. (in Chinese with English abstract). doi:10.1002/cjg2.1217

Reading, H. G. (2009). *Sedimentary Environments: Processes, Facies and Stratigraphy*. 3rd ed. John Wiley & Sons, 83–106.

Schomacker, E. R., Kjemperud, A. V., Nystuen, J. P., and Jahren, J. S. (2010). Recognition and Significance of Sharp-Based Mouth-Bar Deposits in the Eocene Green River Formation, Uinta Basin, Utah. *Sedimentology* 57, 1069–1087. doi:10.1111/j.1365-3091.2009.01136.x

Shanxi Bureau of Geology and Mineral Resources (SBGMR) (1989). *Regional Geology of Shanxi Province*. Beijing: Geological Publishing House.

Shi, N., Cao, J., and Lars-König, K. (1993). Late Cenozoic Vegetational History and the Pliocene-Pleistocene Boundary in the Yushe Basin, S. E. Shanxi, China. *Grana* 32 (4-5), 260–271.

Shi, W., Cen, M., Chen, L., Wang, Y., Chen, X., Li, J., et al. (2015). Evolution of the Late Cenozoic Tectonic Stress Regime in the Shanxi Rift, central North China Plate Inferred from New Fault Kinematic Analysis. *J. Asian Earth Sci.* 114, 54–72. doi:10.1016/j.jseaes.2015.04.044

Shi, W., Dong, S., and Hu, J. (2020). Neotectonics Around the Ordos Block, North China: A Review and New Insights. *Earth-Science Rev.* 200, 1–34. doi:10.1016/j.earscirev.2019.102969

Singer, A. (1980). The Paleoclimatic Interpretation of clay Minerals in Soils and Weathering Profiles. *Earth-Science Rev.* 15, 303–326. doi:10.1016/0012-8252(80)90113-0

Su, P., He, H., Tan, X., Liu, Y., Shi, F., and Kirby, E. (2021). Initiation and Evolution of the Shanxi Rift System in North China: Evidence from Low-Temperature Thermochronology in a Plate Reconstruction Framework. *Tectonics* 40 (3), e2020TC006298. doi:10.1029/2020tc006298

Sun, J. (2005). Long-term Fluvial Archives in the Fen Wei Graben, central China, and Their Bearing on the Tectonic History of the India?Asia Collision System during the Quaternary. *Quat. Sci. Rev.* 24, 1279–1286. doi:10.1016/j.quascirev.2004.08.018

Sun, Z. (1997). *Sedimentary Environment and Hydrocarbon Generation of Cenozoic saline Lacustrine in China*. Beijing: Petroleum Industry Press, 125–141.

Tang, Z., Yang, S., Qiao, Q., Yin, F., Huang, B., and Ding, Z. (2016). A High-Resolution Geochemical Record from the Kuche Depression: Constraints on Early Miocene Uplift of South Tian Shan. *Palaeogeogr. Palaeoclimatol. Palaeoecol.* 446, 1–10. doi:10.1016/j.palaeo.2016.01.020

Tao, H., Sun, S., Wang, Q., Yang, X., and Jiang, L. (2014). Petrography and Geochemistry of Lower Carboniferous Greywacke and Mudstones in Northeast Junggar, China: Implications for Provenance, Source Weathering, and Tectonic Setting. *J. Asian Earth Sci.* 87, 11–25. doi:10.1016/j.jseaes.2014.02.007

Tapponnier, P., Peltzer, G., and Armijo, R. (1986). On the Mechanics of the Collision between India and Asia. *Geol. Soc. Lond. Spec. Publications* 19 (1), 113–157. doi:10.1144/gsl.sp.1986.019.01.07

Tapponnier, P., Peltzer, G., Le Dain, A. Y., Armijo, R., and Cobbold, P. (1982). Propagating Extrusion Tectonics in Asia: New Insights from Simple Experiments with Plasticine. *Geol* 10 (12), 611–616. doi:10.1130/0091-7613(1982)10<611:petian>2.0.co;2

Tapponnier, R., and Molnar, R. (1977). Active Faulting and Tectonics in China. *J. Geophys. Res.* 82 (B20), 2905–2930. doi:10.1029/jb082i020p02905

Taylor, S. R., and McLennan, S. M. (1985). *The continental Crust: Its Composition and Evolution*. United States.

The Research Group on Active Fault System around Ordos Massif, State Seismological Bureau (RGAFSO) (1988). *Active Fault System Around Ordos Massif*. Beijing: Seismological Press, 1–335.

Tian, J., and Zhang, X. (2016). *Sedimentary Geochemistry*. Beijing: Geological Publishing House, 67.

Wang, N., Yang, J., Xia, Z., Mo, D., Li, Y., and Pan, M. (1996). *Cenozoic Sedimentary and Tectonic Geomorphology of Shanxi Rift System*. Beijing: Science Press. (in Chinese).

Wang, P., Huang, Z., Mi, N., Xu, M., Wang, L., Li, H., et al. (2014). Crustal Structure beneath the Weihe Graben in central China: Evidence for the Tectonic Regime Transformation in the Cenozoic. *J. Asian Earth Sci.* 81, 105–114. doi:10.1016/j.jseaes.2013.11.010

Wang, X., Wan, Z., Chen, C., and Chen, S. (2021). Geochemical Characteristics of Hydrocarbons in Core Sediments from the Southwest Sub-Basin of the South China Sea and its Implications for the Sedimentary Environment. *Front. Earth Sci.* 9 (317), 1–10. doi:10.3389/feart.2021.664959

Wang, Z., Wang, J., Fu, X., Zhan, W., Armstrong-Altrin, J. S., Yu, F., et al. (2018). Geochemistry of the Upper Triassic Black Mudstones in the Qiangtang Basin, Tibet: Implications for Paleoenvironment, Provenance, and Tectonic Setting. *J. Asian Earth Sci.* 160, 118–135. doi:10.1016/j.jseaes.2018.04.022

Wei, R., Zhuang, Q., Yan, J., Wei, Y., Du, Y., and Fan, J. (2020). *Late Cenozoic Stratigraphic Division and Sedimentary Environment of Jinzhong Basin in Shanxi Province, with the Climate and lake Evolution since the Pre-qin Period*. Geology in China.

Wei, W., and Algeo, T. J. (2020). Elemental Proxies for Paleosalinity Analysis of Ancient Shales and Mudrocks. *Geochimica et Cosmochimica Acta* 287, 341–366. doi:10.1016/j.gca.2019.06.034

Wei, W., Algeo, T. J., Lu, Y., Lu, Y., Liu, H., Zhang, S., et al. (2018). Identifying marine Incursions into the Paleogene Bohai Bay Basin lake System in Northeastern China. *Int. J. Coal Geology.* 200, 1–17. doi:10.1016/j.coal.2018.10.001

Weltje, G. J., and Von Eynatten, H. (2004). Quantitative Provenance Analysis of Sediments: Review and Outlook. *Sediment. Geology.* 171, 1–11. doi:10.1016/j.sedgeo.2004.05.007

Willis, B. (1907). *Research in China,* V. I*, Part* I, 233–236.

Wu, C. (1996). Palaeochannel and Paleodrainage Patterns in the North China Moutains. *Geographical Res.* 15, 33–41. (in Chinese with English abstract).

Wu, N., Pei, Y., Lu, H., Guo, Z., Li, F., and Liu, T. (2006). Marked Ecological Shifts during 6.2–2.4 Ma Revealed by a Terrestrial Molluscan Record from the Chinese Red Clay Formation and Implication for Palaeoclimatic Evolution. *Palaeogeogr. Palaeoclimatol. Palaeoecol.* 233 (3), 287–299. doi:10.1016/j.palaeo.2005.10.006

Xu, X., Ma, X., and Deng, Q. (1993). Neotectonic Activity along the Shanxi Rift System, China. *Tectonophysics* 219, 305–325. doi:10.1016/0040-1951(93)90180-r

Xu, X., and Ma, X. (1992). Geodynamics of the Shanxi Rift System, China. *Tectonophysics* 208, 325–340. doi:10.1016/0040-1951(92)90353-8

Xu, Y. (2012). *A Study on the Late Quaternary Faulting of the Huoshan Piedmont Fault Zone in the central Shanxi Faulted basin belt*. China Earthquake Administration: Institute of Geology. (in Chinese).

Xu, Y., Yue, L., Li, J., Sun, L., Sun, B., Zhang, J., et al. (2009). An 11-Ma-Old Red clay Sequence on the Eastern Chinese Loess Plateau. *Palaeogeogr. Palaeoclimatol. Palaeoecol.* 284, 383–391. doi:10.1016/j.palaeo.2009.10.023

Yan, J., Hu, J., Gong, W., Liu, X., Yin, Y., and Tan, C. (2020). Late Cenozoic Magnetostratigraphy of the Yuncheng Basin, central North China Craton and its Tectonic Implications. *Geol. J.* 55, 7415–7428. doi:10.1002/gj.3744

Yin, A. (2010). Cenozoic Tectonic Evolution of Asia: A Preliminary Synthesis. *Tectonophysics* 488, 293–325. doi:10.1016/j.tecto.2009.06.002

Yue, L., Deng, T., Zhang, Y., Wang, J., Zhang, R., and Yang, J. (2004). Magneto Stratigraphy of Stratotype Section of the Baode Stage. *J.Stratigr.* 1, 51–63.

Zhang, P., Molnar, P., and Downs, W. R. (2001). Increased Sedimentation Rates and Grain Sizes 2–4 Myr Ago Due to the Influence of Climate Change on Erosion Rates. *Nature* 410, 891–897.

Zhang, S., and Liu, X. (2012). "1:50000 Geological Mapping of Kouquan Fault," in *Special Inspection Report of Active Fault Earthquake Risk Evaluation Project in Key Surveillance and Defense Area* (Institute of Crustal Stress, China Earthquake Administration Publication). (in Chinese).

Zhang, Y., and Liao, C. (2006). Transition of the Late Mesozoic–Cenozoic Tectonic Regimes and Modification of the Ordos basin. *Geology. China* 33, 28–40. (in Chinese with English abstract).

Zhang, Y., Ma, Y., Yang, N., Shi, W., and Dong, S. (2003). Cenozoic Extensional Stress Evolution in North China. *J. Geodynamics* 36, 591–613.

Zhang, Y. Q., Mercier, J. L., and Vergély, P. (1998). Extension in the Graben Systems Around the Ordos (China), and its Contribution to the Extrusion Tectonics of south China with Respect to Gobi-Mongolia. *Tectonophysics* 285, 41–75. doi:10.1016/s0040-1951(97)00170-4

Zhao, J., Liu, C., Mountney, N., Lu, J., Cao, J., Yang, Y., et al. (2016). Timing of Uplift and Evolution of the Lüliang Mountains, North China Craton. *Sci. China Earth Sci.* 59 (1), 58–69. doi:10.1007/s11430-015-5153-z

Zhao, J., Liu, C., Wang, X., Ma, Y., and Huang, L. (2009). Uplift and Evolution Characteristics in the LuLiang Mountain and its Adjacent Area during the Meso-Cenozoic. *Geol. Rev.* 55 (5), 663–672. (in Chinese with English abstract).

Zheng, D., Zhang, P.-Z., Wan, J., Yuan, D., Li, C., Yin, G., et al. (2006). Rapid Exhumation at ~8 Ma on the Liupan Shan Thrust Fault from Apatite Fission-Track Thermochronology: Implications for Growth of the Northeastern Tibetan Plateau Margin. *Earth Planet. Sci. Lett.* 248, 198–208. doi:10.1016/j.epsl.2006.05.023

Zhisheng, A., Kutzbach, J. E., Prell, W. L., and Porter, S. C. (2001). Evolution of Asian Monsoons and Phased Uplift of the Himalaya-Tibetan Plateau since Late Miocene Times. *Nature* 411 (6833), 62–66. doi:10.1038/35075035

Conflict of Interest: The authors declare that the research was conducted in the absence of any commercial or financial relationships that could be construed as a potential conflict of interest.

Publisher's Note: All claims expressed in this article are solely those of the authors and do not necessarily represent those of their affiliated organizations, or those of the publisher, the editors, and the reviewers. Any product that may be evaluated in this article, or claim that may be made by its manufacturer, is not guaranteed nor endorsed by the publisher.

Copyright © 2022 Zhuang, Wei and He. This is an open-access article distributed under the terms of the Creative Commons Attribution License (CC BY). The use, distribution or reproduction in other forums is permitted, provided the original author(s) and the copyright owner(s) are credited and that the original publication in this journal is cited, in accordance with accepted academic practice. No use, distribution or reproduction is permitted which does not comply with these terms.

frontiers in Earth Science

ORIGINAL RESEARCH
published: 04 March 2022
doi: 10.3389/feart.2022.824368

Evaluation of the Fluvial Response to Tectonic Uplift From Grain-Size Distribution in Riverbed Gravels at the Northeastern Margin of the Tibetan Plateau

Zijuan Dong[1], Baotian Pan[1,2], Zhenbo Hu[1]*, Qinhong Mo[1], David Bridgland[3], Menghao Li[1], Xiaohua Li[1], Yanan Yang[1] and Dianbao Chen[1]*

[1]Key Laboratory of Western China's Environmental Systems (Ministry of Education), College of Earth and Environmental Sciences, Lanzhou University, Lanzhou, China, [2]Shiyang River Basin Scientific Observing Station of Gansu Province, Lanzhou, China, [3]Department of Geography, Durham University, Durham, United Kingdom

OPEN ACCESS

Edited by:
Rong Yang,
Zhejiang University, China

Reviewed by:
Xiubin Lin,
Zhejiang University, China
Maodu Yan,
Institute of Tibetan Plateau Research (CAS), China

***Correspondence:**
Baotian Pan
panbt@lzu.edu.cn
Zhenbo Hu
zhbhu@lzu.edu.cn

Specialty section:
This article was submitted to Structural Geology and Tectonics, a section of the journal Frontiers in Earth Science

Received: *29 November 2021*
Accepted: *27 January 2022*
Published: *04 March 2022*

Citation:
Dong Z, Pan B, Hu Z, Mo Q, Bridgland D, Li M, Li X, Yang Y and Chen D (2022) Evaluation of the Fluvial Response to Tectonic Uplift From Grain-Size Distribution in Riverbed Gravels at the Northeastern Margin of the Tibetan Plateau. Front. Earth Sci. 10:824368. doi: 10.3389/feart.2022.824368

Downstream fining of riverbed gravels is generally linked with the processes of hydraulic sorting and abrasion. Hydraulic sorting is when larger gravel clasts stop moving in response to decreasing flow energy, whereas, finer grains will continue to be carried downstream. Furthermore, transportation of gravel clasts causes abrasion, bringing about a gradual decrease in grain size. Hydraulic sorting and abrasion have different dominant effects on the downstream fining of clasts in rivers with different climatic and tectonic backgrounds. At present, most studies focus on humid areas, and relatively few studies have explored this issue for the northeastern margin of the Tibetan Plateau in arid and semi-arid areas. Detailed investigations of the grain size, lithology, and roundness of riverbed gravels have been performed here along the Taolai, Hongshuiba, and Fengle Rivers, which flow across the northeastern margin of the Tibetan Plateau and debouch into the arid inland of North China. The obtained data were subsequently employed in a hydraulic pattern of grain-size distribution of riverbed gravels in this area, which is characterized by the combined influences of tectonic activity and climatic aridity. Analysis reveals that there is no new rock type appearing in the lithological compositions of riverbed gravels along these rivers, only showing fluctuations in proportions of lithology even though they are adjacent to uplifting mountains. Fresh gravel material from these mountains does indeed mix into the fluvial bedload, inducing a notable decrease in roundness in the Taolai and Hongshuiba bedloads downstream from here. The downstream fining of gravel along the three rivers, with median grain sizes above 128 mm and falling into the range from 20 to 128 mm, can probably be attributed to hydraulic sorting and abrasion. Further analysis suggests that the former presents a high correlation with channel gradient, which may be sustained by fault activity at the northeastern margin of the Tibetan Plateau. The grain-size distribution in these riverbed gravels thus provides insights into the evaluation of fluvial responses to active tectonic uplift.

Keywords: riverbed gravel, grain size, hydraulic sorting, abrasion, channel slope

1 INTRODUCTION

The interaction between climate and tectonic activity, and their relative roles as driving mechanisms for fluvial processes, have long been topics for debate (e.g., Molnar and England 1990; Molnar 2003), attracting wide attention from geoscientists (e.g., Bridgland 2000; Westaway 2009; Wang et al., 2014). River system evolution is regarded as a result of these two factors in combination, and can record important evidence for their relative influence (e.g., Bridgland et al., 2012; Bridgland and Westaway 2014). In general, riverbed gravels from the same provenance appear to show a downstream decreasing tendency in grain size over tens to hundreds of kilometers (Parker 1991a). Hydraulic sorting occurs when larger gravel clasts stop moving as flow energy declines, whereas finer grains will continue to be carried downstream. Furthermore, transportation of clasts causes abrasion, bringing about a gradual downstream decrease in grain size, unless new material is added. The controlling factors and mechanisms of these two processes remain weakly understood (Rice 1999). A thorough assessment and distinction of their roles in fluvial sediment transportation can provide an excellent insight into river responses to allogenic controls (Hoey and Bluck 1999). Thus, in coarse sediments (>2 mm), downstream clast-size decrease can result from abrasion leading to actual size reduction (Kodama 1994; Humphrey 1997), or from selective transportation and deposition, which is the above-mentioned sorting process (Ferguson et al., 1996), or from their combined action. During the past few decades, the relative influence of these two factors in yielding a downstream decrease in grain size has, however, remained unclear and controversial (Bradley 1970; Shaw and Kellerhals 1982; Ashworth and Ferguson 1989; Parker 1991a; Parker 1991b; Paola et al., 1992; Mikos 1993; Huddard 1994; Ferguson et al., 1996). There is evidence that abrasion can be attributed to mechanical weathering of clasts through corrasion (Rengers and Wohl 2007) and that this is a leading mechanism in producing downstream fining on alluvial fans along many Japanese rivers, flowing through temperate humid climates and active tectonic zones (Kodama 1994). From mathematical analysis on the weight reduction of average clasts, Mikos (1993) also argued that abrasion appears to dominate. In the 1970's and 1980's, opinion swung strongly in favor of sorting, because observed downstream fining of fluvial bedload presented rates an order of magnitude higher than laboratory simulations using the same lithologies (e.g., Adams 1980). Further analysis reveals that selective sorting may be controlled primarily by the limited competence of hydraulic forces, which succeed in transporting small particles but fail to transport large particles (Rengers and Wohl 2007). Moreover, more recent advances suggest that this process is linked with certain fundamental geomorphic properties, such as concavity of stream profile (Rengers and Wohl 2007). As stream gradient decreases, flow competence in the transport of sediments also decreases (Gomez et al., 2001), thereby resulting in selective deposition of coarse particles, while fine particles continue in transport (Parker 1991b; Ferguson and Ashworth 1991; Hoey and Ferguson 1997; Ferguson et al., 1998; Gomez et al., 2001). Evidence from bed-load trap measurements and the dispersion of magnetic tracer pebbles also indicate that rapid downstream fining of clasts along a small river can probably be attributed to sorting rather than abrasion (Ferguson et al., 1996). This suggestion is in good agreement with the combined study of bed-load transport rates, grain-size distribution, shear stresses, and tracer pebble movements along three high-power gravel-bed rivers, in Scotland and Norway (Ashworth and Ferguson 1989).

In addition, quantitative field studies of the phenomenon are rendered difficult by a host of site-specific factors, such as hydrologic regime, tributaries bringing in clasts of different lithologies, base-level variation, and the scale over which fining is manifested (Cui et al., 1996). Researchers have thus resorted to techniques that allow the effects of various parameters to be isolated (e.g., Werritty and Florence 1990; Paola et al., 1992). Theoretical formulations (Sternberg 1875), observations of modern rivers (Bradley et al., 1972; Dawson 1988), flume studies (Elgueta-Astaburuaga and Hassan 2019), and numerical models (Hoey and Ferguson 1994; Cui et al., 1996) have significantly enhanced our understanding of sediment transport in mixed-grain-size river systems (Robinson and Slingerland 1998). The effectiveness of sorting, however, had been doubted as a result of empirical and theoretical work in the 1980's, which suggested that entrainment from mixed-size gravel is almost or entirely unselective, due to hiding and protrusion effects (Andrews 1983; Wiberg and Smith 1987; Kirchner et al., 1990). Further analysis has indicated that high-stage gravel transport probably approaches equal mobility for different sizes, under the impact of these effects (Parker et al., 1982; Ashworth and Ferguson 1989; Wilcock and Southard 1989).

The above arguments have prompted a re-examination of whether the observed downstream fining of fluvial clasts can be generated through sorting alone. Despite its significance, the research on this issue remains inadequate; for example, the influencing factors of sorting have yet to be resolved. Moreover, sorting has been inferred without direct measurement of bed-load transport in the same river, and abrasion has been supported or rejected by comparing downstream fining in one river with abrasion tests of supposedly similar sediment from another river in hydraulic conditions of unknown applicability (Ferguson et al., 1996). At present, few studies have focused on this topic in areas characterized by the combination of arid or semi-arid climate and active tectonic processes. Below we thus examine the grain-size trends along the riverbeds of the Taolai, Hongshuiba and Fengle Rivers, together with their hydraulic parameters. These rivers flow from the Qilian Mountains and debouch into the arid interior of North China, which is generally considered as the northeast margin of the Tibetan Plateau. Gravels were measured in transects along these rivers, using pebble counts of median diameter, lithology, and clast rounding. It is the purpose of this paper to explore downstream distribution of grain sizes along the riverbed of these rivers and then further analyze the potential causes behind these trends.

2 CATCHMENT SETTING

The Beida River, with a length of ~200 km, derives from the Tuolai and Tuolainan Shan, (Shan = Mountain in Chinese) located within the Southern Qilian Shan, and draining an area

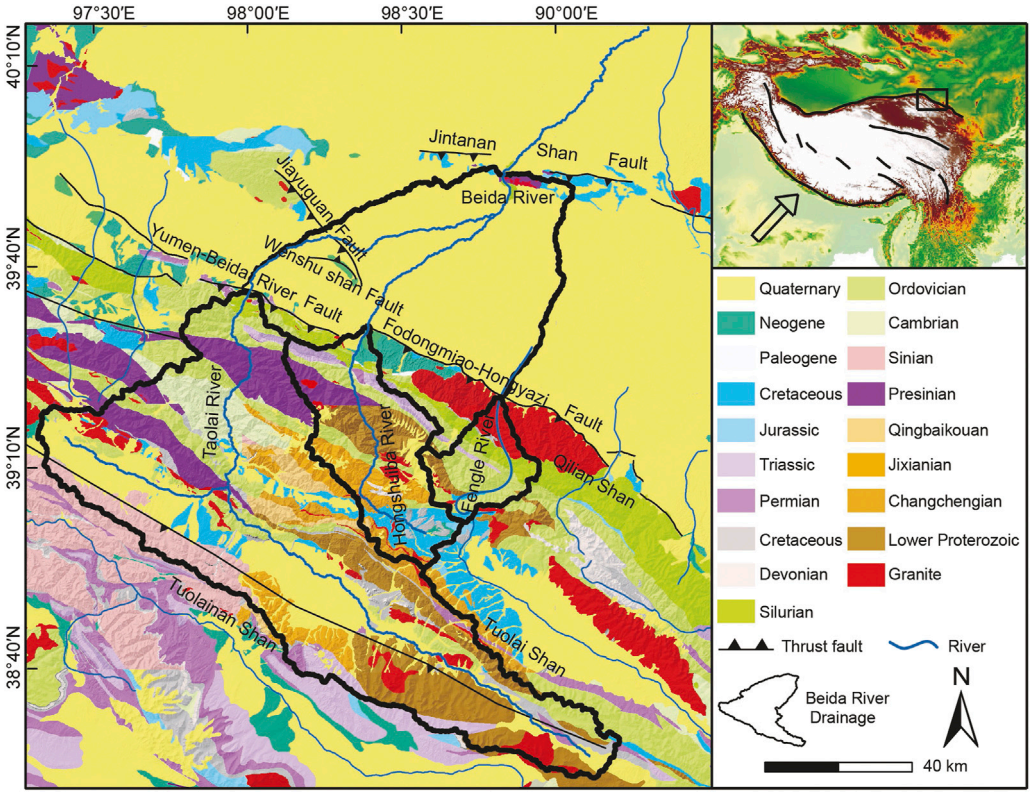

FIGURE 1 | Geological map of the Beida River catchment. Its scale is 1:200,000, revised from the Gansu Geological Bureau (1967). Major faults, rivers, sub-catchments, and mountains have been presented within this catchment. These faults revised from Gansu Geological Bureau (1967). The inset map indicates the location of this catchment in the northeastern margin of the Tibetan Plateau.

of ~8,847 km^2 (Wang 2019). From east to west, this catchment can be divided into the three sub-basins of the Fengle, Hongshuiba, and Taolai Rivers (**Figure 1**). All these tributaries are fed mainly by glacial meltwater, resulting in an approximately constant discharge (Yang 2008). The Taolai and Hongshuiba Rivers flow from the Qilian Shan, and then excavate separately through either side of the Wenshu Shan, converging finally at the southern front of the Jintanan Shan. In contrast, the Fengle River disappears as it flows from the Qilian Shan into the Gobi.

The three rivers debouch northward into the arid interior of North China (Wu et al., 2007; Cai et al., 2012) and between the Qilian Shan and Jintanan Shan are characterized by braided gravel-bed floodplains. The bedrock lithology of the Taolai River catchment mainly comprises limestone, quartzite, schist, gneiss, sandstone, and granite, while the Hongshuiba catchment is dominated by sandstone, gneiss, quartzite, and granite. In comparison with above two sub-catchments, the distribution of bedrock types across the Fengle River catchment points to a relatively simple composition, consisting of granite, sandstone, limestone, and diabase (**Figure 1**). The sediments that have accumulated within the catchments of these three rivers are all fluvial clasts eroded from the Qilian Shan during the Quaternary (Zhang et al., 2020). Moreover, the Wenshu Shan, located between the Qilian Shan and the Jintanan Shan, is mainly composed of conglomerate, presenting a similar lithologic composition in comparison with the catchments of the Taolai and Hongshuiba Rivers (Zhao et al., 2001).

The Beida River catchment is transected by a number of reversed faults, i.e., the Yumen–Beida River fault, the Fodongmiao–Hongyazi fault, the Jiayuguan fault, the Wenshu Shan fault, and the Jintanan Shan fault, which are clearly exposed along the fronts of the Qilian Shan, the Wenshu Shan, and the Jintanan Shan (**Figure 1**). Fault scarps can be readily observed and traced for hundreds of kilometers along these faults, indicating that tectonic activity around these mountains has remained vigorous during the Quaternary (Song 2006). The northern front of the Qilian Shan is constrained by the NW–SE trending Yumen–Beida River fault and Fodongmiao–Hongyazi fault, generating striking relief. In addition, the Wenshu Shan, situated between the Jintanan Shan and Qilian Shan, is bounded by the Jiayuguan fault to the north and Wenshu Shan fault to the south. These two NW–SE-trending reverse faults have led to the uplift of the Wenshu Shan in an anticlinal pattern (Song 2006; Zheng 2009). Owing to their activity and the resultant upward growth of the Qilian Shan and Wenshu Shan, the surface between the two mountain ranges has been uplifted strikingly, forcing the Taolai and Hongshuiba Rivers to incise deeply (**Figures 2A,C**). In contrast, as the two rivers flow northwards far away from the Wenshu Shan, their valleys all show a wide and shallow form (**Figures 2B,D**).

FIGURE 2 | Field photos from the Beida River catchment. **(A)** and **(B)** Two kinds of Taolai River channels. **(C)** and **(D)** View of the Hongshuiba River channel characterized by deep incision and low relief, respectively. **(E)** and **(F)** the Fengle River channel. **(G)** and **(H)** Ephemeral channels overlying the interfluves between the Taolai, Hongshuiba, and Fengle Rivers. **(I)** and **(J)** Sample site illustrating investigation methods in the field. **(K)** and **(L)** Field measurement of riverbed width. **(M)**–**(P)** Field measurement of riverbed depth.

3 METHODS

3.1 Data Collection

Fieldwork along the channels of the Taolai, Hongshuiba, and Fengle Rivers mainly comprised the measurement of hydraulic parameters (width and depth), grain size, lithology, and roundness. Owning to the deep downcutting by these rivers between the Qilian Shan and the Wenshu Shan (**Figures 2A,C**), access to their valleys is rather difficult. These sites, which can be entered by foot into riverbed, thus have been chosen for investigations. Thereafter, measurement sites are more widely spaced downstream. This was partly a reflection of the absence of suitable bars to sample and partly because of the local removal of coarse bed material from the riverbed for local construction purposes. Respectively thirteen, eleven, and seven sites have been used for measurement work along the Taolai, Hongshuiba, and Fengle Rivers (**Table 1**). Furthermore, in view of potential input of material from slopes, twelve measurement sites on the interfluves between these rivers, marked A–L (**Figure 3A**), were also been chosen for investigation. These investigation sites along the three rivers are numbered in downstream sequence (**Figure 3A**), and their downstream distances from the Qilian Shan are employed to mark the location along the river courses. These sites chosen for measurement are generally located within the modern active riverbed, free from artificial disturbance to bed material and thick vegetation cover of the bar surface. River width here refers to the channel width, which was measured using a TruePluse 360 laser rangefinder. Meanwhile, the river depth was measured at 3–5 points along each riverbed cross section to obtain an averaged depth. The riverbed elevation of different reaches was extracted from a DEM with 30-m resolution, yielding the longitudinal profiles of the three rivers. The average riverbed gradient (S) within 2 km upstream and downstream of the measuring points was taken as the riverbed gradient at that point.

The grain size of the sediment was established using sieving (Mosley and Tindale 1985). Within each square, all riverbed clasts were collected to a depth of ~10 cm, although if the largest clasts exceeded this measurement then the sample depth was increased. Collected clasts were then separated into different grain-size

TABLE 1 | Results of analytical indices along the Taolai, Hongshuiba, and Fengle Rivers.

Site	Distance (km)	Width (m)	Depth (m)	D_{95} (mm)	D_{84} (mm)	D_{50} (mm)	D_{16} (mm)	D_5 (mm)	σ	Fs	R	S	τ_b $(g/cms)^2$	τ_c $(g/cms)^2$
Taolai River														
1	0.00	54.2	0.35	1,278.3	996.0	357.1	45.6	1.9	2.5	0.07	4.12	0.021	4076.6	1,133.2
2	1.93	37.0	1.95	675.6	315.2	194.0	41.1	2.3	2.2	0.05	4.10	0.034	5425.8	707.1
3	12.27	36.7	1.63	630.3	458.3	215.3	24.6	1.9	2.3	0.07	4.89	0.015	2370.0	689.6
4	14.98	106.4	0.91	337.8	278.2	148.1	32.0	2.1	1.9	0.06	4.94	0.017	1,545.4	524.9
5	17.17	68.0	1.35	326.3	259.6	54.9	3.4	1.7	2.7	0.13	4.96	0.010	1,349.1	130.9
6	19.40	232.4	1.20	326.3	256.0	69.6	9.1	2.1	2.3	0.06	5.05	0.015	1719.1	244.0
7	20.49	140.1	1.53	296.1	194.0	97.0	11.6	2.8	2.0	0.04	4.72	0.013	1964.4	390.7
8	22.34	209.2	2.60	157.6	113.0	59.7	21.1	1.9	1.6	0.07	4.42	0.014	3506.9	192.0
9	30.91	577.0	1.40	163.1	72.5	39.4	3.5	1.7	1.8	0.15	4.62	0.013	1731.8	88.6
	40.15			78.8	59.7	28.8	2.0	1.6	2.1	0.21	4.72			57.0
10														
	48.74			97.0	55.7	21.1	2.3	1.6	2.1	0.17	4.31			45.6
11														
	55.23			77.7	54.9	26.4	5.2	1.7	1.7	0.12	4.26			66.6
12														
	69.34			61.8	39.9	21.9	5.7	1.7	1.5	0.11	4.51			57.8
13														
Hongshuiba River														
1	0.00	161.3	1.16	675.6	588.1	357.1	48.5	5.0	2.0	0.04	5.21	0.018	2019.6	1,453.5
2	2.31	282.0	0.90	666.3	545.0	145.0	16.2	1.7	2.6	0.10	4.85	0.012	1,036.7	391.6
3	4.82	314.2	0.98	639.1	505.0	170.1	24.9	1.7	2.4	0.13	4.83	0.016	1,541.0	409.6
4	8.34	209.0	1.07	588.1	382.7	145.0	11.4	1.7	2.6	0.13	4.92	0.016	1,668.2	345.8
5	9.84	509.1	1.26	580.0	357.1	157.6	14.0	1.7	2.4	0.12	4.83	0.017	2043.8	398.4
6	13.91	477.2	1.44	621.7	421.7	137.2	27.9	2.1	2.2	0.05	5.03	0.016	2254.5	492.8
7	16.40	315.0	1.34	621.7	421.7	139.1	34.3	2.0	2.2	0.07	5.16	0.013	1745.1	456.1
8	20.91		1.00	278.2	168.9	73.5	14.9	1.7	2.0	0.13	5.05	0.016	1,614.5	178.1
9	29.31		1.00	162.0	128.0	59.7	18.1	1.8	1.7	0.09	4.87	0.015	1,434.1	172.1
	39.70		1.00	157.6	119.4	52.7	11.3	2.0	1.8	0.07	4.56	0.004	390.8	172.7
10														
	54.95		1.50	66.3	41.6	21.1	4.9	1.7	1.6	0.11	4.39	0.004	534.6	54.0
11														
Fengle River														
1	0.00	21.7	1.64	477.7	541.2	235.6	36.8	1.7	2.1	0.04	4.44	0.072	11,645.2	965.3
2	2.77	26.4	0.91	652.6	512.0	219.8	49.2	5.6	1.9	0.02	4.65	0.037	3263.4	1,029.7
3	6.16	147.5	0.90	657.1	415.9	194.0	48.5	3.9	2.1	0.07	4.80	0.026	2318.7	617.5
4	7.92	153.6	1.62	608.9	315.2	159.8	27.9	1.9	2.0	0.10	4.84	0.022	3521.5	439.2
5	10.94	103.5	1.17	319.6	256.0	89.3	18.6	1.9	2.1	0.08	4.99	0.020	2347.1	278.2
6	13.14	151.7	0.60	304.4	171.3	68.6	4.1	1.7	2.5	0.13	5.08	0.016	946.1	165.9
7	15.67	613.0	0.88	159.8	126.2	55.7	4.0	1.6	2.2	0.14	5.05	0.018	1,560.0	130.7

groups by sieving (**Figures 2I,J**). They were further weighed in the field. Particles with a grain size of 0–2 mm are recorded as sand, while > 2-mm clasts are classified as gravel. The gravel was then divided into the following grain-size groups (unit: mm): 2.0–2.5, 2.5–5, 5–10, 10–20, 20–32, 32–64, 64–128, 128–256, 256–512, and 512–1,024. At each site, a total of 200 gravel clasts were investigated to determine their intermediate axis, lithology, and roundness, based on the random measurement method (Stock et al., 2008).

3.2 Analytical Index

In order to make a consistent comparison, the median clast diameter of each size group has been transformed into φ by the following equation:

$$\phi = -\log_2(D/D_0) \quad (1)$$

in which D represents the median clast diameter of each size group, D_0 represents 1 mm to standardize the measuring data to make it free from measurement unit.

The percentage weight of each grain-size group relative to the total riverbed clasts at a site constitutes a frequency distribution curve, which can be further translated into a cumulative frequency curve. The gravel median diameter corresponding to 5, 16, 50, 84, and 95%, in this cumulative frequency curve then have been employed as characteristic particle sizes (Krumbein 1934; Chen et al., 2018), marked by D_5, D_{16}, D_{50}, D_{84}, and D_{95}, respectively. Moreover, based on φ, the sorting property of gravels accumulated at one site can be readily evaluated by the standard deviation of their grain size, which is generally marked as σ, with larger values signifying poorer sorting. According to Folk and Ward (1957), this can be calculated using the formula:

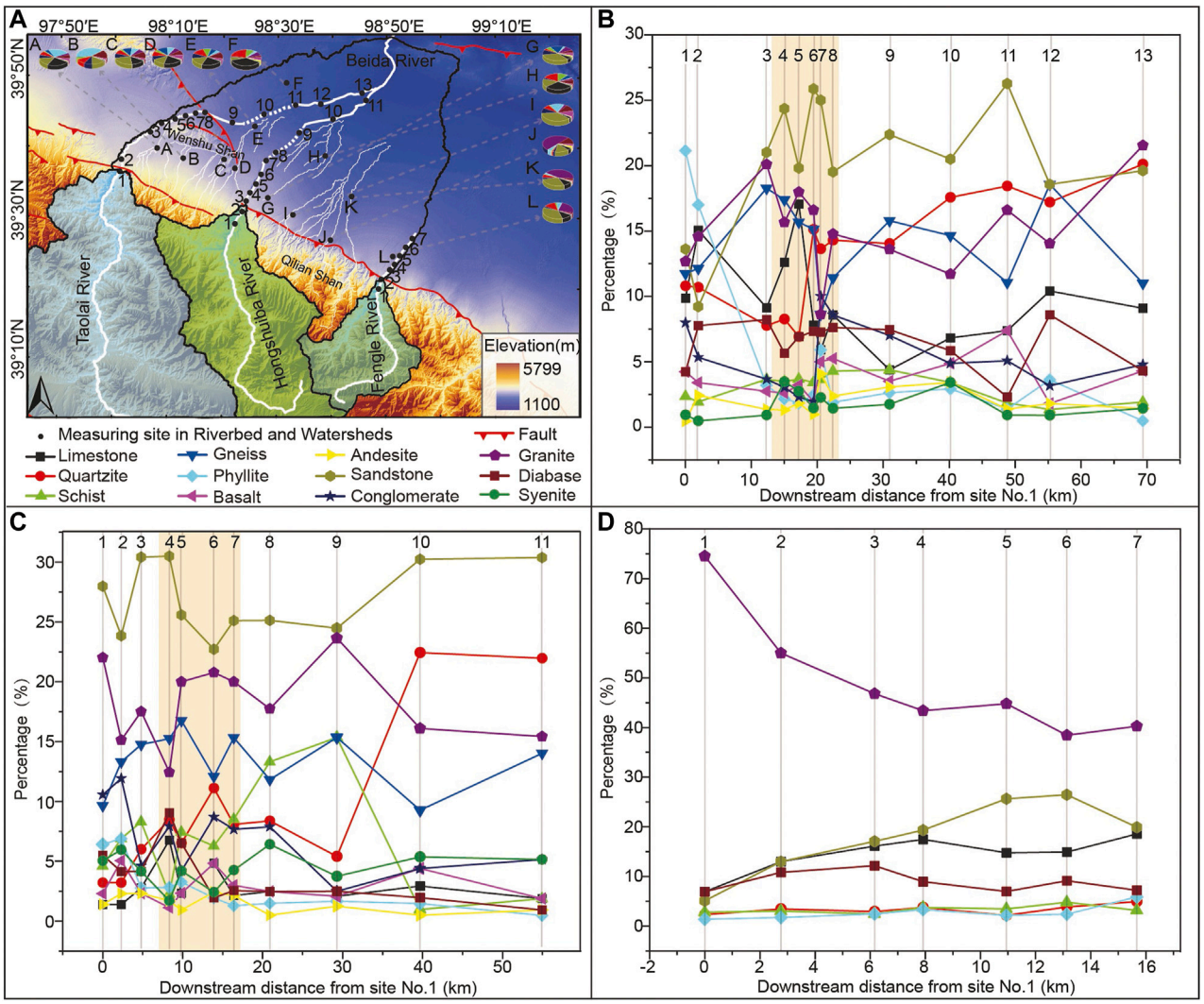

FIGURE 3 | Statistical data on bedload gravel lithology. **(A)** The Beida River catchment. All sampling sites and correspondent lithological composition of bedload gravels have been numbered in downstream sequence along its three tributaries, the Taolai, Hongshuiba, and Fengle Rivers. Furthermore, a total of 12 samples taken from the watersheds between these tributaries has been marked from A to L. Fine white lines indicate watershed gullies. **(B)**, **(C)** and **(D)** Downstream variations in lithological proportion of the bedload gravels along the Taolai Hongshuiba, and Fengle Rivers, respectively. All the sampling sites are marked by number sequence which is coincident with **(A)**, the shaded area in **(B)** and **(C)** indicates that the rivers flow through the Wenshu Shan.

$$\sigma = \frac{\varphi 84 - \varphi 16}{4} + \frac{\varphi 95 - \varphi 5}{6.6} \tag{2}$$

in which $\varphi 95 = -\log_2 D_5$, $\varphi 84 = -\log_2 D_{16}$, $\varphi 16 = -\log_2 D_{84}$, and $\varphi 5 = -\log_2 D_{95}$.

τ_c here is defined as the critical shear stress, which is required for the initial movement of fluvial clasts, while τ_b is used to describe the riverbed shear stress. They can be obtained from the Shields constant equations (Meyer-Peter and Muller 1948):

$$\tau_c^* = \frac{\tau_c}{(s-1)\rho g D} \tag{3}$$

$$\tau_b = \rho g h S \tag{4}$$

Where, τ_c^* is a dimensionless constant, s is the ratio of the density of the sediment to the flowing water, ρ is water density, g is gravitational acceleration, D refers to D_{50}, h is the depth of river water, and S is riverbed slope. Wilcock and Kenworthy (2002) have calculated τ_c^* successfully by using the empirical formula:

$$\tau_c^* = (\tau_c^*)_1 + \left[(\tau_c^*)_0 - (\tau_c^*)_1\right] e^{-14Fs} \tag{5}$$

In which Fs is the sand content of a riverbed clast sample, while $(\tau_c^*)_1$ and $(\tau_c^*)_0$, corresponding to Fs = 1 and Fs = 0, respectively, can be calculated to be 0.011 and 0.035.

Based on the rounding-classification standard of Krumbein (1941a), bedload gravels at each site have been classified as 1 = very angular, 2 = angular, 3 = sub angular, 4 = sub rounded, 5 =

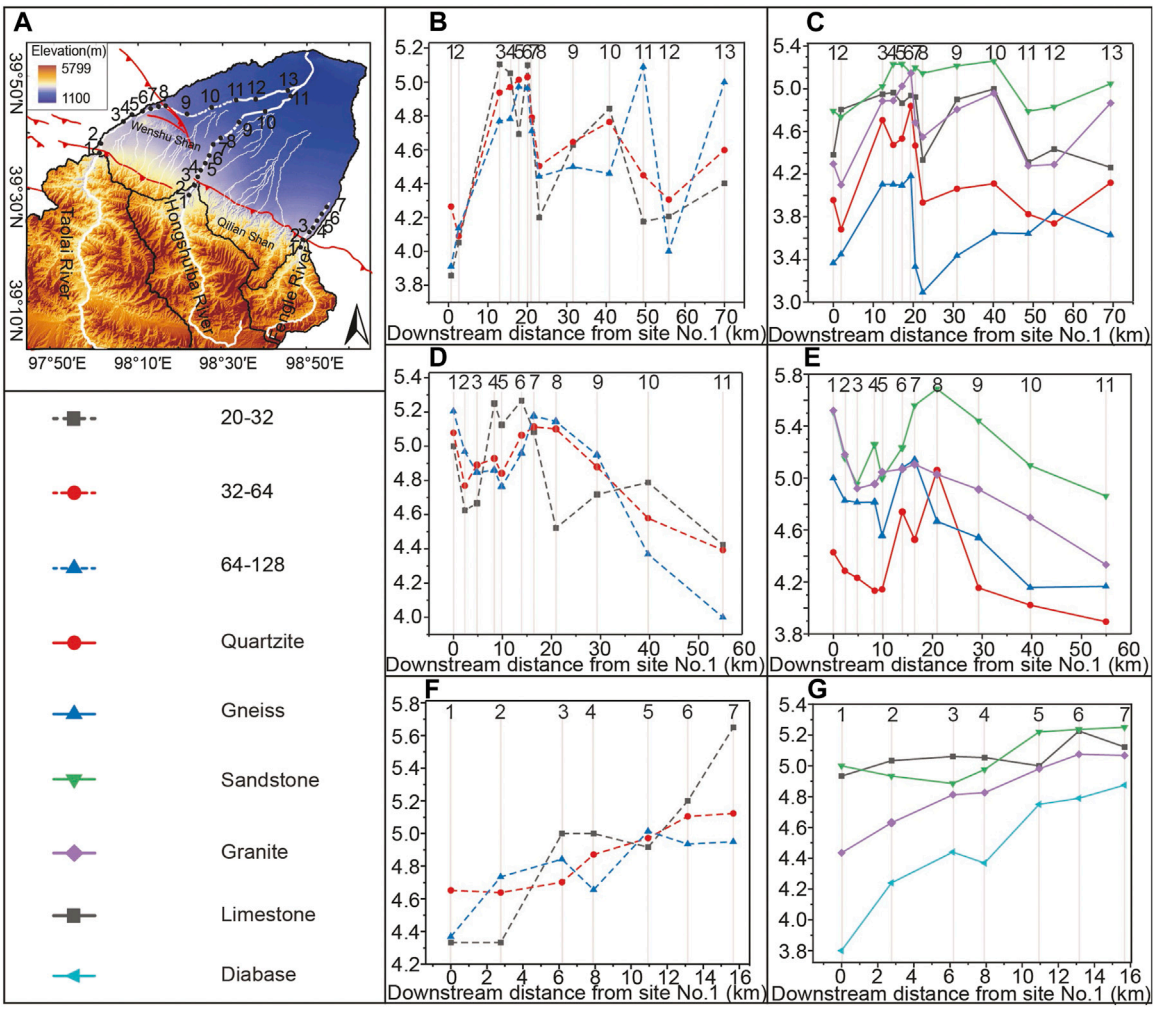

FIGURE 4 | The downstream variation in bedload gravel roundness along the Taolai, Hongshuiba, and Fengle Rivers. **(A)** The Beida River catchment. It can be divided into the three sub-catchments of the Taolai, Hongshuiba, and Fengle Rivers, in which all sampling sites are marked and numbered in downstream sequence. Dashed lines along the courses of the Taolai and Hongshuiba Rivers indicate their dry riverbeds. **(B)**–**(G)** The downstream variation in bedload gravel roundness for different gravel sizes and lithologies, respectively, along the Taolai, Hongshuiba, and Fengle Rivers. Their sampling sites are numbered in correspondence with **(A)**.

TABLE 2 | Results of roundness for the clasts eroded from the interfluves between the Taolai, Hongshuiba, and Fengle Rivers.

Site	A	B	C	D	E	F
R	3.80	3.33	3.85	3.99	4.08	3.44
Site	G	H	I	J	K	L
R	3.97	3.78	3.07	4.07	3.40	3.46

Reply to the figures used by reviewer 2

rounded and 6 = well rounded in the field (Powers 1953), and then their proportions can be calculated in terms of an individual number. An average roundness value (R) is employed here to further describe the rounding characteristics of the gravels at each site, which is defined as the sum of these proportions (Li et al., 2014), with higher value indicating better rounding and vice versa.

4 RESULTS

These results of the above analyses have been calculated and tabulated in **Table 1**. In order to elucidate transportation process of the bedload gravels along the Taolai, Hongshuiba, and Fengle Rivers, their lithology, roundness, and grain size, in combination with the calculated indices, have been analyzed in detail.

4.1 Lithology

Apart from twelve sampling sites located on the watersheds between the tributaries of the Beida River, a total of thirteen, eleven, and seven sites has been investigated along its tributaries: the Taolai, Hongshuiba, and Fengle Rivers, respectively (**Figure 3A**). The lithological composition of the gravels accumulated at the thirteen locations along the Taolai River shows that the proportion of phyllite decreases rapidly downstream from ~20 to 2%, within 10 km from the Qilian

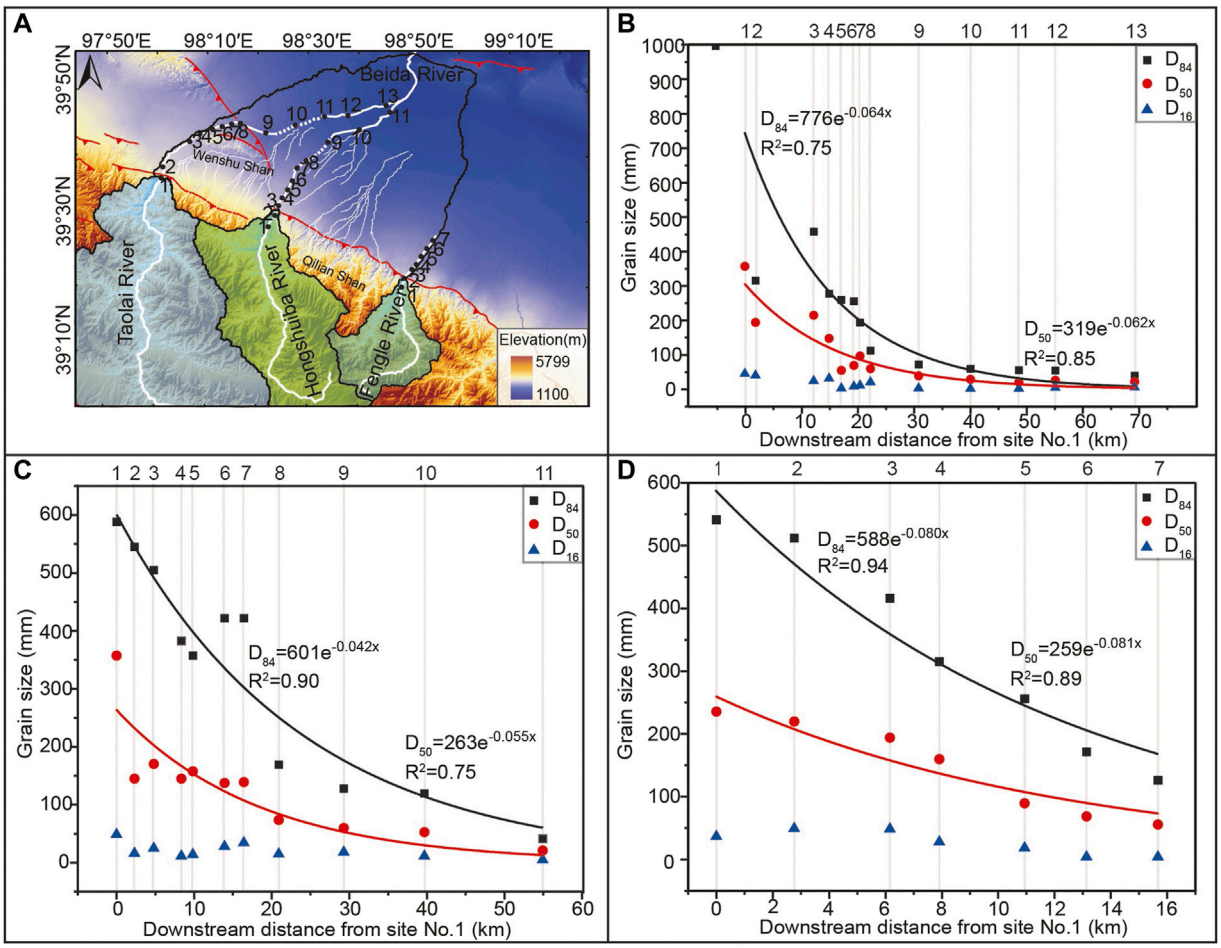

FIGURE 5 | Variation pattern of D_{84}, D_{50}, and D_{16} toward downstream. **(A)** The Beida River catchment. **(B)**, **(C)** and **(D)** Downstream variation in the three indexes along the Taolai, Hongshuiba, and Fengle Rivers, respectively. Their variations all follow an exponential fitting pattern, in which the fitting correlation coefficients for D_{84} and D_{50} can reach up to >0.75. All the sampling sites are marked by number sequence which is coincident with **(A)**.

Shan. In contrast, the proportion of quartzite gradually increases from ~10 to 20% over the same reach (**Figure 3B**). Near the Wenshu Shan, fluctuation of lithological proportions, however, occurs again, with both phyllite and limestone increasing slightly, and then declining to a stable level, while quartzite and sandstone appear to increase progressively. According to Zhao et al. (2001), the lithostratigraphy over the Wenshu Shan is mainly conglomerate and characterized by sandstone and quartzite, so this fluctuation may be attributable to clast input to the Taolai River bedload from these mountains. In the distribution of bedload gravel lithology at the eleven sampling sites along the Hongshuiba River, the proportions of diabase and phyllite both decrease rapidly downstream from ~5 to ~5%–~1% within 10 km from the Qilian Shan and then turn to a stable tendency (**Figure 3C**). In contrast, the proportion of quartzite increase remarkably from ~3% up to 22%. In the vicinity of the Wenshu Shan, the proportion of schist in comparison with other lithologies presents a great fluctuation, which can probably be correlated with the high proportion of schist occurring on the watershed between the Taolai and Hongshuiba Rivers (**Figure 3A**), given that the Wenshu Shan is composed of sandstone and quartzite (Zhao et al., 2001). This lithological fluctuation therefore demonstrates the input of material to the Hongshuiba bedload from small gullies over the watershed (**Figure 3A**). Along the Fengle River, granite decreases from ~74 to 40%, while sandstone increases to reach a relatively steady proportion of ~20% (**Figure 3D**) and other lithologies tend towards stability. Some sampling sites within gullies on the watershed between the Hongshuiba and Fengle Rivers show a high sandstone percentage (**Figure 3A**), suggesting a possible clast contribution to the Fengle River bedload.

4.2 Roundness

Along the Taolai, Hongshuiba, and Fengle Rivers, the results of bedload gravel roundness analysis for different lithologies and grain sizes are presented in **Figure 4**. As the Taolai River flows away from the Qilian Shan, the variation in its bedload gravel roundness falls into a complex pattern in which it first decreases

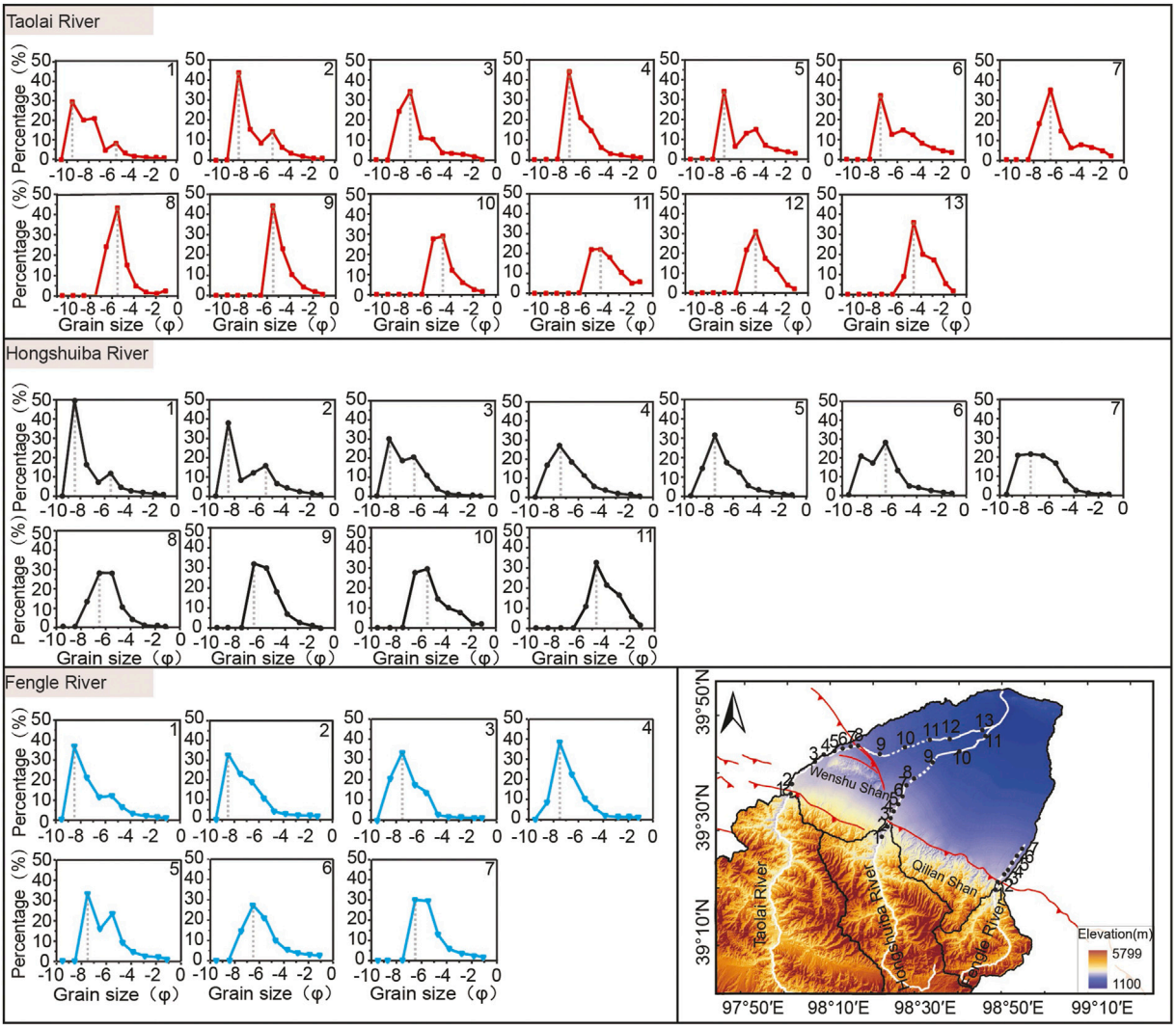

FIGURE 6 | Grain-size frequency distribution curves of bedload gravel along the Taolai, Hongshuiba, and Fengle Rivers. The sampling sites are numbered in downstream sequence and in correspondence with the inset map.

and then increases, twice over, forming two troughs (**Figures 4B,C**). Based on field investigation, they are in good correspondence with two reaches affected by the clast input from the Wenshu Shan and human activities (**Table 2**). Published data have revealed that gravel roundness of clasts formed of the conglomerate constructing the Wenshu Shan is indeed rather low (Zhao et al., 2001). The course of lower Taolai River has been restricted within an artificial channel, leading to original riverbed exposure (**Figure 4A**). Frost weathering seems to be vigorous here (Chen et al., 2019) causing the gravels accumulated on the dry riverbed to shatter. The bedload gravel roundness for different lithologies and grain sizes in the two reaches perhaps respond to the two styles of influence and yield two correspondent troughs. The downstream variation in bedload gravel roundness along the Hongshuiba River for different lithologies and grain sizes also shows two decreasing tendencies, which are against our expectations (**Figures 4D,E**). The statistical data on bedload gravel lithology has suggested that the small gullies on the watershed between the Taolai and Hongshuiba Rivers have a steady material contribution to the latter bedload (**Figure 3A**). Due to artificial reconstruction on the Taolai River, the whole riverbed of the lower Hongshuiba is now also exposed and suffers frost weathering. In view of this good spatial correlation, the two decreasing tendencies in bedload gravel roundness along the Hongshuiba River, therefore, can probably be linked with the two recognized influences: frost weathering and artificial reconstruction. In contrast, the downstream variation in bedload gravel roundness along the Fengle River for different lithologies and grain sizes shows a gradually increasing pattern (**Figures 4F,G**) which conforms to the universal rule (Krumbein 1941b).

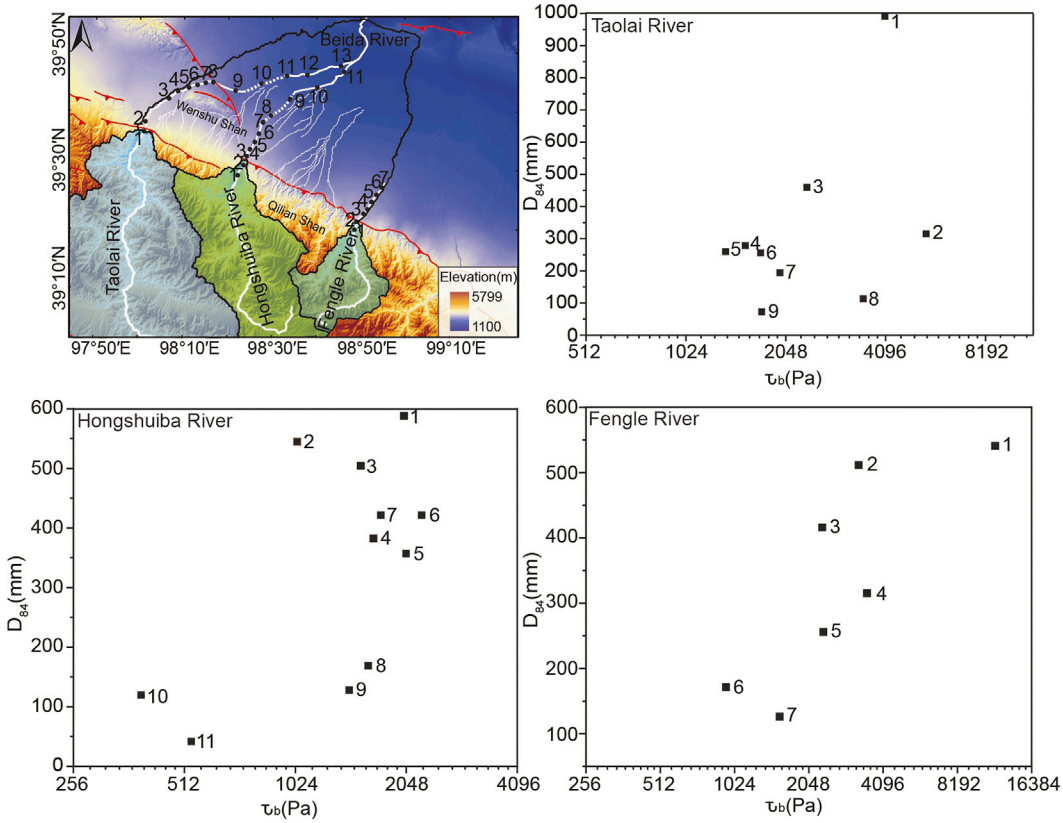

FIGURE 7 | Positive correlation checks between D_{84} and τ_b along the Taolai, Hongshuiba, and Fengle Rivers.

4.3 Grain Size

In general, the three indices D_{84}, D_{50}, and D_{16} can be employed as indicators to evaluate the downstream decrease in grain size of bedload gravel (Hoey and Bluck 1999). Along the Taolai, Hongshuiba, and Fengle Rivers, the three indices all show an obvious downstream diminishing tendency, amongst which D_{84} presents the widest variation range (**Table 1**). Further analysis reveals that the downstream decrease of D_{84} and D_{50} follows a more precise exponential fitting pattern compared with D_{16} (**Figure 5**). Their fit coefficients are all rather high, reaching up to >0.75 along the three rivers (**Figures 5B–D**). This variation pattern is in good agreement with the general rule for gravel-size distribution along riverbeds suggested by Sternberg (1875). Despite a gentle decrease tendency in the downstream direction for D_{16}, its major decline can be clearly observed to occur in the 30-km reaches of the longer Taolai and Hongshuiba Rivers, progressively downstream from the Qilian Shan, in correspondence with D_{84} and D_{50}. The grain-size frequency distribution curves of bedload gravel along the Taolai and Hongshuiba Rivers show a transformation from bimodal to unimodal pattern, with the peak progressively moving to finer particle sizes in a downstream direction (**Figure 6**). Meanwhile, they appear to become narrower and combined with decreasing standard deviation σ (**Table 1**), indicating that the bedload gravel tends towards an enhanced sorting property in the downstream direction. In contrast, the grain-size frequency distribution curves of bedload gravel and standard deviation along the short Fengle River seem to show negligible variation. Moreover, the sand contents of riverbed clast composition are almost constant along the three rivers.

5 DISCUSSION

5.1 Analysis of the Downstream Decrease in Grain Size of Bedload Gravel Based on the Hydraulic Sorting and Abrasion

The investigation results for bedload gravel lithology and roundness suggest that the clasts eroded from the interfluves between the Taolai, Hongshuiba, and Fengle Rivers can indeed be mixed into their riverbeds (**Figure 3A**; **Table 2**). Despite a notable fluctuation in lithological percentage due to this intrusion, the lithological composition of the bedload gravels presents a stable pattern along the three rivers (**Figure 3**), implying that the fluvial clasts transported through the northeastern margin of the Tibetan Plateau, characterized by active tectonism and dry climate, appear to represent material that has been recycled from earlier deposits (Zhang et al., 2020). Moreover, clast influx here perhaps has little effect on bedload gravel transportation. The downstream

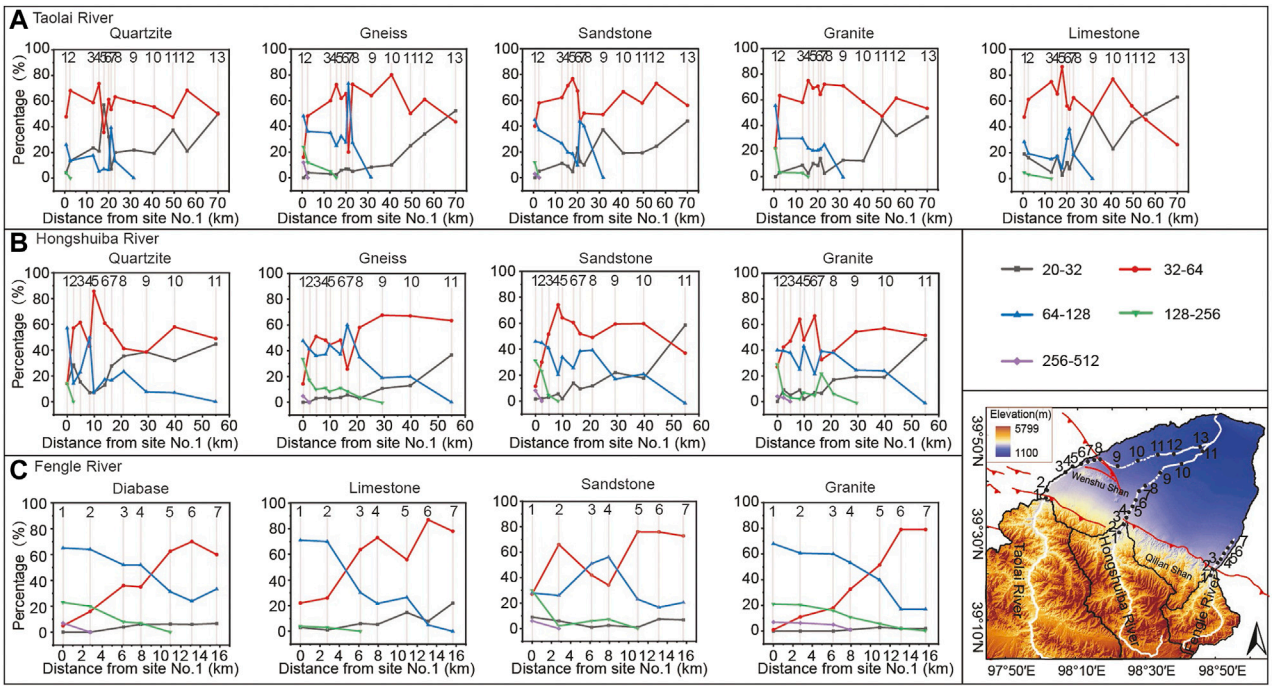

FIGURE 8 | Variation in the percentages of grain-size groups with different lithologies along the Taolai, Hongshuiba, and Fengle Rivers. The bedload gravels collected from every sampling site were classified according to their lithologies. For each lithology, the variation in the percentages of grain-size groups along the three rivers was then analyzed. **(A)**, **(B)**, and **(C)** Downstream variations in the percentages of grain-size groups with different lithologies, along the Taolai, Hongshuiba, and Fengle Rivers, respectively. The reduced percentages of grain-size groups >128 mm toward downstream are not seen in the smaller grain-size groups. In contrast, for the groups <128 mm, the reverse applies.

decrease in grain size in these bedload gravels thus also follows a good exponential fitting pattern (**Figure 5**), in good agreement with the general rule for gravel size distribution along riverbeds suggested by Sternberg (1875). Over the past century, numerous studies have attributed the downstream fining of bedload gravel to hydraulic sorting and abrasion (Mackin 1948; Rice 1998; Rice and Church 1998; Gomez et al., 2001; Rice and Church 2001; Sklar et al., 2006). Nevertheless, a debate on the dominant role in both of these can still be enlarged (e.g., Menting et al., 2015). According to the grain-size distribution of the bedload gravels along the three rivers, downstream fining has indeed been demonstrated by the work reported in this paper.

Along the Taolai, Hongshuiba, and Fengle Rivers, the reaches that are free of clast influx and human activities all present a tendency for bedload gravel roundness to increase downstream (**Figure 4**), linked to the contribution of abrasion to the downstream fining of bedload gravel. However, the sand content amongst bedload clasts seems not to increase due to abrasion, but tends to be almost constant along the three rivers (**Table 1**). This result suggests that the downstream fining of bedload gravel in this region at the northeastern margin of the Tibetan Plateau can also probably be attributed to hydraulic sorting, in addition to abrasion. In recent years, more studies have focused upon this influence, in which D_{84} has been argued to decrease in direct proportion to the decline of riverbed shear stress τ_b (Dunne and Jerolmack 2018). Our data however reveal that some sampling sites along the three rivers do not comply with this relationship (**Figure 7**). In this way, it seems that hydraulic sorting cannot be regarded as the only explanation for downstream fining of bedload gravel in the study area. Further analysis therefore pays attention to the variation in percentages of grain-size groups for different lithologies. Along the Taolai, Hongshuiba, and Fengle Rivers, the downstream reduction of percentages of grain-size groups >128 mm seems not to be seen in adjacent and smaller grain-size groups, in which the reverse occurs: percentages increase downstream (**Figure 8**). Based on this variation pattern, the bedload gravels transported by the three rivers can be divided into two parts, with grain sizes >128 mm and <128 mm, for which downstream fining can be attributed to hydraulic sorting and abrasion, respectively.

5.2 The Linkage Between Hydraulic Sorting and Hydrodynamic Force

In general, hydraulic sorting ability in rivers is dependent on "hiding effect" and hydrodynamic force (Robinson and Slingerland 1998). Under certain hydraulic conditions, coarse particles in fluvial bedload can be moved more readily by flowing water due to their greater exposure, whereas fine particles in contrast are generally hidden (Einstein 1950; Paola et al., 1992). This phenomenon, which has been defined by Diplas (1987) as "hiding effect", can reduce the difference in τ_c, leading to an

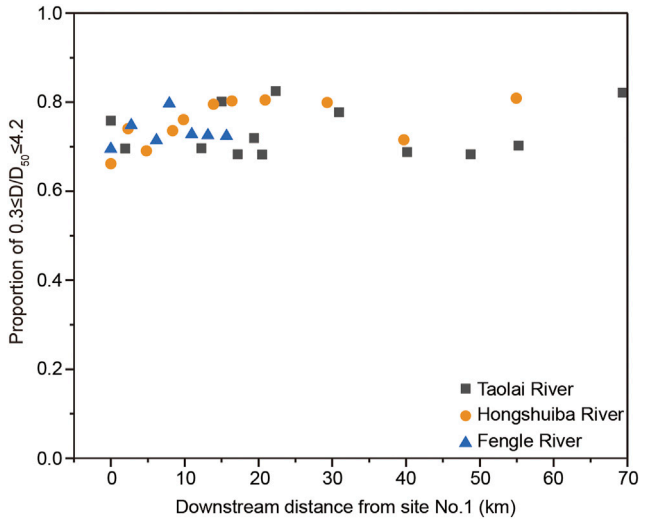

FIGURE 9 | Downstream variation in the ratio of those grain-size groups with D/D_{50} in the range between 0.3 and 4.2 to all the clasts collected at each site. Different symbols are used for the three study rivers. It can be clearly seen that this ratio is maintained in the narrow range 0.66–0.82 moving downstream.

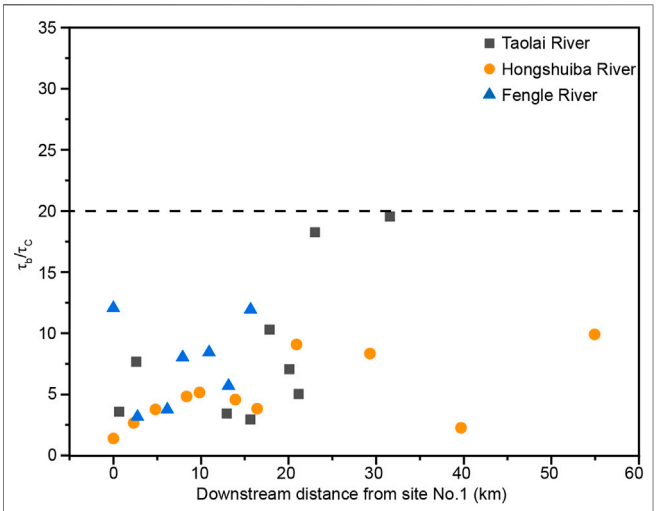

FIGURE 10 | Downstream variation in the ratio of τ_b to τ_c at each sampling site. All the ratios obtained are <20.

almost simultaneous movement for clasts of different grain-size (Parker et al., 1982). Further numerical simulation by Robinson and Slingerland (1998) has revealed how this effect inhibits progressive downstream hydraulic sorting. In order to evaluate this effect, Andrews (1983) has provided an empirical correlation, in which the mass ratio of D to D_{50} falls into a range between 0.3 and 4.2, implying that the correspondent grain-size group perhaps suffers from a closely similar critical shear stress. Following Andrews, we obtained, at each site, the ratio of the mass of those grain-size groups meeting this standard to the total clasts. Along the Taolai, Hongshuiba, and Fengle Rivers, these ratios show only a gentle fluctuation (**Figure 9**), indicating little impact on hydraulic sorting from this "hiding effect" (Robinson and Slingerland 1998).

Since the "hiding effect" has been excluded, hydraulic sorting in the study area can only be linked with hydrodynamic force. Numerical simulation has suggested that it will fluctuate within the variation range of τ_c, if the ratio of τ_b to τ_c is lower than 20, and favoring deposition of the coarse clasts with $\tau_{c>}\tau_b$ (Robinson and Slingerland 1998). Therefore, this ratio is employed here to evaluate the influence of hydrodynamic force on hydraulic sorting. The obtained results show that the ratios of τ_b to τ_c at every sampling site are <20 (**Figure 10**), implying an inadequate deviation between hydrodynamic force and the critical shear stress τ_c that would be required for the initial movement of fluvial clasts (Robinson and Slingerland 1998); thus sorting seems to be an important factor in causing downstream fining in the study area.

5.3 Influence of Tectonic Uplift on Grain-Size Distribution

During the past century, numerous works have focused on fluvial clasts to obtain some general variation patterns of downstream changes in their roundness and grain size, based on a series of flume experiments (Krumbein 1941b; Paola et al., 1992; Elgueta-Astaburuaga and Hassan 2019). Further numerical simulations have subsequently established some driving mechanisms for these patterns (Hoey and Ferguson 1994; Cui et al., 1996), in which downstream fining of bedload gravel has often been attributed to hydraulic sorting and abrasion (Parker 1991a; Paola et al., 1992, Hoey and Bluck 1999; Wilcock and Kenworthy 2002; Rice 2005). However, there is still no consensus on the factors that control their function in river systems. In this paper, hydraulic sorting has been linked with hydrodynamic force, leading to downstream fining of bedload gravels with grain size >128 mm. According to Schumm (1977), riverbed gradient and discharge have been regarded as potential controlling factors on hydrodynamic force. In recent studies, these are also confirmed to be able to drive variation in hydrodynamic force along riverbeds (Gilet et al., 2020). The Taolai, Hongshuiba, and Fengle Rivers originate from the Qilian Shan, and then debouch northward into the arid interior of North China (**Figure 1**). Owing to glacial meltwater supply, they seem to have had almost stable discharge over timescales of years (Yang 2008), which has been proved from hydraulic monitoring data (http://www.ncdc.ac.cn). The prominent hydraulic sorting as a mechanism for downstream fining of bedload gravels >128 mm in the three rivers can, therefore, probably only be correlated with riverbed gradient, rather than discharge.

In view of the excellent match between the 30-m-resolution DEM and the landscape across the northeastern margin of the Tibetan Plateau (Pan et al., 2015), it has been possible to extract the riverbed elevations of the Taolai, Hongshuiba, and Fengle from these data, in which high values show close correspondence to the occurrence of thrust faults (**Figure 11**). The smoothing method of the extracted longitudinal profiles refers to Schwanghart and Scherler 2017. At

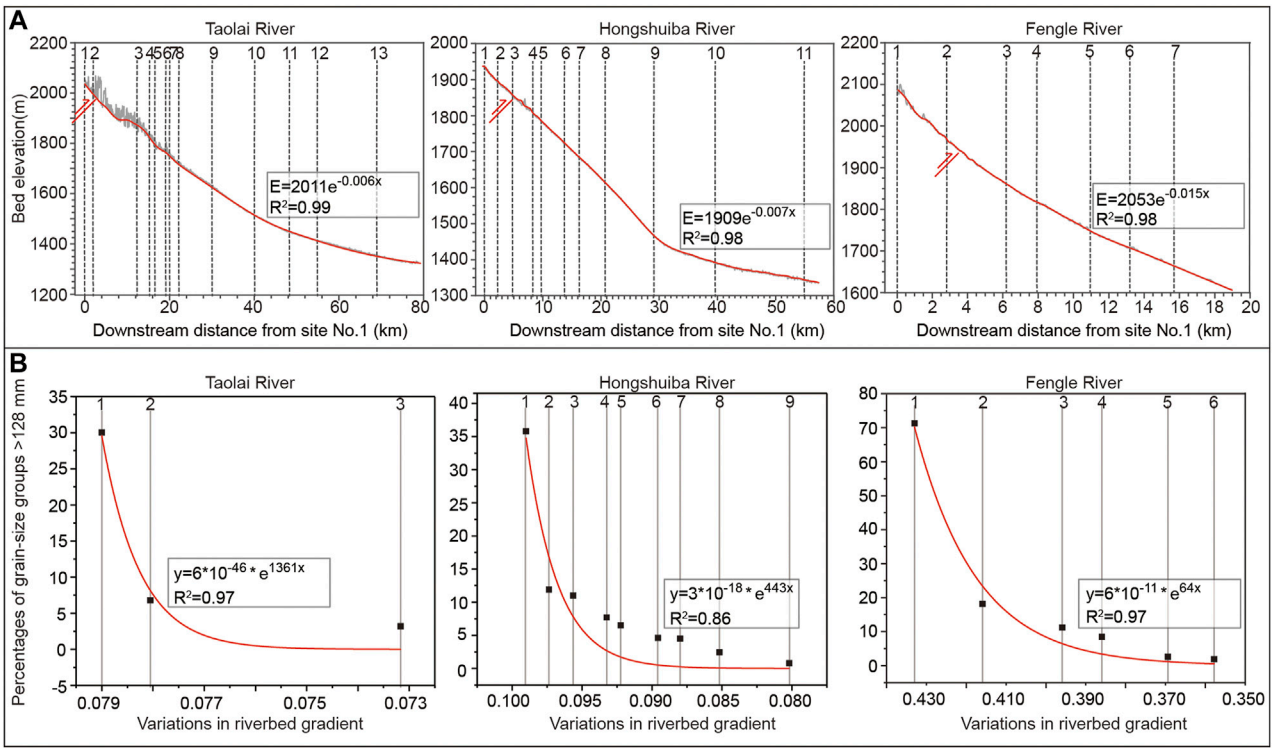

FIGURE 11 | Correlation analysis between the percentages of grain-size groups >128 mm and gradient variations along the Taolai, Hongshuiba, and Fengle Rivers. **(A)** Riverbed elevations along the three rivers. These are extracted from a 30-m-resolution DEM, in which high values correspond closely with thrust fault occurrences. At the sampling sites with some grain-size groups >128 mm, the second derivatives of the three curves were then calculated as a measurement for gradient variations. **(B)** Positive correlation between the obtained variations in riverbed gradient and the percentages of grain-size groups >128 mm. There seems to be an excellent exponential relationship along the three rivers.

sampling sites with bedload gravels >128 mm, the second derivatives of the obtained three curves were then calculated as a measurement for their gradient variations. Correlation analysis between the percentages of grain-size groups >128 mm and gradient variations at these sites shows a notable positive relationship (**Figure 11**). Since the ratios of τ_b to τ_c at every sampling site are all <20 (**Figure 10**), the adjustment in hydrodynamic force due to gradient variation along the three rivers can probably explain the deposition of coarse gravels >128 mm, creating a hydraulic sorting effect. For gravel beds, intrinsic fluvial behaviors can however provide timely adjustment to offset the variation in riverbed gradient by means of deposition and/or incision (Thayer et al., 2016). Thus, the persistence of perturbations in downstream gradient along the study rivers perhaps requires the continued influence of tectonic activity, such as fault movements. The three rivers excavating through the tectonically active northeastern margin of the Tibetan Plateau are transected by the Yumen-Beida River fault and Fodongmiao-Hongyazi fault (**Figure 1**). Previous work has constrained the vertical uplift rates along these reverse faults to be 0.7–1.2 mm/a, since the Late Pleistocene (Liu 2017; Yang et al., 2018; Hetzel et al., 2019), which is consistent with the present GPS data (Zhao et al., 2015; Hetzel et al., 2019). The persistent variation in riverbed gradient along the three rivers can probably be attributed to tectonic uplift generated by these faults (Yang et al., 2018; Hetzel et al., 2019; Wang et al., 2020). The link between grain-size distribution in riverbed gravels and tectonic uplift thus seems to be confirmed in the study area. In fact, grain-size distribution in riverbed gravel has also been employed as an indicator for tectonic activity in the Central Alps, northern frontal Himalayas, around Taiwan and the Mediterranean (Attal and Lavé 2006; Whittaker et al., 2010; Wang et al., 2015; Gilet et al., 2020). The percentages of grain-size groups >128 mm in the riverbed gravels along the three study-area rivers can thus be understood as an evaluator of the fluvial response to tectonic uplift.

6 CONCLUSION

The Taolai, Hongshuiba, and Fengle Rivers, as the three sub-catchments of the Beida River system, cut through the northeastern margin of the Tibetan Plateau. Despite a notable fluctuation in bedload lithologies, caused by clast input from neighboring uplands, the composition of their bedload gravels shows a stable downstream trend, implying transportational recycling of fluvial clasts through a region that is characterized by active tectonism and dry climate. Detailed investigation and analysis of grain-size distribution suggest that downstream fining of bedload gravel in these rivers follows the general rule, within

which the downstream fining of the gravels with grain size >128 mm has been attributed in these study-area rivers to hydraulic sorting. Moreover, the variation in riverbed gradient of the three rivers, explained as a driving force for hydraulic sorting, may be linked with active tectonism. The percentages of grain-size groups >128 mm in the riverbed clasts along the three rivers, therefore, can be understood as an evaluator of the fluvial response to tectonic uplift in the northeastern margin of the Tibetan Plateau.

DATA AVAILABILITY STATEMENT

The original contributions presented in the study are included in the article/Supplementary Material, further inquiries can be directed to the corresponding authors.

AUTHOR CONTRIBUTIONS

ZD completed the writing and editing to the article. ZH designed the research and improve this manuscript. ZH, DB, BP, and DC focused on the scientific issues involved in the article. ZD and QM finished the data collection in the field. ML, XL, YY, and DC performed the data analyses and then prepared the figures and tables. All authors contributed to the article and approved the submitted version.

FUNDING

This research is financially supported by the National Natural Science Foundation of China (Grant no. 41730637, 42041006, and 41871001) and 111 Program from State Administration of Foreign Experts Affairs and Ministry of Education of the People's Republic of China (Grant no. BP2018001).

ACKNOWLEDGMENTS

We really appreciate the driver Shiping Wei for helping us to collect data in the field. This paper has benefited from valuable suggestions and data analysis by Yanan Zhang, Weijin Guan and Jiakun Wu.

REFERENCES

Adams, J. (1980). Contemporary Uplift and Erosion of the Southern Alps, New Zealand: Summary. *Geol. Soc. America Bull.* 91 (1), 2–4. doi:10.1130/0016-7606(1980)91<2:cuaeot>2.0.co;2

Andrews, E. D. (1983). Entrainment of Gravel from Naturally Sorted Riverbed Material. *Geol. Soc. America Bull.* 94, 1225–1231. doi:10.1130/0016-7606(1983)94<1225:eogfns>2.0.co;2

Ashworth, P. J., and Ferguson, R. I. (1989). Size-selective Entrainment of Bed Load in Gravel Bed Streams. *Water Resour. Res.* 25, 627–634. doi:10.1029/WR025i004p00627

Attal, M., and Lavé, J. (2006). Changes of Bedload Characteristics along the Marsyandi River (central Nepal): Implications for Understanding Hillslope Sediment Supply, Sediment Load Evolution along Fluvial Networks, and Denudation in Active Orogenic Belts. *Geol. Soc. America Spec. Paper* 398, 143–171. doi:10.1130/2006.2398(09

Bradley, W. C. (1970). Effect of Weathering on Abrasion of Granitic Gravel, Colorado River (Texas). *Geol. Soc. America Bull.* 81, 61–80. doi:10.1130/0016-7606(1970)81[61:eowoao]2.0.co;2

Bradley, W. C., Fahnestock, R. K., and Rowekamp, E. T. (1972). Coarse Sediment Transport by Flood Flows on Knik River, Alaska. *Geol. Soc. America Bull.* 83, 1261–1284. doi:10.1130/0016-7606(1972)83[1261:cstbff]2.0.co;2

Bridgland, D. R. (2000). River Terrace Systems in north-west Europe: an Archive of Environmental Change, Uplift and Early Human Occupation. *Quat. Sci. Rev.* 19 (13), 1293–1303. doi:10.1016/S0277-3791(99)00095-5

Bridgland, D. R., and Westaway, R. (2014). Quaternary Fluvial Archives and Landscape Evolution: a Global Synthesis. *Proc. Geologists' Assoc.* 125 (5), 600–629. doi:10.1016/j.pgeola.2014.10.009

Bridgland, D. R., Westaway, R., Romieh, M. A., Candy, I., Daoud, M., Demir, T., et al. (2012). The River Orontes in Syria and Turkey: Downstream Variation of Fluvial Archives in Different Crustal Blocks. *Geomorphology* 165-166, 25–49. doi:10.1016/j.geomorph.2012.01.011

Cai, M., Fang, X., Wu, F., Miao, Y., and Appel, E. (2012). Pliocene-Pleistocene Stepwise Drying of Central Asia: Evidence from Paleomagnetism and Sporopollen Record of the Deep Borehole SG-3 in the Western Qaidam Basin, NE Tibetan Plateau. *Glob. Planet. Change* 94-95, 72–81. doi:10.1016/j.gloplacha.2012.07.002

Chen, D. B., Chen, J. J., Hu, X. F., Su, H., Chen, Y., and Zhang, J. (2018). Characteristics and Analysis on the Sediment Grain Size along the Liyuan River on the North Piedmont of the Qilian Shan and its Geological Significance. *Quat. Sci.* 38 (6), 1336–1347. doi:10.11928/j.issn.1001-7410.2018.06.02

Chen, L. P., Geng, H. P., Zhang, J., Zhao, Q. M., and Pan, B. T. (2019). Spatial Distribution of Bedrock Rebound Value (Schmidt Hammer) across the Heihe River basin and its Implication. *J. Glaciology Geocryology* 41 (2), 364–373. doi:10.7522/j.issn.1000-0240.2019.0302

Cui, Y., Paola, C., and Parker, G. (1996). Numerical Simulation of Aggradation and Downstream Fining. *J. Hydraulic Res.* 34 (2), 185–204. doi:10.1080/00221689609498496

Huddart, D. (1994). Rock-type Controls on Downstream Changes in Clast Parameters in Sandur Systems in Southeast Iceland. *Sepm Jsr* 64A (2a), 215–225. doi:10.1306/D4267D61-2B26-11D7-8648000102C1865D

Dawson, M. (1988). Sediment Size Variation in a Braided Reach of the Sunwapta River, Alberta, Canada. *Earth Surf. Process. Landforms* 13, 599–618. doi:10.1002/esp.3290130705

Diplas, P. (1987). Bedload Transport in Gravel-Bed Streams. *J. Hydraulic Eng.* 113 (11), 277–292. doi:10.1061/(asce)0733-9429(1987)113:3(277)

Dunne, K. B. J., and Jerolmack, D. J. (2018). Evidence of, and a Proposed Explanation for, Bimodal Transport States in Alluvial Rivers. *Earth Surf. Dynam.* 6 (3), 583–594. doi:10.5194/esurf-6-583-2018

Einstein, H. A. (1950). The Bed-Load Function for Sediment Transport in Open Channel flowsTechnical Bulletin. *U.S. Department Agric. Soil Conservation Serv.* 1026 (9), 1–89.

Elgueta-Astaburuaga, M. A., and Hassan, M. A. (2019). Sediment Storage, Partial Transport, and the Evolution of an Experimental Gravel Bed under Changing Sediment Supply Regimes. *Geomorphology* 330, 1–12. doi:10.1016/j.geomorph.2018.12.018

Ferguson, R., and Ashworth, P. (1991). Slope-induced Changes in Channel Character along a Gravel-Bed Stream: the Allt Dubhaig, Scotland. *Earth Surf. Process. Landforms* 16 (1), 65–82. doi:10.1002/esp.3290160108

Ferguson, R., Hoey, T., Wathen, S., and Werritty, A. (1996). Field Evidence for Rapid Downstream Fining of River Gravels through Selective Transport. *Geol* 24 (2), 179–182. doi:10.1130/0091-7613(1996)024<0179:fefrdf>2.3.co;2

Ferguson, R. I., Hoey, T. B., Wathen, S. J., Werrity, A., Hardwick, R. I., and Sambrook-Smith, G. H. (1998). "Downstream Fining of River Gravels: Integrated Field, Laboratory and Modeling Study," in *Gravel-Bed Rivers in the Environment*. Editors Klingeman, P. C., Beschta, R. L., Komar, P. D., and Bradley, J. B. (Highlands Ranch, CO: Water Resources Publications), 85–114.

Folk, R. L., and Ward, W. C. (1957). Brazos River Bar [Texas]; a Study in the Significance of Grain Size Parameters. *J. Sediment. Res.* 27 (1), 3–26. doi:10.1306/74D70646-2B21-11D7-8648000102C1865D

Gilet, L., Gob, F., Gautier, E., Houbrechts, G., Virmoux, C., and Thommeret, N. (2020). Hydro-morphometric Parameters Controlling Travel Distance of Pebbles and Cobbles in Three Gravel Bed Streams. *Geomorphology* 358, 107117. doi:10.1016/j.geomorph.2020.107117

Gomez, B., Rosser, B. J., Peacock, D. H., Hicks, D. M., and Palmer, J. A. (2001). Downstream Fining in a Rapidly Aggrading Gravel Bed River. *Water Resour. Res.* 37 (6), 1813–1823. doi:10.1029/2001WR900007

Hetzel, R., Hampel, A., Gebbeken, P., Xu, Q., and Gold, R. D. (2019). A Constant Slip Rate for the Western Qilian Shan Frontal Thrust during the Last 200 Ka Consistent with GPS-Derived and Geological Shortening Rates. *Earth Planet. Sci. Lett.* 509, 100–113. doi:10.1016/j.epsl.2018.12.032

Hoey, T. B., and Bluck, B. J. (1999). Identifying the Controls over Downstream Fining of River Gravels. *J. Sediment. Res.* 69 (1), 40–50. doi:10.2110/jsr.69.40

Hoey, T. B., and Ferguson, R. I. (1997). Controls of Strength and Rate of Downstream Fining above a River Base Level. *Water Resour. Res.* 33 (11), 2601–2608. doi:10.1029/97WR02324

Hoey, T. B., and Ferguson, R. (1994). Numerical Simulation of Downstream Fining by Selective Transport in Gravel Bed Rivers: Model Development and Illustration. *Water Resour. Res.* 30, 2251–2260. doi:10.1029/94WR00556

Hoover Mackin, J. (1948). Concept of the Graded River. *Geol. Soc. America Bull.* 59, 463–512. doi:10.1130/0016-7606(1948)59[463:cotgr]2.0.co;2

Humphrey, L. (1997). Weathering-controlled Abrasion in a Coarse-Grained, Meandering Reach of the rio grande: Implications for the Rock Record. *GSA Bull.* 109 (9), 1080–1088. doi:10.1130/0016-7606(1997)109<1080:WCAIAC>2.3.CO;2

Kirchner, J. W., Dietrich, W. E., Iseya, F., and Ikeda, H. (1990). The Variability of Critical Shear Stress, Friction Angle, and Grain Protrusion in Water-Worked Sediments. *Sedimentology* 37, 647–672. doi:10.1111/j.1365-3091.1990.tb00627.x

Kodama, Y. (1994). Experimental Study of Abrasion and its Role in Producing Downstream Fining in Gravel-Bed Rivers. *J. Sediment. Res.* 64 (1), 76–85. doi:10.2110/jsr.64.76

Krumbein, W. C. (1941b). The Effects of Abrasion on the Size, Shape and Roundness of Rock Fragments. *J. Geology.* 49 (5), 482–520. doi:10.1086/624985

Li, Y., Jin, Z. K., Jin, T., and Shi, L. (2014). Geological Significance of Magmatic Gravel Roundness. *Acta Sedimentologica Sinica* 32 (2), 189–197. doi:10.14027/j.cnki.cjxb.2014.02.004

Liu, X. W. (2017). "Characteristics of Active Tectonics and the Deformation Pattern of the Jiuxi Basin at the Western Qilian Shan," (Lanzhou: Lanzhou University). Doctoral dissertation.

Menting, F., Langston, A. L., and Temme, A. J. A. M. (2015). Downstream Fining, Selective Transport, and Hillslope Influence on Channel Bed Sediment in Mountain Streams, Colorado Front Range, USA. *Geomorphology* 239, 91–105. doi:10.1016/j.geomorph.2015.03.018

Meyer-Peter, E., and Muller, R. (1948). "Formulation for Bed Load Transport," in Proceedings of 2nd meeting of the International Association for Hydraulic Structures Research, Delft, June 7, 1948, 39–64.

Mikos, M. (1993). Fluvial abrasion of gravel sediments: ETH Zurich, Mitteilungen der Versuchsanstalt für Wasserbau. *Hydrologie und Glaziologie* 123, 321.

Molnar, P., and England, P. (1990). Late Cenozoic Uplift of Mountain Ranges and Global Climate Change: Chicken or Egg?. *Nature* 346, 29–34. doi:10.1038/346029a0

Molnar, P. (2003). Nature, Nurture and Landscape. *Nature* 426, 612–613. doi:10.1038/426612a

Mosley, M. P., and Tindale, D. S. (1985). Sediment Variability and Bed Material Sampling in Gravel-Bed Rivers. *Earth Surf. Process. Landforms* 10 (5), 465–482. doi:10.1002/esp.3290100506

Pan, B., Li, Q., Hu, X., Geng, H., and Gao, H. (2015). Bedrock Channels Response to Differential Rock Uplift in Eastern Qilian Mountain along the Northeastern Margin of the Tibetan Plateau. *J. Asian Earth Sci.* 100, 1–19. doi:10.1016/j.jseaes.2014.12.009

Paola, C., Parker, G., Seal, R., Sinha, S. K., Southard, J. B., and Wilcock, P. R. (1992). Downstream Fining by Selective Deposition in a Laboratory Flume. *Science* 258 (5089), 1757–1760. doi:10.1126/science.258.5089.1757

Parker, G., Klingeman, P. C., and McLean, D. G. (1982). Bedload and Size Distribution in Paved Gravel-Bed Streams. *J. Hydr. Div.* 108, 544–571. doi:10.1061/jyceaj.0005854

Parker, G. (1991a). Selective Sorting and Abrasion of River Gravel. I: Theory. *J. Hydraulic Eng.* 117, 131–147. doi:10.1061/(asce)0733-9429(1991)117:2(131)

Parker, G. (1991b). Selective Sorting and Abrasion of River Gravel. II: Applications. *J. Hydraulic Eng.* 117 (7), 150–171. doi:10.1061/(asce)0733-9429(1991)117:2(150)

Powers, M. C. (1953). A New Roundness Scale for Sedimentary Particles. *Sepm Jsr* 23, 117–119. doi:10.1306/D4269567-2B26-11D7-8648000102C1865D

Rengers, F., and Wohl, E. (2007). Trends of Grain Sizes on Gravel Bars in the Rio Chagres, Panama. *Geomorphology* 83 (3-4), 282–293. doi:10.1016/j.geomorph.2006.02.019

Rice, S., and Church, M. (1998). Grain Size along Two Gravel-Bed Rivers: Statistical Variation, Spatial Pattern and Sedimentary Links. *Earth Surf. Process. Landforms* 23, 345–363. doi:10.1002/(sici)1096-9837(199804)23:4<345:aid-esp850>3.0.co;2-b

Rice, S. P., and Church, M. (2001). Longitudinal Profiles in Simple Alluvial Systems. *Water Resour. Res.* 37, 417–426. doi:10.1029/2000WR900266

Rice, S. P., and Haschenburger, J. K. (2004). A Hybrid Method for Size Characterization of Coarse Subsurface Fluvial Sediments. *Earth Surf. Process. Landforms* 29, 373–389. doi:10.1002/esp.1043

Rice, S. (1999). The Nature and Controls on Downstream Fining within Sedimentary Links. *J. Sediment. Res.* 69 (1), 32–39. doi:10.2110/jsr.69.32

Rice, S. (1998). Which Tributaries Disrupt Downstream Fining along Gravel-Bed Rivers?. *Geomorphology* 22, 39–56. doi:10.1016/S0169-555X(97)00052-4

Robinson, R. A. J., and Slingerland, R. L. (1998). Origin of Fluvial Grain-Size Trends in a Foreland basin; the Pocono Formation on the central Appalachian Basin. *J. Sediment. Res.* 68 (3), 473–486. doi:10.2110/jsr.68.473

Schumm, S. A. (1977). Arroyos and Environmental Change in the American Southwest. *Earth Sci. Rev.* 13 (2), 211–212. doi:10.1016/0012-8252(77)90042-3

Schwanghart, W., and Scherler, D. (2017). Bumps in River Profiles: Uncertainty Assessment and Smoothing Using Quantile Regression Techniques. *Earth Surf. Dynam.* 5 (4), 821–839. doi:10.5194/esurf-5-821-2017

Shaw, J., and Kellerhals, R. (1982). The Composition of Recent Alluvial Gravels in Alberta Riverbeds. *Alberta Res. Counc. Bull.* 41, 151.

Sklar, L. S., Dietrich, W. E., Foufoula-Georgiou, E., Lashermes, B., and Bellugi, D. (2006). Do gravel Bed River Size Distributions Record Channel Network Structure?. *Water Resour. Res.* 42 (6). doi:10.1029/2006WR005035

Song, C. H. (2006). "Tectonic Uplift and Cenozoic Sedimentary Evolution in the Northern Margin of the Tibetan Plateau," (Lanzhou, Gansu Province, the People's Republic of China: College of Earth and Environment Sciences, Lanzhou University). [dissertation].

Sternberg, H. (1875). Untersuchungen über längen-und querprofil geschiebeführender flüss. *Z. für Bauwesen.* 25, 483–550.

Stock, J. D., Schmidt, K. M., and Miller, D. M. (2008). Controls on Alluvial Fan Long-Profiles. *Geol. Soc. America Bull.* 120 (5-6), 619–640. doi:10.1130/B26208.1

Thayer, J. B., Phillips, R. T. J., and Desloges, J. R. (2016). Downstream Channel Adjustment in a Low-Relief, Glacially Conditioned Watershed. *Geomorphology* 262, 101–111. doi:10.1016/j.geomorph.2016.03.019

Wang, J. F. (2019). Analysis on Runoff Variation in the Beida River Basin under the Influence of Climate Change and Human Activities. *J. Arid Land Resour. Environ.* 33 (3), 86–91. doi:10.13448/j.cnki.jalre.2019.079

Wang, J., Li, A., Xu, K., Zheng, X., and Huang, J. (2015). Clay mineral and Grain Size Studies of Sediment Provenances and Paleoenvironment Evolution in the Middle Okinawa Trough since 17ka. *Mar. Geology.* 366, 49–61. doi:10.1016/j.margeo.2015.04.007

Wang, Y., Oskin, M. E., Zhang, H., Li, Y., Hu, X., and Lei, J. (2020). Deducing Crustal-Scale Reverse-Fault Geometry and Slip Distribution from Folded River Terraces, Qilian Shan, China. *Tectonics* 39 (1), 1–18. doi:10.1029/2019TC005901

W. C. Krumbein, W. C. (1941a). Measurement and Geological Significance of Shape and Roundness of Sedimentary Particles. *Sepm Jsr* 11, 64–72. doi:10.1306/D42690F3-2B26-11D7-8648000102C1865D

W. C. Krumbein, W. C. (1934). Size Frequency Distributions of Sediments. *Sepm Jsr* 4 (2), 65–77. doi:10.1306/D4268EB9-2B26-11D7-8648000102C1865D

Werritty, A., and Florence, S. (1990). *Downstream Fining in a Gravel-Bed River in S. Poland: Lithologic Controls and the Role of Abrasion*. St. Andrews, Fife, Scotland, U.K: Department of Geography and Geology, University of St. Andrews.

Westaway, R. (2009). Active Crustal Deformation beyond the SE Margin of the Tibetan Plateau: Constraints from the Evolution of Fluvial Systems. *Glob. Planet. Change* 68 (4), 395–417. doi:10.1016/j.gloplacha.2009.03.008

Whittaker, A. C., Attal, M. l., and Allen, P. A. (2009). Characterising the Origin, Nature and Fate of Sediment Exported from Catchments Perturbed by Active Tectonics. *Basin Res.* 22 (6), 809–828. doi:10.1111/j.1365-2117.2009.00447.x

Wiberg, P. L., and Smith, J. D. (1987). Calculations of the Critical Shear Stress for Motion of Uniform and Heterogeneous Sediments. *Water Resour. Res.* 23, 1471–1480. doi:10.1029/WR023i008p01471

Wilcock, P. R., and Kenworthy, S. T. (2002). A Two-Fraction Model for the Transport of Sand/gravel Mixtures. *Water Resour. Res.* 38 (10), 12–21. doi:10.1029/2001WR000684

Wilcock, P. R., and Southard, J. B. (1989). Bed Load Transport of Mixed Size Sediment: Fractional Transport Rates, Bed Forms, and the Development of a Coarse Bed Surface Layer. *Water Resour. Res.* 25, 1629–1641. doi:10.1029/WR025i007p01629

Wu, F., Fang, X., Ma, Y., Herrmann, M., Mosbrugger, V., An, Z., et al. (2007). Plio-Quaternary Stepwise Drying of Asia: Evidence from a 3-Ma Pollen Record from the Chinese Loess Plateau. *Earth Planet. Sci. Lett.* 257 (1–2), 160–169. doi:10.1016/j.epsl.2007.02.029

Yang, H., Yang, X., Huang, X., Li, A., Huang, W., and Zhang, L. (2018). New Constraints on Slip Rates of the Fodongmiao-Hongyazi Fault in the Northern Qilian Shan, NE Tibet, from the 10Be Exposure Dating of Offset Terraces. *J. Asian Earth Sci.* 151, 131–147. doi:10.1016/j.jseaes.2017.10.034

Yang, S. X. (2008). "Water Resources Research on the Phase I of the Jia-Jiu Coal Electricity's Base in Gansu Province, China," (Shaanxi: Northwest Agriculture and Forestry University). [master's thesis].

Yizhou, W., Huiping, Z., Dewen, Z., Wenjun, Z., Zhuqi, Z., Weitao, W., et al. (2014). Controls on Decadal Erosion Rates in Qilian Shan: Re-evaluation and New Insights into Landscape Evolution in north-east Tibet. *Geomorphology* 223, 117–128. doi:10.1016/j.geomorph.2014.07.002

Zhang, J., Geng, H., Pan, B., Hu, X., Chen, L., Wang, W., et al. (2020). Climatic Zonation Complicated the Lithology Controls on the Mineralogy and Geochemistry of Fluvial Sediments in the Heihe River basin, NE Tibetan Plateau. *Quat. Int.* 537, 33–47. doi:10.1016/j.quaint.2020.01.016

Zhao, B., Huang, Y., Zhang, C., Wang, W., Tan, K., and Du, R. (2015). Crustal Deformation on the Chinese mainland during 1998-2014 Based on GPS Data. *Geodesy and Geodynamics* 6 (1), 7–15. doi:10.1016/j.geog.2014.12.006

Zhao, Z., Fang, X., and Li, J. (2001). Late Cenozoic Magnetic Polarity Stratigraphy in the Jiudong Basin, Northern Qilian Mountain. *Sci. China Ser. D-earth Sci.* 44 (1), 243–250. doi:10.1007/bf02911993

Zheng, W. J. (2009). "Geometric Pattern and Active Tectonies of the Hexi Corridor and its Adjacent Regions," (China: Institute of Geology). [dissertation].

Conflict of Interest: The authors declare that the research was conducted in the absence of any commercial or financial relationships that could be construed as a potential conflict of interest.

Publisher's Note: All claims expressed in this article are solely those of the authors and do not necessarily represent those of their affiliated organizations, or those of the publisher, the editors and the reviewers. Any product that may be evaluated in this article, or claim that may be made by its manufacturer, is not guaranteed or endorsed by the publisher.

Copyright © 2022 Dong, Pan, Hu, Mo, Bridgland, Li, Li, Yang and Chen. This is an open-access article distributed under the terms of the Creative Commons Attribution License (CC BY). The use, distribution or reproduction in other forums is permitted, provided the original author(s) and the copyright owner(s) are credited and that the original publication in this journal is cited, in accordance with accepted academic practice. No use, distribution or reproduction is permitted which does not comply with these terms.

frontiers in Earth Science

ORIGINAL RESEARCH
published: 10 March 2022
doi: 10.3389/feart.2022.849181

Miocene Provenance Changes in Taiwan Caused by Southward Input of Sediments From East China Sea Basin

Xiaowei Fu, Lichen Hu, Weilin Zhu, Xiangtong Huang, Kailong Feng and Zengyuan Zhou*

State Key Laboratory of Marine Geology, Tongji University, Shanghai, China

The Cenozoic sediments in marginal basins of East Asia ultimately reflected coupling between the tectonics, landscape evolution, and drainage reorganization. Recently, the provenance of Miocene sediments in the East China Sea Basin (ECSB) and Taiwan has been in hot debate, and several models were proposed to interpret the provenance changes. Most of them are related to river reorganization in East Asia and highly relied on detrital zircon U-Pb dating. In this study, a large number of detrital zircon U-Pb ages of Miocene sediments from the ECSB, Taiwan region, and the potential source areas have been compiled for quantitative provenance analysis. The results suggested that all the early–middle Miocene sediments in Taiwan and the ECSB were closely linked to North China and the Korean Peninsula. Over 80% sediments in Taiwan were delivered from the ECSB whose sediments were predominantly contributed by North China and the Korean Peninsula (70%). However, for the late Miocene to Quaternary sediments in the ECSB, the contribution of the Yangtze River system was 72%, which indicates distinct reorganization of river networks and initial formation of the Yangtze River in the late Miocene. The quantitative provenance analysis together with southward environmental changes from dominantly fluvial sediments in the northern and middle ECSB to shallow marine sediments in Taiwan region suggested that the early–middle Miocene sediments of Taiwan were mainly sourced from the North China and the Korean Peninsula by passing the ECSB. Thus, these sediments in Taiwan region would experience the river–delta–shallow marine route from the ECSB to Taiwan region.

Keywords: Taiwan region, East China Sea Basin, detrital zircon age, Yangtze River (Changjiang River), Miocene provenance changes

OPEN ACCESS

Edited by:
Xuhua Shi,
Zhejiang University, China

Reviewed by:
Rong Yang,
Zhejiang University, China
Xinong Xie,
China University of Geosciences Wuhan, China

****Correspondence:***
Weilin Zhu
zhuwl@tongji.edu.cn

Specialty section:
This article was submitted to Structural Geology and Tectonics, a section of the journal Frontiers in Earth Science

Received: *05 January 2022*
Accepted: *04 February 2022*
Published: *10 March 2022*

Citation:
Fu X, Hu L, Zhu W, Huang X, Feng K and Zhou Z (2022) Miocene Provenance Changes in Taiwan Caused by Southward Input of Sediments From East China Sea Basin. Front. Earth Sci. 10:849181. doi: 10.3389/feart.2022.849181

INTRODUCTION

The Cenozoic East Asia has experienced great tectonic movement, especially the uplift of Tibetan Plateau by India–Asia collision and the subsidence of East Asia margin associated with evolving of numerous rift basins, followed by contrasting topography and climatic changes and reorganization of continental river networks (Wang, 2004; Zheng, 2015) (**Figure 1**). The sedimentary record in marginal basins was believed to ultimately reflect the coupling between these deep earth and surface processes (Clift, 2006; Richardson et al., 2010).

As one of the ultimate destination of sediments derived from the Tibetan Plateau, the East China margin might preserve crucial evidence associated with the links between Tibetan Plateau and the sea. Recently, the provenance of Miocene sediments of the East China Sea Basin (ECSB) and Taiwan has attracted great interest and been in hot debate. A sharp provenance change was recognized at the

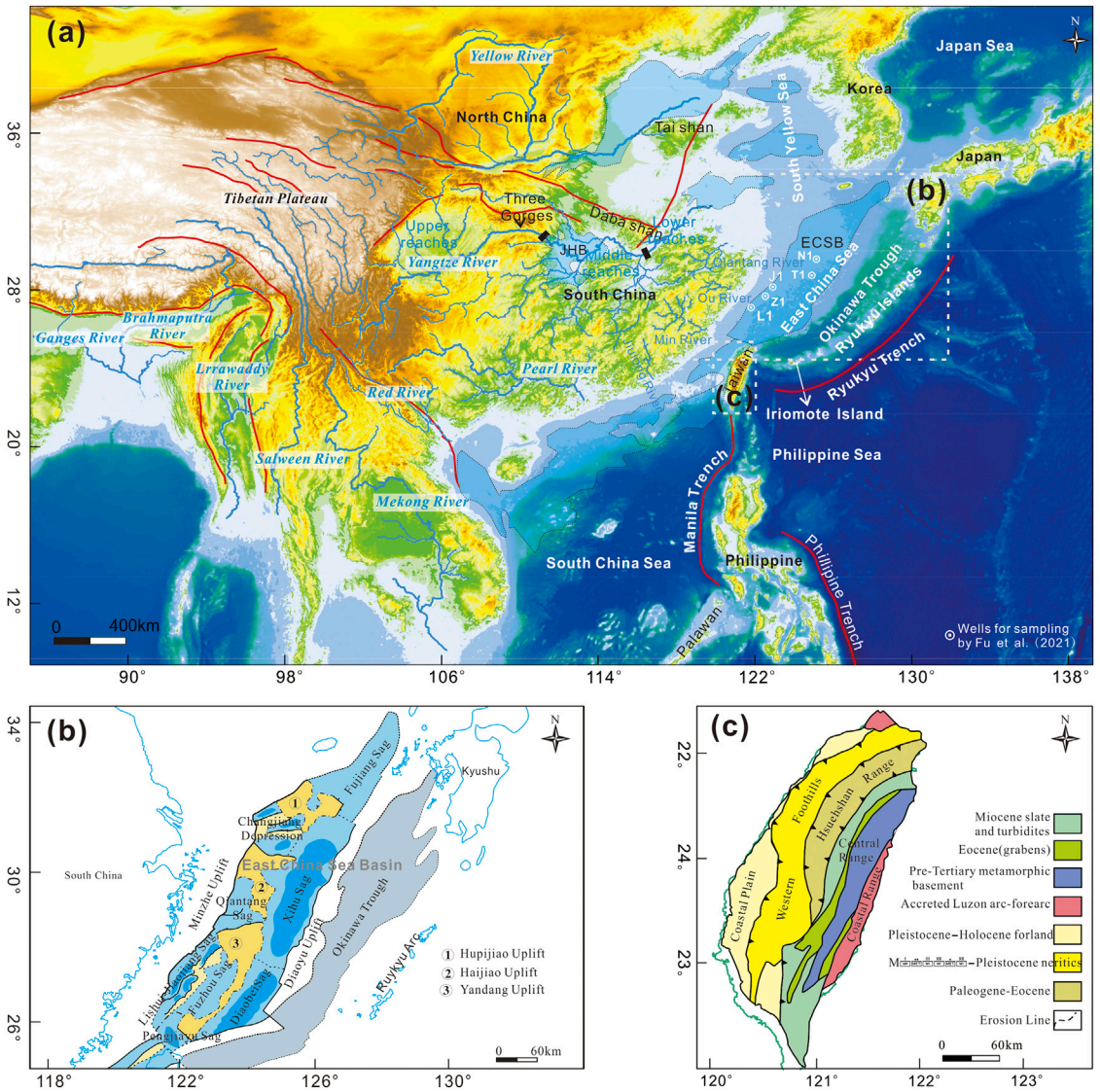

FIGURE 1 | (A) Topographic map of East Asia showing major basins and rivers. **(B)** Tectonic sketch of the East China Sea Basin (modified from Zhu et al., 2019). **(C)** Tectonic framework of Taiwan (modified from Huang et al., 2012). The basins are modified from Ren et al. (2002). ECSB, East China Sea Basin; JHB, Jianghan Basin.

beginning of the Miocene in the Taiwan region that the provenance of western foothills of Taiwan changed from the adjacent South China to new source areas characterized by an obvious increase in old zircon ages (Lan et al., 2014; Deng et al., 2017; Zhang et al., 2017; Chen et al., 2019). Lan et al. (2016) claimed that an enlarged paleo-Min River that extended to the Yangtze Block contributed to this change. Zhang et al. (2017) proposed that this provenance change was caused by the establishment of the Yangtze River, and Deng et al. (2017) suggested the North China Craton (NCC) also supplied detritus. In contrast to these large-scale drainage reorganization models, most recently, Chen et al. (2019) suggested that an unknown macroblock that collided with the Asian margin and now covered by thick sediments resulted in this change. Wang et al. (2018) noticed the similarities between Miocene sediments in western Taiwan and Oligocene sediments in Xihu Sag, one of the subordinate subsiding centers in the ECSB, and suggested that erosion and reworking of these Oligocene sediments were responsible for the Miocene provenance changes in western Taiwan.

Although some authors agreed with the view that Miocene sediments in Taiwan were closely linked with the contemporaneous sediments of the ECSB, the routes for sediment derived from the ECSB to paleo-Taiwan region are also under debate. Deng et al. (2017) suggested that longshore current played an important role in sediment transport from shallow marine environments of the east of the present Yangtze Delta to the Taiwan region. Xu et al. (2007) argued that the transport ability of a longshore current is limited. Zhang et al. (2017) and Zhang et al. (2021a) preferred river transport along the ECSB.

Although several different methods have been applied to trace the Miocene provenance change in Taiwan region (Lan et al., 2014; Lan et al., 2016; Chen et al., 2019), the most powerful and widely used one is the detrital zircon U-Pb dating that clearly shows obvious increase in the proportion of zircon grains with ages peaking at 220, 1800, and 2,500 Ma (Lan et al., 2016; Zhang et al., 2017). Advances in quantitative and statistical provenance analysis of detrital zircon U-Pb dating (Vermeesch et al., 2016; Sundell and Saylor, 2017), especially inverse Monte Carlo modeling, can be used to calculate mixing proportions of every source area (Sundell and Saylor, 2017). These quantitative methods together with rapid increase in detrital zircon U-Pb dating of potential areas and Cenozoic sediments in the ECSB and Taiwan region make it possible to re-examine the Miocene provenance change that occurred in Taiwan region.

In this study, we have compiled a large number of literature detrital zircon ages from Cenozoic sedimentary rocks of Taiwan region, the ECSB, and the potential areas including the adjacent rivers in South China and far inland areas of Yangtze block, North China, and Korean Peninsula to determine the proportions of different sources that fed the Miocene sediments in Taiwan region and the ECSB by inverse Monte Carlo modeling. Considering tectonics and changes of sedimentary environment in east China margin, we provide a more comprehensive understanding on drainage reorganization from the sediments in marginal basins and further constraints on sediments transported along the marginal basins.

Geological Background

The Taiwan island is located in the south of the East China Sea and is subducting by South China Sea plate and Luzon arc (Huang et al., 2012). The arc–continent collision between the Luzon arc and Eurasia since 6.5 Ma resulted in the basic tectonic pattern of Taiwan region (Huang, 2017). Consequently, narrow N-S tectonic belts and the high mountain ranges were formed (Chen et al., 2019). The Taiwan island can be divided into five zones: coastal plain, western foothills, the Hsuehshan Range, the Central Range, and the Coastal Range (**Figure 1C**). The coastal plain, western foothills, and Hsuehshan Range are located in the fold-thrust belt resulted from the deformed and uplifted passive continental margin sediments (Huang et al., 2012). The Central Range and Coastal Range are composed of accretionary prism and forearc basin–volcanic island arc, respectively. Before this collision, Taiwan region received Paleogene sediments of the rift basin and Oligocene to Miocene sediments in the passive margin setting after the opening of South China Sea (Lin et al., 2003).

The ECSB is located in the east of the present Yangtze Estuary (**Figure 1**). This basin is the largest Cenozoic rift basin in the east Asia margin and deposited relatively complete Cenozoic sediments and thus was believed to be one of the crucial places to trace reorganization of river networks in East Asia (Richardson et al., 2010; Fu et al., 2021). The ECSB roughly consists of two subsequently rifted zones (**Figure 1B**), the west zone mainly rifted from the late Mesozoic to the Paleocene and the east zone rifted during Eocene to Oligocene (Zhu et al., 2019). Both of them are composed of several sub-basins that are controlled by boundary faults. Since the Miocene, the uplifts in the ECSB were covered by sedimentary strata due to post-rift subsidence, and the ECSB became a broad continental shelf (Lee et al., 2006).

The rift and its associated sediments of the southern ECSB connected with basins around the Taiwan region (**Figure 1**), and the evolution of these basins have been profoundly affected by the opening of the South China Sea (Huang et al., 2012; Zhu et al., 2019).

Samples and Methods

We compiled most of the detrital zircon U-Pb ages reported by Lan et al. (2016), which covered Eocene to middle Miocene sedimentary rocks of western foothills in Taiwan. Two sand samples from the Zhuoshui River, two samples from the beach sand in northwestern and southwestern Taiwan Island, respectively (**Table 1**). In the ECSB, thirteen detrital zircon samples with a total of 1,161 grain ages from the Miocene to Quaternary sediments were compiled from Fu et al. (2021).

Previous studies suggested that the adjacent South China, Yangtze Block, North China Block, and Korean Peninsula could be the potential areas for the Miocene sediments in Taiwan region and the ECSB (Deng et al., 2017; Fu et al., 2021; Zhang J. et al., 2021). We used the fluvial samples that were collected from the rivers covering most part of these potential areas (**Table 1**; **Figure 2**) to represent the provenance features of the source areas, rather than the bedrock U-Pb ages, as the previous studies did (e.g., Deng et al., 2017; Fu et al., 2021). The fluvial samples are concise to represent general distribution of U-Pb ages of source areas and efficiently used to provenance analysis in East Asia (Cao et al., 2018; He et al., 2020; Zheng et al., 2020). Despite that, hydraulic sorting, mechanical abrasion, and weathering might bias the detrital zircon ages of source regions (Malusà et al., 2013). For geological time, it is hard to determine the erosion patterns of the paleo rivers, which also have a great influence on the age distributions yielded by source rocks (Wissink and Hoke, 2016).

The qualitative and quantitative statistical provenance analyses were both applied to compare the large detrital data set (**Table 1**). The R package (Vermeesch et al., 2016) and DZmix (Sundell and Saylor, 2017) were utilized for qualitative and quantitative analyses, respectively. Kernel density estimates (KDE) showed the probability distributions of samples (Vermeesch, 2013). Multidimensional scaling (MDS), which was applied to detrital zircon U-Pb age data sets to measure dissimilarities between samples, was used to highlight differences (Vermeesch, 2013; Vermeesch et al., 2016) and identify source areas which appear to be the most similar to Miocene sedimentary rocks in Taiwan and the ECSB. The DZmix can calculate the contributions of different source areas by Monte Carlo mixture modeling (Sundell and Saylor, 2017) and further assist to determine if the sediments in the ECSB and Taiwan were fed by the same sources.

RESULTS

The kernel density estimates (KDE) using a 20 Ma bandwidth show that a sharp provenance change occurred in Miocene in

TABLE 1 | Compilation of detrital zircon ages for provenance analysis.

Sample location	Region	No. of ages (n)	Samples	Depositional age	References
Potential areas					
YR Mainstream LD	—	567	Fluvial sands	Present	He et al. (2014)
YR Mainstream LD		426	Fluvial sands	Present	Yang et al. (2012)
YR Mainstream LD		155	Fluvial sands	Present	Iizuka et al. (2010)
YR branches in midstream		548	Fluvial sands	Present	He et al. (2014)
Yongding River	North China Craton	86	Fluvial sands	Present	Yang et al. (2009)
Luan River		108	Fluvial sands	Present	Yang et al. (2009)
Yellow River		729	Fluvial sands	Present	Nie et al. (2016); Yang et al. (2009)
Chongchon River	North Korea	66	Fluvial sands	Present	Wu et al. (2007)
Taedong River		54	Fluvial sands	Present	Wu et al. (2007)
Hantan River	South Korea	83	Fluvial sands	Present	Choi et al. (2016)
Han River		82	Fluvial sands	Present	Choi et al. (2016)
Geum River		60	Fluvial sands	Present	Choi et al. (2016)
Seomjin River		80	Fluvial sands	Present	Choi et al. (2016)
Nam River		80	Fluvial sands	Present	Choi et al. (2016)
Nakdong River		71	Fluvial sands	Present	Choi et al. (2016)
Qiantang River	Cathaysia	322	Fluvial sands	Present	Zhang et al. (2015)
Ou River		126	Fluvial sands	Present	Xu et al. (2007)
Min River		395	Fluvial sands	Present	Xu et al. (2016); Zhang et al. (2017)
Jiulong River		205	Fluvial sands	Present	
Marginal basins					
Western foothills	Taiwan	1,034	Outcrop	Eocene–Miocene	Lan et al. (2016)
Boreholes of offshore basins	East China Sea Basin	1,161	Cuttings	Miocene–Quaternary	Fu et al. (2021)
Fluvial sediments	Taiwan and Penghu Island	426	Fluvial sands	present	Deng et al. (2017), Chen et al. (2019)

Taiwan region characterized by obvious increase in zircon age populations with peaks at ~220 Ma, ~800 Ma, ~1800 Ma, and ~2,500 Ma (**Figure 2**). This change in the age distribution after Oligocene was first reported by Lan et al. (2016). The similar age distribution also can be observed from the early–middle Miocene sedimentary rocks in the ECSB and present sediments from Coast Plain in Taiwan Island (**Figure 2**).

The MDS plot with a stress value of 0.056 suggests good quality of the fit (**Figure 3**). In the MDS plot (**Figure 3**), three clusters are clearly exhibited. The early–middle Miocene samples from Taiwan, the synchronous deposits in the ECSB, and present sands from Taiwan fall in the same cluster with Korea and North China affinity. The late Miocene–Quaternary samples from the ECSB links best with mainstream of the middle–lower Yangtze River, which is consistent with the view that the present-day Yangtze River initially was formed in the late Miocene (Fu et al., 2021). The Eocene samples from Taiwan are closely linked to the Min River, while the Oligocene samples links with the Qiantang River and the Late Miocene–Quaternary of the ECSB, despite of obviously different age distribution in KDE plots (**Figure 2**).

Three contradictory views that enlarged Min River (Lan et al., 2016), concealed microcontinent (Chen et al., 2019), and far inland sources by passing the ECSB (Deng et al., 2017; Zhang et al., 2017; Zhang J. et al., 2021) have been suggested to interpret the provenance change in Miocene. The age features of enlarged Min River and concealed microcontinent cannot be conclusively drawn though associated hypotheses were proposed. If the Miocene provenance change resulted from the sediments that were delivered by passing the ECSB, the contemporaneous deposits in the ECSB and the adjacent rivers in South China would represent the potential sources. According to this, Monte Carlo mixture modeling was constructed by DZmix using the cross-correlation coefficient for finite mixture distributions of probability density plots (Sundell and Saylor, 2017). The mixing model shows source contributions of 88% for the ECSB and 10% for the Min River (**Figure 4A**). Both contributions of the Jiulong River and Ou River are 1%, suggesting very limited contribution. For the present sediments in the coastal plain of Taiwan, which were believed to be mainly derived from the Miocene sedimentary rocks (Deng et al., 2017), and the mixing model with a mean cross-correlation coefficient of 0.89 and very low standard deviation demonstrates reliable evaluation (**Figure 4B**). Similarly, source contributions of 81% are from the ECSB, 8% from the Min River, 3% from the Jiulong River, and 7% from the Ou River. All these indicate that the early–middle Miocene sediments in Taiwan mainly were supplied by detrital materials from the ECSB and mixed with a small amount of sediments from the Min River, Jiulong River, and Ou River, and did not require an enlarged Min River or the microcontinent.

To determine if the early–middle Miocene sediments in Taiwan region were associated with the Yangtze River, samples were taken from middle–lower mainstream of the Yangtze River, branches of the middle Yangtze River, North China, Korea, and other local rivers near Taiwan region to represent the features of the potential source (**Figure 5A**). Since ~90% of sediments in mainstream of present middle and lower reaches of the Yangtze River were eroded from the eastern margin of the Tibetan Plateau (Wissink and Hoke, 2016), we compiled samples from the mainstream and branches to represent the Yangtze River and local contributions from

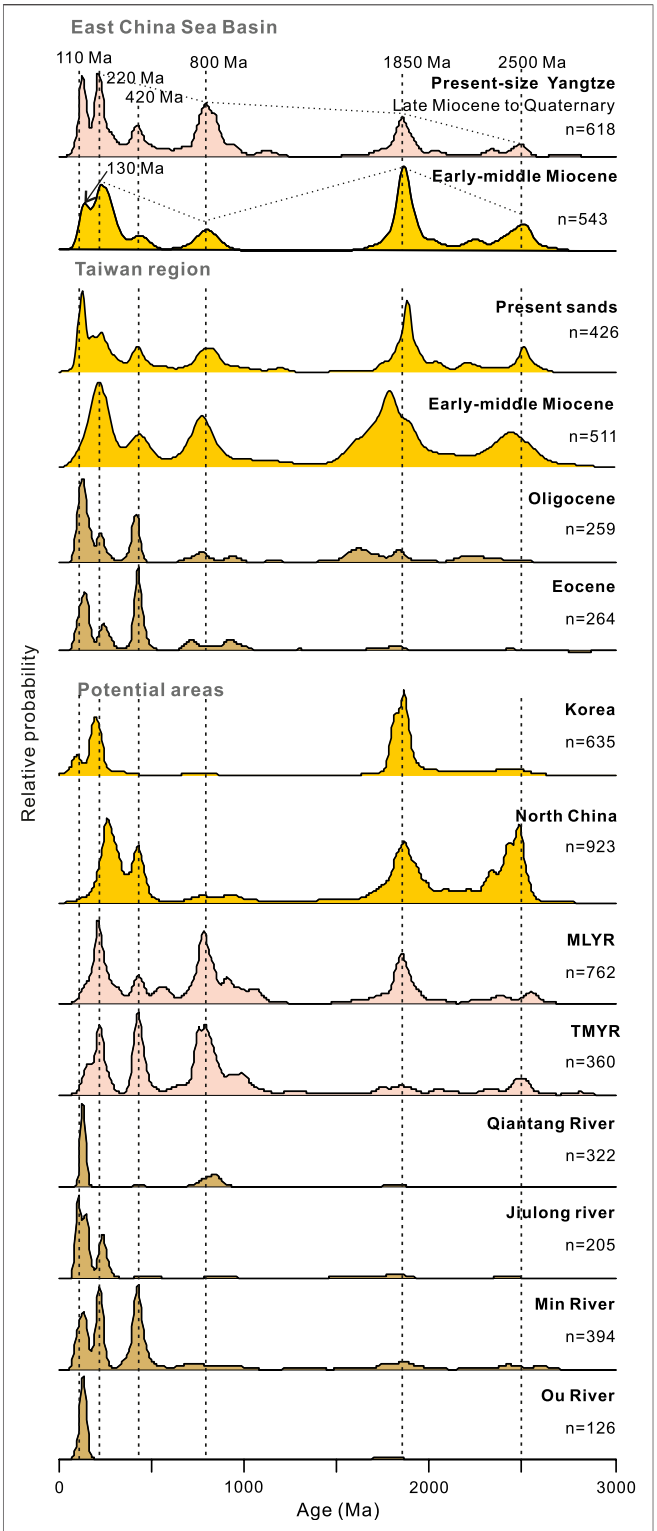

FIGURE 2 | Spectra of detrital zircon ages from the ECSB, Taiwan, and potential areas. The provenance package in R (Vermeesch et al., 2016) was used to make the KDE plots (bin = 20). See **Table 1** for source of literature data. MLYR, middle and lower reaches of the Yangtze River trunk stream; TMYR, tributaries in the middle reaches of the Yangtze River.

middle reaches of the Yangtze River, respectively, to distinguish the contribution of the middle Yangtze River system before the establishment of the present-size Yangtze River. Monte Carlo mixing models of early–middle Miocene sedimentary rocks in Taiwan suggest that the source contributions of 33% were from the Yangtze River and 28% from North China (**Figure 5A**). Korea and branches of the lower Yangtze River contributed roughly the same sediments (14%). In contrary, present sediments in Taiwan were mainly contributed by North China (22%) and Korea (25%), minor by the Yangtze River (16%), and branches of the middle Yangtze River (12%) (**Figure 5B**).

For the early–middle Miocene sediments in the ECSB, they were predominantly derived from the North China (40%) and Korea (30%) and the contributions of the Yangtze River system were limited: mainstream (15%) and branches in middle reaches (7%) (**Figure 5C**). However, for the late Miocene–Quaternary sediments in the ECSB, the Yangtze River contributed the most sediments that the contributions of mainstream were 52% and the branches in middle reaches were 20%, while Korea and North China only contributed a total of 13% sediments (**Figure 5D**). The cross-correlation coefficient (R^2) of modeling for the ECSB sediments was over 0.9, indicating a high level of confidence.

DISCUSSION

Implications for the Evolving of the Yangtze River

Previous studies suggested that the Miocene provenance changes are closely linked with the Yangtze River system (Zhang et al., 2017; Zhang J. et al., 2021). However, most recent studies suggested that the Yangtze River might not have been established until the late Miocene (12 Ma -10 Ma) (Fu et al., 2021; Sun et al., 2021; Zhang Z. et al., 2021). The ECSB would be one of the most possible places to preserve the crucial evidence for evolution of the Yangtze River (Richardson et al., 2010; Fu et al., 2021). Our MDS plot (**Figure 3**) clearly shows that the late Miocene–Quaternary sediments in the ECSB were closely linked with the present Yangtze River systems, but the early–middle Miocene sediments in the ECSB and Taiwan region fall into the same cluster with North China and Korea, which was consistent with the most recent view that the Yangtze River was initially formed in the late Miocene (Zhang Z. et al., 2021; Fu et al., 2021; Guo et al., 2021). The modeling also suggested the change in provenance from 70% sediments derived from North China and Korea in the early–middle Miocene to 72% sediments sourced from the Yangtze River system since the late Miocene. Contrasting to our results, Zhang et al. (2021) proposed that about 50% sediments fed by the Yangtze River system in the early Miocene for ECSB sediments. As we have compiled much larger data (**Table 1**; **Figure 5**) and obtained mixing models with higher mean cross-correlation coefficient of 0.92 for the early–middle Miocene samples and 0.94 for late Miocene–Quaternary samples than those (0.843) models (**Figure 5**), our results are more reliable. The

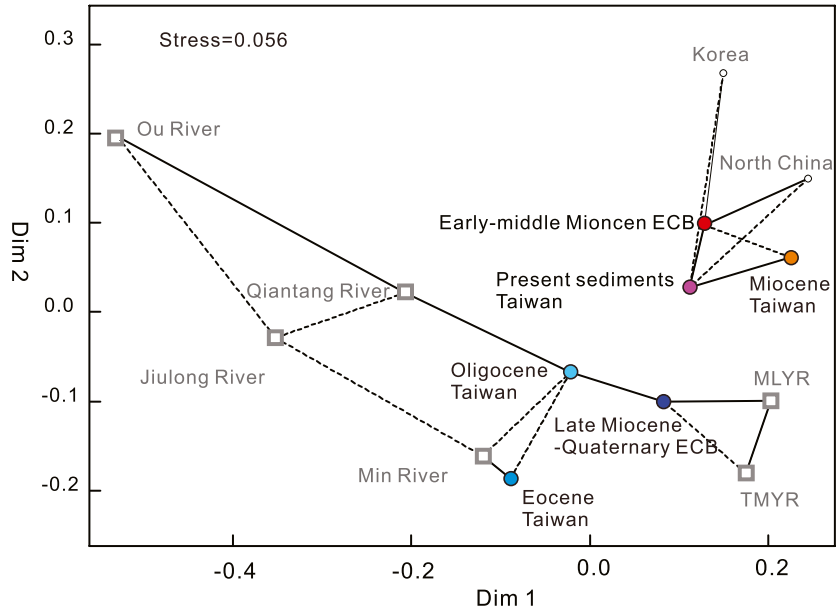

FIGURE 3 | Non-metric multidimensional scaling (MDS, Vermeesch et al., 2016) plot of detrital zircon data. See **Table 1** for source of literature data.

contrasting contributions of sediments for the Yangtze River system before and after the late Miocene support the view that the Yangtze River with present-day erosion patterns and similar size of catchment established in the late Miocene, as proposed by Fu et al. (2021).

Provenance of the Taiwan Region in the Miocene

The provenance of the Miocene sediments in the western foothills of the Taiwan region has been a hot topic of debate, despite a large amount of data obtained (Deng et al., 2017; Lan et al., 2016; Zhang et al., 2017; Chen et al., 2019). The provenance transition from ~31 to 25 Ma has been inferred from elaborate interpretations of major elements, trace elements, rare elements, and Nd isotopes (Lan et al., 2014). The Miocene sediments show a much higher proportion of old zircons and monazite (~1850 Ma) (**Figure 2**) and lower Nd isotope values (Lan et al., 2014; Lan et al., 2016; Chen et al., 2019). It is widely accepted that these sediments were not largely supplied by adjacent small local rivers that derived from the Cathaysia Block (Lan et al., 2016; Deng et al., 2017; Zhang et al., 2017; Chen et al., 2019). However, Chen et al. (2019) claimed that the sediments forming the Miocene strata were from a microcontinent that has been concealed under western Taiwan by overlying strata. Another competitive view is that these sediments were supplied by a large distal river derived from Eurasia, despite the transport routes being a hot debate. Lan et al. (2016) proposed that an enlarged paleo-Min River reached the lower Yangtze craton, resulting in provenance changes. Zhang et al. (2017) suggested that the Yangtze River supplied most of the sediments. Additionally, North China might also have contributed terrigenous clastics (Deng et al., 2017). Wang et al. (2018) noticed similarities in zircon age distribution between Oligocene sediments from the Xihu Sag and Miocene sediments from the Taiwan region. They proposed a mixed model of the Yangtze River and reworked sediment of pre-Miocene sediments of the ECSB.

Several pieces of evidence make the microcontinent model seem impossible. First, in their research, the Yangtze River and rivers derived from the Cathaysia Block were regarded as potential source areas without considering the possibility of North China and Korea, which contributed the most zircons according to our quantitative mixing models (**Figures 4**, **5**); second, seismic sections across the region containing the proposed microcontinental block have revealed that the pre-rift basement is covered by Eocene and Miocene marine strata (Lin et al., 2003). This scenario indicates that even if this "concealed block" existed, it could not have provided a large amount of detritus. Furthermore, it cannot explain why the Eocene sediments in Taiwan are predominantly from nearby South China (Lan et al., 2014; Lan et al., 2016) in the rifting stage (Lin et al., 2003) and why the Miocene sediments sourced from local uplifts concealed the microcontinent as they suggested especially during passive margin subsidence (Huang et al., 2012).

The samples from the Miocene sequences in the western foothills of Taiwan exhibit detrital zircon features similar to the contemporaneous sediments in the ECSB in the KDE plots (**Figure 2**). The MDS plot also suggests that the Taiwan sediment has a close affinity with that in the ECSB (**Figure 3**). The mixing modeling clearly shows that approximate 80–90% of zircons were contributed by ECSB sediments (**Figure 4**). And the 70% of zircons in ECSB sediments were derived from North China and Korea (**Figure 5C**). Thus, we suggest that the Miocene sediments of western foothills in Taiwan have nearly the same sources with the ECSB and were mainly derived from North China and Korea.

The cross-correlation coefficient is 0.6 for early–middle Miocene sedimentary rocks and 0.89 for present sediments which are mainly derived from these rocks. All the model

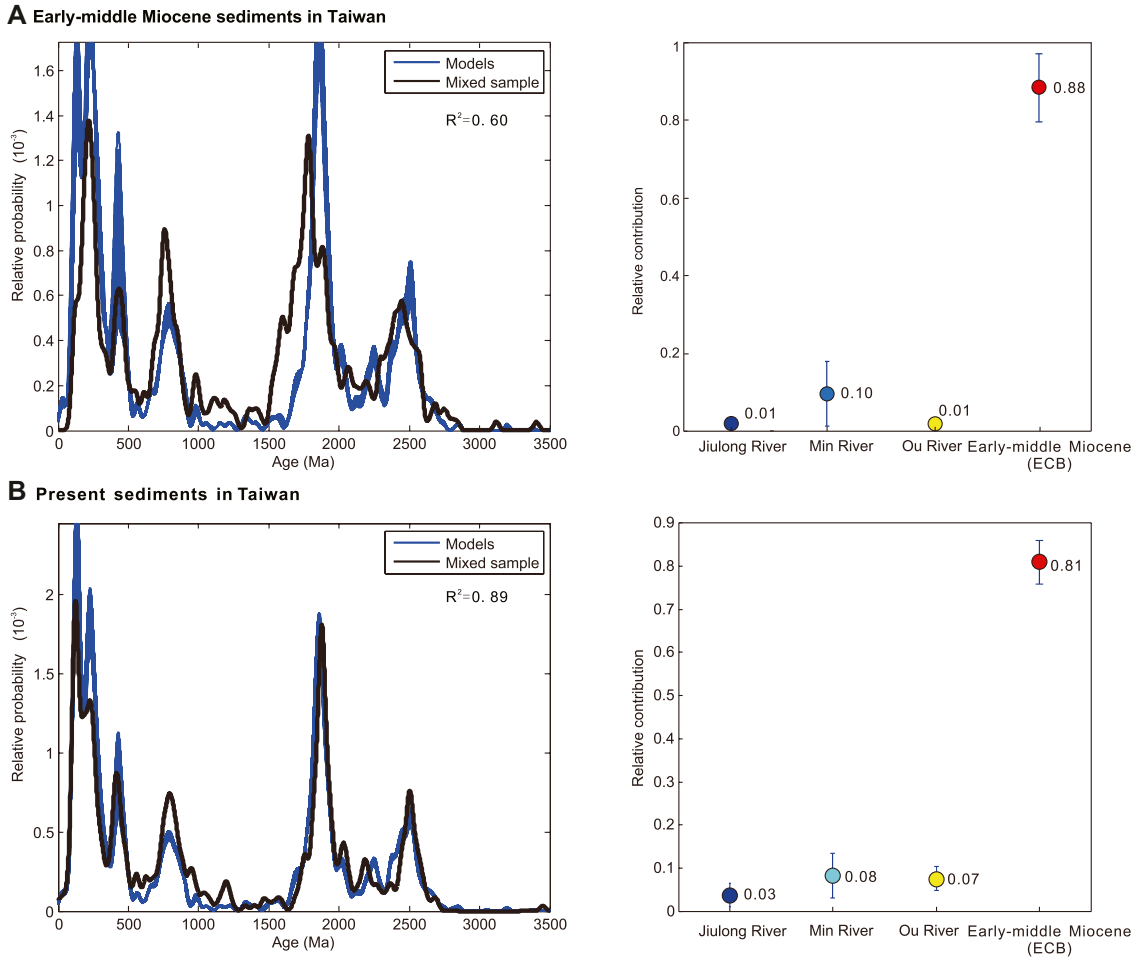

FIGURE 4 | The mixing modelling showing contribution of source areas for early-middle Miocene sandstones and present sediments from Taiwan. The modelling was generated by the Monte Carlo model (Sundell and Saylor, 2017). The Jiulong River, Min River, Ou River and the early-middle Miocene sediments in ECSB were considered as the potential sources to observe the links between sediments in ECSB and the Taiwan. MLYR, middle and lower reaches of the Yangtze River trunk stream; TMYR, tributaries in the middle reaches of the Yangtze River.

trails of finite mixture distributions yield a high peak at ~1.8 Ga with much narrower age range than the counterpart of mixed samples from Miocene sediments in Taiwan but show identical age range with the present sediments from Taiwan and Miocene sedimentary rocks from the ECSB (**Figures 4**, **5**). We noticed that the zircon ages of early–middle Miocene sediments reported by Lan et al. (2016) show obvious variations between samples and the grains for dating per sample between 75 and 91 are also significantly less than the suggested number (120 grains per sample) for provenance analysis proposed by Vermeesch (2004). Therefore, it would produce much better fits for MDS and mixing modelling if high quality of detrital zircon age data can be obtained from the Miocene sedimentary rocks in Taiwan.

Routes of Sediments From East China Sea Basin to Paleo-Taiwan Region

Notably, the routes for sediments delivered from the ECSB to paleo-Taiwan region are under debate. Deng et al. (2017) suggested that a longshore current played an important role in sediment transport from shallow marine environments to the east of the present Yangtze Delta to the Taiwan region. Xu et al. (2007) argued that the transport ability of a longshore current is limited. Zhang et al. (2017) preferred river transport along the ECSB.

The depositional environment from northern ECSB to Paleao-Taiwan region suggests southward tilting, which was consistent with southward delivering of the detrital material. The ECSB formed a wide continental shelf (Lee et al., 2006). In the northern ECSB, the strata of early–middle Miocene dominantly consists of sandstone and mudstone conglomerate interbedded by coal, conglomerate, and freshwater limestone, indicating fluvial to lacustrine environments (Kwon and Boggs, 2002). For the middle ECSB, the lithology predominantly composed of fluvial coarse sandstone and red glutenite mudstone with interbred of coal (Fu et al., 2021).

In the southern ECSB, the Miocene strata consist of alternating lacustrine–flood plain and shallow marine sediments, showing frequent fluctuation of the sea level (Yu and Chow, 1997). The sea

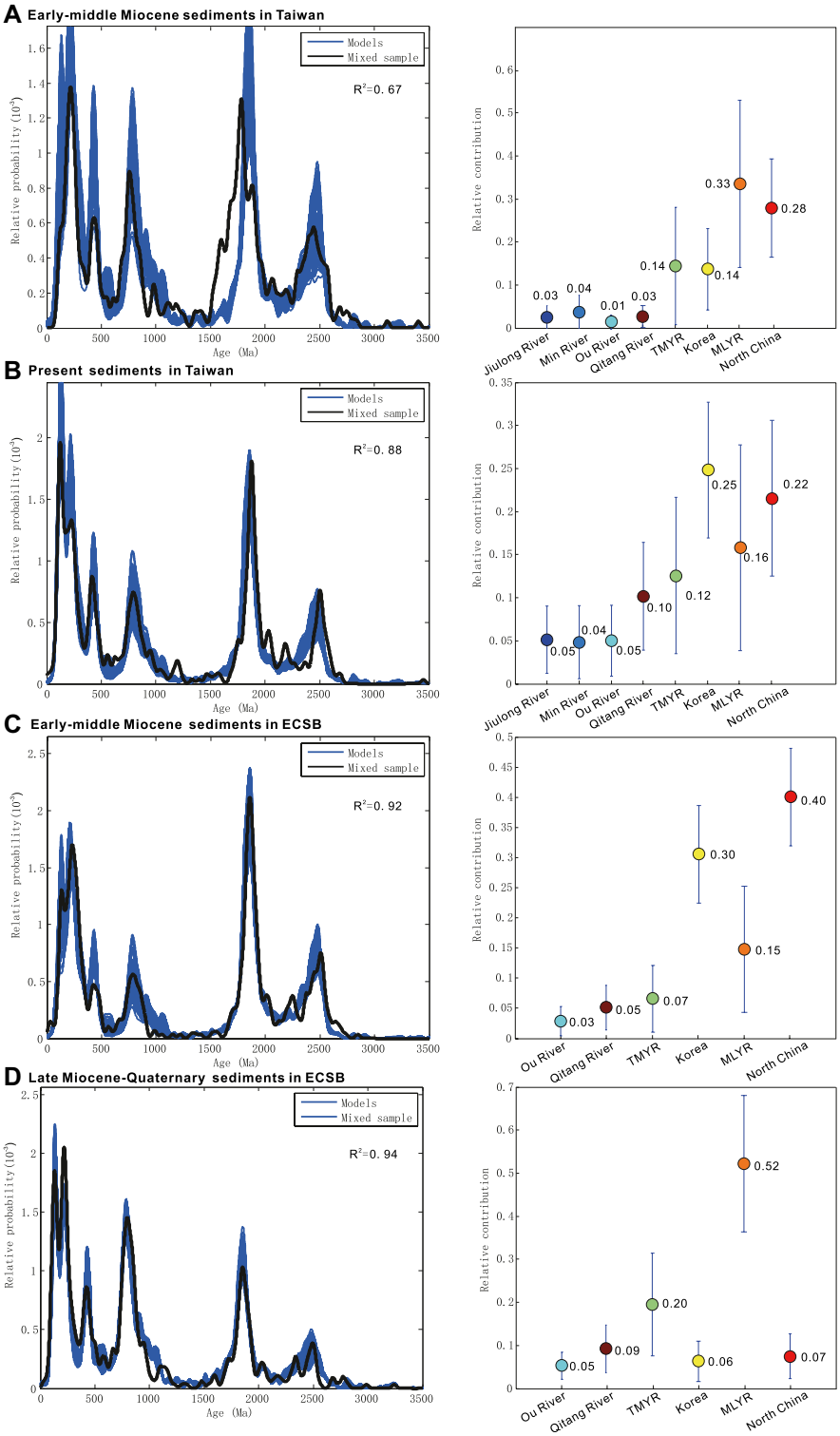

FIGURE 5 | The mixing modelling showing contribution of source areas for early-middle Miocene sandstones and present sediments from Taiwan, Miocene-Quaternary sandstone from ECSB. The modelling was generated by the Monte Carlo model (Sundell and Saylor, 2017). The fluvial samples in the source areas were compiled to quantitatively determine the ultimate contributions from different sources. Note that the Min River and Jiulong River are not used in the modelling for ECSB. MLYR, middle and lower reaches of the Yangtze River trunk stream; TMYR, tributaries in the middle reaches of the Yangtze River.

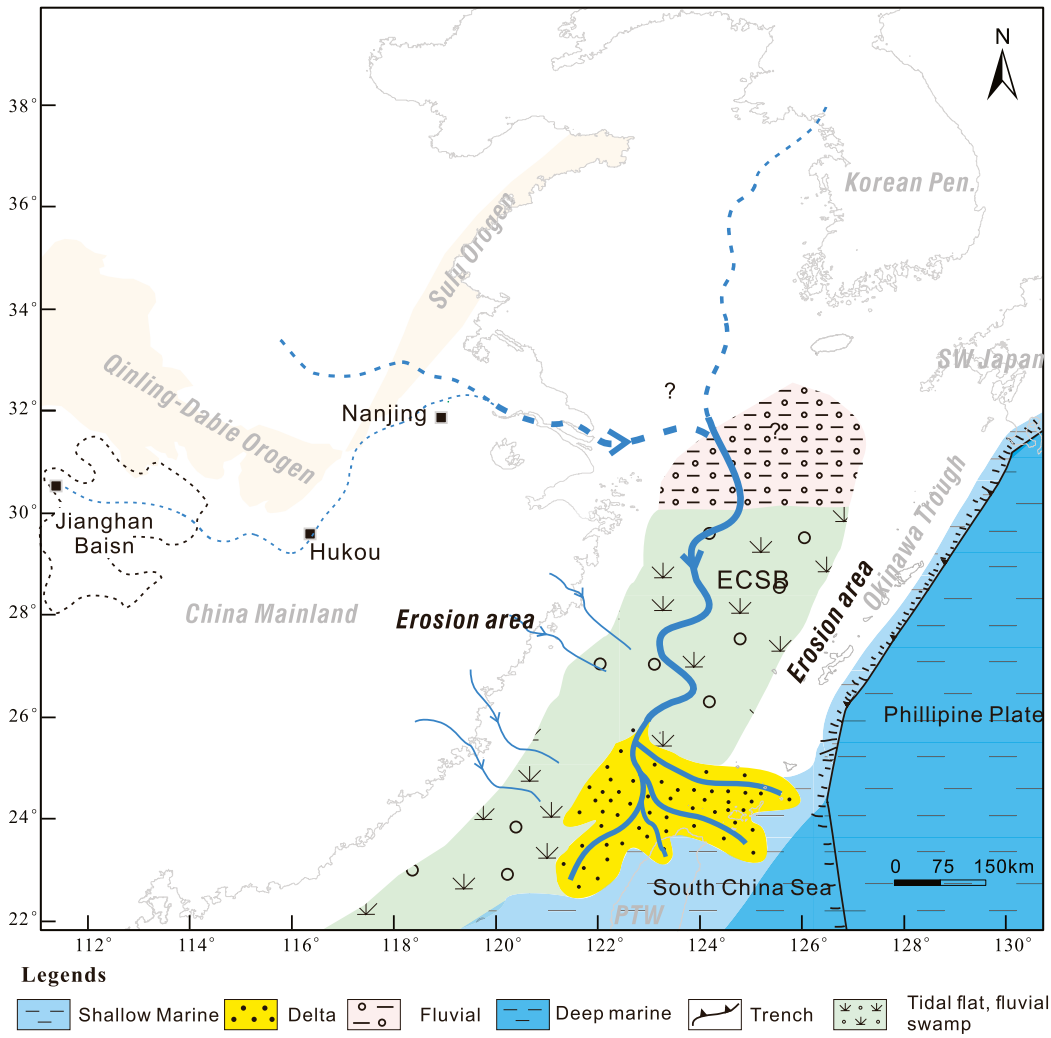

FIGURE 6 | Schematic map showing the sediments delivered from the source areas to the paleo-Taiwan region. PTW, paleo-Taiwan.

water deepened to the east of the southern ECSB. In the southern Ryukyu Islands, the Iriomote Island (**Figure 1A**) is mostly covered by the lower Miocene Iriomote Formation, which was subdivided into A-G member from lower to upper (Saitoh and Masuda, 2004). Iriomote Formation was mainly deposited in a shallow marine setting, but member F containing fossilized roots and coal indicate the terrestrial environment. The well-sorted and roundness sandstone grains combining with framework modes of sandstones that enriched in quartz demonstrate that the siliciclastics were derived from Eurasian continent (Saitoh and Masuda, 2004). In the Taiwan region, the passive continental sediments of early–middle Miocene with well-developed marine microfossils were mainly formed in shallow marine setting (Huang et al., 2012).

Furthermore, back-arc rifting in the northern Okinawa Trough initiated in the middle Miocene and has developed widely since the late Miocene (Letouzey and Kimura, 1985; Letouzey and Kimura, 1986), which was based on observations of the acoustic basement in seismic sections (Gungor et al., 2012). Before that, this region was possibly a zone of uplift, as inferred from the absence of pre-Miocene sediments (Shang et al., 2017), which blocked the sediments of the ECSB to be delivered eastward (**Figure 6**). Although previous studies did not report the existence of a large Miocene delta, we infer there might be a delta somewhere in the southern ECSB between the river system and the shallow marine sea (**Figure 6**). The widespread coal and high frequency sea level fluctuations in the southern ECSB (Yu and Chow, 1997; Saitoh and Masuda, 2004) might imply a Miocene delta system. Therefore, from the northern ECSB to the paleo-Taiwan region, a complete sediment delivering system from the river and delta to shallow marine can be suggested (**Figure 6**). If that was the case, southward delivery by fluvial processes played a major role in the ECSB. The longshore current, wave, and tidal current cannot be neglected, since the Miocene Taiwan region was largely controlled by marine setting (Huang

et al., 2012), and the sediments need to be delivered from the delta to the shallow marine.

Moreover, the early–middle Miocene Paleogeographic characteristics in East Asia might be different from the present, which can be inferred from the predominantly terrestrial deposits in region of the South Yellow Sea (Song et al., 2020). Thus, the river systems which are entirely different from the present might play an important role in the sedimentary transporting system from the North China and Korean Peninsula to the ECSB, but further research is required to trace the detailed routes.

CONCLUSION

In this study, quantitative and qualitative analyses were applied to determine the provenance of early–middle Miocene sediments in the ECSB and Taiwan region based on a large number of detrital zircon age data, together with regional trend in the sedimentary environment. We have drawn the following conclusions:

1) Early–middle Miocene sediments in the ECSB and Taiwan show close affinity with North China and Korea, and the contribution of 70% was from the two source areas for the ECSB.
2) Over 80% sediments in Taiwan were supplied from the ECSB, possibly by the river in the middle and northern ECSB, and by longshore current, wave, and tidal current from the southern ECSB to paleo-Taiwan region.
3) The contribution of the Yangtze River system was 72% for late Miocene–Quaternary sediments in the ECSB, which was consistent with the late Miocene establishment of the Yangtze River.

DATA AVAILABILITY STATEMENT

The original contributions presented in the study are included in the article/Supplementary Material, further inquiries can be directed to the corresponding author.

AUTHOR CONTRIBUTIONS

XF processed the data processing, wrote the manuscript, and provided funding and helped with conception of idea. LH compiled the data, drew plots and edited the manuscript. WZ contributed to the conception, reviewed and edited the manuscript. XH contributed to data processing and participated in discussion. KF and ZZ reviewed and edited the manuscript.

FUNDING

We declare that this work was supported by Natural Science Foundation of Shanghai (22ZR1463300) and National Natural Science Foundation of China (41702228).

REFERENCES

Cao, L., Shao, L., Qiao, P., Zhao, Z., and van Hinsbergen, D. J. J. (2018). Early Miocene Birth of Modern Pearl River Recorded Low-Relief, High-Elevation Surface Formation of SE Tibetan Plateau. *Earth Planet. Sci. Lett.* 496, 120–131. doi:10.1016/j.epsl.2018.05.039

Chen, C.-H., Lee, C.-Y., Lin, J.-W., and Chu, M.-F. (2019). Provenance of Sediments in Western Foothills and Hsuehshan Range (Taiwan): A New View Based on the EMP Monazite versus LA-ICPMS Zircon Geochronology of Detrital Grains. *Earth-Science Rev.* 190, 224–246. doi:10.1016/j.earscirev.2018.12.015

Choi, T., Lee, Y. I., and Orihashi, Y. (2016). Crustal Growth History of the Korean Peninsula: Constraints from Detrital Zircon Ages in Modern River Sediments. *Geosci. Front.* 7, 707–714. doi:10.1016/j.gsf.2016.05.003

Clift, P. D. (2006). Controls on the Erosion of Cenozoic Asia and the Flux of Clastic Sediment to the Ocean. *Earth Planet. Sci. Lett.* 241, 571–580. doi:10.1016/j.epsl.2005.11.028

Deng, K., Yang, S., Li, C., Su, N., Bi, L., Chang, Y.-P., et al. (2017). Detrital Zircon Geochronology of River Sands from Taiwan: Implications for Sedimentary Provenance of Taiwan and its Source Link with the east China mainland. *Earth-Science Rev.* 164, 31–47. doi:10.1016/j.earscirev.2016.10.015

Fu, X., Zhu, W., Geng, J., Yang, S., Zhong, K., Huang, X., et al. (2021). The Present-Day Yangtze River Was Established in the Late Miocene: Evidence from Detrital Zircon Ages. *J. Asian Earth Sci.* 205, 104600. doi:10.1016/j.jseaes.2020.104600

Gungor, A., Lee, G. H., Kim, H.-J., Han, H.-C., Kang, M.-H., Kim, J., et al. (2012). Structural Characteristics of the Northern Okinawa Trough and Adjacent Areas from Regional Seismic Reflection Data: Geologic and Tectonic Implications. *Tectonophysics* 522-523, 198–207. doi:10.1016/j.tecto.2011.11.027

Guo, R., Sun, X., Li, C. a., Li, Y., Wei, C., Zhang, Z., et al. (2021). Cenozoic Evolution of the Yangtze River: Constraints from Detrital Zircon U Pb Ages. *Palaeogeogr. Palaeoclimatol. Palaeoecol.* 579, 110586. doi:10.1016/j.palaeo.2021.110586

He, J., Garzanti, E., Cao, L., and Wang, H. (2020). The Zircon story of the Pearl River (China) from Cretaceous to Present. *Earth-Science Rev.* 201, 103078. doi:10.1016/j.earscirev.2019.103078

He, M., Zheng, H., Bookhagen, B., and Clift, P. D. (2014). Controls on Erosion Intensity in the Yangtze River basin Tracked by U-Pb Detrital Zircon Dating. *Earth-Science Rev.* 136, 121–140. doi:10.1016/j.earscirev.2014.05.014

Huang, C.-Y., Yen, Y., Zhao, Q., and Lin, C.-T. (2012). Cenozoic Stratigraphy of Taiwan: Window into Rifting, Stratigraphy and Paleoceanography of South China Sea. *Chin. Sci. Bull.* 57, 3130–3149. doi:10.1007/s11434-012-5349-y

Huang, C. Y. (2017). Geological Ages of Taiwan Stratigraphy and Tectonic Events (In Chinese). *Sci. Sin.-Terrae* 47, 394–405. doi:10.1360/N072017-00023

Iizuka, T., Komiya, T., Rino, S., Maruyama, S., and Hirata, T. (2010). Detrital Zircon Evidence for Hf Isotopic Evolution of Granitoid Crust and continental Growth. *Geochimica et Cosmochimica Acta* 74, 2450–2472. doi:10.1016/j.gca.2010.01.023

Kwon, Y.-I., and Boggs, S. (2002). Provenance Interpretation of Tertiary Sandstones from the Cheju Basin (NE East China Sea): a Comparison of Conventional Petrographic and Scanning Cathodoluminescence Techniques. *Sediment. Geology.* 152, 29–43. doi:10.1016/S0037-0738(01)00284-6

Lan, Q., Yan, Y., Huang, C.-Y., Clift, P. D., Li, X., Chen, W., et al. (2014). Tectonics, Topography, and River System Transition in East Tibet: Insights from the Sedimentary Record in Taiwan. *Geochem. Geophys. Geosyst.* 15, 3658–3674. doi:10.1002/2014GC005310

Lan, Q., Yan, Y., Huang, C.-Y., Santosh, M., Shan, Y.-H., Chen, W., et al. (2016). Topographic Architecture and Drainage Reorganization in Southeast China: Zircon U-Pb Chronology and Hf Isotope Evidence from Taiwan. *Gondwana Res.* 36, 376–389. doi:10.1016/j.gr.2015.07.008

Lee, G. H., Kim, B., Shin, K. S., and Sunwoo, D. (2006). Geologic Evolution and Aspects of the Petroleum Geology of the Northern East China Sea Shelf basin. *Bulletin* 90, 237–260. doi:10.1306/08010505020

Letouzey, J., and Kimura, M. (1985). Okinawa Trough Genesis: Structure and Evolution of a Backarc basin Developed in a Continent. *Mar. Pet. Geology.* 2, 111–130. doi:10.1016/0264-8172(85)90002-9

Letouzey, J., and Kimura, M. (1986). The Okinawa Trough: Genesis of a Back-Arc basin Developing along a continental Margin. *Tectonophysics* 125, 209–230. doi:10.1016/0040-1951(86)90015-6

Lin, A. T., Watts, A. B., and Hesselbo, S. P. (2003). Cenozoic Stratigraphy and Subsidence History of the South China Sea Margin in the Taiwan Region. *Basin Res.* 15, 453–478. doi:10.1046/j.1365-2117.2003.00215.x

Malusà, M. G., Carter, A., Limoncelli, M., Villa, I. M., and Garzanti, E. (2013). Bias in Detrital Zircon Geochronology and Thermochronometry. *Chem. Geology.* 359, 90–107. doi:10.1016/j.chemgeo.2013.09.016

Nie, J., Stevens, T., Rittner, M., Stockli, D., Garzanti, E., Limonta, M., et al. (2015). Loess Plateau Storage of Northeastern Tibetan Plateau-Derived Yellow River Sediment. *Nat. Commun.* 6, 27. doi:10.1038/ncomms9511

Ren, J., Tamaki, K., Li, S., and Junxia, Z. (2002). Late Mesozoic and Cenozoic Rifting and its Dynamic Setting in Eastern China and Adjacent Areas. *Tectonophysics* 344, 175–205. doi:10.1016/s0040-1951(01)00271-2

Richardson, N. J., Densmore, A. L., Seward, D., Wipf, M., and Yong, L. (2010). Did Incision of the Three Gorges Begin in the Eocene? *Geology* 38, 551–554. doi:10.1130/G30527.1

Saitoh, Y., and Masuda, F. (2004). Miocene sandstone of 'continental' Origin on Iriomote Island, Southwest Ryukyu Arc, Eastern Asia. *J. Asian Earth Sci.* 24, 137–144. doi:10.1016/j.jseaes.2003.10.002

Shang, L.-N., Zhang, X.-H., Jia, Y.-G., Han, B., Yang, C.-S., Geng, W., et al. (2017). Late Cenozoic Evolution of the East China continental Margin: Insights from Seismic, Gravity, and Magnetic Analyses. *Tectonophysics* 698, 1–15. doi:10.1016/j.tecto.2017.01.003

Song, Y., Hu, S., Xu, J., Shen, C., Li, S., Su, P., et al. (2020). Lacustrine Environmental Evolution and Implications on Source Rock Deposition in the Upper Cretaceous-Paleocene of the South Yellow Sea Basin, Offshore Eastern China. *Mar. Pet. Geology.* 113, 104135. doi:10.1016/j.marpetgeo.2019.104135

Sun, X., Tian, Y., Kuiper, K. F., Li, C. a., Zhang, Z., and Wijbrans, J. R. (2021). No Yangtze River Prior to the Late Miocene: Evidence from Detrital Muscovite and K-Feldspar $^{40}Ar/^{39}Ar$ Geochronology. *Geophys. Res. Lett.* 48, e2020GL089903. doi:10.1029/2020GL089903

Sundell, K. E., and Saylor, J. E. (2017). Unmixing Detrital Geochronology Age Distributions. *Geochem. Geophys. Geosyst.* 18, 2872–2886. doi:10.1002/2016GC006774

Vermeesch, P. (2004). How many Grains Are Needed for a Provenance Study? *Earth Planet. Sci. Lett.* 224, 441–451. doi:10.1016/j.epsl.2004.05.037

Vermeesch, P. (2013). Multi-sample Comparison of Detrital Age Distributions. *Chem. Geology.* 341, 140–146. doi:10.1016/j.chemgeo.2013.01.010

Vermeesch, P., Resentini, A., and Garzanti, E. (2016). An R Package for Statistical Provenance Analysis. *Sediment. Geology.* 336, 14–25. doi:10.1016/j.sedgeo.2016.01.009

Wang, W., Bidgoli, T., Yang, X., and Ye, J. (2018). Source-To-Sink Links Between East Asia and Taiwan From Detrital Zircon Geochronology of the Oligocene Huagang Formation in the East China Sea Shelf Basin. Geochemistry. *Geochem. Geophys. Geosyst.* 19, 3673–3688. doi:10.1029/2018GC007576

Wang, P. (2004). Cenozoic Deformation and the History of Sea-Land Interactions in Asia. *Geophys. Monogr. Ser.* 1, 1–22. doi:10.1029/149GM01

Weilin, Z., Kai, Z., Xiaowei, F., Chunfeng, C., Minqiang, Z., and Shunli, G. (2019). The Formation and Evolution of the East China Sea Shelf Basin: A New View. *Earth-Science Rev.* 190, 89–111. doi:10.1016/j.earscirev.2018.12.009

Wissink, G. K., and Hoke, G. D. (2016). Eastern Margin of Tibet Supplies Most Sediment to the Yangtze River. *Lithosphere* 8, 601–614. doi:10.1130/L570.1

Wu, F., Yang, J., Wilde, S., Liu, X., Guo, J., and Zhai, M. (2007). Detrital Zircon U-Pb and Hf Isotopic Constraints on the Crustal Evolution of North Korea. *Precambrian Res.* 159, 155–177. doi:10.1016/j.precamres.2007.06.007

Xu, X., O'Reilly, S. Y., Griffin, W. L., Wang, X., Pearson, N. J., and He, Z. (2007). The Crust of Cathaysia: Age, Assembly and Reworking of Two Terranes. *Precambrian Res.* 158, 51–78. doi:10.1016/j.precamres.2007.04.010

Xu, Y., Wang, C. Y., and Zhao, T. (2016). Using Detrital Zircons from River Sands to Constrain Major Tectono-thermal Events of the Cathaysia Block, SE China. *J. Asian Earth Sci.* 124, 1–13. doi:10.1016/j.jseaes.2016.04.012

Yang, J., Gao, S., Chen, C., Tang, Y., Yuan, H., Gong, H., et al. (2009). Episodic Crustal Growth of North China as Revealed by U-Pb Age and Hf Isotopes of Detrital Zircons from Modern Rivers. *Geochimica et Cosmochimica Acta* 73, 2660–2673. doi:10.1016/j.gca.2009.02.007

Yang, S., Zhang, F., and Wang, Z. (2012). Grain Size Distribution and Age Population of Detrital Zircons from the Changjiang (Yangtze) River System, China. *Chem. Geology.* 296-297, 26–38. doi:10.1016/j.chemgeo.2011.12.016

Yu, H.-S., and Chow, J. (1997). Cenozoic Basins in Northern Taiwan and Tectonic Implications for the Development of the Eastern Asian continental Margin. *Palaeogeogr. Palaeoclimatol. Palaeoecol.* 131, 133–144. doi:10.1016/S0031-0182(96)00124-1

Zhang, J., Krijgsman, W., Lu, Y., Liu, J., Li, X., Du, X., et al. (2021a). Detrital Zircon Ages Reveal Yangtze Provenance since the Early Oligocene in the East China Sea Shelf Basin. *Palaeogeogr. Palaeoclimatol. Palaeoecol.* 577, 110548. doi:10.1016/j.palaeo.2021.110548

Zhang, X., Dalrymple, R. W., Yang, S.-Y., Lin, C.-M., and Wang, P. (2015). Provenance of Holocene Sediments in the Outer Part of the Paleo-Qiantang River Estuary, China. *Mar. Geology.* 366, 1–15. doi:10.1016/j.margeo.2015.04.008

Zhang, X., Huang, C., Wang, Y., Clift, P. D., Yan, Y., Fu, X., et al. (2017). Evolving Yangtze River Reconstructed by Detrital Zircon U-Pb Dating and Petrographic Analysis of Miocene Marginal Sea Sedimentary Rocks of the Western Foothills and Hengchun Peninsula, Taiwan. *Tectonics* 36, 634–651. doi:10.1002/2016TC004357

Zhang, Z., Daly, J. S., Li, C. a., Tyrrell, S., Sun, X., Badenszki, E., et al. (2021b). Formation of the Three Gorges (Yangtze River) No Earlier Than 10 Ma. *Earth-Science Rev.* 216, 103601. doi:10.1016/j.earscirev.2021.103601

Zheng, H. (2015). Birth of the Yangtze River: Age and Tectonic-Geomorphic Implications. *Natl. Sci. Rev.* 2, 438–453. doi:10.1093/nsr/nwv063

Zheng, H., Clift, P. D., He, M., Bian, Z., Liu, G., Liu, X., et al. (2020). Formation of the First Bend in the Late Eocene Gave Birth to the Modern Yangtze River, China. *Geology* 49, 35–39. doi:10.1130/G48149.1

Conflict of Interest: The authors declare that the research was conducted in the absence of any commercial or financial relationships that could be construed as a potential conflict of interest.

Publisher's Note: All claims expressed in this article are solely those of the authors and do not necessarily represent those of their affiliated organizations, or those of the publisher, the editors, and the reviewers. Any product that may be evaluated in this article, or claim that may be made by its manufacturer, is not guaranteed or endorsed by the publisher.

Copyright © 2022 Fu, Hu, Zhu, Huang, Feng and Zhou. This is an open-access article distributed under the terms of the Creative Commons Attribution License (CC BY). The use, distribution or reproduction in other forums is permitted, provided the original author(s) and the copyright owner(s) are credited and that the original publication in this journal is cited, in accordance with accepted academic practice. No use, distribution or reproduction is permitted which does not comply with these terms.

frontiers in Earth Science

ORIGINAL RESEARCH
published: 11 March 2022
doi: 10.3389/feart.2022.849167

Time Constraints of Late Cenozoic Tectonic Deformation of the Atushi Anticline, Southwestern Tian Shan: Evidence From Cosmogenic Nuclide Burial Age

Qingyu Chen[1,2], *Bihong Fu*[1]*, *Pilong Shi*[1] *and Ping Kong*[3]

[1]Aerospace Information Research Institute, Chinese Academy of Sciences, Beijing, China, [2]University of Chinese Academy of Sciences, Beijing, China, [3]Institute of Geology and Geophysics, Chinese Academy of Sciences, Beijing, China

With the latest uplift episode of Tian Shan occurring since early Miocene, a series of thrust–fold belts were formed in front of Tian Shan. The Kashi foreland thrust–fold belt (KFTB) provided a unique case to understand the ongoing intracontinental deformation within the Pamir–Tian Shan convergence zone (PTCZ). Previous cosmogenic nuclide chronological studies on growth folds suggested that the young thrust–fold belt in front of Pamir formed during 6–1.07 Ma. However, the age constraints of late Cenozoic deformation in front of southwestern Tian Shan are still debated. In this study, we attempt to constrain the initial deformation time of the NEE-striking Atushi anticline (ATA) in the KFTB through the cosmogenic nuclide burial dating data of growth strata near the boundary between Pliocene–Pleistocene Atushi Formation and Xiyu Formation (Xiyu Conglomerate), which are exposed in the southern limb of ATA. Moreover, detailed geological interpretations of multiple remote sensing images and field investigations are also carried out to document the late Cenozoic structural deformation and geomorphologic features of ATA. The $^{26}Al/^{10}Be$ burial dating data of four fine-grained samples reveal that the syntectonic deposit of ATA initiated at 1.79 ± 0.16 Ma, and the deposit of Xiyu Conglomerate started since 1.67 ± 0.18 Ma. Thus, we suggest that the thrust–folding of ATA began at ca.1.79 Ma and is currently still active.

Keywords: growth strata, Pliocene-Pleistocene sedimentary strata, $^{26}Al/^{10}Be$ burial age, tectonic deformation, Atushi anticline

OPEN ACCESS

Edited by:
Xuhua Shi,
Zhejiang University, China

Reviewed by:
Honghua Lu,
East China Normal University, China
Tao Li,
China Earthquake Administration, China

***Correspondence:**
Bihong Fu
fubh@aircas.ac.cn

Specialty section:
This article was submitted to Structural Geology and Tectonics, a section of the journal Frontiers in Earth Science

Received: *05 January 2022*
Accepted: *07 February 2022*
Published: *11 March 2022*

Citation:
Chen Q, Fu B, Shi P and Kong P (2022) Time Constraints of Late Cenozoic Tectonic Deformation of the Atushi Anticline, Southwestern Tian Shan: Evidence From Cosmogenic Nuclide Burial Age. Front. Earth Sci. 10:849167. doi: 10.3389/feart.2022.849167

INTRODUCTION

The Pamir–Tian Shan convergence zone (PTCZ) in western Tarim (**Figure 1A**) has resulted from the northward indentation of the India plate into the Eurasia plate since ~55 Ma (Molnar and Tapponnier, 1975; Burtman and Molnar, 1993). The ongoing India–Eurasia collision has caused a rejuvenation of Tian Shan orogen since early Miocene (Sobel and Dumitru, 1997; Yin et al., 1998; Sobel et al., 2006). After that, an accelerated uplift episode of Tian Shan and a rapid deformation of the Kashi foreland thrust–fold belt (KFTB) have generated 4 to 5 rows of thrust–fold belts in front of southwestern Tian Shan since Pliocene (Chen et al., 2002; Scharer et al., 2004; Heermance et al., 2008; Fu et al., 2010; Jia et al., 2015; Thompson-Jobe et al., 2018). The precisely constrained history of

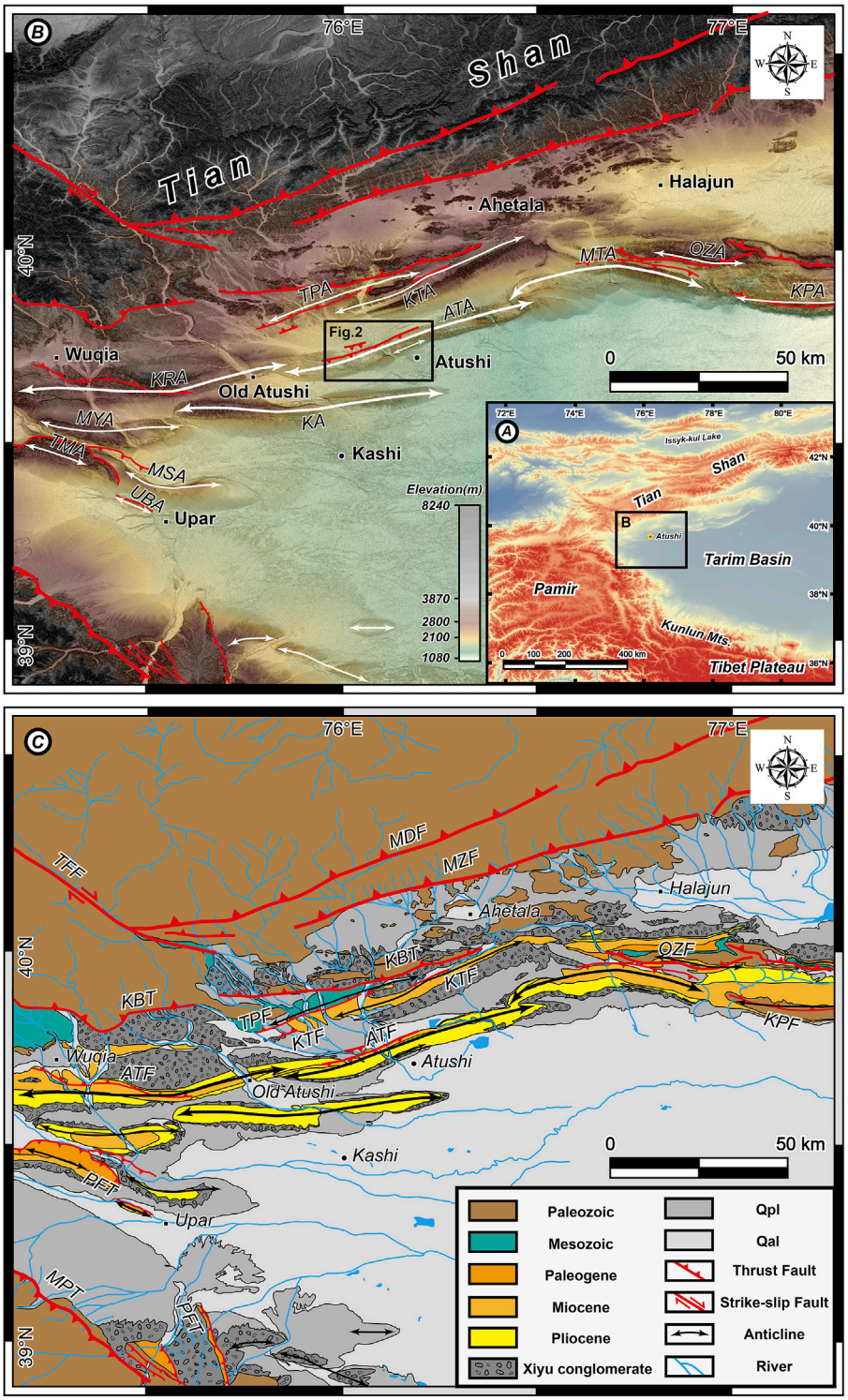

FIGURE 1 | Geological and geomorphological interpretation map of western Tarim. **(A)** Topographic features of Central Asia. The black polygon shows the location of the Pamir–Tian Shan convergence zone (PTCZ). The elevation data are from the 90-m SRTM DEM. **(B)** Major anticlines in PTCZ. The shaded relief map is based on the ALOS World 3D-30 m (AW3D30) **(C)** Geological interpretation map of PTCZ (based on our field investigation combined with interpretation of ASTER and Sentinel-2 multispectral images; Fu et al., 2010; Thompson-Jobe et al., 2018; Li et al., 2018). TPA, Tashipisake anticline; KTA, Keketamu Anticline; MTA, Mutule anticline; OZA, Ozr Goltau anticline; KPA, Kepingtage anticline; ATA, Atushi anticline; KRA, Kerato anticline; KA, Kashi anticline; MYA, Mingyaole anticline; TMA, Tumuan anticline; MSA, Mushi anticline; UBA, Ubulake anticline; TFF, Talas-Ferghana fault; MDF, Maidan fault; MZF, Muziduke fault; KBT, Kashi Basin thrust; TPF, Tashipisake fault; KTF, Keketamu fault; ATF, Atushi fault; OZF, Ozr Goltau fault; KPF, Kepingtage fault; PFT, Pamir frontal thrust; MPT, Main Pamir thrust.

tectonic deformation of thrust-related folds will provide a unique insight into the Cenozoic tectono-geomorphologic growth of PTCZ.

Syntectonic growth strata in foreland basins recorded the kinematic process of tectonic deformation. Since the early pioneer study of unique angular unconformity in the south of Pyrenees, Spain (Riba, 1976), the growth strata have been widely used to explore the coupling mechanisms between sedimentary basin and adjacent orogenic belt (Suppe et al., 1992; Shaw and Suppe, 1994; Chen et al., 2002; Heermance et al., 2008; Sun et al., 2009; Hardy and Cardozo 2021). Various age dating methods have been applied to document the basal age of growth strata, which could chronologically constrain the initiation of a fold growth (Chen et al., 2002; Sobel et al., 2006; Chen et al., 2007a; Heermance et al., 2008; Kong et al., 2011; Li et al., 2013; Thompson-Jobe et al., 2015).

Previous studies indicated that the growth strata are well developed around the thrust–fold belts in front of Pamir and Tian Shan (Chen et al., 2002; Scharer et al., 2004; Hubert-Ferrari et al., 2007; Sun and Zhang, 2009; Thompson-Jobe et al., 2018). In the recent studies (Thompson-Jobe et al., 2018; Thompson-Jobe et al., 2017), the $^{26}Al/^{10}Be$ dating data of Pliocene–Pleistocene growth strata and sedimentary units beneath the active faults developed along the Kerato anticline (KRA), Mingyaole anticline (MYA), Tumuan anticline (TMA), and Mushi anticline (MSA) in PTCZ have constrained the northward propagation of the northeastern Pamir thrust system since >5 Ma. However, the spatio-temporal process on the southward propagation of the KFTB in front of southwestern Tian Shan, particularly the initial deformation timing of the ATA, the southernmost thrust–fold belt in the KFTB, remains unclear (Chen et al., 2002; Heermance et al., 2007; Jia et al., 2015). It is difficult to date the thick coarse-grained Pliocene–Pleistocene sedimentary units, which are widely developed in the KFTB, with traditional chronological methods (Heermance et al., 2007; Balco and Shuster, 2009; Fu et al., 2010). Moreover, due to the tectonic uplift and long-term erosion in this region, the sedimentary facies frequently changed in the KFTB during the Neogene. Thus, the geological age of Pliocene–Pleistocene deposits in the KFTB is still controversial (Chen et al., 2002; Heermance et al., 2008).

The purpose of this study is to determine the initial deformation timing of ATA. To do this, we document in detail the late Cenozoic sedimentary units exposed at the ATA based on geological and geomorphological interpretations of the high-resolution multispectral satellite remote sensing images as well as the field investigations. Particularly, we meticulously recorded geometrical changes between the Pliocene–Pleistocene pre-growth strata and the growth strata along the cross-geological section in the western bank of Boguzi River by using unmanned aerial vehicle (UAV) horizontal imitating ground flight and field measurements. Finally, four fine-grained samples were collected from the Pliocene–Pleistocene sedimentary strata of the ATA to constrain the timing of late Cenozoic tectonic deformation of the anticline *via* $^{26}Al/^{10}Be$ burial age dating.

GEOLOGICAL SETTING

The KFTB is located in front of southwestern Tian Shan, where tectonic deformation and sedimentary response resulted from the interaction of Pamir, western Tarim, and southwestern Tian Shan (**Figure 1A**) (Allen et al., 1999; Avouac et al., 1993; Yin et al., 1998; Zhao et al., 2001; Scharer et al., 2004; Sobel et al., 2006; Fu et al., 2010; Gao et al., 2013). The KFTB is composed of a series of tight anticlines and broad synclines (**Figure 1B**) as well as the NE-NEE-striking thrust faults. Successively from north to south, they are Tashipisake Anticline (TPA), Keketamu anticline (KTA), Atushi anticline (ATA), and Kashi anticline (KA) (**Figure 1B**). The corresponding faults are Maidan fault (MDF), Muziduke fault (MZF), Kashi basin thrust fault (KBT), Tashipisake fault (TPF), Keketamu fault (KTF), and Atushi fault (ATF) (**Figure 1C**). MDF, MZF, KBT, and TPF dip to the north, which are exposed on the south flank of the anticlines. The south-dipping ATF and KTF are exposed on the north flank of the anticlines (Wu et al., 2019; Zhao et al., 2001; Chen et al., 2002; Scharer et al., 2004; Sobel et al., 2006; Heermance et al., 2007; Heermance et al., 2008; Fu et al., 2010; Jia et al., 2015; Li et al., 2018).

Affected by the southward expansion of southwestern Tian Shan, the sedimentary strata exposed on the surface are diverse and complex (**Figure 1C**). The Paleozoic strata exposed at the hanging wall of KBT are composed of Carboniferous limestone, shale, and Permian sandstone. The Mesozoic strata consist of Cretaceous thick red and orange sandstone interbedded with grayish-green siltstone (Chen et al., 2001; Scharer et al., 2004; Heermance et al., 2007). The Cenozoic strata mainly consist of the Miocene Pakabulake Formation (Pakabulake Formation), Pliocene Atushi Formation, and Xiyu Conglomerate (Chen et al., 2001; Heermance et al., 2007). The Pakabulake Formation is composed of brownish-red sandstone, siltstone, and gypsum at the upper layer (Fu et al., 2010). The Atushi Formation consists of grayish-yellow sandstone interbedded with thin brownish-red siltstone and mudstone. The Xiyu Formation is known as the Xiyu Conglomerate, distributed widely in the piedmonts of active orogenic belts in Xinjiang (Liu et al., 1996; Chen et al., 2001; Sun et al., 2004; Chen et al., 2007a; Sun et al., 2009; Sun and Zhang, 2009; Thompson-Jobe et al., 2018). The lithology and sedimentary facies of Xiyu Conglomerate are significantly different from its underlying strata. It is dark gray, gray massive conglomerate with grayish-yellow sandstone, siltstone layers or lens, main laminar flow, braided channel accumulation, and mostly alluvial–diluvial facies (Chen et al., 2000; Chen et al., 2007b).

Low-temperature thermochronological studies suggested that rapid topographical growth on the hanging wall of MDF and MZF could be constrained in 25–20 Ma. Afterwards, the structural stress delivered to KBT at 18–15 Ma (Sobel et al., 2006; Jia et al., 2015). The initial deformation age of TPA is constrained to 15–13.5 Ma according to sedimentary facies change, crosscutting relationships, and sedimentation rate (Heermance et al., 2008) as well as the detrital zircon age (Jia et al., 2015). The initial deforming age of KTA was defined at ~4 Ma that originated from the dating age of the growth strata and the sedimentation rate (Heermance et al., 2008).

At the southernmost part of KFTB, about 20-km-wide ATA and KA are developed themselves as shown in **Figure 1B** (Chen et al., 2001; Chen et al., 2002; Sobel et al., 2006; Tian et al., 2006; Yang et al., 2009; Li et al., 2018). Concerning the spatial distribution of ATA, some studies suggested that ATA is a reversed-S-shaped anticline, extending to near Wuqia county in the west and interacting with Mutule anticline (MTA) in the east (Scharer et al., 2004; Thompsom-Jobe et al., 2018). However, other researches considered that ATA is terminated at the Old Atushi town, and the western part belongs to the KRA (Heermance et al., 2008; Fu et al., 2010). Numerous studies have documented the Pliocene–Pleistocene strata exposed in ATA (Chen et al., 2002; Scharer et al., 2004; Sobel et al., 2006; Heermance et al., 2007; Heermance et al., 2008; Fu et al., 2010; Zhang et al., 2013; Jia et al., 2015; Thompson-Jobe et al., 2018). The NEE-SWW-striking ATF, a south-dipping thrust fault located at the northern flank of the ATA, is basically paralleled to the axis of ATA (**Figure 1B**). The age constraints from the magnetostratigraphy proposed that the northeastward lateral propagation and the growth of the ATA initiated at ~1.4 and ~1.2 Ma, respectively, in the eastern bank of Boguzi River and Ganhangou sections (Chen et al., 2002). Six pedestal terraces (including flood plain as T_0) are developed along the Boguzi River. All terraces are pedestal terraces, and the consolidated bed rock consisted of Pliocene mudstone, sandstone, and Lower Pleistocene conglomerate. The sediments of the terraces are mainly comprised of dark gray gravel and interbedded with a grayish-yellow sand layer containing sandy clay lenses. The diameter of the gravel is generally 2–10 cm, and the diameter of the individual large boulder is 20–30 cm. It is well rounded, and the main component is metamorphic sandstone. The deformation of the six terraces revealed that the ATA has experienced multi-stage uplifting and folding during the late Pleistocene (Yang et al., 2009). The youngest KA in the southernmost part of KFTB, a doubly plunging detachment fold with a steep northern limb and a gentle southern limb, extended over 60-km long (Chen et al., 2007a; Li et al., 2018; Li et al., 2019). The magnetostratigraphic data from two geologic sections at the south and north flanks of KA indicate that the anticline began growing at ~1.4 and ~1.07 Ma, respectively (Chen et al., 2007a).

DATA AND METHODS

Multiple Remote Sensing Data

Multispectral satellite remote sensing images are very useful to interpret the structural features and sedimentary units in the Pamir–Tian Shan convergence zone with an arid and semi-arid climate condition (Fu et al., 2010). Moreover, the duplication and the absence of strata and weathering make it difficult to identify the spatial distribution of stratigraphic units in the field (Heermance et al., 2007). In this study, multiple sources of satellite remote sensing data were used, which include the ASTER Visible and Near Infrared (VNIR, 15-m ground resolution) and short-wave infrared data (30-m ground resolution) and Sentinel-2 VNIR data (10-m ground resolution). For multispectral remote sensing data, an appropriate band selection of remote sensing data plays a key role in image enhancement, which is useful for geological interpretation and lithological extraction (**Figure 2A**). The ASTER false-color composite image (R: band ratio 2/1, G: band 3, and B: band ratio 5/8, **Figure 2A**) was able to distinguish different lithological units in this region. We also imposed ASTER multispectral image on the DEM data from ALOS World 3D-30 m (AW3D30) to generate 3D perspective images of a typical area (**Figure 4A**), which is beneficial for the geomorphologic feature analysis of KFTB.

Cosmogenic Nuclide Burial Dating

Cosmogenic nuclide burial dating, first proposed by Lal and Arnold (1985), relies on various decay constants for ^{10}Be and ^{26}Al (Granger and Muzikar, 2001). The assumption behind the method is that quartz is exposed to the cosmic rays at the Earth's surface for a period of time, acquiring certain amounts of ^{10}Be and ^{26}Al, respectively. When quartz is buried at a sufficient depth, the production of cosmogenic nuclides ceases, and decay becomes the dominant process affecting the concentrations of ^{10}Be and ^{26}Al (Granger and Muzikar, 2001; Granger et al., 2013). Cosmogenic nuclide burial data were widely used in interpreting exposed and the burial history of sediments or terrace surfaces (Balco and Shuster, 2009; Jungers and Heimsath, 2016) and dating the age of Late Cenozoic conglomerates (Kong et al., 2011; Thompson-Jobe et al., 2018). Compared with other means, cosmogenic nuclide dating is a direct way to measure samples without relying on existing symbolic age (like fossils and volcanic ash), which provided the numerical age of the samples instead of the correlated age or relative age (McCalpin and Nelson, 1996). ^{26}Al/^{10}Be burial dating is an advantage for dating Pliocene–Pleistocene clastic sediments that are challenging to be dated by other methods (Balco and Shuster, 2009; Thompson-Jobe et al., 2018). So far, we have selected ^{26}Al/^{10}Be burial dating method to constrain the geological age of Pliocene–Pleistocene conglomerates, which are exposed along the southern flank of ATA. Four samples were collected from the boundary between Atushi Formation and Xiyu Conglomerate (**Table 1**; **Figure 5B**). The sample preparations were processed at the cosmogenic nuclide laboratory of the Institute of Geology and Geophysics, Chinese Academy of Sciences in Beijing. The oxides were mixed with niobium and silver metal powders, and both ^{10}Be and ^{26}Al concentrations were measured by AMS at PRIME Lab at Purdue University. The concentrations of ^{10}Be/^{9}Be were normalized to the NIST standard SRM4325. Half-lives of 1.39 Ma (Korschinek et al., 2010) and 0.71 Ma and high-latitude, sea-level production rates of 4.6 and 31.1 atoms/g/year were used for ^{10}Be and ^{26}Al in the age calculation, respectively.

RESULTS

Geological and Geomorphological Interpretation of ATA

Based on the geological and geomorphological interpretation of satellite images and field investigations, our work depicted the geomorphologic expression and stratigraphic units of ATA in detail (**Figure 1**).

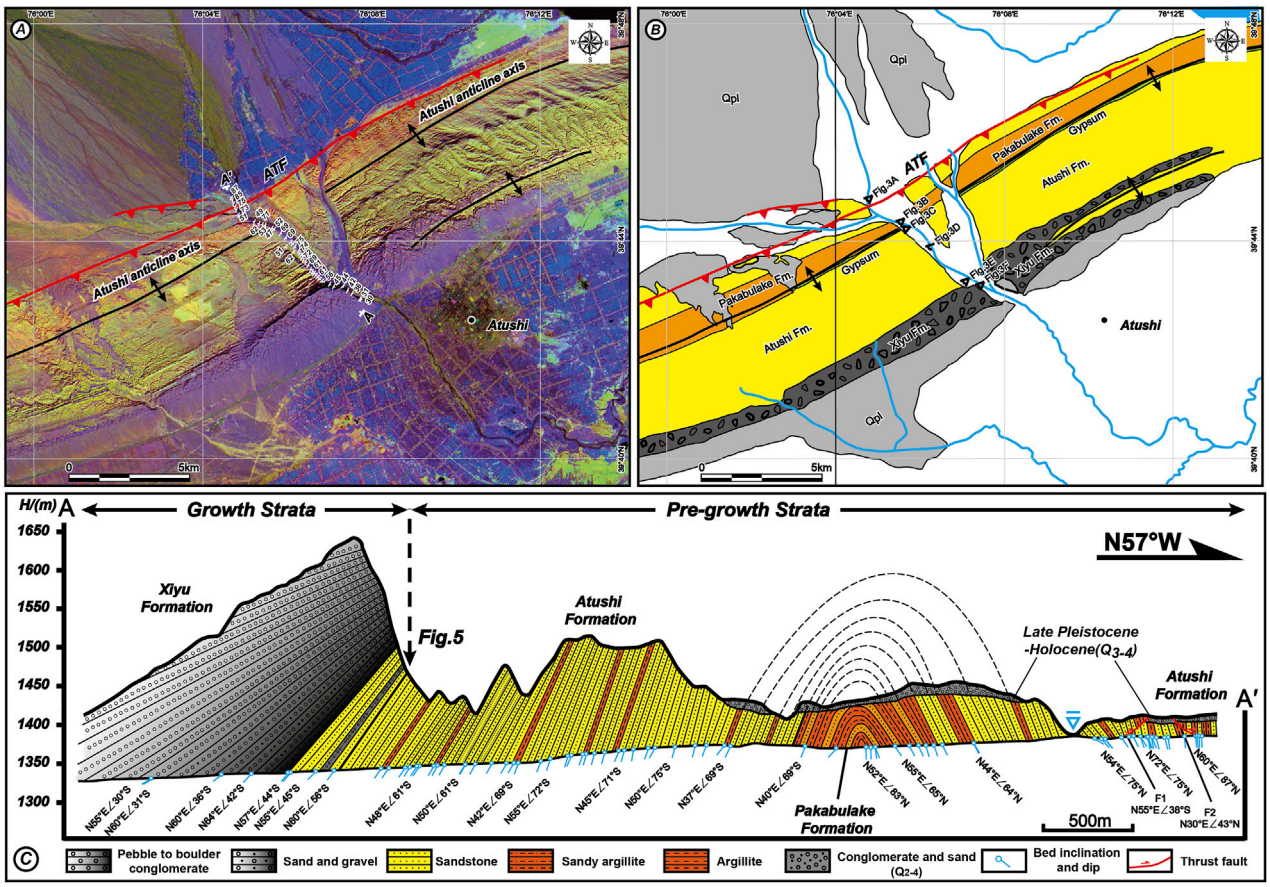

FIGURE 2 | (A) False-color ASTER composite image of 2/1(R), 3(G), and 5/8(B) of Atushi anticline. **(B)** Interpretation of satellite image. **(C)** Geological section observed on the western bank of Boguzi River (section A–A′ in **Figure 2A**).

TABLE 1 | Burial age of the upper layer of Atushi Formation and the lower layer of Xiyu Conglomerate.

Sample	Latitude (north)	Longitude (east)	Elevation (m)	Burial depth (m)	^{10}Be concentration ($\times10^4$ atg^{-1})	^{26}Al concentration ($\times10^4$ atg^{-1})	^{26}Al/^{10}Be	Burial age (Ma)
XY01	39°43.262′	76°06.856′	1,369	40	3.47 ± 0.13	9.2 ± 1.3	2.64 ± 0.38	1.94 ± 0.27
XY02	39°43.266′	76°06.845′	1,371	40	3.26 ± 0.15	8.4 ± 0.8	2.58 ± 0.27	1.99 ± 0.19
XY03	39°43.219′	76°06.897′	1,375	40	3.77 ± 0.16	10.7 ± 0.9	2.84 ± 0.26	1.79 ± 0.16
XY04	39°43.190′	76°06.940′	1,375	40	4.53 ± 0.16	13.7 ± 1.3	3.02 ± 0.30	1.67 ± 0.18

ATA is a growing fold with two asymmetric limbs (steep and narrow in the northern limb and gentle in the southern limb) and a tight hinge zone, with an axial surface dip to the south (**Figure 2C**). The surface expression of ATA extends to the Old Atushi town in the west and is interacted with MTA in the east, exceeding about 60 km along the axis of the fold (**Figure 1C**). A water gap formed in the middle part of ATA by the erosion of Boguzi River, and it provides an excellent geological section to observe and document the structural deformation and sedimentary features of ATA (**Figure 2**). Notably, our results indicated that a tight anticline developed at the east bank of Boguzi River along the southern flank of ATA (**Figure 2**).

The ATA has deformed Miocene Pakabulake Formation to Xiyu Conglomerate stratigraphic units (**Figure 2**). As shown in the ASTER false-color composite image (**Figure 2A**), the color patterns of Pakabulake Formation, Atushi Formation, and Xiyu Conglomerate are displayed as brownish-red, yellowish-green, and purplish-gray, respectively. The field investigations show that the Pakabulake Formation, exposed in the core of the anticline, is consisting of brownish-red argillite, sandy argillite, siltstone, and gypsum (**Figures**

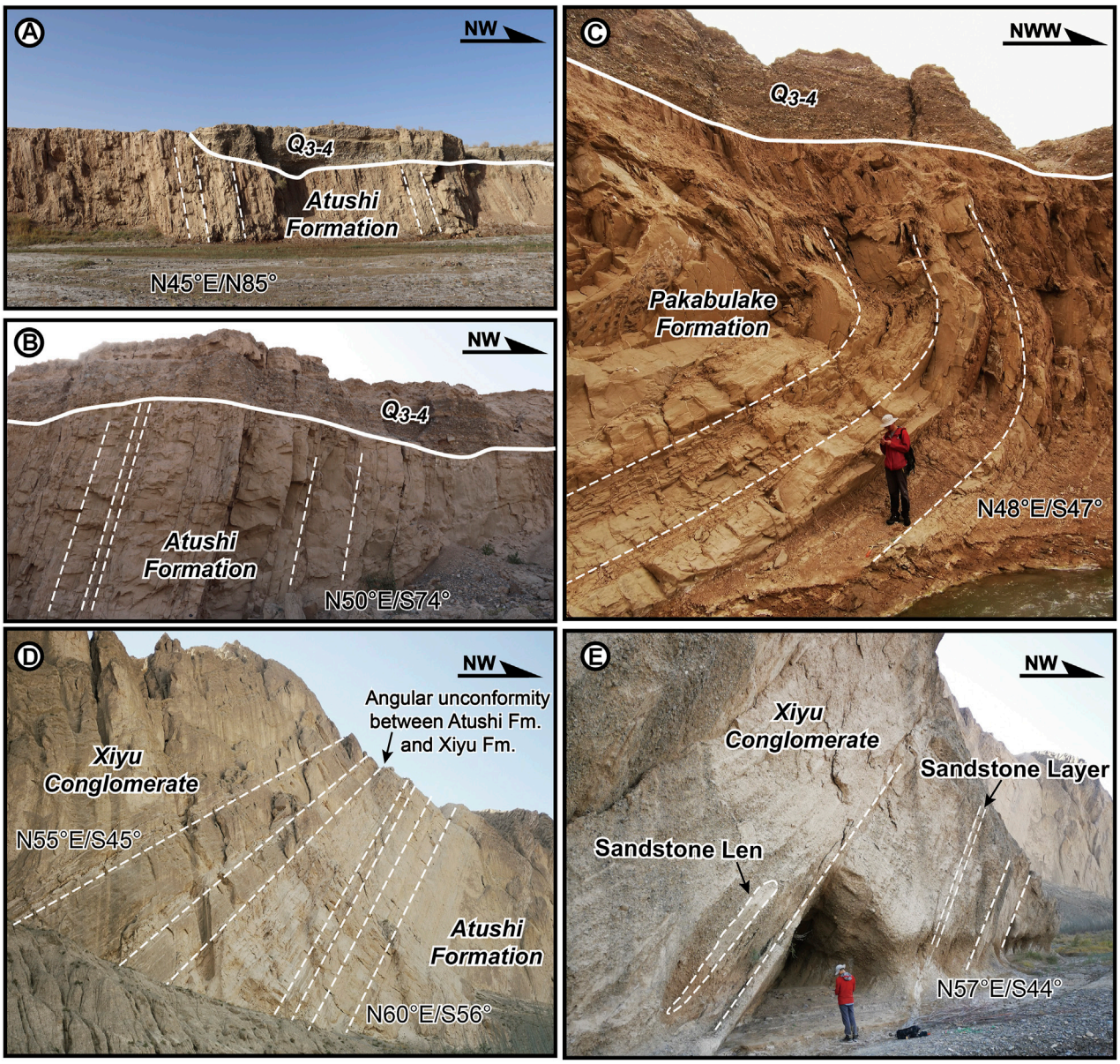

FIGURE 3 | Field photographs of the folded strata. **(A)** Picture of north-dipping Atushi Formation at the northern limb. **(B)** Picture of south-dipping Atushi Formation at the southern limb. **(C)** Intensive deformation of Pakabulake Formation in the core. **(D)** Angular unconformity between Atushi Formation and Xiyu Conglomerate. **(E)** Sandstone len and layer in gray Xiyu Conglomerate.

2B,C). The Atushi Formation is mainly composed of thick pale grayish-yellow sandstone, interbedded with thin brownish-red mudstone and containing a dark gray conglomerate at its top layer. The Xiyu Conglomerate is composed of a massive gray conglomerate containing grayish-yellow thin-bedded sandstone, siltstone layers, or lens (**Figure 3E**). The contact between Atushi Formation and Xiyu Conglomerate is displayed as a low-angular unconformity (**Figure 3D**).

The ATF is a south-dipping thrust fault extending along the north flank of ATA, which is affected by a northward thrusting deformation (**Figure 1B**; Yang et al., 2009; Fu et al., 2010). The fault scarps are developed on Late Quaternary proluvial and alluvial deposits of the Boguzi River along the ATF, showing that ATA is currently still active (**Figures 2B,C**).

$^{26}Al/^{10}Be$ Burial Age

Four fine-grained sandstone and siltstone samples were collected from the upper layer of Atushi Formation to the lower layer of the Xiyu Conglomerate at the southern flank of ATA (XY-01 to XY-04, **Figures 5B,C**). The sedimentary features of the upper layer of Atushi Formation and Xiyu Conglomerate are quite different. The upper layer of Atushi Formation is characterized by grayish

yellow sandstone interbedded with gray conglomerate, which is consisting of small-sized pebbles (1–3 cm) with fair sorting and subrounded psephicity. The Xiyu Formation is composed of dark gray, gray massive conglomerate, containing grayish-yellow thin-bedded sandstone, and siltstone layers or lens. The Xiyu Conglomerate is consisting of large- to medium-sized pebbles (5–10 cm) with bad sorting and subangular psephicity (**Figures 5D,E**). XY-01 and XY-02 were collected from the grayish-yellow sandstone and siltstone layers. XY-03 was sampled from the sandstone layer interbedded with conglomerate, where a low-angular unconformity has developed. These three samples were collected from the upper layer of Atushi Formation. XY-04 was sampled from the lenticular sandstone layer of Xiyu Conglomerate, near the boundary between the Atushi and Xiyu formations. To minimize production during incision and exhumation after the initial deposition, we collected samples from the sites that were well shielded by at least 30 m of rock. Sample information and ^{10}Be and ^{26}Al concentrations together with data on burial ages are shown in **Table 1**.

The ^{26}Al/^{10}Be ratios of XY-01, XY-02, XY-03, and XY-04, are 2.64 ± 0.38, 2.58 ± 0.27, 2.84 ± 0.26, and 3.02 ± 0.30, respectively. Although the ^{26}Al/^{10}Be ratio has a statistical difference from the model ^{26}Al/^{10}Be ratio of 6.76 ± 0.88 at the Earth's surface, the ^{26}Al/^{10}Be values of the four buried samples are consistent with each other. For buried samples that are within the range of muon production, the ^{10}Be and ^{26}Al concentrations will be functions of the initial concentrations at the time of burial, the burial time, and the burial depth as a function of time. Using the ^{26}Al/^{10}Be ratios, the burial ages range from 1.94 to 1.67 Ma. Our burial ages are almost equal to 1.7 Ma as obtained from the Boguzi River stratigraphic section (Sobel et al., 2006), but these are different from ~1.9 Ma for Xiyu Conglomerate as obtained by Chen et al. (2002) using magnetostratigraphy.

DISCUSSION

Geometries of the Growth Strata of ATA

Previous studies constrained the initial timing of deformation by dating the geologic age of the growth strata but rarely paid attention to the relationship between the growth mechanism of the fold and the sedimentary features of the growth strata (Sobel et al., 2006; Sun et al., 2009; Sun and Zhang, 2009). From the perspective of structural analysis, the growth mechanism of the thrust-related fold is mainly divided into two categories: hinge migration and hinge rotation (Shaw and Suppe, 1994; John and David, 1997; Hubert-Ferrari et al., 2007; Li et al., 2015; Li et al., 2018). Among the folds deformed by hinge migration, the geological age of the growth strata cannot simply represent the initial deformation timing of the fold. In this case, the hinge widening and dip angle might change over the hinge area in the pre-growth strata (Suppe et al., 1992; Salvini and Storti, 2002). On the other hand, the growth of the hinge rotation fold is through limb rotation, with the constant limb length and variable limb dip angle. The measurement of the onset age of the growth strata enabled us to constrain the initial deforming age of the limb rotation fold (Poblet et al., 1997).

Previous studies have already suggested that ATA belongs to the fold of the limb rotation growth mechanism based on the analyses of the geometry and dip panel (Chen et al., 2002), interpretation of seismic profile (Qu et al., 2001; Gao et al., 2013), and the measurement of the fold scarps (Li et al., 2018). According to our field investigation and mapping, we confirmed that the growth mechanism of ATA belongs to limb rotation (**Figure 4C**). The initial deposition of the growth strata could represent the beginning of the tectonic deformation of ATA.

Our results also show that the deformed late Cenozoic strata of Miocene Pakabulake Formation, Pliocene Atushi Formation, and Xiyu Conglomerate developed from the core to the southern limb of ATA (**Figure 2C**). Particularly, we carefully document the subtle change of bed dipping angles, bed width, and sedimentary features around the boundary of the growth and the pre-growth strata. Based on these criteria, we identified the sign layer that can represent the initial deposition of the growth strata (**Figure 5**). The sign layer consists of alluvial conglomerate interbedding with sandstone at the top layer of Atushi Formation. The low-angular unconformity starting from the dip angles of the sign layer are abruptly varying from 56° to 45° (**Figures 2C**, **5B**). Meanwhile, the width of the strata under the sign layer is constant (W_4, W_5, and W_6 in **Figure 5C**), but upward of the sign layer, the width of the strata is distinctly becoming thinner toward the crest, indicating that they accumulated during deformation (W_1, W_2, and W_3 in **Figure 5C**).

Timing of Syntectonic Deformation of ATA

The geological age of Pliocene–Pleistocene deposits in the KFTB is still controversial in previous studies (Chen et al., 2002; Sobel et al., 2006; Heermance et al., 2008). By using magnetostratigraphy dating data, Chen et al. (2002) suggested that the boundary ages between the Atushi Formation and Xiyu Conglomerate on the east bank of the Boguzi River and Ganhangou sections are ~1.9 and ~1.0 Ma, respectively. Consequently, they firstly proposed that the initial deformation time of ATA might start at ~1.4 and ~1.2 Ma in the above-mentioned two sections. However, the magnetostratigraphic sampling section located on the east bank of Boguzi River, where a secondary-scale anticline developed, led to the duplication of the Pliocene–Pleistocene strata (**Figures 2**, **4A**). The duplication of sedimentary stratigraphic units might bring confusion to the magnetochronological age data which relies on the continuous deposition of sedimentary strata. Moreover, the fine sandstone and argillite layers suitable for paleomagnetic study are very limited in the boundary between Atushi Formation and Xiyu Conglomerate. Thus, the timing of Xiyu Conglomerate age from a magnetochronological study remains uncertain, and accurate age dating of the growth strata and detailed research of structural deformation are urgently needed to constrain the Pliocene–Pleistocene tectonic deformation of ATA.

In this study, the ^{26}Al/^{10}Be burial age of the growth strata indicates that the initial deformation time of ATA can be traced to 1.79 ± 0.16 Ma, which is almost equal to 1.7 Ma (Sobel et al.,

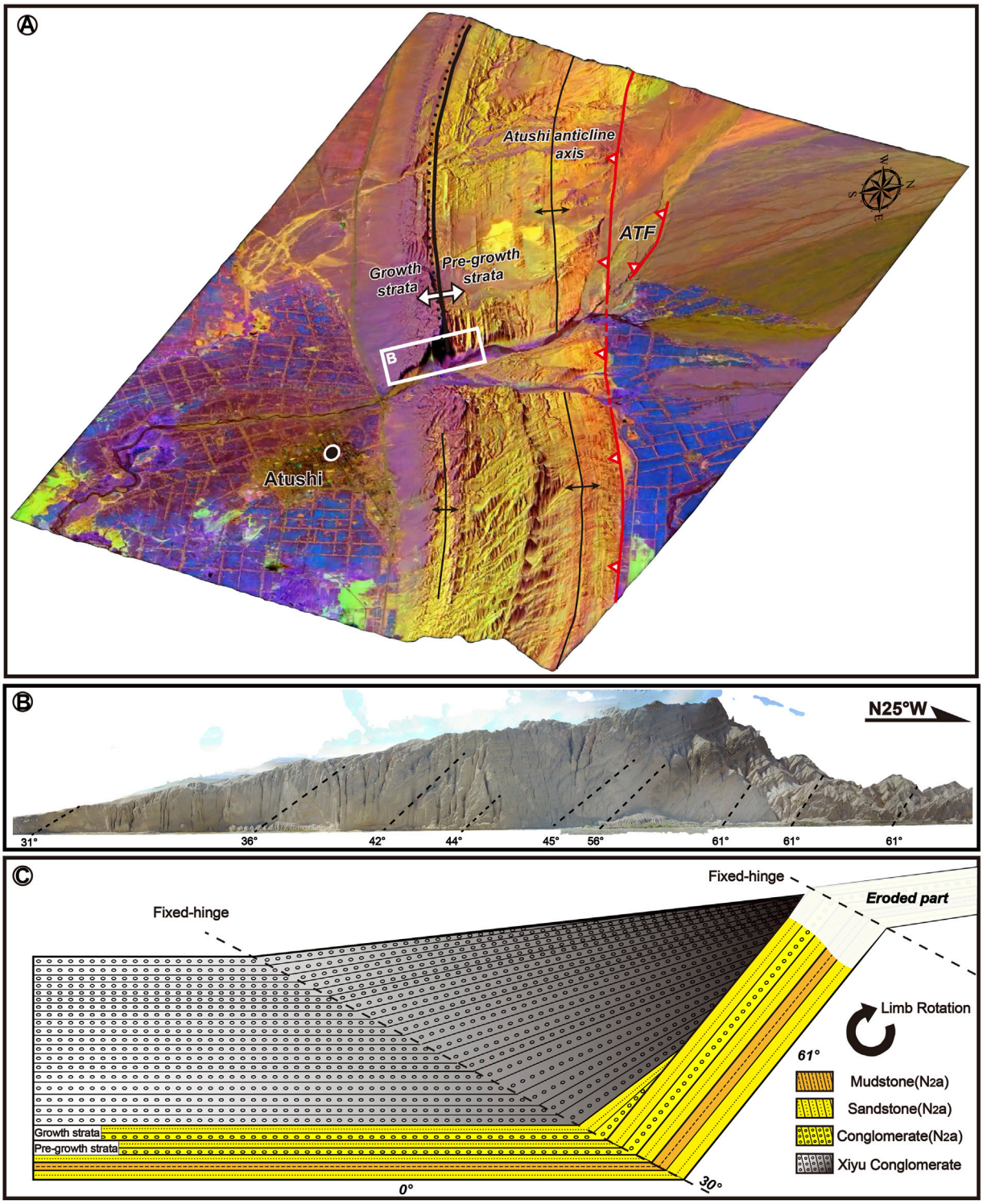

FIGURE 4 | (A) The 3D model of Boguzi River section. **(B)** Spliced pictures of the UAV horizontal imitating ground flight. **(C)** Geometry of the southern limb of Atushi anticline (ATA) and growth mechanism model of ATA based on our field mapping and the cross-section of ATA (Chen et al., 2002; Scharer et al., 2004; Li et al., 2018).

2006) and is different from ~1.4 Ma (Chen et al., 2002). Meanwhile, we proposed that the initial deposit time of Xiyu Conglomerate is about 1.67 ± 0.18 Ma, which is different from ~1.9 Ma in the eastern bank of Boguzi River section and ~1.0 Ma at the Ganhangou section. This phenomenon may be caused by the diachronous deposition of Xiyu Conglomerate (Chen et al.,

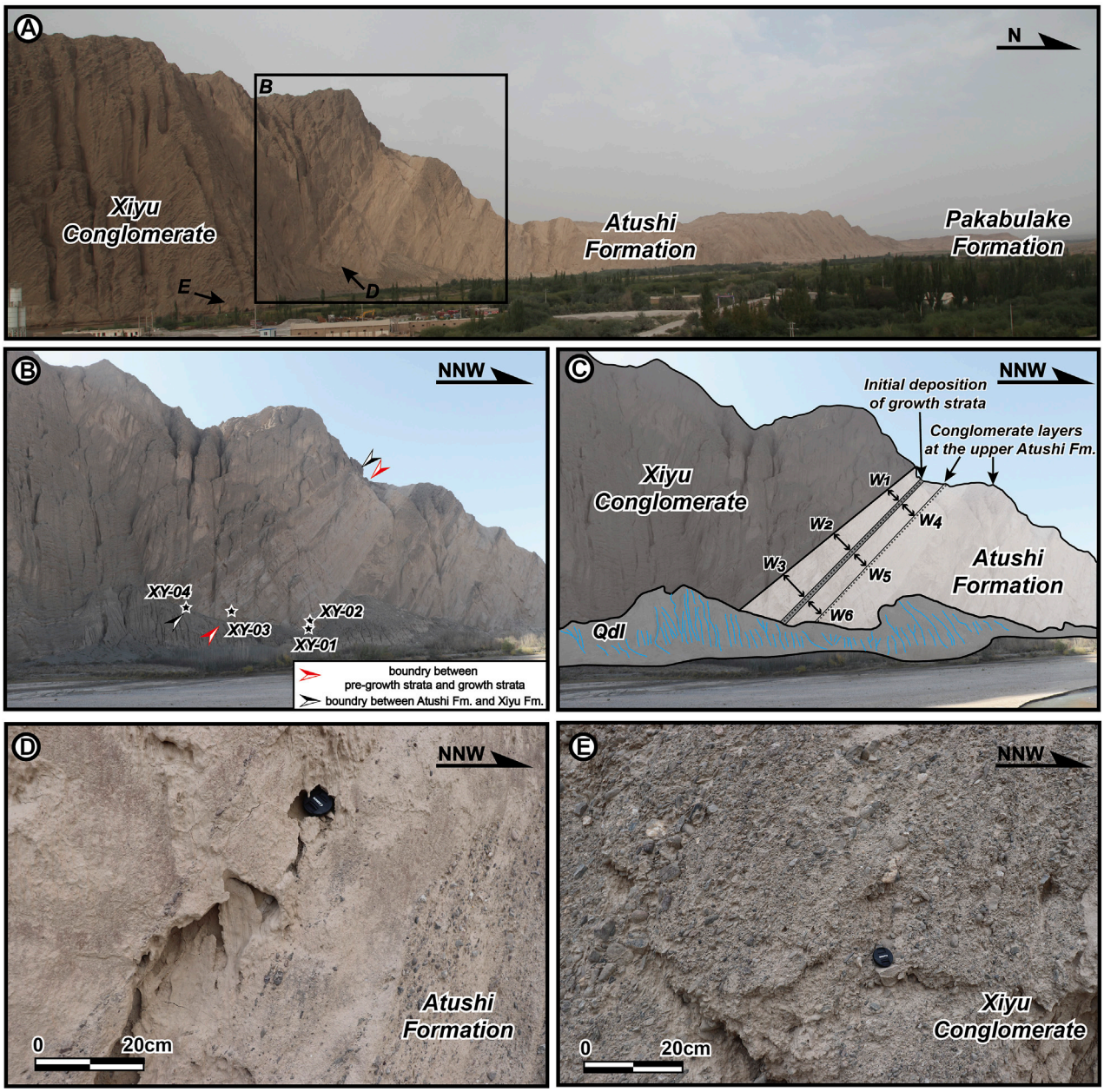

FIGURE 5 | Photographs showing the sedimentary strata near the boundary between Atushi Formation and Xiyu Conglomerate. **(A)** Photograph showing the geological section in the western bank of Boguzi River section. **(B)** Pliocene–Pleistocene strata. The black–white stars show the sampling points of four samples (XY01–XY04). The red arrow means the initial deposition boundary of growth strata and pre-growth strata. The black arrow represents the boundary between Atushi Formation and Xiyu Conglomerate. **(C)** Interpretation of photographs: W_1–W_6 indicated the internal width of adjacent coarse-grained layers, which developed at the top layer of Atushi Formation. **(D)** Photograph showing the sedimentary features of Atushi Fm. **(E)** Photograph showing the sedimentary features of Xiyu Conglomerate.

2000; Chen et al., 2007a; Chen et al., 2007b; Heermance et al., 2007; Qiao et al., 2016). The initial tectonic deformation age of ATA is similar to the middle Kalayuergun anticline (2.6–1.7 Ma) located at the western end of Baicheng-Kuqa foreland fold-and-thrust belt (Lv et al., 2019).

The previous studies have constrained the initial deformation time of west Atushi anticline (ca.3.8 Ma; Thompson-Jobe et al., 2018) and the Ganhangou section of Atushi anticline (1.2 Ma, Chen et al., 2002), respectively. Combined with the initial deformation age of the west bank of the Boguzi River section of Atushi anticline (1.79 Ma in this study), it can be concluded that the ages of the growth strata eastward along the Atushi anticline were younger. Therefore, the fold might have propagated eastward during the Pliocene to Quaternary, and the rate of lateral propagation is 18.6–24.3 km/Ma.

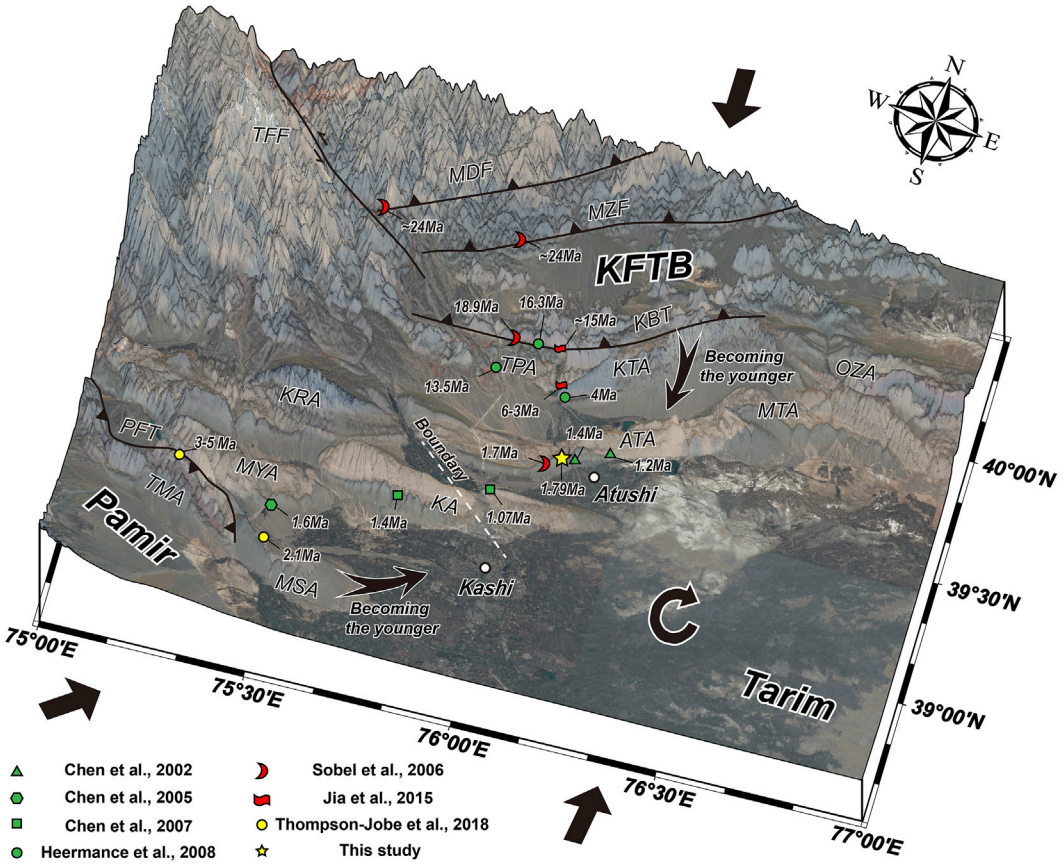

FIGURE 6 | Late Cenozoic deformation age of thrust–fold belts in the Pamir–Tian Shan convergence zone. The initial deformation ages of thrust–fold belts are becoming younger from Muziduke fault to the north flank of Kashi anticline in front of southwestern Tian Shan, displaying a southward propagation process in the Kashi foreland thrust–fold belt. The initial deformation ages of thrust–fold belts in front of northeastern Pamir are also becoming younger, suggesting a northward propagation process in northeastern Pamir.

Figure 6 shows that the initial deformation ages of thrust–fold belts are becoming younger from MZF to the north flank of KA in front of southwestern Tian Shan (Chen et al., 2002; Sobel et al., 2006; Chen et al., 2007a; Heermance et al., 2008; Jia et al., 2015), which indicated the southward multi-stage propagation processes in the KFTB. Meanwhile, recent studies also proposed that the initial deformation ages of the thrust–fold belts in front of northeastern Pamir are also becoming younger, which suggests a northward propagation process in northeastern Pamir (**Figure 6**; Chen et al., 2005, Chen et al., 2007a; Thompson-Jobe et al., 2018). The boundary of two opposite-verging thrust–fold belts along the PTCZ is likely distributed along KA (**Figure 6**; Fu et al., 2010).

CONCLUSION

The tectonic deformation of syntectonic growth strata related to a natural growth fold can provide a key to understand the coupling mechanisms of the sedimentary basin (KFTB) and adjacent southwestern Tian Shan orogenic belt. Our results from the geological and geomorphological interpretations of multiple remote sensing images as well as field investigations conclude that:

(1) The NEE-striking ATA extends about 60 km from the Old Atushi town in the west to the MTA in the east, with a steep limb at the north and a gentle limb at the south. The Miocene Pakabulake Formation is developed in the core, and the Pliocene–Pleistocene Atushi Formation and Xiyu Conglomerate are exposed in the southern limb.

(2) Syntectonic growth strata developed at the southern limb of ATA, which caused the dip angles of Pliocene–Pleistocene strata abruptly changing southward from 56° to 45°, and the width of the strata is distinctly becoming thinner toward the crest at the top part of Atushi Formation. The initial deposit of the growth strata could represent the onset of limb rotation deformation of ATA.

(3) The cosmogenic nuclide $^{26}Al/^{10}Be$ burial age could be constrained as the initial time of growth strata at 1.79 ± 0.16 Ma. The initial deposit of the diachronous Xiyu

Conglomerate began at about 1.67 ± 0.18 Ma. The late Pliocene to early Pleistocene is an important episode of intracontinental deformation in the KFTB, which is a tectonic–sedimentary response to the ongoing convergence between Pamir and Tian Shan.

DATA AVAILABILITY STATEMENT

The original contributions presented in the study are included in the article/Supplementary Material, further inquiries can be directed to the corresponding author.

AUTHOR CONTRIBUTIONS

QC and BF designed the study, did the fieldwork, and wrote the manuscript. PS worked on the processing of UAV remote sensing data and field investigations. PK contributed to age dating of the cosmogenic nuclide samples.

FUNDING

This work was funded by the Strategic Priority Research Program of the Chinese Academy of Sciences (XDA 20070202) and the Second Tibetan Plateau Scientific Expedition and Research Program (STEP, grant no. 2019QZKK0901).

ACKNOWLEDGMENTS

We appreciate the two reviewers for their constructive comments and suggestions, which help to largely improve the quality of this paper. We also gratefully acknowledge the beneficial discussion of Dr. Zhenyu Wang of the Institute of Earthquake Forecasting, China Earthquake Administration.

REFERENCES

Allen, M. B., Vincent, S. J., and Wheeler, P. J. (1999). Late Cenozoic Tectonics of the Kepingtage Thrust Zone: Interactions of the Tien Shan and Tarim Basin, Northwest China. *Tectonics* 18 (4), 639–654. doi:10.1029/1999TC900019

Avouac, J. P., Tapponnier, P., Bai, M., You, H., and Wang, G. (1993). Active Thrusting and Folding along the Northern Tien Shan and Late Cenozoic Rotation of the Tarim Relative to Dzungaria and Kazakhstan. *J. Geophys. Res.* 98, 6755–6804. doi:10.1029/92JB01963

Balco, G., and Shuster, D. L. (2009). ^{26}Al–^{10}Be–^{21}Ne Burial Dating. *Earth Planet. Sci. Lett.* 286 (3-4), 570–575. doi:10.1016/j.epsl.2009.07.025

Burtman, V. S., and Molnar, P. (1993). Geological and Geophysical Evidence for Deep Subduction of Continental Crust beneath the Pamir. *Geol. Soc. America* 281, 1–76. doi:10.1130/SPE281-p1

Chen, J., Ding, G., Burbank, D. W., Scharer, K., Rubin, C., Sobel, E., et al. (2001). Late Cenozoic Tectonics and Seismicity in the Southwestern Tianshan, China. *Earthquake research in China* 17 (2), 134–155. [in Chinese with English abstract]. CNKI:SUN:ZGZD.0.2001-02-003.

Chen, H. L., Chen, Y. G., Chen, S. Q., Lin, X. B., Yang, R., Cheng, X. G., et al. (2019). The Tectonic Processes and Geomorphic Characteristics of Pamir Salient. *Acta Geoscientica Sinica* 40 (1), 55–75. [in Chinese with English abstract]. doi:10.3975/cagsb.2018.092603

Chen, J., Burbank, D. W., Scharer, K. M., Sobel, E., Yin, J. H., Rubin, C., et al. (2002). Magnetochronology of the Upper Cenozoic Strata in the Southwestern Chinese Tian Shan: Rates of Pleistocene Folding and Thrusting. *Earth Planet. Sci. Lett.* 195 (1-2), 113–130. doi:10.1016/S0012-821X(01)00579-9

Chen, J., Heermance, R., Burbank, D. W., Scharer, K. M., Miao, J., and Wang, C. (2007a). Quantification of Growth and Lateral Propagation of the Kashi Anticline, Southwest Chinese Tian Shan. *J. Geophys. Res.* 112 (B3). doi:10.1029/2006jb004345

Chen, J., Heermance, R. V., Burbank, D. W., Scharer, K. M., and Wang, C. S. (2007b). Magnetochronology and its Implications of the Xiyu Conglomerate in the Southwestern Chinese Tian Shan Foreland. *Quat. Sci.* 27 (4), 576–587. [in Chinese with English abstract]. doi:10.3321/j.issn:1001-7410.2007.04.014

Chen, J., Scharer, K. M., Burbank, D. W., Heermance, R. V., and Wang, C. S. (2005). Quaternary Detachment Folding of the Mingyaole Anticline, Southwestern Tian Shan. *Seismology Geology.* 27 (4), 530–547. [in Chinese with English abstract]. doi:10.3969/j.issn.0253-4967.2005.04.002

Chen, J., Yin, J. H., Qu, G. S., and Zhang, K. Q. (2000). Timing, Lower Boundary, Genesis, and Deformation of Xiyu Formation Around the Western Margins of the Tarim basin. *Seismology Geology.* 22, 104–116. [in Chinese with English abstract] CNKI:SUN:DZDZ.0.2000-S1-014. doi:10.3969/j.issn.0253-4967.2005.04.002

Fu, B., Ninomiya, Y., and Guo, J. (2010). Slip Partitioning in the Northeast Pamir-Tian Shan Convergence Zone. *Tectonophysics* 483 (3-4), 344–364. doi:10.1016/j.tecto.2009.11.003

Gao, R., Hou, H., Cai, X., Knapp, J. H., He, R., Liu, J., et al. (2013). Fine Crustal Structure beneath the junction of the Southwest Tian Shan and Tarim Basin, NW China. *Lithosphere* 5 (4), 382–392. doi:10.1130/l248.1

Granger, D. E., Lifton, N. A., and Willenbring, J. K. (2013). A Cosmic Trip: 25 Years of Cosmogenic Nuclides in Geology. *Geol. Soc. America Bull.* 125 (9-10), 1379–1402. doi:10.1130/b30774.1

Granger, D. E., and Muzikar, P. F. (2001). Dating Sediment Burial with In Situ-produced Cosmogenic Nuclides: Theory, Techniques, and Limitations. *Earth Planet. Sci. Lett.* 188, 269–281. doi:10.1016/S0012-821X(01)00309-0

Hardy, S., and Cardozo, N. (2021). Discrete Element Modelling of Sedimentation and Tectonics: Implications for the Growth of Thrust Faults and Thrust Wedges in Space and Time, and the Interpretation of Syn-Tectonic (Growth) Strata. *Front. Earth Sci.* 9. doi:10.3389/feart.2021.742204

Heermance, R. V., Chen, J., Burbank, D. W., and Miao, J. J. (2008). Temporal Constraints and Pulsed Late Cenozoic Deformation during the Structural Disruption of the Active Kashi Foreland, Northwest China. *Tectonics* 27 (6). doi:10.1029/2007tc002226

Heermance, R. V., Chen, J., Burbank, D. W., and Wang, C. (2007). Chronology and Tectonic Controls of Late Tertiary Deposition in the Southwestern Tian Shan Foreland, NW China. *Basin Res.* 19 (4), 599–632. doi:10.1111/j.1365-2117.2007.00339.x

Hubert-Ferrari, A., Suppe, J., Gonzalez-Mieres, R., and Wang, X. (2007). Mechanisms of Active Folding of the Landscape (Southern Tian Shan, China). *J. Geophys. Res.* 112 (B3). doi:10.1029/2006jb004362

Jia, Y., Fu, B., Jolivet, M., and Zheng, S. (2015). Cenozoic Tectono-Geomorphological Growth of the SW Chinese Tian Shan: Insight from AFT and Detrital Zircon U-Pb Data. *J. Asian Earth Sci.* 111, 395–413. doi:10.1016/j.jseaes.2015.06.023

John, H. S., and David, A. M. (1997). Effect of Initial Fault Geometry on the Development of Fixed-Hinge, Fault-Propagation Folds. *J. Struct. Geology.* 19 (12), 1537–1541. doi:10.1016/S0191-8141(97)00065-5

Jungers, M. C., and Heimsath, A. M. (2015). Post-tectonic Landscape Evolution of a Coupled basin and Range: Pinaleño Mountains and Safford Basin, southeastern Arizona. *Geol. Soc. America Bull.* 128 (3-4), 469–486. doi:10.1130/b31276.1

Kong, P., Zheng, Y., and Fu, B. (2011). Cosmogenic Nuclide Burial Ages and Provenance of Late Cenozoic Deposits in the Sichuan Basin: Implications for Early Quaternary Glaciations in East Tibet. *Quat. Geochronol.* 6 (3-4), 304–312. doi:10.1016/j.quageo.2011.03.006

Korschinek, G., Bergmaier, A., Faestermann, T., Gerstmann, U. C., Knie, K., Rugel, G., et al. (2010). A New Value for the Half-Life of 10Be by Heavy-Ion Elastic

Recoil Detection and Liquid Scintillation Counting. *Nucl. Instr. Methods Phys. Res. Section B: Beam Interactions Mater. Atoms* 268 (2), 187–191. doi:10.1016/j.nimb.2009.09.020

Lal, D., and Arnold, J. R. (1985). Tracing Quartz through the Environment. *J. Earth Syst. Sci.* 94 (1), 1–5. doi:10.1007/bf02863403

Li, T., Chen, J., Thompson, J. A., Burbank, D. W., and Yang, H. (2015). Hinge-migrated Fold-scarp Model Based on an Analysis of Bed Geometry: A Study from the Mingyaole Anticline, Southern Foreland of Chinese Tian Shan. *J. Geophys. Res. Solid Earth* 120 (9), 6592–6613. doi:10.1002/2015jb012102

Li, T., Chen, J., Thompson, J. A., Burbank, D. W., and Yang, X. (2013). Quantification of Three-Dimensional Folding Using Fluvial Terraces: A Case Study from the Mushi Anticline, Northern Margin of the Chinese Pamir. *J. Geophys. Res. Solid Earth* 118 (8), 4628–4647. doi:10.1002/jgrb.50316

Li, T., Chen, J., Thompson Jobe, J. A., Burbank, D. W., Cheng, X., Xu, J., et al. (2018). Active Bending-Moment Faulting: Geomorphic Expression, Controlling Conditions, Accommodation of Fold Deformation. *Tectonics* 37, 2278–2306. doi:10.1029/2018TC004982

Li, Z., Li, T., Almeida, R., Zhang, P., Zheng, W., Sun, C., et al. (2019). Lateral Fault Growth in the Kashi Anticline (Chinese Tian Shan): Insights from Seismic Interpretation, Shortening Distribution, and Trishear Methods. *J. Geophys. Res. Solid Earth* 124 (7), 7303–7319. doi:10.1029/2018jb017186

Liu, T. S., Ding, M. L., and Edward, D. (1996). Gravel Deposits on the Margins of the Qinghai-Xizang Plateau, and Their Environmental Significance. *Palaeogeogr. Palaeoclimatol. Palaeoecol.* 120 (1-2), 159–170. doi:10.1016/0031-0182(95)00039-9

Lü, L., Sun, J., Zhang, Z., Jia, Y., Li, T., Li, C., et al. (2019). Cenozoic Deformation and Crustal Shortening in the Foreland of Southern Tian Shan, NW China, as a Response to the India-Asia Collision. *J. Asian Earth Sci.* 183, 103960. doi:10.1016/j.jseaes.2019.103960

McCalpin, J. P., and Nelson, A. R. (1996). Chapter 1 Introduction to Paleoseismology. *Int. Geophys.* 62, 1–32. doi:10.1016/s0074-6142(96)80068-4

Molnar, P., and Tapponnier, P. (1975). Cenozoic Tectonics of Asia: Effects of a Continental Collision: Features of Recent continental Tectonics in Asia Can Be Interpreted as Results of the India-Eurasia Collision. *Science* 189 (4201), 419–426. doi:10.1126/science.189.4201.419

Poblet, J., McClay, K., Storti, F., and Mufioz, J. A. (1997). Geometries of Syntectonic Sediments Associated with Single-Layer Detachment Folds. *J. Struct. Geology.* 19 (3), 369–381. doi:10.1016/S0191-8141(96)00113-7

Qiao, Q., Huang, B., Piper, J. D. A., Deng, T., and Liu, C. (2016). Neogene Magnetostratigraphy and Rock Magnetic Study of the Kashi Depression, NW China: Implications to Neotectonics in the SW Tianshan Mountains. *J. Geophys. Res. Solid Earth* 121 (3), 1280–1296. doi:10.1002/2015jb012687

Qu, G., Chen, J., Chen, X., Canerot, J., and Li, Y. (2001). A Study on the Back-Thrusting System at Atushi-Bapanshuimo in Tarim Basin. *Seismology and Geology* 23, 1–14. [in Chinese with English abstract].

Riba, O. (1976). Syntectonic Unconformities of the Alto Cardener, Spanish Pyrenees: a Genetic Interpretation. *Sediment. Geology.* 15, 213–233. doi:10.1016/0037-0738(76)90017-8

Salvini, F., and Storti, F. (2002). Three-dimensional Architecture of Growth Strata Associated to fault-bend, Fault-Propagation, and Décollement Anticlines in Non-erosional Environments. *Sediment. Geology.* 146, 57–73. doi:10.1016/S0037-0738(01)00166-X

Scharer, K. M., Burbank, D. W., Chen, J., Weldon, R. J., Rubin, C., Zhao, R., et al. (2004). Detachment Folding in the Southwestern Tian Shan-Tarim Foreland, China: Shortening Estimates and Rates. *J. Struct. Geology.* 26, 2119–2137. doi:10.1016/j.jsg.2004.02.016

Shaw, J. H., and Suppe, J. (1994). Active Faulting and Growth Folding in the Eastern Santa Barbara Channel, California. *Geol. Soc. America Bull.* 106 (5), 607–626. doi:10.1130/0016-7606(1994)106<0607:afagfi>2.3.co;2

Sobel, E., Chen, J., and Heermance, R. (2006). Late Oligocene-Early Miocene Initiation of Shortening in the Southwestern Chinese Tian Shan: Implications for Neogene Shortening Rate Variations. *Earth Planet. Sci. Lett.* 247 (1-2), 70–81. doi:10.1016/j.epsl.2006.03.048

Sobel, E. R., and Dumitru, T. A. (1997). Thrusting and Exhumation Around the Margins of the Western Tarim basin during the India-Asia Collision. *J. Geophys. Res.* 102 (B3), 5043–5063. doi:10.1029/96jb03267

Sun, J., Li, Y., Zhang, Z., and Fu, B. (2009). Magnetostratigraphic Data on Neogene Growth Folding in the Foreland basin of the Southern Tianshan Mountains. *Geology* 37 (11), 1051–1054. doi:10.1130/g30278a.1

Sun, J. M., Zhu, R. X., and Bowler, J. (2004). Timing of the Tianshan Mountains Uplift Constrained by Magnetostratigraphic Analysis of Molasse Deposits. *Earth Planet. Sci. Lett.* 219 (3-4), 239–253. doi:10.1016/s0012-821x(04)00008-1

Sun, J., and Zhang, Z. (2009). Syntectonic Growth Strata and Implications for Late Cenozoic Tectonic Uplift in the Northern Tian Shan, China. *Tectonophysics* 463 (1-4), 60–68. doi:10.1016/j.tecto.2008.09.008

Suppe, J., Chou, G. T., and Hook, S. C. (1992). Rates of Folding and Faulting Determined from Growth Strata. *Thrust Tectonics*, 105–121. doi:10.1007/978-94-011-3066-0_9

Thompson-Jobe, J. A., Burbank, D. W., Li, T., Chen, J., and Bookhagen, B. (2015). Late Miocene Northward Propagation of the Northeast Pamir Thrust System, Northwest China. *Tectonics* 34 (3), 510–534. doi:10.1002/2014tc003690

Thompson-Jobe, J. A., Li, T., Bookhagen, B., Chen, J., and Burbank, D. (2018). Dating Growth Strata and basin Fill by Combining 26Al/10Be Burial Dating and Magnetostratigraphy: Constraining Active Deformation in the Pamir-Tian Shan Convergence Zone, NW China. *Lithosphere* 10 (6), 806–828. doi:10.1130/L727.1

Thompson-Jobe, J. A., Li, T., Chen, J., Burbank, D. W., and Bufe, A. (2017). Quaternary Tectonic Evolution of the Pamir-Tian Shan Convergence Zone, Northwest China. *Tectonics* 36 (12), 2748–2776. doi:10.1002/2017tc004541

Tian, Q., Ding, G., Hao, P., Canerot, J., and Li, Y. (2006). Seismotectonic Study on West Part of the Interaction Zone Between Southern Tianshan and Northern Tarim. *Seismology and Geology* 28, 213–223. [in Chinese with English abstract].

Wu, C., Zheng, W., Zhang, P., Zhang, Z., Jia, Q., Yu, J., et al. (2019). Oblique Thrust of the Maidan Fault and Late Quaternary Tectonic Deformation in the Southwestern Tian Shan, Northwestern China. *Tectonics* 38 (8), 2625–2645. doi:10.1029/2018tc005248

Yang, X., Chen, L., Li, A., Du, L., and Deng, Q. (2009). Late Quaternary Phased Uplift of the Atushi Anticline in the Southwestern Tianshan. *Earth Science Frontiers* 16 (3), 160–170. [in Chinese with English abstract] CNKI:SUN:DXQY.0.2009-03-018.

Yin, A., Nie, S., Craig, P., Harrison, T. M., Ryerson, F. J., Xianglin, Q., et al. (1998). Late Cenozoic Tectonic Evolution of the Southern Chinese Tian Shan. *Tectonics* 17 (1), 1–27. doi:10.1029/97tc03140

Zhang, Z., Han, W., Fang, X., Song, C., and Li, X. (2013). Late Miocene-Pleistocene Aridification of Asian Inland Revealed by Geochemical Records of Lacustrine-Fan delta Sediments from the Western Tarim Basin, NW China. *Palaeogeogr. Palaeoclimatol. Palaeoecol.* 377, 52–61. doi:10.1016/j.palaeo.2013.03.008

Zhao, R. B., Li, J., and Shen, J. (2001). Preliminary Study on the Deformation Features and Seismogenic Model of the 1902 Artux, Xinjiang Earthquake of Ms8¼. *Seismology Geology.* 23 (4), 581–587. [in Chinese with English abstract]. doi:10.1007/s11769-000-0051-4

Conflict of Interest: The authors declare that the research was conducted in the absence of any commercial or financial relationships that could be construed as a potential conflict of interest.

Publisher's Note: All claims expressed in this article are solely those of the authors and do not necessarily represent those of their affiliated organizations, or those of the publisher, the editors and the reviewers. Any product that may be evaluated in this article, or claim that may be made by its manufacturer, is not guaranteed or endorsed by the publisher.

Copyright © 2022 Chen, Fu, Shi and Kong. This is an open-access article distributed under the terms of the Creative Commons Attribution License (CC BY). The use, distribution or reproduction in other forums is permitted, provided the original author(s) and the copyright owner(s) are credited and that the original publication in this journal is cited, in accordance with accepted academic practice. No use, distribution or reproduction is permitted which does not comply with these terms.

frontiers | Frontiers in Earth Science

ORIGINAL RESEARCH
published: 05 April 2022
doi: 10.3389/feart.2022.846949

Strain Distribution Along the Qilian Fold-and-Thrust Belt Determined From GPS Velocity Decomposition and Cluster Analysis: Implications for Regional Tectonics and Deformation Kinematics

*Guoqiang Zhao and Zhengyang Pan**

Key Laboratory of Earthquake Forecasting, Institute of Earthquake Forecasting, China Earthquake Administration, Beijing, China

OPEN ACCESS

Edited by:
Xuhua Shi,
Zhejiang University, China

Reviewed by:
Yiran Wang,
Nanyang Technological University, Singapore
Keliang Zhang,
Institute of Geology China Earthquake Administration, China

****Correspondence:***
Zhengyang Pan
panzhengyang@ief.ac.cn

Specialty section:
This article was submitted to Structural Geology and Tectonics, a section of the journal Frontiers in Earth Science

Received: *31 December 2021*
Accepted: *10 March 2022*
Published: *05 April 2022*

Citation:
Zhao G and Pan Z (2022) Strain Distribution Along the Qilian Fold-and-Thrust Belt Determined From GPS Velocity Decomposition and Cluster Analysis: Implications for Regional Tectonics and Deformation Kinematics. Front. Earth Sci. 10:846949. doi: 10.3389/feart.2022.846949

The Qilian fold-and-thrust belt (QFTB) offers an excellent example to demonstrate the strain transition from strike–slip shearing to oblique crustal shortening, which plays an important role in dissecting the stress propagation of Indian–Eurasian convergence from the plateau interior to the surrounding blocks. Various geological or numerical models have attempted to describe the regional tectonic characteristics of the QFTB. However, these models only interpret one or part of the deformation behaviors in the QFTB, and the strain distribution across and along the QFTB as well as its deformation kinematics remains to be determined. Therefore, in this work, we applied the method of velocity decomposition and cluster analysis using combined GPS data to determine the strain partition or accommodation in different parts of the QFTB as well as tectonic relationships with surrounding blocks, which will contribute to distinguishing which model is more suitable for delineating the present-day deformation kinematics of the QFTB. Our analysis indicates that the western part of the QFTB is dominated mainly by crustal shortening perpendicular to the trend of the QFTB, coupled with lateral extension along the trend of the QFTB, while the eastern part of the QFTB is characterized mainly by lateral extrusion owing to the impact of two large eastward-striking left-slip faults (East Kunlun fault and Haiyuan fault), which are accommodated by an obvious velocity gradient boundary belt centered on two diamond basins (Qinghaihu and Gonghe basins) associated with their boundary faults. The active tectonics of the QFTB are obviously divided into two distinct groups: one group is a pure shear–strain pattern, accounting for strong crustal shortening in the western part of the QFTB, and the other group is a simple shear–strain pattern, accounting for the obvious lateral extrusion in the eastern part of the QFTB.

Keywords: Qilian fold-and-thrust belt, GPS velocity decomposition, cluster analysis, pure shear–strain pattern, simple shear–strain pattern

1 INTRODUCTION

The Qilian fold-and-thrust belt (QFTB) is located on the northeastern forefront boundary of the Tibetan Plateau, adjoining the Alashan Block and Ordos Block, which provides a natural laboratory to study how the deformation pattern of the periphery of the Tibetan Plateau is influenced by the remote effect of Indian–Eurasian convergence (Burchfiel et al., 1989; Tapponnier et al., 1990; Meyer et al., 1998; Dupont-Nivet et al., 2004; Lease et al., 2012; Yuan et al., 2013). At the same time, the QFTB also offers the best place to quantify the formation and evolution of large left-lateral strike–slip faults (Altyn Tagh fault, Haiyuan fault, and East Kunlun fault), partitioning or accommodating the strain diffusion of Indian–Eurasian convergence (Burchfiel et al., 1991; Meyer et al., 1996; Kirby et al., 2007; Zheng D. et al., 2017). The junction between the North–South Seismic Belt and the Haiyuan–Liupanshan–Luohe Seismic Belt has hosted more than ten earthquakes of magnitude 7 or higher in the past several hundred years in the QFTB, including the famous Haiyuan 8.5 earthquake and the Gulang 8.0 earthquake (Gaudemer et al., 1995; Zhang, 2013). These intense tectonic activities are inextricably linked to fault strain accumulation and regional stress concentrations in the QFTB (Hu et al., 2017; Pan et al., 2020). Therefore, studying contemporary deformation around the QFTB can not only contribute to a better understanding of how the strain from the Indian–Eurasian convergence is allocated between these large-scale strike–slip faults and their surrounding blocks but also facilitate comprehending intracontinental earthquake occurrence processes and fault dynamic behavior and better assessing the risk of earthquakes and geological disasters in this region.

Therefore, in this study, we utilized the updated GPS velocity field and improved the analysis method to further discover subtle deformation characteristics and detailed tectonic kinematics of the QFTB and advanced ongoing research regarding the kinetic mechanisms. First, we combined the previous GPS velocity field and transferred this to a common reference frame and provided a full new map of crustal movement of the QFTB. Next, we decomposed the combined GPS velocity field into the crustal shortening parallel and perpendicular to the trend of the QFTB, which helped quantify how the velocities varied across the different parts of the QFTB. Then, we applied cluster analysis to the combined GPS velocity field, and on each cluster, we utilized the spherical GPS strain algorithm by least-square estimation to discover detailed kinematic characteristics. Finally, by combining the aforementioned results with previous geodetic, geological, and geophysical data, the deformation patterns and the dominant kinematic mechanisms in the QFTB were examined. The results of our study have important significance for further research on the dynamic mechanisms and evolving processes of plateau growth and expansion.

2 TECTONIC SETTING OF THE QFTB

The QFTB defines the northeastern boundary of the Tibetan Plateau, which is characterized by folds, thrust faults, strike–slip faults, and intermontane basins spaced at ~30–40 km that partially accommodate Indian–Eurasian convergence (Tapponnier et al., 1990; Meyer et al., 1998). It is bounded by several tectonic blocks, which include the Alashan Block to the northeast, Ordos Block to the east of the western North China Craton, Qaidam Block to the southwest, and Tarim Block to the northwest. This orogenic belt is ~100 km wide and ~1,000 km long, and its average elevation is ~4.5 km. Its boundaries comprise several left-lateral strike–slip faults, including the left strike–slip East Kunlun, Altyn Tagh, and Haiyuan faults that extend for ~1,500, ~2000, and ~1,000 km, respectively, which are the longest and most continuous structures on the northeastern Tibetan Plateau (Zuza and Yin, 2016). Among these large strike–slip faults, the NNW- to NWW-trending faults (Riyueshan fault, Elashan fault, Qilian Nanshan thrust faults, and Qaidam Basin thrust faults), associated with secondary tectonic structures, including two diamond basins (Qinghaihu and Gonghe basins), accommodate the internal tectonic deformation of the QFTB (Duvall et al., 2011; Yuan et al., 2013; Lease, 2014; Zuza and Yin, 2016). The formation of the QFTB originated from the closure of the Qilian Ocean during the collision between the Qaidam–Kunlun terrane and North China Craton, which has been considered an example of an ancient oceanic subduction zone that records a complete history of the Proto-Tethyan Ocean from the seafloor spreading and subduction to the ultimate continental collision (Gehrels et al., 2011; Song et al., 2013). To date, it still suffers significant crustal shortening and intensive active deformation (Meyer et al., 1998).

A great deal of achievements has been made on active tectonics of the QFTB and its surrounding regions. For example, horizontal GPS velocities show that the QFTB is experiencing crustal shortening with a horizontal shortening rate of 8.7 ± 1.8 mm/yr in the NE-SW direction (Zhang et al., 2004; Zheng G. et al., 2017; Ma et al., 2017); of this shortening rate, approximately 5.5 ± 1.8 mm/yr is accommodated across the Qilian Shan. This indicates that in the northeastward movement of the Indian continent at a rate of 36–40 mm/yr, the Qilian Shan, together with the Qaidam–Kunlun terranes, accommodates 20–25% of Indian–Eurasian convergence (Zhang et al., 2004; Gan et al., 2007; Zhao et al., 2015; Zheng G. et al., 2017). Vertical GPS velocities confirm that ongoing uplift is occurring along the Qilian Mountains at a rate of 1~2 mm/yr, which is analogous to most of the Tibetan Plateau (Liang et al., 2013). The new GPS strain rate field indicates that NE-SW shortening and NW-SE extension are predominant deformation characteristics in the QFTB, and the deformation is distributed across a series of faults and blocks (Wang and Shen, 2020), which is consistent with the results of geological surveying (Yin and Harrison, 2000). Receiver-function studies also support this surface deformation pattern, which suggests that the formation of the Qilian fold-and-thrust belt was mainly influenced by the superposition of crustal blocks during the collision of the Eurasian and Indian plates (Li et al., 2015). This pattern emphasizes limited, passive deformation of the bounding Asian lithosphere as it encounters the growing Tibetan Plateau (Shen et al., 2015), and suggests vertical coherent deformation within the lithosphere beneath the Qilian fold-and-thrust belt and its

surrounding areas in response to the Indian–Eurasian collision (Wang et al., 2016). Likewise, seismic anisotropy studies also support that the vertical coherent deformation of the lithosphere is the dominant mechanism for the deformation pattern of the QFTB (Li et al., 2011; Eken et al., 2013; Chang et al., 2017). However, recent seismic tomography (Zhang et al., 2011; Li et al., 2014; Wang et al., 2014) and seismic refraction studies (Zhang et al., 2013) suggest that actively deforming middle NE Tibetan crust is dominated by discrete subhorizontal simple-shear zones associated with hypothetic channel flow or asthenospheric flow that decouple the deformation in the crust from that in the mantle (Yu and Chen, 2016). High-resolution 3D images of the crustal S-wave velocity structure also support ductile lower crustal flow accompanied by upper crustal shortening as the main driving mechanism for the growth and extension of the QFTB (Zhao et al., 2021). Considering these different interpretations of the kinematics and dynamics of the QFTB, it is necessary to clarify the kinematic interplay among the tectonic units of the QFTB and the tectonic interaction of the QFTB with adjacent blocks, such as the Alashan Block to the north and the Ordos Block to the east, which would allow us to better understand how the strain from Indian–Eurasian convergence is transferred from the plateau interior to the plateau margin.

3 DATA AND METHODS

3.1 GPS Data Compilation and Velocity Field Decomposition

Over several decades, a number of GPS velocity fields have been published to constrain the fault activity and regional kinematics of the Tibetan Plateau (Zhang et al., 2004; Gan et al., 2007; Zhao et al., 2015; Zheng G. et al., 2017). On the basis of these results, we can establish a more detailed and delicate crustal movement image by combining the individual velocities relative to a common reference frame, which is achieved by calculating a six-parameter Helmert solution (three rotations and three translations) from the individual frames. Thus, we compiled the recent GPS velocity field of Wang and Shen (2020) covering the plateau and its surroundings, which is based mainly on datasets collected by the Crustal Movement Observation Network of China with relatively long time spans exceeding ~15 years. Then, we supplemented these solutions with other published GPS velocity data, including the 36 GPS sites reported previously (Su et al., 2018), which are based on datasets collected by the Institute of Earthquake Forecasting Network and local agencies with relatively long time spans exceeding ~10 years. For more details of the datasets and their processing, refer to Wang and Shen (2020). Here, we used the GPS data of Wang and Shen (2020) as our reference data and transferred the other GPS data by estimating translation and rotation parameters with the program VELROT, which is a part of GAMIT/GLOBK software with a Euler pole (wx = −0.02350 deg/Myr, wy = −0.14760 deg/Myr, and wz = 0.21400 deg/Myr) (Herring et al., 2010). Furthermore, we picked the GPS velocity vectors with one standard deviation < 1.5 mm/yr to obtain the self-consistent resolution, which was directed to avoid contaminating the subsequent strain rate estimation and cluster analysis. Finally, the combined velocity field, including ~335 GPS stations, is presented in **Figure 1**.

In view of the principal stress associated with NE-SW or NEE-SW orientations for most of the Qilian orogenic belt in Pan (2020), which is almost consistent with the orientation of Indian–Eurasian convergence, we decompose the combined GPS velocities into two components: along (or tangential to) and normal (or perpendicular) to the trend of the QFTB (~NE110 is approximately perpendicular to the aforementioned stress orientation) and calculate the velocity gradient on each of them by the spline in the tension algorithm described previously (Wessel and Bercovici, 1998; Hackl et al., 2009) in **Figure 2**. To fully reveal the delicate deformation characteristics and regional kinematics, we also present a series of velocity profiles to examine the regional deformation fields in **Figures 3**, **4**.

3.2 Cluster Analysis of the Velocity Field and Surface Strain Estimation

The cluster analysis applied in the GPS velocity field can help us recognize the characteristics of regional crustal movement in an agnostic way without referencing geologic information (Thatcher et al., 2016). At the same time, it also allows us to discover regional boundaries purely based on the velocity field independent of any geophysical model (Granat et al., 2021). The core of the clustering method is to group the available observations and separate the members of each group with similar features from the members of all other groups. This facilitates the discovery of novel boundary features and/or the independent confirmation of other models or theories (Savage and Simpson, 2013). As the number of clusters increases, it will discern which fault plays an important role in the regional deformation (Granat et al., 2021). Here, we adopted k-means clustering according to Simpon (2012) to distinguish the regional feature depending only on the velocity field. Considering the spatial distribution of several large strike–slip faults and many secondary strike–slip and thrust faults within the QFTB, we define the number of microblocks divided by Li (2018) as the largest cluster in cluster analysis and test the different numbers of clusters (k = 2–10) to identify groups of velocities. The results are shown by color coding in **Figures 5**, **6**.

Then, we use the method introduced by Savage (2001) to calculate the average strain rate across the regions separated by the cluster analysis to determine how uniform the average strains and rotations are (Savage et al., 2001). The principal strain rate tensors (i.e., the maximum and minimum strain rate tensors) and rotational strain rate are computed as follows:

$$\lambda_{1,2} = \frac{1}{2}\left(\dot{\varepsilon}_{ii} + \dot{\varepsilon}_{jj}\right) \pm \left\{\dot{\varepsilon}_{ij}^2 + \frac{1}{4}\left(\dot{\varepsilon}_{ii} - \dot{\varepsilon}_{jj}\right)^2\right\}^{\frac{1}{2}}, \quad (1)$$

$$\theta = \frac{1}{2}\arctan\left(\frac{2\dot{\varepsilon}_{ij}}{\dot{\varepsilon}_{ii} - \dot{\varepsilon}_{jj}}\right), \quad (2)$$

$$\omega_{1,2} = \frac{1}{2}\left(\dot{\varepsilon}_{ij} - \dot{\varepsilon}_{ji}\right) \quad (3)$$

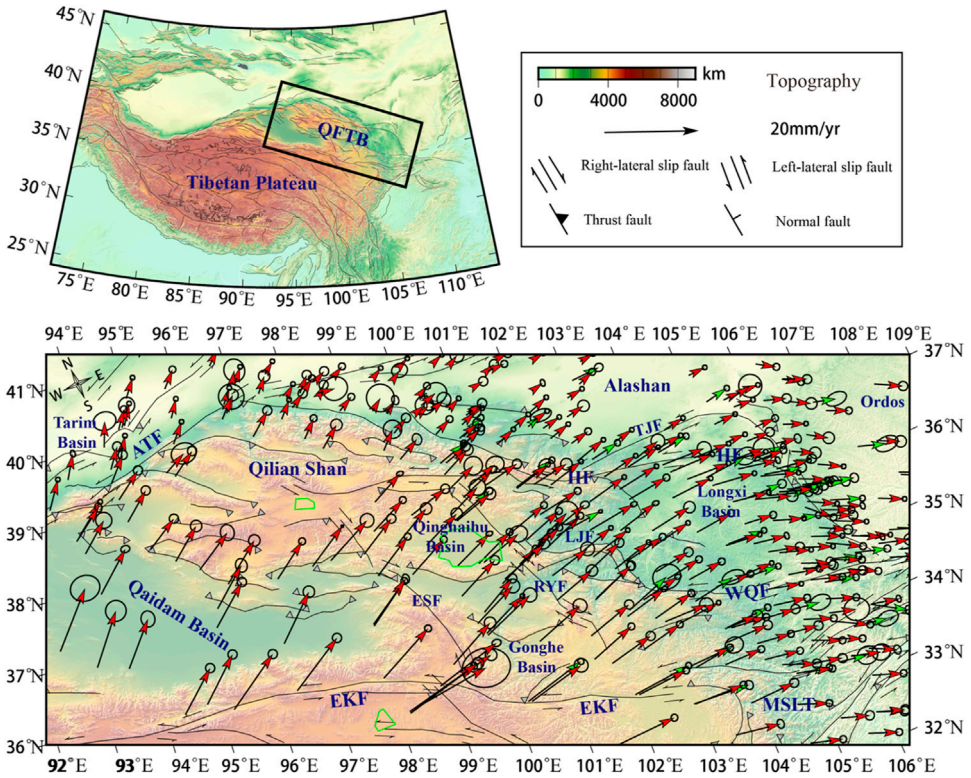

FIGURE 1 | Tectonic map of the Qilian fold-and-thrust belt (a) located in the India–Eurasia collisional belt (b) with the combined GPS velocity field including uncertainties (95% confidence ellipses) relative to a Eurasian reference frame. Velocity with red arrows from Wang and Shen (2020) and velocity with green arrows from Su et al., 2018. The black solid lines represent faults from Styron et al. (2010); Zuza and Yin (2016). Abbreviations (from north to south): QFTB = Qilian fold-and-thrust belt; ATF = Altyn Tagh fault; HF = Haiyuan fault; EKF = East Kunlun fault; TJF = Tianjingshan fault; RYF = Riyueshan fault; ESF = Elashan fault; WQF = West Qinling fault; LJF = Laji fault; MSLT = Min Shan–Longmen thrust belt.

where i and j are the indices for the east and north directions, respectively, $\dot{\varepsilon}_{ii}, \dot{\varepsilon}_{jj}\dot{\varepsilon}_{ij}$ represent the strain rate tensor, λ_1 and λ_2 represent the values of the maximum and minimum strain rate tensors, respectively, and θ represents the azimuth of λ_2 (the minimum strain rate tensor) counterclockwise from north in radians. Positive values of the maximum and minimum strain rate tensors indicate extension, while negative values indicate compression. $\omega_{1,2}$ represents the antisymmetric rotation rate tensor.

4 RESULTS

The results clearly show that the velocities decrease from south of the East Kunlun fault to north of the Qilian Mountains perpendicular to the trend of the QFTB, and present a relatively obvious clockwise rotation from the west to the east along the trend of the QFTB. On a larger scale, this velocity field explicitly reflects distributed and diffusive deformation throughout the QFTB and the surrounding regions as has been discussed by previous geodetic studies (Zhang et al., 2004; Gan et al., 2007; Zhao et al., 2015; Zheng G. et al., 2017; Wang and Shen, 2020). The velocity component perpendicular to the trend of the QFTB indicates that the gradient of velocity from south to north decreases from west to east (**Figure 2**). The velocity rate in southern Qaidam is approximately 12~13 mm/yr, and the velocity rate north of the Qilian Shan is approximately 1–3 mm/yr. Meanwhile, the velocity components remain almost unchanged east of the Riyueshan fault at a rate of approximately 1–4 mm/yr. However, along the trend of the QFTB (**Figure 2B**), the values of the velocity component increase from approximately 2–3 mm/yr west of the Qaidam Basin to approximately 8–11 mm/yr in the region adjoining the Riyueshan fault, while the values of the velocity component have a rate of approximately 5~8 mm/yr east of the Riyueshan fault. These results imply that the region adjoining the Riyueshan fault plays an important role in accommodating the deformation of the QFTB.

The GPS velocity along the trend of the QFTB in Profile TPro1-3 in **Figure 3** shows evidence for the eastward extrusion of the QFTB, and the velocity in the eastern part of the QFTB is obviously larger than that in the western part of the QFTB. Not surprisingly, the velocity in the Gonghe Basin in Profile Tpro3 has a rate of 7–9 mm/yr, which may be related to the properties of the basin, in which the filled weak materials or sediments flow more easily under the same circumstances. As mentioned previously, the surface movement decreases gradually from south to northwest of the Riyueshan fault, which is shown clearly in GPS velocity Profile Npro1-4 in **Figure 4**, while the velocity

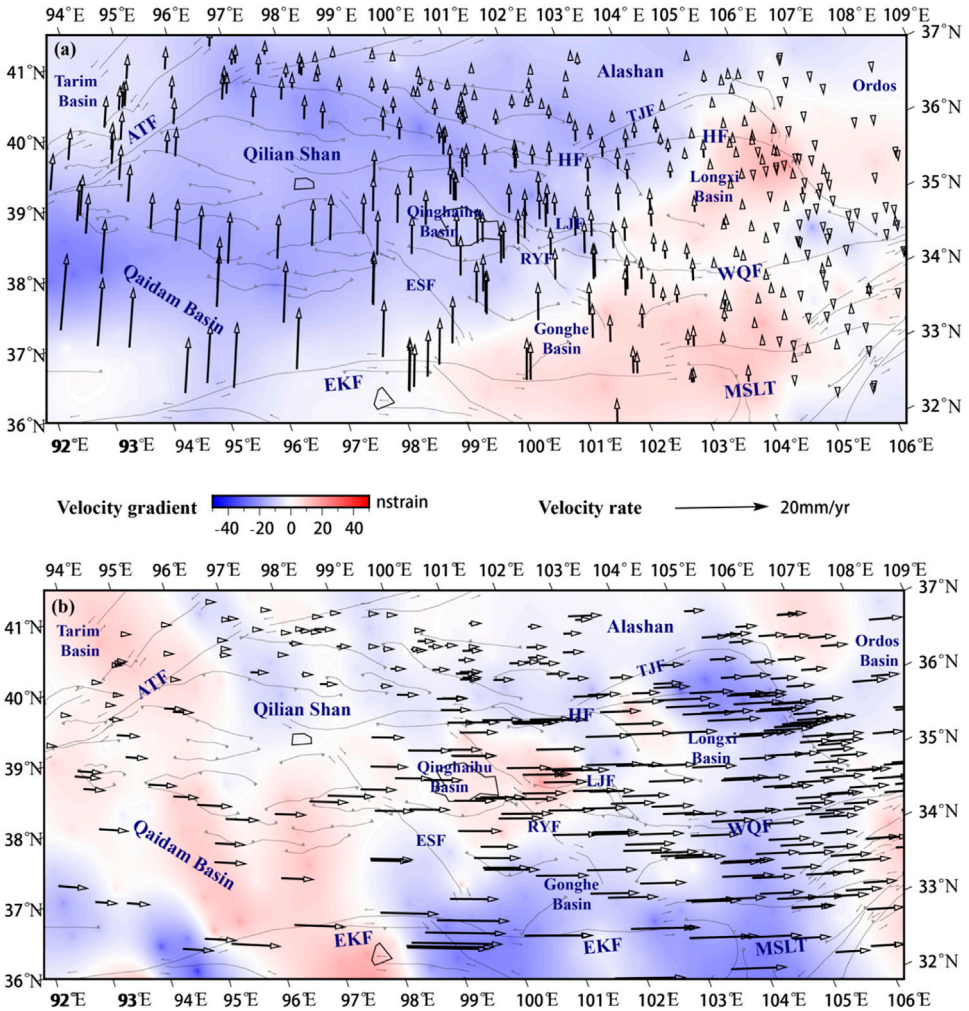

FIGURE 2 | (A) GPS velocity component perpendicular to the trend of the QFTB superimposed on the map of its gradient. **(B)** GPS velocity component along the QFTB superimposed on the map of its gradient.

has fewer or no obvious changes east of the Riyueshan fault on GPS velocity Profile Npro5-6 in **Figure 4**. Crustal shortening was detected in the Qilian Shan and Qaidam Basin between the East Kunlun fault and North Qilian front fault, and east–west extension was clearly identified through a comparison of GPS sites in the western and eastern QFTB, which is consistent with the results inferred from previous geophysical and geological data (Zhang et al., 2004; Gan et al., 2007; Zhao et al., 2015; Zheng G. et al., 2017; Wang and Shen, 2020).

In cluster analysis of GPS velocities, one boundary for k = 2 can be identified from the intersection between the East Kunlun and Elashan faults, following the Gonghe Basin and Riyueshan faults, and then follows the central part of the Haiyuan fault. The Qilian Nanshan thrust fault and Qaidam Basin thrust faults are identified when k > 2, suggesting that these faults could act as the boundary between the Qilian Shan and Qaidam Basin. East of the Qilian Shan and Qaidam Basin, the Haiyuan fault can be identified when k > 6, which is consistent with the identification of the western Qinling fault. However, remarkably, an underlying boundary located at approximately 104°E is identified when k > 3; it begins from the eastern end of the East Kunlun fault, follows the central part of the western Qinling fault and the Longxi Basin, and then follows the arc-shaped Haiyuan fault. This boundary can be related to part of the horizontal motion induced by subsidence in the Longxi Basin (Liang et al., 2013).

The results for the principal strain rate and rotational strain rate field are presented at the center of the cluster in **Figures 5**, **6**. The strain rates computed from the updated GPS velocities for k = 2–10 indicate that most of the QFTB experienced high magnitudes of contraction strain directed perpendicular to the trend of the QFTB and relatively lower magnitudes of extension strain along the trend of the QFTB. Generally, the deformation pattern in the QFTB can be divided into two distinct groups—the shortening regime accompanied by anticlockwise rotation in the western part of the QFTB and the strike-slipping regime along with obvious clockwise rotation in the eastern part of the QFTB. Based on the aforementioned

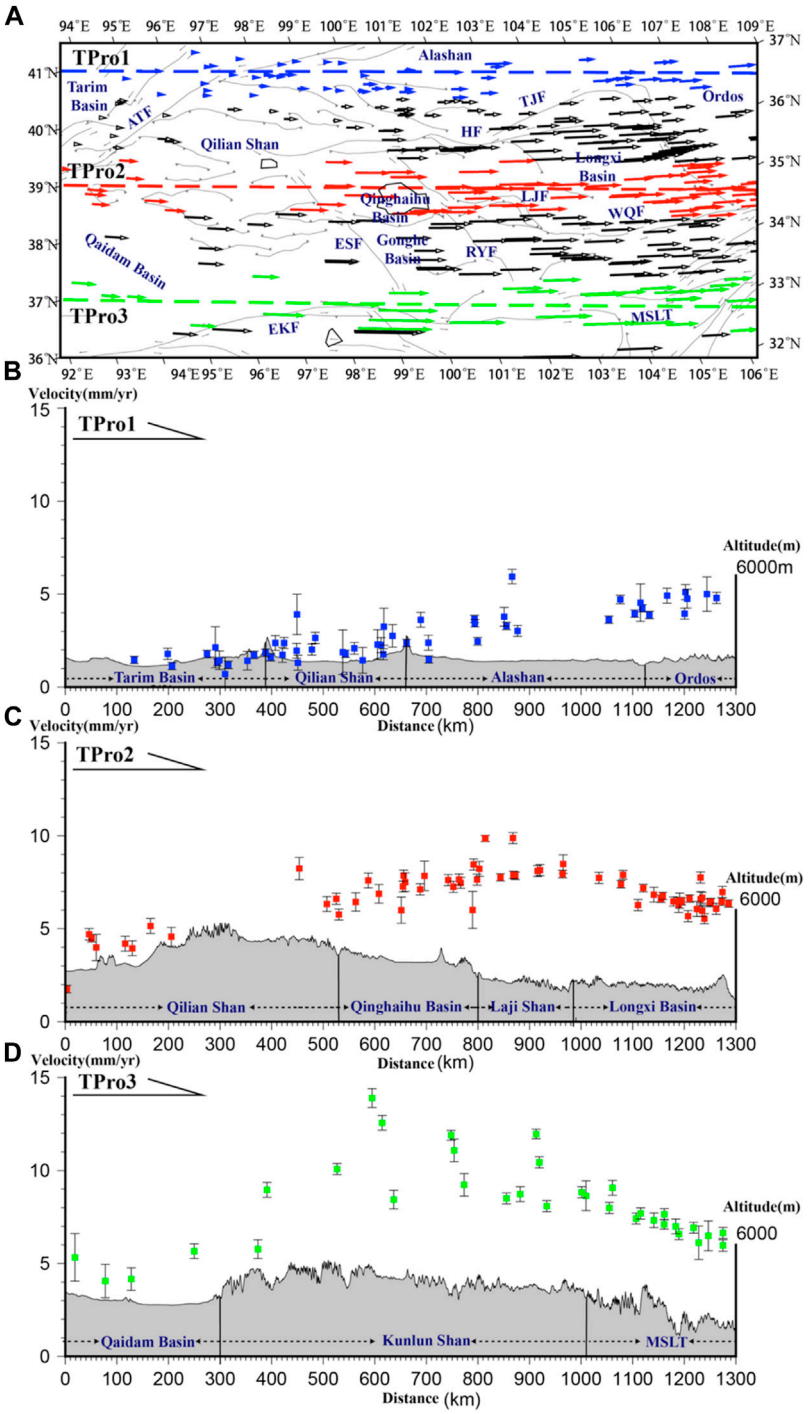

FIGURE 3 | (A) Location of three GPS velocity profiles in QFTB. **(B)** Profile TPro1 of GPS velocity along the trend of the QFTB with 1 error bar. **(C)** Profile TPro2 of GPS velocity along the trend of the QFTB with 1 error bar. **(D)** Profile TPro3 of GPS velocity along the trend of the QFTB with 1 error bar.

results, we regard that the boundary of strain transfer seems to begin from the East Kunlun fault adjoining the Gonghe Basin and follows the Qinghaihu Basin joining the Riyueshan fault, which then follows the central part of the Haiyuan fault. This transfer zone within the strain rate field is consistent with the previously mentioned results of velocity decomposition, which illustrates that the diamond basin associated with boundary faults plays a considerable role in accommodating the far-field effect of Indian–Eurasian convergence. In the western part of the QFTB, the contraction strain has a value of approximately

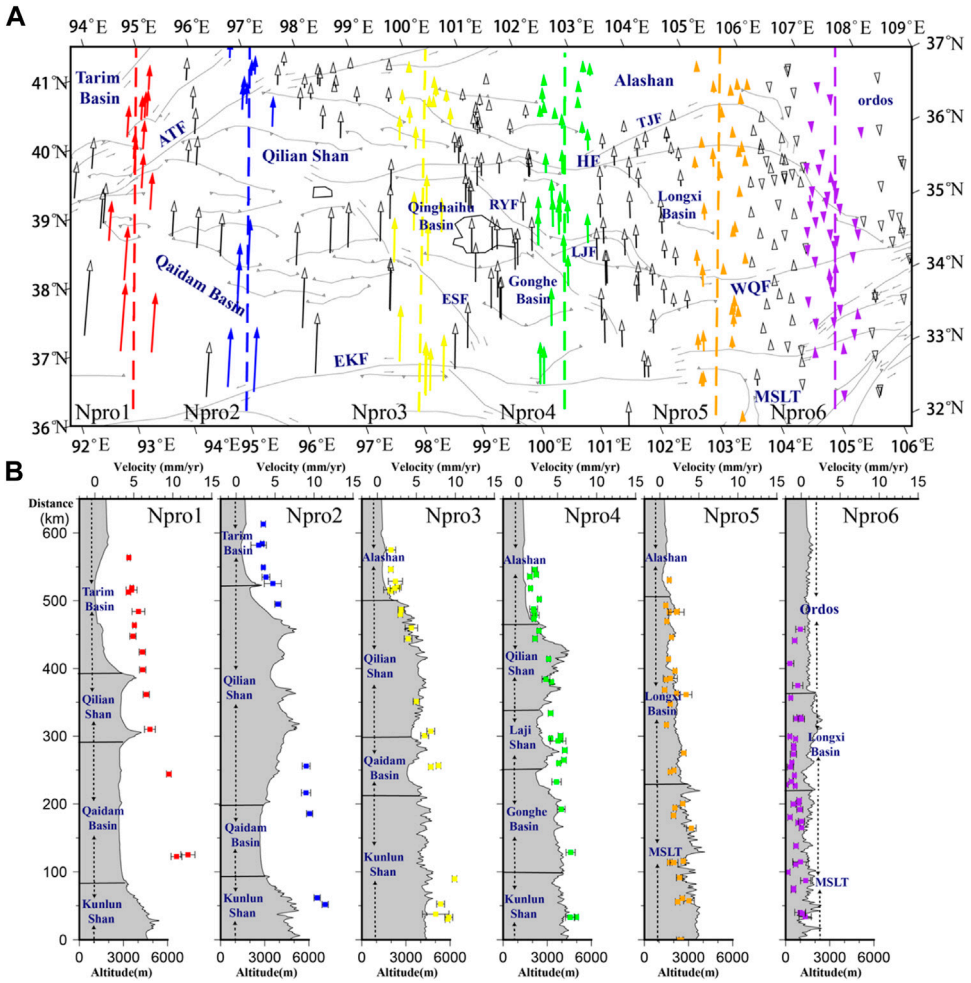

FIGURE 4 | (A) Location of six GPS velocity profiles in QFTB. **(B)** Profile NPro1–6 of GPS velocity perpendicular to the trend of the QFTB with 1 error bar. The colors represent the different velocity profiles and their available GPS stations.

40–50 nstrain/yr, but the extension rate is relatively low, with a value of less than 20 nstrain/yr. On the eastern Qilian Shan margin near the Qinghaihu Basin and Riyueshan faults, the inferred rotational rate field displays an anticlockwise rotation, while in the interior of the Qilian Shan and the majority of the Qaidam Basin, it shows very little rotation, which we suggest is possibly related to the combined effects of mountain growth and fault adjustment subjected by convergence stress propagated from the Indian–Eurasian collision. In the eastern part of the QFTB, the rotational rate field shows an obvious clockwise rotation between the East Kunlun fault and Haiyuan fault. We believe that this relative rotation may also have been related to lateral extrusion of the material, which is compatible with geological and seismological evidence (Li et al., 2011; Eken et al., 2013; Chang et al., 2017). Both the extension strain rate and the contraction strain rate have similar magnitudes, with values of approximately 30–40 nstrain/yr, which are ascribed to the accommodation of the eastward strike of the East Kunlun fault and Haiyuan fault.

5 DISCUSSION

Understanding the strain distribution will not only allow us to test and improve models of the active tectonics of the QFTB but also provide much more related information to assess future regional seismic hazards. Our findings indicate that stronger contraction strain is mainly concentrated west of the Riyueshan fault, where the focal mechanisms are mainly dominated by thrust faulting (Pan et al., 2020). This is in accordance with geological findings that a series of imbricate thrust faults and active folds in the Qilian Shan accommodate the remote effects of Indian–Eurasian convergence (Liu et al., 2017; Bi et al., 2018; Yang et al., 2018; Hetzel et al., 2019). The map of the velocity gradient perpendicular to and parallel to the trend of the QFTB also exhibits consistent characteristics, which imply that the region adjoining the Riyueshan fault plays an important role in accommodating the deformation of the QFTB. Considering the northward and eastward velocity gradient and the high contraction strain rate, the deformation characteristics of the western part of the QFTB can be viewed as an analog of the

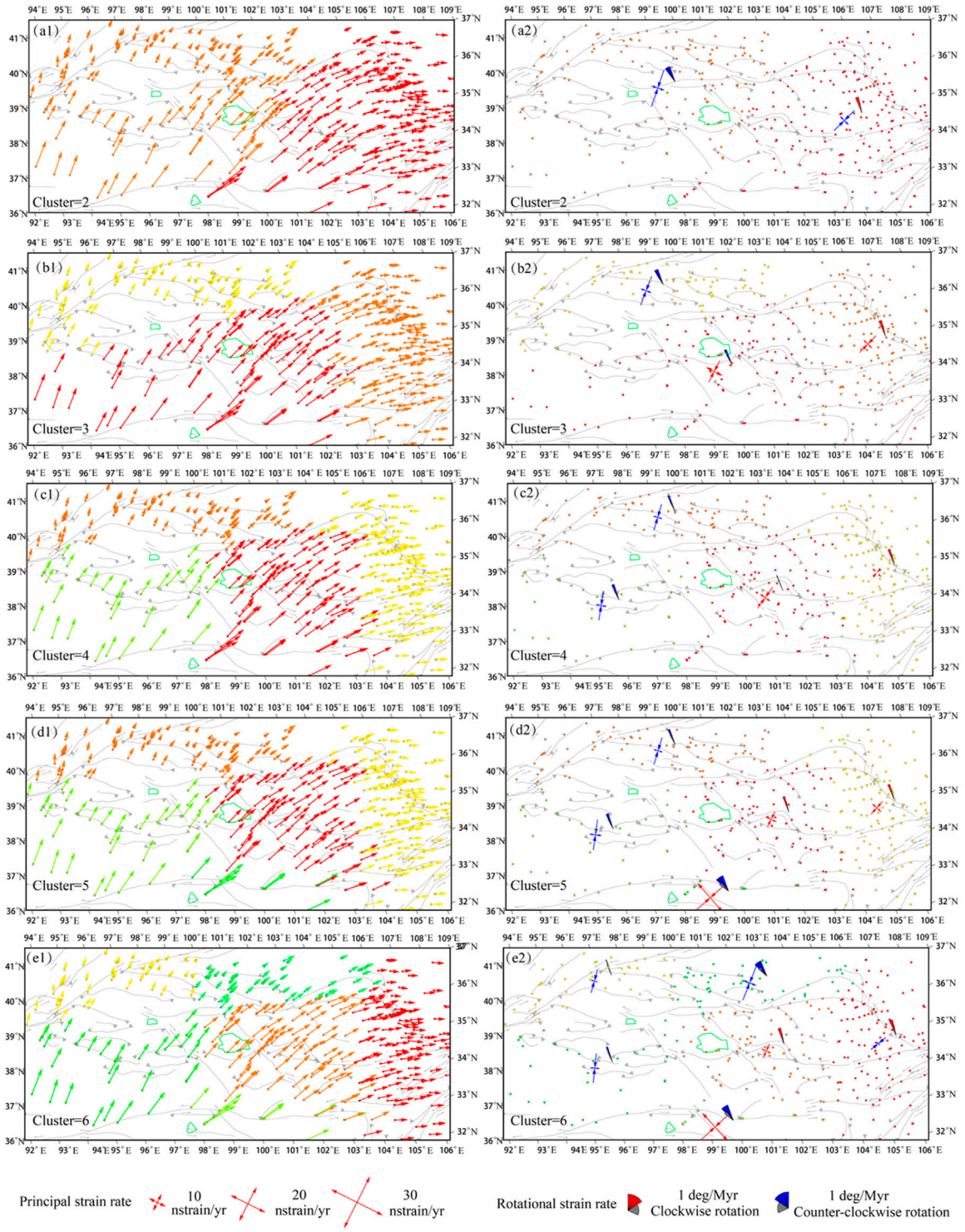

FIGURE 5 | Clustering velocity result for K = 2–6 and their calculated principal strain rate and rotational strain rate. a1–e1 represent the velocity result of cluster analysis, and a2–e2 represent the strain rate for each cluster.

pure shear–strain pattern, which suggests that the deformation of the QFTB can be interpreted by faulting, folding in the upper crust, and horizontal shortening (Lease et al., 2012; Zheng D. et al., 2017). Moreover, the deflection of GPS velocities across the East Kunlun fault also suggests the occurrence of strain partitioning due to the strength of the lithosphere (He et al.,

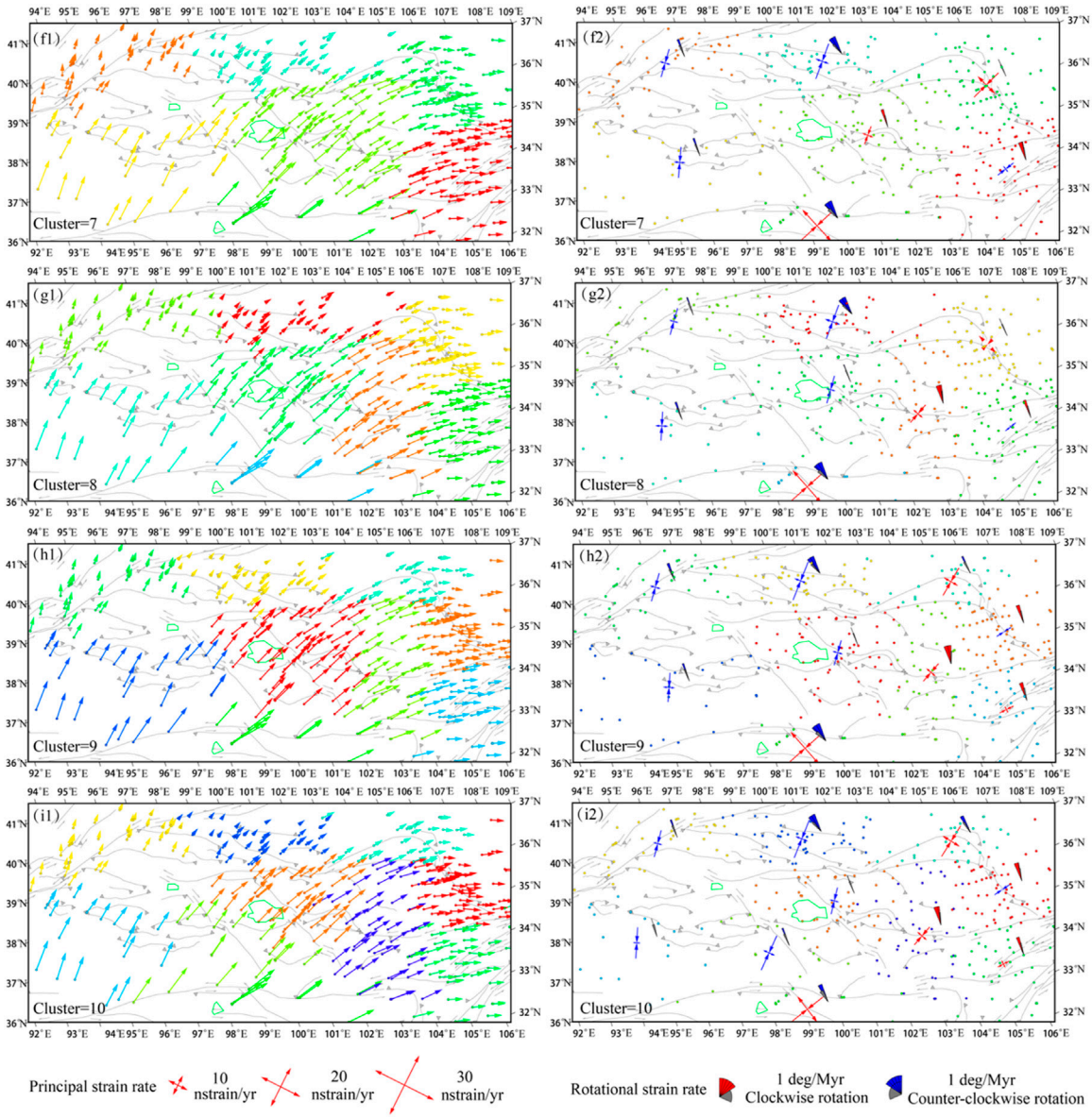

FIGURE 6 | Clustering velocity result for K = 7–10 and their calculated principal strain rate and rotational strain rate. f1–i1 represent the velocity result of cluster analysis, and f2–i2 represent the strain rate for each cluster.

2013), suggesting strong compression perpendicular to the trend of the QFTB.

In contrast, the extensional strains are localized along the East Kunlun fault and Haiyuan fault east of the Riyueshan fault, where the majority of shallow crustal earthquakes are strike–slip faulting regimes. These results are consistent with our velocity decomposition results. However, the Longxi Basin between the Haiyuan and Kunlun faults shows a weak northward velocity gradient and an obvious clockwise rotation, which supports the idea of the strain transfer of the Kunlun fault motion (Duvall and Clark, 2010). The underlying boundary identified by cluster analysis from the eastern end of the East Kunlun fault to the arc-shaped Haiyuan faults could serve as a channel for this strain transfer. Combining the results of cluster analysis and the velocity gradient, the deformation characteristics of the eastern QFTB can be deciphered by the simple shear–strain pattern, which suggests that the kinematics of the QFTB can be explained by a combination of block rotation and lateral transport of crustal materials (England and Molnar, 1990; Gan et al., 2021). As boundary faults, a number of studies have revealed that the strong activity of the Haiyuan and East Kunlun faults plays an important role in accommodating the eastward extrusion of northeastern Tibet relative to the surrounding block. The Ms 6.9 Menyuan earthquake on 8 Jan 2022 with a strike–slip faulting regime offers an example to illustrate the strain mode on these large faults. At the same time, InSAR observations indicate that

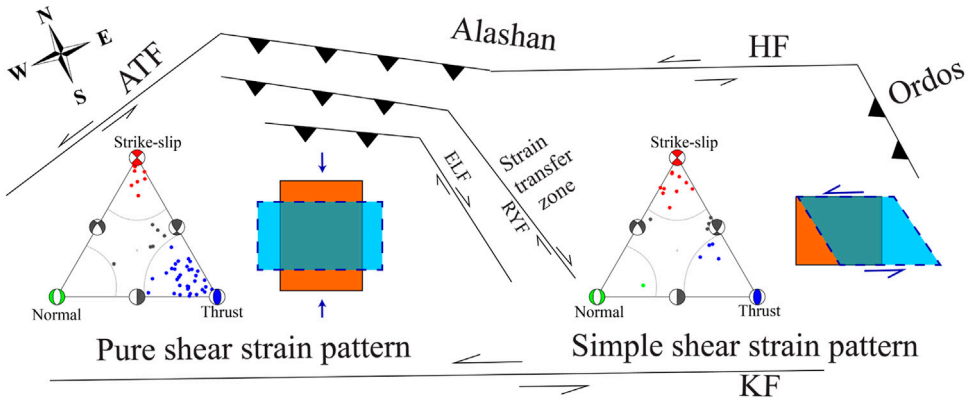

FIGURE 7 | Schematic illustrations of the model for the deformation pattern of QFTB.

the slip rates along the Haiyuan fault decrease from the center of the Lenglongling fault to the east of the Liupanshan fault (Daout et al., 2016), confirming our proposed simple shear model.

In light of the aforementioned results of the GPS profiles perpendicular to the trend of the orogenic belts, we observe statistically significant differential motion between the stations located to the west and east of the Riyueshan fault, reflecting a velocity offset. On the one hand, this could be invoked as strain partitioning and transfer along these crustal faults over the orogenic belt due to the heterogeneity and strength of the crustal material (i.e., the properties of the Gonghe Basin and the effect of fault geometry and segmentation) (He et al., 2013; Zhu et al., 2020). On the other hand, previous geological and geomorphological results indicate that the secondary faults in the QFTB are tectonically active (Craddock et al., 2011; Craddock et al., 2014). The Qinghai Nanshan fault, the southern boundary fault of the Qinghaihu Basin, and the Gonghe Nanshan fault, located on the southern margin of the Gognhe Basin, have experienced obvious crustal shortening and variable uplift based on the analysis of their landscape features (Su et al., 2022; Zhang et al., 2012). Combined with the results of GPS velocity decomposition, cluster analysis in GPS velocity, and the different regimes displayed by the ternary diagram of focal mechanisms (Frohlich, 1992) (**Figure 7**), we suggest that two diamond basins (Qinghaihu Basin and Gonghe Basin) associated with their boundary faults could play a considerable role in accommodating and absorbing crustal deformation within the QFTB. The stress and strain results also demonstrate that the axis of the compressive stress orientation changes from trending approximately NE-SW to the west of the QFTB to NEE-SWW to the east (Pan et al., 2020; Pan et al., 2021). The results of the velocity profile and strain estimation in this study can be better described by the diffuse model, which is different from the continuous model indicating that the convergence is accommodated by the widely distributed deformation (Flesch et al., 2001; England and Molnar, 2005) because the lengths of the boundary faults around the QFTB that accommodate the regional deformation are of the same order of magnitude as the dimensions of the deforming region. At the same time, the slip rates on several major faults estimated by geological and geodetic surveying are relatively slow (Hetzel et al., 2002; Li et al., 2019), such as the Altyn Tagh fault and the East Kunlun fault, and the deformation within the tectonic units of the QFTB derived from cluster analysis of GPS velocity is not negligible. These results contradict the block model assuming that the deformation is mainly localized near the major strike–slip faults (Tapponnier et al., 2001; Thatcher, 2007, 2009). In addition, the nonrigid bookshelf rotation model proposed by Zuza and Yin (2016) cannot explain the regional and local scale of deformation in the QFTB because the magnitude and style of the strain in the QFTB vary considerably among those boundary strike–slip faults.

In summary, the active tectonics of the QFTB are obviously divided into two distinct groups: one group is a pure shear–strain pattern mainly accounting for strong crustal shortening in the western QFTB, and the other group is a simple shear–strain pattern describing obvious lateral extrusion in the eastern QFTB. Indeed, when considering these local variations and different inhomogeneities, the variations in topography and crustal thickness and other deep geophysical processes should be considered. In addition, more observational strain indicators and numerical models (regional to local scales) are required to investigate the potential mechanisms and dynamic processes behind this surface deformation and tectonics.

6 CONCLUSION

The purpose of this study was to use velocity decomposition and cluster analysis to place better constraints on the regional tectonics and kinematics of the QFTB, relying only on the updated GPS velocity field without any geological constraints or model limitations (i.e., fault locations, fault locking, and creeping). In our analysis, the main conclusions are as follows:

(1) The velocity decomposition and velocity gradient results indicate that the deformation in the west of the Riyueshan

fault is characterized mainly by crustal shortening perpendicular to the trend of the QFTB, coupled with lateral extension along the trend of the QFTB, while the deformation in the east of Riyueshan is characterized mainly by lateral extrusion owing to the impact of two large eastward striking left-slip faults (East Kunlun fault and Haiyuan fault).

(2) The clustering analysis and strain estimation illustrate that the deformation of the QFTB can be divided into two groups: the shortening regime accompanied by anticlockwise rotation in the western QFTB and the strike-slipping regime along with obvious clockwise rotation in the eastern QFTB. The dividing line begins where the East Kunlun fault adjoins the Gonghe Basin, following which the Qinghaihu Basin joins the Riyueshan fault, and then follows the central part of the Haiyuan fault.

(3) The active tectonics of the QFTB are obviously divided into two distinct groups: one group is a pure shear–strain pattern mainly accounting for strong crustal shortening in the western part of the QFTB, and the other group is a simple shear–strain pattern describing obvious lateral extrusion in the eastern part of the QFTB. As the strain transfer zone, two diamond basins (Qinghaihu Basin and Gonghe Basin) associated with their boundary faults play a considerable role in accommodating and absorbing crustal deformation within the QFTB.

DATA AVAILABILITY STATEMENT

The raw data supporting the conclusion of this article will be made available by the authors, without undue reservation.

AUTHOR CONTRIBUTIONS

GZ carried out data analysis and wrote the manuscript. ZP conceptualized the problem, model implementation and validation, wrote the modeling section, and participated in discussions of all aspects of the manuscript.

ACKNOWLEDGMENTS

The authors are very grateful to the editor and three anonymous reviewers for their constructive reviews that have significantly improved the manuscript. We are grateful to all the people who contributed to the Crustal Movement Observation Network of China (CMONOC). This work was supported by National Natural Science Foundation of China (42104056) and the Special Fund of the Institute of Earthquake Forecasting, China Earthquake Administration (2021IEF0105). All figures in this manuscript were prepared with The Generic Mapping Tools (GMT) (Wessel et al., 2013).

REFERENCES

Bi, H., Zheng, W., Ge, W., Zhang, P., Zeng, J., and Yu, J. (2018). Constraining the Distribution of Vertical Slip on the South Heli Shan Fault (Northeastern Tibet) from High-Resolution Topographic Data. *J. Geophys. Res. Solid Earth* 0 (0).

Burchfiel, B. C., Quidong, D., Molnar, P., Royden, L., Yipeng, W., Peizhen, Z., et al. (1989). Intracrustal Detachment within Zones of continental Deformation. *Geol* 17 (8), 748–752. doi:10.1130/0091-7613(1989)017<0448:idwzoc>2.3.co;2

Burchfiel, B. C., Zhang, P., Wang, Y., Zhang, W., Song, F., Deng, Q., et al. (1991). Geology of the Haiyuan Fault Zone, Ningxia-Hui Autonomous Region, China, and its Relation to the Evolution of the Northeastern Margin of the Tibetan Plateau. *Tectonics* 10 (6), 1091–1110. doi:10.1029/90tc02685

Chang, L., Ding, Z., Wang, C., and Flesch, L. M. (2017). Vertical Coherence of Deformation in Lithosphere in the NE Margin of the Tibetan Plateau Using GPS and Shear-Wave Splitting Data. *Tectonophysics* 699, 93–101. doi:10.1016/j.tecto.2017.01.025

Craddock, W. H., Kirby, E., Zhang, H., Clark, M. K., Champagnac, J.-D., and Yuan, D. (2014). Rates and Style of Cenozoic Deformation Around the Gonghe Basin, Northeastern Tibetan Plateau. *Geosphere* 10 (6), 1255–1282. doi:10.1130/ges01024.1

Craddock, W., Kirby, E., and Zhang, H. (2011). Late Miocene-Pliocene Range Growth in the interior of the Northeastern Tibetan Plateau. *Lithosphere* 3 (6), 420–438. doi:10.1130/l159.1

Daout, S., Jolivet, R., Lasserre, C., Doin, M.-P., Barbot, S., Tapponnier, P., et al. (2016). Along-strike Variations of the Partitioning of Convergence across the Haiyuan Fault System Detected by InSAR. *Geophys. J. Int.* 205 (1), 536–547. doi:10.1093/gji/ggw028

Dupont-Nivet, G., Horton, B. K., Butler, R. F., Wang, J., Zhou, J., and Waanders, G. L. (2004). Paleogene Clockwise Tectonic Rotation of the Xining-Lanzhou Region, Northeastern Tibetan Plateau. *J. Geophys. Res. Solid Earth* 109 (B4). doi:10.1029/2003jb002620

Duvall, A. R., and Clark, M. K. (2010). Dissipation of Fast Strike-Slip Faulting within and beyond Northeastern Tibet. *Geology* 38 (3), 223–226. doi:10.1130/g30711.1

Duvall, A. R., Clark, M. K., van der Pluijm, B. A., and Li, C. (2011). Direct Dating of Eocene Reverse Faulting in Northeastern Tibet Using Ar-Dating of Fault Clays and Low-Temperature Thermochronometry. *Earth Planet. Sci. Lett.* 304 (3–4), 520–526. doi:10.1016/j.epsl.2011.02.028

Eken, T., Tilmann, F., Mechie, J., Zhao, W., Kind, R., Su, H., et al. (2013). Seismic Anisotropy from SKS Splitting beneath Northeastern Tibet. *Bull. Seismological Soc. America* 103 (6), 3362–3371. doi:10.1785/0120130054

England, P., and Molnar, P. (1990). Right-lateral Shear and Rotation as the Explanation for Strike-Slip Faulting in Eastern Tibet. *Nature* 344 (6262), 140–142. doi:10.1038/344140a0

Frohlich, C. (1992). Triangle Diagrams: Ternary Graphs to Display Similarity and Diversity of Earthquake Focal Mechanisms. *Phys. Earth Planet. Interiors* 75 (1), 193–198. doi:10.1016/0031-9201(92)90130-n

Gan, C., Ming, A., Wenjun, Z., Haiyun, B., Jinrui, L., Yipeng, Z., et al. (2021). *Nonrigid Bookshelf Kinematics of Northeastern Tibet: Constrains from Fault Slip Rates Around the Qinghai Lake and Chaka-Gonghe Basins*. Lithosphere, 2021. (Special 2).

Gan, W., Zhang, P., Shen, Z.-K., Niu, Z., Wang, M., Wan, Y., et al. (2007). Present-day Crustal Motion within the Tibetan Plateau Inferred from GPS Measurements. *J. Geophys. Res.* 112 (B8). doi:10.1029/2005jb004120

Gaudemer, Y., Tapponnier, P., Meyer, B., Peltzer, G., Shunmin, G., Zhitai, C., et al. (1995). Partitioning of Crustal Slip between Linked, Active Faults in the Eastern Qilian Shan, and Evidence for a Major Seismic gap, the 'Tianzhu gap', on the Western Haiyuan Fault, Gansu (China). *Geophys. J. Int.* 120 (3), 599–645. doi:10.1111/j.1365-246x.1995.tb01842.x

Gehrels, G., Kapp, P., DeCelles, P., Pullen, A., Blakey, R., Weislogel, A., et al. (2011). Detrital Zircon Geochronology of Pre-tertiary Strata in the Tibetan-Himalayan Orogen. *Tectonics* 30 (5). doi:10.1029/2011tc002868

Granat, R., Donnellan, A., Heflin, M., Lyzenga, G., Glasscoe, M., Parker, J., et al. (2021). Clustering Analysis Methods for GNSS Observations: A Data-Driven Approach to Identifying California's Major Faults. *Earth Space Sci.* (n). n/a, e2021EA001680.

Hackl, M., Malservisi, R., and Wdowinski, S. (2009). Strain Rate Patterns from Dense GPS Networks. *Nat. Hazards Earth Syst. Sci.* 9 (4), 1177–1187. doi:10.5194/nhess-9-1177-2009

He, J., Lu, S., and Wang, W. (2013). Three-dimensional Mechanical Modeling of the GPS Velocity Field Around the Northeastern Tibetan Plateau and Surrounding Regions. *Tectonophysics* 584, 257–266. doi:10.1016/j.tecto.2012.03.025

Herring, T. A., King, R. W., and McClusky, S. C. (2010). *GLOBK Reference Manual. Global Kalman Filter VLBI and GPS Analysis Program*, 10.4. Cambridge, MA: Massachussetts Institute Technology.

Hetzel, R., Hampel, A., Gebbeken, P., Xu, Q., and Gold, R. D. (2019). A Constant Slip Rate for the Western Qilian Shan Frontal Thrust during the Last 200 Ka Consistent with GPS-Derived and Geological Shortening Rates. *Earth Planet. Sci. Lett.* 509, 100–113. doi:10.1016/j.epsl.2018.12.032

Hetzel, R., Niedermann, S., Tao, M., Kubik, P. W., Ivy-Ochs, S., Gao, B., et al. (2002). Low Slip Rates and Long-Term Preservation of Geomorphic Features in Central Asia. *Nature* 417 (6887), 428–432. doi:10.1038/417428a

Hu, X., Zang, A., Heidbach, O., Cui, X., Xie, F., and Chen, J. (2017). Crustal Stress Pattern in China and its Adjacent Areas. *J. Asian Earth Sci.* 149, 20–28. doi:10.1016/j.jseaes.2017.07.005

Kirby, E., Harkins, N., Wang, E., Shi, X., Fan, C., and Burbank, D. (2007). Slip Rate Gradients along the Eastern Kunlun Fault. *Tectonics* 26 (2), n/a. doi:10.1029/2006tc002033

Lease, R. O. (2014). *Cenozoic Mountain Building on the Northeastern Tibetan Plateau*. Geological Society of America Special Papers 507. doi:10.1130/2014.2507(06)

Lease, R. O., Burbank, D. W., Zhang, H., Liu, J., and Yuan, D. (2012). Cenozoic Shortening Budget for the Northeastern Edge of the Tibetan Plateau: Is Lower Crustal Flow Necessary? *Tectonics* 31 (3), n/a–n. doi:10.1029/2011tc003066

Li, X., Li, C., Pierce, I. K. D., Zhang, P., Zheng, W., Dong, J., et al. (2019). *New Slip Rates for the Tianjingshan Fault Using Optically Simulated Luminescence, GPS, and Paleoseismic Data, NE Tibet, China*. Tectonophysics 755, 64–74. doi:10.1016/j.tecto.2019.02.007

Li, X., Santosh, M., Cheng, S., Xu, X., and Zhong, W. (2015). Crustal Structure and Composition beneath the Northeastern Tibetan Plateau from Receiver Function Analysis. *Phys. Earth Planet. Interiors* 249, 51–58. doi:10.1016/j.pepi.2015.10.001

Li, Y., Liu, M., Wang, Q., and Cui, D. (2018). Present-day Crustal Deformation and Strain Transfer in Northeastern Tibetan Plateau. *Earth Planet. Sci. Lett.* 487, 179–189. doi:10.1016/j.epsl.2018.01.024

Li, Y., Wu, Q., Zhang, F., Feng, Q., and Zhang, R. (2011). Seismic Anisotropy of the Northeastern Tibetan Plateau from Shear Wave Splitting Analysis. *Earth Planet. Sci. Lett.* 304 (1–2), 147–157. doi:10.1016/j.epsl.2011.01.026

Li, Z., Ni, S., and Roecker, S. (2014). Interstation Pg and Sg Differential Traveltime Tomography in the Northeastern Margin of the Tibetan Plateau: Implications for Spatial Extent of Crustal Flow and Segmentation of the Longmenshan Fault Zone. *Phys. Earth Planet. Interiors* 227, 30–40. doi:10.1016/j.pepi.2013.11.016

Liang, S., Gan, W., Shen, C., Xiao, G., Liu, J., Chen, W., et al. (2013). Three-dimensional Velocity Field of Present-Day Crustal Motion of the Tibetan Plateau Derived from GPS Measurements. *J. Geophys. Res. Solid Earth*. n/a. doi:10.1002/2013jb010503

Liu, X.-W., Yuan, D.-Y., and Su, Q. (2017). Late Pleistocene Slip Rate of the Northern Qilian Shan Frontal Thrust, Western Hexi Corridor, China. *Terra Nova* 29 (4), 238–244. doi:10.1111/ter.12270

Ma, H., Wu, Y., Feng, J. g., Xu, R., Wu, S., and Wang, Q. (2017). Research on Recent GPS Crustal Deformation Characteristics in the Northeastern Edge of Qinghai-Tibet Plateau. *J. Phys. Conf. Ser.* 910, 012028. doi:10.1088/1742-6596/910/1/012028

Meyer, B., Tapponnier, P., Bourjot, L., Métivier, F., Gaudemer, Y., Peltzer, G., et al. (1998). Crustal Thickening in Gansu-Qinghai, Lithospheric Mantle Subduction, and Oblique, Strike-Slip Controlled Growth of the Tibet Plateau. *Geophys. J. Int.* 135 (1), 1–47. doi:10.1046/j.1365-246x.1998.00567.x

Meyer, B., Tapponnier, P., Gaudemer, Y., Peltzer, G., Shunmin, G., and Zhitai, C. (1996). Rate of Left-Lateral Movement along the Easternmost Segment of the Altyn Tagh Fault, East of 96°E (China). *Geophys. J. Int.* 124 (1), 29–44. doi:10.1111/j.1365-246x.1996.tb06350.x

Pan, Z., He, J., and Shao, Z. (2020). Spatial Variation in the Present-Day Stress Field and Tectonic Regime of Northeast Tibet from Moment Tensor Solutions of Local Earthquake Data. *Geophys. J. Int.* 221 (1), 478–491. doi:10.1093/gji/ggaa013

Pan, Z., Zhang, Z., Shao, Z., and Zhao, G. (2021). *Block Motions and Strain Partition on Active Faults in Northeast Tibet and Their Geodynamic Implications*. Terra Nova 33, 356–363. doi:10.1111/ter.12520

Savage, J. C., Gan, W., and Svarc, J. L. (2001). Strain Accumulation and Rotation in the Eastern California Shear Zone. *J. Geophys. Res.* 106 (B10), 21995–22007. doi:10.1029/2000jb000127

Savage, J. C., and Simpson, R. W. (2013). Clustering of Velocities in a GPS Network Spanning the Sierra Nevada Block, the Northern Walker Lane Belt, and the Central Nevada Seismic Belt, California-Nevada. *J. Geophys. Res. Solid Earth* 118 (9), 4937–4947. doi:10.1002/jgrb.50340

Shen, X., Yuan, X., and Liu, M. (2015). Is the Asian Lithosphere Underthrusting beneath Northeastern Tibetan Plateau? Insights from Seismic Receiver Functions. *Earth Planet. Sci. Lett.* 428, 172–180. doi:10.1016/j.epsl.2015.07.041

Simpson, R. W., Thatcher, W., and Savage, J. C. (2012). Using Cluster Analysis to Organize and Explore Regional GPS Velocities. *Geophys. Res. Lett.* 39 (18), L18307. doi:10.1029/2012gl052755

Song, S., Niu, Y., Su, L., and Xia, X. (2013). Tectonics of the North Qilian Orogen, NW China. *Gondwana Res.* 23 (4), 1378–1401. doi:10.1016/j.gr.2012.02.004

Su, Q., Wang, X., Yuan, D., Zhang, H., Lu, H., and Xie, H. (2022). *Secondary Faulting Plays a Key Role in Regulating the Cenozoic Crustal Deformation in the Northeastern Qinghai-Tibet Plateau*. Terra Nova, 1–13. doi:10.1111/ter.12583

Su, X., Yao, L., Wu, W., Meng, G., Su, L., Xiong, R., et al. (2018). Crustal Deformation on the Northeastern Margin of the Tibetan Plateau from Continuous GPS Observations. *Remote Sensing* 11 (1). doi:10.3390/rs11010034

Tapponnier, P., Meyer, B., Avouac, J. P., Peltzer, G., Gaudemer, Y., Guo, S., et al. (1990). Active Thrusting and Folding in the Qilian Shan, and Decoupling between Upper Crust and Mantle in Northeastern Tibet. *Earth Planet. Sci. Lett.* 97 (3), 382–403. doi:10.1016/0012-821x(90)90053-z

Thatcher, W., Savage, J. C., and Simpson, R. W. (2016). The Eastern California Shear Zone as the Northward Extension of the Southern San Andreas Fault. *J. Geophys. Res. Solid Earth*, 2015JB012678. doi:10.1002/2015jb012678

Wang, H., Gao, R., Zeng, L., Kuang, Z., Xue, A., Li, W., et al. (2014). Crustal Structure and Moho Geometry of the Northeastern Tibetan Plateau as Revealed by SinoProbe-02 Deep Seismic-Reflection Profiling. *Tectonophysics* 636, 32–39. doi:10.1016/j.tecto.2014.08.010

Wang, M., and Shen, Z.-K. (2020). Present-Day Crustal Deformation of Continental China Derived from GPS and its Tectonic Implications. *J. Geophys. Res. Solid Earth* (n/a), e2019JB018774. n/a.

Wang, Q., Niu, F., Gao, Y., and Chen, Y. (2016). Crustal Structure and Deformation beneath the NE Margin of the Tibetan Plateau Constrained by Teleseismic Receiver Function Data. *Geophys. J. Int.* 204 (1), 167–179. doi:10.1093/gji/ggv420

Wessel, P., and Bercovici, D. (1998). Interpolation with Splines in Tension: A Green's Function Approach. *Math. Geology*. 30 (1), 77–93. doi:10.1023/a:1021713421882

Wessel, P., Smith, W. H. F., Scharroo, R., Luis, J., and Wobbe, F. (2013). Generic Mapping Tools: Improved Version Released. *Eos Trans. AGU* 94 (45), 409–410. doi:10.1002/2013eo450001

Yang, H., Yang, X., Zhang, H., Huang, X., Huang, W., and Zhang, N. (2018). Active Fold Deformation and Crustal Shortening Rates of the Qilian Shan Foreland Thrust Belt, NE Tibet, since the Late Pleistocene. *Tectonophysics* 742-743, 84–100. doi:10.1016/j.tecto.2018.05.019

Yin, A., and Harrison, T. M. (2000). Geologic Evolution of the Himalayan-Tibetan Orogen. *Annu. Rev. Earth Planet. Sci.* 28 (1), 211–280. doi:10.1146/annurev.earth.28.1.211

Yu, Y., and Chen, Y. J. (2016). Seismic Anisotropy beneath the Southern Ordos Block and the Qinling-Dabie Orogen, China: Eastward Tibetan Asthenospheric Flow Around the Southern Ordos. *Earth Planet. Sci. Lett.* 455, 1–6. doi:10.1016/j.epsl.2016.08.026

Yuan, D. Y., Ge, W. P., Chen, Z. W., Li, C. Y., Wang, Z. C., Zhang, H. P., et al. (2013). The Growth of Northeastern Tibet and its Relevance to Large-scale continental Geodynamics: A Review of Recent Studies. *Tectonics* 32 (5), 1358–1370. doi:10.1002/tect.20081

Zhang, H.-P., Craddock, W. H., Lease, R. O., Wang, W.-t., Yuan, D.-Y., Zhang, P.-Z., et al. (2012). Magnetostratigraphy of the Neogene Chaka basin and its Implications for Mountain Building Processes in the north-eastern Tibetan Plateau. *Basin Res.* 24 (1), 31–50. doi:10.1111/j.1365-2117.2011.00512.x

Zhang, P.-Z. (2013). A Review on Active Tectonics and Deep Crustal Processes of the Western Sichuan Region, Eastern Margin of the Tibetan Plateau. *Tectonophysics* 584, 7–22. doi:10.1016/j.tecto.2012.02.021

Zhang, P.-Z., Shen, Z., Wang, M., Gan, W., Bürgmann, R., Molnar, P., et al. (2004). Continuous Deformation of the Tibetan Plateau from Global Positioning System Data. *Geol* 32 (9), 809. doi:10.1130/g20554.1

Zhang, Q., Sandvol, E., Ni, J., Yang, Y., and Chen, Y. J. (2011). Rayleigh Wave Tomography of the Northeastern Margin of the Tibetan Plateau. *Earth Planet. Sci. Lett.* 304 (1–2), 103–112. doi:10.1016/j.epsl.2011.01.021

Zhang, Z., Bai, Z., Klemperer, S. L., Tian, X., Xu, T., Chen, Y., et al. (2013). Crustal Structure across Northeastern Tibet from Wide-Angle Seismic Profiling: Constraints on the Caledonian Qilian Orogeny and its Reactivation. *Tectonophysics* 606, 140–159. doi:10.1016/j.tecto.2013.02.040

Zhao, B., Huang, Y., Zhang, C., Wang, W., Tan, K., and Du, R. (2015). Crustal Deformation on the Chinese mainland during 1998-2014 Based on GPS Data. *Geodesy and Geodynamics* 6 (1), 7–15. doi:10.1016/j.geog.2014.12.006

Zhao, P., Chen, J., Li, Y., Liu, Q., Chen, Y., Guo, B., et al. (2021). Growth of the Northeastern Tibetan Plateau Driven by Crustal Channel Flow: Evidence from High-Resolution Ambient Noise Imaging. *Geophys. Res. Lett.* 48 (13), e2021GL093387. doi:10.1029/2021gl093387

Zheng, D., Wang, W., Wan, J., Yuan, D., Liu, C., Zheng, W., et al. (2017a). Progressive Northward Growth of the Northern Qilian Shan-Hexi Corridor (Northeastern Tibet) during the Cenozoic. *Lithosphere* 9 (3), 408–416. doi:10.1130/l587.1

Zheng, G., Wang, H., Wright, T. J., Lou, Y., Zhang, R., Zhang, W., et al. (2017b). Crustal Deformation in the India-Eurasia Collision Zone from 25 Years of GPS Measurements. *J. Geophys. Res. Solid Earth*. doi:10.1002/2017jb014465

Zhu, X., He, J., Xiao, J., and Wang, X. (2020). *Uniform Slip Rates of the Altyn Tagh and the Kunlun Faults Likely Reflect Lateral Variation of Frictional Strength of the Faults*. Terra Nova 32, 381–389. doi:10.1111/ter.12467

Zuza, A. V., and Yin, A. (2016). Continental Deformation Accommodated by Non-rigid Passive Bookshelf Faulting: An Example from the Cenozoic Tectonic Development of Northern Tibet. *Tectonophysics* 677-678, 227–240. doi:10.1016/j.tecto.2016.04.007

Conflict of Interest: The authors declare that the research was conducted in the absence of any commercial or financial relationships that could be construed as a potential conflict of interest.

Publisher's Note: All claims expressed in this article are solely those of the authors and do not necessarily represent those of their affiliated organizations, or those of the publisher, the editors, and the reviewers. Any product that may be evaluated in this article, or claim that may be made by its manufacturer, is not guaranteed or endorsed by the publisher.

Copyright © 2022 Zhao and Pan. This is an open-access article distributed under the terms of the Creative Commons Attribution License (CC BY). The use, distribution or reproduction in other forums is permitted, provided the original author(s) and the copyright owner(s) are credited and that the original publication in this journal is cited, in accordance with accepted academic practice. No use, distribution or reproduction is permitted which does not comply with these terms.

Advantages of publishing in Frontiers

OPEN ACCESS
Articles are free to read for greatest visibility and readership

FAST PUBLICATION
Around 90 days from submission to decision

HIGH QUALITY PEER-REVIEW
Rigorous, collaborative, and constructive peer-review

TRANSPARENT PEER-REVIEW
Editors and reviewers acknowledged by name on published articles

Frontiers
Avenue du Tribunal-Fédéral 34
1005 Lausanne | Switzerland

Visit us: www.frontiersin.org
Contact us: frontiersin.org/about/contact

REPRODUCIBILITY OF RESEARCH
Support open data and methods to enhance research reproducibility

DIGITAL PUBLISHING
Articles designed for optimal readership across devices

FOLLOW US
@frontiersin

IMPACT METRICS
Advanced article metrics track visibility across digital media

EXTENSIVE PROMOTION
Marketing and promotion of impactful research

LOOP RESEARCH NETWORK
Our network increases your article's readership